POP-Type Rhodium Complexes in Amine Borane Dehydropolymerisation

Gemma M. Adams

A thesis submitted in partial fulfilment of the requirements for the degree of

Doctor of Philosophy at the University of Oxford





Linacre College

September 2018

The work presented in this thesis was carried out between October 2014 and June 2018 under the supervision of Professor Andrew S. Weller. All of the work is my own, unless otherwise stated, and has not been submitted previously for any degree at this, or any other, university.

Gemma M. Adams

September 2018

Acknowledgements

First and foremost, a massive thank you to Professor Andrew Weller for being a fantastic DPhil supervisor. Thank you for all of your sound advice over the past 4 years, and for believing in me at times when I didn't believe in myself. I'm so sorry that I just can't stand those horrible celebratory pink drinks, but there's nothing quite like the feeling of being offered one.

I count myself very lucky to have worked with everyone who has passed through the Weller group during my DPhil. Thanks to all of the postdocs who were a never-ending source of advice: Drs Amparo Prades, Tom Hooper, Mark Chadwick, Annie Colebatch, Alasdair McKay, Antonio Martínez-Martínez and Alice Johnson. In particular thank you to Annie for being the best team amine borane companion I could have wished for, hosting Bake Off and googly eye-ing everything in sight. Thank you to Alasdair for doing everything in his power to get us that borylene structure, and for always being willing to drop his own work to help out. Thanks to Big Tone for teaching me that Spanish minutes are a variable unit of time and that it is possible to be a calm chemist. Thank you to Alice for always being up for another round of drinks and a game of table football.

Thank you to the DPhil students I have worked with throughout my time in the group, I have had so much fun with you all: Dr Heather Johnson, Dr Amit Kumar, James Barwick-Silk, Anna Spearing-Ewyn, Alex Bukvic, Tim Morgan Boyd and David Ryan. Thanks to Heather for enjoying a refreshing Thatcher's Gold with me every Friday at the UC without fail. Thanks to Amit for all of the yummy curry and love life gossip. To James for being a great fume hood partner – I hope you'll still be willing to go for a drink with me and one other person in the future. Thanks to Anna for the introduction to folk music and sword dancing. To Tim for having his best night's sleep on a rock, but I guess it was better than the cupboard under the stairs. Well done to David for starting the Weller peloton before even Andy did; good luck with the amine complexes. Thank you to Alex (Buttflick) for being my best friend in the lab from day 1, for all the honking and dabbing, and for being the funniest, most talented, and supportive person I know.

Thanks to the Part II students who definitely kept the group interesting year on year: Amy, Isobel, Nick, Joe, Hannah, Ben, Louisa, Hollie, Max and Tom. In particular, big shout outs to Joe Skornia for all his hard work in the initial stages of the Xantphos-^{i}Pr work, and to Louisa Britton for catching that piece of cake – who knew it would lead to a great friendship.

Thanks to Dr Nick Rees for NMR help and opening my eyes to new music genres, and to Drs Colin Sparrow and James Wickens for mass spec assistance. Thank you to the always helpful workshop staff, including Ron, Jude and Bill, and to Terri for keeping our glassware top-notch.

Thanks to Professor Ian Manners, Dr George Whittell and Nicola Oldroyd for the amine borane discussions at BrisOx, GPC help and mass spec help. Thank you to Professor Guy Lloyd-Jones for the kinetic modelling in Chapter 3. Thanks also to Professor Stuart Macgregor and Dr Nick Beattie for all of the hard work put into the DFT in Chapters 2 and 4, as well as the great fun had on Macgreller research retreats.

I have loved my time at Linacre College. Thank you to everyone who battled those early mornings at the river or in the gym with me. In particular, to the Dream Team (Beth, Gemma, Hannah and Marie) for always being there and encouraging me to replace all calories burned rowing/cycling/running with GBK Deliveroo. Thank you to Josh for all the late nights on the phone, trips to the US that I'll never forget, and for developing the GPC peak fitting tool in Chapter 3. Clancy, thank you for being an incredible friend and keeping me sane the past two years! Outside of Linacre, thank you to Lauren, Sammie, Simon, Sam and Grant for being the best friends I could wish for.

Most importantly, thank you to Mum, Dad and Olivia for really trying hard to understand what on earth the dehydropolymerisation of amine boranes is! Thank you so much for always being there for me, especially whenever I was finding things tough. You are the reason that I managed to make it to Oxford in the first place.

Abbreviations

Å	Angstrom
$[Al(O^tBu^F)_4]^-$	$[Al\{OC(CF_3)_3\}_4]^-$
$[BAr^{Cl}{}_4]^-$	$[B\{3,5\text{-}C_6H_3Cl_2\}_4]^-$
$[BAr^F{}_4]^-$	$[B\{3,5\text{-}C_6H_3(CF_3)_2\}_4]^-$
bpy	2,2′-bipyridine
Bz	benzyl
calc.	calculated
[cat]	catalyst
1,5-COD	1,5-cyclooctadiene
Cp	cyclopentadienyl
Cp*	pentamethylcyclopentadienyl
Cy	cyclohexyl
Cyp	cyclopentyl
δ	chemical shift in ppm
Đ	dispersity index (M_w/M_n)
DFT	density functional theory
ΔG	change in Gibb's free energy
ΔH	change in enthalpy
ΔS	change in entropy
DPEphos	bis[(2-diphenylphosphino)phenyl]ether
DTBP	2,6-ditertbutylpyridine
eq	equivalents
ESI-MS	electrospray ionisation mass spectrometry
Et	ethyl
fac	facial
GPC	gel permeation chromatography
HBcat	catecholborane
HBpin	pinacolborane
Hex	hexyl
Hz	hertz
I	nuclear spin
^{i}Bu	isobutyl
ICP-MS	inductively coupled plasma mass spectrometry
IMes	N,N′-bis(2,4,6-trimethylphenyl)imidazol-2-ylidene
^{i}Pr	isopropyl
IR	infrared
J	coupling constant in Hz
K	Kelvin
k	rate constant
KIE	kinetic isotope effect

kV	kilovolt
M	mol dm^{-3}
Me	methyl
mer	meridional
mL	millilitre
μmol	micromole
M_n	number average molecular weight
M_w	weight average molecular weight
m/z	mass to charge ratio
NBA	norbornane
NBD	norbornadiene
^{n}Bu	normal butyl
NMR	nuclear magnetic resonance
$[OTf]^-$	triflate
Ph	phenyl
PN*H*P	$HN(CH_2CH_2P^iPr_2)_2$
POCOP-^{t}Bu	1,3-$C_6H_3(OP^tBu_2)_2$
ppm	parts per million
Pr	propyl
σ CAM	sigma complex assisted metathesis
TBA	3,3-dimethylbutane
TBE	3,3-dimethylbut-1-ene
^{t}Bu	tertbutyl
$^{t}Bu^F$	nonafluoro-tertbutyl
THF	tetrahydrofuran
TOF	turnover frequency
TON	turnover number
Xantphos-^{i}Pr	4,5-bis(diisopropylphosphino)-9,9-dimethylxanthene
Xantphos-Ph	4,5-bis(diphenylphosphino)-9,9-dimethylxanthene
Xantphos-Ph′	4-phenylphosphido-5-diphenylphosphino-9,9-dimethylxanthene
°C	degrees Celsius

Abstract

This thesis explores the catalytic dehydropolymerisation of N-methylamine borane, $H_3B{\cdot}NMeH_2$, to form N-methylpolyaminoborane, $(H_2BNMeH)_n$, using POP-type rhodium complexes based upon the $\{Rh(Xantphos\text{-}^iPr)\}^+$ and $\{Rh(DPEphos)\}^+$ fragments. A comparison of these metal-ligand frameworks provides a structure/activity relationship in order to gain mechanistic insight into the $H_3B{\cdot}NMeH_2$ dehydropolymerisation process.

Chapter 2 describes the synthesis of a suitable $\{Rh(Xantphos\text{-}^iPr)\}^+$ precatalyst for $H_3B{\cdot}NMeH_2$ dehydropolymerisation. Its reactivity with $H_3B{\cdot}NMeH_2$ is examined by NMR spectroscopy, and independent synthetic routes to the complexes observed are described. From this, a dimetalloborylene is isolated and crystallographically characterised. The kinetics of $H_3B{\cdot}NMeH_2$ dehydrogenation and $(H_2BNMeH)_n$ growth using the $\{Rh(Xantphos\text{-}^iPr)\}^+$ fragment are reported in Chapter 3, which combined with the speciation studies in Chapter 2, allows for a mechanistic proposal for dehydropolymerisation. The formation and subsequent deprotonation of a boronium cation is postulated to lead to the monomer, $H_2B{=}NMeH$, which forms $(H_2BNMeH)_n$ via an on-metal end-chain propagation mechanism.

In Chapter 4 the focus shifts to synthesise a suitable $\{Rh(DPEphos)\}^+$ precatalyst for $H_3B{\cdot}NMeH_2$ dehydropolymerisation. Here, speciation studies of the $\{Rh(DPEphos)\}^+$ fragment with $H_3B{\cdot}NMeH_2$ enables the observation of bimetallic complexes, one of which is considered an amidodiboryl complex. An in-depth dehydropolymerisation kinetic study using the $\{Rh(DPEphos)\}^+$ system is undertaken in Chapter 5, and strong dependence of $(H_2BNMeH)_n$ molecular weight on H_2 pressure and catalyst loading indicates that an on-metal coordination/dehydrogenation/insertion mechanism operates, contrasting that proposed for the $\{Rh(Xantphos\text{-}^iPr)\}^+$ system. The bimetallic amidodiboryl complex described in Chapter 4 and $NMeH_2$-derived $\{Rh(DPEphos)\}^+$ species are also tested in catalysis, and appear close in identity to the true active catalytic species, due to the lack of induction period observed prior to H_2 evolution.

Contents

Declaration i
Acknowledgements ii
Abbreviations iv
Abstract vi
Contents vii
1 Introduction 1
1.1 Overview 1
1.2 Rhodium in organotransition metal catalysis 1
1.3 Phosphine ligands 3
1.3.1 Multidentate POP-type ligands 5
1.4 Weakly coordinating anions 8
1.5 Sigma complexes 9
1.5.1 Sigma dihydrogen complexes 9
1.5.2 Sigma amine borane complexes 11
1.5.3 Sigma aminoborane complexes 13
1.6 Dehydropolymerisation of amine boranes 13
1.6.1 General pathways for the dehydrocoupling/polymerisation of amine boranes 14
1.6.2 Observation and trapping of aminoboranes 15
1.6.3 Types of polymerisation mechanism 17
1.6.4 Catalyst free routes to polyaminoboranes 18
1.6.5 Metal catalysed dehydrocoupling of amine boranes 19
1.6.6 Heterogeneous transition metal catalysts for amine borane dehydrocoupling 20
1.6.7 Homogeneous transition metal catalysts for amine borane dehydrocoupling 22
1.7 Xantphos-^{i}Pr and DPEphos ligands in catalysis 37
1.7.1 Xantphos-^{i}Pr 38
1.7.2 DPEphos 41
1.8 Summary 46
1.9 References 47
2 {Rh(Xantphos-^{i}Pr)}$^{+}$ complexes as precatalysts for the dehydropolymerisation of $H_3B{\cdot}NMeH_2$ 53
2.1 Introduction 53
2.2 Formation of [Rh(Xantphos-^{i}Pr)(NBD)][BAr^{F}_{4}] (**1**) 53
2.3 Formation of [Rh(Xantphos-^{i}Pr)$(H)_2(H_3B{\cdot}NMe_3)$][BAr^{F}_{4}] (**2**) 58
2.4 Reactivity of [Rh(Xantphos-^{i}Pr)$(H)_2(H_3B{\cdot}NMe_3)$][BAr^{F}_{4}] (**2**) 63
2.4.1 Reaction of **2** with D_2: H/D exchange 63
2.4.2 Speciation studies of **2** with 10 equivalents of $H_3B{\cdot}NMeH_2$ 64
2.5 Formation of {Rh(Xantphos-^{i}Pr)}$^{+}$ amine borane complexes 66

2.5.1 Formation of [Rh(Xantphos-^{i}Pr)(H)$_2$(H$_3$B·NMeH$_2$)][BAr$^{F}_4$] (**3**) 67
2.5.2 Formation of [Rh(Xantphos-^{i}Pr)(H)$_2$(H$_3$B·NMeHBH$_2$·NMeH$_2$)][BAr$^{F}_4$] (**4**) 69
2.5.3 Formation of [Rh(Xantphos-^{i}Pr)(H)$_2$(H$_3$B·NMe$_2$H)][BAr$^{F}_4$] (**5**) 71
2.5.4 Conclusions: formation of {Rh(Xantphos-^{i}Pr)}$^+$ amine borane complexes 72
2.6 Formation of {Rh(Xantphos-^{i}Pr)}$^+$ complexes from NMeH$_2$ or BH$_3$ 73
2.6.1 Formation of [Rh(Xantphos-^{i}Pr)(H)$_2$(NMeH$_2$)][BAr$^{F}_4$] (**6**) 73
2.6.2 Formation of [{Rh(Xantphos-^{i}Pr)(H)$_2$}$_2$(BH$_4$)][BAr$^{F}_4$] (**7**) 75
2.6.3 Conclusions: formation of {Rh(Xantphos-^{i}Pr)}$^+$ complexes from NMeH$_2$ or BH$_3$ .. 77
2.7 Formation of a {Rh(Xantphos-^{i}Pr)}$^+$ dimetalloborylene complex 78
2.7.1 Formation of [{Rh(Xantphos-^{i}Pr)}$_2$B][BAr$^{F}_4$] (**8**) 78
2.8 Structure of [{Rh(Xantphos-^{i}Pr)}$_2$B][BAr$^{Cl}_4$] (**8-[BAr$^{Cl}_4$]**) 80
2.9 Connecting complexes **2**, **3**, **7** and **8** 84
2.10 Exploring possible Lewis acidity of [{Rh(Xantphos-^{i}Pr)}$_2$B][BAr$^{Cl}_4$] (**8-[BAr$^{Cl}_4$]**): formation of [Rh(Xantphos-^{i}Pr)(CO)][BAr$^{Cl}_4$] (**9**) 88
2.11 Catalyst poisoning: formation of [Rh(Xantphos-^{i}Pr)(PPh$_3$)][BAr$^{F}_4$] (**10**) 90
2.12 Summary 91
2.13 References 92
3 Dehydropolymerisation of H$_3$B·NMeH$_2$ using the {Rh(Xantphos-^{i}Pr)}$^+$ system 95
3.1 Introduction 95
3.2 Dehydropolymerisation of H$_3$B·NMeH$_2$ using precatalyst [Rh(Xantphos-^{i}Pr)(H)$_2$(H$_3$B·NMe$_3$)][BAr$^{F}_4$] (**2**): initial screening 96
3.3 Amine borane dehydrogenation kinetics 97
3.3.1 Induction period prior to the onset of H$_2$ evolution 99
3.3.2 Tests for catalyst homogeneity 101
3.3.3 Determining order in precatalyst **2** and H$_3$B·NMeH$_2$ 102
3.3.4 Catalyst recharging experiments 105
3.3.5 Kinetic isotope effects 106
3.4 Polyaminoborane growth kinetics 108
3.4.1 Aminoborane trapping experiments 108
3.4.2 Polyaminoborane analysis: NMR spectroscopy 109
3.4.3 Polyaminoborane analysis: GPC 111
3.4.4 Polyaminoborane molecular weight versus conversion 114
3.4.5 Polyaminoborane molecular weight versus catalyst loading and dependence on H$_2$ pressure 116
3.5 Involvement of complexes **3**, **6**, **7** and **8** in the dehydropolymerisation of H$_3$B·NMeH$_2$ using **2** 118
3.5.1 Testing [Rh(Xantphos-^{i}Pr)(H)$_2$(NMeH$_2$)][BAr$^{F}_4$] (**6**) as a H$_3$B·NMeH$_2$ dehydropolymerisation catalyst 119
3.5.2 Involvement of complexes **3**, **7** and **8** in the dehydropolymerisation of H$_3$B·NMeH$_2$ under true catalytic conditions 120

3.6 Proposed mechanism for the dehydropolymerisation of $H_3B{\cdot}NMeH_2$ using the $\{Rh(Xantphos\text{-}^{i}Pr)\}^+$ system 123

3.7 Summary 128

3.8 References 129

4 $\{Rh(DPEphos)\}^+$ complexes as precatalysts for the dehydropolymerisation of $H_3B{\cdot}NMeH_2$ 132

4.1 Introduction 132

4.2 Formation of $[Rh(DPEphos)(NBD)][BAr^F{}_4]$ (**12**) and $[Rh(DPEphos)(NBD)][Al(O^tBu^F)_4]$ (**12-[Al(O^{t}Bu^F)$_4$]**) 133

4.3 Formation of a suitable $\{Rh(DPEphos)\}^+$ amine borane dehydropolymerisation precatalyst 134

4.4 Reactivity of $[Rh(DPEphos)(H_2B(CH_2CH_2{}^tBu){\cdot}NMe_3)][BAr^F{}_4]$ (**13**) 138

4.4.1 Reaction of **13** with D_2: H/D exchange 138

4.4.2 Speciation studies of **13** with 10 equivalents of $H_3B{\cdot}NMeH_2$ 140

4.5 Formation of $\{Rh(DPEphos)\}^+$ complexes from $H_3B{\cdot}NMeH_2$ 143

4.5.1 Formation of $[\{Rh(DPEphos)\}_2(H)(H_2BNMeH)][BAr^F{}_4]$ (**14**) 143

4.5.2 Formation of $[\{Rh(DPEphos)\}_2\{(H_2B)_2NMeH\}][BAr^F{}_4]$ (**15**) and $[\{Rh(DPEphos)\}_2\{(H_2B)_2NMeH\}][Al(O^tBu^F)_4]$ (**15-[Al(O^{t}Bu^F)$_4$]**) 147

4.5.3 Conclusions: formation of $\{Rh(DPEphos)\}^+$ complexes from $H_3B{\cdot}NMeH_2$ 157

4.6 Reactivity of the $\{Rh(DPEphos)\}^+$ fragment with BH_3 or $NMeH_2$ 158

4.6.1 Formation of $[\{Rh(DPEphos)\}_2(B_2H_5)][BAr^F{}_4]$ (**16**) 158

4.6.2 Formation of $[Rh(DPEphos)(H)_2(NMeH_2)_x][BAr^F{}_4]$ (x = 1 or 2, **17**) 160

4.6.3 Formation of $[Rh(DPEphos)(NMeH_2)_x][BAr^F{}_4]$ (x = 1 or 2, **18**) 163

4.6.4 Conclusions: formation of $\{Rh(DPEphos)\}^+$ complexes from BH_3 or $NMeH_2$ 165

4.7 Catalyst poisoning: $[Rh(DPEphos)(PPh_3)][BAr^F{}_4]$ 166

4.8 Summary 167

4.9 References 168

5 Dehydropolymerisation of $H_3B{\cdot}NMeH_2$ using the $\{Rh(DPEphos)\}^+$ system 171

5.1 Introduction 171

5.2 Dehydropolymerisation of $H_3B{\cdot}NMeH_2$ using precatalyst $[Rh(DPEphos)(H_2B(CH_2CH_2{}^tBu){\cdot}NMe_3)][BAr^F{}_4]$ (**13**): initial screening 172

5.3 Polyaminoborane growth kinetics 174

5.3.1 Polyaminoborane molecular weight versus conversion 174

5.3.2 Polyaminoborane molecular weight versus catalyst loading 175

5.3.3 H_2 dependence on polyaminoborane molecular weight 177

5.3.4 Further polyaminoborane analysis 179

5.3.5 Probing for living polymerisation 183

5.3.6 Aminoborane trapping experiments 183

5.4 Amine borane dehydrogenation kinetics 184

5.4.1 Tests for catalyst homogeneity 186

5.4.2 Determining order in precatalyst **13** and $H_3B{\cdot}NMeH_2$ 186

5.4.3 Induction period prior to the onset of H_2 evolution 188

5.4.4 Catalyst recharging experiments 189
5.4.5 Kinetic isotope effect on dehydrogenation catalysis 190
5.5 Involvement of $[\{Rh(DPEphos)\}_2(H)(H_2BNMeH)]^+$ (**14**) and $[\{Rh(DPEphos)\}_2\{(H_2B)_2NMeH\}]^+$ (**15**) in the dehydropolymerisation of $H_3B{\cdot}NMeH_2$ using $[Rh(DPEphos)(H_2B(CH_2CH_2{}^tBu){\cdot}NMe_3)]^+$ (**13**) 193
5.5.1 Role of $[\{Rh(DPEphos)\}_2(H)(H_2BNMeH)]^+$ (**14**) 194
5.5.2 Role of $[\{Rh(DPEphos)\}_2\{(H_2B)_2NMeH\}]^+$ (**15**) 195
5.6 Involvement of $[BH_2(NMeH_2)_2][BAr^F{}_4]$ (**11**), BH_3 and $NMeH_2$ in the dehydropolymerisation of $H_3B{\cdot}NMeH_2$ using $[Rh(DPEphos)(H_2B(CH_2CH_2{}^tBu){\cdot}NMe_3)]^+$ (**13**) 199
5.6.1 Doping the reaction with $[BH_2(NMeH_2)_2][BAr^F{}_4]$ (**11**) 200
5.6.2 Doping the reaction with THF solutions of BH_3 or $NMeH_2$ 201
5.7 Involvement of $NMeH_2$ complexes $[Rh(DPEphos)(H)_2(NMeH_2)_x][BAr^F{}_4]$ (x = 1 or 2, **17**) and $[Rh(DPEphos)(NMeH_2)_x][BAr^F{}_4]$ (x = 1 or 2, **18**) in the dehydropolymerisation of $H_3B{\cdot}NMeH_2$ 207
5.8 Proposed mechanism for the dehydropolymerisation of $H_3B{\cdot}NMeH_2$ using the $\{Rh(DPEphos)\}^+$ system 210
5.9 Summary and future of the $\{Rh(DPEphos)\}^+$ system 216
5.10 References 216
6 Summary and future outlook 219
7 Experimental methods 220
7.1 General techniques 220
7.1.1 Procedure for hydrogenation 220
7.1.2 Nuclear magnetic resonance (NMR) spectroscopy 220
7.1.3 Mass spectrometry 221
7.1.4 Gel permeation chromatography (GPC) 221
7.1.5 Elemental microanalysis 221
7.1.6 Infrared spectroscopy 222
7.2 Synthesis and characterisation 222
7.2.1 Starting materials 222
7.2.2 Synthesis of $[Rh(Xantphos\text{-}^iPr)(NBD)][BAr^F{}_4]$ (**1**) 222
7.2.3 Synthesis of $[Rh(Xantphos\text{-}^iPr)(H)_2(H_3B{\cdot}NMe_3)][BAr^F{}_4]$ (**2**) 223
7.2.4 Synthesis of $[Rh(Xantphos\text{-}^iPr)(H)_2(H_3B{\cdot}NMe_3)][BAr^{Cl}{}_4]$ (**2-[BAr$^{Cl}_4$]**) 224
7.2.5 Synthesis of $[Rh(Xantphos\text{-}^iPr)(H)_2(H_3B{\cdot}NMeH_2)][BAr^F{}_4]$ (**3**) 225
7.2.6 Synthesis of $[Rh(Xantphos\text{-}^iPr)(H)_2(H_3B{\cdot}NMeHBH_2{\cdot}NMeH_2)][BAr^F{}_4]$ (**4**) 225
7.2.7 Synthesis of $[Rh(Xantphos\text{-}^iPr)(H)_2(H_3B{\cdot}NMe_2H)][BAr^F{}_4]$ (**5**) 226
7.2.8 Synthesis of $[Rh(Xantphos\text{-}^iPr)(H)_2(NMeH_2)][BAr^F{}_4]$ (**6**) 226
7.2.9 Synthesis of $[\{Rh(Xantphos\text{-}^iPr)(H)_2\}_2BH_4][BAr^F{}_4]$ (**7**) 227
7.2.10 Synthesis of $[\{Rh(Xantphos\text{-}^iPr)\}_2B][BAr^F{}_4]$ (**8**) 227
7.2.11 Synthesis of $[\{Rh(Xantphos\text{-}^iPr)\}_2B][BAr^{Cl}{}_4]$ (**8-[BAr$^{Cl}_4$]**) 228
7.2.12 Synthesis of $[Rh(Xantphos\text{-}^iPr)(CO)][BAr^{Cl}{}_4]$ (**9**) 229
7.2.13 Synthesis of $[Rh(Xantphos\text{-}^iPr)(PPh_3)][BAr^F{}_4]$ (**10**) 229

7.2.14 Synthesis of $[BH_2(NMeH_2)_2][BAr^F{}_4]$ (**11**) 230
7.2.15 Synthesis of $[Rh(DPEphos)(NBD)][Al(O^tBu^F)_4]$ (**12-[Al(O^{t}Bu^F)$_4$]**) 231
7.2.16 Synthesis of $[Rh(DPEphos)(H_2B(CH_2CH_2{}^tBu)\cdot NMe_3)][BAr^F{}_4]$ (**13**) 231
7.2.17 Synthesis of $[\{Rh(DPEphos)\}_2(H)(H_2BNMeH)][BAr^F{}_4]$ (**14**) 232
7.2.18 Synthesis of $[\{Rh(DPEphos)\}_2\{(H_2B)_2NMeH\}][BAr^F{}_4]$ (**15**) 233
7.2.19 Synthesis of $[\{Rh(DPEphos)\}_2\{(H_2B)_2NMeH\}][Al(O^tBu^F)_4]$ (**15-[Al(O^{t}Bu^F)$_4$]**) 233
7.2.20 Synthesis of $[\{Rh(DPEphos)\}_2(B_2H_5)][BAr^F{}_4]$ (**16**) 234
7.2.21 Synthesis of $[Rh(DPEphos)(H)_2(NMeH_2)_x][BAr^F{}_4]$ (x = 1 or 2, **17**) 235
7.2.22 Synthesis of $[Rh(DPEphos)(NMeH_2)_x][BAr^F{}_4]$ (x = 1 or 2, **18**) 236
7.3 Catalytic procedures 237
7.3.1 Dehydropolymerisation under open conditions 237
7.3.2 Dehydropolymerisation under hydrogen evolution measurement conditions 238
7.3.3 Dehydropolymerisation under closed conditions 238
7.3.4 Dehydropolymerisation in the presence of cyclohexene 239
7.3.5 Dehydropolymerisation recycling experiments 239
7.3.6 Molecular weight versus conversion procedure 240
7.3.7 Tests for catalyst homogeneity: mercury poisoning 240
7.3.8 Tests for catalyst homogeneity: PPh_3 fractional poisoning 240
7.3.9 Dehydropolymerisation under THF, BH_3 or $NMeH_2$-doped conditions 240
7.4 Computational details 241
7.5 X-ray crystallography 241
7.5.1 Crystallographic data 244
7.6 References 247
8 Electronic appendices ..... inside back cover

1 Introduction

1.1 Overview

This thesis explores the synthesis of rhodium complexes containing the POP-type ligands Xantphos-^{i}Pr and DPEphos, and their subsequent reactivity with N-monomethylamine borane, $H_3B{\cdot}NMeH_2$, to form polyaminoborane, $(H_2BNMeH)_n$, by catalytic dehydropolymerisation (Figure 1.1). Building on previous success achieved using structurally similar diphenylphosphinopropane ($Ph_2P(CH_2)_3PPh_2$) and Xantphos-Ph (4,5-bis(diphenylphosphino)-9,9-dimethylxanthene) transition metal complexes in amine borane dehydrocoupling,[1-5] a comparison of Xantphos-^{i}Pr and DPEphos provides new insight into possible mechanisms for amine borane dehydropolymerisation.

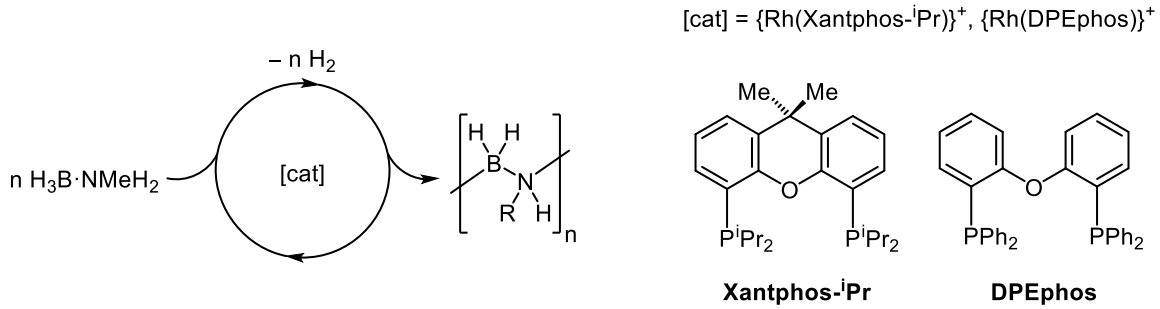
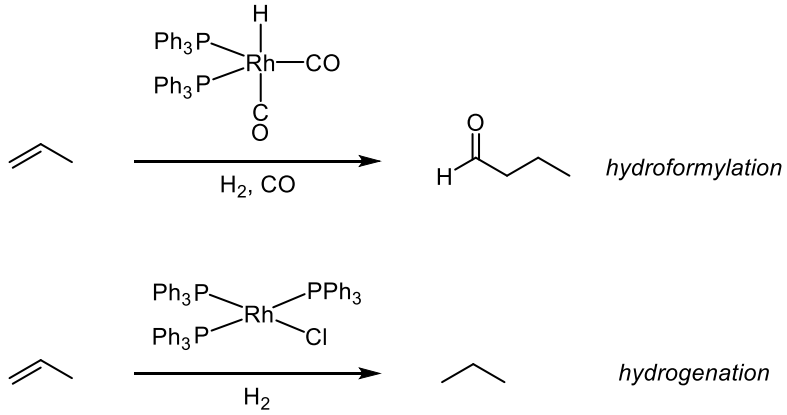


Figure 1.1 The dehydropolymerisation of $H_3B{\cdot}NMeH_2$ to form $(H_2BNMeH)_n$ using rhodium complexes containing Xantphos-^{i}Pr and DPEphos POP-type ligands.

1.2 Rhodium in organotransition metal catalysis

Organotransition metal complexes have a wide range of uses in catalytic reactions for high value processes including natural product synthesis and the production of commodity chemicals.[6-7] For example, the polymerisation of α-olefins can be achieved by both early,[8] and late,[9] transition metal catalysts, and both rhodium and iridium catalysts can be used for the carbonylation of methanol.[6] Whilst most well-known organometallic catalytic processes create new carbon-element bonds, there are fewer examples where focus lies on the formation of main group-main group bonds, however homonuclear and heteronuclear dehydrocoupling of many main group elements such as B, N, Si, P and Ge, have provided a range of new main group oligomeric and polymeric materials.[10-11]

Rhodium is a late, second row transition metal with a [Kr]$4d^8 5s^1$ electronic ground state. The most common oxidation states for rhodium are Rh(I) and Rh(III), therefore its ability to switch between these oxidation states make it an ideal candidate for transition metal catalysis, in order to support bond activation processes such as oxidative addition and reductive elimination steps throughout a catalytic cycle.[7] As a catalyst it is found in catalytic convertors present in automobiles to control exhaust emissions, however it is also used in other processes, such as catalytic hydroformylation[12] and catalytic hydrogenation (Scheme 1.1).[13]



Scheme 1.1 Catalytic hydroformylation and hydrogenation reactions achieved using rhodium complexes.

Along a catalytic reaction pathway, a metal-ligand complex may be required to form vacant sites to allow the capture of substrates prior to activation, or stabilise resultant vacant sites when a substrate is released. Latent low coordinate rhodium complexes have been studied in which agostic or solvent interactions "mask" the vacant site (Figure 1.2),[14-15] as well as stabilising key intermediates. If these complexes can be independently synthesised, they provide insight into catalytic pathways. For example, 14 electron rhodium complexes have been isolated with only three two electron donor ligands attached (Figure 1.2), supporting the idea that rhodium can form low coordinate, formally electron deficient, complexes during catalysis.[16]

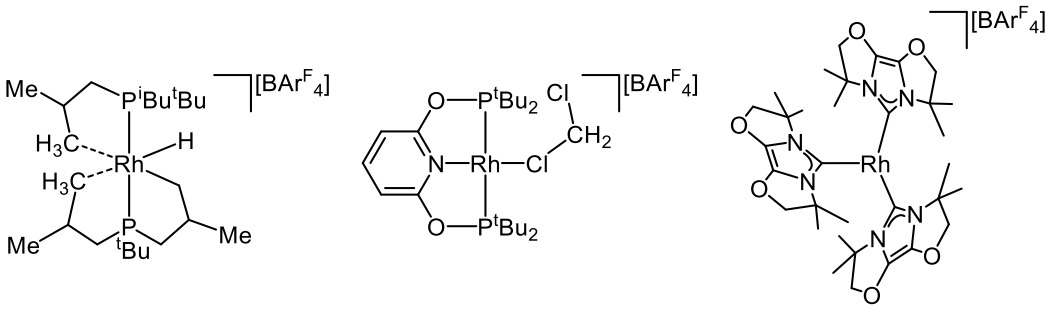


Figure 1.2 Examples of latent, low coordinate complexes of rhodium.

These properties of rhodium make it an ideal candidate for exploring the fundamentals of relatively new catalytic reactions. One example is the subject of this thesis, in which well-defined rhodium-phosphine complexes are utilised in amine borane dehydropolymerisation.

1.3 Phosphine ligands

Phosphines (PR_3) are a popular choice of ligand for many organometallic reactions due to their ability to support a variety of transition metal complexes, and stabilise either an electron rich or electron deficient metal over the course of a reaction. This can be achieved by modulation of the ligand through both steric and electronic effects.

Sigma donation from the phosphorus lone pair to the metal centre acts alongside backdonation from the filled metal dπ orbitals into the P–R σ* antibonding orbital,[6] and the extent of this interaction can be tuned by the identity of the R groups (Figure 1.3).[17] Electron withdrawing substituents such as aryl or alkoxy groups, or halides, lower the energy of the P–R σ*, enabling a greater interaction with the relevant metal based orbital and decreasing the electron density at the metal.[18] The Tolman electronic parameter measures the electron donating ability of the ligand by comparing the frequency of the A_1 C–O vibrational mode of the CO ligands between different $Ni(CO)_3(PR_3)$ complexes.[19] Greater π acceptor character of the phosphine leads to an increase in the C–O stretching frequency as backbonding to the CO ligands is reduced.

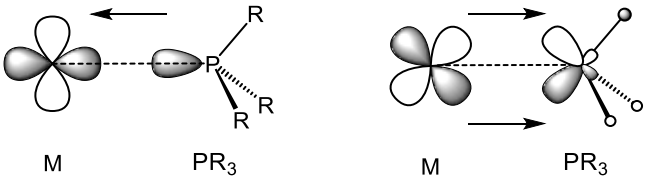


Figure 1.3 Left: σ bonding in a M–PR_3 fragment. Right: π backbonding in a M–PR_3 fragment.

The steric properties of a PR_3 ligand may also be tuned and can be measured by the Tolman cone angle (θ) of the resulting transition metal complex.[19] The M–P bond length is fixed at 2.28 Å, where M lies at the vertex and θ is the angle between the outer edges of the R groups in a space fill model of the M–PR_3 fragment (Figure 1.4). Bulkier R substituents invoke a larger cone angle, for example P(mesityl)$_3$ has a cone angle of 212°, whereas for PH_3, θ = 87°.

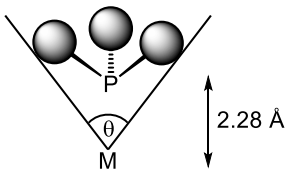


Figure 1.4 Tolman cone angle (θ).

Bidentate phosphine ligands, such as those based upon $Ph_2P(CH_2)_xPPh_2$ (x = 2 – 5, Figure 1.5), can additionally be characterised by ligand bite angle.[20] Bite angle (β) was defined by Casey and Whiteker in 1990 to quantify the preferred chelation angle of a multidentate disphosphine ligand determined computationally by the constraints of the ligand backbone (Figure 1.5).[21] Bite angles within 3 kcal mol^{-1} of the preferred bite angle were considered to be within the allowed flexibility range (FR) of the ligand, and have also been used to describe multidentate POP-type ligands (Figure 1.5).

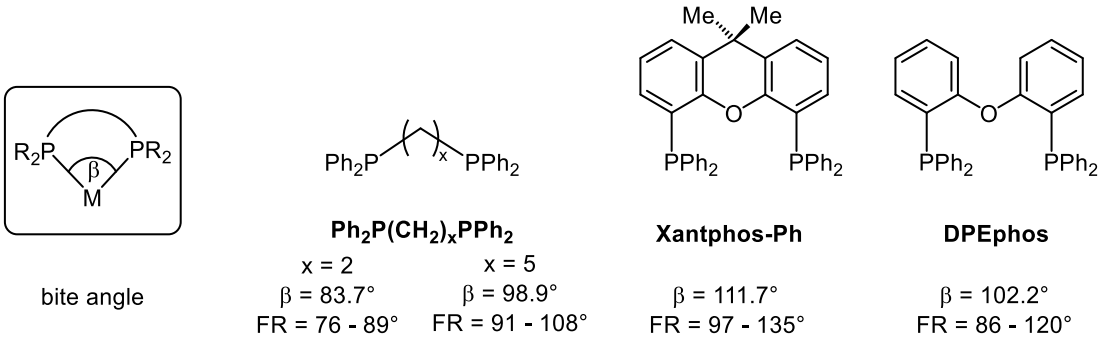


Figure 1.5 Representation of the bite angle (β), and the calculated bite angles and flexibility ranges for $Ph_2P(CH_2)_xPPh_2$ (x = 2, 5), Xantphos-Ph and DPEphos.

1.3.1 Multidentate POP-type ligands

The coordination chemistry of multidentate ligands based upon diphosphine ligand frameworks with an additional ether linkage, POP-type ligands, has been known for some decades.[22] Their use in catalysis has been significant, especially ligand frameworks based upon Xantphos-Ph (4,5-bis(diphenylphosphino)-9,9-dimethylxanthene) and DPEphos (bis[(2-diphenylphosphino)phenyl] ether) (Figure 1.5), which were originally developed by van Leeuwen and co-workers as wide bite angle bidentate ligands for rhodium catalysed hydroformylation.[23] Although principally bidentate in coordination mode, the ability for POP-type ligands to coordinate the central ether gives ligand geometries that are related to classical tridentate pincer ligands.[24] This offers the ability of the ligand set to adapt to the specific requirements of the metal (i.e. variable oxidation states and resulting geometric constraints), including the binding of substrates or release of products during synthesis, or during a catalytic cycle.

Flexibility between tridentate and bidentate coordination of POP-type ligands to a metal centre generally involves the reversible decoordination of the ether group, although P-dechelation has been proposed,[25] leading to hemilabile behaviour.[26] The metal centre is rendered operationally unsaturated by the reversible decoordination of a ligand, but one that still remains associated with the coordination sphere of the metal. One donor is labile, such as the ether group in a POP-type ligand, however the other donor group(s), i.e. the phosphines, remain bound to the metal centre

(Figure 1.6). The energy difference, with an appropriately small barrier, between such "open" and "closed" geometries should be of the order of 50 kJ mol^{-1} in order to make this process reversible and kinetically compentent.[27]

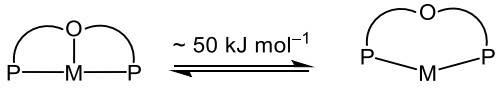


Figure 1.6 Representation of hemilabile ligand behaviour in a POP-type ligand.

The breadth of coordination geometries that are available to POP-type ligands make them valuable ligands in catalytic organometallic chemistry. In 2018, Adams and Weller reviewed the P–M–P angles and M–O distances of crystallographically characterised POP-type ligand complexes,[25] building on previous work by Haynes and co-workers.[28] A plot of P–M–P angle versus M–O distance showed clustering of data which allowed for demarcation of the four possible coordination geometries of POP-type ligands in transition metal complexes (Figure 1.7). The majority of the complexes reported contained long M–O distances and small bite angles (M–O > 2.5 Å, P–M–P < 125°) – considered to be cis κ^2-P,P complexes with no formal metal-oxygen bond. Less common were trans κ^2-P,P complexes where the bite angle is larger (> 130°), but the M–O distance remains long (> 2.4 Å). Inspection of complexes occupying the bottom right of the graph were shown to be mer κ^3-P,O,P complexes, in which M–O distances are shorter and the phosphine ligands are situated trans to one another (M–O < 2.4 Å, P–M–P > 145°). This subset of ligand geometry can be considered to be pincer-like. The final set of coordination complexes are found at the bottom left of the plot, containing complexes with both short M–O distances and narrow bite angles (M–O < 2.4 Å, P–M–P < 130°), which are examples of rarer fac κ^3-P,O,P structures, where the phosphine ligands lie cis to one another, and the ether linker lies in the apical position of the complex, also cis to both phosphines.

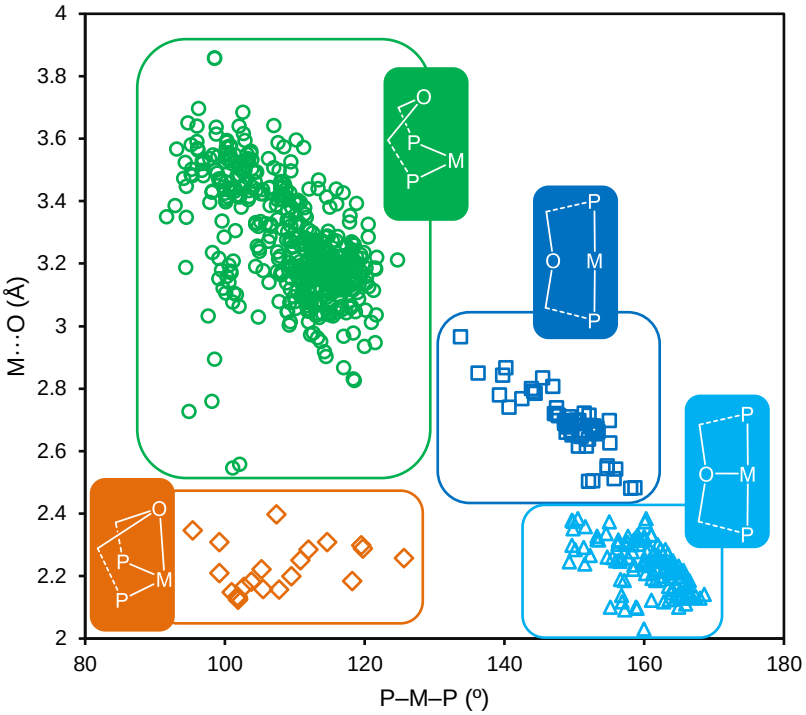


Figure 1.7 Plot of M–O distance (Å) versus P–M–P bite angle (°) in crystallographically characterised transition metal complexes containing POP-type ligands. Ligand coordination geometries as follows: ○ = cis κ^2-P,P; □ = trans κ^2-P,P; △ = mer κ^3-P,O,P; ◇ = fac κ^3-P,O,P. Adapted with permission from G. M. Adams; A. S. Weller, POP-type ligands: Variable coordination and hemilabile behaviour, *Coord. Chem. Rev.* **2018**, *355*, 150-172.

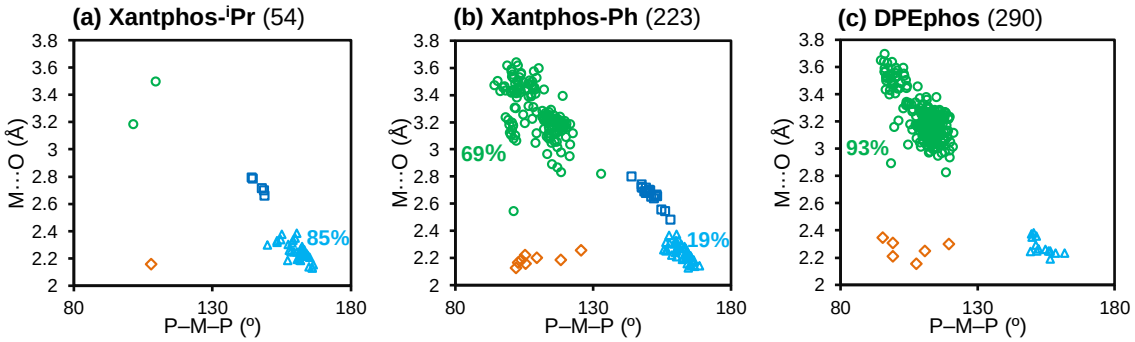


Figure 1.8 Plot of M–O distance (Å) versus P–M–P bite angle (°) in crystallographically characterised transition metal complexes containing (a) Xantphos-^{i}Pr (54 complexes), (b) Xantphos-Ph (223 complexes) and (c) DPEphos (290 complexes). Number of complexes examined in parentheses. Ligand coordination geometries as follows: ○ = cis κ^2-P,P; □ = trans κ^2-P,P; △ = mer κ^3-P,O,P; ◇ = fac κ^3-P,O,P.

Relevant to this thesis are the POP-type ligands Xantphos-^{i}Pr and DPEphos, as well as their comparison with the parent ligand, Xantphos-Ph. These three ligands show different spreads of coordination modes as shown by the crystallographically characterised examples contained in the

Cambridge Structural Database.[29-31] The M–O distances and P–M–P angles of these complexes are detailed in Figure 1.8, and show that Xantphos-^{i}Pr has the greatest propensity for mer κ^3-P,O,P coordination (85% of 54 examples), whilst DPEphos is most likely to exist in a cis κ^2-P,P conformation (93% of 290 complexes). Interestingly, Xantphos-Ph appears to be an intermediate between these two coordination extremes, with 69% of its 223 complexes reported to be cis κ^2-P,P bound, whilst 19% are mer κ^3-P,O,P ligated. These coordination preferences may lead to differences in catalytic ability of each of these ligands, which will be explored in more detail for Xantphos-^{i}Pr versus DPEphos in this thesis.

1.4 Weakly coordinating anions

In order to form reactive cationic rhodium complexes for use in organometallic catalysis by an inner sphere bond activation process, the counterion must be weakly coordinating to ensure that when a vacant site is required, the anion does not occupy it and allow full reactivity to be revealed.[32] Traditional counterions such as $[PF_6]^-$ and $[BF_4]^-$ are unsuitable for this purpose as these have been shown to be coordinating or react with low coordinate cationic partners by hydrolysis,[33] or fluoride abstraction,[34] respectively.

The $[BAr^F{}_4]^-$ anion (Ar^F = 3,5-$C_6H_3(CF_3)_2$, Figure 1.9) is an ideal weakly coordinating anion as the bulky, electronegative aryl groups allow the negative charge to be symmetrically delocalised throughout the whole structure.[35] Coordination of the $[BAr^F{}_4]^-$ anion is rare, but can occur via the η^6 interaction of one of the aryl rings in the case of rhodium.[36-37] Figure 1.9 also shows other, related, weakly coordinating anions such as $[BAr^{Cl}{}_4]^-$ (Ar^{Cl} = 3,5-$C_6H_3Cl_2$),[38] and $[Al(O^tBu^F)_4]^-$ ($^tBu^F$ = $C(CF_3)_3$),[39] which have also been utilised in organometallic chemistry. $[BAr^{Cl}{}_4]^-$ is a particularly useful anion for obtaining good quality crystals for single crystal X-ray diffraction studies, and it lacks rotational disorder in the resultant crystal structure compared to the disorder often observed in the CF_3 groups present in analogous $[BAr^F{}_4]^-$ complexes. $[Al(O^tBu^F)_4]^-$, which has been most extensively developed by Krossing,[39] cannot undergo unwanted η^6 binding of aryl

substituents and this negates any unwanted side reactions, and may aid the synthesis of good quality single crystals. All three of these anions have been utilised in this thesis.

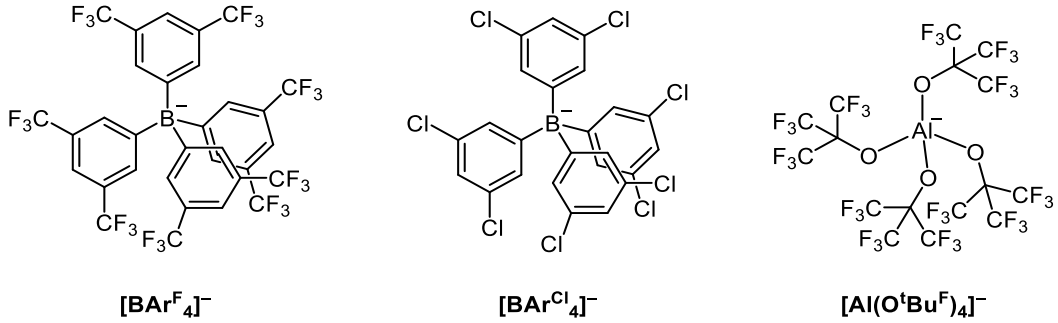
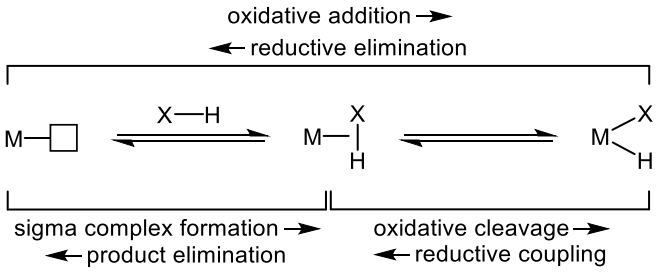


Figure 1.9 Weakly coordinating anions $[BAr^{F}_4]^-$, $[BAr^{Cl}_4]^-$ and $[Al(O^tBu^F)_4]^-$.

1.5 Sigma complexes

Complexes containing a ligand where an intermolecular X–H (X = e.g. H, C, Si, B) bonding pair of electrons also acts as a donor to a metal centre are collectively named metal sigma complexes. These systems are an area of significant interest as they are often postulated to be the intermediates of oxidative cleavage and reductive bond forming steps during reaction pathways in catalysis (Scheme 1.2). Therefore, investigation of these X–H complexes is vital to widen the understanding of bond activation processes and hence enable further exploration of catalytic processes, as well as the fundamental challenges involved in their synthesis and characterisation.



Scheme 1.2 Generalised steps in oxidative addition and reductive elimination and the role of sigma complexes. (X = e.g. H, C, Si, B).

1.5.1 Sigma dihydrogen complexes

The simplest sigma X–H complexes are those of dihydrogen, X = H. Figure 1.10 shows the first σ complex, characterised by Kubas in 1984, $W(CO)_3(P^iPr_3)_2(\eta^2\text{-}H_2)$.[40] Many other dihydrogen

complexes have since been documented,[41] and offer the blueprint for the synthesis and characterisation of σ complexes. The neutral H_2 molecule is a formal two electron donor: creating a three centre, two electron bond on coordination to a metal centre. These electrons are donated from the H–H σ bonding molecular orbital into an appropriately orientated and vacant metal d orbital, and there is also a backbonding component from the metal into the H–H σ* antibonding orbital (Figure 1.10), leading to side on binding of H_2. These bonding effects are signalled by NMR spectroscopy, single crystal X-ray and neutron diffraction studies, and IR spectroscopy of the dihydrogen transition metal complexes and its comparison with free H_2, as the H–H bond is weakened on binding to a transition metal centre.

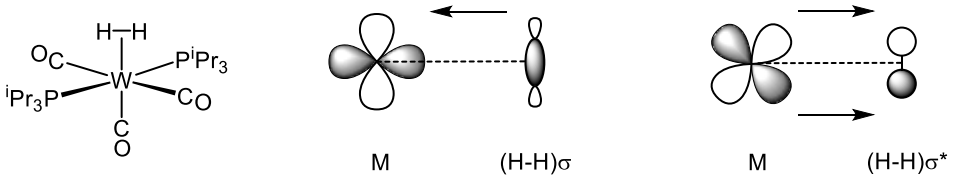


Figure 1.10 Left: Kubas's dihydrogen complex. Right: Bonding model for dihydrogen coordination.

The extent of backbonding into the σ* molecular orbital determines whether a dihydrogen complex is formed or if the H–H σ bond is cleaved, resulting in the dihydride species (Figure 1.11). The presence of strongly π accepting co-ligands leads to modest back donation to H_2 and the dihydrogen will more likely remain intact. The metal also has a significant effect on the balance of the bonding: classical hydrides are preferred for metals with greater radial extension of the d orbitals, with non-classical behaviour (η^2 bound dihydrogen) increasing across a period, and the dihydride species favoured when descending a group. Generally, H–H distances, which can be directly measured using neutron diffraction, or indirectly from the $^1J_{HD}$ value and T_1 time of the HD resonance in analogous HD complexes,[42] are in the region of 0.8 – 0.9 Å for dihydrogen complexes and in excess of 1.6 Å for the dihydride, with intermediate stages of bond cleavage showing accordant values.[43] Using HD in place of H_2 allows measurement of the H–D coupling constant which has a value of 43.2 Hz in free HD. Dihydride complexes exhibit $^2J_{HD}$ values of less than 5

Hz whereas dihydrogen species generally show $^1J_{HD}$ values greater than 25 Hz, but less than free HD.[43]

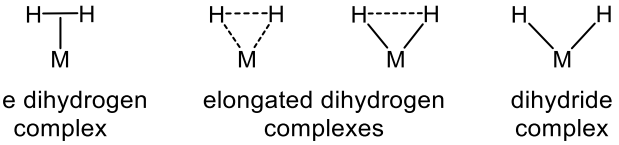


Figure 1.11 Stages of dihydrogen cleavage at a transition metal centre.

1.5.2 Sigma amine borane complexes

Sigma complexes of amine boranes are of interest as these likely precede an oxidative bond cleavage event, the first key step, in amine borane dehydrocoupling or dehydropolymerisation via an inner sphere mechanism (Section 1.6.7). Therefore isolation and the study of fundamental reactivity of sigma amine borane complexes are considered important challenges in this research area. An amine borane generally coordinates to a metal centre via a three centre, two electron bond through the hydridic B–H sigma bond.[44] The B–H σ orbital donates electron density to the metal, however in comparison to H_2 sigma complexes (Figure 1.10), the B–H σ* is too high in energy for significant back donation. This effect, coupled with additional steric constraints imposed onto the boron atom by the amine group and other R groups (such as alkyl, aryl or H), relative to H_2, leads to more end on binding of the B–H fragment rather than the side on binding observed in H–H complexes.

The first example of amine borane coordination to a metal centre was achieved by Shimoi and co-workers in 1999.[45] Photolysis of $M(CO)_6$ (M = Cr, Mo, W) in the presence of the tertiary amine borane $H_3B{\cdot}NMe_3$ gave $M(CO)_5(\eta^1\text{-}H_3B{\cdot}NMe_3)$ (Figure 1.12). Interestingly, the B–H protons were fluxional on the NMR timescale due to rapid exchange between the η bound B–H and terminal B–H proton environments.[45-46] Other η^1 amine borane sigma complexes have also been reported (Figure 1.12).[4, 47-48] Amine boranes can also bind to a metal in an η^2 fashion through two of the B–H bonds.[1, 49-50] Selected examples of these types of amine borane sigma complexes are displayed in Figure 1.12.

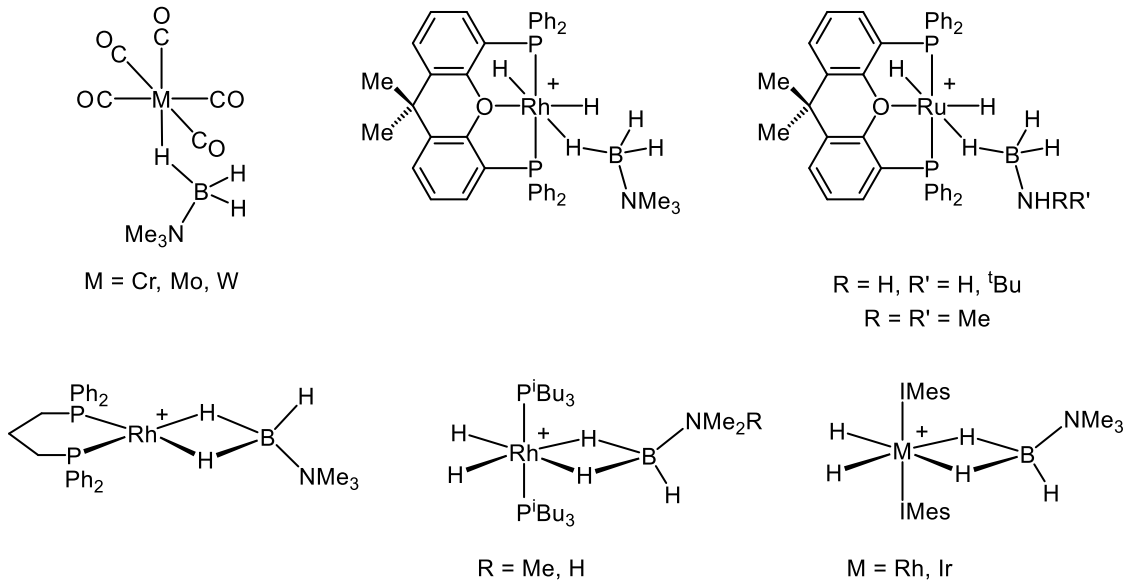


Figure 1.12 Selected examples of $\eta^1$and η^2 sigma amine borane complexes. IMes = N,N′-bis(2,4,6-trimethylphenyl)imidazol-2-ylidene. $[BAr^F{}_4]^-$ anions not shown for clarity.

Weller and co-workers have reported a rhodium complex in which both η^1 and η^2 bound amine boranes are present in the same complex (Figure 1.13), which may be indicative of intermediates involved in the coupling of two amine boranes together.[51] Furthermore, sigma complexes of the likely result of these coupling events, e.g. linear borazanes or cyclic borazanes, have been observed – including $H_3B{\cdot}NMeHBH_2{\cdot}NMeH_2$,[52] $H_3B{\cdot}NH_2(BH_2NH_2)_nBH_2{\cdot}NH_3$ (n = 0 – 3),[53] and $(H_2BNMe_2)_2$ (Figure 1.13).[54]

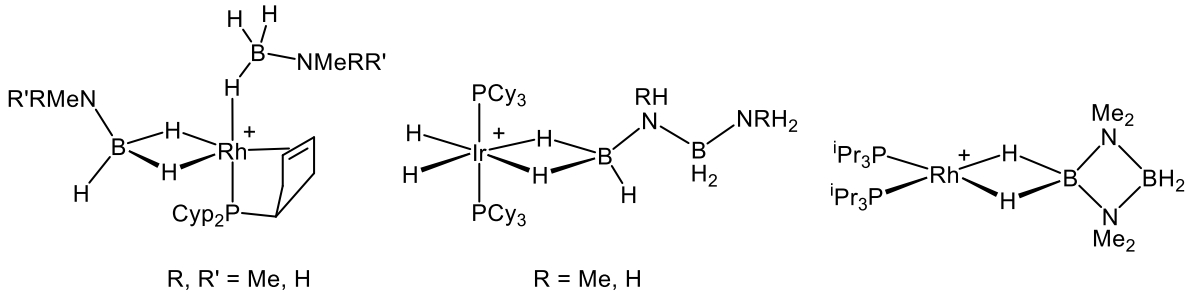


Figure 1.13 Weller's rhodium complex containing both $\eta^1$and η^2 bound amine borane ligands and sigma complexes of linear and cyclic borazanes. $[BAr^F{}_4]^-$ anions not shown for clarity.

1.5.3 Sigma aminoborane complexes

The dehydrogenation of amine boranes to form aminoboranes is considered to be the initial step in metal catalysed amine borane dehydrocoupling mechanisms. Therefore their generation and interaction with metal centres represents fundamental steps in dehydrocoupling. Sigma complexes of aminoboranes arise from donation of the aminoborane B–H bond into a vacant metal orbital, with back donation from the metal into the B–N π* orbital also possible. Many examples have been characterised, including both η^1,[55] and η^2 aminoborane coordination (Figure 1.14).[56-57] In 2016, Weller and co-workers isolated an unusual binding mode of the simplest aminoborane $H_2B{=}NH_2$ to a bimetallic Rh_2 fragment, noting that the observation of bimetallic σ aminoborane complexes in amine borane dehydrocoupling gave interesting insight into the possible nature of the true active species in these systems (Figure 1.14).[2]

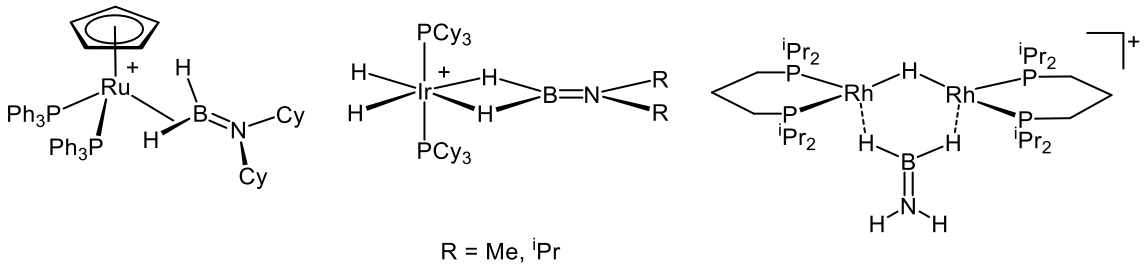


Figure 1.14 Selected sigma complexes of aminoboranes. Counterions not shown for clarity.

1.6 Dehydropolymerisation of amine boranes

Amine boranes are Lewis acid/Lewis base adducts with the molecular formula $R_3B{\cdot}NR_3$, with examples incorporating R = H, alkyl, or aryl, and combinations thereof.[11] For amine boranes containing hydrogen substituents on boron and nitrogen, the protic N–H bonds and hydridic B–H bonds enables dihydrogen loss which is much more energetically feasible than for their alkane analogues.[58] The air stable parent amine borane, ammonia borane ($H_3B{\cdot}NH_3$), has been of particular interest due to its high weight percentage of hydrogen (19.6%), and ability to thermally release gaseous H_2 – which may prove valuable for the evolution of hydrogen powered fuel cells by storage of hydrogen by chemical hydrides.[59] Structurally similar hydrazine borane ($H_3B{\cdot}NH_2NH_2$) has also been explored in the literature as it also contains a relatively high weight percentage of

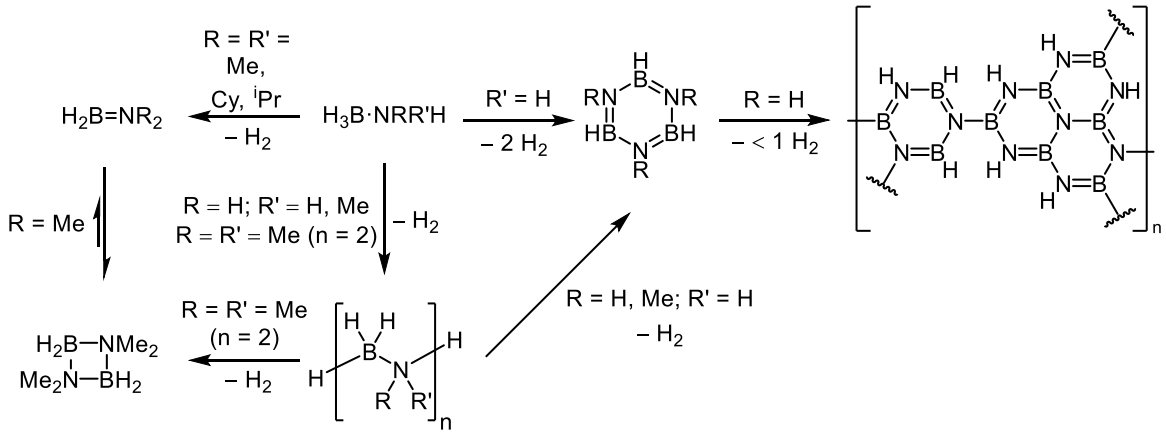
hydrogen (15.4%).[60-61] Relying on the thermal dehydrogenation of $H_3B{\cdot}NH_3$ to produce H_2 alone, however, leads to mixtures of BN coupled by-products such as polyaminoboranes, $(H_2BNH_2)_n$, and polyborazylene, (BNH_x), therefore the incorporation of metal catalysts into this process may improve dehydrogenation control and efficiency to ensure maximum H_2 output for its use as a fuel. However, the viability of these materials as hydrogen stores is uncertain, as even the state of the art method to regenerate $H_3B{\cdot}NH_3$ from the dehydrogenated polymeric spent fuel is energetically uphill.[62] However, the BN coupled products may prove useful in their own right, as unexplored polymeric materials in the case of polyaminoboranes, or as precursors to thermally and chemically resistant hexagonal boron nitride, also known as "white graphene", in the case of polyborazylene. Recently, Manners and co-workers formed the first boron-nitrogen analogue of polystyrene, $(PhHBNH_2)_n$, via catalytic dehydropolymerisation of $PhH_2B{\cdot}NH_3$,[63] further demonstrating the potential viability and scope for these new polymers.

1.6.1 General pathways for the dehydrocoupling/polymerisation of amine boranes

Depending on the nature of the substituents bound to nitrogen, amine boranes may form different dehydrocoupling products, liberating varying equivalents of H_2. Ammonia borane ($H_3B{\cdot}NH_3$), which has been well documented as a potential hydrogen storage medium,[64] can in principle release up to 3 equivalents of H_2 to form pure boron nitride (BN); however there are currently no catalytic methods for this process. Instead, a variety of dehydrocoupling products may result with corresponding H_2 release: polyaminoborane $(H_2BNH_2)_n$ (1 equivalent H_2), borazine $(HBNH)_3$ (2 equivalents H_2) or polyborazylene BNH_x (> 2 equivalents H_2) (Scheme 1.3). For the primary amine borane ($H_3B{\cdot}NMeH_2$), analogous polyaminoboranes and borazines may form (Scheme 1.3).

Secondary amine boranes containing two non-hydrogen substituents at the nitrogen atom are capable of releasing one equivalent of H_2 only. For the simplest secondary amine borane $H_3B{\cdot}NMe_2H$, the major dehydrocoupling product is the cyclic dimer $(H_2BNMe_2)_2$, and this can be formed from the dimerisation of two aminoborane $H_2B{=}NMe_2$ molecules or alternatively via the

cyclisation of the linear diborazane $H_3B{\cdot}NMe_2BH_2{\cdot}NMe_2H$. Amine boranes $H_3B{\cdot}NCy_2H$ and $H_3B{\cdot}N^iPr_2H$ lose an equivalent of H_2 to form the analogous aminoboranes, which do not dimerise due to the steric bulk surrounding nitrogen. Scheme 1.3 details the generalised pathways involved in the dehydrogenation and dehydrocoupling of parent, primary and secondary amine boranes.

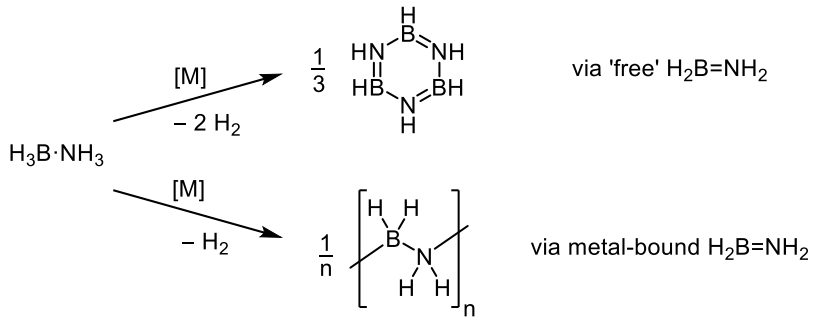


Scheme 1.3 Generalised pathways for the dehydrocoupling or dehydropolymerisation of amine boranes. All steps may be metal mediated.

1.6.2 Observation and trapping of aminoboranes

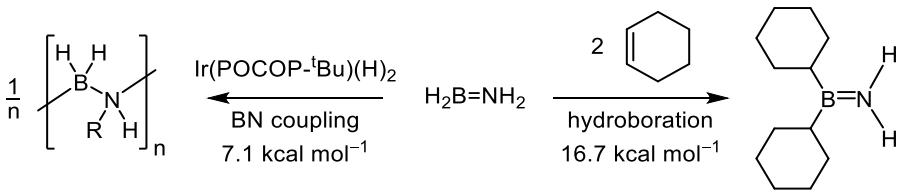
Amine borane dehydrocoupling is proposed to occur via initial formation of the corresponding aminoborane ($H_2B{=}NRR'$), with loss of H_2. For aminoboranes which have the ability to BN couple, these are only transient species prior to the B–N bond forming event. $H_2B{=}N^tBuH$ and $H_2B{=}NMe_2$, for example, have been directly observed as transient species in the catalytic dehydrocoupling of $H_3B{\cdot}N^tBuH_2$ and $H_3B{\cdot}NMe_2H$ respectively.[65-66] Less bulky aminoboranes which can eventually form polyaminoboranes, such as $H_2B{=}NMeH$ and $H_2B{=}NH_2$, have not been directly observed during their metal catalysed dehydrocoupling, though the former has been observed in situ under metal free conditions at −10°C (see Section 1.6.4), and both have been stabilised by coordination to a transition metal fragment (Section 1.5.3). Mechanistically speaking, the trapping of aminoboranes such as $H_2B{=}NMeH$ and $H_2B{=}NH_2$ is considered important for determining whether the aminoborane is not only formed during dehydrocoupling, but if it is liberated from the metal or alternatively remains bound to the metal centre. In 2008, Baker and Dixon proposed that borazine, $(HBNH)_3$, was the product of trimerisation and dehydrogenation of free $H_2B{=}NH_2$, whereas

oligomeric or polymeric $(H_2BNH_2)_n$ resulted if the aminoborane was metal bound throughout the reaction (Scheme 1.4).[67]



Scheme 1.4 Baker and Dixon's hypothesis on the outcome of metal catalysed dehydrocoupling of $H_3B{\cdot}NH_3$ depending on whether the aminoborane is metal bound or free.

Probing the hydroboration of cyclohexene by aminoboranes formed during dehydrocoupling reactions is one method, suggested by Baker and Dixon,[67] which may allow the trapping of free aminoboranes in solution (Scheme 1.5). For example, cyclohexene added to the dehydrocoupling of $H_3B{\cdot}NH_3$ by $[Rh(1,5\text{-COD})(\mu\text{-Cl})]_2$ (1,5-COD = 1,5-cyclooctadiene) formed hydroborated $H_2B{=}NH_2$, $Cy_2B{=}NH_2$, as the major product instead of borazine,[68] however no $Cy_2B{=}NH_2$ was observed when Ir(POCOP-^{t}Bu)$(H)_2$ was utilised – only oligomeric products were produced by head-to-tail BN coupling.[69] These observations support that only metal bound aminoboranes form oligomeric/polymeric material, however more recent studies suggest that lack of hydroboration of cyclohexene does not necessarily reflect an absence of free aminoborane in solution. For example, if metal mediated oligomerisation/polymerisation is kinetically favoured over borazine formation or hydroboration of aminoboranes, $Cy_2B{=}NRH$ will not be observed, even if free aminoborane is liberated during dehydrocoupling. In fact, Paul has shown that BN coupling in oligomerisation/polymerisation using the Ir(POCOP-^{t}Bu)$(H)_2$ system is a lower energy process than hydroboration,[70] with barriers of 7.1 kcal mol^{-1} and 16.7 kcal mol^{-1} respectively (Scheme 1.5).



Scheme 1.5 Trapping of aminoboranes via the hydroboration of cyclohexene versus BN coupling.

1.6.3 Types of polymerisation mechanism

Chain propagation in polymer formation can generally be assigned to one of three fundamental polymer growth mechanisms: chain growth, step growth or living polymerisation (Figure 1.15), determined by the analysis of the molecular weight of the polymer over the course of the reaction. In this thesis, polyaminoborane molecular weight is defined by its number average molecular weight (M_n, g mol^{-1}), and its dispersity (Đ = M_w (g mol^{-1}, weight average molecular weight) / M_n),[71] as measured relative to polystyrene standards. Chain growth polymerisation is indicated by polymer of appreciable M_n formed at short reaction times (or low substrate conversion) (Figure 1.15(a)).[71-72] Here, monomers add to the growing polymer chain in turn, and an inherent chain termination event is in operation which leads to a levelling off of the molecular weight of the material produced. In contrast, during step growth polymerisation, low M_n material forms at short – medium reaction times (Figure 1.15(b)).[71] All of the substrate is initially consumed to form short chain oligomers, which subsequently couple together to form longer chains later in the reaction. This means that high molecular weight material is only observed at longer reaction times. Lastly, living polymerisation (Figure 1.15(c)) is a type of chain growth polymerisation where chain transfer and chain termination events are absent, and the rate of chain initiation is much higher than the rate of propagation. Therefore, every initiating site propagates at a similar rate, leading to a narrow molecular weight distribution of the resulting polymer, with a Đ value close to unity.[71] Living polymerisation is therefore considered the most desirable polymerisation mechanism, due to control of polymer molecular weight governed by user-imposed catalyst loading and termination processes.

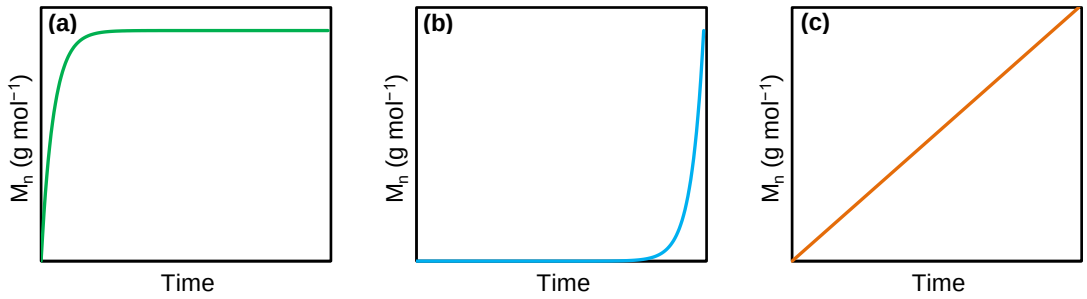
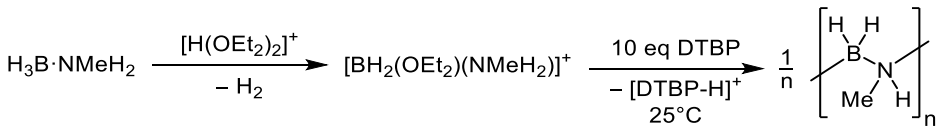


Figure 1.15 Types of polymerisation mechanism. (a) Chain growth. (b) Step growth. (c) Living.

1.6.4 Catalyst free routes to polyaminoboranes

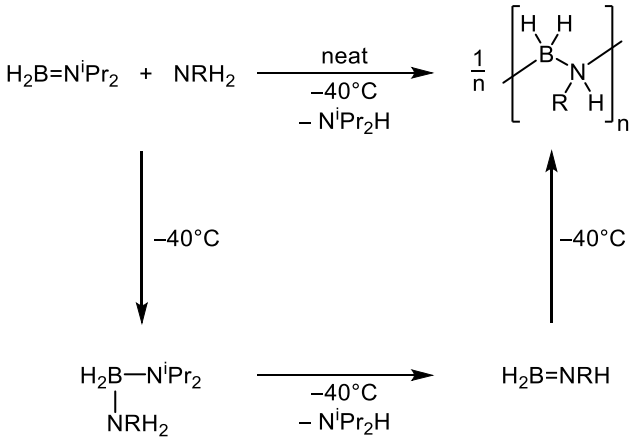
Whilst thermally induced dehydrocoupling of amine boranes often forms mixtures of BN products,[10] catalyst free routes to selectively produce polyaminoboranes, though scarce, have been reported, with two known examples in the literature. In 2014, Wass and Manners documented the generation of aminoborane monomers from amine boronium cations which could then undergo uncontrolled BN coupling.[73] For example, low molecular weight $(H_2BNMeH)_n$ (M_n < 5,000 g mol^{-1}) was prepared according to Scheme 1.6. Protonation of $H_3B{\cdot}NMeH_2$ using the Brønsted acid $[H(OEt_2)_2][B(C_6F_5)_4]$ gave the boronium cation $[BH_2(OEt_2)(NMeH_2)][B(C_6F_5)_4]$ with loss of H_2. Deprotonation of cationic $[BH_2(OEt_2)(NMeH_2)]^+$ by 2,6-ditertbutylpyridine (DTBP) generated $H_2B{=}NMeH$, which could be directly observed for the first time by ^{11}B NMR spectroscopy of the reaction mixture at −10°C, which subsequently polymerised.



Scheme 1.6 Manners's and Wass's metal free dehydropolymerisation of $H_3B{\cdot}NMeH_2$ to form low molecular weight polyaminoborane. $[B(C_6H_5)_4]^-$ anions not shown for clarity.

More recently, higher molecular weight polyaminoboranes produced via catalyst and solvent free methods have been achieved by Alcaraz and co-workers.[74] The stable aminoborane $H_2B{=}N^iPr_2$ was utilised as a BH_2 transfer agent, as its solvent free, stoichiometric reaction with a variety of primary

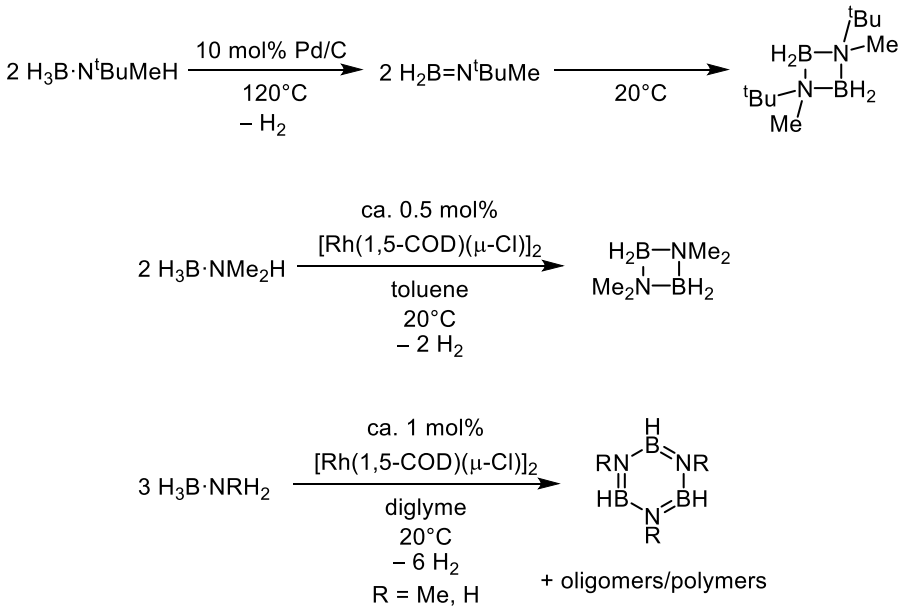
amines (NRH_2, R = allyl, ^nBu, Pr, Et, Me, H) at −40°C gave $(H_2BNRH)_n$ (Scheme 1.7) with impressive molecular weights for a metal free system, albeit with relatively high dispersities (e.g. for R = Me, M_n = 201,000 g mol^{-1}, Đ = 10.2). Excitingly, the reported synthesis of polyallylaminoborane (R = allyl) was the first to provide polyaminoborane with an unsaturated side chain appended to the amine, and this material was of reasonably high molecular weight with a promising, narrow dispersity index (M_n = 58,000 g mol^{-1}, Đ = 1.2).



Scheme 1.7 Alcaraz's routes to high molecular weight polyaminoboranes, utilising the bulky aminoborane $H_2B{=}N^iPr_2$ as a source of BH_2.

1.6.5 Metal catalysed dehydrocoupling of amine boranes

The first example of amine borane dehydrocoupling mediated by a transition metal catalyst was reported in 1989 by Roberts and co-workers.[75] $H_3B{\cdot}N^tBuMeH$ was dehydrogenated to $H_2B{=}N^tBuMe$ using 10 mol% palladium on charcoal at 120°C under an inert atmosphere. The target liquid aminoborane was found to slowly solidify at room temperature and underwent BN coupling to yield two isomeric dimers, E/Z-$(H_2BN^tBuMe)_2$, with the E isomer proposed to be the major form on steric grounds (Scheme 1.8). However, it was not until over ten years later that the Manners group utilised $[Rh(1,5\text{-COD})(\mu\text{-Cl})]_2$ (1,5-COD = 1,5-cyclooctadiene) to achieve catalytic $H_3B{\cdot}NMe_2H$, $H_3B{\cdot}NMeH_2$ and $H_3B{\cdot}NH_3$ dehydrocoupling at room temperature (Scheme 1.8).[68, 76] This catalyst negated the need for the high temperatures typically used for thermally induced dehydrocoupling – previously the state of the art in the synthesis of cyclic BN compounds and borazines.[77-78]



Scheme 1.8 The first examples of metal catalysed amine borane dehydrocoupling.

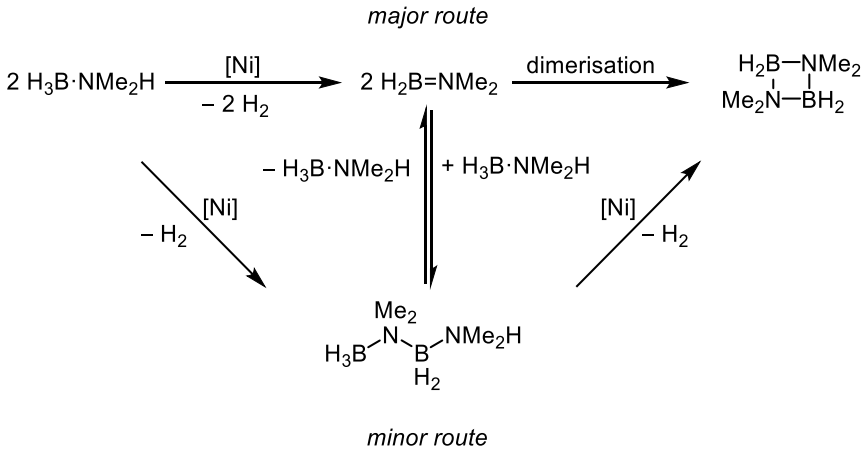
Since these first examples, both heterogeneous and homogeneous transition metals have been utilised in the dehydrocoupling of amine boranes.

1.6.6 Heterogeneous transition metal catalysts for amine borane dehydrocoupling

Heterogeneous catalysis is an appealing method to achieve dehydrocoupling of amine boranes, with the greatest benefit being straightforward separation of products from the catalyst. Manners's $[Rh(1,5\text{-}COD)(\mu\text{-}Cl)]_2$ (1,5-COD = 1,5-cyclooctadiene) system was studied in depth in 2004 with $H_3B{\cdot}NMe_2H$ as the substrate, and shown to be heterogeneous in nature.[79] At 2 mol% catalyst loading, conversion of $H_3B{\cdot}NMe_2H$ was monitored by ^{11}B NMR spectroscopy which showed an induction period of ~200 minutes, alongside a colour change of the reaction mixture from orange to black. The presence of an induction period may indicate heterogeneous (i.e. colloidal) catalysis due to slow nucleation in the formation of the catalytically active nanoparticles. Finke's ensemble of tests for heterogeneous catalysis were therefore performed,[80] with addition of excess mercury to a catalytically active sample halting catalysis completely, and sub-stoichiometric amounts of PPh_3 resulting in a substantial slowing of dehydrocoupling rate. Fulton, Linehan and Autrey later

suggested that soluble Rh_6 clusters were the active species in Manners's system, as determined by in operando X-ray absorption fine structure spectroscopy.[81]

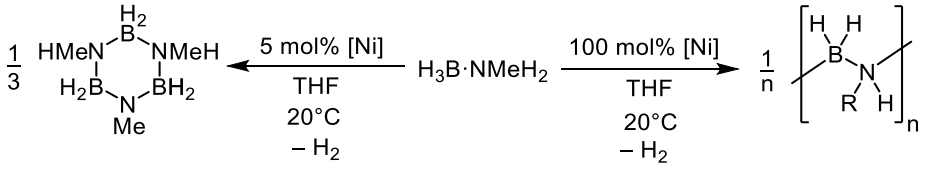
In 2011, the Manners group reported a skeletal nickel catalyst, produced by the selective leaching of Al from a Ni/Al alloy, for the dehydrocoupling of $H_3B{\cdot}NMe_2H$, $H_3B{\cdot}NEt_2H$ and $H_3B{\cdot}NMeH_2$.[82] Full conversion of $H_3B{\cdot}NMe_2H$ to cyclic $(H_2BNMe_2)_2$ was achieved using 5 mol% Ni in toluene at 20°C after 6 hours. Over the reaction course, small amounts of the linear diborazane $H_3B{\cdot}NMe_2BH_2{\cdot}NMe_2H$ could be identified in the ^{11}B NMR spectrum, which led to the proposal of two possible routes for the dehydrocoupling pathway (Scheme 1.9). After dehydrogenation of $H_3B{\cdot}NMe_2H$ to the aminoborane $H_2B{=}NMe_2$, off metal dimerisation to the cyclic species may result (proposed major pathway), or alternatively on metal BN coupling to form the linear species followed by cyclisation and concomitant loss of H_2 was proposed to be the minor pathway.



Scheme 1.9 The mechanism of the dehydrocoupling of $H_3B{\cdot}NMe_2H$ using skeletal nickel, proposed by Manners.

The same skeletal nickel system when combined with the primary amine borane $H_3B{\cdot}NMeH_2$ showed different product selectivity depending on the relative concentration of the catalyst. Using 5 mol% catalyst led to the cyclic triborazane $(H_2BNMeH)_3$, however 100 mol% skeletal nickel (i.e. stoichiometric quantities) produced polyaminoborane $(H_2BNMeH)_n$ (M_n = 51,300 g mol^{-1}, Đ = 1.5) (Scheme 1.10). This difference was postulated to be due to the higher local concentration of the monomer $H_2B{=}NMeH$ at high catalyst loading which kinetically favoured polymerisation over

cyclisation. This was also observed with parent amine borane $H_3B{\cdot}NH_3$ which cyclised to B-(cyclodiborazanyl)-aminoborohydride or polymerised to $(H_2BNH_2)_n$ using 5 mol% or 100 mol% skeletal nickel respectively.

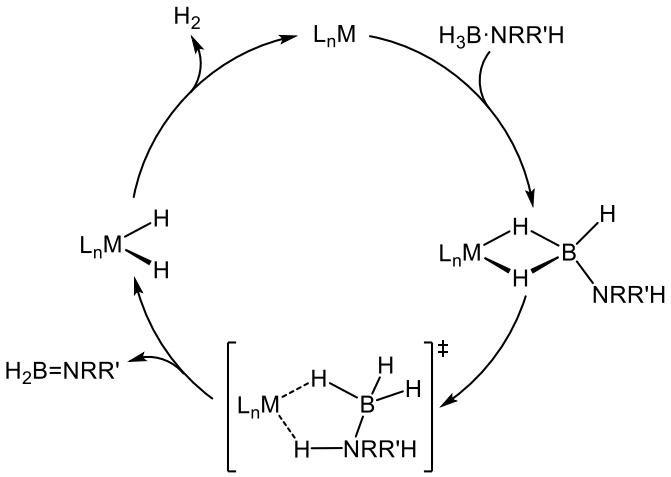


Scheme 1.10 Manners's skeletal nickel system which showed product selectivity dependent on catalyst loading.

1.6.7 *Homogeneous transition metal catalysts for amine borane dehydrocoupling*

Compared to heterogeneous catalysts, homogeneous transition metal systems have well defined coordination sites, and these can be systematically changed in terms of both the metal centre and the ligand. This approach allows for more detailed insight to be gained into amine borane dehydrocoupling mechanisms, as different intermediates may be stabilised according to the identity of the metal fragment. In addition, soluble and well-defined catalyst systems allow for detailed kinetic studies to be performed for both the dehydrogenation step and B–N bond formation.

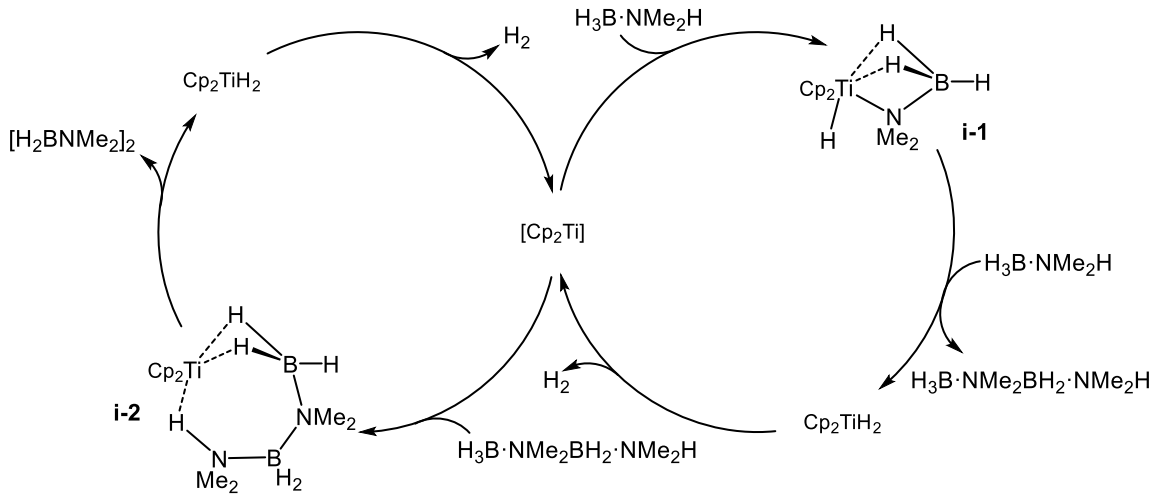
Inner or outer sphere mechanisms may operate depending on the system in question. Inner sphere mechanisms are generally thought to proceed via initial coordination of the amine borane to the metal to form a sigma complex (Section 1.5.2). This bound amine borane can dehydrogenate through B–H/N–H transfer to form the corresponding aminoborane which can then form system dependent products (Scheme 1.3). A general and simplified pathway for this process is detailed in Scheme 1.11. In contrast, outer sphere mechanisms involve the dehydrogenation of the amine borane without its direct coordination to a metal centre. A third type of mechanism, proposed by Conejero and López-Serrano in 2013 and discussed in more detail later,[83] involves the formation of boronium cations, e.g. $[BH_2(NMe_2H)(THF)]^+$, which can then be deprotonated by a metal hydride to form H_2 and aminoborane, which can subsequently undergo B–N coupling. Each of these mechanisms will be discussed throughout this Section.



Scheme 1.11 Simplified, general pathway for inner sphere amine borane dehydrogenation to form the corresponding aminoborane.

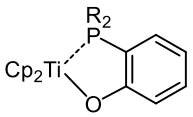
The first relatively well defined amine borane dehydrocoupling system mediated by a homogeneous transition metal catalyst was reported by Manners and co-workers in 2006.[84] Cp_2TiCl_2 was reacted with 2 equivalents of ^{n}BuLi at −15°C to form [Cp_2Ti] in situ, and subsequently reacted with $H_3B{\cdot}NMe_2H$ in toluene at 2 mol% catalyst loading at 20°C to form cyclic $(H_2BNMe_2)_2$. The kinetic profile of the reaction did not involve an induction period and addition of excess mercury did not alter catalysis – both features indicative of homogeneity. Four years later an in depth mechanistic study on the [Cp_2Ti] system was carried out by Manners and Lloyd-Jones.[85] A significant amount of linear $H_3B{\cdot}NMe_2BH_2{\cdot}NMe_2H$ was formed at low $H_3B{\cdot}NMe_2H$ conversion, followed by its consumption to form $(H_2BNMe_2)_2$. This was supported by the reaction of independently synthesised $H_3B{\cdot}NMe_2BH_2{\cdot}NMe_2H$ with 2 mol% [Cp_2Ti] which formed only ca. 0.5% $H_2B{=}NMe_2$ over the course of the reaction by ^{11}B NMR spectroscopy, indicating that the linear diborazane is the likely sole intermediate on the dehydrocoupling pathway. The proposed mechanism is detailed in Scheme 1.12 and involves two connected cycles, where coordination of $H_3B{\cdot}NMe_2H$ to the Ti centre forms [$Cp_2Ti(\eta^2\text{-}H_3B{\cdot}NMe_2H)$] which undergoes N–H activation to give the amidoborane complex [$Cp_2Ti(H)(NMe_2{\cdot}BH_3)$] (**i-1**). A second equivalent of $H_3B{\cdot}NMe_2H$ reacts with **i-1** in a BN coupling event to give $H_3B{\cdot}NMe_2BH_2{\cdot}NMe_2H$, reforming [$Cp_2Ti$] via Cp_2TiH_2 with loss of H_2. Coordination of the linear diborazane to [Cp_2Ti] forms sigma complex **i-2**, which undergoes on metal dehydrocyclisation to

form Cp_2TiH_2 and $(H_2BNMe_2)_2$. Later work suggested further complexity in this system, as Ti(III) complexes may be important in the dehydrocoupling reaction, as opposed to the straightforward Ti(II)/Ti(IV) cycle depicted in Scheme 1.12.[86]



Scheme 1.12 Mechanism of $H_3B{\cdot}NMe_2H$ dehydrocoupling using $[Cp_2Ti]$, proposed to occur via cyclisation of the linear diborazane $H_3B{\cdot}NMe_2BH_2{\cdot}NMeH_2$ to form $(H_2BNMe_2)_2$.

Building on this, and work by Wass and co-workers on titanocene phosphinoaryloxide complexes with ^{t}Bu groups at the phosphorus atom,[87] Beweries's studies on analogous complexes containing ^{i}Pr or Ph moieties in place of ^{t}Bu (Figure 1.16) demonstrated that Ti(III) species were present throughout the dehydrocoupling of $H_3B{\cdot}NMe_2H$.[88] It was found that the influence of ^{i}Pr over Ph gave a higher activity (TOF = 0.39 h^{-1} for ^{i}Pr, 0.16 h^{-1} for Ph), proposed to be due to the potential for increased steric hindrance on using Ph.



R = ^{t}Bu, ^{i}Pr, Ph

Figure 1.16 Examples of titanocene phosphinoaryloxide complexes developed independently by Wass and Beweries for the dehydrocoupling of $H_3B{\cdot}NMe_2H$.

Related metallocene $H_3B{\cdot}NMe_2H$ dehydrocoupling catalysts were developed by Rosenthal and co-workers in 2011 of the type $[Cp_2M(\eta^2\text{-}Me_3SiCCSiMe_3)(L)]$ (M = Ti, Zr; L = pyridine for Zr, no L

for Ti) as isolable sources of [Cp_2M].[89] For M = Ti, a turnover frequency of 3 h^{-1} was reported. The zirconium complex was still active, albeit slower. This was proposed to be due to the stronger complexation of $Me_3SiCCSiMe_3$ in the precatalyst to Zr than Ti, hence the lower ability for generation of the free, active metallocene. Replacing Cp with Cp* produced a catalyst which showed no dehydrocoupling activity, highlighting the importance of sterics in this system. Later, the influence of steric and electronic parameters of substituents at the Cp ligands was further probed by installing an ^{i}Pr group on each of the Cp rings.[90] The catalyst [(η^5-$C_5H_4{}^{i}Pr)_2Ti(\eta^2$-$Me_3SiCCSiMe_3$)] showed improved activity (TOF = 32 h^{-1} at 40°C, 6 h^{-1} at 24°C) compared to its Cp analogue, hence showing that the electronic effect of ^{i}Pr dominates the additional steric effect imposed. Only a small amount of linear diborazane $H_3B{\cdot}NMe_2BH_2{\cdot}NMe_2H$ was formed during the reaction, suggesting that this system operated by a different mechanism to that of Manners and Lloyd-Jones (Scheme 1.12).[85] In addition, the reaction was shown to be half order in concentration of catalyst, therefore a dinuclear mechanism or bimetallic active species was speculated upon.

A further comparison of Ti versus Zr catalysts for the dehydrocoupling of $H_3B{\cdot}NMe_2H$ was documented by Chirik in 2007.[91] The most active catalyst with a TOF of 420 h^{-1} in benzene was a bimetallic bis(cyclopentadienyl)titanium dinitrogen complex (**i-3**, Figure 1.17), however on changing the solvent to THF a much slower turnover frequency of 0.29 h^{-1} was reported. The zirconium complexes exhibited poor turnover frequencies, speculated to be due to the formation of lower activity zirconocene borohydride hydride complexes during the reaction. $(C_5Me_4H)_2Zr(\eta^2$-$BH_4)H$ (**i-4**) was isolated, and found to have a lower activity than its $(C_5Me_4H)_2Zr(H)_2$ (**i-5**) precursor (Figure 1.17). These borohydride complexes most likely arose from the B–N cleavage and capture of free BH_3 by the zirconocene dihydride.

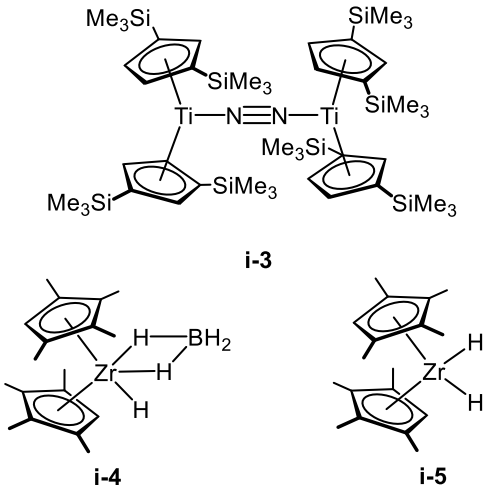
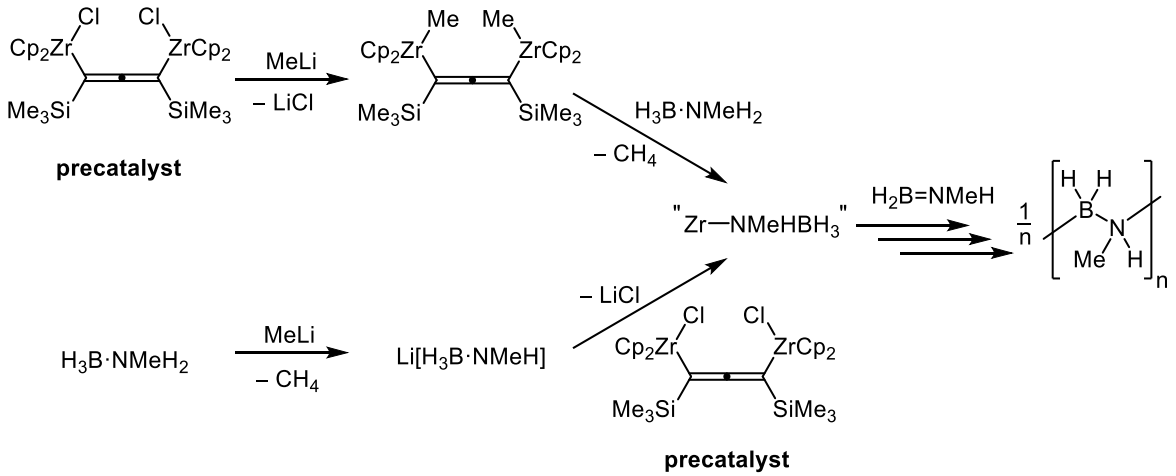


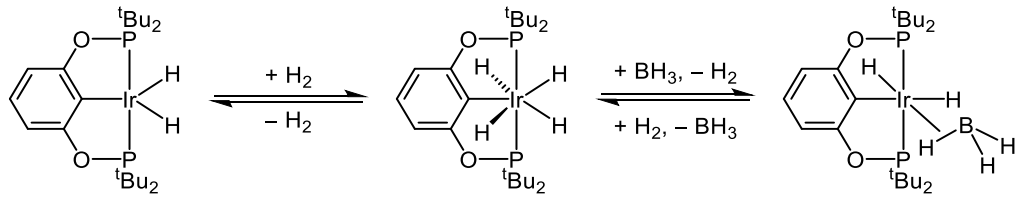
Figure 1.17 Top: Chirik's most active titanocene dehydrocoupling catalyst. Bottom: An example of Chirik's zirconocene dehydrocoupling catalysts, which were shown to react with BH_3 during the reaction.

It was not until 2018 that the dehydropolymerisation of primary amine boranes mediated by early transition metals was first reported. Manners and co-workers presented the dehydropolymerisation of $H_3B{\cdot}NMeH_2$ using a $Cp^*TiCl_2/{}^nBuLi$ system,[92] which was proposed to proceed via a step growth polymerisation mechanism (Figure 1.15). In addition, the substrate scope of dehydropolymerisation was extended to incorporate N-benzyl substituents, such as $H_3B{\cdot}NBzH_2$.[92] Even more recently, Reiß, Beweries and co-workers have reported a highly active dinuclear 1,3-allenediyl bridged zirconocene complex (Scheme 1.13) for the dehydropolymerisation of $H_3B{\cdot}NMeH_2$ to form low molecular weight $(H_2BNMeH)_n$.[93] Activation of the precatalyst by MeLi was proposed, via two possible pathways, to form a zirconium amidoborane intermediate which could enable further chain propagation of $H_2B{=}NMeH$ (Scheme 1.13).



Scheme 1.13 Reiß's and Beweries's highly active dinuclear 1,3-allenediyl bridged zirconocene precatalyst for the dehydropolymerisation of $H_3B{\cdot}NMeH_2$, and two possible pathways for its activation by MeLi to form a zirconium amidoborane species which may be involved in chain propagation.

Until recently, mainly mid-late transition metal catalysts have enabled the dehydropolymerisation of $H_3B{\cdot}NH_3$ and $H_3B{\cdot}NMeH_2$. For example, Brookhart's catalyst, Ir(POCOP-^{t}Bu)$(H)_2$ **i-6** (POCOP-^{t}Bu = κ^3-P,O,P-1,3-$(OP^tBu_2)_2C_6H_3$), was utilised by Heinekey and Goldberg in 2006 to dehydrogenate $H_3B{\cdot}NH_3$.[69] At 0.5 mol% catalyst loading 1 equivalent of H_2 was released (TOF = 860 h^{-1}) to form the postulated cyclic species $(H_2BNH_2)_5$. Later, Manners and co-workers identified the BN product to be $(H_2BNH_2)_n$ ($n \approx 20$) using solid state NMR spectroscopy.[94] On addition of ammonia borane to Ir(POCOP-^{t}Bu)$(H)_2$, the tetrahydride complex Ir(POCOP-^{t}Bu)$(H)_4$ (**i-7**) formed straightaway due to the reaction of **i-6** with H_2 generated in the reaction mixture. At long reaction times a new species was observed, later assigned to contain a sigma borane motif: Ir(POCOP-^{t}Bu)$(H)_2(\eta^1\text{-}BH_3)$ (**i-8**).[95] Complex **i-8** can be converted back to tetrahydride **i-7** on addition of H_2. The relationship between these complexes in catalysis is shown in Scheme 1.14.

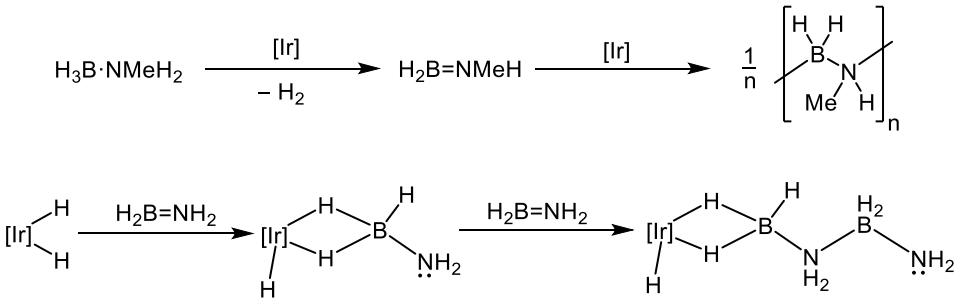


i-6 **i-7** **i-8**

Scheme 1.14 Organometallic complexes involved in the dehydrocoupling of $H_3B{\cdot}NH_3$ using Ir(POCOP-^{t}Bu)$(H)_2$.

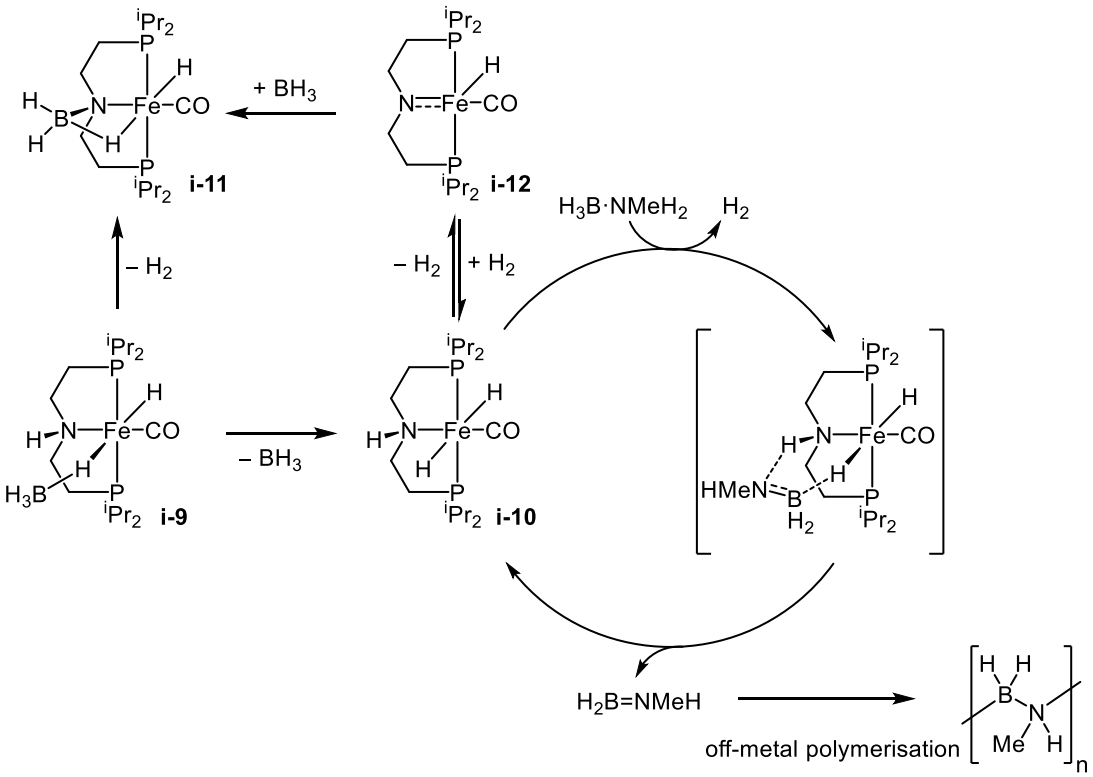
Following this work, Manners increased the scope of Brookhart's catalyst in amine borane dehydrocoupling by studying $H_3B{\cdot}NMeH_2$ and $H_3B{\cdot}N^nBuH_2$ as well as previously reported $H_3B{\cdot}NH_3$.[94, 96] High molecular weight $(H_2BNMeH)_n$ (M_n = 55,200 g mol^{-1}, Đ = 2.9) was formed using 0.3 mol% Ir(POCOP-^{t}Bu)$(H)_2$ when $H_3B{\cdot}NMeH_2$ was used as the amine borane substrate. Medium molecular weight material using 0.1 mol% **i-6** was observed at low $H_3B{\cdot}NMeH_2$ conversion ($M_n \approx$ 20,000 g mol^{-1}, < 40% conversion), however M_n increased as conversion increased ($M_n \approx$ 60,000 g mol^{-1}, 100% conversion), indicating that whilst the polymerisation did not operate via a step growth mechanism, it differed from classical chain growth (Figure 1.15). In addition, increased catalyst loadings led to increased M_n, whereas metal mediated single site controlled chain growth polymerisation generally shows an inverse relationship between these two variables. There was also no difference in the molecular weight of the polyaminoborane formed in a closed system compared to an open, showing that the build-up of hydrogen had no appreciable effect, therefore is unlikely to be involved in chain termination. These experimental observations were consistent with dual action of the metal centre: first, slow generation of $H_2B{=}NMeH$ from $H_3B{\cdot}NMeH_2$, followed by fast chain growth polymerisation of $H_2B{=}NMeH$ (Scheme 1.15), as formation of high M_n polymer would be dependent on the availability of the monomer, which increases at higher conversions. Later work undertaken by Paul and co-workers suggested a mechanism for the polymerisation step using DFT calculations, with $H_3B{\cdot}NH_3$ as the substrate (dehydrogenation to form $H_2B{=}NH_2$ was not calculated). This involved an on metal end chain growth mechanism, where the NH_2-based lone pair of an aminoborohydride complex interacts with the Lewis acidic BH_2 group of a free aminoborane molecule (Scheme 1.15),[97] which subsequently

forms a lone pair on the end of the growing polyaminoborane chain to allow further end chain propagation.



Scheme 1.15 Top: Manners's proposed dual action of the iridium metal centre in $H_3B{\cdot}NMeH_2$ dehydropolymerisation using Ir(POCOP-^{t}Bu)$(H)_2$ ([Ir] = {Ir(POCOP-^{t}Bu)}). Bottom: Paul's proposed on metal end chain growth polymerisation mechanism.

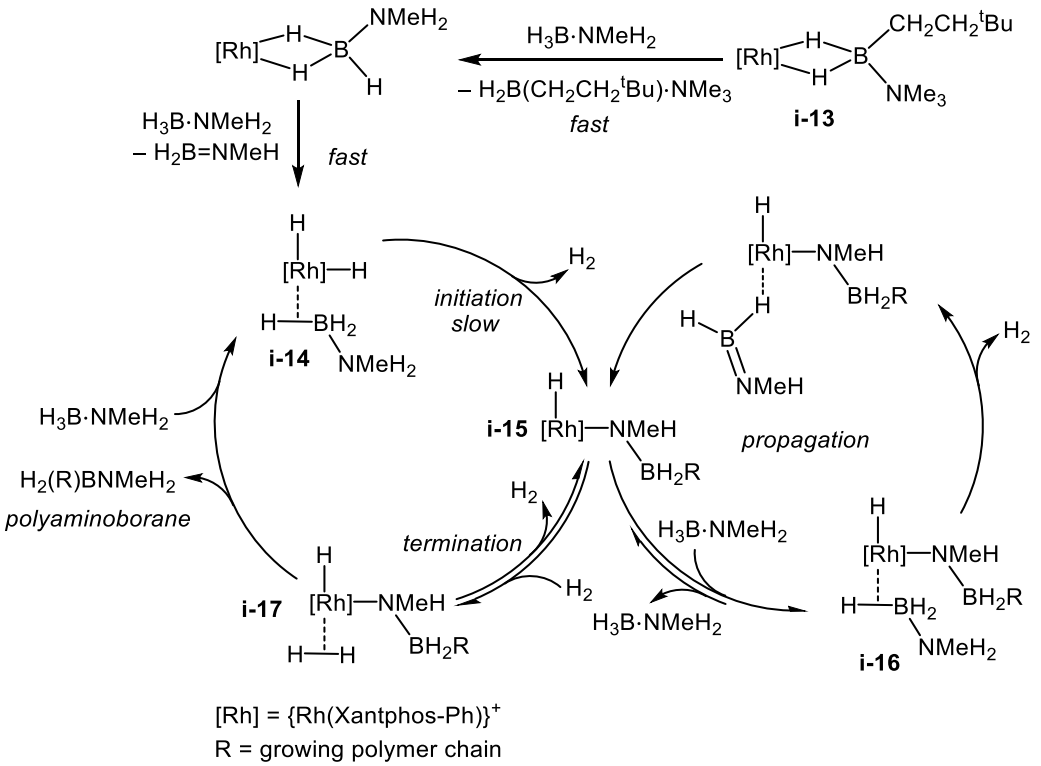
In 2017, Beweries and co-workers explored the dehydropolymerisation of $H_3B{\cdot}NMeH_2$ using FeH(PN*H*P)(CO)(HBH_3) **i-9** (PN*H*P = $HN(CH_2CH_2P^iPr_2)_2$)[98] to form medium/high molecular weight $(H_2BNMeH)_n$.[99] They proposed a mechanism in THF solvent in which $H_3B{\cdot}NMeH_2$ is dehydrogenated on metal by an outer sphere mechanism, similar to that proposed by Schneider in $H_3B{\cdot}NH_3$ dehydrogenation,[100] to form H_2B=NMeH, which subsequently polymerises off metal (Scheme 1.16). This was suggested as carrying out the reaction in a sealed system where H_2 was allowed to build up did not affect $(H_2BNMeH)_n$ molecular weight, and changing the catalyst loading between 1 mol% – 5 mol% did not lead to a substantial deviation of M_n – indicative of a chain propagation mechanism which is not strongly metal-based. Three complexes (**i-9**, **i-10** and **i-11**, Scheme 1.16) were observed using ^{1}H and ^{31}P NMR spectroscopy during catalysis and hence implicated in the proposed catalytic cycle. Off cycle complex **i-11** was corroborated by the addition of BH_3 to proposed but unobserved **i-12**, indicating possible involvement of borane during the reaction.



Scheme 1.16 Beweries's proposed outer sphere mechanism for the dehydrogenation of $H_3B{\cdot}NMeH_2$, where polymerisation is suggested to occur off metal.

Weller, in collaboration with Lloyd-Jones and Manners, undertook mechanistic studies of the dehydrocoupling and dehydropolymerisation of $H_3B{\cdot}NMe_2H$ and $H_3B{\cdot}NMeH_2$ respectively, using $[Rh(\kappa^2\text{-P,P-Xantphos-Ph})(\eta^2\text{-}H_2B(CH_2CH_2{}^tBu){\cdot}NMe_3)][BAr^F{}_4]$ **i-13** (Xantphos-Ph = 4,5-bis(diphenylphosphino)-9,9-dimethylxanthene).[4] The primary and secondary amine borane systems showed very similar dehydrogenation reaction profiles: both possessed an induction period, apparent saturation kinetics and analogous speciation with the $\{Rh(Xantphos\text{-}Ph)\}^+$ fragment. The catalytic cycle in Scheme 1.17 was proposed for the $H_3B{\cdot}NMeH_2$ substrate, in which initial addition of $H_3B{\cdot}NMeH_2$ to **i-13** formed the Rh(III) dihydride species **i-14** with loss of H_2 and $H_2B{=}NMeH$. The formation of the tentatively assigned amidoborane complex **i-15** was postulated to be the active catalytic species on the basis of the slow induction period in which N–H activation was rate limiting. Reversible $H_3B{\cdot}NMeH_2$ coordination (saturation kinetics) to **i-15** forms the strongly favoured amine borane bound complex **i-16** which undergoes B–H/N–H transfer, producing $H_2B{=}NMeH$ which can then polymerise to furnish $(H_2B{\cdot}NMeH)_n$. For $H_3B{\cdot}NMe_2H$,

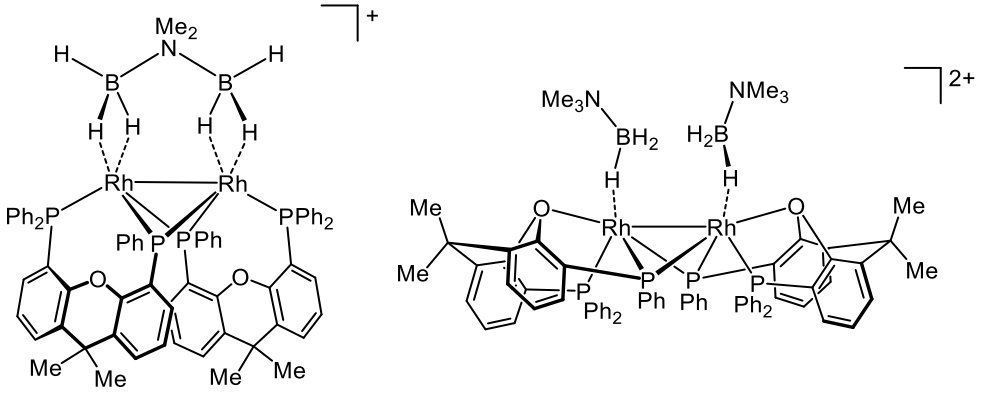
$H_2B{=}NMe_2$ would form and cyclise to give $(H_2BNMe_2)_2$. Chain propagation was proposed to operate by a coordination/insertion process (analogous to single site Ziegler Natta polymerisation of olefins),[101] and the chain termination event of the polymerisation was proposed to occur via hydrogenolysis of complex **i-17**. The role of H_2 was corroborated by comparison of polymer molecular weight which was much longer in the open system (M_n = 22,700 g mol^{-1}, Đ = 2.1) versus the closed system (M_n = 2,800 g mol^{-1}, Đ = 1.8) where H_2 pressure was able to build up.



Scheme 1.17 Weller's mechanistic proposal for on-metal dehydropolymerisation of $H_3B{\cdot}NMeH_2$ using the precatalyst [Rh(κ^2-P,P-Xantphos-Ph)(η^2-$H_2B(CH_2CH_2{}^tBu){\cdot}NMe_3$][BAr$^F{}_4$] (**i-13**). [BAr$^F{}_4$]$^-$ anions not shown for clarity.

Later work on the {Rh(Xantphos-Ph)}$^+$ system led to the isolation a bimetallic Rh_2 complex in which one of the phosphines on each Xantphos-Ph ligand had undergone P–C activation.[5] At 5 mol% catalyst loading, the reaction of **i-13** with $H_3B{\cdot}NMe_2H$ revealed that [{Rh(κ^2-P,P-Xantphos-Ph′)}$_2$(η^{2}η^2-$H_3BNMe_2BH_3$)][BAr$^F{}_4$] (**i-18**, Figure 1.18, Xantphos-Ph′ = 4-phenylphosphido-5-diphenylphosphino-9,9-dimethylxanthene) was the major organometallic product at the end of catalysis. This complex could be fully characterised, and its crystal structure reported. The related bimetallic complex [{Rh(κ^3-P,O,P-Xantphos-Ph′)}$_2$(η^1-$H_3B{\cdot}NMe_3$)$_2$][BAr$^F{}_4$]$_2$

(**i-19**) was also reported, and tested in catalysis with $H_3B{\cdot}NMe_2H$ (Figure 1.18). This showed similar kinetic behaviour to that of monometallic complex **i-13** reported in 2014,[4] hence the monometallic or bimetallic nature of the active catalytic species in the $\{Rh(Xantphos\text{-}Ph)\}^+$ system could not be confirmed. This hypothesis was further supported as polyaminoborane, $(H_2BNMeH)_n$, formed using complex **i-19** (0.1 mol% loading) with $H_3B{\cdot}NMeH_2$ had similar molecular weight and dispersity values (M_n = 28,700 g mol^{-1}, Đ = 1.7) to that reported using 0.2 mol% **i-13** (vide supra).

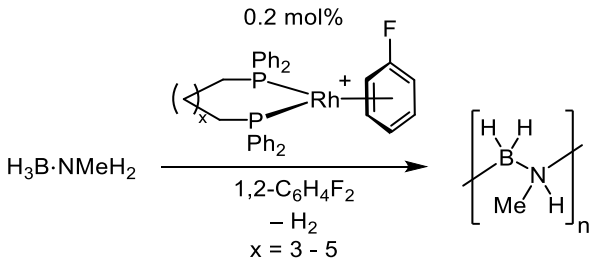


i-18 **i-19**

Figure 1.18 P–C activated Xantphos-Ph complex **i-18** observed at the end of $H_3B{\cdot}NMe_2H$ dehydrocoupling using precatalyst **i-13**. Complex **i-19** is a closely related $H_3B{\cdot}NMe_3$ analogue of **i-18** which could be reliably prepared and crystallised. $[BAr^F{}_4]^-$ anions not shown for clarity.

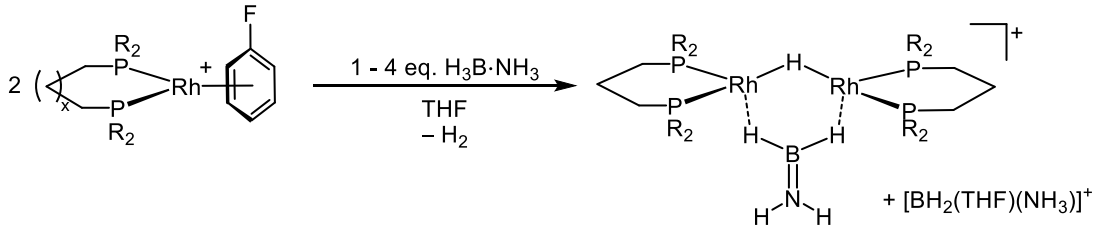
In 2011, Weller and Manners reported the dehydrocoupling of $H_3B{\cdot}NMe_2H$ and $H_3B{\cdot}NMeH_2$ using $[Rh(Ph_2P(CH_2)_xPPh_2)(\eta^6\text{-}C_6H_5F)][BAr^F{}_4]$ (x = 3 – 5) in 1,2-$C_6H_4F_2$ solvent (Scheme 1.18).[1] Investigating the kinetics using $H_3B{\cdot}NMe_2H$ showed TOF values which decreased with increasing chain length of the bisphosphine ligand backbone (i.e. for x = 3, TOF ≈ 1,250 h^{-1}), proposed to be due to influence of bisphosphine ligand bite angle. If the first step of the reaction is to coordinate the amine borane to the rhodium centre, as per the generally accepted inner sphere mechanism (Scheme 1.11), a smaller bite angle was proposed to provide the weakest Rh···H_3B interaction and hence the highest activity.[54] An induction period was also observed before productive catalysis, which increased in length on increasing the catalyst loading, however classical heterogeneous testing suggested the reaction was in fact homogeneous. This was speculated to be due to the formation of inactive bimetallic complexes, since $[\{Rh(PPh_2(CH_2)_xPPh_2)\}_2(H)(H_2BNMe_2)][BAr^F{}_4]$

(x = 3 – 5) species were implicated by ESI-MS studies on stoichiometric reactions of each catalyst with $H_3B{\cdot}NMe_2H$. The dehydropolymerisation ability of the catalysts with $H_3B{\cdot}NMeH_2$ showed the formation of high molecular weight polymer (M_n = 77,700 g mol^{-1}, Đ = 2.2 for x = 3).



Scheme 1.18 Weller's small bite angle systems for the dehydropolymerisation of $H_3B{\cdot}NMeH_2$. $[BAr^F{}_4]^-$ anions not shown for clarity.

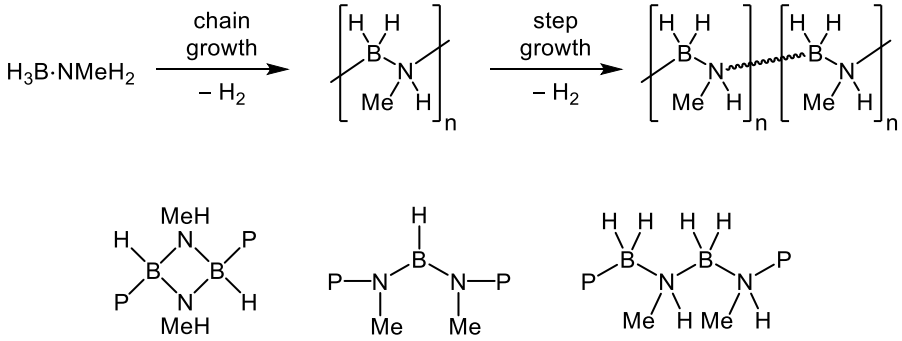
The same catalyst system was further probed in 2016 by Macgregor and Weller, where reaction of $[Rh(R_2P(CH_2)_3PR_2)(\eta^6\text{-}C_6H_5F)][BAr^F{}_4]$ (R = Ph **i-20**, ^{i}Pr **i-21**) with a slight excess of $H_3B{\cdot}NH_3$ in THF resulted in $[\{Rh(R_2P(CH_2)_3PR_2)\}_2(\mu\text{-}H)(\mu\text{-}H_2BNH_2)][BAr^F{}_4]$ (R = Ph **i-22**, ^{i}Pr **i-23**) (Scheme 1.19) alongside 1 equivalent of the boronium cation $[BH_2(THF)(NH_3)][BAr^F{}_4]$.[2] Both **i-22** and **i-23** could be characterised by single crystal X-ray crystallography, however reliable NMR spectroscopic data could only be obtained for the ^{i}Pr complex **i-23**. The analogous $\mu\text{-}H_2B{=}NMeH$ complex to **i-22** could also be observed in the reactions of **i-20** with $H_3B{\cdot}NMeH_2$, however could not be crystallographically characterised. In situ formed $[\{Rh(Ph_2P(CH_2)_3PPh_2)\}_2(\mu\text{-}H)(\mu\text{-}H_2BNMeH)][BAr^F{}_4]$ is an active catalyst for $H_3B{\cdot}NMeH_2$ dehydropolymerisation at 0.25 mol% catalyst loading (i.e. 0.5 mol% relative to Rh_1), and due to the very similar kinetic profile and TOF value found for this reaction compared to that using 0.5 mol% **i-20** (monometallic Rh_1), it could not be determined whether the active catalytic species was in fact monometallic or bimetallic, much like in the $\{Rh(Xantphos\text{-}Ph)\}^+$ system described previously.[5]



R = Ph (**i-20**), ^{i}Pr (**i-21**) R = Ph (**i-22**), ^{i}Pr (**i-23**)

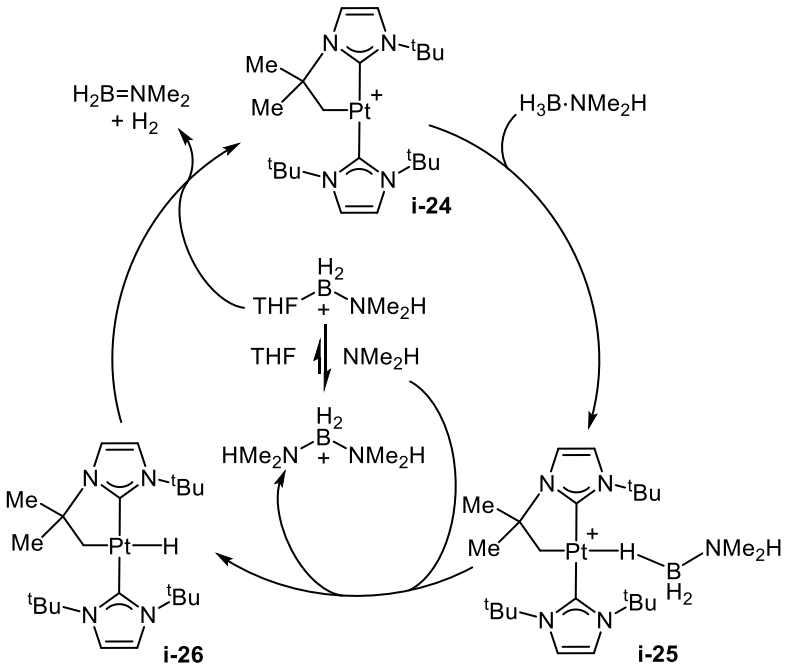
Scheme 1.19 Formation of bimetallic rhodium complex with the simplest aminoborane $H_2B{=}NH_2$ trapped in a bridging manner to the two rhodium atoms. $[BAr^F{}_4]^-$ anions not shown for clarity.

Two years later, the Weller group revisited $H_3B{\cdot}NMeH_2$ dehydropolymerisation in the presence of **i-20** for the synthesis of deuterated N-methylpolyaminoboranes.[3] Polymer growth kinetics using protio $H_3B{\cdot}NMeH_2$ pointed to an unusual hybrid chain growth/step growth polymerisation mechanism, as medium molecular weight polymer (0.5 mol% catalyst loading, $M_n \approx 10{,}000$ g mol^{-1}) was formed at conversions between 10% – 90% (indicative of chain growth), however at conversions greater than 90% a dramatic increase in M_n was observed – indicative of step growth polymerisation ($M_n = 30{,}000$ g mol^{-1} at 0.5 mol% catalyst loading) (Figure 1.15). The early stage mechanism at less than 90% conversion was proposed to be dehydrogenation/coordination/insertion, and the later step growth polymerisation amplified this, as an inverse dependence of M_n versus catalyst loading was observed (0.5 mol% **i-20**: $M_n = 30{,}000$ g mol^{-1}; 1.0 mol% **i-20**: $M_n = 10{,}100$ g mol^{-1}), and H_2 build up in the system led to shorter chains (0.5 mol% **i-20**: $M_n = 4{,}700$ g mol^{-1}), as seen previously for the Xantphos-Ph system **i-13**.[4] The late stage, step growth mechanism was supported by treatment of low molecular weight $(H_2BNMeH)_n$ ($M_n = 6{,}900$ g mol^{-1}) with 0.5 mol% **i-20** for 90 minutes in which polymer molecular weight approximately doubled. This mechanism is outlined in Scheme 1.20, alongside proposed possible motifs for the step growth polymer coupling process.



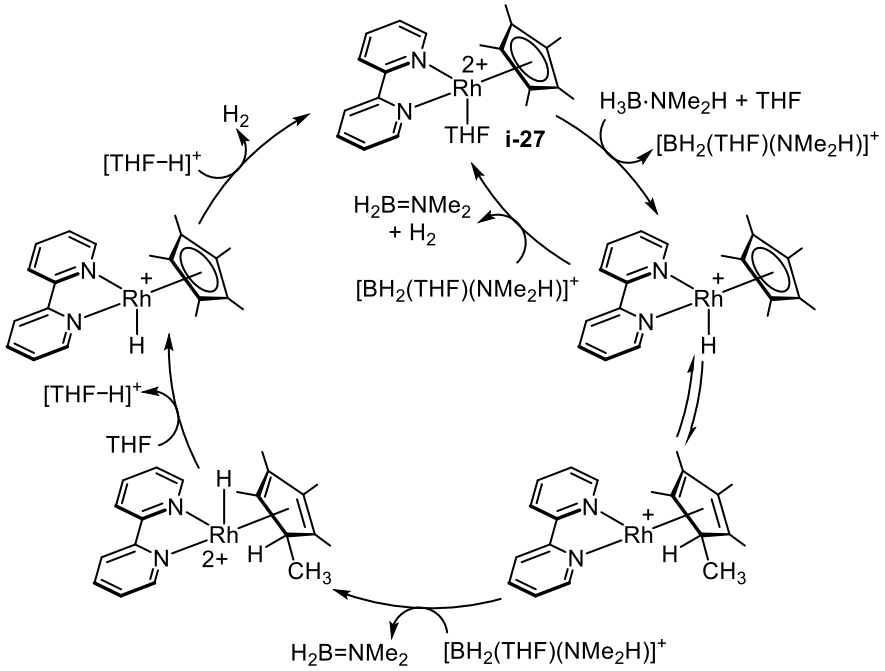
Scheme 1.20 Top: Weller's proposed hybrid chain growth/step growth polymerisation mechanism. Bottom: Possible coupling motifs formed by step growth polymerisation.

Formation of boronium cations may play a role in the dehydrocoupling of amine boranes. For example, $[BH_2(NH_3)_2][BAr^F{}_4]$ is formed as a by-product in the dehydrocoupling of $H_3B{\cdot}NH_3$ by Weller's $[Rh(R_2P(CH_2)_3PR_2)(\eta^6\text{-}C_6H_5F)][BAr^F{}_4]$ (R = Ph **i-20**, ^{i}Pr **i-21**) systems, however any other role of the boronium species was not speculated.[2] In 2013 Conejero and López-Serrano reported the dehydrocoupling of $H_3B{\cdot}NMe_2H$ to $(H_2BNMe_2)_2$ using $[Pt(I^tBu')(I^tBu)][BAr^F{}_4]$ **i-24** (I^tBu = 1,3-ditertbutylimidazol-2-ylidene, I^tBu' = cyclometallated I^tBu).[83] An experimental and DFT supported mechanism for this process is detailed in Scheme 1.21. Complex **i-24** initially reacts with the amine borane to form the sigma complex **i-25**. Hydrogen transfer from the BH_3 fragment to the platinum centre is assisted by free NMe_2H (resulting from B–N cleavage of $H_3B{\cdot}NMe_2H$), giving the neutral species $Pt(I^tBu')(I^tBu)H$ and boronium, $[BH_2(NMe_2H)_2]^+$, which in THF solution is in equilibrium with $[BH_2(THF)(NMe_2H)]^+$. This THF based boronium cation protonates neutral **i-26**, releasing $H_2B{=}NMe_2$, H_2 and reforming catalyst **i-24**.



Scheme 1.21 Proposed mechanism for the dehydrocoupling of $H_3B{\cdot}NMeH_2$ incorporating the involvement of boronium cations. $[BAr^F{}_4]^-$ anions not shown for clarity.

Similarly, in Freixa's half sandwich Ru system, [Ru(para-cymene)(bpy)(Cl)][Cl] (para-cymene = 4-isopropyltoluene, bpy = 2,2′-bipyridine), the dehydrocoupling of $H_3B{\cdot}NH_3$ was also proposed to proceed via protonation of the ruthenium hydride centre by $[BH_2(THF)(NH_3)]^+$ to form $H_2B{=}NH_2$ – in this instance boronium formation was confirmed using ESI-MS.[102] Shortly after, Nozaki also implicated the role of boronium in the dehydrocoupling of $H_3B{\cdot}NMe_2H$ using the THF adduct of $[M(Cp^*)(bpy)][OTf]_2$ (M = Rh (**i-27**), Ir, Cp* = = η^5-pentamethylcyclopentadienyl, bpy = 2,2′-bipyridine).[103] Two related mechanisms were hypothesised in these systems: a direct protonolysis pathway and a Cp* non-innocence mediated pathway. Interestingly, the rhodium complexes were found to be much more active than their iridium analogues, and this was supported by DFT calculations in which a lower energy was required for Cp* non-innocence for M = Rh. The proposed mechanism in shown in Scheme 1.22.



Scheme 1.22 Nozaki's direct protonolysis and Cp* non-innocence pathways for the dehydrocoupling of $H_3B{\cdot}NMe_2H$ which require the production of boronium cations. $[OTf]^-$ anions not shown for clarity.

Thus far, efforts to elucidate a universal mechanism for the dehydrocoupling or dehydropolymerisation of amine boranes have resulted in a complex landscape in which it is clear that these processes are system and substrate specific. Details such as the formation of bimetallic complexes from mononuclear precatalysts, the effect of B–N cleavage of the amine borane to give the corresponding amine and borane, and the role of boronium cations provide a plethora of possibilities, and complications, with much still to be explored.

1.7 Xantphos-^{i}Pr and DPEphos ligands in catalysis

With the success of Weller's Xantphos-Ph (complex **i-13**) and $Ph_2P(CH_2)_3PPh_2$ (complex **i-20**) systems in $H_3B{\cdot}NMeH_2$ dehydropolymerisation, systematic tuning of the ligand was proposed to give further insight into these mechanisms. Therefore, changing the phenyl groups of Xantphos-Ph to isopropyl to give Xantphos-^{i}Pr, or removing the Xantphos-Ph CMe_2 backbone to give DPEphos (Figure 1.19) may give further mechanistic insight and control of the dehydropolymerisation process. Both of these ligands have previously been utilised in organometallic chemistry.

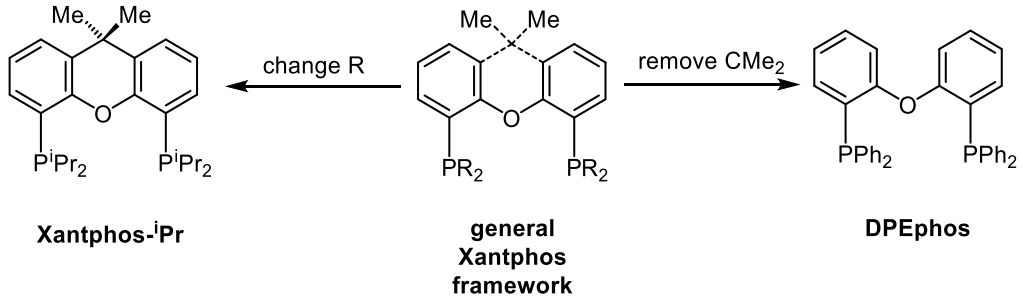


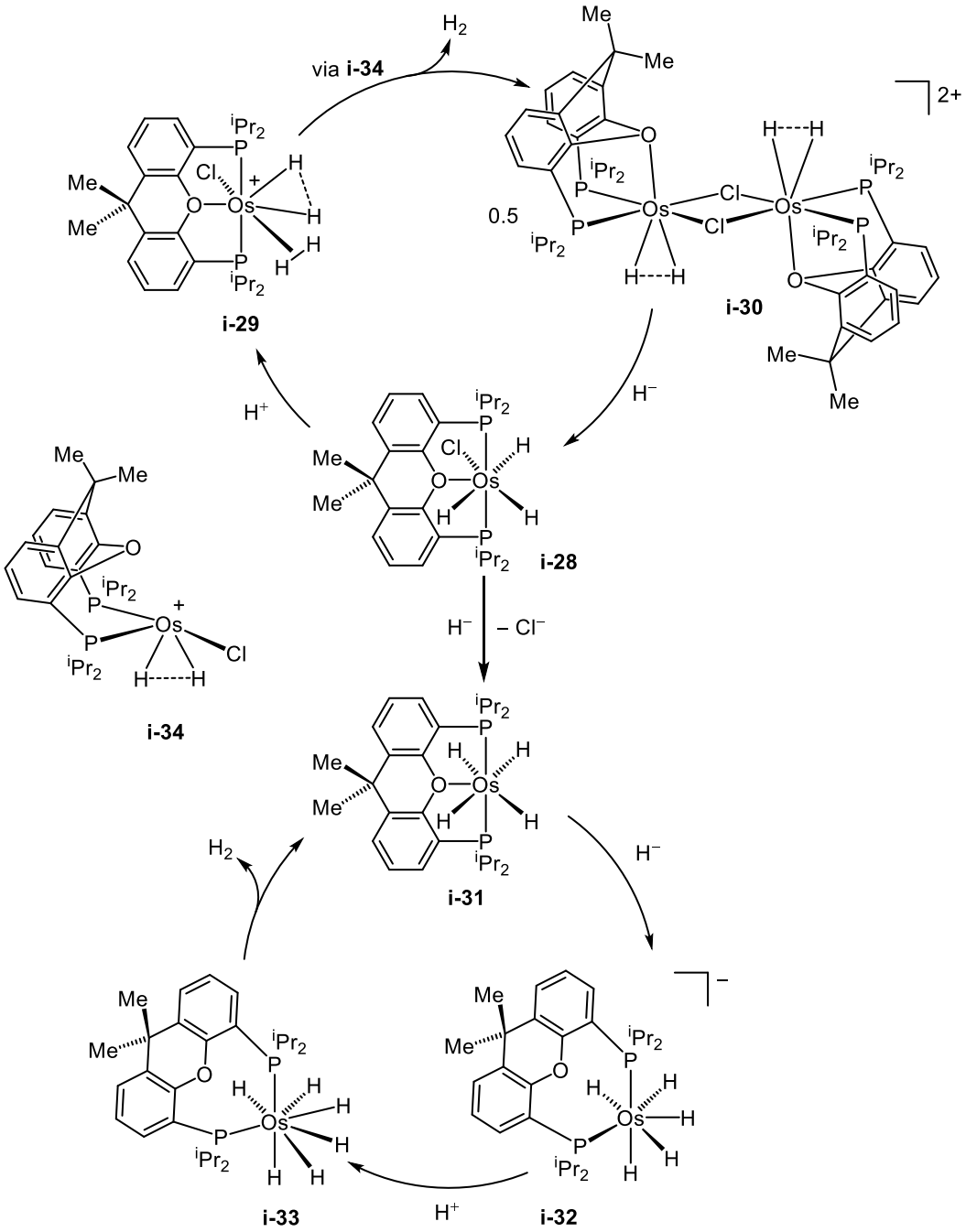
Figure 1.19 Altering the Xantphos ligand framework to give Xantphos-^{i}Pr and DPEphos ligands.

1.7.1 Xantphos-^{i}Pr

The Xantphos-^{i}Pr ligand (4,5-bis(diisopropylphosphino)-9,9-dimethylxanthene) was first synthesised by Esteruelas and co-workers in 2010,[104] and ligated to both ruthenium and osmium to form the tridentate complexes M(κ^3-P,O,P-Xantphos-^{i}Pr)(Cl)$_3$ (M = Ru, Os). Later, in 2013, Goldman and co-workers ligated Xantphos-^{i}Pr to rhodium also in a κ^3-P,O,P fashion.[105]

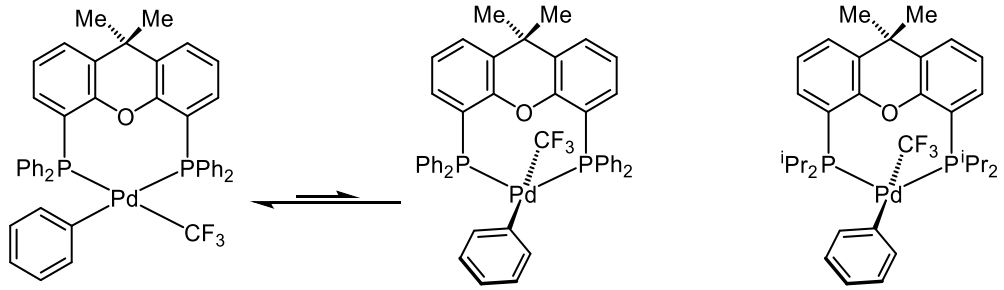
Esteruelas has extensively explored Xantphos-^{i}Pr transition metal complexes, such as cis κ^2-P,P, fac κ^3-P,O,P and mer κ^3-P,O,P Xantphos-^{i}Pr osmium complexes (Scheme 1.23).[106-107] For example, sequential addition of H^+ and H^- or alternatively H^- then H^+ to the trihydride complex mer-Os(κ^3-P,O,P-Xantphos-^{i}Pr)(H)$_3$(Cl) (**i-28**) promotes changes in ligand binding mode. Addition of H^+ to **i-28** forms the compressed dihydride dihydrogen complex mer-[Os(κ^3-P,O,P-Xantphos-^{i}Pr)(Cl)(H···H)(μ^2-H$_2$)]$^+$ (**i-29**), which can lose H_2 to form fac-[Os(κ^3-P,O,P-Xantphos-^{i}Pr)$_2$(H···H)(μ-Cl)]$^{2+}$ (**i-30**). Addition of H^- to **i-30** reforms trihydride complex **i-28**. Hydride addition to **i-28** gives mer-Os(κ^3-P,O,P-Xantphos-^{i}Pr)(H)$_4$ (**i-31**) with displacement of the chloride ligand. Further hydride addition displaces the Xantphos-^{i}Pr ether to give cis-[Os(κ^2-P,P-Xantphos-^{i}Pr)(H)$_5$]$^-$ (**i-32**). The κ^2-P,P geometry of the ligand is retained on proton addition to **i-32**, yielding cis-Os(κ^2-P,P-Xantphos-^{i}Pr)(H)$_6$ (**i-33**), though over time, this slowly lost one equivalent of H_2, reforming the tetrahydride complex **i-31** and closing the cycle. A more recent study by the same group proposed that H_2 loss to form **i-30** from **i-29** proceeded through cis-[Os(κ^2-P,P-Xantphos-^{i}Pr)(H···H)(Cl)]$^+$ (**i-34**, Scheme 1.23), which could be trapped by HBpin and HBcat to form mer-

[Os(κ^3-P,O,P-Xantphos-^{i}Pr)(H)(Cl)(η^2-HBpin)] and mer-[Os(κ^3-P,O,P-Xantphos-^{i}Pr)](H)(Cl)(η^2-HBcat))] respectively.[108] From these results, the Xantphos-^{i}Pr ligand favoured trans phosphine coordination in the κ^3-P,O,P complexes, and in line with this, complex **i-30** is the only crystallographically characterised example of the Xantphos-^{i}Pr ligand in a fac κ^3-P,O,P geometry and it is notable that this has strongly bound, geometry-directing bridging chlorides.



Scheme 1.23 Variable coordination modes of the Xantphos-^{i}Pr ligand obtained by Esteruelas. Counterions not shown for clarity.

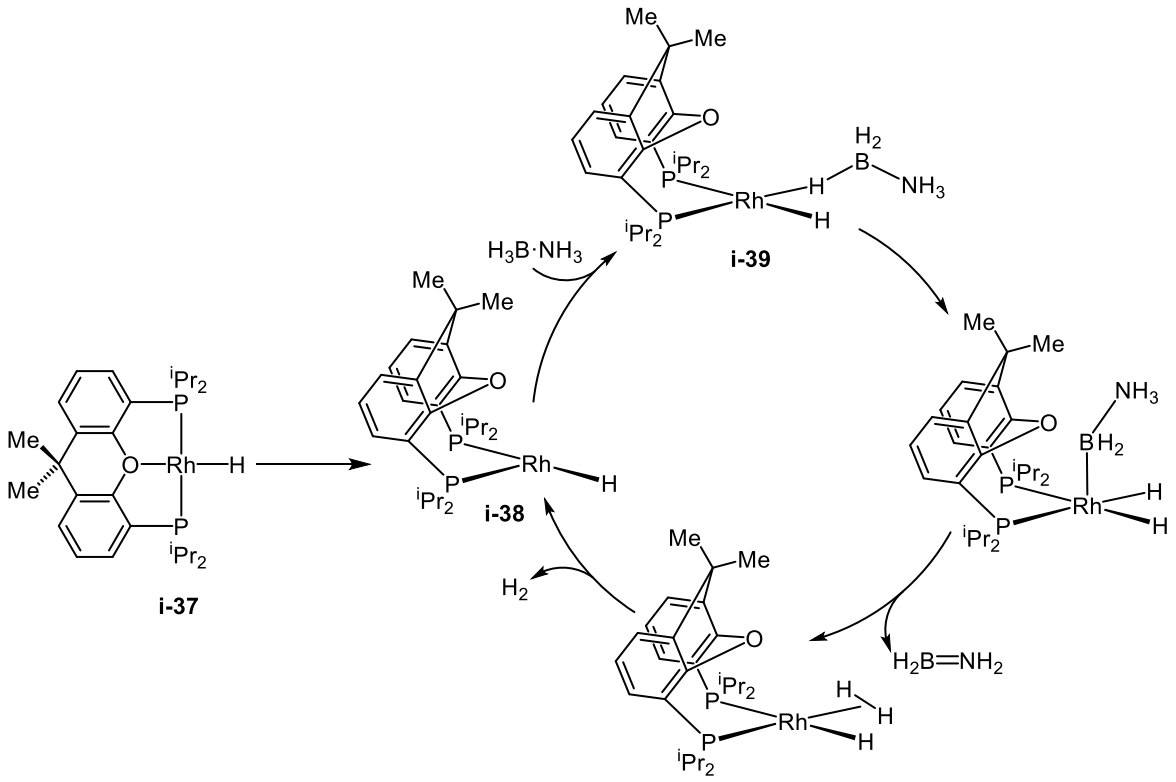
A direct comparison of Xantphos-^{i}Pr and Xantphos-Ph ligands coordinated to palladium was made by Bakhmutov, Grushin, Macgregor and co-workers in their synthesis of Pd(Xantphos-R)(Ph)(CF_3) complexes (R = ^{i}Pr, Ph).[109] For Xantphos-Ph, both cis and trans isomers were observed in solution, and the cis isomer could be crystallographically characterised (**i-35**, Scheme 1.24). However the analogous Xantphos-^{i}Pr complex was found to be exclusively trans κ^2-P,P bound in both the solid state and in solution (**i-36**, Scheme 1.24). In addition, reductive elimination from trans-Pd(κ^2-P,P-Xantphos-^{i}Pr)(Ph)(CF_3) to form Ph–CF_3 was much slower in comparison to the Xantphos-Ph analogue, presumably due to the lower propensity for the Xantphos-^{i}Pr ligand to bind in a cis manner required for this process.



cis-**i-35** trans-**i-35** **i-36**

Scheme 1.24 The difference in binding of the Xantphos-^{i}Pr ligand compared to Xantphos-Ph.

Esteruelas studied the Xantphos-^{i}Pr ligand in catalytic ammonia borane and dimethylamine borane dehydrogenation using neutral Rh(κ^3-P,O,P-Xantphos-^{i}Pr)(H) (**i-37**).[110] Turnover frequency values at 50% conversion for $H_3B{\cdot}NH_3$ and $H_3B{\cdot}NMe_2H$ substrates were 3,150 h^{-1} and 1,725 h^{-1} respectively, the increased steric bulk at nitrogen in $H_3B{\cdot}NMe_2H$ likely to cause a slower rate. The mechanism for $H_3B{\cdot}NH_3$ dehydrogenation was probed by DFT calculations and showed that dissociation of the oxygen atom of the Xantphos-^{i}Pr ligand occurred to form a tricoordinate T-shaped intermediate (**i-38**) to which the amine borane could bind to form a sigma complex (**i-39**) (Scheme 1.25). The mechanism suggested proposed that the ligand remained cis κ^2-P,P coordinated to the rhodium centre throughout the catalytic cycle, although there was no experimental evidence to support this.



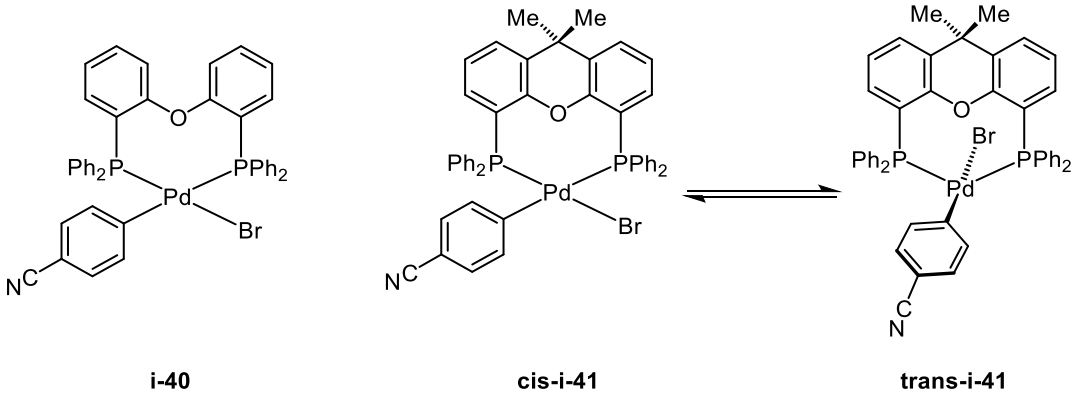
Scheme 1.25 The proposed mechanism of $H_3B{\cdot}NH_3$ dehydrocoupling by a neutral {Rh(Xantphos-^{i}Pr)} complex.

Given the relatively few examples of the Xantphos-^{i}Pr ligand in catalysis, and its success in $H_3B{\cdot}NH_3$ dehydrocoupling, exploring this ligand in terms of its transition metal complexes and reactivity with amine boranes may provide new avenues into main group dehydrocoupling mechanisms.

1.7.2 DPEphos

DPEphos was initially synthesised by van Leeuwen and co-workers in 1995 for use as a κ^2-P,P bidentate ligand.[23] Its natural bite angle of 102.2° was calculated to be lower than that of Xantphos-type ligands.[23] This, combined with the data in Figure 1.8, suggests that the DPEphos ligand may be more likely to form cis κ^2-P,P bound complexes than Xantphos-Ph. A kinetic study on the palladium catalysed amination of aryl triflates and aryl bromides was reported by van Leeuwen using neutral complexes Pd(L)(para-C_6H_4CN)(Br) (L = e.g. DPEphos, Xantphos-Ph).[111] The

DPEphos ligand provided cis κ^2-P,P coordination to the metal centre only (**i-40**), whilst Pd(Xantphos-Ph)(para-C_6H_4CN)(Br) (**i-41**) showed cis-trans isomerisation in solution, with the trans complexes shown to be the crystallographically characterised form (Scheme 1.26). For the Xantphos-Ph complex, a weak Pd···O interaction was proposed, with a Pd–O distance of 2.698(2) Å.[112] Only the complexes capable of cis-trans isomerisation gave appreciable conversions during the amination of bromobenzene, which suggested that the ability of the ligand to adopt different coordination motifs was important. In particular, the lower propensity for DPEphos to form trans P,P-bound complexes compared to Xantphos-Ph was of interest.

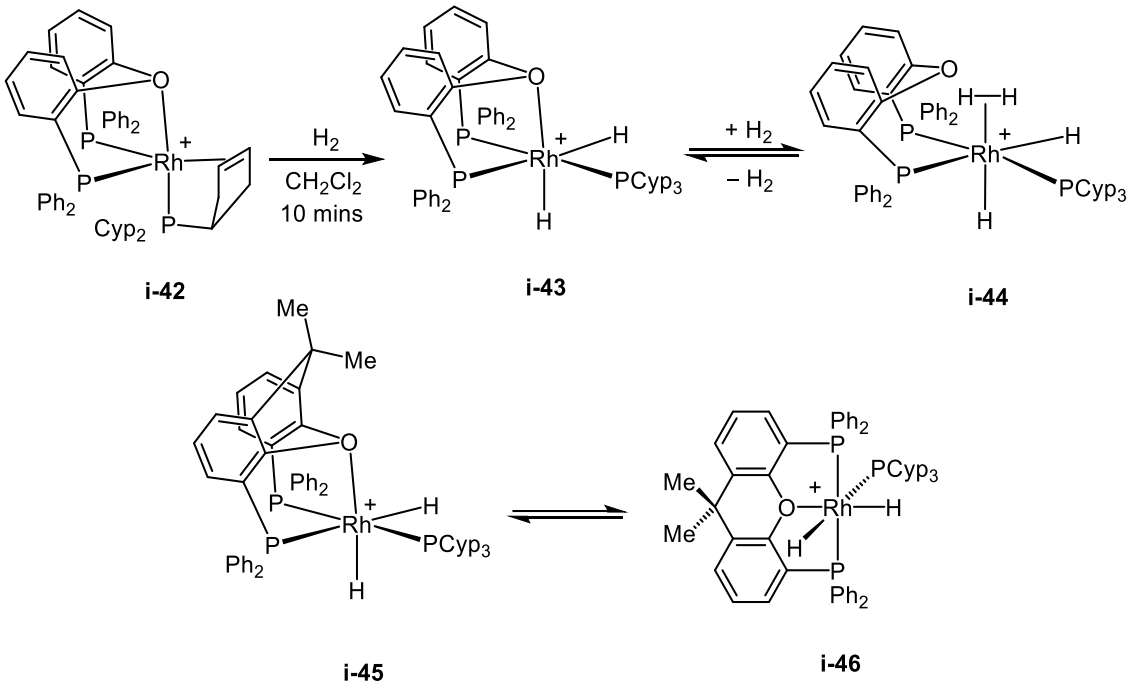


i-40 **cis-i-41** **trans-i-41**

Scheme 1.26 The difference in binding of the DPEphos ligand compared to Xantphos-Ph.

The Weller group reported that on placing fac-[Rh(κ^3-P,O,P-DPEphos){$PCyp_2(\eta^2$-C_5H_7)}][BAr^F_4] (**i-42**) under a H_2 atmosphere, the bound alkene was hydrogenated and at room temperature the major species formed was fac-[Rh(κ^3-P,O,P-DPEphos)$(H)_2(PCyp_3)$][BAr^F_4] (**i-43**) (Scheme 1.27), which was characterised by single crystal X-ray diffraction.[113] At −50°C under H_2 this complex was in equilibrium with the dihydrogen dihydride complex [Rh(κ^2-P,P-DPEphos)(η^2-H_2)$(H)_2(PCyp_3)$][BAr^F_4] (**i-44**). In order for this equilibrium to occur, the central ether linkage of the DPEphos ligand must dissociate from the metal to allow coordination of a dihydrogen molecule, hence acting in a hemilabile manner (Scheme 1.27). In comparison, the analogous study using the Xantphos-Ph ligand showed that the dihydrogen adduct [Rh(κ^2-P,P-Xantphos-Ph)(η^2-H_2)$(H)_2(PCyp_3)$][BAr^F_4] was not formed in equilibrium with fac-[Rh(κ^3-P,O,P-Xantphos-Ph)$(H)_2(PCyp_3)$][BAr^F_4] (**i-45**), but instead fac-mer isomerisation occurred from which the

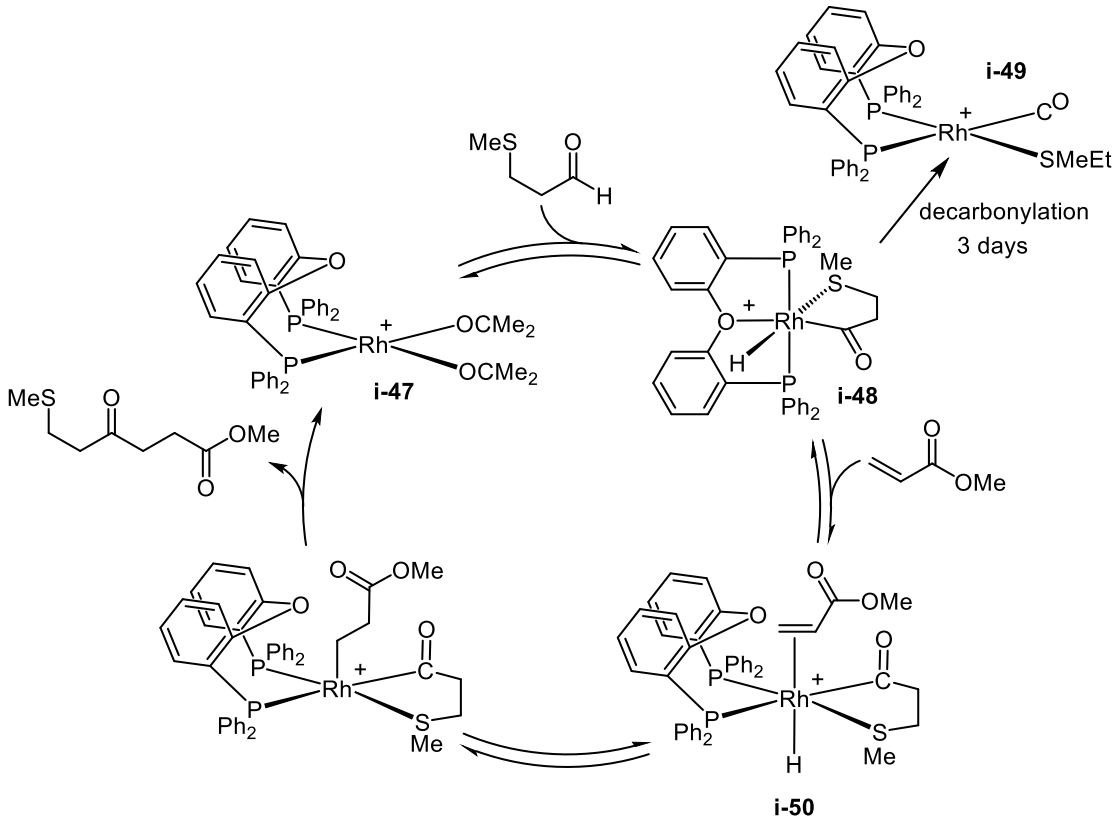
corresponding mer isomer, mer-[Rh(κ^3-P,O,P-Xantphos-Ph)$(H)_2(PCyp_3)$][$BAr^F{}_4$] (**i-46**), could be observed (Scheme 1.27) – indicating that the Rh–O bond in the Xantphos-Ph complexes were more persistent than in the analogous DPEphos complexes, and must outcompete H_2 binding. Equilibrium studies showed that the fac isomer **i-45** was slightly favoured over the mer (**i-46**), due to entropic factors.



Scheme 1.27 Variable binding modes of DPEphos and the difference in ability for the DPEphos ligand to dissociate the ether linker during the coordination of H_2 compared to that of Xantphos-Ph. $[BAr^F{}_4]^-$ anions not shown for clarity.

The hemilabile nature of DPEphos has been exploited by Weller and Willis in studies centred on the hydroacylation reaction of alkenes using β-S-substituted aldehydes.[114-117] C–H activation of an aldehyde at a Rh(I) centre to form an acyl hydride intermediate, followed by insertion of an olefin/alkyne and reductive elimination of a ketone product requires oxidation state changes and the formation of latent coordination sites during catalysis. However, catalyst deactivation may occur due to reductive decarbonylation of the low coordinate acyl hydride intermediate. The DPEphos ligand was shown to be able to stabilise the acyl hydride intermediate formed by aldehyde addition to **i-47** by coordination of the ether linker, forming [Rh(κ^3-P,O,P-DPEphos (H)($MeSCH_2CH_2CO$)][$CB_{11}H_6Cl_6$] (**i-48**). As reductive decarbonylation of this species to form **i-49**

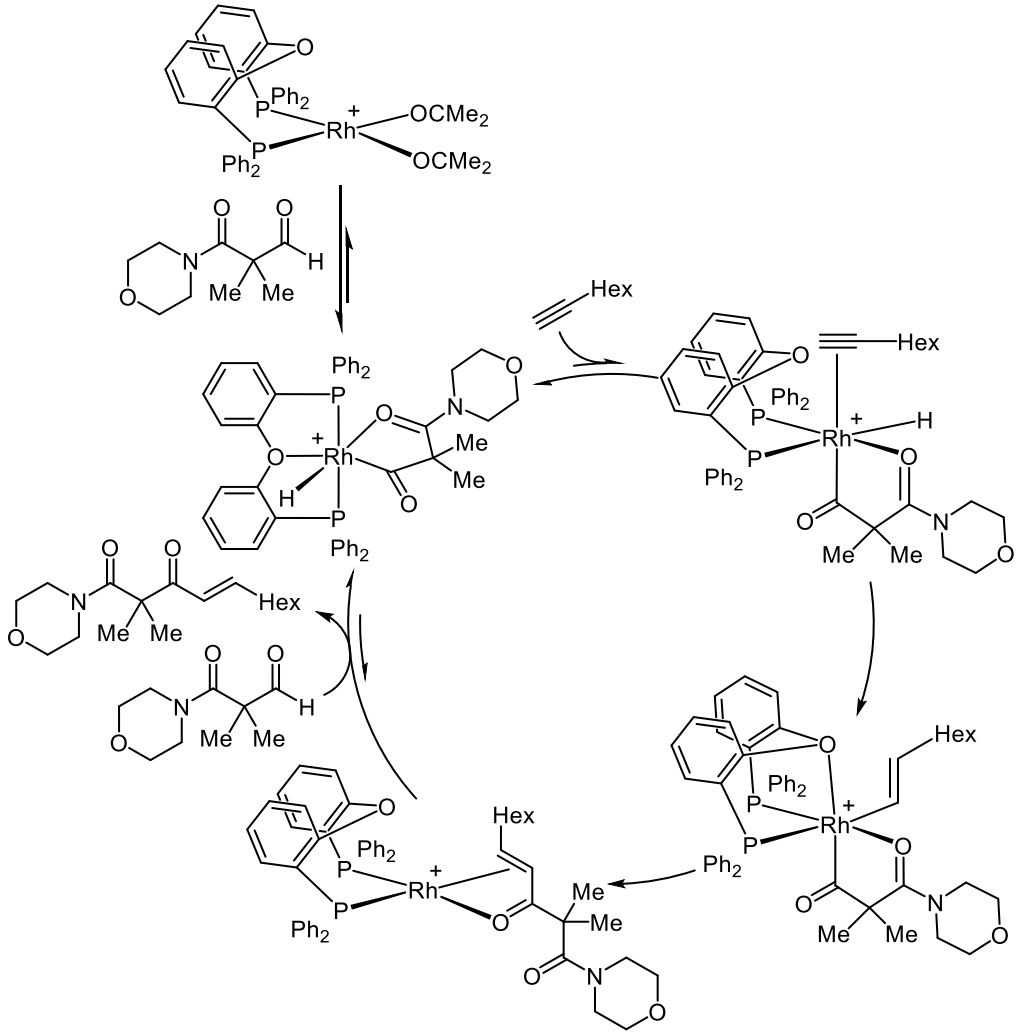
was much slower than with other non-hemilabile ligands, such as dppe, this allowed for more challenging substrates to be tackled in hydroacylation catalysis. For productive hydroacylation to occur, however, dissociation of the bound oxygen is required prior to binding of alkene, which was expected to form [Rh(κ^2-P,P-DPEphos)(H)(η^2-H_2C=CHCOOMe)(MeSCH_2CH_2CO)][$CB_{11}H_6Cl_6$] (**i-50**). The overall proposed catalytic cycle for this transformation is detailed in Scheme 1.28 and shows the importance of the ability for the DPEphos ether group to bind to the metal centre to stabilise intermediates, as well as dissociate from rhodium in order to allow further reactivity to occur. Notably, the use of Xantphos-Ph in place of DPEphos gave a significantly lower turnover frequency,[117] as the central oxygen atom was too strongly bound in the mer κ^3-P,O,P geometry (analogous to complex **i-48**) to allow for alkene complexation.



Scheme 1.28 Proposed catalytic cycle for the hydroacylation of alkenes using the {Rh(DPEphos)} fragment. [$CB_{11}H_6Cl_6$]$^-$ anions not shown for clarity.

Continuing the theme of hydroacylation, an extensive mechanistic study of the hydroacylation of 2,2-dimethyl-3-morpholino-3-oxopropanal with 1-octyne using {Rh(κ^2-P,P-DPEphos)}$^+$ led to a

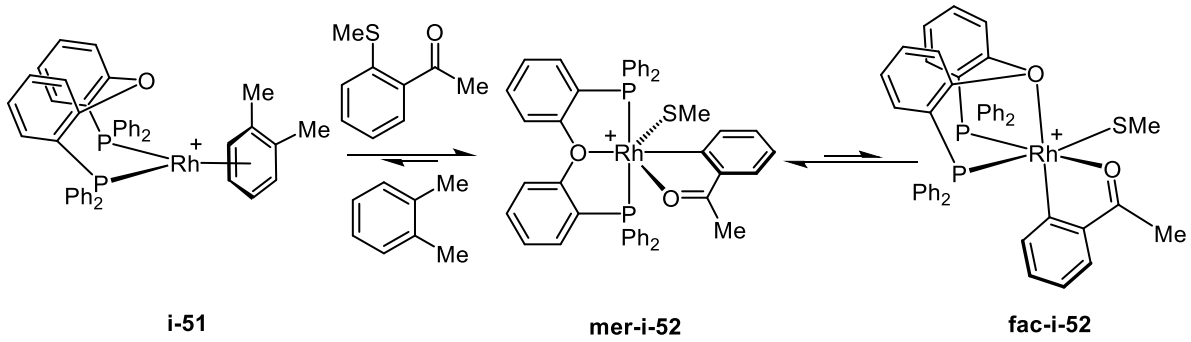
reaction with no decarbonylation, controlled selectivity and gram scale synthesis of the product.[118] The mechanism detailed in Scheme 1.29 importantly shows the necessity and ability for the DPEphos ligand to occupy cis κ^2-PP, fac κ^3-POP and mer κ^3-POP geometries in this process.



Scheme 1.29 Weller's proposed mechanism for the hydroacylation of 1-octyne in a system which showed no decarbonylation. $[BAr^F{}_4]^-$ anions not shown for clarity.

Another example of catalysis in which the DPEphos was used with success, and the flexible nature of the ligand shown, was in alkyne carbothiolation.[119] The Rh(I) κ^2-P,P-DPEphos precatalyst (**i-51**) oxidatively added an aryl methyl sulphide to form a mer κ^3-P,O,P-DPEphos complex (**i-52**), which was in equilibrium with its analogous fac κ^3-P,O,P complex (Scheme 1.30). This equilibrium was proposed to operate through a five coordinate intermediate where the DPEphos ether dissociated from the metal in order to access a conformationally flexible species required for fac-mer

isomerisation. Similar behaviour was noted with the Xantphos-Ph ligand in which it was demonstrated that the fac κ^3-P,O,P-Xantphos-Ph catalyst was a more active catalyst than the mer.[120]



Scheme 1.30 Isomerisation of the catalyst resting state and requirement of DPEphos to obtain variable coordination modes during the carbothiolation of alkynes using a {Rh(DPEphos)} fragment. [BAr$^F{}_4$]$^-$ anions not shown for clarity.

A DFT study on alkene hydroamination reactions catalysed by Hartwig's {Rh(DPEphos)}$^+$ fragment[121] was published by Couce-Rios et al. in 2016.[122] In this, structural isomers (κ^2-P,P-DPEphos versus κ^3-P,O,P-DPEphos) of proposed intermediates along the calculated reaction pathway were studied. Interestingly, the structures for which DPEphos occupied κ^3-P,O,P coordination sites were more than 6 kcal mol^{-1} higher in energy than their κ^2-P,P-DPEphos analogues, suggesting that bidentate coordination of the DPEphos phosphines was energetically more favourable than tridentate coordination with involvement of the central ether.

With these examples in mind, it is apparent that whilst structurally similar, the DPEphos ligand generally prefers to bind in a κ^2-P,P manner in comparison to Xantphos-Ph, where ether binding is more accessible. This difference in reactivity may be interesting to probe and compared with the successful Xantphos-Ph, catalyst **i-13**.

1.8 Summary

This thesis aims to obtain further insight into the mechanism of $H_3B{\cdot}NMeH_2$ dehydropolymerisation. The cationic {Rh(Xantphos-^{i}Pr)}$^+$ and {Rh(DPEphos)}$^+$ fragments have

been selected as systems related to the successful Xantphos-Ph catalyst, as both ligands can obtain κ^2 and κ^3 geometries (Figure 1.8) which have been required in previous mechanistic studies.

In Chapter 2, the coordination chemistry and stoichiometric reactivity of $\{Rh(Xantphos\text{-}^{i}Pr)\}^+$ with $H_3B{\cdot}NMeH_2$ is explored, and the catalytic dehydropolymerisation ability of this system is detailed in Chapter 3. In Chapter 4, a suitable DPEphos-ligated precatalyst is synthesised and its reactivity with amine boranes is probed, with kinetic studies of $H_3B{\cdot}NMeH_2$ dehydropolymerisation using this system undertaken in Chapter 5.

1.9 References

1. Dallanegra, R.; Robertson, A. P. M.; Chaplin, A. B.; Manners, I.; Weller, A. S., Tuning the $[L_2Rh{\cdots}H_3B{\cdot}NR_3]^+$ interaction using phosphine bite angle. Demonstration by the catalytic formation of polyaminoboranes. *Chem. Commun.* **2011,** *47* (13), 3763-3765.
2. Kumar, A.; Beattie, N. A.; Pike, S. D.; Macgregor, S. A.; Weller, A. S., The Simplest Amino-Borane $H_2B{=}NH_2$ Trapped on a Rhodium Dimer: Pre-Catalysts for Amine-Borane Dehydropolymerization. *Angew. Chem. Int. Ed.* **2016,** *55* (23), 6651-6656.
3. Colebatch, A. L.; Hawkey Gilder, B. W.; Whittell, G. R.; Oldroyd, N. L.; Manners, I.; Weller, A. S., A General, Rhodium-Catalyzed, Synthesis of Deuterated Boranes and N-Methyl Polyaminoboranes. *Chem. Eur. J.* **2018,** *24* (21), 5450-5455.
4. Johnson, H. C.; Leitao, E. M.; Whittell, G. R.; Manners, I.; Lloyd-Jones, G. C.; Weller, A. S., Mechanistic Studies of the Dehydrocoupling and Dehydropolymerization of Amine-Boranes Using a $[Rh(Xantphos)]^+$ Catalyst. *J. Am. Chem. Soc.* **2014,** *136* (25), 9078-9093.
5. Johnson, H. C.; Weller, A. S., P–C-Activated Bimetallic Rhodium Xantphos Complexes: Formation and Catalytic Dehydrocoupling of Amine-Boranes. *Angew. Chem. Int. Ed.* **2015,** *54* (35), 10173-10177.
6. Crabtree, R. H., *The Organometallic Chemistry of the Transition Metals*. 4th ed.; John Wiley & Sons, Inc.: 2005.
7. Hartwig, J. F., *Organotransition Metal Chemistry*. University Science Books: 2010.
8. Ziegler, K.; Holzkamp, E.; Breil, H.; Martin, H., Polymerisation von Äthylen und anderen Olefinen. *Angew. Chem.* **1955,** *67* (16), 426-426.
9. Small, B. L.; Brookhart, M., Polymerization of Propylene by a New Generation of Iron Catalysts: Mechanisms of Chain Initiation, Propagation, and Termination. *Macromolecules* **1999,** *32* (7), 2120-2130.
10. Clark, T. J.; Lee, K.; Manners, I., Transition-metal-catalyzed dehydrocoupling: A convenient route to bonds between main-group elements. *Chem. Eur. J.* **2006,** *12* (34), 8634-8648.
11. Leitao, E. M.; Jurca, T.; Manners, I., Catalysis in service of main group chemistry offers a versatile approach to p-block molecules and materials. *Nat. Chem.* **2013,** *5*, 817.
12. Evans, D.; Osborn, J. A.; Wilkinson, G., Hydroformylation of alkenes by use of rhodium complex catalysts. *J. Chem. Soc. A* **1968,** (0), 3133-3142.
13. Osborn, J. A.; Jardine, F. H.; Young, J. F.; Wilkinson, G., The preparation and properties of tris(triphenylphosphine)halogenorhodium(I) and some reactions thereof including catalytic homogeneous hydrogenation of olefins and acetylenes and their derivatives. *J. Chem. Soc. A* **1966,** (12), 1711-1732.
14. Adams, G. M.; Chadwick, F. M.; Pike, S. D.; Weller, A. S., A CH_2Cl_2 complex of a $[Rh(pincer)]^+$ cation. *Dalton Trans.* **2015,** *44* (14), 6340-6342.
15. Sewell, L. J.; Chaplin, A. B.; Abdalla, J. A. B.; Weller, A. S., Reversible C–H activation of a $P^tBu^iBu_2$ ligand to reveal a masked 12 electron $[Rh(PR_3)_2]^+$ cation. *Dalton Trans.* **2010,** *39* (32), 7437-7439.
16. Chaplin, A. B., Rhodium(I) Complexes of the Conformationally Rigid $IBioxMe_4$ Ligand: Isolation of a Stable Low-Coordinate T-Shaped Complex. *Organometallics* **2014,** *33* (3), 624-626.

17. Orpen, A. G.; Connelly, N. G., Structural evidence for the participation of P–X σ* orbitals in metal–PX_3 bonding. *J. Chem. Soc., Chem. Commun.* **1985,** (19), 1310-1311.
18. Dias, P. B.; Minas de Piedade, M. E.; Simões, J. A. M., Bonding and energetics of phosphorus(III) ligands in transition metal complexes. *Coord. Chem. Rev.* **1994,** *135-136*, 737-807.
19. Tolman, C. A., Steric effects of phosphorus ligands in organometallic chemistry and homogeneous catalysis. *Chem. Rev.* **1977,** *77* (3), 313-348.
20. Achord, P. D.; Kiprof, P.; Barker, B., Study of bite angle effects in hydroformylation. *J. Mol. Struct. (Theochem)* **2008,** *849* (1), 103-111.
21. Casey, C. P.; Whiteker, G. T., The Natural Bite Angle of Chelating Diphosphines. *Isr. J. Chem.* **1990,** *30* (4), 299-304.
22. Alcock, N. W.; Brown, J. M.; Jeffery, J. C., Structural and chemical aspects of phosphino-ethers as chelating ligands in rhodium(I) cationic complexes. X-ray crystal structures of two phosphino ether rhodium carbonyl complexes. *J. Chem. Soc., Chem. Commun.* **1974,** (20), 829-830.
23. Kranenburg, M.; van der Burgt, Y. E. M.; Kamer, P. C. J.; van Leeuwen, P. W. N. M.; Goubitz, K.; Fraanje, J., New Diphosphine Ligands Based on Heterocyclic Aromatics Inducing Very High Regioselectivity in Rhodium-Catalyzed Hydroformylation: Effect of the Bite Angle. *Organometallics* **1995,** *14* (6), 3081-3089.
24. Morales-Morales, D.; Jensen, C., *The Chemistry of Pincer Compounds*. Elsevier: Amsterdam, 2007.
25. Adams, G. M.; Weller, A. S., POP-type ligands: Variable coordination and hemilabile behaviour. *Coord. Chem. Rev.* **2018,** *355*, 150-172.
26. Jeffrey, J. C.; Rauchfuss, T. B., Metal complexes of hemilabile ligands. Reactivity and structure of dichlorobis(o-(diphenylphosphino)anisole)ruthenium(II). *Inorg. Chem.* **1979,** *18* (10), 2658-2666.
27. Braunstein, P.; Naud, F., Hemilability of Hybrid Ligands and the Coordination Chemistry of Oxazoline-Based Systems. *Angew. Chem. Int. Ed.* **2001,** *40* (4), 680-699.
28. Williams, G. L.; Parks, C. M.; Smith, C. R.; Adams, H.; Haynes, A.; Meijer, A. J. H. M.; Sunley, G. J.; Gaemers, S., Mechanistic Study of Rhodium/Xantphos-Catalyzed Methanol Carbonylation. *Organometallics* **2011,** *30* (22), 6166-6179.
29. Bruno, I. J.; Cole, J. C.; Edgington, P. R.; Kessler, M.; Macrae, C. F.; McCabe, P.; Pearson, J.; Taylor, R., New software for searching the Cambridge Structural Database and visualizing crystal structures. *Acta Cryst.* **2002,** *B58*, 389-397.
30. Groom, C. R.; Bruno, I. J.; Lightfoot, M. P.; Ward, S. C., The Cambridge Structural Database. *Acta Cryst.* **2016,** *B72*, 171-179.
31. The Cambridge Structural Database (CSD) search was conducted using the ConQuest package (August 2018). The outputs from this search can be found in the electronic appendices.
32. Krossing, I.; Raabe, I., Noncoordinating Anions-Fact or Fiction? A Survey of Likely Candidates. *Angew. Chem. Int. Ed.* **2004,** *43* (16), 2066-2090.
33. Paul, R. L.; Amoroso, A. J.; Jones, P. L.; Couchman, S. M.; Reeves, Z. R.; Rees, L. H.; Jeffery, J. C.; McCleverty, J. A.; Ward, M. D., Effects of metal co-ordination geometry on self-assembly: a monomeric complex with trigonal prismatic metal co-ordination *vs.* tetrameric complexes with octahedral metal co-ordination. *J. Chem. Soc., Dalton Trans.* **1999,** (10), 1563-1568.
34. Kannan, S.; Moody, M. A.; Barnes, C. L.; Duval, P. B., Fluoride Abstraction and Reversible Photochemical Reduction of Cationic Uranyl(VI) Phosphine Oxide Complexes. *Inorg. Chem.* **2006,** *45* (23), 9206-9212.
35. Kobayashi, H.; Sonoda, T.; Iwamoto, H.; Yoshimura, M., Tetrakis[3,5-di(*F*-methyl)phenyl]borate as the first efficient negatively charged phase transfer catalyst. Kinetic evidences. *Chem. Lett.* **1981,** *10* (5), 579-580.
36. Pike, S. D.; Thompson, A. L.; Algarra, A. G.; Apperley, D. C.; Macgregor, S. A.; Weller, A. S., Synthesis and Characterization of a Rhodium(I) σ-Alkane Complex in the Solid State. *Science* **2012,** *337* (6102), 1648-1651.
37. Douglas, T. M.; Molinos, E.; Brayshaw, S. K.; Weller, A. S., Rhodium Phosphine Olefin Complexes of the Weakly Coordinating Anions $[BArf_4]^-$ and $[1\text{-}closo\text{-}CB_{11}H_6Br_6]^-$. Kinetic versus Thermodynamic Factors in Anion Coordination and Complex Reactivity. *Organometallics* **2007,** *26* (3), 463-465.
38. Chaplin, A. B.; Weller, A. S., $[B(3,5\text{-}C_6H_3Cl_2)_4]^-$ as a Useful Anion for Organometallic Chemistry. *Eur. J. Inorg. Chem.* **2010,** *2010* (32), 5124-5128.
39. Krossing, I., The Facile Preparation of Weakly Coordinating Anions: Structure and Characterisation of Silverpolyfluoroalkoxyaluminates $AgAl(OR_F)_4$, Calculation of the Alkoxide Ion Affinity. *Chem. Eur. J.* **2001,** *7* (2), 490-502.
40. Kubas, G. J.; Ryan, R. R.; Swanson, B. I.; Vergamini, P. J.; Wasserman, H. J., Characterization of the First Examples of Isolable Molecular Hydrogen Complexes, $M(CO)_3(PR_3)(H_2)$ (M = Mo, W; R = Cy, *i*-Pr). Evidence for a Side-on Bonded H_2 Ligand. *J. Am. Chem. Soc.* **1984,** *106* (2), 451-452.

41. Kubas, G. J., Fundamentals of H_2 Binding and Reactivity on Transition Metals Underlying Hydrogenase Function and H_2 Production and Storage. *Chem. Rev.* **2007,** *107* (10), 4152-4205.
42. Heinekey, D. M.; Oldham, W. J., Coordination chemistry of dihydrogen. *Chem. Rev.* **1993,** *93* (3), 913-926.
43. McGrady, G. S.; Guilera, G., The multifarious world of transition metal hydrides. *Chem. Soc. Rev.* **2003,** *32* (6), 383-392.
44. Kubas, G. J., *Metal Dihydrogen and σ-Bond Complexes*. Kluwer: New York, 2001.
45. Shimoi, M.; Nagai, S.; Ichikawa, M.; Kawano, Y.; Katoh, K.; Uruichi, M.; Ogino, H., Coordination Compounds of Monoborane-Lewis Base Adducts: Syntheses and Structures of $[M(CO)_5(\eta^1\text{-}BH_3\cdot L)]$ (M = Cr, Mo, W; L = NMe_3, PMe_3, PPh_3). *J. Am. Chem. Soc.* **1999,** *121* (50), 11704-11712.
46. Algarra, A. G.; Sewell, L. J.; Johnson, H. C.; Macgregor, S. A.; Weller, A. S., A combined experimental and computational study of fluxional processes in sigma amine-borane complexes of rhodium and iridium. *Dalton Trans.* **2014,** *43* (29), 11118-11128.
47. Kawano, Y.; Hashiva, M.; Shimoi, M., Syntheses and Reactivity of Cationic Borane-Ruthenium Complexes $[(\eta^5\text{-}C_5R_5)Ru(PMe_3)_2(\eta^1\text{-}BH_3\cdot EMe_3)][BArf_4]$ (R = H, Me; E = N, P; $BArf_4$= $[B\{3,5\text{-}C_6H_3(CF_3)_2\}_4]$). *Organometallics* **2006,** *25* (18), 4420-4426.
48. Ledger, A. E. W.; Ellul, C. E.; Mahon, M. F.; Williams, J. M. J.; Whittlesey, M. K., Ruthenium Bidentate Phosphine Complexes for the Coordination and Catalytic Dehydrogenation of Amine- and Phosphine-Boranes. *Chem. Eur. J.* **2011,** *17* (31), 8704-8713.
49. Douglas, T. M.; Chaplin, A. B.; Weller, A. S.; Yang, X.; Hall, M. B., Monomeric and Oligomeric Amine-Borane σ-Complexes of Rhodium. Intermediates in the Catalytic Dehydrogenation of Amine-Boranes. *J. Am. Chem. Soc.* **2009,** *131* (42), 15440-15456.
50. Tang, C. Y.; Thompson, A. L.; Aldridge, S., Dehydrogenation of Saturated CC and BN Bonds at Cationic N-Heterocyclic Carbene Stabilized M(III) Centers (M = Rh, Ir). *J. Am. Chem. Soc.* **2010,** *132* (30), 10578-10591.
51. Dallanegra, R.; Chaplin, A. B.; Weller, A. S., Bis(σ-amine-borane) Complexes: An Unusual Binding Mode at a Transition-Metal Center. *Angew. Chem. Int. Ed.* **2009,** *48* (37), 6875-6878.
52. Johnson, H. C.; Robertson, A. P. M.; Chaplin, A. B.; Sewell, L. J.; Thompson, A. L.; Haddow, M. F.; Manners, I.; Weller, A. S., Catching the First Oligomerization Event in the Catalytic Formation of Polyaminoboranes: $H_3B\cdot NMeHBH_2\cdot NMeH_2$ Bound to Iridium. *J. Am. Chem. Soc.* **2011,** *133* (29), 11076-11079.
53. Kumar, A.; Johnson, H. C.; Hooper, T. N.; Weller, A. S.; Algarra, A. G.; Macgregor, S. A., Multiple metal-bound oligomers from Ir-catalysed dehydropolymerisation of $H_3B\cdot NH_3$ as probed by experiment and computation. *Chem. Sci.* **2014,** *5* (6), 2546-2553.
54. Chaplin, A. B.; Weller, A. S., Amine- and Dimeric Amino-Borane Complexes of the $\{Rh(P^iPr_3)_2\}^+$ Fragment and Their Relevance to the Transition-Metal-Mediated Dehydrocoupling of Amine-Boranes. *Inorg. Chem.* **2010,** *49* (3), 1111-1121.
55. Vidovic, D.; Addy, D. A.; Krämer, T.; McGrady, J.; Aldridge, S., Probing the Intrinisic Structure and Dynamics of Aminoborane Coordination at Late Transition Metal Centers: Mono(σ-BH) Binding in $[CpRu(PR_3)_2(H_2BNCy_2)]^+$. *J. Am. Chem. Soc.* **2011,** *133* (22), 8494-8497.
56. Stevens, C. J.; Dallanegra, R.; Chaplin, A. B.; Weller, A. S.; Macgregor, S. A.; Ward, B.; McKay, D.; Alcaraz, G.; Sabo-Etienne, S., $[Ir(PCy_3)_2(H)_2(H_2B\text{–}NMe_2)]^+$ as a Latent Source of Aminoborane: Probing the Role of Metal in the Dehydrocoupling of $H_3B\cdot NMe_2H$ and Retrodimerisation of $[H_2BNMe_2]_2$. *Chem. Eur. J.* **2011,** *17* (10), 3011-3020.
57. Alcaraz, G.; Chaplin, A. B.; Stevens, C. J.; Clot, E.; Vendier, L.; Weller, A. S.; Sabo-Etienne, S., Ruthenium, Rhodium, and Iridium Bis(σ-B–H) Diisopropylaminoborane Complexes. *Organometallics* **2010,** *29* (21), 5591-5595.
58. Grant, D. J.; Matus, M. H.; Anderson, K. D.; Camaioni, D. M.; Neufeldt, S. R.; Lane, C. F.; Dixon, D. A., Thermochemistry for the Dehydrogenation of Methyl-Substituted Ammonia Borane Compounds. *J. Phys. Chem. A* **2009,** *113* (21), 6121-6132.
59. Beweries, T., Organometallics for Hydrogen Storage Applications. In *Organometallics and Related Molecules for Energy Conversion*, Wong, W.-Y., Ed. Springer: Berlin, Heidelberg, 2015; pp 469-495.
60. Thomas, J.; Klahn, M.; Spannenberg, A.; Beweries, T., Group 4 metallocene catalysed full dehydrogenation of hydrazine borane. *Dalton Trans.* **2013,** *42* (41), 14668-14672.
61. Han, D.; Joksch, M.; Klahn, M.; Spannenberg, A.; Drexler, H. J.; Baumann, W.; Jiao, H.; Knitsch, R.; Hansen, M. R.; Eckert, H.; Beweries, T., Iridium(III) hydrido complexes for the catalytic dehydrogenation of hydrazine borane. *Dalton Trans.* **2016,** *45* (44), 17697-17704.
62. Sutton, A. D.; Burrell, A. K.; Dixon, D. A.; Garner, E. B.; Gordon, J. C.; Nakagawa, T.; Ott, K. C.; Robinson, J. P.; Vasiliu, M., Regeneration of Ammonia Borane Spent Fuel by Direct Reaction with Hydrazine and Liquid Ammonia. *Science* **2011,** *331* (6023), 1426-1429.

63. Resendiz-Lara, D. A.; Stubbs, N. E.; Arz, M. I.; Pridmore, N. E.; Sparkes, H. A.; Manners, I., Boron–nitrogen main chain analogues of polystyrene: poly(B-aryl)aminoboranes via catalytic dehydrocoupling. *Chem. Commun.* **2017,** *53* (85), 11701-11704.
64. Stephens, F. H.; Pons, V.; Tom Baker, R., Ammonia-borane: the hydrogen source par excellence? *Dalton Trans.* **2007,** (25), 2613-2626.
65. Johnson, H. C.; Weller, A. S., A *tert*-butyl-substituted amino-borane bound to an iridium fragment: A latent source of free $H_2B{=}N^tBuH$. *J. Organomet. Chem.* **2012,** *721-722*, 17-22.
66. García-Vivó, D.; Huergo, E.; Ruiz, M. A.; Travieso-Puente, R., Thermally Induced Dehydrogenation of Amine-Borane Adducts and Ammonia-Borane by Group 6 Cyclopentadienyl Complexes Having Single and Triple Metal–Metal Bonds. *Eur. J. Inorg. Chem.* **2013,** *2013* (28), 4998-5008.
67. Pons, V.; Baker, R. T.; Szymczak, N. K.; Heldebrant, D. J.; Linehan, J. C.; Matus, M. H.; Grant, D. J.; Dixon, D. A., Coordination of aminoborane, NH_2BH_2, dictates selectivity and extent of H_2 release in metal-catalysed ammonia borane dehydrogenation. *Chem. Commun.* **2008,** *48*, 6597-6599.
68. Jaska, C. A.; Temple, K.; Lough, A. J.; Manners, I., Rhodium-catalyzed formation of boron-nitrogen bonds: a mild route to cyclic aminoboranes and borazines. *Chem. Commun.* **2001,** (11), 962-963.
69. Denney, M. C.; Pons, V.; Hebden, T. J.; Heinekey, D. M.; Goldberg, K. I., Efficient Catalysis of Ammonia Borane Dehydrogenation. *J. Am. Chem. Soc.* **2006,** *128* (37), 12048-12049.
70. Bhunya, S.; Malakar, T.; Ganguly, G.; Paul, A., Combining Protons and Hydrides by Homogeneous Catalysis for Controlling the Release of Hydrogen from Ammonia-Borane: Present Status and Challenges. *ACS Catal.* **2016,** *6* (11), 7907-7934.
71. Raave, A., *Principles of Polymer Chemistry*. 3rd ed.; Springer: New York, USA, 2012.
72. Chen, E. Y. X., Coordination Polymerization of Polar Vinyl Monomers by Single-Site Metal Catalysts. *Chem. Rev.* **2009,** *109* (11), 5157-5214.
73. Metters, O. J.; Chapman, A. M.; Robertson, A. P. M.; Woodall, C. H.; Gates, P. J.; Wass, D. F.; Manners, I., Generation of aminoborane monomers $RR'NH{=}BH_2$ from amine-boronium cations $[RR'NH{-}BH_2L]^+$: metal catalyst-free formation of polyaminoboranes at ambient temperature. *Chem. Commun.* **2014,** *50* (81), 12146-12149.
74. De Albuquerque Pinheiro, C. A.; Roiland, C.; Jehan, P.; Alcaraz, G., Solventless and Metal-Free Synthesis of High-Molecular-Mass Polyaminoboranes from Diisopropylaminoborane and Primary Amines. *Angew. Chem. Int. Ed.* **2018,** *57* (6), 1519-1522.
75. Green, I. G.; Johnson, K. M.; Roberts, B. P., Homolytic reactions of ligated boranes. Part 13. An electron spin resonance study of radical addition to aminoboranes. *J. Chem. Soc., Perkin Trans. 2* **1989,** (12), 1963-1972.
76. Jaska, C. A.; Temple, K.; Lough, A. J.; Manners, I., Transition Metal-Catalyzed Formation of Boron–Nitrogen Bonds: Catalytic Dehydrocoupling of Amine-Borane Adducts to Form Aminoboranes and Borazines. *J. Am. Chem. Soc.* **2003,** *125* (31), 9424-9434.
77. Burg, A. B.; Randolph, C. L., The N-Methyl Derivatives of B_2H_7N. *J. Am. Chem. Soc.* **1949,** *71* (10), 3451-3455.
78. Staubitz, A.; Robertson, A. P. M.; Manners, I., Ammonia-Borane and Related Compounds as Dihydrogen Sources. *Chem. Rev.* **2010,** *110* (7), 4079-4124.
79. Jaska, C. A.; Manners, I., Heterogeneous or Homogeneous Catalysis? Mechanistic Studies of the Rhodium-Catalyzed Dehydrocoupling of Amine-Borane and Phosphine-Borane Adducts. *J. Am. Chem. Soc.* **2004,** *126* (31), 9776-9785.
80. Widegren, J. A.; Finke, R. G., A review of the problem of distinguishing true homogeneous catalysis from soluble or other metal-particle heterogeneous catalysis under reducing conditions. *J. Mol. Catal. A: Chem.* **2003,** *198* (1-2), 317-341.
81. Chen, Y.; Fulton, J. L.; Linehan, J. C.; Autrey, T., In Situ XAFS and NMR Study of Rhodium-Catalyzed Dehydrogenation of Dimethylamine Borane. *J. Am. Chem. Soc.* **2005,** *127* (10), 3254-3255.
82. Robertson, A. P. M.; Suter, R.; Chabanne, L.; Whittell, G. R.; Manners, I., Heterogeneous Dehydrocoupling of Amine-Borane Adducts by Skeletal Nickel Catalysts. *Inorg. Chem.* **2011,** *50* (24), 12680-12691.
83. Roselló-Merino, M.; López-Serrano, J.; Conejero, S., Dehydrocoupling Reactions of Dimethylamine-Borane by Pt(II) Complexes: A New Mechanism Involving Deprotonation of Boronium Cations. *J. Am. Chem. Soc.* **2013,** *135* (30), 10910-10913.
84. Clark, T. J.; Russell, C. A.; Manners, I., Homogeneous, Titanocene-Catalyzed Dehydrocoupling of Amine-Borane Adducts. *J. Am. Chem. Soc.* **2006,** *128* (30), 9582-9583.
85. Sloan, M. E.; Staubitz, A.; Clark, T. J.; Russell, C. A.; Lloyd-Jones, G. C.; Manners, I., Homogeneous Catalytic Dehydrocoupling/Dehydrogenation of Amine-Borane Adducts by Early Transition Metal, Group 4 Metallocene Complexes. *J. Am. Chem. Soc.* **2010,** *132* (11), 3831-3841.

86. Helten, H.; Dutta, B.; Vance, J. R.; Sloan, M. E.; Haddow, M. F.; Sproules, S.; Collison, D.; Whittell, G. R.; Lloyd-Jones, G. C.; Manners, I., Paramagnetic Titanium(III) and Zirconium(III) Metallocene Complexes as Precatalysts for the Dehydrocoupling/Dehydrogenation of Amine-Boranes. *Angew. Chem. Int. Ed.* **2013,** *52* (1), 437-440.
87. Chapman, A. M.; Wass, D. F., Cationic Ti(IV) and neutral Ti(III) titanocene-phosphinoaryloxide frustrated Lewis pairs: hydrogen activation and catalytic amine-borane dehydrogenation. *Dalton Trans.* **2012,** *41* (30), 9067-9072.
88. Klahn, M.; Hollmann, D.; Spannenberg, A.; Bruckner, A.; Beweries, T., Titanocene(III) complexes with 2-phosphinoaryloxide ligands for the catalytic dehydrogenation of dimethylamine borane. *Dalton Trans.* **2015,** *44* (27), 12103-12111.
89. Beweries, T.; Hansen, S.; Kessler, M.; Klahn, M.; Rosenthal, U., Catalytic dehydrogenation of dimethylamine borane by group 4 metallocene alkyne complexes and homoleptic amido compounds. *Dalton Trans.* **2011,** *40* (30), 7689-7692.
90. Beweries, T.; Thomas, J.; Klahn, M.; Schulz, A.; Heller, D.; Rosenthal, U., Catalytic and Kinetic Studies of the Dehydrogenation of Dimethylamine Borane with an *i*Pr Substituted Titanocene Catalyst. *ChemCatChem* **2011,** *3* (12), 1865-1868.
91. Pun, D.; Lobkovsky, E.; Chirik, P. J., Amineborane dehydrogenation promoted by isolable zirconium sandwich, titanium sandwich and N_2 complexes. *Chem. Commun.* **2007,** (31), 3297-3299.
92. Jurca, T.; Dellermann, T.; Stubbs, N. E.; Resendiz-Lara, D. A.; Whittell, G. R.; Manners, I., Step-growth titanium-catalysed dehydropolymerisation of amine-boranes. *Chem. Sci.* **2018,** *9* (13), 3360-3366.
93. Trose, M.; Reiß, M.; Reiß, F.; Anke, F.; Spannenberg, A.; Boye, S.; Lederer, A.; Arndt, P.; Beweries, T., Dehydropolymerisation of methylamine borane using a dinuclear 1,3-allenediyl bridged zirconocene complex. *Dalton Trans.* **2018,** *Advance Article*, DOI: 10.1039/c8dt03311k.
94. Staubitz, A.; Sloan, M. E.; Robertson, A. P. M.; Friedrich, A.; Schneider, S.; Gates, P. J.; Schmedt auf der Günne, J.; Manners, I., Catalytic Dehydrocoupling/Dehydrogenation of N-Methylamine-Borane and Ammonia-Borane: Synthesis and Characterization of High Molecular Weight Polyaminoboranes. *J. Am. Chem. Soc.* **2010,** *132* (38), 13332-13345.
95. Hebden, T. J.; Denney, M. C.; Pons, V.; Piccoli, P. M. B.; Koetzle, T. F.; Schultz, A. J.; Kaminsky, W.; Goldberg, K. I.; Heinekey, D. M., σ-Borane Complexes of Iridium: Synthesis and Structural Characterization. *J. Am. Chem. Soc.* **2008,** *130* (32), 10812-10820.
96. Staubitz, A.; Presa Soto, A.; Manners, I., Iridium-Catalyzed Dehydrocoupling of Primary Amine-Borane Adducts: A Route to High Molecular Weight Polyaminoboranes, Boron–Nitrogen Analogues of Polyolefins. *Angew. Chem. Int. Ed.* **2008,** *47* (33), 6212-6215.
97. Bhunya, S.; Malakar, T.; Paul, A., Unfolding the crucial role of a nucleophile in Ziegler-Natta type Ir catalyzed polyaminoborane formation. *Chem. Commun.* **2014,** *50* (44), 5919-5922.
98. Alberico, E.; Sponholz, P.; Cordes, C.; Nielsen, M.; Drexler, H. J.; Baumann, W.; Junge, H.; Beller, M., Selective Hydrogen Production from Methanol with a Defined Iron Pincer Catalyst under Mild Conditions. *Angew. Chem. Int. Ed.* **2013,** *52* (52), 14162-14166.
99. Anke, F.; Han, D.; Klahn, M.; Spannenberg, A.; Beweries, T., Formation of high-molecular weight polyaminoborane by Fe hydride catalysed dehydrocoupling of methylamine borane. *Dalton Trans.* **2017,** *46* (21), 6843-6847.
100. Glüer, A.; Förster, M.; Celinski, V. R.; Schmedt auf der Günne, J.; Holthausen, M. C.; Schneider, S., Highly Active Iron Catalyst for Ammonia Borane Dehydrocoupling at Room Temperature. *ACS Catal.* **2015,** *5* (12), 7214-7217.
101. Alt, H. G.; Köppl, A., Effect of the Nature of Metallocene Complexes of Group IV Metals on Their Performance in Catalytic Ethylene and Propylene Polymerization. *Chem. Rev.* **2000,** *100* (4), 1205-1222.
102. Telleria, A.; Vicent, C.; San Nacianceno, V.; Garralda, M. A.; Freixa, Z., Experimental Evidence Supporting Related Mechanisms for Ru(II)-Catalyzed Dehydrocoupling and Hydrolysis of Amine-Boranes. *ACS Catal.* **2017,** *7* (12), 8394-8405.
103. Pal, S.; Kusumoto, S.; Nozaki, K., Dehydrogenation of Dimethylamine-Borane Catalyzed by Half-Sandwich Ir and Rh Complexes: Mechanism and the Role of Cp* Noninnocence. *Organometallics* **2018,** *37* (6), 906-914.
104. Asensio, G.; Cuenca, A. B.; Esteruelas, M. A.; Medio-Simón, M.; Oliván, M.; Valencia, M., Osmium(III) Complexes with POP Pincer Ligands: Preparation from Commercially Available $OsCl_3 \cdot 3H_2O$ and Their X-ray Structures. *Inorg. Chem.* **2010,** *49* (19), 8665-8667.
105. Haibach, M. C.; Wang, D. Y.; Emge, T. J.; Krogh-Jespersen, K.; Goldman, A. S., (POP)Rh pincer hydride complexes: unusual reactivity and selectivity in oxidative addition and olefin insertion reactions. *Chem. Sci.* **2013,** *4* (9), 3683-3692.
106. Alós, J.; Bolaño, T.; Esteruelas, M. A.; Oliván, M.; Oñate, E.; Valencia, M., POP-Pincer Osmium-Polyhydrides: Head-to-Head (Z)-Dimerization of Terminal Alkynes. *Inorg. Chem.* **2013,** *52* (10), 6199-6213.

107. Esteruelas, M. A.; García-Yebra, C.; Martín, J.; Oñate, E., *mer*, *fac*, and Bidentate Coordination of an Alkyl-POP Ligand in the Chemistry of Nonclassical Osmium Hydrides. *Inorg. Chem.* **2017,** *56* (1), 676-683.
108. Esteruelas, M. A.; Fernández, I.; García-Yebra, C.; Martín, J.; Oñate, E., Elongated σ-Borane versus σ-Borane in Pincer-POP-Osmium Complexes. *Organometallics* **2017,** *36* (12), 2298-2307.
109. Bakhmutov, V. I.; Bozoglian, F.; Gómez, K.; González, G.; Grushin, V. V.; Macgregor, S. A.; Martin, E.; Miloserdov, F. M.; Novikov, M. A.; Panetier, J. A.; Romashov, L. V., CF_3–Ph Reductive Elimination from [(Xantphos)Pd(CF_3)(Ph)]. *Organometallics* **2012,** *31* (4), 1315-1328.
110. Esteruelas, M. A.; Nolis, P.; Oliván, M.; Oñate, E.; Vallribera, A.; Vélez, A., Ammonia Borane Dehydrogenation Promoted by a Pincer-Square-Planar Rhodium(I) Monohydride: A Stepwise Hydrogen Transfer from the Substrate to the Catalyst. *Inorg. Chem.* **2016,** *55* (14), 7176-7181.
111. Guari, Y.; van Strijdonck, G. P. F.; Boele, M. D. K.; Reek, J. N. H.; Kamer, P. C. J.; van Leeuwen, P. W. N. M., Palladium-Catalyzed Amination of Aryl Bromides and Aryl Triflates Using Diphosphane Ligands: A Kinetic Study. *Chem. Eur. J.* **2001,** *7* (2), 475-482.
112. Zuideveld, M. A.; Swennenhuis, B. H. G.; Boele, M. D. K.; Guari, Y.; van Strijdonck, G. P. F.; Reek, J. N. H.; Kamer, P. C. J.; Goubitz, K.; Fraanje, J.; Lutz, M.; Spek, A. L.; van Leeuwen, P. W. N. M., The coordination behaviour of large natural bite angle diphosphine ligands towards methyl and 4-cyanophenylpalladium(II) complexes. *J. Chem. Soc., Dalton Trans.* **2002,** (11), 2308-2317.
113. Dallanegra, R.; Chaplin, A. B.; Weller, A. S., Rhodium Cyclopentyl Phosphine Complexes of Wide-Bite-Angle Ligands DPEphos and Xantphos. *Organometallics* **2012,** *31* (7), 2720-2728.
114. Moxham, G. L.; Randell-Sly, H. E.; Brayshaw, S. K.; Woodward, R. L.; Weller, A. S.; Willis, M. C., A Second-Generation Catalyst for Intermolecular Hydroacylation of Alkenes and Alkynes Using β-S-Substituted Aldehydes: The Role of a Hemilabile P-O-P Ligand. *Angew. Chem. Int. Ed.* **2006,** *45* (45), 7618-7622.
115. Moxham, G. L.; Randell-Sly, H.; Brayshaw, S. K.; Weller, A. S.; Willis, M. C., Intermolecular Alkene and Alkyne Hydroacylation with β-S-Substituted Aldehydes: Mechanistic Insight into the Role of a Hemilabile P–O–P Ligand. *Chem. Eur. J.* **2008,** *14* (27), 8383-8397.
116. Pawley, R. J.; Huertos, M. A.; Lloyd-Jones, G. C.; Weller, A. S.; Willis, M. C., Intermolecular Alkyne Hydroacylation. Mechanistic Insight from the Isolation of the Vinyl Intermediate That Precedes Reductive Elimination. *Organometallics* **2012,** *31* (15), 5650-5659.
117. Pawley, R. J.; Moxham, G. L.; Dallanegra, R.; Chaplin, A. B.; Brayshaw, S. K.; Weller, A. S.; Willis, M. C., Controlling Selectivity in Intermolecular Alkene or Aldehyde Hydroacylation Reactions Catalyzed by $\{Rh(L_2)\}^+$ Fragments. *Organometallics* **2010,** *29* (7), 1717-1728.
118. Barwick-Silk, J.; Hardy, S.; Willis, M. C.; Weller, A. S., Rh(DPEPhos)-Catalyzed Alkyne Hydroacylation Using β-Carbonyl-Substituted Aldehydes: Mechanistic Insight Leads to Low Catalyst Loadings that Enables Selective Catalysis on Gram-Scale. *J. Am. Chem. Soc.* **2018,** *140* (23), 7347-7357.
119. Hooper, J. F.; Chaplin, A. B.; González-Rodríguez, C.; Thompson, A. L.; Weller, A. S.; Willis, M. C., Aryl Methyl Sulfides as Substrates for Rhodium-Catalyzed Alkyne Carbothiolation: Arene Functionalization with Activating Group Recycling. *J. Am. Chem. Soc.* **2012,** *134* (6), 2906-2909.
120. Ren, P.; Pike, S. D.; Pernik, I.; Weller, A. S.; Willis, M. C., Rh–POP Pincer Xantphos Complexes for C–S and C–H Activation. Implications for Carbothiolation Catalysis. *Organometallics* **2015,** *34* (4), 711-723.
121. Utsunomiya, M.; Kuwano, R.; Kawatsura, M.; Hartwig, J. F., Rhodium-Catalyzed Anti-Markovnikov Hydroamination of Vinylarenes. *J. Am. Chem. Soc.* **2003,** *125* (19), 5608-5609.
122. Couce-Rios, A.; Lledós, A.; Ujaque, G., The Origin of Anti-Markovnikov Regioselectivity in Alkene Hydroamination Reactions Catalyzed by $[Rh(DPEphos)]^+$. *Chem. Eur. J.* **2016,** *22* (27), 9311-9320.

2 {Rh(Xantphos-^{i}Pr)}$^{+}$ complexes as precatalysts for the dehydropolymerisation of $H_3B{\cdot}NMeH_2$

2.1 Introduction

Xantphos-^{i}Pr was selected as a suitable ligand to further probe the mechanism of amine borane dehydropolymerisation, due to its structural similarities to Xantphos-Ph (Figure 2.1), but comparatively less well-known chemistry. For example, since its initial synthesis by Esteruelas in 2010,[1] the Xantphos-^{i}Pr ligand has appeared in only 17 publications, however 1228 publications and patents utilised Xantphos-Ph in the same timeframe.[2] Xantphos-^{i}Pr has been employed as a ligand (mainly bound to rhodium and osmium) for the dimerisation of terminal alkynes,[3] the alcoholysis of silanes,[4] C–H activation of ketones and aldehydes,[5] decyanative borylation,[6] the diboration of internal alkynes,[7] as well as, most pertinently to this work, the dehydrocoupling of $H_3B{\cdot}NH_3$.[8]

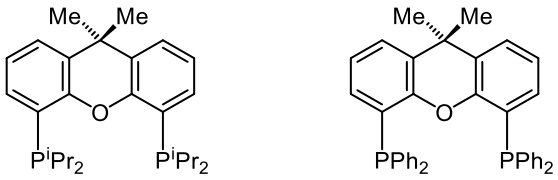


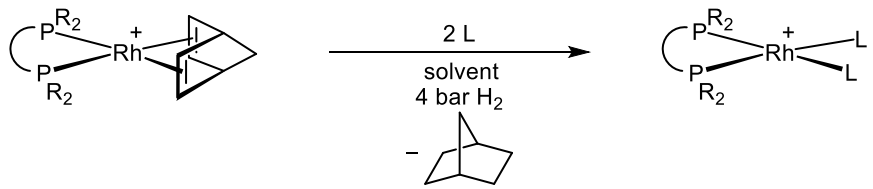
Figure 2.1 Structures of Xantphos-^{i}Pr and Xantphos-Ph.

This Chapter involves the synthesis of a suitable {Rh(Xantphos-^{i}Pr)}$^{+}$ precatalyst for amine borane dehydropolymerisation and investigates its reactivity with $H_3B{\cdot}NMeH_2$. {Rh(Xantphos-^{i}Pr)}$^{+}$ complexes that are implicated or observed during catalysis, which is outlined in more detail in Chapter 3, are also reported.

2.2 Formation of [Rh(Xantphos-^{i}Pr)(NBD)][BAr$^{F}{}_4$] (**1**)

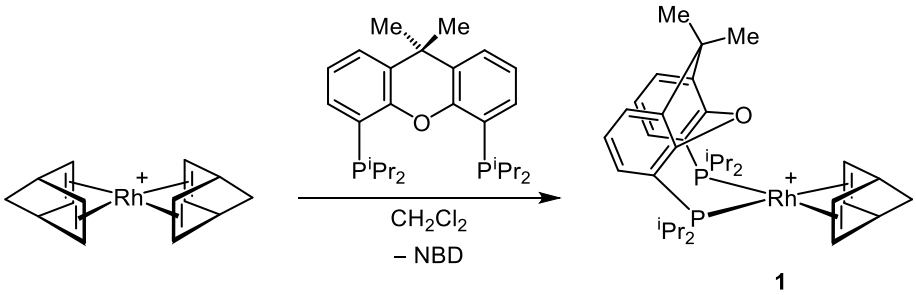
Suitable precursors for accessing {Rh(P$_2$)}$^{+}$ (P$_2$ = bidentate bisphosphine) complexes often involve a strained norbornadiene (NBD) ligand, i.e. [Rh(P$_2$)(NBD)]$^{+}$, for which there are many examples in

the literature.[9-11] The two metal bound NBD alkene groups can be hydrogenated, forming free norbornane (NBA), and replaced by the desired ligand(s) (L, Scheme 2.1). A weakly coordinating anion, such as $[BAr^F_4]^-$ (Ar^F = 3,5-$C_6H_3(CF_3)_2$), decreases the likelihood of competitive anion coordination or decomposition by anion reactivity (Section 1.4). Therefore [Rh(Xantphos-^{i}Pr)(NBD)][BAr^F_4] was considered to be an appropriate initial target for synthesising {Rh(Xantphos-^{i}Pr)}$^+$ complexes.



Scheme 2.1 Synthesis of $[Rh(P_2)(L)_2]^+$ complexes from a general $[Rh(P_2)(NBD)]^+$ precursor. Anions not shown for clarity. P_2 = bidentate phosphine, L = desired ancillary ligand.

[Rh(κ^2-P,P-Xantphos-^{i}Pr)(NBD)][BAr^F_4] (**1**) was synthesised by the dropwise addition of Xantphos-^{i}Pr to a solution of $[Rh(NBD)_2][BAr^F_4]$,[12] in CH_2Cl_2 (Scheme 2.2). Complex **1** was characterised by NMR spectroscopy, electrospray ionisation mass spectrometry (ESI-MS) and elemental microanalysis. Single crystals of **1** suitable for single crystal X-ray diffraction were formed by diffusion of a CH_2Cl_2 solution of **1** into pentane.



Scheme 2.2 Synthesis of [Rh(κ^2-P,P-Xantphos-^{i}Pr)(NBD)][BAr^F_4] (**1**). $[BAr^F_4]^-$ anions not shown for clarity.

The solid state structure of **1** (Figure 2.2), shows approximate non-crystallographic C_s symmetry in which the Xantphos-^{i}Pr ligand adopts a cis κ^2-P,P coordination mode. There is a close H···H contact between two ^{i}Pr methine groups (C11 and C17) of 1.973 Å (Figure 2.3), which is shorter than the sum of their van der Waals radii (r_v(H) = 1.20 Å).[13] In comparison to the analogous Xantphos-Ph

complex, [Rh(κ^2-P,P-Xantphos-Ph)(NBD)][BAr$^F{}_4$] (**1-Ph**),[10] there are no such interactions as the phosphine phenyl substituents lie parallel, 3.426 Å apart (Figure 2.3).[14] This difference between Xantphos-Ph and Xantphos-^{i}Pr potentially destabilises the ground state geometry in **1** and may influence any preference for κ^3-P,O,P versus κ^2-P,P coordination in the latter.[15] This may be further confirmed by the plots of P–M–P bond angle versus M···O bond lengths for both Xantphos-Ph and Xantphos-^{i}Pr in Figure 1.8 which show that crystallographically characterised Xantphos-^{i}Pr complexes have a much greater propensity for mer κ^3-P,O,P coordination to transition metals compared to Xantphos-Ph. Interestingly Goldman and co-workers commented that [Rh(κ^2-P,P-Xantphos-^{t}Bu)(NBD)]$^+$ could not be prepared – this is likely due to the increase of these destabilising H···H contacts between the methyl groups present in the even bulkier tertbutyl phosphines.[16]

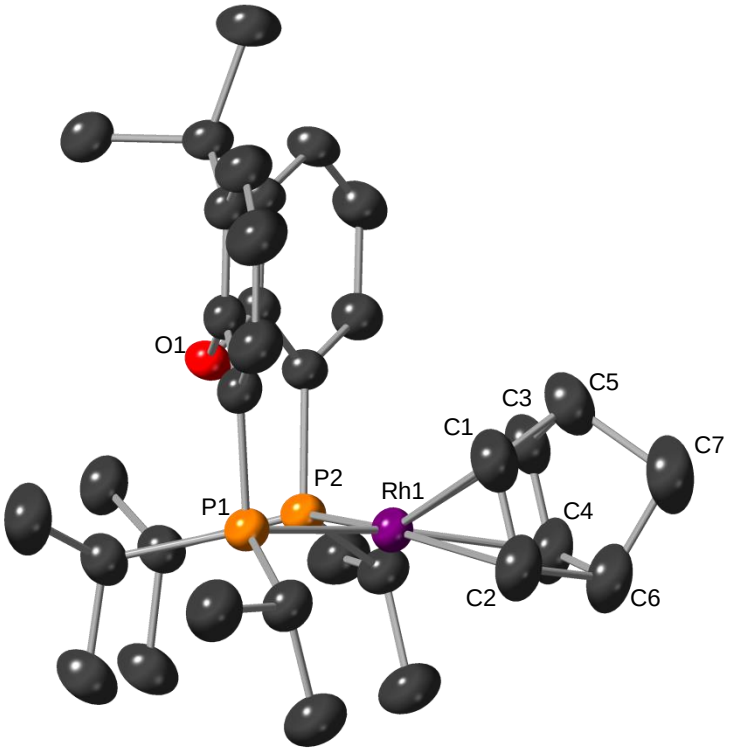


Figure 2.2 Crystal structure of the cationic portion of [Rh(κ^2-P,P-Xantphos-^{i}Pr)(NBD)][BAr$^F{}_4$] (**1**). Displacement ellipsoids are drawn at the 30% probability level. H atoms are not shown for clarity. Selected bond lengths (Å) and angles (°): Rh1–P1, 2.3897(8); Rh1–P2, 2.3659(8); Rh1–O1, 3.161(2); Rh1–C1, 2.187(3); Rh1–C2, 2.213(3); Rh1–C3, 2.165(4); Rh1–C4, 2.194(4); C1–C2, 1.385(6); C3–C4, 1.373(6); P1–Rh1–P2, 101.72(3).

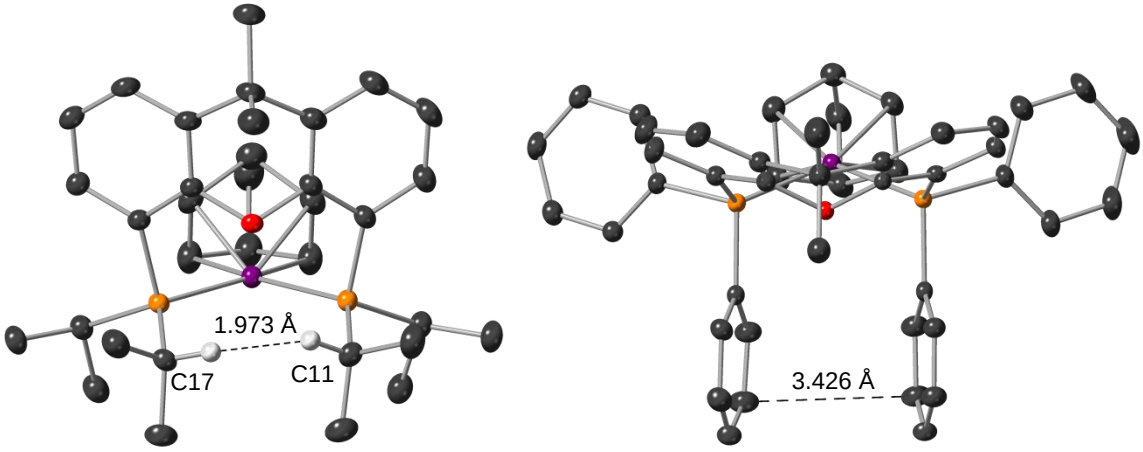


Figure 2.3 Crystal structures of the cationic portions of **1** (left) and **1-Ph** (right), highlighting the close H···H methine contacts on the alkyl phosphines in **1**, and the longer distance between the phenyl phosphines in **1-Ph**. H atoms (except those bound to C11 and C17 in **1**) are not shown for clarity.

The room temperature NMR spectroscopic data for **1** in CD_2Cl_2 suggest a structure that contrasts with that determined in the solid state. The $^{31}P\{^1H\}$ NMR spectrum shows a Rh(I) centre[17] coordinated to equivalent ^{31}P environments at δ 26.3 (d, $^1J_{RhP}$ 145 Hz), and the ^1H NMR spectrum shows a singlet of integral 6 H for the gem-dimethyl protons on the backbone of the Xantphos-^{i}Pr ligand, and magnetically equivalent norbornadiene alkene protons, indicated by a singlet of integral 4 H with respect to the $[BAr^F_4]^-$ anion. This data suggests that a fluxional process occurs in solution at 298 K. However, on cooling to 188 K the system becomes static, and two resonances each of integral 2 H are seen for each alkene environment, in addition to two resonances of 3 H for each methyl environment in the Xantphos-^{i}Pr backbone, consistent with the solid state structure.

The mechanism of exchange for the norbornadiene alkene protons in complex **1** was studied using variable temperature ^1H NMR spectroscopy and subsequent line shape analysis of the relevant peaks across eight temperatures using gNMR software (lineshape analysis at four temperatures are shown in Figure 2.4).[18] Fluxionality of complexes containing Xantphos-types ligands has been detailed previously,[19-20] in particular, a report by Vogt and co-workers describes fluxional behaviour in Ru(κ^2-P,P-Xantphos-Ph)(H)(Cl)(CO)(PPh_3),[20] leading to a time averaged mirror plane through the ruthenium metal centre and phosphine ligands.

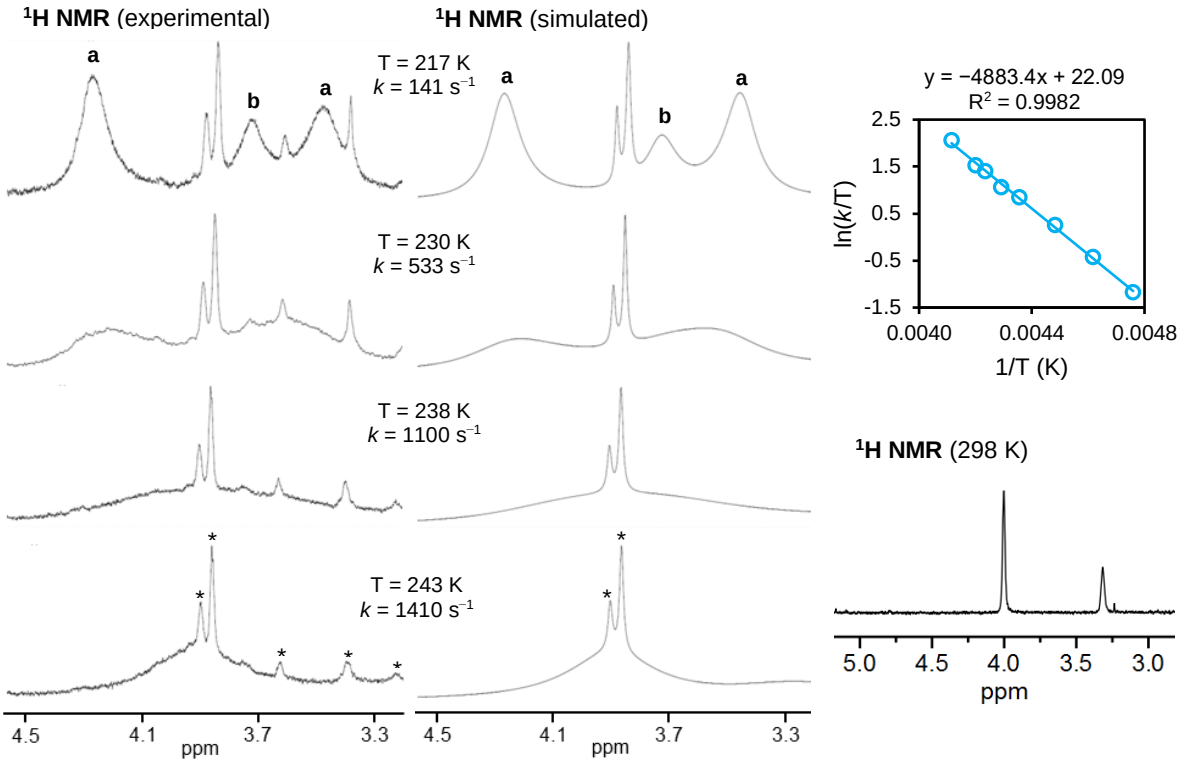
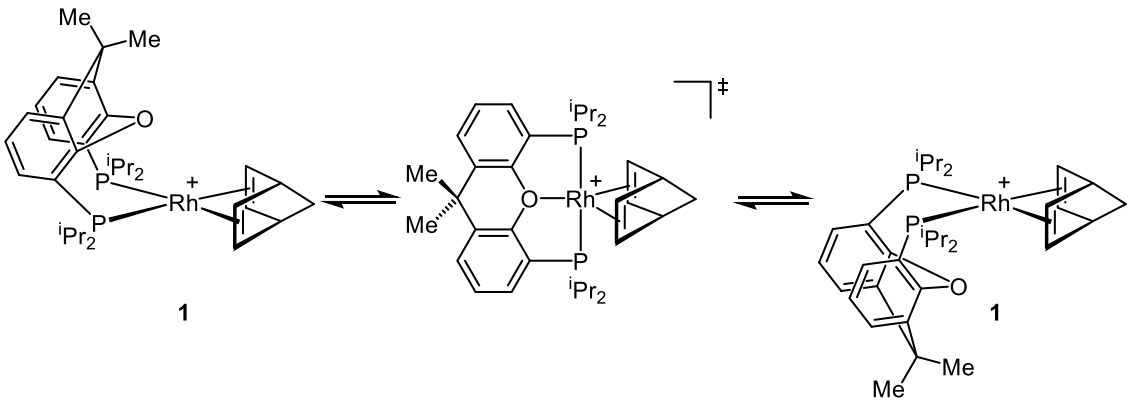


Figure 2.4 Left: Line shape analysis of the variable temperature ^{1}H NMR spectroscopic data of the NBD alkene resonances in **1**. * = impurities in the sample noticeable at low temperature, a = the two NBD alkene environments, b = one of the NBD bridgehead environments. Right: Eyring plot for **1** (top) and ^{1}H NMR spectrum of **1** between δ 5.0 and δ 3.0 at 298 K showing the resonance corresponding to the NBD alkene environment (δ 4.00, s, 4 H) and the NBD bridgehead environment (δ 3.32, s, 2 H) (bottom).

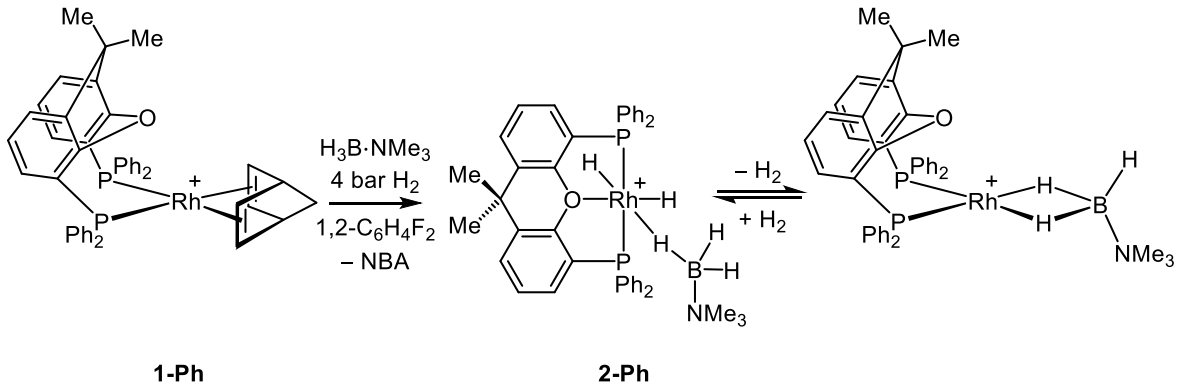
Using the rates of exchange obtained from gNMR analysis, an Eyring analysis was carried out and the kinetic parameters of **1** for this exchange process were calculated to be $\Delta H^{\ddagger}$ = +4 (± 1) kJ mol^{-1}, $\Delta S^{\ddagger}$ = −14 (± 3) J K^{-1} mol^{-1} and $\Delta G_{298}^{\ddagger}$ = 45(± 1) kJ mol^{-1}. The small, negative, $\Delta S^{\ddagger}$ value suggests a slightly more ordered transition state for the fluxional process, and is consistent with Vogt's findings that suggest an intramolecular exchange process, such as flipping of the Xanthene backbone, leads to the fluxionality of the norbornadiene alkene protons.[20] Therefore backbone flipping, possibly via a mer κ^{3}-P,O,P-Xantphos-^{i}Pr transition state, may be the cause for the fluxional behaviour seen in complex **1** in solution (Scheme 2.3).



Scheme 2.3 Proposed fluxional process of **1**. $[BAr^F_4]^-$ anions not shown for clarity.

2.3 Formation of $[Rh(Xantphos\text{-}^iPr)(H)_2(H_3B{\cdot}NMe_3)][BAr^F_4]$ (**2**)

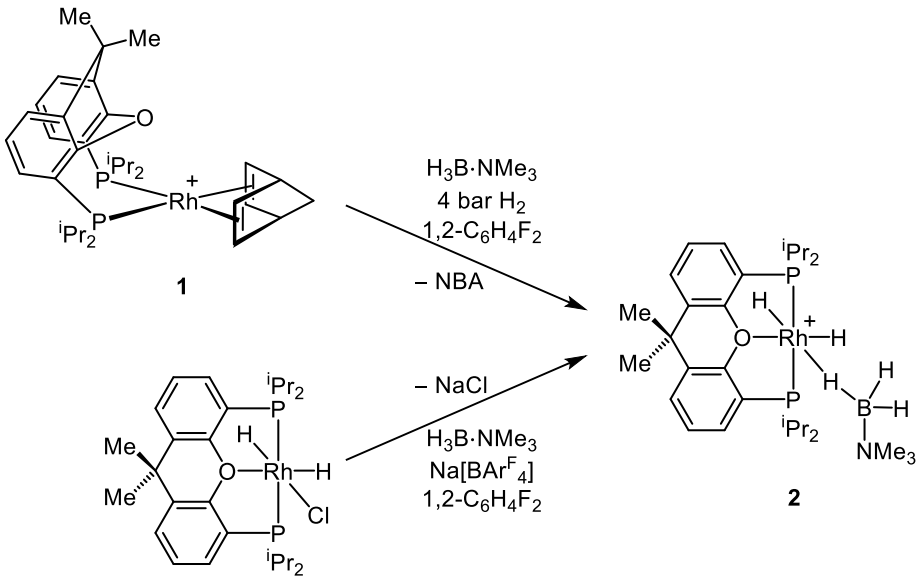
With complex **1** in hand, a suitable $\{Rh(Xantphos\text{-}^iPr)\}^+$-containing precatalyst was targeted. Previously reported hydrogenation of **1-Ph** in the presence of $H_3B{\cdot}NMe_3$ yielded $[Rh(\kappa^3\text{-P,O,P-Xantphos-Ph})(H)_2(\eta^1\text{-}H_3B{\cdot}NMe_3)][BAr^F_4]$ (**2-Ph**), though this complex was only stable under an H_2 atmosphere, losing H_2 under argon to form $[Rh(\kappa^2\text{-P,P-Xantphos-Ph})(\eta^2\text{-}H_3B{\cdot}NMe_3)][BAr^F_4]$ (Scheme 2.4).[21] Metal bound $H_3B{\cdot}NMe_3$ can be considered a model for complexes likely formed during the first step of dehydrocoupling of amine boranes via inner sphere processes (Section 1.6.7), as it does not contain protic N–H groups which may otherwise dehydrogenate in the presence of the hydridic B–H groups.[22] In addition, given that sigma coordination of an amine borane to a metal centre is generally weak (Section 1.5.2), $H_3B{\cdot}NMe_3$ may be a suitable masking ligand for the formation of an operationally unsaturated, catalytically active $\{Rh(Xantphos\text{-}^iPr)\}^+$ species.



1-Ph **2-Ph**

Scheme 2.4 Conversion of **1-Ph** to [Rh(κ^3-P,O,P-Xantphos-Ph)(H)$_2$(η^1-H$_3$B·NMe$_3$)][BAr$^F_4$] (**2-Ph**), which loses H_2 under an argon atmosphere to form [Rh(κ^3-P,O,P-Xantphos-Ph)(η^2-H$_3$B·NMe$_3$)][BAr$^F_4$]. [BAr$^F_4$]$^-$ anions not shown for clarity.

Hydrogenation of **1** in the presence of a stoichiometric quantity of H$_3$B·NMe$_3$ yielded [Rh(κ^3-P,O,P-Xantphos-^{i}Pr)(H)$_2$(η^1-H$_3$B·NMe$_3$)][BAr$^F_4$] (**2**, Scheme 2.5), which could be characterised by NMR spectroscopy, ESI-MS and elemental microanalysis. Single crystals of **2** suitable for single crystal X-ray diffraction were grown from 1,2-C$_6$H$_4$F$_2$/pentane. In contrast to **2-Ph**, complex **2** was stable to H_2 loss even after prolonged exposure to vacuum (72 hours, 6×10^{-3} mbar), suggesting that during catalysis the Rh(III) oxidation state may be persistent. An alternative route to **2** was also achieved through chloride abstraction of previously reported Rh(κ^3-P,O,P-Xantphos-^{i}Pr)(H)$_2$Cl,[16, 23] using Na[BAr$^F_4$] in the presence of one equivalent of H$_3$B·NMe$_3$ (Scheme 2.5). The analogous [BAr$^{Cl}_4$]$^-$ complex (Ar^{Cl} = 3,5-C$_6$H$_3$Cl$_2$),[24] **2-[BAr$^{Cl}_4$]**, could also be synthesised by the latter route, instead using Na[BAr$^{Cl}_4$] as the chloride abstraction agent.



Scheme 2.5 Synthesis of [Rh(κ^3-P,O,P-Xantphos-^{i}Pr)(H)$_2$(η^1-H$_3$B·NMe$_3$)][BAr$^F_4$] (**2**). [BAr$^F_4$]$^-$ anions not shown for clarity.

Examination of the solid state structure of **2** (Figure 2.5) shows mer κ^3-P,O,P binding of Xantphos-^{i}Pr to the rhodium centre. The hydride ligands could not be located in the Fourier map, therefore they were placed in calculated positions – their presence confirmed by the NMR spectroscopic data (vide infra). In the solid state, the hydrides are inequivalent and cis orientated to one another – one trans to the Xantphos-^{i}Pr ether and the other trans to the supporting H$_3$B·NMe$_3$ ligand. The Rh1–B1 distance of 2.783(6) Å is longer than the sum of the covalent radii (r_c) of rhodium and boron (r_c(Rh) = 1.42 Å, r_c(B) = 0.84 Å),[25] however it is shorter than the sum of their van der Waals radii (r_v; r_v(Rh) = 2.44 Å; r_v(B) = 1.91 Å).[13] This suggests a weak Rh···B interaction, where the borane component predominantly binds to the metal through a bridging hydride in an η^1 fashion.[26] Similar geometries to **2** have also been reported in **2-Ph** (Rh···B, 2.759(6) Å),[21] as well as [Ru(κ^3-P,O,P-Xantphos-Ph)(PPh$_3$)(H)(η^1-H$_3$B·NH$_3$)][BPh$_4$] (Ru···B, 2.94 Å).[27] For comparison, the covalent radius of ruthenium is 1.46 Å,[25] and its van der Waals radius is 2.46 Å.[13] Notably, the P1–Rh1–P2 angle of 160.45(5)° in **2** is more compressed than that in **2-Ph** (162.40(5)°), likely due to the increased steric bulk of the ^{i}Pr groups compared to Ph.

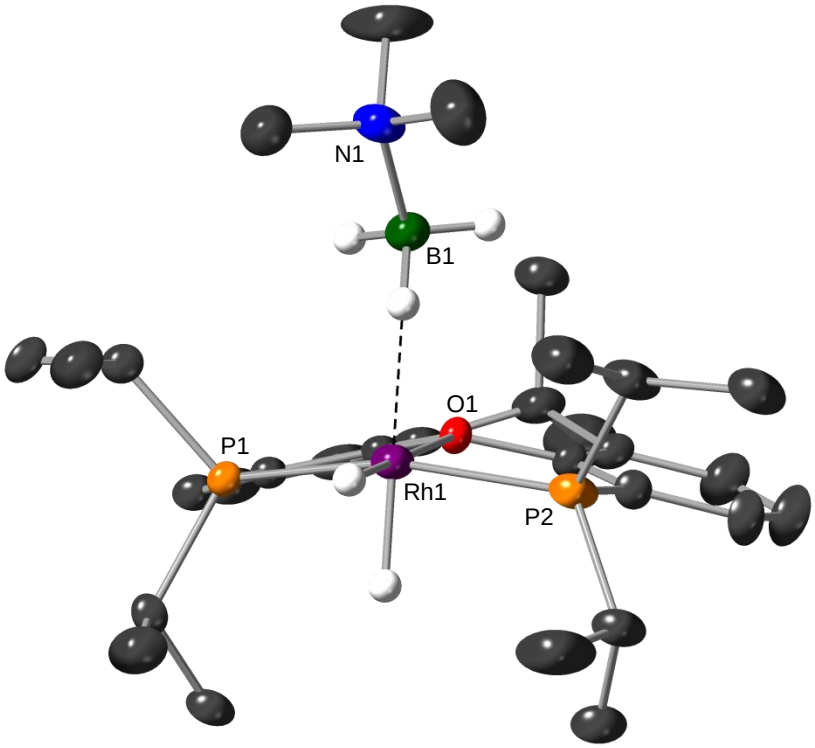


Figure 2.5 Crystal structure of the cationic portion of [Rh(κ^3-P,O,P-Xantphos-^{i}Pr)(H)$_2$(η^1-H$_3$B·NMe$_3$)][BAr$^F{}_4$] (**2**). Displacement ellipsoids are drawn at the 30% probability level. C-bound H atoms are not shown for clarity. Selected bond lengths (Å) and angles (°): Rh1–P1, 2.2650(13); Rh1–P2, 2.2490(15); Rh1–O1, 2.192(3); Rh1–B1, 2.783(6); B1–N1, 1.607(7); P1–Rh1–P2, 160.45(5).

The room temperature (298 K) ^{31}P{^{1}H} NMR spectrum of complex **2** in CD_2Cl_2 shows one environment at δ 66.5 (d, $^1J_{RhP}$ 111 Hz), with a coupling constant indicative of Xantphos-^{i}Pr bound to a cationic Rh(III) centre.[4] A broad signal is observed at δ −9.9 in the ^{11}B{^{1}H} NMR spectrum, consistent with the η^1 bound amine borane found in the solid state structure – characteristically only slightly upfield shifted relative to the chemical shift of free H$_3$B·NMe$_3$ in 1,2-C$_6$H$_4$F$_2$,[28] δ −8.4, q, $^1J_{BH}$ 97 Hz.[29] This, in addition to the solid state structure, suggests a weak interaction between the rhodium centre and the borane fragment. In contrast, η^2 amine borane complexes show ^{11}B NMR chemical shifts downfield from the free amine borane.[30] This is due to differing orbital contributions to the metal between η^1 and η^2 amine borane complexes,[31] although such analysis remains to be quantitatively determined.

In ^{1}H NMR spectrum at 298 K, there are two environments observed at δ 0.08 and δ −19.09, of integrals 3 H and 2 H respectively. The former resonance is quadrupolar broadened and sharpens significantly on ^{11}B decoupling, indicative of the bound η^1-BH_3 group where the terminal B–H and bridging Rh···H–B exchange rapidly compared to the NMR timescale.[26-27, 32] The latter resonance shows that the two Rh–H groups are magnetically equivalent at 298 K (Figure 2.6), however this contrasts with the solid state structure shown in Figure 2.5, indicating that a fluxional hydride exchange process is operating at higher temperatures. Upon cooling to 200 K, the single Rh–H signal splits to give two resonances, each of integral 1 H at δ −17.62 and δ −19.97 (Figure 2.6). Variable temperature ^{1}H NMR spectroscopy, line shape analysis and Eyring analysis of these hydride peaks was performed, and the kinetic parameters for the hydride exchange process were calculated to be $\Delta H^{\ddagger}$ = +59 (± 4) kJ mol^{-1}, $\Delta S^{\ddagger}$ = +37 (± 15) J K^{-1} mol^{-1} and $\Delta G_{298}^{\ddagger}$ = 49(± 8) kJ mol^{-1}.

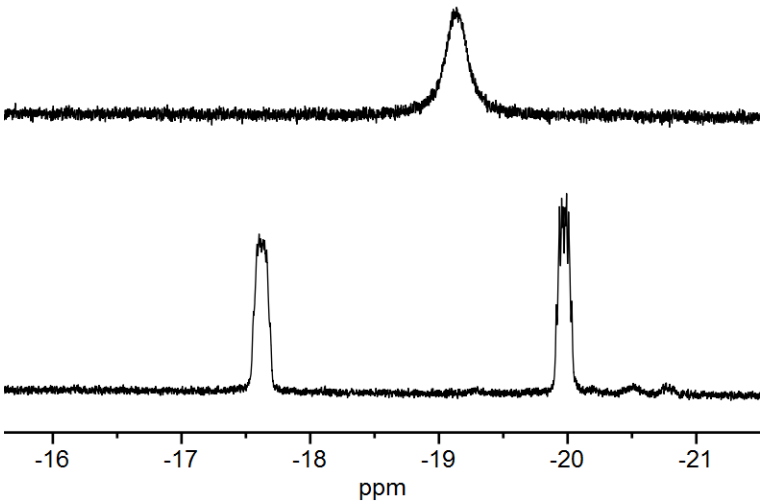
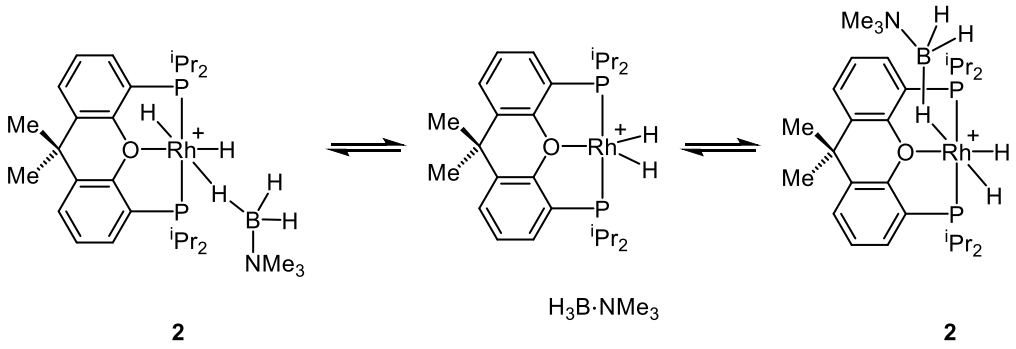


Figure 2.6 ^{1}H NMR spectra of complex **2**, showing the hydride region. Top: 298 K. Bottom: 200 K.

The positive, but modest, activation entropy suggests that the hydride exchange is dissociative in nature.[23] The simplest explanation for this process is that the hydrides are fluxional via a mechanism in which the $H_3B{\cdot}NMe_3$ ligand dissociates and recoordinates on the other side via a symmetric 16 electron [Rh(κ^3-P,O,P-Xantphos-^{i}Pr)(H)$_2$]$^{+}$ intermediate (Scheme 2.6), previously reported by Goldman.[16] These activation parameters are similar to those reported for related

fluxional processes in complexes [Rh(κ^3-P,O,P-Xantphos-^{i}Pr)(H)$_2$][OTf] ($\Delta H^{\ddagger}$ = +65 (± 3) kJ mol^{-1}, $\Delta S^{\ddagger}$ = +67 (± 8) J K^{-1} mol^{-1}),[23] and [Rh(κ^3-P,O,P-Xantphos-Ph)(H)$_2$(OCMe$_2$)][BAr$^F{}_4$] ($\Delta H^{\ddagger}$ = +61 (± 2) kJ mol^{-1}, $\Delta S^{\ddagger}$ = +13 (± 6) J K^{-1} mol^{-1}).[33] This additionally suggests that the σ bound $H_3B{\cdot}NMe_3$ moiety has the ability to dissociate from the rhodium metal centre in order to reveal a vacant site necessary for catalysis. The small but positive activation entropy may also indicate the formation of an encounter complex between $H_3B{\cdot}NMe_3$ and [Rh(κ^3-P,O,P-Xantphos-^{i}Pr)(H)$_2$]$^+$, therefore suggesting the amine borane may remain in the coordination sphere of the rhodium centre, or alternatively that a solvent cage operates to stabilise the transition state in this process.



2 **2**

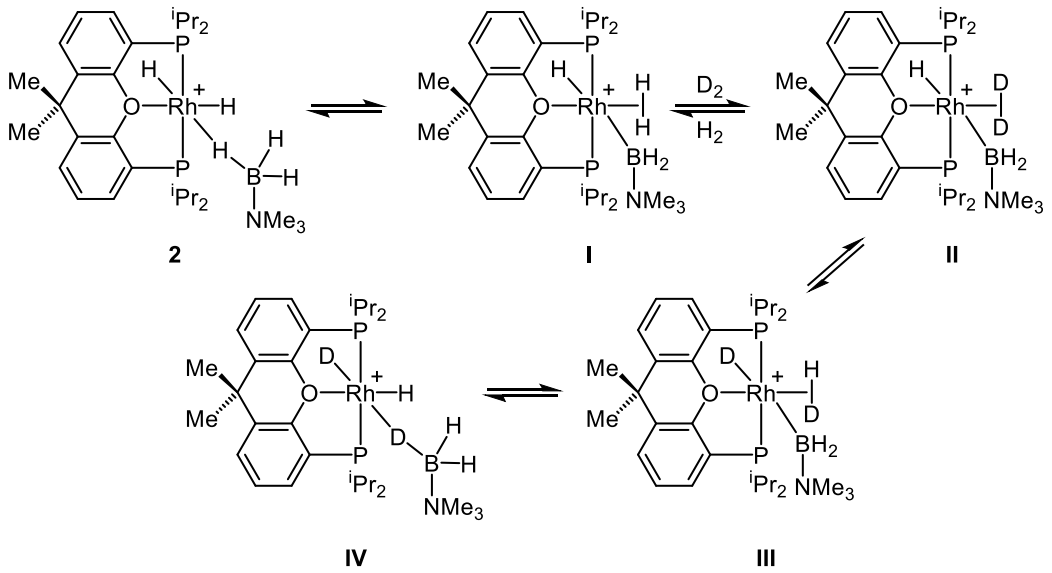
Scheme 2.6 Proposed fluxional process for **2**. [BAr$^F{}_4$]$^-$ anions not shown for clarity.

2.4 Reactivity of [Rh(Xantphos-^{i}Pr)(H)$_2$(H$_3$B·NMe$_3$)][BAr$^F{}_4$] (**2**)

*2.4.1 Reaction of **2** with D$_2$: H/D exchange*

As B–H activation at a metal centre is a key step during inner sphere dehydrogenation of amine boranes (Section 1.6.6),[34] isolated complex **2** was dissolved in CD_2Cl_2 under an atmosphere of D_2 (298 K, ~1 bar) to probe deuterium incorporation into the complex via metal mediated H/D exchange. After 5 minutes, H/D exchange had occurred at both the Rh–H and the BH_3 groups.[35] The ^{1}H NMR spectrum showed reduced integrals of 2 H for the Rh···H–B environment and 0.7 H for the Rh–H environment, from 3 H and 2 H respectively, relative to 8 H for the [BAr$^F{}_4$]$^-$ anion. This was additionally confirmed by the presence of corresponding Rh···D–B and Rh–D peaks in the ^{2}H NMR spectrum at δ 0.05 and δ −18.88 respectively. Given that **2** is stable with respect to H_2 loss (Section 2.3), H/D exchange likely operates through a σ complex assisted metathesis (σ CAM)

mechanism in a Rh(III) manifold (Scheme 2.7),[36] similar to Weller and Macgregor's $[M(PCy_3)_2(H)_2(H_3B{\cdot}NMe_3)][BAr^F{}_4]$ systems (M = Rh, Ir).[35] Scheme 2.7 suggests a mechanism for this process where B–H activation at the Rh(III) centre gives a rhodium dihydrogen base stabilised boryl complex, **I**. Subsequent loss of H_2 and binding of D_2 gives **II** which can rearrange to form **III** via a σ CAM process, resulting in **IV** where deuterium incorporation has occurred at both the $Rh(H)_2$ and BH_3 positions.



Scheme 2.7 Proposed mechanism for the H/D exchange between **2** and D_2. $[BAr^F{}_4]^-$ anions not shown for clarity. Not all pathways or H/D combinations are shown.

This indicates that fast, reversible Rh–H(D)/B–H(D) exchange occurs in complex **2**, therefore there is a low energetic barrier to the formation of boryl dihydrogen complexes such as **I**. This may have further implications in terms of possible mechanisms for amine borane dehydrocoupling using the $\{Rh(Xantphos\text{-}^iPr)\}^+$ system, and will be discussed further in Chapter 3.

*2.4.2 Speciation studies of **2** with 10 equivalents of $H_3B{\cdot}NMeH_2$*

To provide insight into the organometallic species that may be formed during the dehydropolymerisation of $H_3B{\cdot}NMeH_2$ using **2**, 10 equivalents of $H_3B{\cdot}NMeH_2$ were added to complex **2** (i.e. 10 mol% catalyst loading) in 1,2-$C_6H_4F_2$ solvent in a sealed NMR tube.

The initial ^{11}B NMR spectrum (t = 30 s) showed that full consumption of $H_3B{\cdot}NMeH_2$ had already occurred – forming $(HBNMe)_3$ as the major product. Free $H_3B{\cdot}NMe_3$ is also present, suggesting that during catalysis $H_3B{\cdot}NMe_3$ is completely displaced – the signal is a well resolved quartet (δ −8.1, $^1J_{BH}$ 97 Hz), as opposed to a broad resonance which would correspond to η^1 bound $H_3B{\cdot}NMe_3$ (Section 2.3). Initially, $^{31}P\{^1H\}$ NMR spectroscopy of the reaction mixture shows two overlapping environments at δ 67.6 (d, br, $^1J_{RhP}$ ~110 Hz) (assigned to a complex **A**) and δ 67.2 (d, $^1J_{RhP}$ 111 Hz) (assigned to a complex **B**), as shown in Figure 2.7. The corresponding ^{1}H NMR spectrum shows a number of peaks upfield of 0 ppm: quadrupolar broadened resonances at δ −0.56 and δ −2.77, which sharpen on ^{11}B decoupling, indicate Rh···H–B environments, while peaks at δ −16.07, δ −16.63, δ −20.18 and δ −20.41 are in the region expected for classical Rh–H groups (Figure 2.7). From these data it was proposed that two distinct Rh(III) species were present, both containing equivalent phosphines, with rhodium bound BH_3 groups and static Rh–H environments likely, due to similar NMR spectral data to complex **2** (Section 2.3). After 20 minutes, a new resonance in the $^{31}P\{^1H\}$ NMR spectrum appears at δ 47.5 (d, $^1J_{RhP}$ 174 Hz) (Figure 2.7, a complex **C**), the larger coupling constant indicative of a cationic Xantphos-type Rh(I) complex.[17] Interestingly, in the ^{1}H NMR spectrum, no additional resonances upfield of 0 ppm are seen (Figure 2.7), suggesting that **C** may not contain metal bound B–H groups or hydrides in its structure.

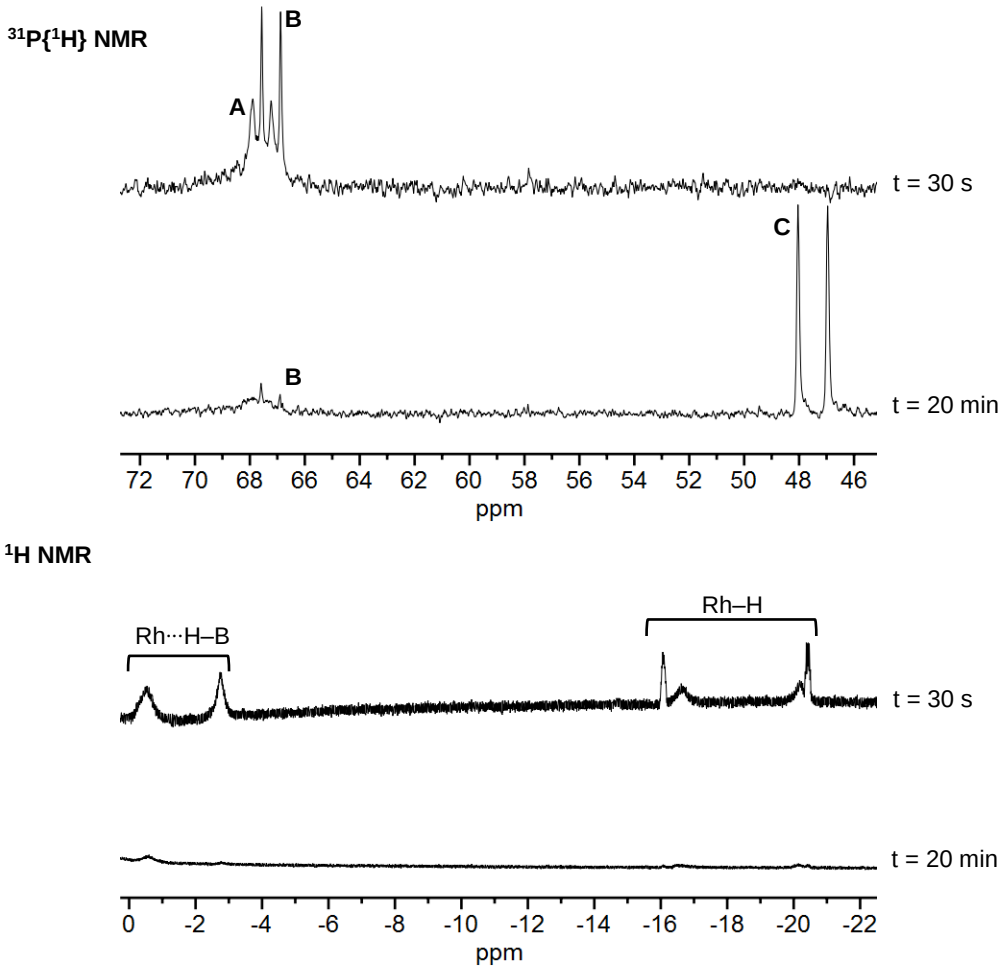


Figure 2.7 Stacked NMR spectra of the reaction of $H_3B{\cdot}NMeH_2$ with 10 mol% **2** in 1,2-$C_6H_4F_2$ over time. Top: $^{31}P\{^1H\}$ NMR spectra. Bottom: Hydride region of the ^1H NMR spectra.

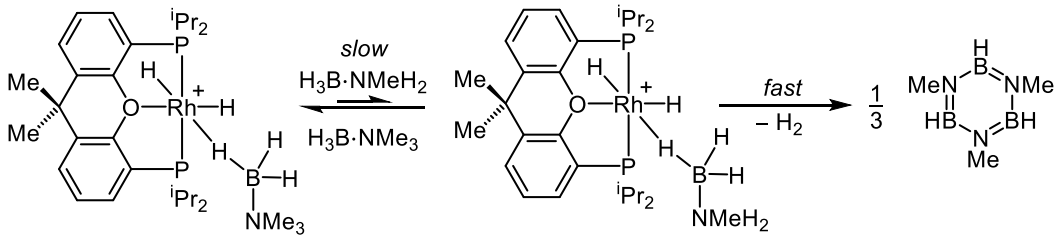
With this information in hand, the identities of these three complexes, **A**; **B**; and **C**, were probed.

2.5 Formation of {Rh(Xantphos-^{i}Pr)}$^+$ amine borane complexes

Given that $H_3B{\cdot}NMe_3$ was displaced at the beginning of catalysis at 10 mol%, it was speculated that one of the initially formed Rh(III) complexes **A** or **B** could be a product of straightforward exchange of the tertiary amine borane with $H_3B{\cdot}NMeH_2$. Therefore the synthesis of a $H_3B{\cdot}NMeH_2$ complex of the {Rh(Xantphos-^{i}Pr)}$^+$ fragment was investigated.

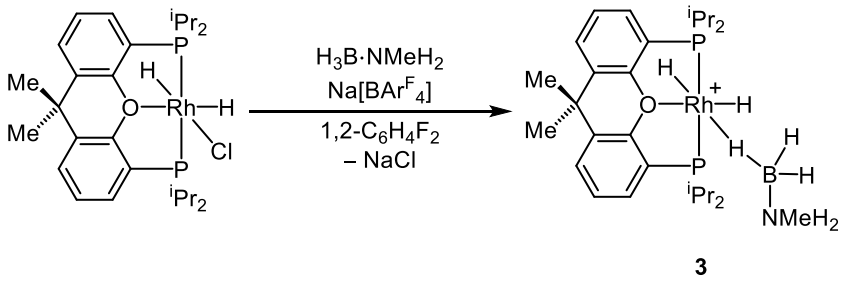
*2.5.1 Formation of [Rh(Xantphos-^{i}Pr)(H)$_2$(H$_3$B·NMeH$_2$)][BAr$^{F}_4$] (**3**)*

Addition of one equivalent of $H_3B{\cdot}NMeH_2$ to complex **2** in 1,2-$C_6H_4F_2$ solvent resulted in the dehydrocoupling of $H_3B{\cdot}NMeH_2$ to $(HBNMe)_3$, with **2** the only complex identified by $^{31}P\{^{1}H\}$ NMR spectroscopy. This may occur if substitution of the $H_3B{\cdot}NMe_3$ ligand in **2** by $H_3B{\cdot}NMeH_2$ to form the potential intermediate [Rh(κ^3-P,O,P-Xantphos-^{i}Pr)(H)$_2$(η^1-$H_3B{\cdot}NMeH_2$)][BAr$^{F}_4$] (**3**) is slow when only one equivalent of $H_2B{\cdot}NMeH_2$ is present (Scheme 2.8). However if once **3** is formed, dehydrocoupling to $(HBNMe)_3$ is fast, only **2** will be observed during the reaction (Scheme 2.8). Hence, another route to [Rh(κ^3-P,O,P-Xantphos-^{i}Pr)(H)$_2$(η^1-$H_3B{\cdot}NMeH_2$)][BAr$^{F}_4$] was sought.



Scheme 2.8 Proposed reaction profile of **2** → **3**, forming $(HBNMe)_3$ using one equivalent of $H_3B{\cdot}NMeH_2$. $[BAr^{F}_4]^-$ anions not shown for clarity.

[Rh(κ^3-P,O,P-Xantphos-^{i}Pr)(H)$_2$(η^1-$H_3B{\cdot}NMeH_2$)][BAr$^{F}_4$] (**3**) was thus independently synthesised by another route by chloride abstraction of Rh(κ^3-P,O,P-Xantphos-^{i}Pr)(H)$_2$Cl using Na[BAr$^{F}_4$] in the presence of one equivalent of $H_3B{\cdot}NMeH_2$ (Scheme 2.9). This complex could only be characterised by in situ by NMR spectroscopy, as attempts to crystallise this complex by layering the filtered 1,2-$C_6H_4F_2$ solution with pentane yielded intractable oils.



Scheme 2.9 Synthesis of [Rh(κ^3-P,O,P-Xantphos-^{i}Pr)(H)$_2$(η^1-$H_3B{\cdot}NMeH_2$)][BAr$^{F}_4$] (**3**). $[BAr^{F}_4]^-$ anion not shown for clarity.

The $^{31}P\{^{1}H\}$ NMR spectrum of **3** showed a doublet at δ 67.6 with a $^{1}J_{RhP}$ coupling of 110 Hz, indicative of a Rh(III) centre,[4] similar to complex **2** (Section 2.3) and unknown complex **A** (Figure 2.8). In the $^{11}B\{^{11}H\}$ NMR spectrum, a broad singlet at δ −19.0 was observed for the Rh···H_3B groups, slightly upfield shifted from free $H_3B{\cdot}NMeH_2$ (δ −17.1, q, $^{1}J_{BH}$ 96 Hz), suggesting an η^1 amine borane complex.[21] Whilst the ^{31}P environment of **3** seemed to be in agreement with complex **A**, its ^{1}H NMR spectrum differed from that of both **A** and **B** slightly (Figure 2.8). The hydride region of **3** showed three environments with relative integrals 3 H, 1 H and 1 H, as expected for metal bound BH_3 and static, though broad, Rh–H resonances. Interestingly, these differ from the fluxional Rh–H environments in complex **2**, which may be due to the decreased steric bulk centred on the nitrogen atom in primary **3** compared to tertiary **2**. However with chemical shifts of δ −0.33 (3 H, Rh···H–B), δ −16.75 (1 Rh–H) and δ −20.18 (1 H, Rh–H), these resonances are close to, but do not exactly match any of those reported in the hydride region for either complex **A** or **B** (Section 2.4.2).

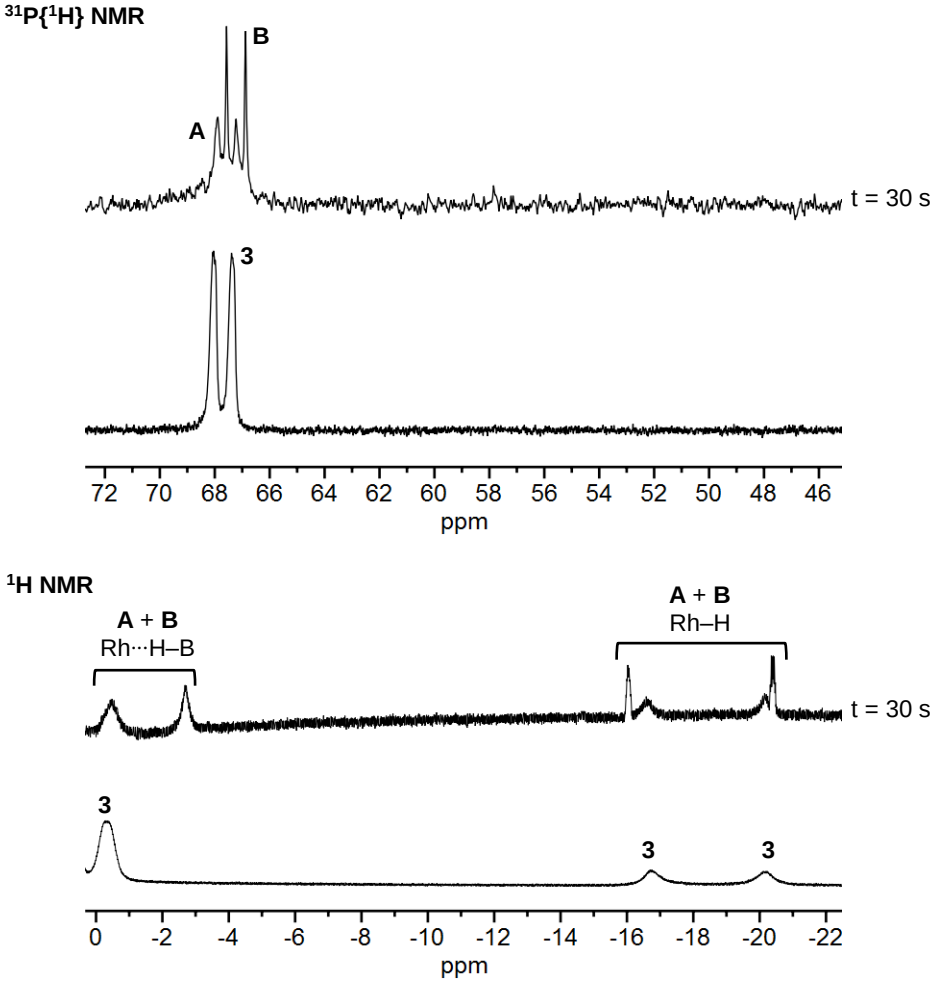


Figure 2.8 Stacked $^{31}P\{^{1}H\}$ (top) and ^{1}H NMR (bottom) spectra of complex **3** compared to that of complexes **A** and **B** at t = 30 s in 1,2-$C_6H_4F_2$ solvent.

With these small chemical shift differences in mind, another potential amine borane complex was postulated. A single dehydrocoupling event of $H_3B{\cdot}NMeH_2$ would form the linear diborazane $H_3B{\cdot}NMeHBH_2{\cdot}NMeH_2$,[37] therefore synthesis of the linear diborazane analogue of complex **3** was attempted.

*2.5.2 Formation of [Rh(Xantphos-^{i}Pr)(H)$_2$(H$_3$B·NMeHBH$_2$·NMeH$_2$)][BAr$^{F}_4$] (**4**)*

$[Rh(\kappa^3\text{-P,O,P-Xantphos-}^{i}Pr)(H)_2(\eta^1\text{-}H_3B{\cdot}NMeHBH_2{\cdot}NMeH_2)][BAr^{F}_4]$ (**4**) was formed in situ via chloride abstraction using the same reaction conditions as Scheme 2.9, only replacing $H_3B{\cdot}NMeH_2$ with $H_3B{\cdot}NMeHBH_2{\cdot}NMeH_2$.[37] The hydride region in the ^{1}H NMR spectrum of complex **4**, similar to **3**, showed three environments, though each were now centred at δ −0.53 (Rh···H–B), δ −16.62

(Rh–H) and δ −20.19 (Rh–H). These show a slightly improved match with three of the ^{1}H NMR resonances detailed for unknown complexes **A** and **B** (Figure 2.9), in particular the chemical shift for the likely Rh···H–B environment at δ −0.56. Both the BH_2 and BH_3 environments of the linear diborazane are broadened in the ^{11}B NMR spectrum at δ −4.8 and δ −18.0 respectively. The ^{31}P{^{1}H} NMR spectrum of **4** showed a resonance centred at δ 68.1, which is at a higher chemical shift than both complexes **A** and **B** (δ 67.6 and δ 67.2 respectively), but closer to **A**. This peak appears as an apparent triplet due to the presence of two, tightly coupled, phosphorus environments with similar chemical shifts. Each of the phosphorus atoms couples to rhodium ($^{1}J_{RhP}$ 112 Hz) and the other, magnetically inequivalent, trans positioned phosphorus environment ($^{2}J_{PP}$ ~340 Hz),[38] leading to two heavily roofed doublets of doublets (Figure 2.9).

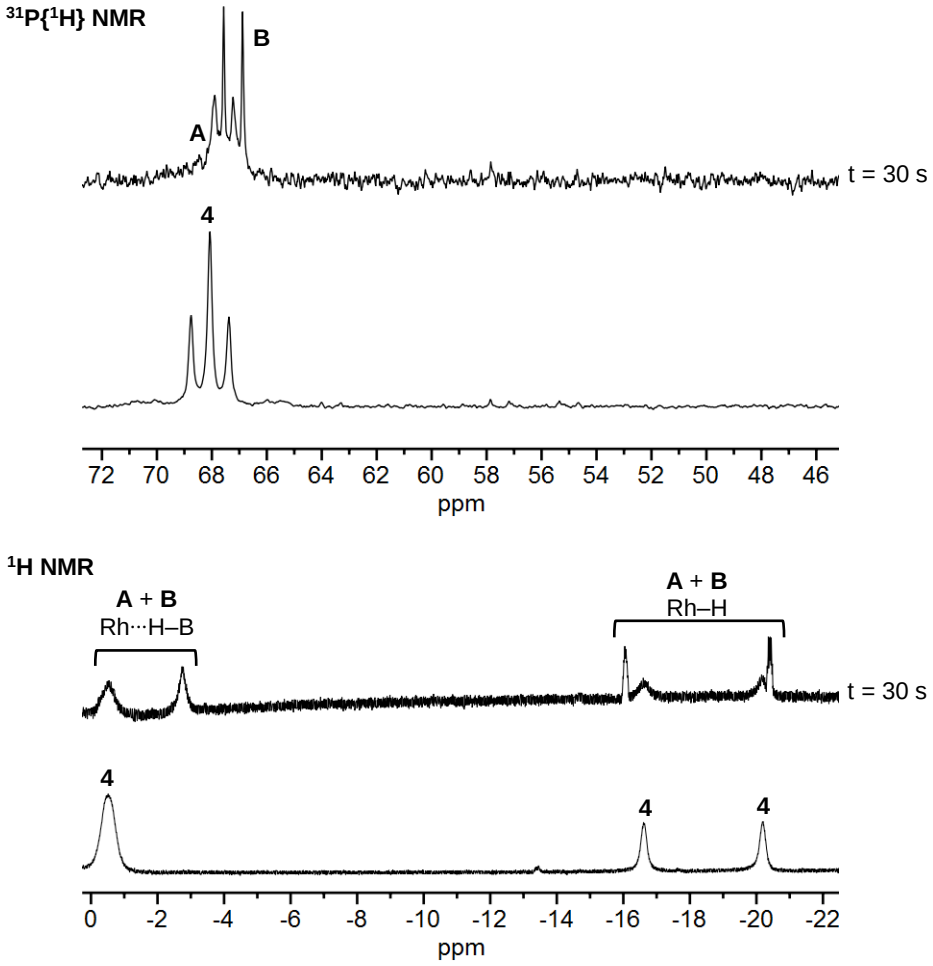


Figure 2.9 Stacked ^{31}P{^{1}H} (top) and ^{1}H NMR (bottom) spectra of complex **4** compared to that of complexes **A** and **B** at t = 30 s in 1,2-$C_6H_4F_2$ solvent.

*2.5.3 Formation of [Rh(Xantphos-^{i}Pr)(H)$_2$(H$_3$B·NMe$_2$H)][BAr$^F{}_4$] (**5**)*

It is noteworthy that both **3** and **4**, in comparison to **2**, show static hydride environments at 298 K. As **3** and **4** both contain primary amine boranes rather than the tertiary amine borane in complex **2**, this may simply be a steric effect. Whilst the crystal structures of **3** and **4** could not be obtained, the solid state structure of an analogous complex containing the secondary amine borane $H_3B{\cdot}NMe_2H$ could be determined. Chloride abstraction of Rh(κ^3-P,O,P-Xantphos-^{i}Pr)(H)$_2$Cl using Na[BAr$^F{}_4$] in the presence of one equivalent of $H_3B{\cdot}NMe_2H$ (analogous to the synthesis of **2** in Scheme 2.9) gave [Rh(κ^3-P,O,P-Xantphos-^{i}Pr)(H)$_2$(η^1-H$_3$B·NMe$_2$H)][BAr$^F{}_4$] (**5**). After filtration of the reaction mixture and subsequent diffusion into pentane, crystals of **5** were formed which were suitable for single crystal X-ray diffraction studies (Figure 2.10).

The ^{1}H NMR spectrum of the in situ reaction mixture containing **5** showed similar data to both **3** and **4**. Notably, static hydride resonances at δ −17.30 and δ −19.86, and a peak at δ −0.38 of integral 3 H that indicated a fluxional η^1-BH$_3$ environment. The ^{31}P{^{1}H} NMR spectrum showed a doublet at δ 67.8 ($^1J_{RhP}$ 111 Hz), whilst the ^{11}B NMR spectrum contained a broad signal indicative of η^1 bound $H_3B{\cdot}NMe_2H$ at δ −14.9, only slightly upfield shifted compared to free $H_3B{\cdot}NMeH_2$ which resonates at δ −12.8 (q, $^1J_{BH}$ 96 Hz) in 1,2-C$_6$H$_4$F$_2$ solvent.[28] The position of the hydride ligands was supported by the solid state structure of **5** (Figure 2.10). Although the B–H and Rh–H groups were placed in their calculated positions, it is possible that the static structure found in both the solid state and in solution may be stabilised by a dihydrogen bond between the N–H group in the bound $H_3B{\cdot}NMe_2H$ fragment and one of the isopropyl C–H groups on the Xantphos-^{i}Pr ligand, in addition to the reduced steric profile compared to **2** (Figure 2.5). The C–H···H–N distance of 2.234 Å (Figure 2.10) is smaller than the sum of the van der Vaal's radii of two hydrogen atoms (2.40 Å),[13] and may be within the range of what would be expected for a dihydrogen interaction, for example a LiCCH···HNC interaction of 2.356 Å has been calculated.[39] This may therefore explain, in the solution phase, the structural differences of **2** versus **3**, **4** and **5** beyond steric size arguments.

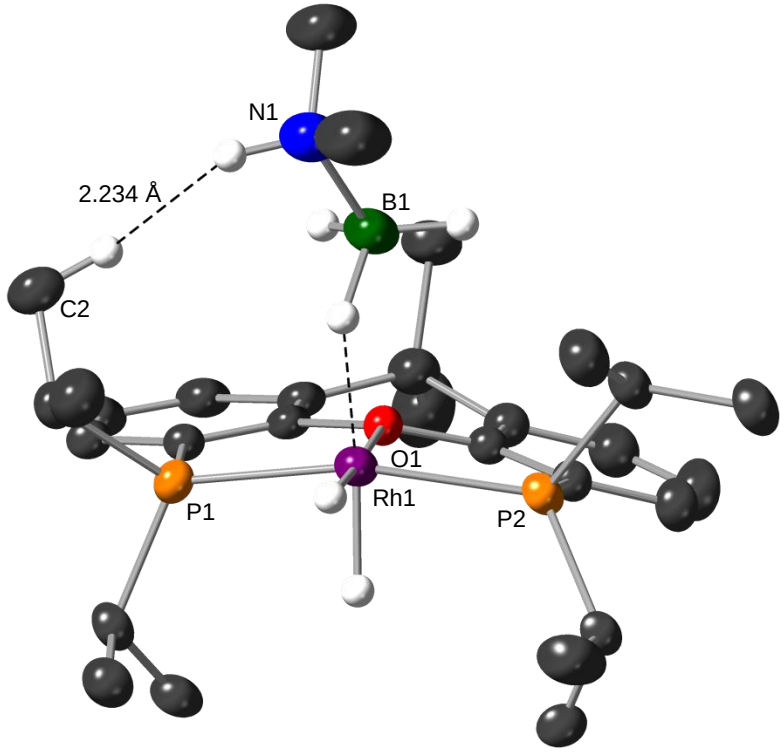


Figure 2.10 Crystal structure of the cationic portion of [Rh(κ^3-P,O,P-Xantphos-^{i}Pr)(H)$_2$(η^1-H$_3$B·NMe$_2$H)][BAr$^F{}_4$] (**5**). Displacement ellipsoids are drawn at the 30% probability level. C-bound H atoms (except one H atom bound to C2) are not shown for clarity. Selected bond lengths (Å) and angles (°): Rh1–P1, 2.2670(19); Rh1–P2, 2.252(2); Rh1–O1, 2.206(5); Rh1–B1, 2.821(11); B1–N1, 1.612(18), P1–Rh1–P2, 159.92(8). The possible C–H···N–H interaction of 2.234 Å is shown.

2.5.4 Conclusions: formation of {Rh(Xantphos-^{i}Pr)}$^+$ amine borane complexes

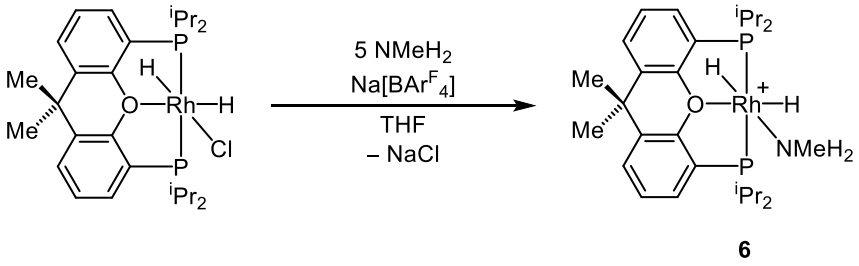
With complexes **3** and **4** independently synthesised in situ, whilst neither were a conclusive match for complexes **A** or **B** in Section 2.4.2, both show closer spectral similarities to **A** which resonates at δ 67.6 (d, $^1J_{RhP}$ 110 Hz) in the ^{31}P{^{1}H} NMR spectrum (Figure 2.7). It was hence proposed that the peaks at δ −0.56, δ −16.63 and δ −20.18 in the ^{1}H NMR spectrum of the initial 10 mol% reaction mixture of **2** with H$_3$B·NMeH$_2$ (Figure 2.7), were features of **A**. On balance, the ^{31}P{^{1}H} NMR spectrum of **3** which shows a doublet at δ 67.6 (rather than an apparent triplet that occurs in **4**) suggests that **A** is most likely to be **3**, i.e. [Rh(κ^3-P,O,P-Xantphos-^{i}Pr)(H)$_2$(η^1-H$_3$B·NMeH$_2$)][BAr$^F{}_4$].

2.6 Formation of {Rh(Xantphos-^{i}Pr)}$^{+}$ complexes from $NMeH_2$ or BH_3

The second, unknown, complex identified in the initial stages of 10 mol% catalysis (complex **B**) is assigned to having ^{1}H NMR spectral data of δ −2.77, δ −16.07 and δ −20.41, and a ^{31}P environment at δ 67.2 (Section 2.4.2). The sharp Rh–H peaks indicate a complex with static hydrides alongside another ligand which likely contains a B–H environment resonating at δ −2.77. The amine borane complexes **3** and **4** gave broader hydride resonances than those in complex **B**; hence ligands other than that of typical amine borane type fragments (investigated in Section 2.5) were postulated. As discussed in Chapter 1, B–N bond cleavage to form free amine and free borane may result during catalysis; therefore the synthesis of $NMeH_2$ and BH_3 complexes of {Rh(Xantphos-^{i}Pr)}$^{+}$ were pursued.

*2.6.1 Formation of [Rh(Xantphos-^{i}Pr)(H)$_2$(NMeH$_2$)][BAr$^{F}_4$] (**6**)*

Amine complexes of Xantphos-type ligands have previously been reported. For example, [Rh(κ^3-P,O,P-Xantphos-Ph)(H)$_2$(NMe$_2$H)][BAr$^{F}_4$] was formed by addition of $Et_3B{\cdot}NMe_2H$ to complex **2-Ph**, in which B–N bond cleavage of the amine borane occurred to give the free amine.[40] [Rh(κ^3-P,O,P-Xantphos-Ph)(H)$_2$(NMe$_2$H)][BAr$^{F}_4$] contained static Rh–H resonances in the ^{1}H NMR spectrum, though could not be crystallographically characterised.[40] [Rh(κ^3-P,O,P-Xantphos-^{i}Pr)(H)$_2$(NMeH$_2$)][BAr$^{F}_4$] (**6**) was formed in a THF solution using the same route used for complexes **3**, **4** and **5** with 5 equivalents of $NMeH_2$ instead of the corresponding amine borane (Scheme 2.10). Complex **6** was fully characterised by NMR spectroscopy, ESI-MS, elemental microanalysis and single crystal X-ray diffraction, the solid state structure shown in Figure 2.11. Likewise to the solid state structure of **5** in Figure 2.10, there appears to be close C–H···H–N interactions in complex **6**,[39] which may further stabilise the structure.



6

Scheme 2.10 Synthesis of [Rh(κ^3-P,O,P-Xantphos-Ph)(H)$_2$(NMe$_2$H)][BAr$^F{}_4$] (**6**). [BAr$^F{}_4$]$^-$ anion not shown for clarity.

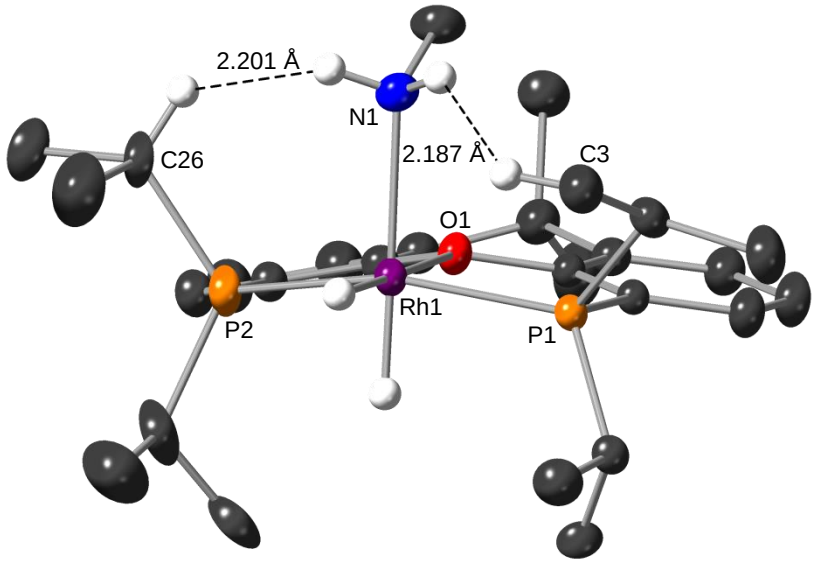


Figure 2.11 Crystal structure of the cationic portion of [Rh(κ^3-P,O,P-Xantphos-^{i}Pr)(H)$_2$(NMeH$_2$)][BAr$^F{}_4$] (**6**). Displacement ellipsoids are drawn at the 30% probability level. C-bound H atoms (except one H atom bound to C3 and the H atom bound to C26) are not shown for clarity. Selected bond lengths (Å) and angles (°): Rh1–P1, 2.2757(8); Rh1–P2, 2.2662(9); Rh1–O1, 2.213(2); Rh1–N1, 2.242(3); P1–Rh1–P2, 158.72(4).

The hydride resonances of **6** were found in the ^{1}H NMR spectrum (CD_2Cl_2) at δ −17.73 and δ −20.40, indicating a non-fluxional structure, however no other signals were present < 0 ppm. The ^{31}P{^{1}H} NMR spectrum indicates one phosphorus environment at δ 64.0 ($^1J_{RhP}$ 111 Hz), different from the signal at δ 67.2 observed for complex **B**, therefore it is unlikely that **6** is complex **B**. The involvement of **6** in the dehydropolymerisation of $H_3B{\cdot}NMeH_2$, however, cannot be ruled out if **6** is simply not formed under these conditions at 10 mol% catalyst loading.

*2.6.2 Formation of [{Rh(Xantphos-^{i}Pr)(H)$_2$}$_2$(BH$_4$)][BAr$^F_4$] (**7**)*

The presence of a Rh···H–B interaction is highly likely in complex **B** due to the characteristic signal observed at δ −2.77 in the ^{1}H NMR spectrum, which sharpened on ^{11}B decoupling. This was probed by addition of 1 equivalent of $H_3B{\cdot}THF$ to complex **2**. The reaction mixture was immediately monitored by NMR spectroscopy. A resonance in the $^{31}P\{^{1}H\}$ spectrum at δ 67.9 ($^{1}J_{RhP}$ 111 Hz) was responsible for 35% of the phosphorus in the reaction mixture, the coupling constant suggesting a Rh(III) species,[4] which may therefore contain hydride ligands. Also present were signals at δ 64.7 (50% total P, v br), δ 52.1 (10% total P, m) and δ 48.1 (5% total P, d, $^{1}J_{RhP}$ 174 Hz). In the ^{1}H NMR spectrum, a broad signal centred at δ −2.94 was observed alongside sharper peaks at δ −16.25 and δ −20.69 in an approximate 2:1:1 ratio. In the ^{11}B NMR spectrum a broad resonance at δ −36.9 was observed, which is in the region associated with a borohydride ligand.[41] However, given the variety of complexes present in the $^{31}P\{^{1}H\}$ NMR spectrum of this reaction mixture, a cleaner route was required to form this complex and enable its unequivocal characterisation.

With this preliminary data, and speculated $[BH_4]^-$ involvement, complex **2** was reacted with $[N^nBu_4][BH_4]$ in 1,2-$C_6H_4F_2$ solvent (Scheme 2.11). Monitoring of this reaction mixture by NMR spectroscopy showed a much cleaner $^{31}P\{^{1}H\}$ NMR spectrum compared to the reaction of **2** with $H_3B{\cdot}THF$. 80% of the total phosphorus in solution could be assigned to a peak at δ 67.2 (d, $^{1}J_{RhP}$ 111 Hz), the rest of the phosphorus contribution attributed to a signal at δ 47.5 (d, $^{1}J_{RhP}$ 174 Hz) (Figure 2.12). The peak at δ 47.5 will be discussed later (Section 2.7). Resonances in the hydride region of the ^{1}H NMR spectrum (Figure 2.12) were present at δ −2.77 (2 H), δ −16.07 (1 H) and δ −20.41 (1 H), as was a broad signal at δ −37.5 in the ^{11}B NMR spectrum.

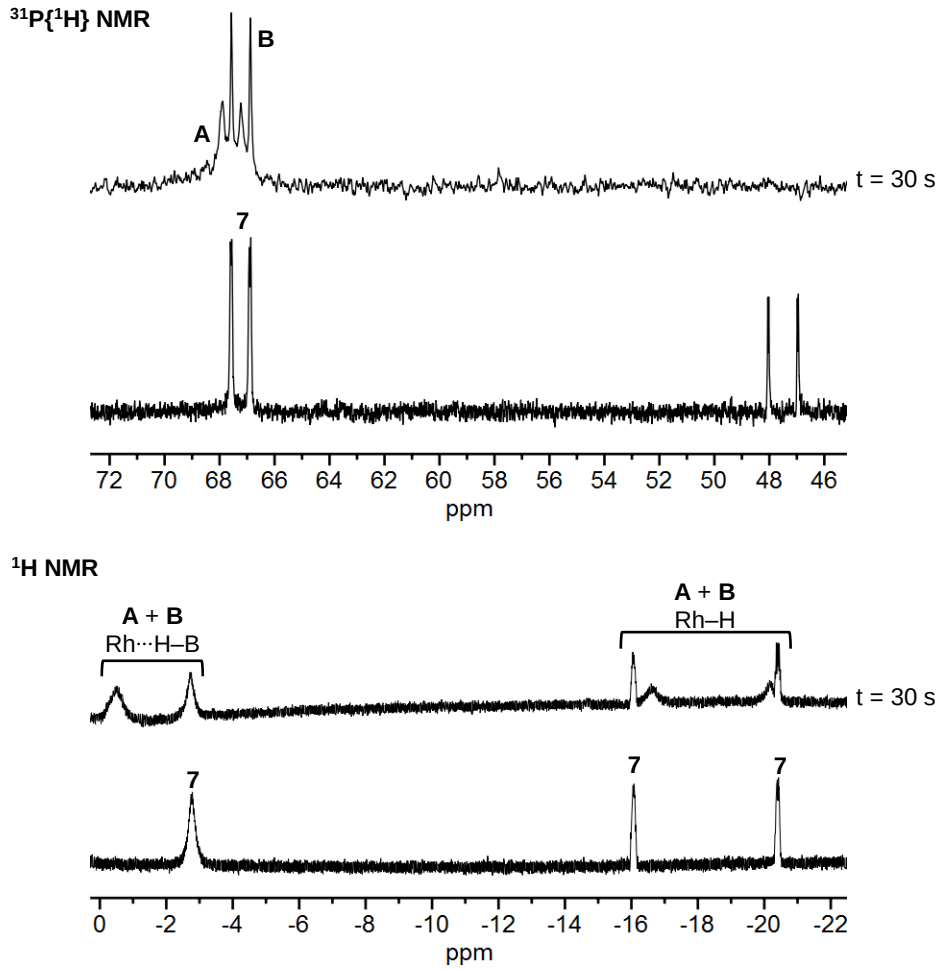


Figure 2.12 Stacked $^{31}P\{^{1}H\}$ (top) and ^{1}H NMR (bottom) spectra of complex **7** compared to that of complexes **A** and **B** at t = 30 s in 1,2-$C_6H_4F_2$ solvent.

These observed spectroscopic data are a very good match of that described for complex **B**, and are similar to those reported for the bimetallic, monocationic, complex [{PNP-^{i}Pr)FeH(CO)}$_2$(μ,$\eta^1\eta^1$-H_2BH_2)][BPh_4] (PNP-^{i}Pr = HN{$CH_2CH_2(P^iPr_2)$}$_2$, Figure 2.13).[42] The ^{1}H NMR spectrum of the iron complex showed that all of the protons associated with the $\mu,\eta^1\eta^1$-H_2BH_2 ligand were equivalent at room temperature (δ −5.7), showing a fluxional process for the B–H environments, however its ^{11}B NMR spectra was not reported. The crystal structure of [{PNP-^{i}Pr)FeH(CO)}$_2$(μ,$\eta^1\eta^1$-H_2BH_2)][BPh_4] showed no Fe–Fe bond, nor any bridging hydride ligands. Instead, the borohydride ligand coordinated to both iron centres through a single B–H bond. The other two, terminal, B–H bonds interacted with one of the PNP-^{i}Pr ligands through a dihydrogen bond with the N–H group, which act to stabilise the $\mu,\eta^1\eta^1$-H_2BH_2 fragment.

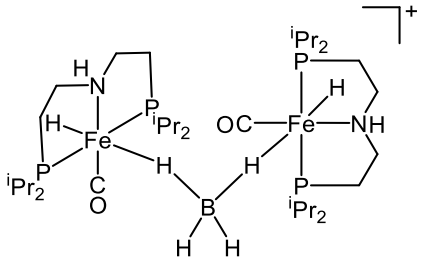
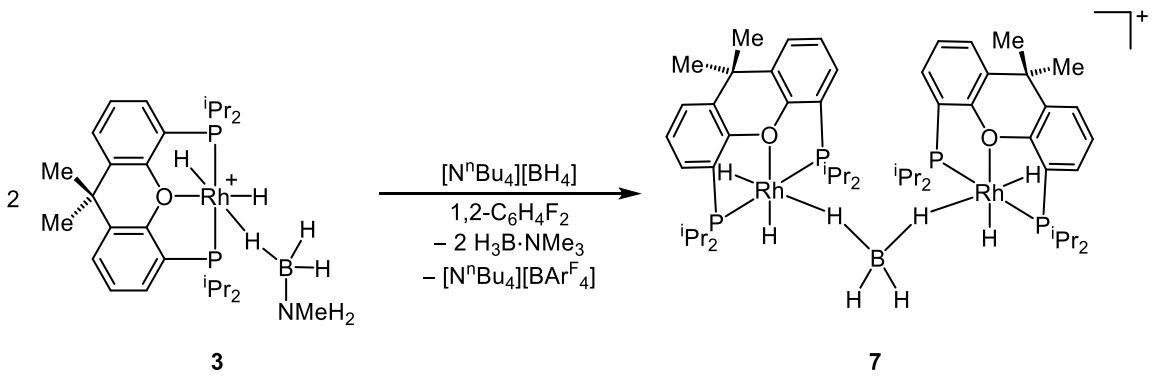


Figure 2.13 Structure of [{PNP-^{i}Pr)FeH(CO)}$_2$(μ,η^{1}η^1-H_2BH_2)][BPh_4]. The dihydrogen bonding interaction between the terminal B–H bonds and the N–H group of the adjacent PNP-^{i}Pr ligand is not shown for simplicity. [BPh_4]$^-$ anion not shown for clarity.

Hence it was proposed that **B** is a bimetallic bridging borohydride complex, [{Rh(κ^3-P,O,P-Xantphos-^{i}Pr)$(H)_2$}$_2$(μ,η^{1}η^1-H_2BH_2)][BAr^F_4] (**7**, Scheme 2.11). These data points towards η^1-BH_4 coordination of the borohydride ligand to each rhodium centre, where rapid exchange between terminal and bridging B–H resonances occurs, and two static Rh–H groups per rhodium that do not undergo exchange. This accounts for the 2:1:1 ratio of resonances in the hydride region of the ^{1}H NMR spectrum of complex **7**. Unfortunately, complex **7** could not be crystallographically characterised, or isolated, as over 30 minutes, steady effervescence of the reaction mixture occurs and the complex at δ 47.5 becomes the major species in the ^{31}P{^{1}H} NMR spectrum. The identity of this complex is discussed further in Section 2.7.



Scheme 2.11 Synthesis of [{Rh(κ^3-P,O,P-Xantphos-^{i}Pr)$(H)_2$}$_2$(μ,η^{1}η^1-H_2BH_2)][BAr^F_4] (**7**). [BAr^F_4]$^-$ anions not shown for clarity.

2.6.3 Conclusions: formation of {Rh(Xantphos-^{i}Pr)}$^+$ complexes from $NMeH_2$ or BH_3

From the formation of [Rh(κ^3-P,O,P-Xantphos-^{i}Pr)$(H)_2(NMeH_2)$][BAr^F_4] (**6**) and postulated [{Rh(κ^3-P,O,P-Xantphos-^{i}Pr)$(H)_2$}$_2$(μ,η^{1}η^1-H_2BH_2)][BAr^F_4] (**7**), using free $NMeH_2$ or free

BH_3/$[BH_4]^-$ sources respectively, it is likely that complex **7** is present in the initial stages of the dehydrocoupling of $H_3B{\cdot}NMeH_2$ using 10 mol% **2**, previously labelled complex **B**. This may therefore indicate that B–N bond cleavage of $H_3B{\cdot}NMeH_2$ to form BH_3, which is then trapped by a hydride to form a $[BH_4]^-$ complex (Scheme 2.14), as well as $NMeH_2$, may be important in the mechanism of dehydropolymerisation of $H_3B{\cdot}NMeH_2$ using $\{Rh(Xantphos\text{-}^iPr)\}^+$ complexes. Complex **6** is not observed – suggesting a different fate for the amine.

2.7 Formation of a $\{Rh(Xantphos\text{-}^iPr)\}^+$ dimetalloborylene complex

The end organometallic product at 10 mol% catalysis, complex **C**, showed NMR spectroscopic data consistent with a Rh(I) centre and no visible metal hydride or metal bound BH_3 resonances in the ^1H spectrum (Figure 2.7). This resonance was also observed as a minor product in the initial reaction mixtures of complex **2** with $H_3B{\cdot}THF$ or with $[N^nBu_4][BH_4]$ (Figure 2.12). and is the major product formed in the latter reaction after 30 minutes.

*2.7.1 Formation of [{Rh(Xantphos-^{i}Pr)}$_2$B][BAr$^F{}_4$] (**8**)*

The addition of 0.5 equivalents of $[N^nBu_4][BH_4]$ to complex **2** initially formed **7** in 1,2-$C_6H_4F_2$ solvent, giving a light yellow solution. Over 30 minutes, steady effervescence could be observed and a darkening of the colour of the solution to orange. $^{31}P\{^1H\}$ NMR spectroscopy of this aged reaction mixture showed that it now contained 80% of the new complex (**8**) by a signal δ 47.5, which appears as a doublet of doublets. This finding shows that in the reaction profile of 10 mol% $H_3B{\cdot}NMeH_2$ using **2** (Figure 2.7) complex **B** (i.e. **7**) evolves into complex **C** (**8**) over time. ESI-MS of the aged reaction mixture after 30 minutes showed the dominant cationic species to be singly charged with an isotope pattern that matched very well with a formulation of $[\{Rh(Xantphos\text{-}^iPr)\}_2B]^+$ (*m/z* 1101.34, calculated 1101.33, Figure 2.14). The ^1H NMR spectrum of **8** shows an absence of hydride signals (between δ 0 and δ −50), while in the ^{11}B NMR spectrum a very broad resonance at δ 135 is observed. This is consistent with complexes in which there is a significant M···B multiple bonding component,[43] and is considerably downfield shifted from the regions

associated with amine boranes[28] or aminoboranes[44] interacting with metal centres. Given these data, the structure of **8** was proposed to be that shown in Scheme 2.12. The doublet of doublets (δ 47.5, $^{1}J_{RhP}$ 174 Hz, $^{3}J_{RhP}$ 6 Hz) observed in the $^{31}P\{^{1}H\}$ NMR spectrum (Figure 2.14) can therefore be rationalised by a one bond and a three bond ^{103}Rh–^{31}P coupling (i.e. an $A_2XX'A'_2$ system), the size of the former (174 Hz) being consistent with a Rh(I) centre,[17] while smaller couplings (such as 6 Hz) to distal Rh centres in dimeric systems have been noted before,[45] as observed in **8**. A further discussion on the structure of **8** is described in Section 2.8.

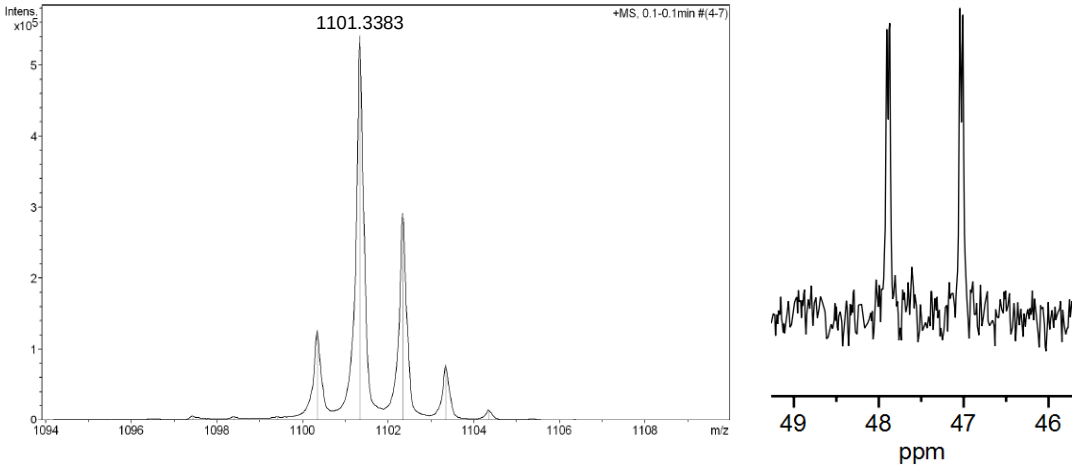
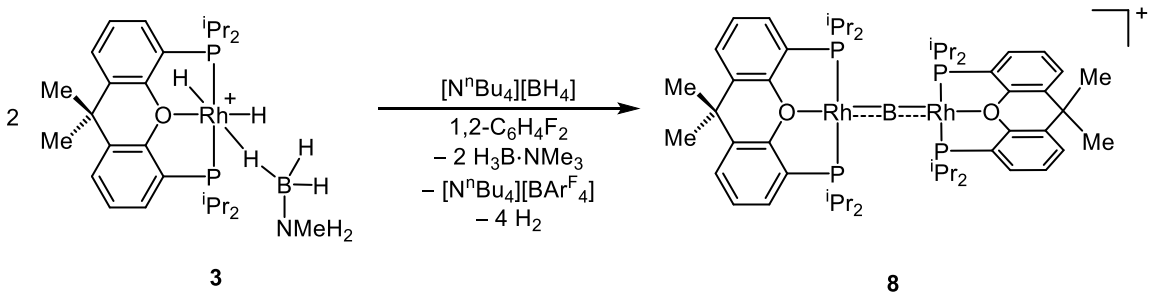


Figure 2.14 Left: ESI-MS spectrum of **8**. Right: $^{31}P\{^{1}H\}$ NMR spectrum of **8** in 1,2-$C_6H_4F_2$ solvent.



Scheme 2.12 Synthesis of [{Rh(κ^3-P,O,P-Xantphos-^{i}Pr)}$_2$B)][BAr$^F_4$] (**8**). [BAr$^F_4$]$^-$ anion not shown for clarity.

Complex **8** is particularly sensitive and attempts to isolate this species – by diffusion of a 1,2-$C_6H_4F_2$ solution of **8** into pentane across a range of temperatures, for example – leads to decomposition of **8** to unidentified products, therefore its solid state structure, at least using the [BAr$^F_4$]$^-$ anion, could not be obtained. It appears that **8** is formed via dehydrogenation of

borohydride complex **7**, and is likely the identity of complex **C** – the organometallic complex formed at the end of the reaction of 10 mol% **2** with $H_3B{\cdot}NMeH_2$.

2.8 Structure of [{Rh(Xantphos-^{i}Pr)}$_2$B][BAr$^{Cl}_4$] (**8-[BAr$^{Cl}_4$]**)

[{Rh(Xantphos-^{i}Pr)}$_2$B][BAr$^{F}_4$] (**8**) could not be crystallographically characterised. However adding 0.5 equivalents of [N^{n}Bu$_4$][BH$_4$] to the [BAr$^{Cl}_4$]$^-$ analogue of complex **2**, **2-[BAr$^{Cl}_4$]**, in CH_2Cl_2 yielded orange single crystals of [{Rh(κ^3-P,O,P-Xantphos-^{i}Pr)}$_2$B][BAr$^{Cl}_4$] (**8-[BAr$^{Cl}_4$]**) suitable for single crystal X-ray diffraction studies. The solid state structure of **8-[BAr$^{Cl}_4$]** is shown as a thermal ellipsoid model in Figure 2.15 and a space-filling model in Figure 2.16.

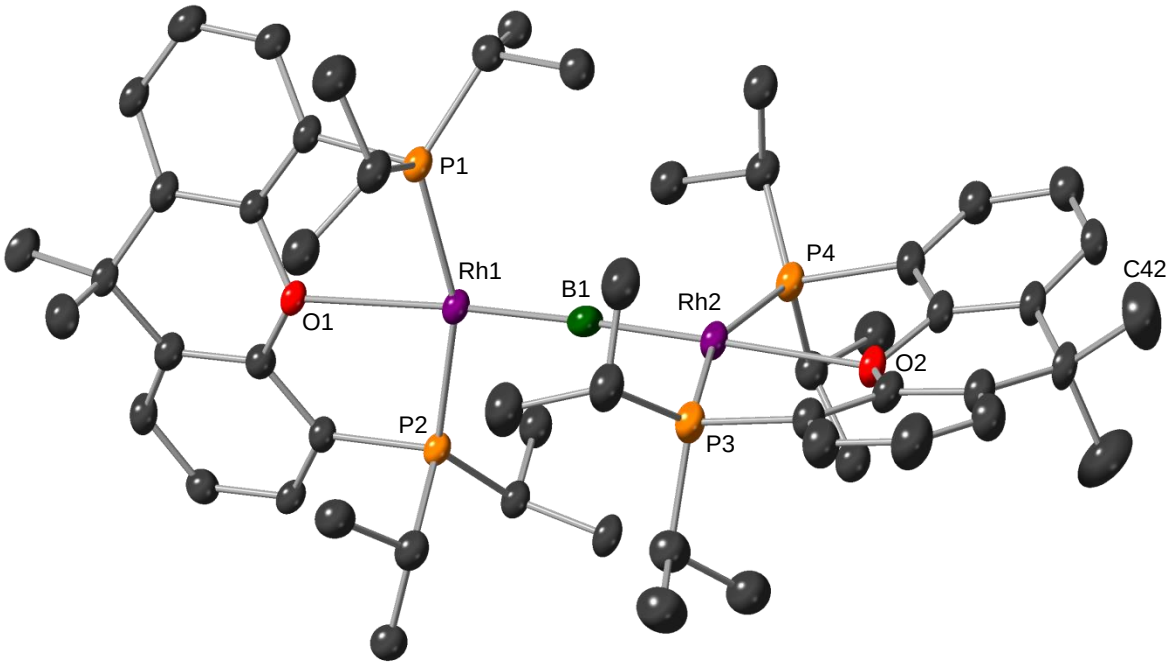


Figure 2.15 Crystal structure of the cationic portion of [{Rh(κ^3-P,O,P-Xantphos-^{i}Pr)}$_2$B][BAr$^{Cl}_4$] (**8-[BAr$^{Cl}_4$]**). Displacement ellipsoids are drawn at the 30% probability level. H atoms are not shown for clarity. Selected bond lengths (Å) and angles (°): Rh1–P1, 2.2961(17); Rh1–P2, 2.2546(17); Rh2–P3, 2.260(2); Rh2–P4, 2.2953(19); Rh1–O1, 2.343(4); Rh2–O2, 2.343(4);Rh1–B1, 1.862(8); Rh2–B1, 1.880(8); Rh1–B1–Rh2, 177.4(5); angle between P1/Rh1/P2/O1 and P3/Rh2/P4/O2 90.2.

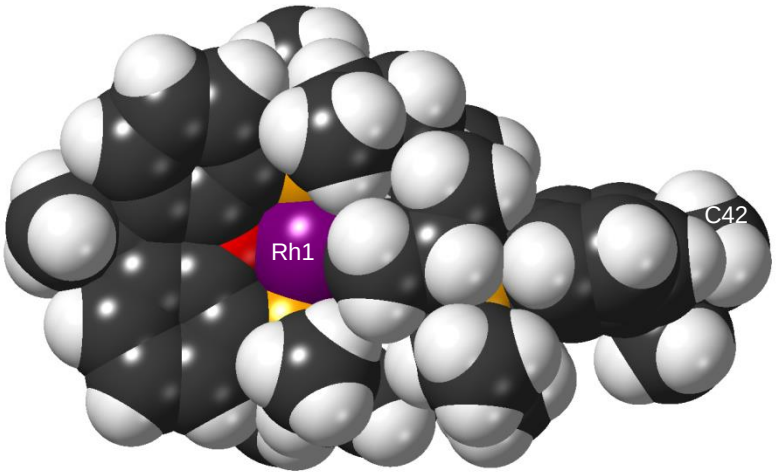


Figure 2.16 Space filling diagram (van der Waals radii) of the cationic portion of [{Rh(κ^3-P,O,P-Xantphos-^{i}Pr)}$_2$B][BAr$^{Cl}_4$] (**8-[BAr$^{Cl}_4$]**), showing the positions of Rh1 and C42 for perspective.

Single crystals of complex **8-[BAr$^{Cl}_4$]** were of relatively poor crystal quality and in addition to the reduction in high angle data, the final crystallographic refinement was only of moderate quality (R = 7.9%). However, the data collected proved adequate for confirming the connectivity and bond metrics, showing a bimetallic borylene structure had been formed. **8-[BAr$^{Cl}_4$]** contains a near linear Rh$_2$ bimetallic unit spanned by a single boron atom (Rh–B–Rh = 177.4(5)°). The Xantphos-^{i}Pr ligands adopt a mer κ^3-P,O,P geometry, placing the central ether group trans to the boron, and the Rh–O distances (2.343(2) and 2.343(4) Å) are longer than that observed in **2** (2.192(3) Å), suggesting that the boron atom exerts a significant trans influence.[46-47] The Rh–B distances (1.880(8) and 1.862(8) Å) are both shorter than the Rh–B distance measured in the boryl complex Rh(κ^3-P,O,P-Xantphos-^{i}Pr)(Bpin) (1.981(4) Å; pin = pinacol; Figure 2.17),[48] which has a formal covalent Rh–B single bond, however are longer than those in monometallic complexes with M=B bonds such as Ru(H)(Cl)(=BMes)(PCy$_3$)$_2$ (1.780(4) Å, Mes = mesityl; Figure 2.17).[49]

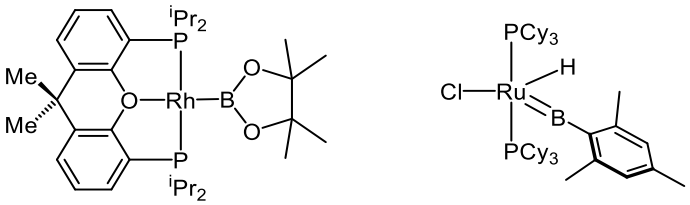


Figure 2.17 Structures of boryl complex Rh(κ^3-P,O,P-Xantphos-^{i}Pr)(Bpin) (left) and monometallic borylene complex Ru(H)(Cl)(=BMes)(PCy$_3$)$_2$ (right).

In fact, the Rh–B distances in **8-[BAr$^{Cl}_4$]** are similar to group 9 aminoborylenes, such as mer-[Ir(PMe$_3$)$_3$(H)(Cl)(=BN^{i}Pr$_2$)][BAr$^F_4$] (1.897(5) Å),[50] in which electronic unsaturation of boron can be attenuated by conjugation with the nitrogen lone pair (Figure 2.18). They are also comparable to closely related iron,[51] and ruthenium,[52] dimetalloborylenes [{(η^5-C$_5$H$_4$R)(CO)$_2$M}$_2$B]$^+$ (M = Fe, R= Me; M = Ru, R = H; the Ru example is detailed in Figure 2.18). For the ruthenium complex, the Ru–B distances are 1.931(3) and 1.963(3) Å, with a Ru–B–Ru angle of 175.5(2)°. These comparisons suggest some partial double bond character to the Rh–B bonding in **8-[BAr$^{Cl}_4$]** by dπ-pπ interactions.[51] This may also be suggested by the orientation of the Xantphos-^{i}Pr ligands, of which the angle between the P1/Rh1/P2/O1 planes is 90.2°, however the steric requirements of the interlocking of the ^{i}Pr groups also are likely to dominate this geometry (Figure 2.16).

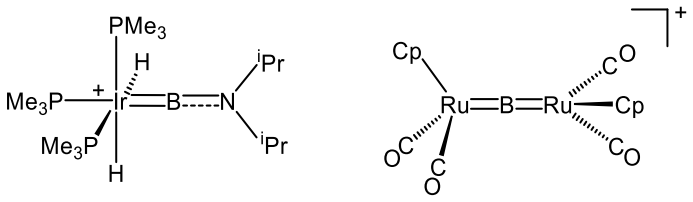


Figure 2.18 Structures of borylene complexes related to **8**/**8-[BAr$^{Cl}_4$]**: mer-[Ir(PMe$_3$)$_3$(H)(Cl)(=BN^{i}Pr$_2$)]$^+$ and [{(η^5-C$_p$)(CO)$_2$Ru}$_2$B]$^+$. Anions not shown for clarity.

Complex **8-[BAr$^{Cl}_4$]** can be described by three valence extremes (Figure 2.19): (a) a dimetalloborylene in which a formally positively charged boron engages in both σ and π bonding with two Rh(I) centres, (b) a cationic borinium with no multiple bonding,[53] and (c) a dimetalloboride with a Rh(III)=B–Rh(I) core.[43] The latter valence extreme (c) was discounted due to the symmetric Rh–B–Rh motif observed and NMR data that indicate equivalent Rh(I) centres.

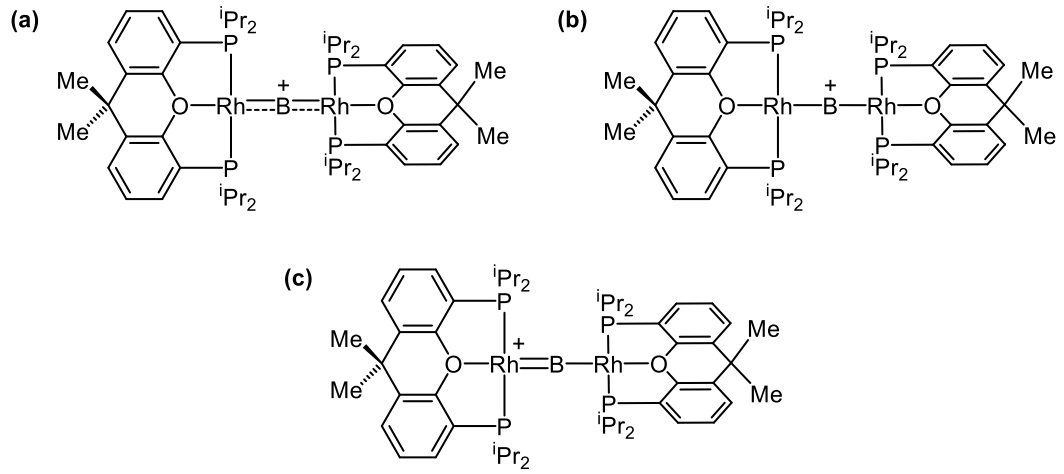


Figure 2.19 Possible bonding schemes for **8-[BAr$^{Cl}_4$]**. (a) A dimetalloborylene. (b) A borinium. (c) A dimetalloboride.

Given that structures (a) and (b) are opaque to experiment, in order to decipher the structure of **8-[BAr$^{Cl}_4$]** as a dimetalloborylene or a cationic borinium, DFT calculations were undertaken by Dr Nicholas A. Beattie and Prof. Stuart A. Macgregor (Heriot-Watt University, Edinburgh). A QTAIM (Quantum Theory of Atoms in Molecules) analysis was carried out.[54] Two important parameters obtained from these calculations are ρ(r) (electron density) and ε (bond ellipticity). A non-zero value of ρ(r) indicates that a bond between two atoms is present, while ε is a measure of the bond anisotropy (i.e. single double bond π character). A cylindrically symmetrical bond (such as C–C) will have very low ellipticity (close to zero) while a C=C bond for example, will have an ellipticity of 1. Bond critical points were located between each rhodium and the central boron atom (Figure 2.20) which suggests a covalent interaction with a ρ(r) value of 0.15, and low ellipticity (ε = 0.03), suggesting a near-spherical electron distribution at the bond critical point. Multiple bonding between orthogonal Rh–B–Rh planes was most readily seen in the delocalised Kohn-Sham orbitals HOMO-5 and HOMO-8 (Figure 2.20). In addition, NBO (Natural Bond Order) calculations were interpreted in terms of there being similar contributions to Rh–B π bonding in both the xz and the yz planes, supporting formulation (a) in Figure 2.19 as the best descriptor for the bonding in **8-[BAr$^{Cl}_4$]** – a dimetalloborylene.

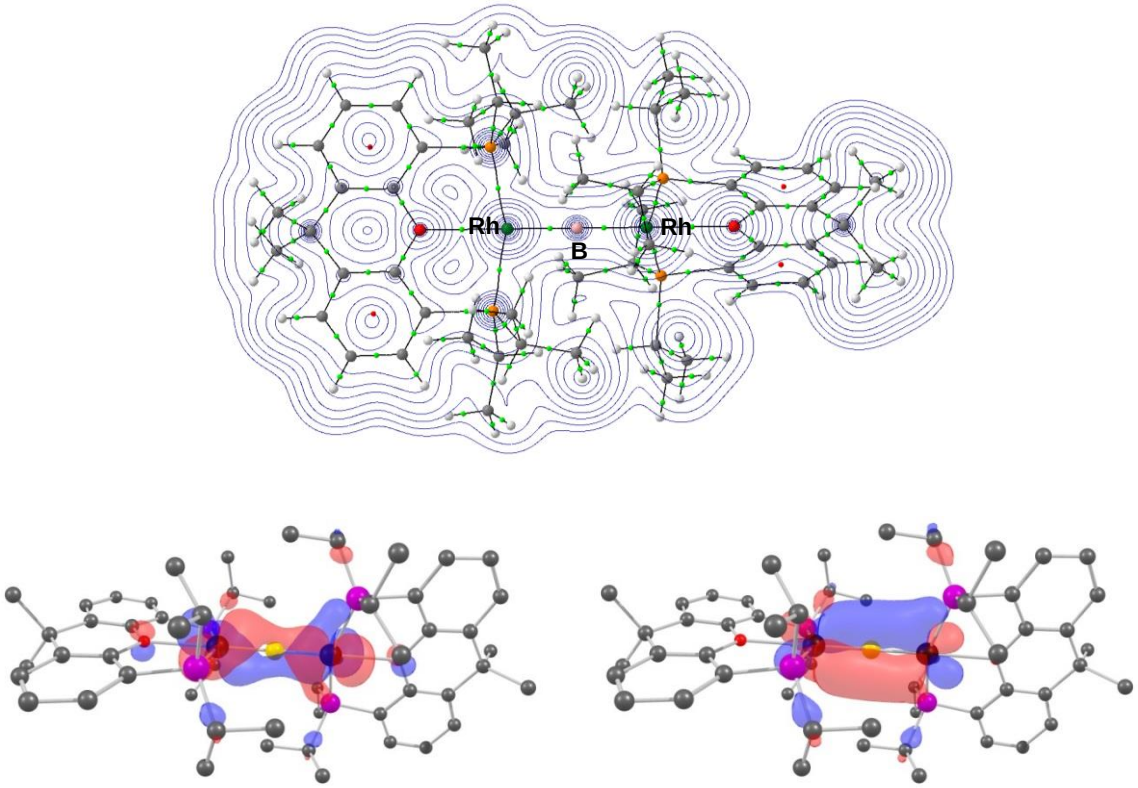


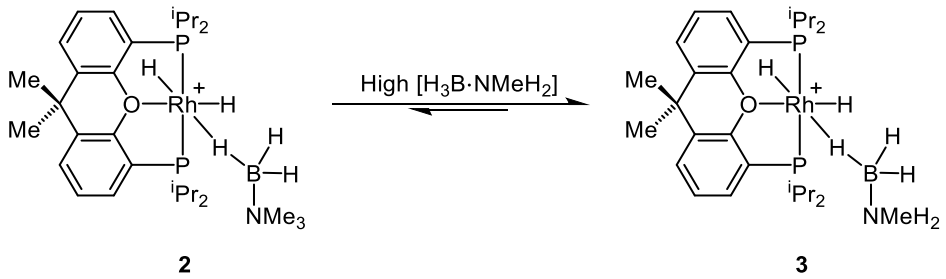
Figure 2.20 Top: Molecular graph of **8-[BAr$^{Cl}_4$]** with 2D contour plot of the electron density in the Rh/P/B plane. Bond critical points are shown in green and ring critical points in red. Bottom: Kohn-Sham orbitals HOMO-5 (left) and HOMO-8 (right) exhibiting Rh–B π bonding in **8-[BAr$^{Cl}_4$]**. All diagrams courtesy of Dr Nicholas A. Beattie and Prof. Stuart A. Macgregor.

2.9 Connecting complexes **2**, **3**, **7** and **8**

In Figure 2.7, $H_3B{\cdot}NMeH_2$ dehydrocoupling using 10 mol% **2** in 1,2-$C_6H_4F_2$ solvent operated via a reaction profile of **2** → **A** + **B** → **C** by $^{31}P\{^1H\}$ and ^1H NMR spectroscopy of the reaction mixture over time. Throughout this Chapter, **A** was shown to be [Rh(κ^3-P,O,P-Xantphos-^{i}Pr)(H)$_2$(η^1-$H_3B{\cdot}NMeH_2$)][BAr$^F_4$] (**3**), the identity of **B** was proposed to be complex **7**, [{Rh(κ^3-P,O,P-Xantphos-^{i}Pr)(H)$_2$}$_2$(μ,η^{1}η^1-H_2BH_2)][BAr$^F_4$] and the final organometallic product of the reaction, **C**, was characterised as [{Rh(κ^3-P,O,P-Xantphos-^{i}Pr)}$_2$B)][BAr$^F_4$] (**8**).

Therefore, the formation of complex **8** from complex **2** is proposed to occur in a reaction manifold described as **2** → **3** → **7** → **8**. This proposed pathway is postulated to be in agreement with the following points:

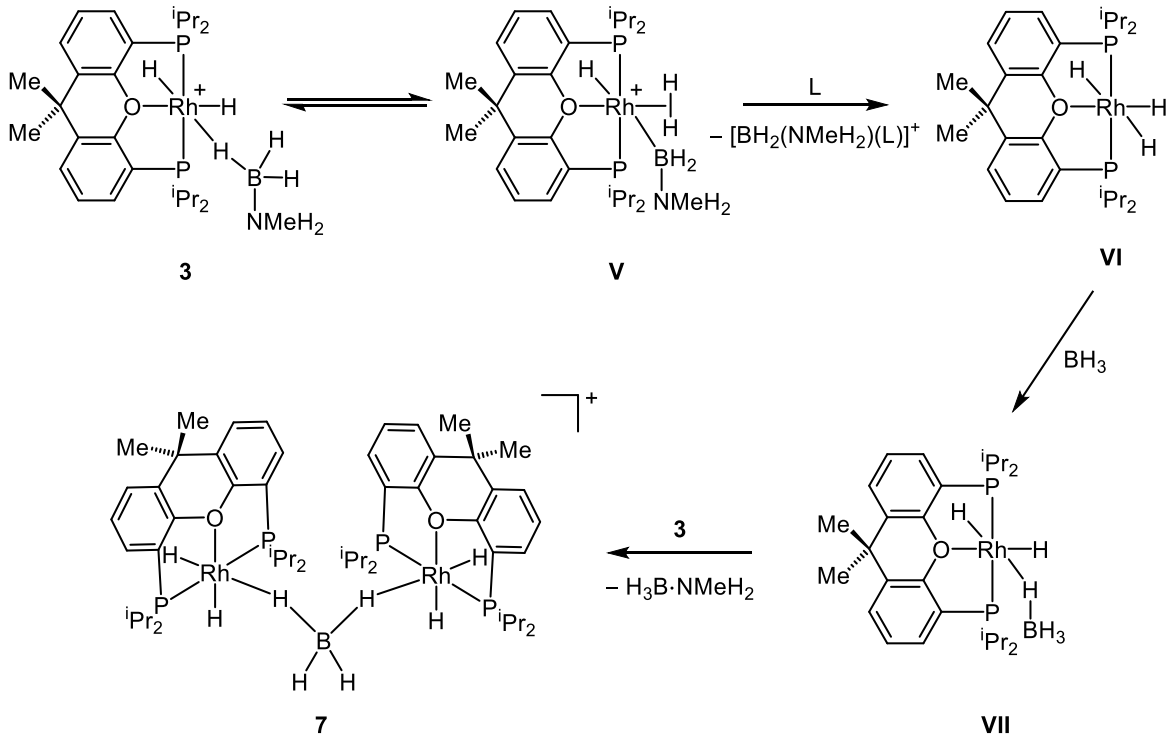
(1) The transformation **2** → **3** may occur through reversible displacement of $H_3B{\cdot}NMe_3$ by $H_3B{\cdot}NMeH_2$ under conditions of excess $H_3B{\cdot}NMeH_2$ (or displacement by $H_3B{\cdot}NMeHBH_2{\cdot}NMeH_2$ to form **4**), as shown in Scheme 2.13, confirmed by the presence of free $H_3B{\cdot}NMe_3$ in the ^{11}B NMR spectrum of the reaction mixture.



2 **3**

Scheme 2.13 Formation of **3** from **2**. $[BAr^F{}_4]^-$ anions not shown for clarity.

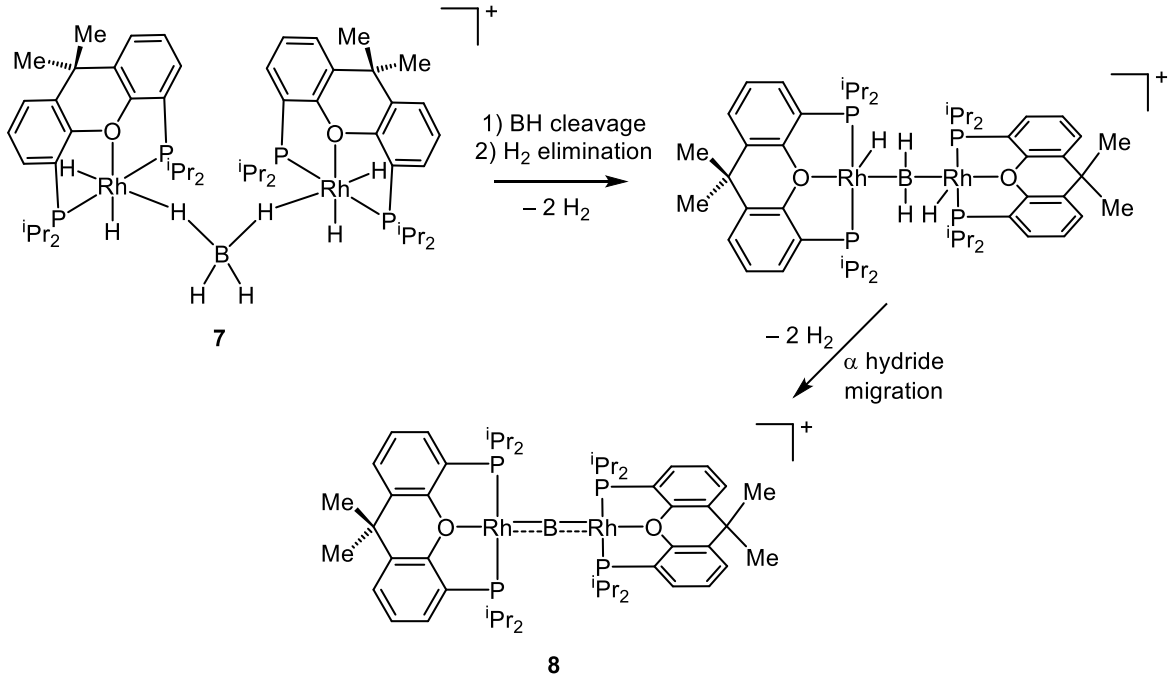
(2) The transformation of **3** → **7** required further investigation. Addition of 10 equivalents of $H_3B{\cdot}NMeH_2$ to in situ formed **3** leads to the observation of **7** and eventually **8**. Noteworthy is a triplet observed at δ −8.9 ($^1J_{BH}$ 108 Hz) in the ^{11}B NMR spectrum, which may indicate boronium formation: $[BH_2(NMeH_2)(L)]^+$ (L = $NMeH_2$ or solvent).[55] This peak cannot be seen in the analogous reaction using complex **2** as the presence of free $H_3B{\cdot}NMe_3$ in the reaction mixture is coincident with this signal. Given that complex **2** undergoes fast H/D exchange under D_2 via a proposed base stabilised boryl dihydrogen intermediate **I** (Scheme 2.7), this may also be accessible in complex **3**. Thus, it is proposed that B–H activation of **3** occurs to form base stabilised boryl dihydrogen complex **V**. Attack of **V** by $NMeH_2$, or solvent, would form a neutral trihydride species Rh(κ^3-P,O,P-Xantphos-^{i}Pr)$(H)_3$ (**VI**) with concomitant production of a boronium cation. **VI** can then be trapped by BH_3 to form **VII**, and fast addition of a $[Rh(\kappa^3\text{-P,O,P-Xantphos-}^i\text{Pr})(H)_2]^+$ fragment (such as **3**, with loss of $H_3B{\cdot}NMeH_2$) to **VII** forms **7** (Scheme 2.14).



Scheme 2.14 Proposed mechanism of the formation of **7** from **3**.

(3) The transformation of **7** → **8** occurs through facile loss of 4 equivalents of H_2. Such reductive loss of H_2 from metalloboranes has previously been reported.[50, 56-57] For example, the loss of H_2 from $[Cp'Fe(\eta^3\text{-}BH_4)]$ to form $[Cp'FeBH_2]_3$ (Cp′ = 1,2,4-tri(tert-butyl)cyclopentadienyl) was reported by Walter and co-workers,[56] however its mechanism was not discussed.

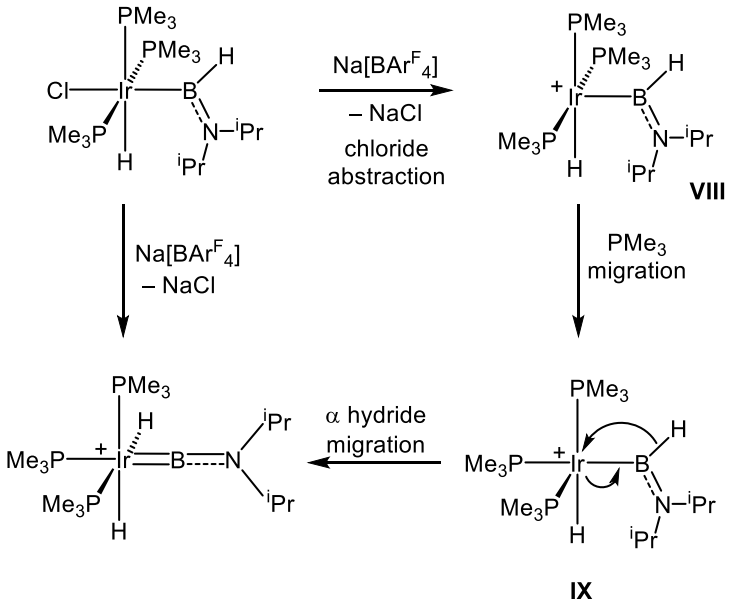
Conversion of **7** to **8** may occur by initial loss of 1 equivalent of H_2 per rhodium through B–H activation of **7**, followed by dihydrogen loss from the resulting boryl complex (Section 2.4.1). Subsequent α migration of the boryl B–H groups,[50] may lead to concerted loss of one equivalent of H_2 per rhodium centre, forming **8** (Scheme 2.15).



7 **8**

Scheme 2.15 Proposed mechanism of the formation of **8** from **7**.

Precedent for α hydride migration from boryl groups has been reported by Aldridge and co-workers.[50] Chloride abstraction of the boryl hydride complex mer-Ir(PMe_3)(H)(Cl){B(H)N^{i}Pr$_2$} by Na[BAr$^F{}_4$] led to the formation of fac-[Ir(PMe_3)$_3$(H)$_2$(NB^{i}Pr$_2$)][BAr$^F{}_4$]. The mechanism for this transformation is shown in Scheme 2.16, and shows phosphine migration in **VIII** gave **IX**, which could undergo α hydride migration to give fac-[Ir(PMe_3)$_3$(H)$_2$(NB^{i}Pr$_2$)][BAr$^F{}_4$].



Scheme 2.16 Aldridge's mechanism of previously unprecedented chloride abstraction, phosphine migration and subsequent α hydride migration of mer-Ir(PMe_3)(H)(Cl){B(H)N^{i}Pr$_2$} to form fac-[Ir(PMe_3)$_3$(H)$_2$(NB^{i}Pr$_2$)][$BAr^F{}_4$].

2.10 Exploring possible Lewis acidity of [{Rh(Xantphos-^{i}Pr)}$_2$B][$BAr^{Cl}{}_4$] (**8-[$BAr^{Cl}{}_4$]**): formation of [Rh(Xantphos-^{i}Pr)(CO)][$BAr^{Cl}{}_4$] (**9**)

The structure of **8-[$BAr^{Cl}{}_4$]** shows a two coordinate cationic boron centre and despite Rh–B π bonding contributions to the electronics, it may possess the ability to behave as a Lewis acid.[53] The addition of CO_2 gas to **8-[$BAr^{Cl}{}_4$]** in CD_2Cl_2 solvent led to the isolation of single crystals of the carbon monoxide complex, [Rh(κ^3-P,O,P-Xantphos-^{i}Pr)(CO)][$BAr^{Cl}{}_4$] (**9**), which was characterised by NMR spectroscopy, ESI-MS and infrared spectroscopy. The solid state structure of **9** is shown in Figure 2.21. The binding of CO (as opposed to N_2) was confirmed by measurement of the CO stretching frequency (1999.7 cm^{-1}) indicative of metal bound CO adduct.[58]

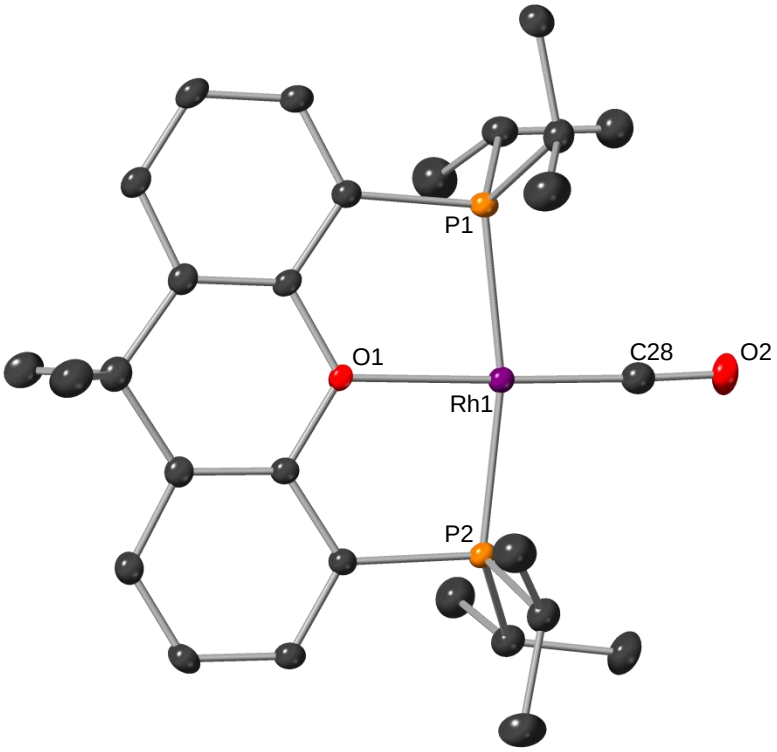
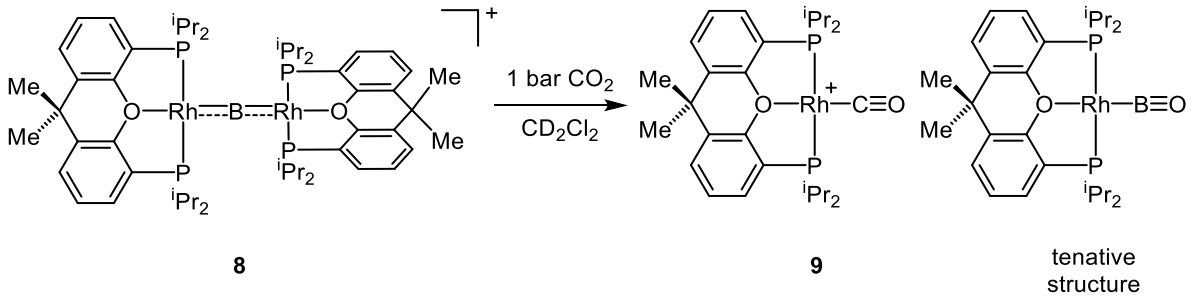


Figure 2.21 Crystal structure of the cationic portion of [Rh(κ^3-P,O,P-Xantphos-^{i}Pr)(CO)][BAr$^{Cl}_4$] (**9**). Displacement ellipsoids are drawn at the 30% probability level. H atoms are not shown for clarity. Selected bond lengths (Å) and angles (°): Rh1–P1, 2.2783(8); Rh1–P2, 2.2901(8); Rh1–O1, 2.134(2); Rh1–C28, 1.802(4); C28–O2, 1.147(5); P1–Rh1–P2, 167.16(3).

The production of **9** indicates that **8-[BAr$^{Cl}_4$]** can accept a lone pair of electrons from CO_2 to cause a deoxygenation reaction. Unfortunately, however, the fate of the boron-containing component of the reaction could not be analysed. Similar studies by Shoji and co-workers reported that the reaction of borinium cations [Mes$_2$B][X] ([X] = [CB$_{11}$HCl$_{11}$] and [B(C$_6$F$_5$)$_4$]) with CO_2 led to the isolation of [MesCO][X], however the proposed coproduct, neutral MesB=O, could not be isolated.[53] Instead, this transformation was studied by DFT calculations which confirmed the energetically favourable process, forming both [MesCO][X] and MesB=O products. Braunschweig and co-workers reported B≡O stabilised by a platinum complex in 2010,[59] therefore it is possible that in the reaction of **8-[BAr$^{Cl}_4$]** with CO_2, complex **9** may form alongside neutral Rh(κ^3-P,O,P-Xantphos-^{i}Pr)(B≡O) (Scheme 2.17), however no data currently support this formulation.



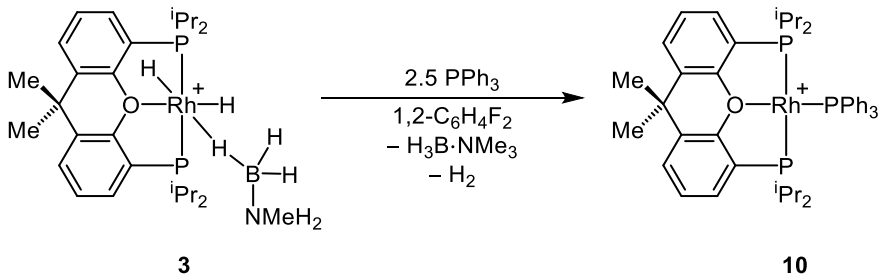
8 9

Scheme 2.17 Proposed formation of **9** and postulated Rh(κ^3-P,O,P-Xantphos-^{i}Pr)(B=O) from the reaction of **8-[BAr$^{Cl}_4$]** with CO_2. $[BAr^{Cl}_4]^-$ anions not shown for clarity.

2.11 Catalyst poisoning: formation of [Rh(Xantphos-^{i}Pr)(PPh_3)][BAr^F_4] (**10**)

Phosphine ligands can be utilised as poisons for metal-based catalytic reactions, as they can strongly coordinate to the metal centre, quenching the active site and halting catalysis.[60] Such reactivity can be used in testing for heterogeneous catalysis if used in sub-stoichiometric quantities.[60]

As halting catalysis using exogeneous PPh_3 will be required in studies of the dehydropolymerisation of $H_3B{\cdot}NMeH_2$ using {Rh(Xantphos-^{i}Pr)}$^+$ complexes (Chapter 3), the identification of products stemming from the addition of PPh_3 to complex **2** were investigated. [Rh(κ^3-P,O,P-Xantphos-^{i}Pr)(PPh_3)][BAr^F_4] (**10**) was obtained from crystallising a reaction mixture containing **2** and 2.5 equivalents of PPh_3 in 1,2-$C_6H_4F_2$ (Scheme 2.18). **10** could be additionally characterised by single crystal X-ray diffraction (the solid state structure is shown in Figure 2.22) NMR spectroscopy, ESI-MS and elemental microanalysis.



3 10

Scheme 2.18 Synthesis of [Rh(κ^3-P,O,P-Xantphos-^{i}Pr)(PPh_3)][BAr^F_4] (**10**). $[BAr^F_4]^-$ anions not shown for clarity.

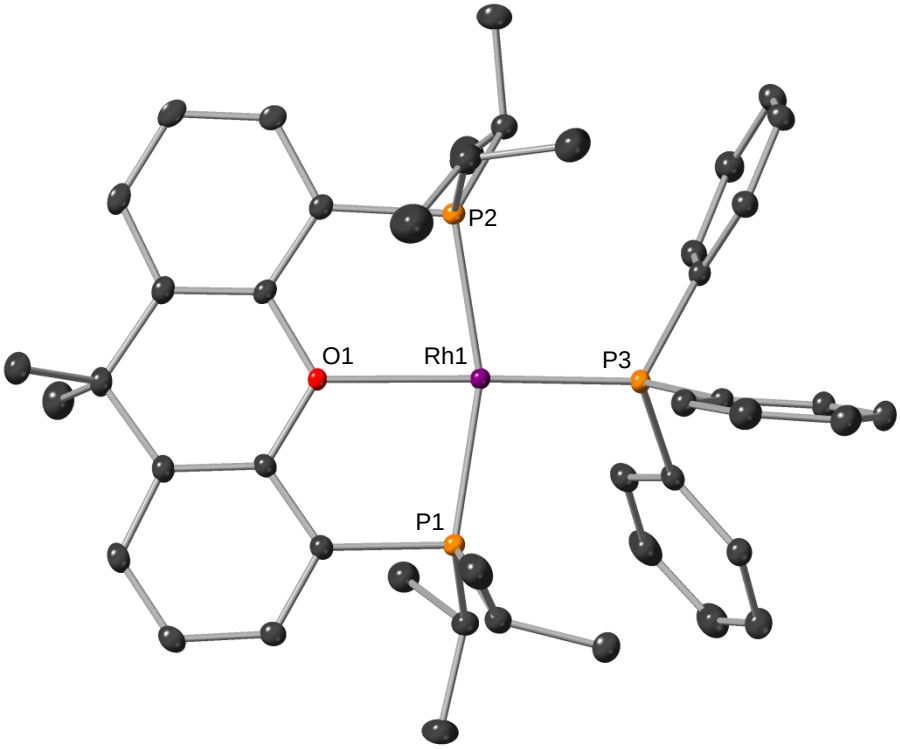


Figure 2.22 Crystal structure of the cationic portion of [Rh(κ^3-P,O,P-Xantphos-^{i}Pr)(PPh$_3$)][BAr$^F{}_4$] (**10**). Displacement ellipsoids are drawn at the 30% probability level. C-bound H atoms are not shown for clarity. Selected bond lengths (Å) and angles (°): Rh1–P1, 2.3227(4); Rh1–P2, 2.2888(4); Rh1–O1, 2.2267(10); Rh1–P3, 2.2160(4); P1–Rh1–P2, 160.003(14).

Addition of 10 equivalents of $H_3B{\cdot}NMeH_2$ to complex **10** in 1,2-$C_6H_4F_2$ led to no observable dehydrocoupling, hence the use of PPh_3 to suppress catalysis by the formation of **10** was utilised in Chapter 3.

2.12 Summary

In this Chapter, a Rh(III) Xantphos-^{i}Pr complex containing η^1 bound $H_3B{\cdot}NMe_3$, [Rh(κ^3-P,O,P-Xantphos-^{i}Pr)(H)$_2$(η^1-$H_3B{\cdot}NMe_3$)][BAr$^F{}_4$] (**2**), was synthesised and found to be a suitable precatalyst for the dehydrocoupling of $H_3B{\cdot}NMeH_2$ at 10 mol% catalyst loading. Speciation experiments suggest that at least three organometallic complexes are involved in the dehydrocoupling mechanism: complexes **3**, **7** and **8**. **7** has been characterised as a bridging borohydride bimetallic complex, which can lose H_2 to form an unusual, symmetric,

dimetalloborylene (**8**). Further exploration of the dehydropolymerisation ability of **2** will be discussed in Chapter 3.

2.13 References

1. Asensio, G.; Cuenca, A. B.; Esteruelas, M. A.; Medio-Simón, M.; Oliván, M.; Valencia, M., Osmium(III) Complexes with POP Pincer Ligands: Preparation from Commercially Available $OsCl_3 \cdot 3H_2O$ and Their X-ray Structures. *Inorg. Chem.* **2010,** *49* (19), 8665-8667.
2. SciFinder, A CAS Solution. American Chemical Society.
3. Alós, J.; Bolaño, T.; Esteruelas, M. A.; Oliván, M.; Oñate, E.; Valencia, M., POP-Pincer Osmium-Polyhydrides: Head-to-Head (Z)-Dimerization of Terminal Alkynes. *Inorg. Chem.* **2013,** *52* (10), 6199-6213.
4. Esteruelas, M. A.; Oliván, M.; Vélez, A., POP-Pincer Silyl Complexes of Group 9: Rhodium versus Iridium. *Inorg. Chem.* **2013,** *52* (20), 12108-12119.
5. Alós, J.; Esteruelas, M. A.; Oliván, M.; Oñate, E.; Puylaert, P., C–H Bond Activation Reactions in Ketones and Aldehydes Promoted by POP-Pincer Osmium and Ruthenium Complexes. *Organometallics* **2015,** *34* (20), 4908-4921.
6. Esteruelas, M. A.; Oliván, M.; Vélez, A., Conclusive Evidence on the Mechanism of the Rhodium-Mediated Decyanative Borylation. *J. Am. Chem. Soc.* **2015,** *137* (38), 12321-12329.
7. Curto, S. G.; Esteruelas, M. A.; Oliván, M.; Oñate, E.; Vélez, A., β-Borylalkenyl Z-E Isomerization in Rhodium-Mediated Diboration of Nonfunctionalized Internal Alkynes. *Organometallics* **2018,** *37* (12), 1970-1978.
8. Esteruelas, M. A.; Nolis, P.; Oliván, M.; Oñate, E.; Vallribera, A.; Vélez, A., Ammonia Borane Dehydrogenation Promoted by a Pincer-Square-Planar Rhodium(I) Monohydride: A Stepwise Hydrogen Transfer from the Substrate to the Catalyst. *Inorg. Chem.* **2016,** *55* (14), 7176-7181.
9. Moxham, G. L.; Randell-Sly, H. E.; Brayshaw, S. K.; Woodward, R. L.; Weller, A. S.; Willis, M. C., A Second-Generation Catalyst for Intermolecular Hydroacylation of Alkenes and Alkynes Using β-S-Substituted Aldehydes: The Role of a Hemilabile P-O-P Ligand. *Angew. Chem. Int. Ed.* **2006,** *45* (45), 7618-7622.
10. Pawley, R. J.; Moxham, G. L.; Dallanegra, R.; Chaplin, A. B.; Brayshaw, S. K.; Weller, A. S.; Willis, M. C., Controlling Selectivity in Intermolecular Alkene or Aldehyde Hydroacylation Reactions Catalyzed by $\{Rh(L_2)\}^+$ Fragments. *Organometallics* **2010,** *29* (7), 1717-1728.
11. Pike, S. D.; Thompson, A. L.; Algarra, A. G.; Apperley, D. C.; Macgregor, S. A.; Weller, A. S., Synthesis and Characterization of a Rhodium(I) σ-Alkane Complex in the Solid State. *Science* **2012,** *337* (6102), 1648-1651.
12. Guzel, B.; Omary, M. A.; Fackler, J. P.; Akgerman, A., Synthesis and characterization of {(COD)Rh(bis-(2R,3R)-2,5-diethylphospholanobenzene)$^+$BARF$^-$} for use in homogeneous catalysis in supercritical carbon dioxide. *Inorg. Chim. Acta* **2001,** *325* (1-2), 45-50.
13. Alvarez, S., A cartography of the van der Waals territories. *Dalton Trans.* **2013,** *42* (24), 8617-8636.
14. Dallanegra, R. Cationic Rhodium Complexes with Chelating Phosphine and Phosphine Alkene Ligands. Application in Dehydrogenation and Dehydrocoupling Reactions. University of Oxford, Oxford, 2011.
15. Adams, G. M.; Weller, A. S., POP-type ligands: Variable coordination and hemilabile behaviour. *Coord. Chem. Rev.* **2018,** *355*, 150-172.
16. Haibach, M. C.; Wang, D. Y.; Emge, T. J.; Krogh-Jespersen, K.; Goldman, A. S., (POP)Rh pincer hydride complexes: unusual reactivity and selectivity in oxidative addition and olefin insertion reactions. *Chem. Sci.* **2013,** *4* (9), 3683-3692.
17. Dallanegra, R.; Chaplin, A. B.; Weller, A. S., Rhodium Cyclopentyl Phosphine Complexes of Wide-Bite-Angle Ligands DPEphos and Xantphos. *Organometallics* **2012,** *31* (7), 2720-2728.
18. Budzelaar, P. H. M., *gNMR 5.1*. Cherwell Scientific Publishing.
19. Goertz, W.; Keim, W.; Vogt, D.; Englert, U.; Boele, M. D. K.; van der Veen, L. A.; Kamer, P. C. J.; van Leeuwen, P. W. N. M., Electronic effects in the nickel-catalysed hydrocyanation of styrene applying chelating phosphorus ligands with large bite angles. *J. Chem. Soc., Dalton Trans.* **1998,** (18), 2981-2988.
20. Pingen, D.; Lebl, T.; Lutz, M.; Nichol, G. S.; Kamer, P. C. J.; Vogt, D., Catalytic Activity and Fluxional Behavior of Complexes Based on $RuHCl(CO)(PPh_3)_3$ and Xantphos-Type Ligands. *Organometallics* **2014,** *33* (11), 2798-2805.

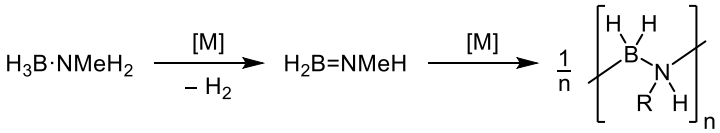
21. Johnson, H. C.; McMullin, C. L.; Pike, S. D.; Macgregor, S. A.; Weller, A. S., Dehydrogenative Boron Homocoupling of an Amine-Borane. *Angew. Chem. Int. Ed.* **2013,** *52* (37), 9776-9780.
22. Grant, D. J.; Matus, M. H.; Anderson, K. D.; Camaioni, D. M.; Neufeldt, S. R.; Lane, C. F.; Dixon, D. A., Thermochemistry for the Dehydrogenation of Methyl-Substituted Ammonia Borane Compounds. *J. Phys. Chem. A* **2009,** *113* (21), 6121-6132.
23. Esteruelas, M. A.; Oliván, M.; Vélez, A., Xantphos-Type Complexes of Group 9: Rhodium versus Iridium. *Inorg. Chem.* **2013,** *52* (9), 5339-5349.
24. Chaplin, A. B.; Weller, A. S., $[B(3,5\text{-}C_6H_3Cl_2)_4]^-$ as a Useful Anion for Organometallic Chemistry. *Eur. J. Inorg. Chem.* **2010,** *2010* (32), 5124-5128.
25. Cordero, B.; Gómez, V.; Platero-Prats, A. E.; Réves, M.; Echeverría, J.; Cremades, E.; Barragán, F.; Alvarez, S., Covalent radii revisited. *Dalton Trans.* **2008,** (21), 2832-2838.
26. Shimoi, M.; Nagai, S.; Ichikawa, M.; Kawano, Y.; Katoh, K.; Uruichi, M.; Ogino, H., Coordination Compounds of Monoborane-Lewis Base Adducts: Syntheses and Structures of $[M(CO)_5(\eta^1\text{-}BH_3\cdot L)]$ (M = Cr, Mo, W; L = NMe_3, PMe_3, PPh_3). *J. Am. Chem. Soc.* **1999,** *121* (50), 11704-11712.
27. Ledger, A. E. W.; Ellul, C. E.; Mahon, M. F.; Williams, J. M. J.; Whittlesey, M. K., Ruthenium Bidentate Phosphine Complexes for the Coordination and Catalytic Dehydrogenation of Amine- and Phosphine-Boranes. *Chem. Eur. J.* **2011,** *17* (31), 8704-8713.
28. Douglas, T. M.; Chaplin, A. B.; Weller, A. S.; Yang, X.; Hall, M. B., Monomeric and Oligomeric Amine-Borane σ-Complexes of Rhodium. Intermediates in the Catalytic Dehydrogenation of Amine-Boranes. *J. Am. Chem. Soc.* **2009,** *131* (42), 15440-15456.
29. Merle, N.; Koicok-Köhn, G.; Mahon, M. F.; Frost, C. G.; Ruggerio, G. D.; Weller, A. S.; Willis, M. C., Transition metal complexes of the chelating phosphine borane ligand $Ph_2PCH_2Ph_2P\cdot BH_3$. *Dalton Trans.* **2004,** (22), 3883-3892.
30. Alcaraz, G.; Sabo-Etienne, S., NMR: A good tool to ascertain σ-silane or σ-borane formulations? *Coord. Chem. Rev.* **2008,** *252* (21), 2395-2409.
31. Halbert, S.; Copéret, C.; Raynaud, C.; Eisenstein, O., Elucidating the Link between NMR Chemical Shifts and Electronic Structure in d^0 Olefin Metathesis Catalysts. *J. Am. Chem. Soc.* **2016,** *138* (7), 2261-2272.
32. Kawano, Y.; Hashiva, M.; Shimoi, M., Syntheses and Reactivity of Cationic Borane-Ruthenium Complexes $[(\eta^5\text{-}C_5R_5)Ru(PMe_3)_2(\eta^1\text{-}BH_3\cdot EMe_3)][BArf_4]$ (R = H, Me; E = N, P; $BArf_4$= $[B\{3,5\text{-}C_6H_3(CF_3)_2\}_4]$). *Organometallics* **2006,** *25* (18), 4420-4426.
33. Pawley, R. J. Controlling Selectivity in the Rhodium-Catalysed Intermolecular Hydroacylation Reaction. University of Oxford, Oxford, 2012.
34. Johnson, H. C.; Hooper, T. N.; Weller, A. S., The Catalytic Dehydrocoupling of Amine-Boranes and Phosphine-Boranes. In *Synthesis and Application of Organoboron Compounds*, Springer-Verlag Berlin: 2015; Vol. 49, pp 153-220.
35. Algarra, A. G.; Sewell, L. J.; Johnson, H. C.; Macgregor, S. A.; Weller, A. S., A combined experimental and computational study of fluxional processes in sigma amine-borane complexes of rhodium and iridium. *Dalton Trans.* **2014,** *43* (29), 11118-11128.
36. Perutz, R. N.; Sabo-Etienne, S., The σ-CAM Mechanism: σ Complexes as the Basis of σ-Bond Metathesis at Late-Transition-Metal Centers. *Angew. Chem. Int. Ed.* **2007,** *46* (15), 2578-2592.
37. Johnson, H. C.; Robertson, A. P. M.; Chaplin, A. B.; Sewell, L. J.; Thompson, A. L.; Haddow, M. F.; Manners, I.; Weller, A. S., Catching the First Oligomerization Event in the Catalytic Formation of Polyaminoboranes: $H_3B\cdot NMeHBH_2\cdot NMeH_2$ Bound to Iridium. *J. Am. Chem. Soc.* **2011,** *133* (29), 11076-11079.
38. Barwick-Silk, J.; Hardy, S.; Willis, M. C.; Weller, A. S., Rh(DPEPhos)-Catalyzed Alkyne Hydroacylation Using β-Carbonyl-Substituted Aldehydes: Mechanistic Insight Leads to Low Catalyst Loadings that Enables Selective Catalysis on Gram-Scale. *J. Am. Chem. Soc.* **2018,** *140* (23), 7347-7357.
39. Robertson, K. N.; Knop, O.; Cameron, T. S., C-H···H-C interactions in organoammonium tetraphenylborates: another look at dihydrogen bonds. *Can. J. Chem.* **2003,** *81* (6), 727-743.
40. Johnson, H. C.; Leitao, E. M.; Whittell, G. R.; Manners, I.; Lloyd-Jones, G. C.; Weller, A. S., Mechanistic Studies of the Dehydrocoupling and Dehydropolymerization of Amine-Boranes Using a $[Rh(Xantphos)]^+$ Catalyst. *J. Am. Chem. Soc.* **2014,** *136* (25), 9078-9093.
41. Carreno, R.; Riera, V.; Ruiz, M. A.; Bois, C.; Jeannin, Y., Reactivity of the Unsaturated Dihydrides $[Mn_2(\mu\text{-}H)_2(CO)_6(\mu\text{-}L_2)]$ (L_2 = $Ph_2PCH_2PPh_2$, $(EtO)_2POP(OEt)_2$) toward Boron Hydrides. X-ray Crystal Structure of $[Mn_2(\mu\text{-}BH_4)(\mu\text{-}H)(CO)_5(\mu\text{-}Ph_2PCH_2PPh_2)]$, a Molecule Displaying a Novel Coordination Mode of the Tetrahydroborate Ligand. *Organometallics* **1993,** *12* (5), 1946-1953.
42. Koehne, I.; Schmeier, T. J.; Bielinski, E. A.; Pan, C. J.; Lagaditis, P. O.; Bernskoetter, W. H.; Takase, M. K.; Würtele, C.; Hazari, N.; Schneider, S., Synthesis and Structure of Six-Coordinate Iron Borohydride Complexes Supported by PNP Ligands. *Inorg. Chem.* **2014,** *53* (4), 2133-2143.

43. Braunschweig, H.; Dewhurst, R. D.; Gessner, V. H., Transition metal borylene complexes. *Chem. Soc. Rev.* **2013,** *42* (8), 3197-3208.
44. Alcaraz, G.; Vendier, L.; Clot, E.; Sabo-Etienne, S., Ruthenium Bis(σ-B–H) Aminoborane Complexes from Dehydrogenation of Amine-Boranes: Trapping of $H_2B–NH_2$. *Angew. Chem. Int. Ed.* **2010,** *49* (5), 918-920.
45. Borrachero, M. V.; Estevan, F.; García-Granda, S.; Lahuerta, P.; Latorre, J.; Peris, E.; Sanaú, M., Crystal Structure of $[Rh_2(\mu^2\text{-}O_2CMe)_2\{\mu^2\text{-}(CH_2)PPh_2\}\{\mu^2\text{-}(C_6H_4)PPh_2\}\cdot PPh_3]\cdot 2CH_2Cl_2$, a Compound with a Diphenylphosphinomethanide Group in a Bridging (P,C) Coordination. *J. Chem. Soc., Chem. Commun.* **1993,** (24), 1864-1865.
46. Braunschweig, H.; Radacki, K.; Uttinger, K., T-Shaped Platinum Boryl Complexes: Synthesis and Structure. *Chem. Eur. J.* **2008,** *14* (26), 7858-7866.
47. Segawa, Y.; Yamashita, M.; Nozaki, K., Syntheses of PBP Pincer Iridium Complexes: A Supporting Boryl Ligand. *J. Am. Chem. Soc.* **2009,** *131* (26), 9201-9203.
48. Esteruelas, M. A.; Oliván, M.; Vélez, A., POP-Rhodium-Promoted C–H and B–H Bond Activation and C–B Bond Formation. *Organometallics* **2015,** *34* (10), 1911-1924.
49. Alcaraz, G.; Helmstedt, U.; Clot, E.; Vendier, L.; Sabo-Etienne, S., A Terminal Borylene Ruthenium Complex: From B–H Activation to Reversible Hydrogen Release. *J. Am. Chem. Soc.* **2008,** *130* (39), 12878-12879.
50. O'Neill, M.; A. Addy, D.; Riddlestone, I.; Kelly, M.; Phillips, N.; Aldridge, S., Borane to Boryl Hydride to Borylene Dihydride: Explicit Demonstration of Boron-to-Metal α-Hydride Migration in Aminoborane Activation. *J. Am. Chem. Soc.* **2011,** *133* (30), 11500-11503.
51. Braunschweig, H.; Kraft, K.; Kupfer, T.; Radacki, K.; Seeler, F., B^+ in the Coordination Sphere of Two Transition Metals. *Angew. Chem. Int. Ed.* **2008,** *47* (26), 4931-4933.
52. Vidovic, D.; Aldridge, S., Coordination and Activation of the BF Molecule. *Angew. Chem. Int. Ed.* **2009,** *48* (20), 3669-3672.
53. Shoji, Y.; Tanaka, N.; Mikami, K.; Uchiyama, M.; Fukushima, T., A two-coordinate boron cation featuring C–B^+–C bonding. *Nature Chem.* **2014,** *6*, 498-503.
54. Bader, R. F. W., *Atoms in Molecules - A Quantum Theory*. Oxford University Press: Oxford, 1990.
55. Robertson, A. P. M.; Haddow, M. F.; Manners, I., Synthesis and the Thermal and Catalytic Dehydrogenation Reactions of Amine-Thioboranes. *Inorg. Chem.* **2012,** *51* (15), 8254-8264.
56. Maekawa, M.; Daniliuc, C. G.; Jones, P. G.; Hohenberger, J.; Sutter, J.; Meyer, K.; Walter, M. D., Synthesis of $[Cp'Fe(\eta^3\text{-}BH_4)]$ and Its Conversion to $[Cp'FeBH_2]_3$. *Eur. J. Inorg. Chem.* **2013,** *2013* (22-23), 4097-4104.
57. Fehlner, T. P., Systematic Metallaborane Chemistry. *Organometallics* **2000,** *19* (14), 2643-2651.
58. Adams, G. M.; Chadwick, F. M.; Pike, S. D.; Weller, A. S., A CH_2Cl_2 complex of a $[Rh(pincer)]^+$ cation. *Dalton Trans.* **2015,** *44* (14), 6340-6342.
59. Braunschweig, H.; Radacki, K.; Schneider, A., Oxoboryl Complexes: Boron−Oxygen Triple Bonds Stabilized in the Coordination Sphere of Platinum. *Science* **2010,** *328* (5976), 345-347.
60. Widegren, J. A.; Finke, R. G., A review of the problem of distinguishing true homogeneous catalysis from soluble or other metal-particle heterogeneous catalysis under reducing conditions. *J. Mol. Catal. A: Chem.* **2003,** *198* (1-2), 317-341.

3 Dehydropolymerisation of $H_3B{\cdot}NMeH_2$ using the $\{Rh(Xantphos\text{-}^iPr)\}^+$ system

3.1 Introduction

Following the characterisation of amine borane complexes of the $\{Rh(Xantphos\text{-}^iPr)\}^+$ fragment as described in Chapter 2, the ability of $[Rh(\kappa^3\text{-}P,O,P\text{-}Xantphos\text{-}^iPr)(H)_2(\eta^1\text{-}H_3B{\cdot}NMe_3)][BAr^F{}_4]$ (**2**) in the dehydropolymerisation of $H_3B{\cdot}NMeH_2$ at low catalyst loadings was of clear interest to investigate. In Section 2.4.2, the reaction of $H_3B{\cdot}NMeH_2$ with a high catalyst loading of **2** (10 mol%) led to the rapid formation of the corresponding borazine $(HBNMe)_3$ as the major dehydrocoupling product after merely 30 seconds, formed by the dehydrotrimerisation of three aminoborane $H_2B{=}NMeH$ molecules formed in situ.[1] However, in the catalytic dehydropolymerisation of $H_3B{\cdot}NMeH_2$, the catalyst is required to operate in a bifunctional manner,[1-2] initially dehydrogenating $H_3B{\cdot}NMeH_2$ (via B–H and N–H activation) to form $H_2B{=}NMeH$ and then subsequently controlling the B–N bond forming events between $H_2B{=}NMeH$ molecules to produce $(H_2BNMeH)_n$, rather than borazine (Scheme 3.1).



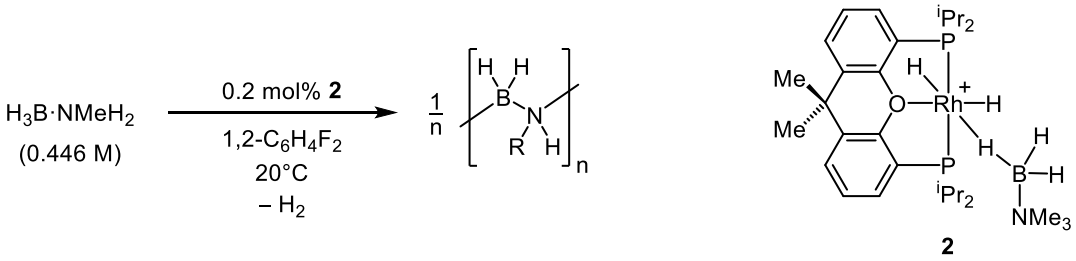
Scheme 3.1 Bifunctional nature of the metal catalyst, [M], required for dehydropolymerisation of $H_3B{\cdot}NMeH_2$ to form $(H_2BNMeH)_n$.

As detailed in Chapter 1, precatalysts based upon $\{Rh(Xantphos\text{-}Ph)\}^+$, such as **i-13** ($[Rh(\kappa^2\text{-}P,P\text{-}Xantphos\text{-}Ph)(\eta^2\text{-}H_2B(CH_2CH_2{}^tBu){\cdot}NMe_3)][BAr^F{}_4]$) or **2-Ph** ($[Rh(\kappa^3\text{-}P,O,P\text{-}Xantphos\text{-}Ph)(H)_2(\eta^1\text{-}H_3B{\cdot}NMe_3)][BAr^F{}_4]$), were effective for the dehydropolymerisation of $H_3B{\cdot}NMeH_2$.[3] A controlled, on metal, coordination/dehydrogenation/insertion chain propagation mechanism for $(H_2BNMeH)_n$ formation and chain termination by hydrogenolysis, were presented (Scheme 1.17). Although the identity of the true catalyst could not be resolved, $[Rh(\kappa^3\text{-}P,O,P\text{-}Xantphos\text{-}Ph)(H)_2(\eta^1\text{-}H_3B{\cdot}NMeH_2)][BAr^F{}_4]$ (**i-14**), analogous to complex **3** ($[Rh(\kappa^3\text{-}P,O,P\text{-}Xantphos\text{-}^iPr)(H)_2(\eta^1\text{-}H_3B{\cdot}NMeH_2)][BAr^F{}_4]$), was implicated as the first formed species. Thus similarities and differences

between the well-studied Xantphos-Ph and novel Xantphos-^{i}Pr systems may become apparent on detailed investigation, and these may be dictated by the preference of Xantphos-^{i}Pr to coordinate to transition metals in a mer κ^3-P,O,P fashion, whereas Xantphos-Ph favours cis κ^2-P,P geometries (Figure 1.8). This work may therefore give further insight into possible amine borane dehydropolymerisation mechanisms.

3.2 Dehydropolymerisation of $H_3B{\cdot}NMeH_2$ using precatalyst [Rh(Xantphos-^{i}Pr)$(H)_2(H_3B{\cdot}NMe_3)][BAr^F{}_4]$ (**2**): initial screening

The ability of [Rh(κ^3-P,O,P-Xantphos-^{i}Pr)$(H)_2(\eta^1$-$H_3B{\cdot}NMe_3)][BAr^F{}_4]$ (**2**) to serve as a suitable precatalyst for the dehydropolymerisation of $H_3B{\cdot}NMeH_2$ was initially tested using the same dehydropolymerisation conditions utilised in the Xantphos-Ph system.[3] Precatalyst **2** (0.2 mol% loading) enabled the complete conversion of $H_3B{\cdot}NMeH_2$ (0.446 M) in 1,2-$C_6H_4F_2$ solvent under open conditions (H_2 released via a mineral oil bubbler under controlled argon flow) to afford polyaminoborane $(H_2BNMeH)_n$ as the major product after only 20 minutes (Scheme 3.2). This was confirmed by a characteristic broad signal in the ^{11}B NMR spectrum of the in situ reaction mixture at δ −5.1, indicative of multiple but similar boron environments within the polyaminoborane chain, and minor amount of borazine, $(HBNMe)_3$, formed (δ 33.2, d, $^1J_{BH}$ 132 Hz) (Figure 3.1). GPC analysis of isolated $(H_2BNMeH)_n$ is discussed in Section 3.4.



Scheme 3.2 Dehydropolymerisation of $H_3B{\cdot}NMeH_2$ using precatalyst **2**. $[BAr^F{}_4]^-$ anion not shown for clarity.

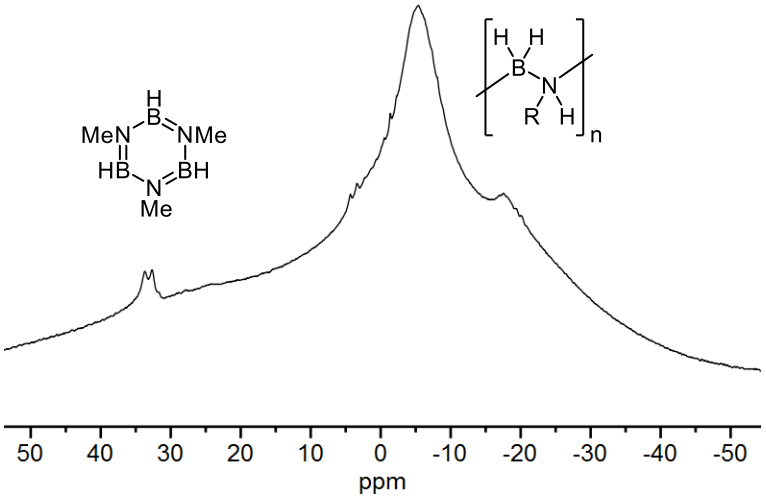


Figure 3.1 ^{11}B NMR spectrum of the reaction mixture corresponding to Scheme 3.2. The broad baseline signal observed in the ^{11}B NMR spectrum at δ ~20.0 is due to background from the tube and probe (borosilicate glass).

Given the success of this initial study, the two proposed components of dehydropolymerisation – (1) dehydrogenation of $H_3B{\cdot}NMeH_2$ to $H_2B{=}NMeH$ and (2) B–N coupling of $H_2B{=}NMeH$ to form $(H_2BNMeH)_n$ – were separately investigated.

3.3 Amine borane dehydrogenation kinetics

By following the evolution of H_2 during dehydropolymerisation, the dehydrogenation of $H_3B{\cdot}NMeH_2$ to form the transient aminoborane $H_2B{=}NMeH$ can be indirectly interrogated. This was achieved by carrying out the reaction in jacketed two-neck Schlenk flask connected to a recirculating cooler to ensure a constant temperature set at 20°C. Connecting the reaction flask to a water-filled gas burette via Teflon tubing, and sealing off the system from the argon supply allows for the measurement of the volume of H_2 gas given off over time.

Using 0.2 mol% **2** and 0.446 M $H_3B{\cdot}NMeH_2$ in 1,2-$C_6H_4F_2$ solvent, 1.1 equivalents of H_2 were released over 18 minutes, consistent with the major product being $(H_2BNMeH)_n$ (i.e. one equivalent of H_2 released) and a small, less than 10%, amount of $(HBNMe)_3$ formed which would correspondingly release 2 equivalents of H_2. This means that measuring the H_2 evolved from the

reaction can be used as an effective proxy for $H_2B{=}NMeH$ generation, which subsequently undergoes polymerisation. Firstly, the volume of H_2 given off in millilitre increments over time is converted to moles using the ideal gas law, which can then be normalised relative to the initial number of moles of $H_3B{\cdot}NMeH_2$ assuming that exactly one equivalent of H_2 is given off by the end of the reaction (Equation 3.1). Then, $[H_2B{=}NMeH]_{normalised}$ evolved (i.e. $[H_2B{=}NMeH]$) can be calculated by Equation 3.2. $[H_2B{=}NMeH]$ can then be used to represent the temporal profile of dehydrogenation over time (Figure 3.2). Dehydrogenation of $H_3B{\cdot}NMeH_2$ under these conditions is therefore fast (TOF ≈ 1700 h^{-1}). This is considerably faster than for the Xantphos-Ph system **i-13** (TOF ≈ 250 h^{-1}),[3] but similar to the well-studied Ir(POCOP-^{t}Bu)$(H)_2$ system (TOF ≈ 2400 h^{-1}, 0.5 M $H_3B{\cdot}NMeH_2$, 0.1 mol% catalyst loading).[4] It is also comparable with the fastest catalysts reported for $H_3B{\cdot}NH_3$ or $H_3B{\cdot}NMe_2H$ dehydrocoupling.[5-7] GPC analysis of the isolated polyaminoborane during these reactions will be discussed in Section 3.4.

$$n(H_2)_{normalised} = \frac{\{n(H_2)_t\}\{n(H_3B{\cdot}NMeH_2)_0\}}{\{n(H_2)_{total}\}}$$

$n(H_2)_t$ = number of moles H_2 evolved at time = t
$n(H_3B{\cdot}NMeH_2)_0$ = number of moles $H_3B{\cdot}NMeH_2$ at t = 0
$n(H_2)_{total}$ = total number of moles H_2 evolved

Equation 3.1 Definition of $n(H_2)_{normalised}$. $n(H_2)$ values are calculated using the ideal gas law.

$$[H_2B{=}NMeH] = [H_2B{=}NMeH]_{normalised} = \frac{1000\{n(H_2)_{normalised}\}}{V}$$

V = volume of reaction mixture (mL)

Equation 3.2 Definition of $[H_2B{=}NMeH]$ used throughout this thesis.

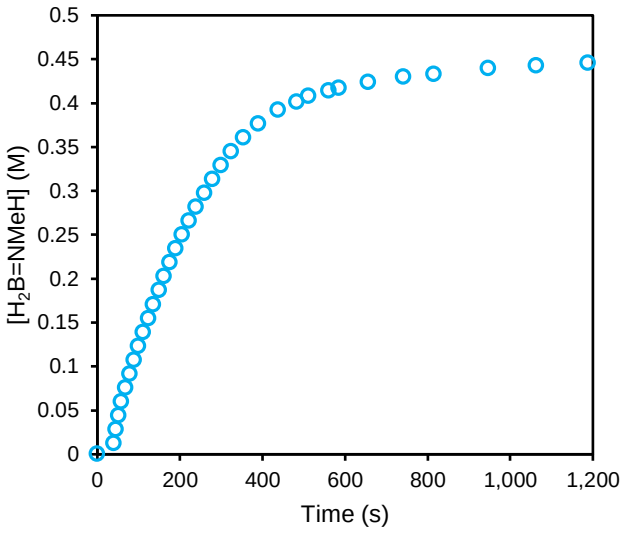


Figure 3.2 Temporal data plot for $H_2B{=}NMeH$ formation (as measured by H_2 evolution). [**2**] = 8.92×10^{-4} M, [$H_3B{\cdot}NMeH_2$] = 0.446 M, 1,2-$C_6H_4F_2$ solvent.

With this initial result, further insight into the kinetics of dehydrogenation of $H_3B{\cdot}NMeH_2$ using precatalyst **2** was sought.

3.3.1 Induction period prior to the onset of H_2 evolution

For all regimes discussed, a small induction period was observed (20 – 150 s) that was also variable between batches of 1,2-$C_6H_4F_2$ solvent, but consistent within each batch for repeat runs, as were the overall temporal profiles for H_2 evolution. Therefore, comparison of kinetic data was achieved using the same batch of solvent. Variability seen between different batches of 1,2-$C_6H_4F_2$ was proposed to be due the presence of trace impurities in the solvent. Impurities present in fluorinated arene solvents has previously been discussed,[8-9] and for this work, GC-MS analysis of 1,2-$C_6H_4F_2$ was carried out by Dr Colin Sparrow (University of Oxford) to determine any likely impurities, as these were below the limit of NMR spectroscopy (i.e. < 1%). The batches of 1,2-$C_6H_4F_2$ solvent tested had been stirred over Al_2O_3 for 1 hour to scavenge unwanted fluoride, dried over CaH_2 and vacuum distilled, and stored under argon in the presence of 3.0 Å molecular sieves in order to ensure sufficiently H_2O, O_2 and N_2-free solvents, in an identical manner to the solvents used in catalysis. All batches showed trace quantities of 1-chloro-2-fluorobenzene, 2-fluorophenol and 2-

chloro-4-fluorotoluene (Figure 3.3). Therefore, it was proposed that impurities such as these could act to modify a small portion of catalyst in both the induction period and during productive catalysis. Importantly, isolated polyaminoborane does not vary in molecular weight significantly when using different batches of solvent for either catalyst, therefore polyaminoborane formed using all batches of 1,2-$C_6H_4F_2$ solvent can be compared in Section 3.4. Due to the variable nature of the induction period, and its short length, rate data will be reported post induction period, with the length of the induction period subtracted from each time point.

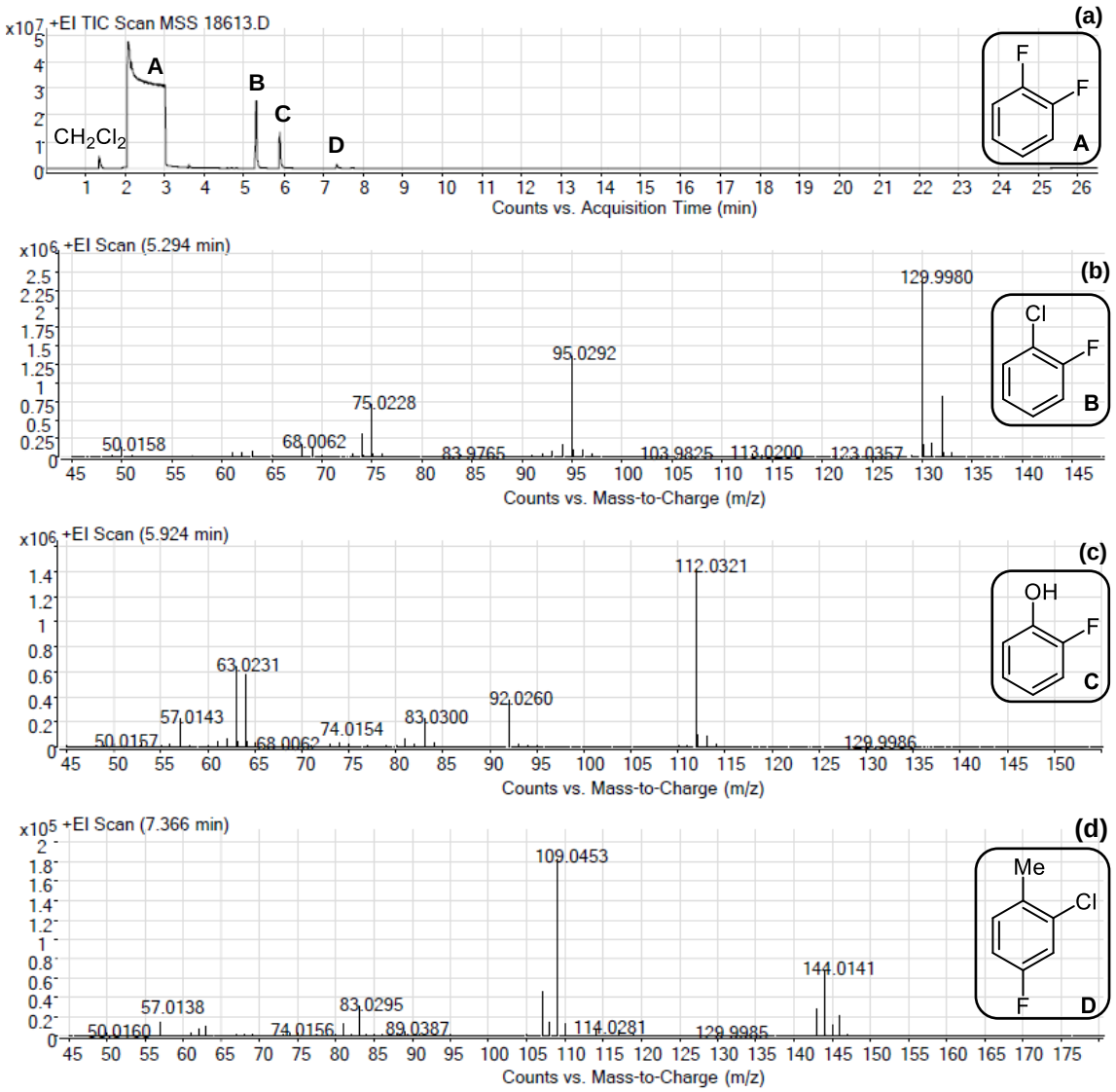


Figure 3.3 GC-MS graph of 1,2-$C_6H_4F_2$ and identification of its contaminants. (a) Full chromatogram of 1,2-$C_6H_4F_2$. The peak at 1.391 minutes is CH_2Cl_2 which is used to wash the autosampler syringe. (b) Peak at 5.294 minutes which is assigned to 1-chloro-2-fluorobenzene. (c) Peak at 5.924 minutes which is assigned to 2-fluorophenol. (d) Peak at 7.366 minutes which is assigned to 2-chloro-4-fluorotoluene.

3.3.2 Tests for catalyst homogeneity

The presence of an induction period before the onset of catalysis may indicate heterogeneous catalysis by the formation of colloidal rhodium nanoparticles, which can take time to become the appropriate size for catalysis to occur.[10] However, induction periods have also been observed in dehydropolymerisation systems which were proposed to be homogeneous through rigorous testing, including $\{Rh(Xantphos\text{-}Ph)\}^+$,[3] and $\{Rh(Ph_2P(CH_2)_3PPh_2)\}^+$.[5] A visual inspection of the reaction mixture using precatalyst **2** showed that it remained light yellow throughout the reaction, with no dark material that may be indicative of colloidal rhodium. However, classical tests for heterogeneous catalysis were still employed.[10]

As briefly described in Section 2.11, exogenous PPh_3 can be used as a poison for catalysis. For a homogeneous reaction mediated by **2**, at least 1 equivalent of PPh_3 would be required to completely halt dehydropolymerisation, in order to suppress every metal site and form $[Rh(\kappa^3\text{-}P,O,P\text{-}Xantphos\text{-}^iPr)(PPh_3)][BAr^F{}_4]$ (**10**, Section 2.11). On the other hand, catalysis mediated by nanoparticles occurs on the surface of the nanoparticle.[10] Given that most of the metal sites sit in the bulk, not on the surface, a sub-stoichiometric quantity should halt catalysis if the reaction is heterogeneous. Addition of 0.2 equivalents of PPh_3 to the catalytic mixture once turnover was established did not act to modify the reaction (Figure 3.4). Alternatively, excess mercury added to a heterogeneous system may prevent further reactivity by the formation of an unreactive metal/mercury amalgam. Addition of ~1500 equivalents of mercury to the reaction mixture post induction period did not halt catalysis (Figure 3.4), whilst addition of mercury did cease catalysis in Manners' heterogeneous $[Rh(1,5\text{-}COD)(\mu\text{-}Cl]$ system which was shown to be heterogeneous by a variety of techniques.[11] Both of these observations using PPh_3 and mercury suggest that the catalysis is in fact homogeneous in this system.[12]

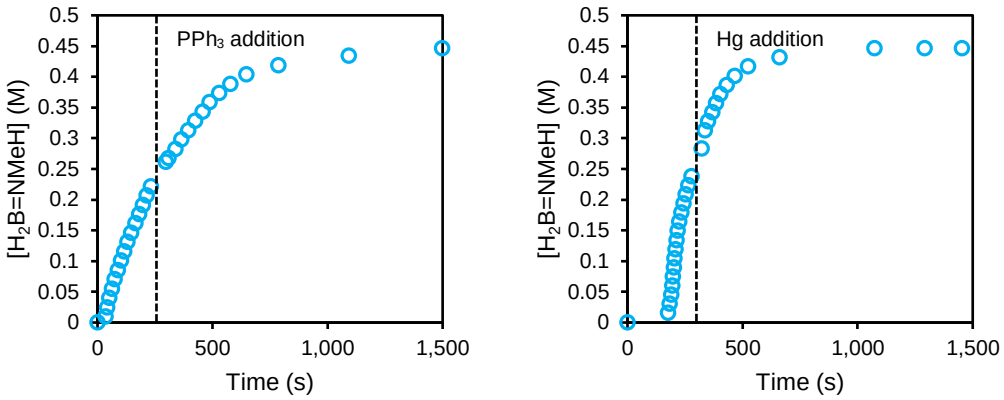


Figure 3.4 Temporal data plots for $H_2B{=}NMeH$ formation (as measured by H_2 evolution). [**2**] = 8.92×10^{-4} M, $[H_3B{\cdot}NMeH_2]$ = 0.446 M, 1,2-$C_6H_4F_2$ solvent. Left: Effect of 0.2 equivalents of PPh_3 added at 200 s. Right: Effect of 1500 equivalents of Hg added at 300 s. Note that these reactions were carried out using different batches of 1,2-$C_6H_4F_2$ solvent.

*3.3.3 Determining order in precatalyst **2** and $H_3B{\cdot}NMeH_2$*

To probe the effect of the concentration of **2** on catalysis, dehydropolymerisation was conducted at 0.446 M $H_3B{\cdot}NMeH_2$ and varied catalyst loadings of 0.1, 0.2 and 0.4 mol% **2**. The kinetics were probed by the initial rates method, monitoring the rate of H_2 evolution (i.e. $H_2B{=}NMeH$ formation) over the first 5% of the reaction post induction period. A plot of initial rate versus initial concentration of **2** is shown in Figure 3.5. This demonstrates that the reaction is approximately first order in [**2**] (R^2 = 0.985), suggesting that a rapid monomer-dimer equilibrium is not in operation.[13] Therefore any possible bimetallic species formed (such as **8**) lie off the catalytic cycle, and can be easily brought back on cycle through conversion to two monometallic active species.[3, 5, 14]

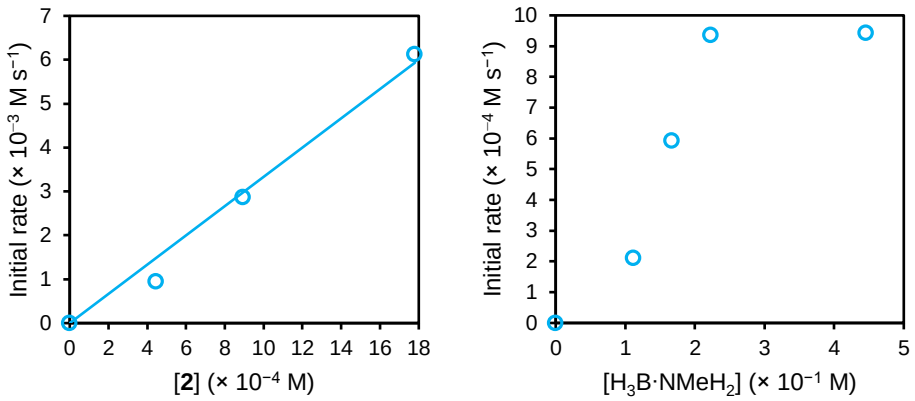
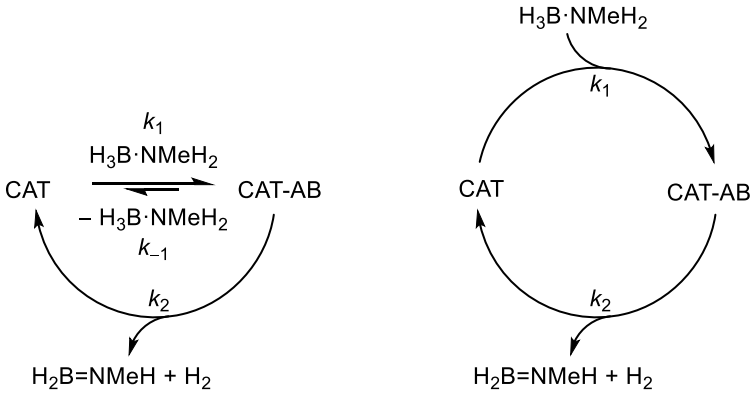


Figure 3.5 Initial rate plots for the dehydropolymerisation of $H_3B{\cdot}NMeH_2$ using **2**. Left: Variation in precatalyst **2** ($[H_3B{\cdot}NMeH_2]$ = 0.446 M). A line of best fit is shown for the proposed first order dependence on [**2**] (R^2 = 0.985). Right: Variation in $H_3B{\cdot}NMeH_2$ ([**2**] = 4.45 × 10^{-4} M).

Examining the effect of initial concentration of $H_3B{\cdot}NMeH_2$ versus initial rate over a 4-fold range (0.111 M, 0.167 M, 0.223 M and 0.446 M) led to the plot detailed in Figure 3.5. Between 0.111 M and 0.223 M, there is a dependence of initial rate on $[H_3B{\cdot}NMeH_2]_0$, however the measurement at 0.111 M appears to be an outlier, which may suggest some $H_3B{\cdot}NMeH_2$ consumption during the induction period which is more apparent at the lowest $H_3B{\cdot}NMeH_2$ concentration. Between 0.223 M and 0.446 M, an apparent zero order region becomes evident. These results suggest a complicated mechanistic landscape and may point to a saturation kinetics regime, as was modelled previously for the Xantphos-Ph system.[3]

If a saturation kinetics regime is in operation, this would suggest quasi-irreversible $H_3B{\cdot}NMeH_2$ coordination to the metal centre at higher $H_3B{\cdot}NMeH_2$ concentration (Scheme 3.3). However, steady-state/saturation kinetics modelling performed by Prof. Guy C. Lloyd-Jones (University of Edinburgh) did not provide a good fit to the data post induction period. Instead, due to the limited solubility of $H_3B{\cdot}NMeH_2$ in 1,2-$C_6H_4F_2$, which has been previously discussed,[3, 5] a simple first order model in both $H_3B{\cdot}NMeH_2$ and **2** (Scheme 3.3) taking into account a solubility limit of $H_3B{\cdot}NMeH_2$ (0.22 M) best accounted for the data involving multiple kinetic runs (Figure 3.6). With this model in hand, overall second order rate constants were simulated, and an average rate constant, k = 5.9 ± 0.5 M^{-1} s^{-1}, was obtained.



Scheme 3.3 Left: Representation of a saturation kinetics regime in [$H_3B{\cdot}NMeH_2$]. Right: Representation of a first order regime in [$H_3B{\cdot}NMeH_2$]. CAT = active catalytic species, CAT-AB = active catalytic species with $H_3B{\cdot}NMeH_2$ bound.

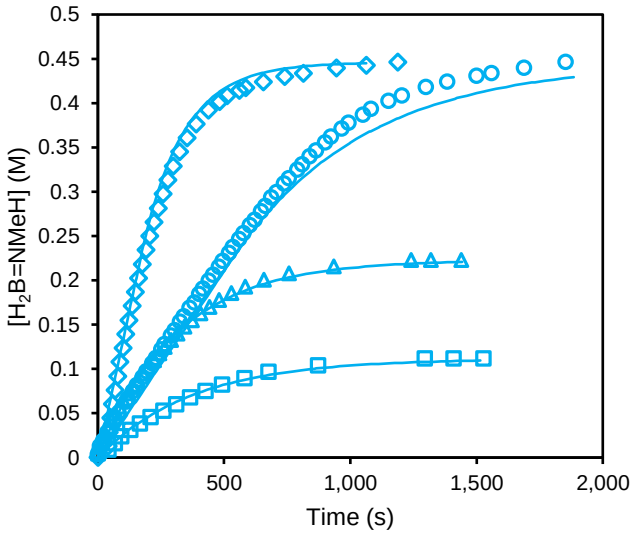


Figure 3.6 Temporal data plots for $H_2B{=}NMeH$ formation (as measured by H_2 evolution) in 1,2-$C_6H_4F_2$ solvent. Selected experimental data: ◇ = 4.45 × 10^{-4} M **2**, 0.446 M $H_3B{\cdot}NMeH_2$; ○ = 8.92 × 10^{-4} M **2**, 0.446 M $H_3B{\cdot}NMeH_2$; △ = 4.45 × 10^{-4} M **2**, 0.223 M $H_3B{\cdot}NMeH_2$; □ = 4.45 × 10^{-4} M **2**, 0.111 M $H_3B{\cdot}NMeH_2$. Selected simulated data: blue lines. Induction periods are not shown for clarity and have been subtracted from each time point.

With the solubility limit of $H_3B{\cdot}NMeH_2$ in 1,2-$C_6H_4F_2$ set at 0.22 M, further in depth kinetic studies in this thesis were carried out at concentrations of $H_3B{\cdot}NMeH_2$ at 0.223 M or lower to decrease complications imposed by $H_3B{\cdot}NMeH_2$ solubility at higher $H_3B{\cdot}NMeH_2$ concentrations.

3.3.4 Catalyst recharging experiments

Addition of two successive batches of $H_3B{\cdot}NMeH_2$ to the catalysis solution post dehydropolymerisation (0.2 mol% **2**, 0.446 M [$H_3B{\cdot}NMeH_2$]) resulted in full consumption of $H_3B{\cdot}NMeH_2$ (TON = 1500). The equivalents of H_2 produced versus time plot for all three consecutive experiments is shown in Figure 3.7. Notably, no induction period was observed for the second and third additions of $H_3B{\cdot}NMeH_2$, indicating that the species present at the end of catalysis remain active, or can be immediately converted to the true catalytic species in the presence of excess $H_3B{\cdot}NMeH_2$. It also suggests that the induction period may be due to the processing of trace impurities in the reaction solvent by the {Rh(Xantphos-^{i}Pr)}$^{+}$ before productive catalysis can occur. The third reaction shows a slight reduction in rate, speculated to be due to slight catalyst deactivation on manipulation of the reaction mixture over time. From the work outlined in Chapter 2, the organometallic species known to be present along the reaction course during the first charge are shown in Figure 3.8: **2**, **3**, **7** and **8**. The identity of the organometallics species present during the second and third charges are explored in Section 3.5 (vide infra).

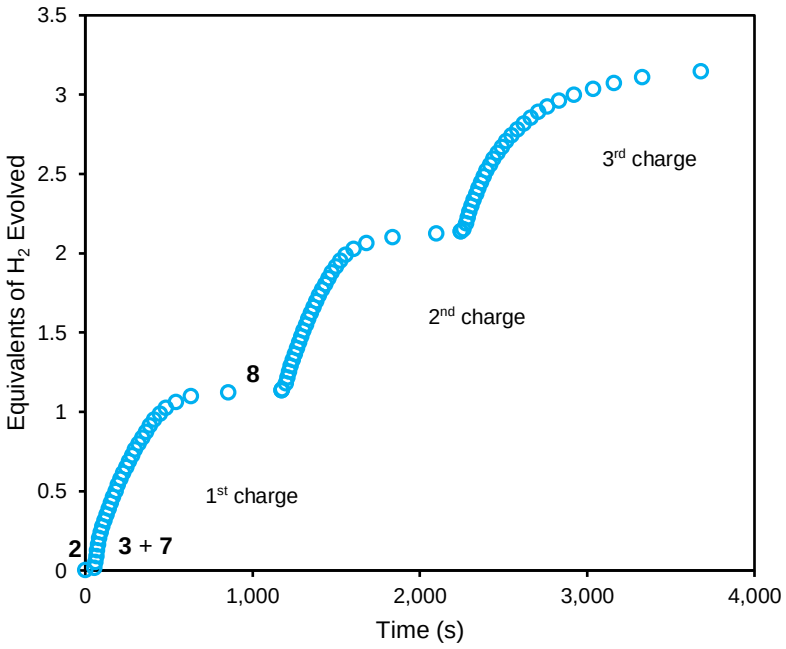


Figure 3.7 Top: Temporal data plots for the equivalents of H_2 formed over 3 successive catalytic runs (as measured by H_2 evolution) in 1,2-$C_6H_4F_2$ solvent. [**2**] = 8.92×10^{-4} M, [$H_3B{\cdot}NMeH_2$] = 0.446 M × 3.

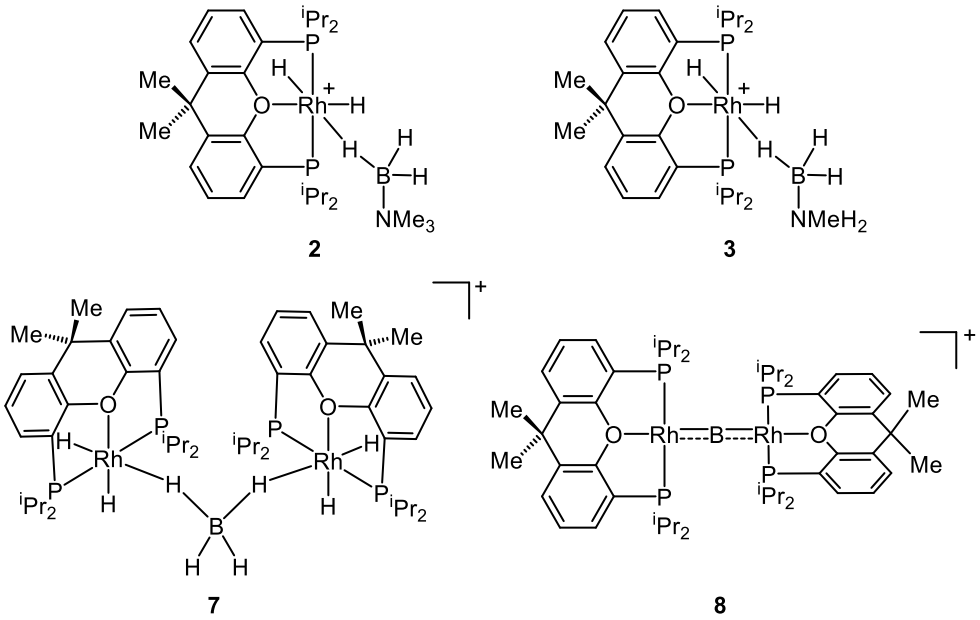


Figure 3.8 Structures of complexes **2**, **3**, **7** and **8**. $[BAr^{F}{}_{4}]^{-}$ anions not shown for clarity.

3.3.5 Kinetic isotope effects

The substrates $D_3B{\cdot}NMeH_2$ and $H_3B{\cdot}NMeD_2$ were used in catalysis to probe any kinetic isotope effects on the dehydrogenation process (KIE = k_H/k_D). By using $D_3B{\cdot}NMeH_2$ at 0.111 M ([**2**] = 2.23×10^{-4} M, 0.2 mol%), a KIE of 0.8 ± 0.1 for B–H/B–D substitution was measured, while $H_3B{\cdot}NMeD_2$ resulted in a KIE of 4.4 ± 0.1 for N–H/N–D substitution (Figure 3.9).

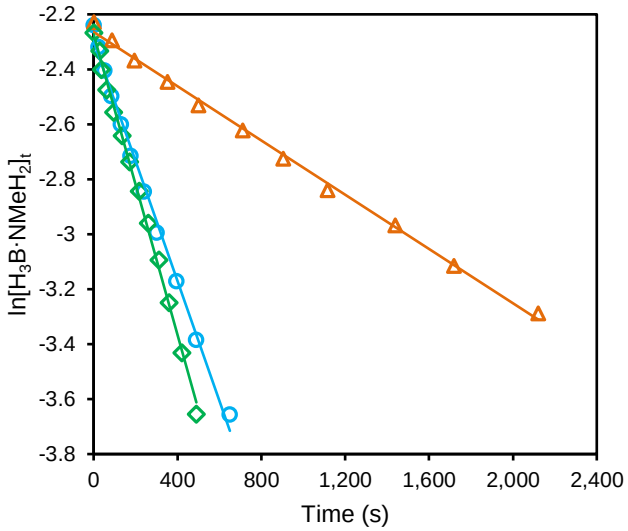


Figure 3.9 First order rate plots for KIE investigations with induction periods subtracted from each time point. ○ = 2.23×10^{-4} M **2**, 0.111 M $H_3B{\cdot}NMeH_2$ (k_{obs} = 2.2 ± 0.1 × 10^{-3} s^{-1}); ◇ = 2.23×10^{-4} M **2**, 0.111 M $D_3B{\cdot}NMeH_2$ (k_{obs} = 2.7 ± 0.1 × 10^{-3} s^{-1}); △ = 2.23×10^{-4} M **2**, 0.111 M $H_3B{\cdot}NMeD_2$ (k_{obs} = 0.5 ± 0.1 × 10^{-3} s^{-1}).

The large KIE associated with deuterium incorporation on the nitrogen suggests that N–H cleavage is involved in the turnover limiting step of dehydrogenation, or though less likely, in an equilibrium process prior to it. Similar KIE values for N–H/N–D substitution were reported for the dehydrocoupling of $H_3B{\cdot}NMe_2H$ using $[Cp_2Ti]$ (3.6 ± 0.3),[15] and $Rh(PCy_3)_2(H)_2Cl$ (5.3 ± 1.3) catalysts,[16] and N–H activation was proposed to be turnover limiting in both cases. On the other hand, for $\{Rh(Xantphos\text{-}Ph)\}^+$ precatalyst **i-13**, in which a coordination/dehydrogenation/insertion mechanism was proposed, the KIE associated with N–H activation in $H_3B{\cdot}NMe_2H$ was smaller (2.1 ± 0.2).[3] This smaller KIE in the Xantphos-Ph system compared to that reported for $\{Rh(Xantphos\text{-}^iPr)\}^+$ may indicate that differing mechanisms for these rate limiting N–H processes.

The small, inverse KIE associated with B–H activation using precatalyst **2** may indicate an equilibrium isotope effect that arises from reversible B–H activation at the metal centre,[17-18] occurring prior to the turnover limiting step. The possible mechanism for this reversible B–H activation using D_2 is detailed in Scheme 2.7. However, within error the KIE for B–H/B–D substitution may be considered to be close to unity, meaning simply that B–H activation may not be contributing to the KIE value. The large difference in KIE for B–H versus N–H, however, suggests that B–H/N–H activation does not occur in a synchronous concerted manner, as has been documented in reports by Baker (e.g. $KIE_{N–H} = 2.3$, $KIE_{B–H} = 1.7$),[19] Guan,[20] and Rossin and Shubina.[21] However, a transition state in which B–H activation occurs much earlier than N–H activation could be the cause of the difference KIE values for N–H versus B–H using precatalyst **2** (Figure 3.10).

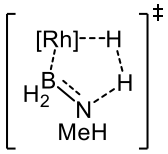


Figure 3.10 Possible transition state in which B–H activation of a bound amine borane moiety has occurred much earlier than N–H activation.

3.4 Polyaminoborane growth kinetics

With information garnered about the dehydrogenation process of $H_3B{\cdot}NMeH_2$ to $H_2B{=}NMeH$ using $\{Rh(Xantphos\text{-}^iPr)\}^+$, the fate of the resultant aminoborane required probing. This can be investigated through aminoborane trapping experiments, as well as gaining information about polyaminoborane chain length via analysing the resultant polyaminoborane formed.

3.4.1 Aminoborane trapping experiments

Described in Section 1.6.2, the presence of free, but transient, $H_2B{=}NMeH$ in dehydrocoupling reaction mixtures may be probed by trapping the aminoborane using cyclohexene, forming $Cy_2B{=}NMeH$ via hydroboration.[22] This may be a useful method for ascertaining whether the aminoborane remains metal bound, and hence whether the B–N coupling event between $H_2B{=}NMeH$ monomers occurs on-metal, or off.

Addition of 2.7 equivalents of cyclohexene (i.e. 270 mol%) to the dehydropolymerisation of $H_3B{\cdot}NMeH_2$ using **2** at 0.2 mol% catalyst loading did not result in the observation of $Cy_2B{=}NMeH$ in the ^{11}B NMR spectrum of the reaction mixture (δ 44.9, br, THF solvent) (Figure 3.11).[23] At 10 mol% **2**, where $(HBNMe)_3$ becomes the major product of the reaction (Section 2.4.2), approximately 1% of the reaction mixture is assigned to $Cy_2B{=}NMeH$ in the ^{11}B NMR spectrum, observed at a chemical shift of δ 45.9 in 1,2-$C_6H_4F_2$ solvent (Figure 3.11). These data suggest that any $H_2B{=}NMeH$ formed is consumed significantly faster than hydroboration, both in chain propagation to form $(H_2BNMeH)_n$ at 0.2 mol% catalyst loading, or $(HBNMe)_3$ formation in the case of 10 mol% catalyst loading. In particular, this suggests that polymerisation of $H_2B{=}NMeH$ is likely to be metal mediated, as $(H_2BNMeH)_n$ formed via metal free methods showed the presence of $Cy_2B{=}NMeH$ on addition of cyclohexene.[24]

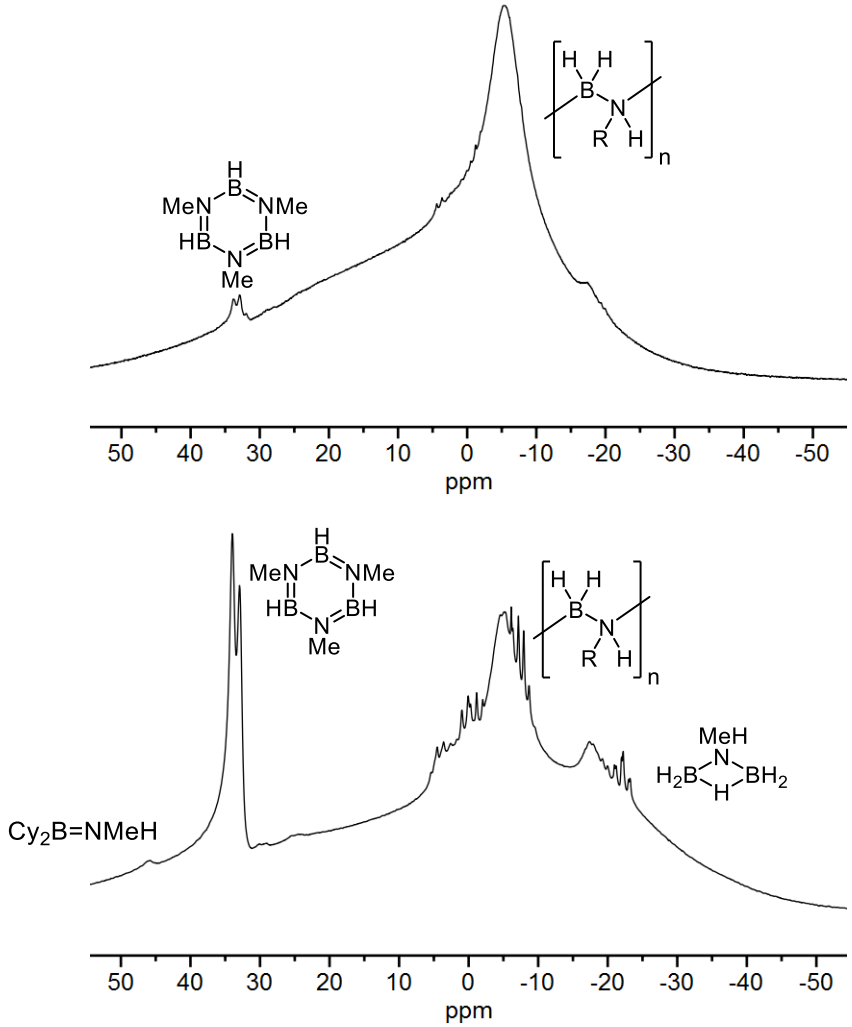


Figure 3.11 ^{11}B NMR spectra of the reaction mixtures of the dehydrocoupling of $H_3B{\cdot}NMeH_2$ (0.446 M) with 2.7 equivalents of cyclohexene (relative to $H_3B{\cdot}NMeH_2$) using precatalyst **2** in 1,2-$C_6H_4F_2$ solvent. Top: 0.2 mol% **2**. Bottom: 10 mol% **2**. The peak at δ 45.9 is assigned to $Cy_2B{=}NMeH$. The broad baseline signals observed in the ^{11}B NMR spectra at δ ~20.0 are due to background from the tube and probe (borosilicate glass).

3.4.2 Polyaminoborane analysis: NMR spectroscopy

Off white polyaminoborane $(H_2BNMeH)_n$ could be isolated in yields between 30 – 75% using precatalyst **2**. Carrying out the dehydropolymerisation on a gram scale of $H_3B{\cdot}NMeH_2$ at 0.2 mol% catalyst loading led to the isolation of 0.6 g (H_2BNMeH_n) (62% yield). The ^{11}B NMR spectra of isolated polyaminoborane produced showed a broad peak, centred at δ −5.0 in CD_2Cl_2 solvent (Figure 3.12). A small shoulder was also apparent at δ ~2.0 which may be indicative of a small amount of chain branching, signalled by the presence of tertiary or quaternary boron centres "BHN_3" or "BN_4", in the polyaminoborane backbone.[2, 25] A signal to lower field has also been

reported in other systems and was distinct when chain branching was proposed.[24] A small, unresolved signal at δ −17.6 suggests some entrained $H_3B{\cdot}NMeH_2$, although this may simply be a BH_3 polyaminoborane end group signal.[26] The ^{1}H NMR spectrum (Figure 3.12) shows environments which could be assigned to NH, NMe, and BH_2, where the BH_2 resonance sharpened slightly on ^{11}B decoupling. A small shoulder on the NMe signal was observed to low field, but this was poorly resolved. The $^{13}C\{^1H\}$ NMR spectra show multiple environments assigned to NMe, for example a sharp signal was observed at δ 36.2 and broader, lower field signals were observed centred at δ ~37.0 (Figure 3.12). Very similar spectral data have been observed for N-methylpolyaminoborane produced using Ir(POCOP-^{t}Bu)$(H)_2$,[4] and FeH(PN*H*P)(CO)(HBH_3),[27] especially the multiple environments in the $^{13}C\{^1H\}$ NMR spectra. The $^{13}C\{^1H\}$ NMR spectrum of the related polyphosphinoborane $(H_2BP^tBuH)_n$ formed by a thermal dehydropolymerisation process ($M_n \approx 30{,}000$ g mol^{-1}, $Đ \approx 1.8$) also showed multiple environments for the ^{t}Bu group, not dissimilar to those observed here for the NMe groups, while in the ^{31}P NMR spectra multiple environments were observed.[28] These data were interpreted as being due to the tactic environments associated with the polyphosphinoborane and, in particular, specific triads. A mixture of R,R and R,S diastereoisomers of the linear triborazane $H_3B(NMeHBH_2)_2NMeH_2$ have also been synthesised, although no ^{13}C NMR data were reported.[29]

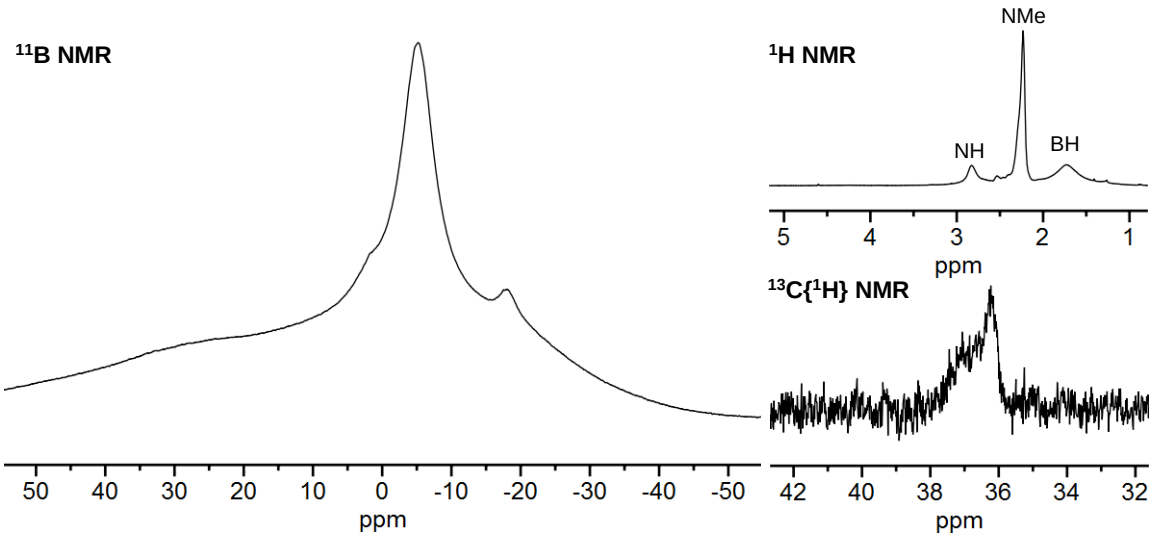


Figure 3.12 NMR spectra (CD_2Cl_2, 298 K) for isolated $(H_2BNMeH)_n$ produced by precatalyst **2** (0.2 mol%, 0.446 M $H_3B{\cdot}NMeH_2$, 1,2-$C_6H_4F_2$ solvent). The broad baseline signal observed in the ^{11}B NMR spectrum at δ ~20.0 is due to background from the tube and probe (borosilicate glass).

Given the possibility for chain branching, as well as ^{1}H and ^{13}C NMR spectra which are complicated due to coupling to both quadrupolar ^{10}B (I = 3, 20% natural abundance) and ^{11}B (I = 3/2, 80% natural abundance) environments, it is difficult to ascertain $(H_2BNMeH)_n$ stereochemistry using this data alone. However, these spectral observations could well be important in future studies of polyaminoborane tacticity.

3.4.3 Polyaminoborane analysis: GPC

Molecular weight analysis of $(H_2BNMeH)_n$ samples was carried out by gel permeation chromatography (GPC) using a refractive index (RI) detector, and compared to polystyrene standards. All of the polyaminoborane samples produced using **2** gave GPC traces which appeared to contain a bimodal distribution of polyaminoborane molecular weights: a broad, low intensity peak characteristic of $(H_2BNMeH)_n$,[4] and a sharper peak that tailed to lower M_n (Figure 3.13(a)). Sharp signals such as these had not previously been reported in the GPC data of $(H_2BNMeH)_n$ for other systems, such as [Rh(κ^2-P,P-Xantphos-Ph)(η^2-$H_2B(CH_2CH_2{}^tBu)\cdot NMe_3$)][$BAr^F{}_4$] **i-13**, and this may be due to variability in polyaminoborane molecular weight separation allowed by the particular column set used. To test this, polyaminoborane produced using Xantphos-^{i}Pr precatalyst **2** and Xantphos-Ph precatalyst **i-13** were compared on the same machine. The sharp peak was now also evident on analysing $(H_2BNMeH)_n$ formed by precatalyst **i-13**. This signal has also been documented in very recent work by the Weller group.[30] Significantly, this sharp signal was absent in $(H_2BNMeH)_n$ samples formed by the neutral catalyst Rh(κ^3-P,O,P-Xantphos-^{i}Pr)H in work pursued by Dr Annie L. Colebatch (Figure 3.13(b)),[31] therefore it was suspected it may be due to the presence of the $[BAr^F{}_4]^-$ anion entrained into the polyaminoborane.

Further evidence that the sharp peak found in the GPC traces of polyaminoborane produced by **2** was due to the $[BAr^F{}_4]^-$ anion came from spiking a sample of $(H_2BNMeH)_n$ produced by neutral Rh(κ^3-P,O,P-Xantphos-^{i}Pr)H with 0.2 mol% complex **2**, and the resultant GPC trace showed the characteristic skewed signal (Figure 3.13(c)). The GPC traces could be deconvoluted,[32] by fitting

the data to a skewed Gaussian bimodal distribution using a standalone program developed by Joshua I. Levy (Northwestern University). The GPC data was initially analysed using OMNISEC software to obtain suitable peak limits for molecular weight analyses. Weight fraction per log molecular weight increment (dw/dlog(M)) versus log molecular weight (log(M)) plots (i.e. the true molecular weight distribution curve),[33] were obtained using OMNISEC. The sum of two skew Gaussian functions was used to model the molecular weight distribution curve; with parameter estimation achieved using the Levenberg-Marquadt nonlinear least-squares method from MINPACK,[34] via the SciPy optimization library for Python. The peak limits found initially using OMNISEC were subsequently applied to the fitted molecular weight distribution curve and the fitted molecular weight parameters were calculated. Coincidently, the relatively sharp peak profile for the $[BAr^{F}{}_{4}]^{-}$ anion, coupled with its co-elution with polyaminoborane which tails into system peaks, results in the modelled fits giving similar M_n and Đ to the raw data for $(H_2BNMeH)_n$ produced using precatalyst **2**. Giving confidence in this approach, fits carried out for the data for $[BAr^{F}{}_{4}]^{-}$-spiked $(H_2BNMeH)_n$ using neutral Rh(κ^3-P,O,P-Xantphos-^{i}Pr)H recovered the unspiked data well (Figure 3.13(c)).

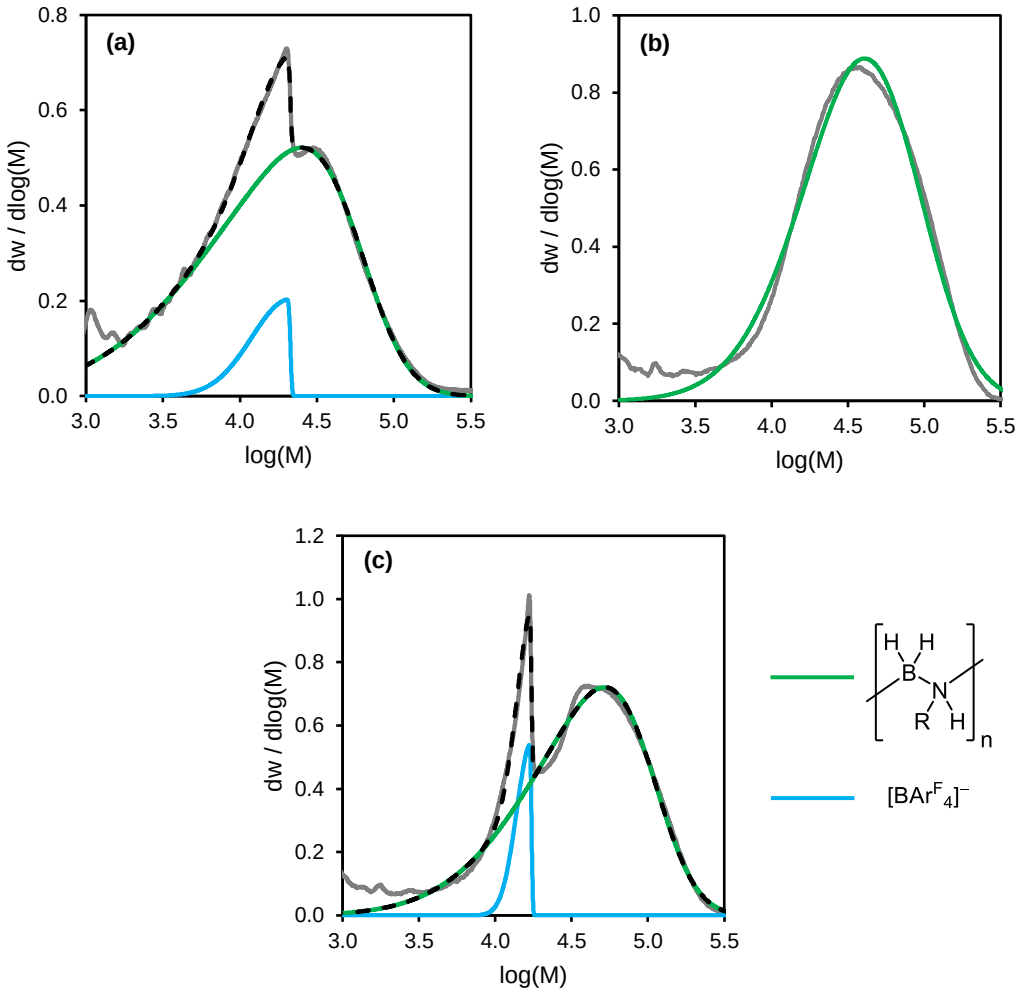


Figure 3.13 Experimental (grey, solid line), combined fitted (black, dashed line), and individual skewed Gaussian fitted (green and blue, solid lines) GPC data for $(H_2BNMeH)_n$. (a) Using precatalyst **2** (0.2 mol%, 0.446 M $H_3B{\cdot}NMeH_2$). (b) Using Rh(κ^3-P,O,P-Xantphos-^{i}Pr)H. (c) Using Rh(κ^3-P,O,P-Xantphos-^{i}Pr)H, spiked with 0.2 mol% precatalyst **2**.

Even though the catalyst is used in low concentration (0.2 – 1.0 mol%) the $[BAr^F_4]^-$ aryl groups might be expected to be significantly more sensitive to RI detection than polyaminoborane, a technique that has been shown to have a positive correlation to the polarisability of any functional group.[35] Hence the sharp signal found for $[BAr^F_4]^-$ may not necessarily be indicative of the relative concentration of $[BAr^F_4]^-$ compared to $(H_2BNMeH)_n$. In fact, for the GPC trace in Figure 3.13(a), 10% of the area of the overall GPC trace was in fact attributed to the sharp $[BAr^F_4]^-$ signal. ^{19}F NMR spectroscopy of polyaminoborane produced using 0.2 mol% **2** showed a signal at δ −63.2 in CD_2Cl_2 solvent, consistent with $[BAr^F_4]^-$, while for that produced using neutral Rh(κ^3-P,O,P-

Xantphos-^{i}Pr)H was, of course, absent.[31] In the ^{1}H NMR spectrum, signals assigned to the $[BAr^{F}_{4}]^{-}$ 3,5-$C_6H_3(CF_3)_2$ groups were observed, and when integrated with respect to the NMe signal a loading of 0.18 mol% was estimated – much lower than the 10% $[BAr^{F}_{4}]^{-}$ contribution suggested by GPC, suggesting a relative ~50-fold enhancement by RI detection.

Knowing that the $[BAr^{F}_{4}]^{-}$ anion remained present in the $(H_2BNMeH)_n$ samples, the presence of rhodium metal was also analysed. Inductively coupled plasma mass spectrometry (ICP-MS) was used to measure the rhodium content in $(H_2BNMeH)_n$ samples, which indicated a loading of ~450 ppm (i.e. 0.045 mol%), suggesting that the anion and cation are both entrained, albeit to differing extents. A similar entrainment of catalyst in phosphine borane dehydropolymerisation has recently been reported.[36] In order for polyaminoboranes to potentially become useful new polymeric materials, the amount of catalyst present should be minimal. For example, the European Union regulates the content of heavy metals in packaging (such as polymeric materials) to 100 ppm by weight.[37-38] Future work into these systems should consider ways to remove catalyst from the polyaminoborane samples, or alternatively develop catalysts which do not become entrained in the resulting polyaminoborane.

3.4.4 Polyaminoborane molecular weight versus conversion

A plot of polyaminoborane molecular weight versus the percentage conversion of $H_3B{\cdot}NMeH_2$ allows for the determination of the nature of polyaminoborane growth, i.e. chain growth, step growth, or living polymerisation (Figure 1.15). At each conversion point, 5.0 equivalents of PPh_3 were added to the reaction mixture to quench catalysis, and the reaction mixture was precipitated with hexane. The resultant solid mixture was isolated, dissolved in THF solvent and analysed by ^{11}B NMR spectroscopy to determine the percentage conversion, and the molecular weight data for the resulting $(H_2BNMeH)_n$ could then be obtained (Figure 3.14).

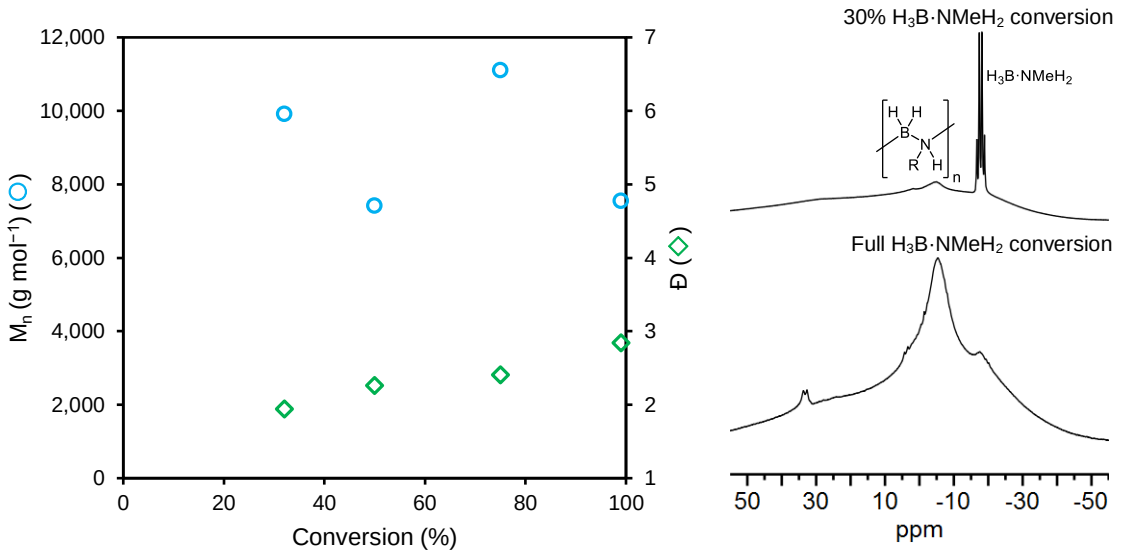


Figure 3.14 M_n (○; g mol^{-1}) and Đ (◇) versus $H_3B{\cdot}NMeH_2$ conversion (%) plot. [**2**] = 8.92 × 10^{-4} M (0.2 mol%), [$H_3B{\cdot}NMeH_2$] = 0.446 M, 1,2-$C_6H_4F_2$ solvent. Open conditions via controlled argon flow. Right: Stacked ^{11}B NMR spectra of the polyaminoborane samples in THF solvent from molecular weight versus conversion reaction mixtures using precatalyst **2** ([**2**] = 8.92 × 10^{-4} M (0.2 mol%), [$H_3B{\cdot}NMeH_2$] = 0.446 M, 1,2-$C_6H_4F_2$, open conditions) at 30% $H_3B{\cdot}NMeH_2$ conversion (top) and full $H_3B{\cdot}NMeH_2$ conversion (bottom). The broad baseline signals observed at δ ~20.0 are due to background from the tube and probe (borosilicate glass).

The data shows that at low conversion of $H_3B{\cdot}NMeH_2$, polyaminoborane of appreciable molecular weight was being formed (M_n = 10,000 g mol^{-1}, Đ = 2.0), and this did not change significantly over the course of dehydropolymerisation. At these low conversions $H_3B{\cdot}NMeH_2$ was the dominant species by ^{11}B NMR spectroscopy, while the signal at δ −5.0 assigned to polyaminoborane was characteristically broad. There was no indication that short chain oligomers such as $H_3B{\cdot}NMeHBH_2{\cdot}NMeH_2$ were formed, as these would be expected to show more resolved B–H coupling in the BH_2 region (δ −5.0) of the ^{11}B NMR spectrum, therefore a step growth polymerisation process was rejected.[39] Instead, these data are consistent with chain growth polyaminoborane propagation in which a reactive aminoborane monomer undergoes polymerisation to give $(H_2BNMeH)_n$, followed by termination.[40-41]

On the other hand, living polymerisation is a type of chain growth polymerisation in which there is no intrinsic chain termination event, therefore polymer molecular weight increases with addition of

further monomer. Whilst both the M_n versus conversion graph in Figure 3.14 and non-unity value of Đ for $(H_2BNMeH)_n$ implies living polymerisation does not occur in this system, living polymerisation was explicitly tested for. Two further additions of $H_3B{\cdot}NMeH_2$ were added to the reaction mixture post dehydropolymerisation (0.2 mol% **2**, 0.446 M [$H_3B{\cdot}NMeH_2$]). No significant change in the molecular weight of isolated polyaminoborane resulted (M_n = 15,000 g mol^{-1}, Đ = 1.9), therefore living polymerisation was discounted, although clearly active organometallic species were still present at the end of each catalytic run.

3.4.5 Polyaminoborane molecular weight versus catalyst loading and dependence on H_2 pressure

With the characteristic chain growth profile of $H_2B{=}NMeH$ polymerisation by **2** demonstrated, further details on its mechanism were probed. In polymerisation via single-site coordination/insertion, reducing the catalyst loading would be expected to increase the degree of polymerisation, as noted for $H_3B{\cdot}NMeH_2$ dehydropolymerisation using Xantphos-Ph precatalyst **i-13**,[3] and $H_3B{\cdot}PPhH_2$ dehydropolymerisation using Fe(η^5-C_5H_5)$(CO)_2(OTf)$.[42] Further support for coordination/insertion in the Xantphos-Ph system (Scheme 1.17) was confirmed by the dependence of polyaminoborane M_n on H_2 pressure. In this mechanism, metal bound $H_3B{\cdot}NMeH_2$ dehydrogenates to form $H_2B{=}NMeH$ on metal. This can then insert into a metal bound $(H_2BNMeH)_n$ chain, such as Rh(H)–$NMeHBH_2R$ (R = growing $(H_2BNMeH)_n$), which is susceptible to hydrogenolysis if H_2 outcompetes further $H_3B{\cdot}NMeH_2$ binding (Figure 3.15). The use of H_2 as a chain termination agent is well established in olefin polymerisation and likely operates through sigma bond metathesis of H_2 with the [M]–CH_2–R′ growing polymer chain to form a metal hydride and free polymer (Figure 3.15).[43-44] Therefore the dependence of $(H_2BNMeH)_n$ chain length on catalyst loading and H_2 pressure was investigated using precatalyst **2**.

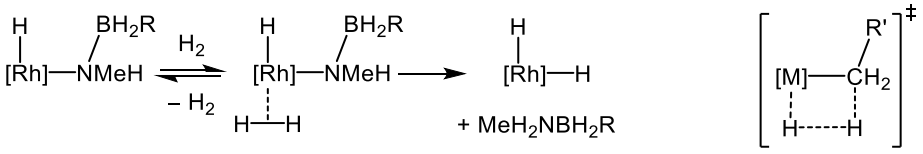


Figure 3.15 Left: Possible intermediates involved in the hydrogenolysis of the growing polyaminoborane chain in the Xantphos-Ph system. [Rh] = {Rh(Xantphos-Ph)}$^{+}$, R = growing polyaminoborane chain. Right: Possible transition state for the chain termination of polyolefins by sigma bond metathesis of H_2 with [M]–CH_2–R′. [M] = early transition metal catalyst, R′ = growing polyolefin chain.

Figure 3.16 shows that increasing the catalyst loading from 0.2 to 1 mol% for **2** resulted in a 2-fold decrease in polyaminoborane molecular weight, rather than the expected 5-fold decrease – uncharacteristic of coordination/insertion chain growth. This was further confirmed by carrying out dehydropolymerisation in a closed system (0.2 mol% **2**, 0.223 M [$H_3B{\cdot}NMeH_2$]). Based on 50.0 mg $H_3B{\cdot}NMeH_2$ (0.223 M), this leads to an approximate 1 bar of H_2 pressure over time. Isolation of the polyaminoborane formed and subsequent GPC analysis showed that a pressure of H_2 did not act to significantly modify the chain length when allowed to build up in a closed system (M_n = 9,000 g mol^{-1}, Đ = 2.5) versus the same catalysis conditions open to argon flow connected to a mineral oil bubbler (M_n = 10,000 g mol^{-1}, Đ = 2.2). This lack of sensitivity to H_2 for catalyst **2** contrasts with Xantphos-Ph system **i-13**, but is similar to Manners' Ir(POCOP-^{t}Bu)$(H)_2$,[4] and Beweries' FeH(PN*H*P)(CO)(HBH_3) systems (Section 1.6.7),[27] where no significant effects were reported. Hence, hydrogenolysis is unlikely to be responsible for polyaminoborane chain termination in this system.

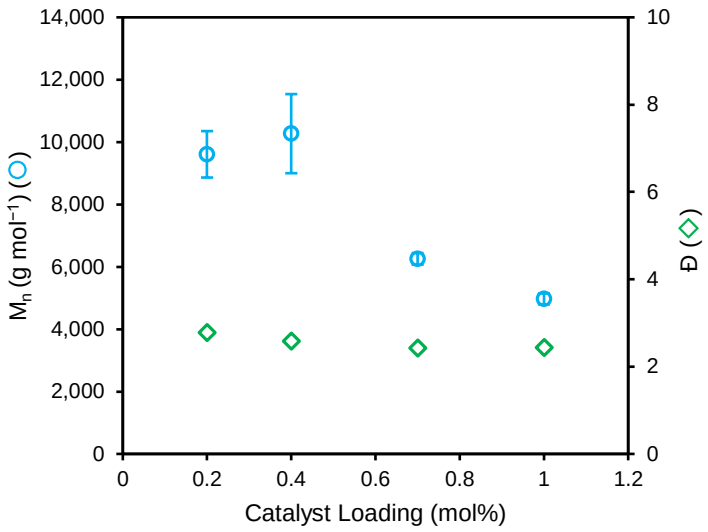


Figure 3.16 M_n (○**;** g mol^{-1}) and Đ (◇) versus catalyst loading of **2** (mol%). [$H_3B{\cdot}NMeH_2$] = 0.446 M, 1,2-$C_6H_4F_2$ solvent. Open conditions via controlled argon flow.

With these results in mind, it is unlikely that dehydropolymerisation using {Rh(Xantphos-^{i}Pr)}$^{+}$ system **2** operates by a single site coordination/dehydrogenation/insertion mechanism as seen in Xantphos-Ph system **i-13**, though it does show clear chain growth characteristics (Figure 3.14). Therefore an alternative chain growth mechanism was proposed (Section 3.6, vide infra).

3.5 Involvement of complexes **3**, **6**, **7** and **8** in the dehydropolymerisation of $H_3B{\cdot}NMeH_2$ using **2**

In Chapter 2 it was shown that during the dehydrocoupling of $H_3B{\cdot}NMeH_2$ using 10 mol% **2**, the transformation **2** → **3** → **7** → **8** operated, therefore the involvement of these complexes at lower catalyst loadings was of interest. Amine complex **6** was also of interest to test in catalysis as free $NMeH_2$ is proposed to form in the reaction, due to the presence of complexes **7** and **8** which are derived from free BH_3, and therefore suggesting that $H_3B{\cdot}NMeH_2$ dissociation operates in this system. The proposed structures of complexes **2**, **3**, **6**, **7** and **8** are shown in Figure 3.17.

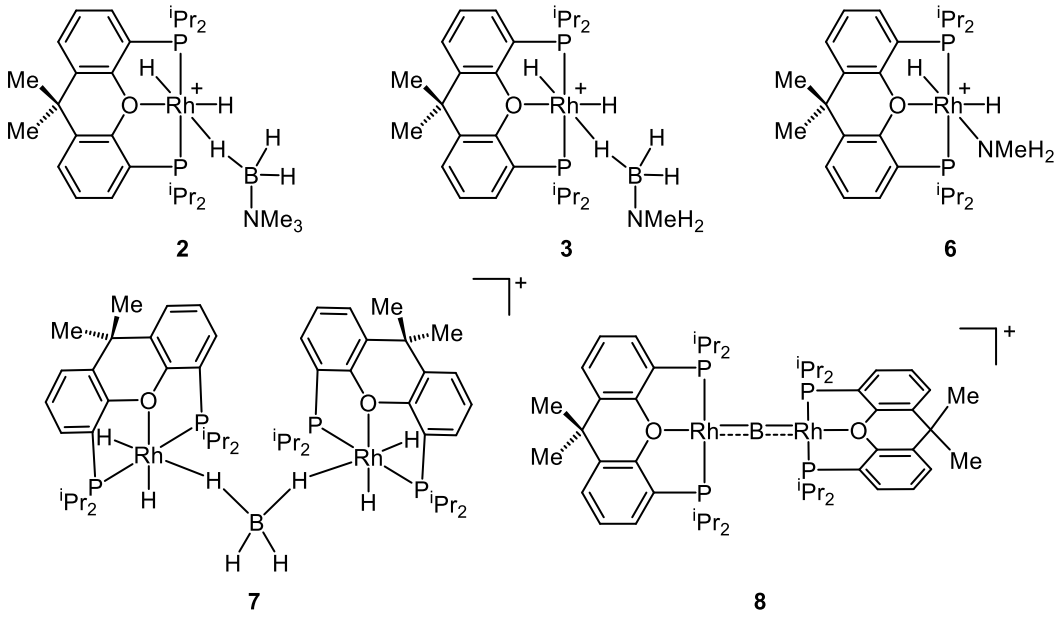
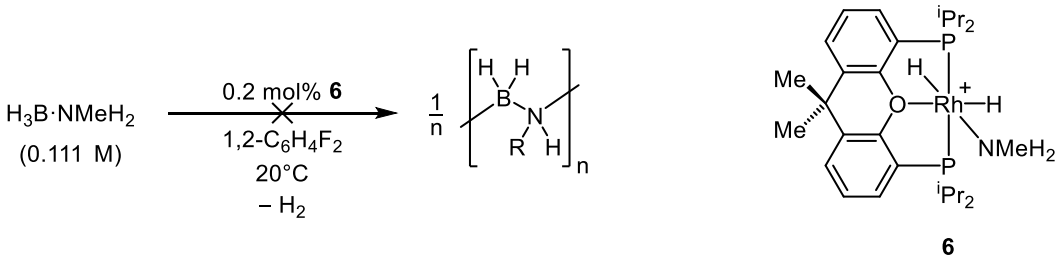


Figure 3.17 Proposed structures of **2**, **3**, **6**, **7** and **8**. $[BAr^F_4]^-$ anions not shown for clarity.

*3.5.1 Testing [Rh(Xantphos-^{i}Pr)(H)$_2$(NMeH$_2$)][BAr$^F_4$] (**6**) as a H$_3$B·NMeH$_2$ dehydropolymerisation catalyst*

Catalysis using the simple amine complex [Rh(κ^3-P,O,P-Xantphos-^{i}Pr)(H)$_2$(NMeH$_2$)][BAr$^F_4$] (**6**) was attempted under the hydrogen evolution measurement conditions employed in Section 3.3 (Scheme 3.4, 0.2 mol% **6**, 0.111 M [H$_3$B·NMeH$_2$]). After 1 hour, no H$_2$ had been evolved from the reaction mixture, and ^{11}B NMR spectroscopy showed that only H$_3$B·NMeH$_2$ was present, hence it is very unlikely that complex **6** is involved in the H$_3$B·NMeH$_2$ dehydrogenation mechanism. Therefore, if free NMeH$_2$ is generated, it may be involved in dehydropolymerisation via an alternative pathway.



Scheme 3.4 Attempted dehydropolymerisation of H$_3$B·NMeH$_2$ using complex **6**. $[BAr^F_4]^-$ anion not shown for clarity.

*3.5.2 Involvement of complexes **3**, **7** and **8** in the dehydropolymerisation of $H_3B{\cdot}NMeH_2$ under true catalytic conditions*

As dehydropolymerisation is performed at low catalyst loadings, directly interrogating reaction mixtures to determine the fate of the catalyst by NMR spectroscopic techniques is difficult. Instead, increasing the catalyst loading to 10 mol% was utilised to aid observation of possible catalytic intermediates as outlined in Section 2.4.2. However, the reaction mixture present at the end of catalysis using 0.4 mol% **2** was still concentrated and interrogated by NMR spectroscopy. Although a weak spectrum resulted, a doublet of doublets at δ 47.5 ($^1J_{RhP}$ 174 Hz, $^3J_{RhP}$ 6 Hz) could be resolved in the $^{31}P\{^1H\}$ NMR spectrum (Figure 3.18), alongside a lack of signals in the hydride region of the ^1H NMR spectrum, characteristic of the dimetalloborylene complex [{Rh(κ^3-P,O,P-Xantphos-^{i}Pr)}$_2$B][BAr$^F{}_4$], complex **8** (Section 2.7).

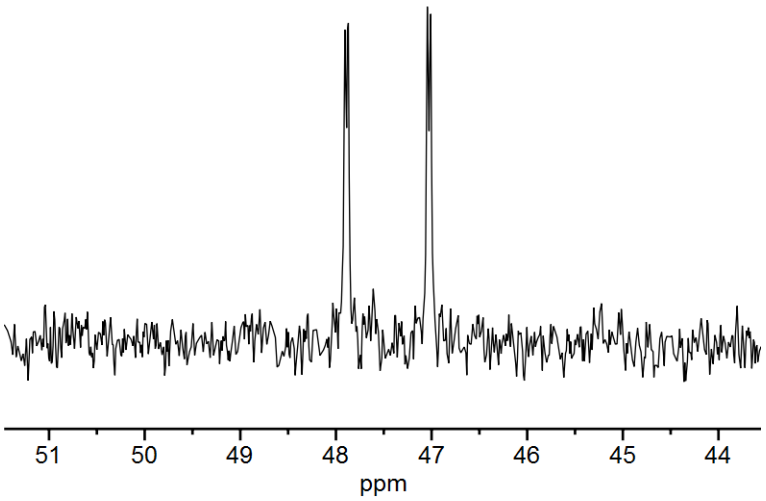


Figure 3.18 $^{31}P\{^1H\}$ NMR spectrum of the concentrated reaction mixture at the end of dehydropolymerisation of $H_3B{\cdot}NMeH_2$ using precatalyst **2** at 0.4 mol% loading. [**2**] = 1.78 × 10^{-3} M, [$H_3B{\cdot}NMeH_2$] = 0.446 M, 1,2-$C_6H_4F_2$ solvent, open conditions.

Given that **8** forms at the end of catalysis, and catalysis restarts on addition of more $H_3B{\cdot}NMeH_2$ substrate (Section 3.3.4), its role as a dehydropolymerisation catalyst was investigated. The use of **8-[BAr$^{Cl}{}_4$]** as a catalyst at 0.2 mol% catalyst loading afforded polymeric material (M_n = 14,000 g mol^{-1}, Đ = 2.7) similar to that starting from 0.4 mol% **2** under open conditions (M_n = 10,300 g mol^{-1}, Đ = 2.6). The dehydrogenation kinetics using in situ formed **8** were also similar to that using precatalyst **2** under the same concentration of Rh_1 (Figure 3.19).

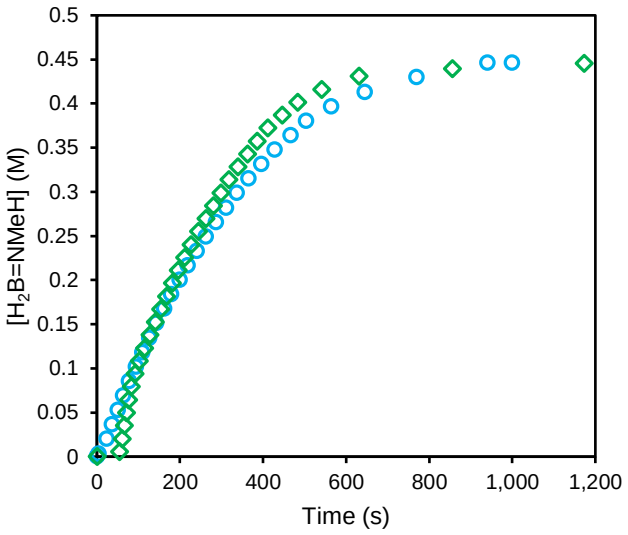
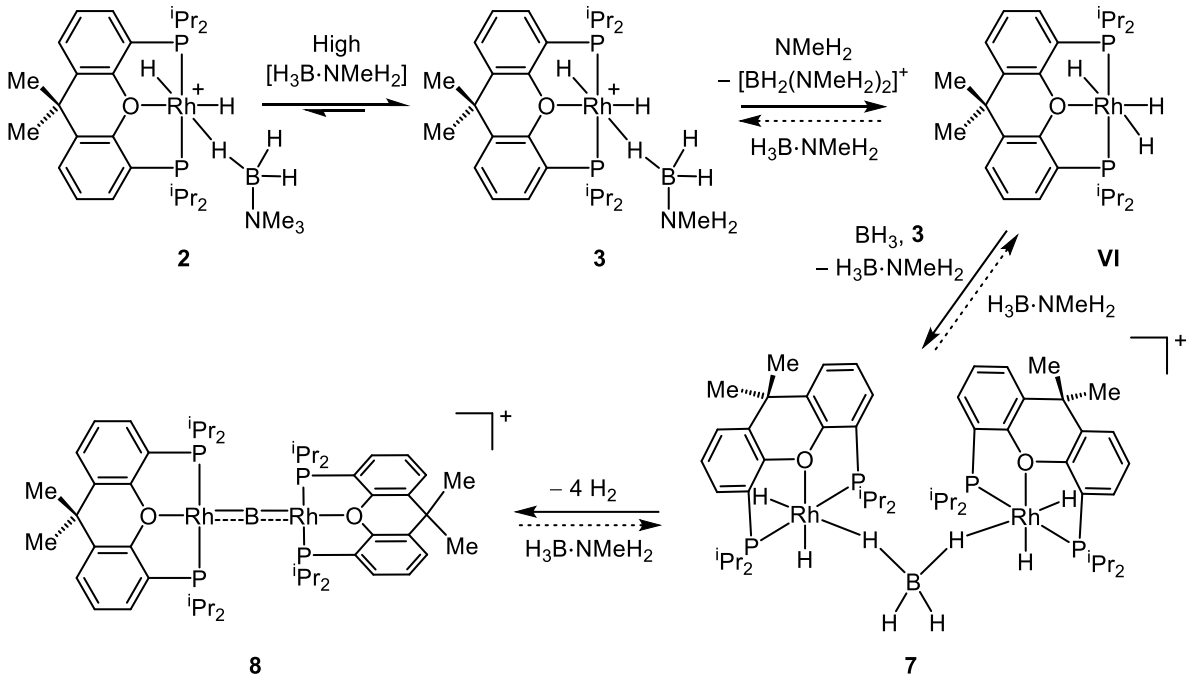


Figure 3.19 Temporal data plots for $H_2B{=}NMeH$ formation (as measured by H_2 evolution). $[H_3B{\cdot}NMeH_2]$ = 0.446 M, 1,2-$C_6H_4F_2$ solvent. ○ = 4.45×10^{-4} M in situ formed **8**; ◇ = 8.92×10^{-4} M **2**.

Further to this, addition of 10 equivalents of $H_3B{\cdot}NMeH_2$ to **8-[BAr$^{Cl}_4$]** in a sealed NMR tube, using the same conditions as in Section 2.4.2, showed that complexes **3-[BAr$^{Cl}_4$]** and **7-[BAr$^{Cl}_4$]** were generated immediately, alongside $(HBNMe)_3$ and $[BH_2(NMeH_2)(L)]^+$ (L = $NMeH_2$ or solvent). Thus, although we cannot rule out that **8** is the true catalytic species, its temporal and reactivity profiles suggest that it is more likely to play a dormant, off-cycle role in the catalytic cycle, with **3** or **7** observed as resting states (Scheme 3.5). The speciation studies in Chapter 2 for complexes **2** and **3**, and reported here for complex **8**, all point to hydride transfer processes in the cationic system, due to the evolution of precatalyst **2** to dimetalloborylene **8** via the pathway shown in Scheme 3.5. Ligand substitution of $H_3B{\cdot}NMe_3$ in **2** by $H_3B{\cdot}NMeH_2$ forms **3**, from which attack by $NMeH_2$ forms proposed, though unobserved, neutral trihydride **VI** with the concomitant formation of a boronium cation such as $[BH_2(NMeH_2)_2]^+$. **VI** can then undergo further reaction with BH_3/**3** to form **7** which can then lose 4 equivalents of H_2 to form **8**. Therefore, it was proposed that neutral hydride species such as **VI** and boronium cations, i.e. $[BH_2(NMeH_2)_2][BAr^F_4]$ (**11**), may be involved in key steps in the dehydrogenation mechanism.



Scheme 3.5 Proposed reactivity profile connecting complex **2** to complex **8** via complexes **3**, **VI** and **7**. $[BAr^F_4]^-$ anions not shown for clarity. Dashed arrows indicate a pathway back to complexes **3** and **7**, and therefore the active catalyst, with excess $H_3B{\cdot}NMeH_2$.

To probe the role of boronium cations, dehydropolymerisation was repeated at 0.111 M $H_3B{\cdot}NMeH_2$, 0.2 mol% **2**, with and without the addition of excess, independently synthesised, $[BH_2(NMeH_2)_2][BAr^F_4]$ (**11**, 2 mol%). Figure 3.20 details the temporal evolution plots obtained alongside the first order rate plots for these data. With additional $[BH_2(NMeH_2)_2][BAr^F_4]$, the induction period increased by ~10 minutes (Figure 3.20). This may be due to increased dihydrogen bonding in the system between boronium and $H_3B{\cdot}NMeH_2$ or $NMeH_2$,[45] which may hamper the formation of the active catalytic species. However, post induction period, during the productive, first order region of dehydrogenation catalysis, a ~3-fold increase in k_{obs} was observed with added $[BH_2(NMeH_2)_2]^+$ (Figure 3.20). This therefore may suggest that boronium is in fact involved in the dehydrogenation mechanism, as increasing its concentration increased rate of catalysis. Further confirmation that boronium could be involved during $H_3B{\cdot}NMeH_2$ dehydrogenation was provided by GPC analysis of the polyaminoborane produced under the conditions of excess boronium. This was of low molecular weight but still characteristic of precatalyst **2** (M_n = 6,000 g mol^{-1}, Đ = 1.7).

The presence of $[BH_2(NMeH_2)_2]^+$ in the reaction mixture has previously been discussed as a potential initiator,[46] but Weller and co-workers have previously demonstrated that similar boronium salts do not promote dehydrocoupling at 0.5 mol% loading,[14] and in turn suggests that $[BH_2(NMeH_2)_2]^+$ acts to positively modify the transition metal catalyst rather than initiate dehydrogenation solely itself.

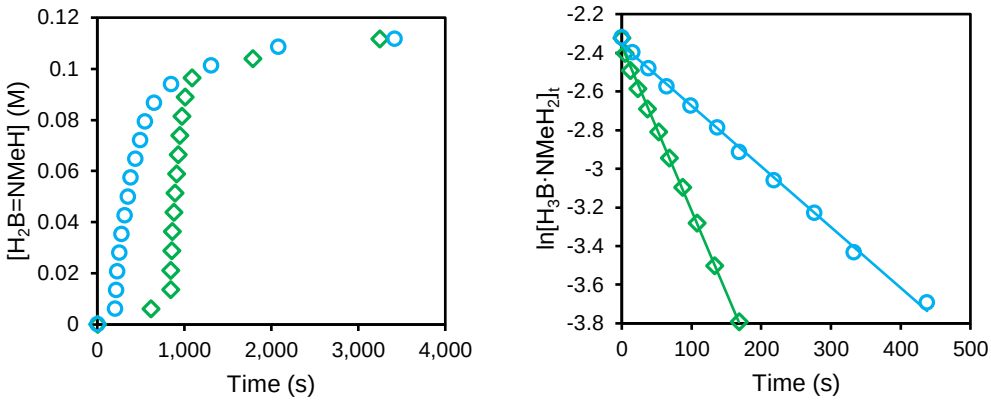


Figure 3.20 Left: Temporal data plots for $H_2B{=}NMeH$ formation (as measured by H_2 evolution). ○ = 2.23 × 10^{-4} M **2**, 0.111 M $H_3B{\cdot}NMeH_2$; ◇ = 2.23 × 10^{-4} M **2**, 2.23 × 10^{-3} M $[BH_2(NMeH_2)_2][BAr^F{}_4]$, 0.111 M $H_3B{\cdot}NMeH_2$. Right: First order rate plots with induction periods subtracted from each time point. ○ = 2.23 × 10^{-4} M **2**, 0.111 M $H_3B{\cdot}NMeH_2$ (k_{obs} = 3.1 ± 0.1 × 10^{-3} s^{-1}); ◇ = 2.23 × 10^{-4} M **2**, 2.23 × 10^{-3} M $[BH_2(NMeH_2)_2][BAr^F{}_4]$, 0.111 M $H_3B{\cdot}NMeH_2$ (k_{obs} = 8.5 ± 0.1 × 10^{-3} s^{-1}).

3.6 Proposed mechanism for the dehydropolymerisation of $H_3B{\cdot}NMeH_2$ using the $\{Rh(Xantphos\text{-}^iPr)\}^+$ system

The catalytic studies presented throughout this Chapter, and speciation experiments performed during Chapter 2, combine together to provide the following observations for the dehydropolymerisation of $H_3B{\cdot}NMeH_2$ using $\{Rh(Xantphos\text{-}^iPr)\}^+$ precatalyst **2**, $[Rh(\kappa^3\text{-}P,O,P\text{-}Xantphos\text{-}^iPr)(H)_2(\eta^1\text{-}H_3B{\cdot}NMe_3)][BAr^F{}_4]$:

(1) Although complicated slightly by solubility effects above concentrations of 0.22 M $H_3B{\cdot}NMeH_2$, dehydrogenation of $H_3B{\cdot}NMeH_2$ to form $H_2B{=}NMeH$ is first order in both precatalyst **2** and $H_3B{\cdot}NMeH_2$.

(2) A KIE for B–H activation of 0.8 ± 0.1 and for N–H activation of 4.4 ± 0.1 suggests that N–H activation is involved in the rate limiting step during the dehydrogenation of $H_3B{\cdot}NMeH_2$, or alternatively that an asynchronous transition state in which B–H activation occurs much earlier than N–H activation operates.

(3) A speciation manifold probed in Chapter 2 that operates **2** → **3** → **7** → **8**.

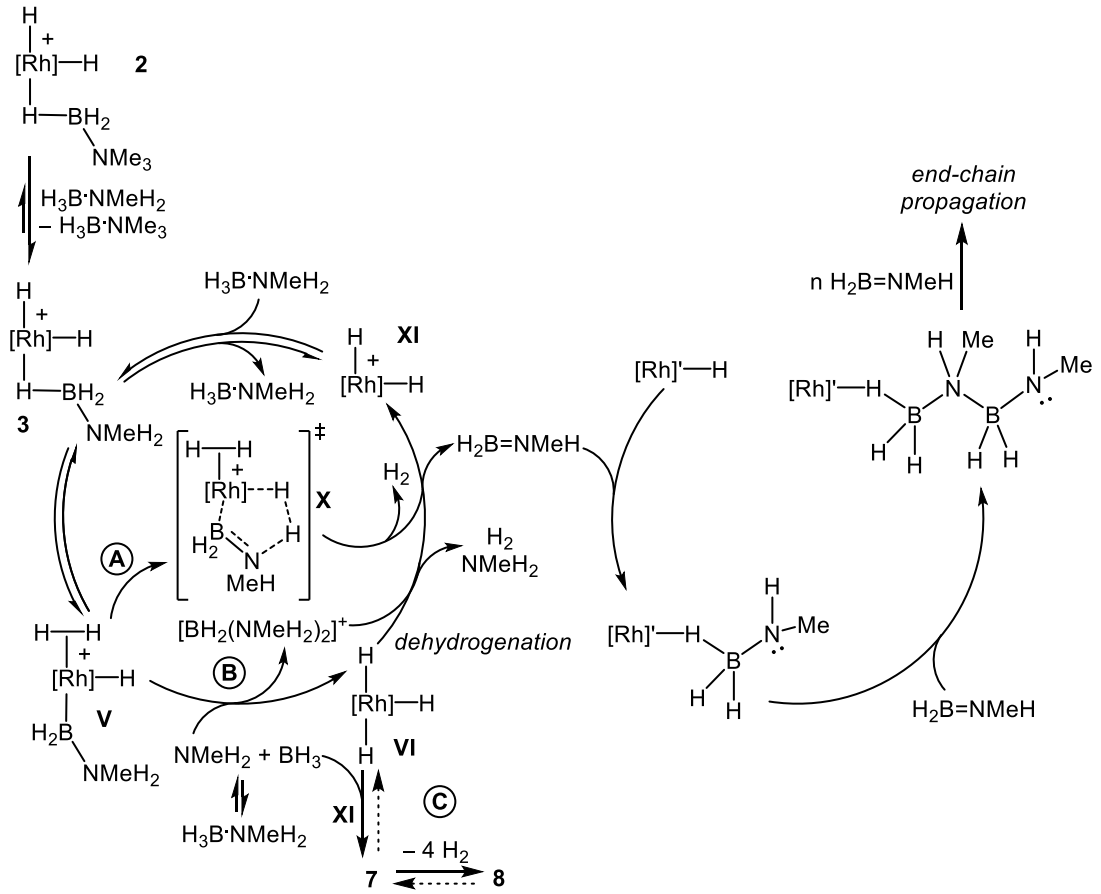
(4) Proposed boronium cations, $[BH_2(NMeH_2)(L)]^+$ (L = $NMeH_2$ or solvent), are observed in the ^{11}B NMR spectra during speciation experiments of complexes **3** or **8** with 10 equivalents of $H_3B{\cdot}NMeH_2$. In addition, the presence of 10 equivalents (relative to rhodium) of independently synthesised $[BH_2(NMeH_2)_2][BAr^F{}_4]$ (**11**) in catalysis using precatalyst **2** leads to a ~3-fold increase in rate of dehydrogenation of $H_3B{\cdot}NMeH_2$ to $H_2B{=}NMeH$, suggesting that it may be intimately involved in the dehydrogenation mechanism.

(5) Recharging experiments show that the catalyst remains active and is not irreversibly consumed in the dehydropolymerisation process. In fact, the end organometallic species of catalysis is complex **8**, $[\{Rh(\kappa^3\text{-P,O,P-Xantphos-}^i\text{Pr})\}_2B]^+$, which forms both $[Rh(\kappa^3\text{-P,O,P-Xantphos-}^i\text{Pr})(H)_2(\eta^1\text{-}H_3B{\cdot}NMeH_2)]^+$ (**3**) and $[\{Rh(\kappa^3\text{-P,O,P-Xantphos-}^i\text{Pr})(H)_2\}_2(\mu,\eta^1\eta^1\text{-}H_2BH_2)]^+$ (**7**) on addition of more substrate.

(6) The essential chain growth characteristics of $H_2B{=}NMeH$ polymerisation suggest a mechanism that involves rapid addition of the reactive monomer $H_2B{=}NMeH$ to a growing polyaminoborane chain.

(7) Absence of a strong effect of catalyst loading on the degree of polymerisation and lack of control of polymerisation using H_2 suggest a polymerisation mechanism alternative to that of single site coordination/dehydrogenation/insertion.

This information led to the proposal for the dehydropolymerisation mechanism as detailed in Scheme 3.6.



Scheme 3.6 Proposed mechanism for the dehydrogenation of $H_3B{\cdot}NMeH_2$ to $H_2B{=}NMeH$ using precatalyst **2**, and the proposed mechanism for end-chain propagation of $H_2B{=}NMeH$ to form $(H_2BNMeH)_n$. [Rh] = {Rh(Xantphos)}, [Rh]′ = {Rh(Xantphos)L_n} (L_n = unknown ancillary ligands). $[BAr^F{}_4]^-$ anions not shown for clarity.

Coordination of $H_3B{\cdot}NMeH_2$ to form $[Rh(\kappa^3\text{-P,O,P-Xantphos-}^i\text{Pr})(H)_2(\eta^1\text{-}H_3B{\cdot}NMeH_2)]^+$ (**3**) and subsequent reversible B–H activation forms boryl dihydrogen hydride complex **V**. This process was shown to be fast in the $\{Rh(\text{Xantphos-}^i\text{Pr})\}^+$ system by H/D exchange experiments on $[Rh(\kappa^3\text{-P,O,P-Xantphos-}^i\text{Pr})(H)_2(\eta^1\text{-}H_3B{\cdot}NMe_3)]^+$ (**2**), with the mechanism detailed in Scheme 2.7. Pathway **A** proceeds through intramolecular N–H activation via transition state **X**,[6, 21] in which rate determining N–H transfer occurs to a cationic rhodium hydride with the formation of the reactive monomer $H_2B{=}NMeH$. Alternatively, intermediate **V** can evolve by attack of $NMeH_2$, leading to boronium formation to give neutral trihydride **VI**, pathway **B**. Subsequently, rate determining, intermolecular protonation by $[BH_2(NMeH_2)_2]^+$ reforms cationic dihydride **XI** and releases

$H_2B{=}NMeH$. This is similar to the mechanism proposed by Conejero for $H_3B{\cdot}NMe_2H$ dehydrocoupling using cationic Pt based catalysts.[47-48] Complex **8** (**(**[{Rh(κ^3-P,O,P-Xantphos-^{i}Pr)}$_2$B]$^+$) is proposed to form in an off-cycle process by reaction of BH_3/**XI** with **VI** (pathway **C**). [{Rh(κ^3-P,O,P-Xantphos-^{i}Pr)(H)$_2$}$_2$(μ,$\eta^1\eta^1$-H_2BH_2)]$^+$ **(7**) could be reformed from **8** by the reaction of **8** with free H_2 present in the reaction mixture, or through concerted B–H/N–H transfer from two $H_3B{\cdot}NMeH_2$ molecules, also releasing two $H_2B{=}NMeH$ molecules which can then polymerise. Boronium $[BH_2(NMeH_2)_2]^+$ thus potentially plays two different roles: as a co-intermediate (pathway **B**) or as a side product bifurcating from pathway **A** that eventually forms dormant species **8** (pathway **C**). The observations observed throughout this thesis are consistent with proposed mechanistic pathway **B**, which closely involves $[BH_2(NMeH_2)_2]^+$; however under these conditions pathway **A** cannot be completely discounted.

In terms of polymerisation, a chain propagation process is proposed in which a low concentration of a separate, likely neutral, rhodium hydride species forms a Lewis acid/Lewis base adduct with $H_2B{=}NMeH$ which thus develops a lone pair on the nitrogen (i.e., an aminoborohydride). Aminoborohydride complexes have previously been reported by Aldridge and co-workers,[49] as well as by Schafer, Love and Weller (Figure 3.21).[50]

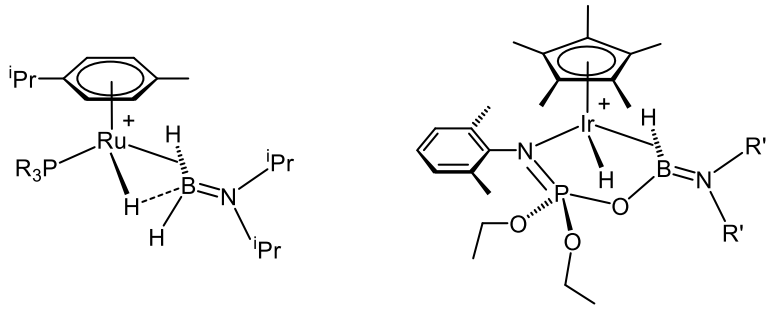
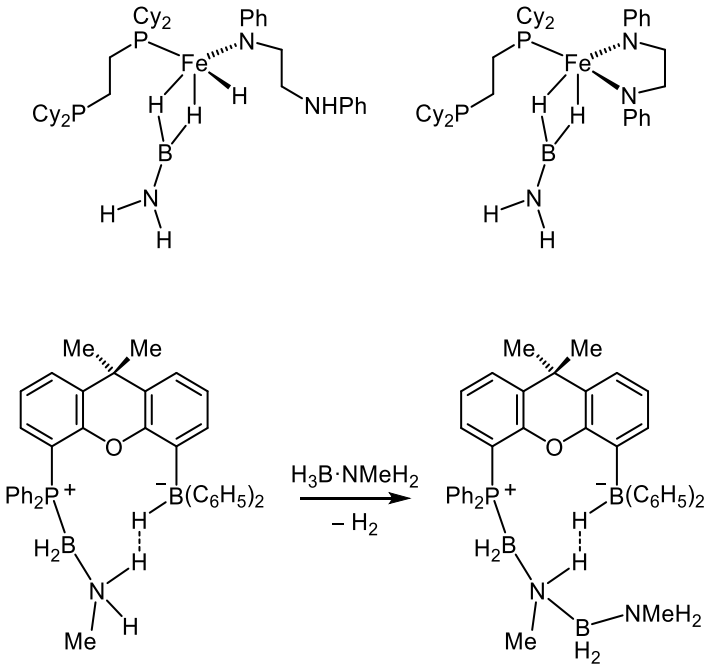


Figure 3.21 Aminoborohydride-type complexes by Aldridge (left) and Schafer, Love and Weller (right). R = Cy, Ph; R′ = Cy, ^{i}Pr. $[BAr^F{}_4]^-$ anions not shown for clarity.

Subsequent fast, head-to-tail end chain B–N bond forming events lead to $(H_2BNMeH)_n$. Further support for this mechanism comes from Manners' experimental observations in the Ir(POCOP-^{t}Bu)(H)$_2$ catalyst system,[4] and Paul's computational studies on the same system which demonstrate

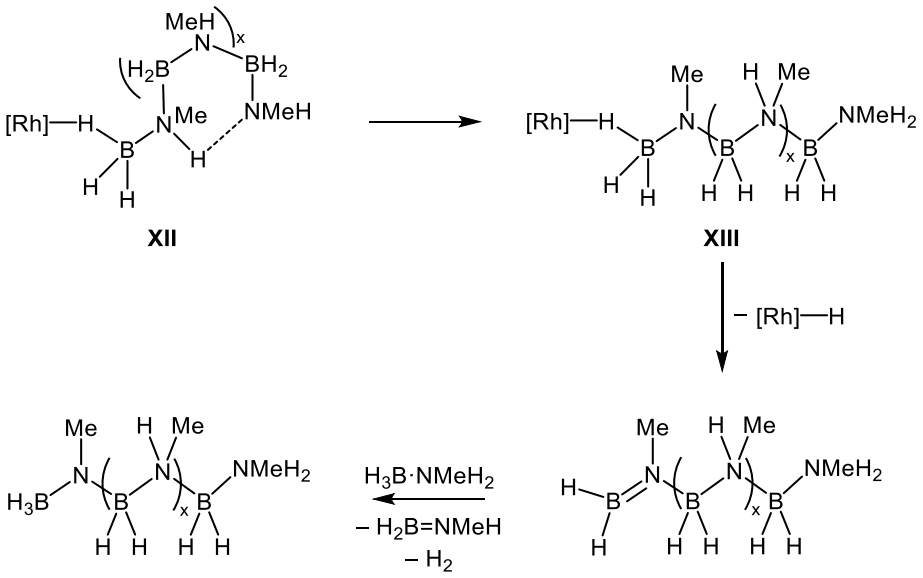
a very low energy pathway (~7 kcal mol^{-1}) for a B–N bond forming process occurring in this nucleophilic head to tail chain growth manner (Scheme 1.15).[51] Given the structural similarities between κ^3-P,O,P-Xantphos ligands and POCOP pincer ligands it is not unreasonable to suggest a similar mechanism is operating here. This polymerisation mechanism is also related to other proposals, such as Baker's Fe(PhNCH$_2$CH$_2$NPh)(Cy$_2$PCH$_2$CH$_2$PCy$_2$) system for the dehydropolymerisation of $H_3B{\cdot}NH_3$, in which two possible motifs were proposed for aminoborane bound complexes which could undergo end chain propagation (Scheme 3.7),[52] and Aldridge's frustrated Lewis pair chain growth dehydrooligomerisation of $H_3B{\cdot}NMeH_2$ (Scheme 3.7).[53]



Scheme 3.7 Top: Baker's proposed motifs that could operate in end chain propagation for the dehydropolymerisation of $H_3B{\cdot}NH_3$ using the Fe(PhNCH$_2$CH$_2$NPh)(Cy$_2$PCH$_2$CH$_2$PCy$_2$) system. Bottom: Aldridge's Frustrated Lewis Pair end chain growth system for the dehydrooligomerisation of $H_3B{\cdot}NMeH_2$.

The chain termination event in this system is currently opaque to experiment. Notably, the lack of H_2 influence on polyaminoborane molecular weight suggests chain termination does not occur by hydrogenolysis, in contrast to observations for the Xantphos-Ph system.[3] In the nucleophilic end-chain polymerisation mechanism computationally confirmed by Paul and co-workers for the dehydropolymerisation of $H_3B{\cdot}NH_3$ using Ir(POCOP-^{t}Bu)(H)$_2$, an energetically viable chain termination pathway was also proposed.[51] Therefore an analogous process may operate in this

{Rh(Xantphos-^{i}Pr)}$^{+}$ system (Scheme 3.8). Proton transfer from the NMeH group adjacent to the rhodium bound BH_3 group to the terminal NMeH group in **XII** occurs to give intermediate **XIII**. Dissociation of the metal complex forms Rh–H and $H_2B{=}NMe(BH_2NMeH)_xBH_2NMeH_2$. Finally, hydrogenation of the terminal aminoborane may occur via concerted N–H and B–H shift from a molecule of $H_3B{\cdot}NMeH_2$ to form $H_3B(NMeHBH_2)_xNMeH_2$ and free $H_2B{=}NMeH$.



Scheme 3.8 Possible mechanism, analogous to that of Paul's, for polyaminoborane chain termination in the dehydropolymerisation of $H_3B{\cdot}NMeH_2$ using precatalyst **2**. [Rh] = an unknown {Rh(Xantphos-^{i}Pr)} fragment.

3.7 Summary

This Chapter has described a mechanistic investigation into the dehydropolymerisation of $H_3B{\cdot}NMeH_2$ using [Rh(κ^3-P,O,P-Xantphos-^{i}Pr)(H)$_2$(η^1-$H_3B{\cdot}NMe_3$)][BAr^F_4] (**2**), which provides fast turnovers and good selectivity for $(H_2BNMeH)_n$. In addition to the speciation studies carried out in Chapter 2, neutral hydride active catalysts were proposed to be on cycle for the dehydrogenation of $H_3B{\cdot}NMeH_2$ to $H_2B{=}NMeH$, formed by hydride transfer routes from the cationic species using BH_3. In terms of polymerisation of $H_2B{=}NMeH$, a head-to-tail end chain process was suggested. In Chapters 4 and 5, structure/activity relationships for the dehydropolymerisation of $H_3B{\cdot}NMeH_2$ are further probed, as this methodology – so heavily exploited in olefin polymerisation[43] – may be central to harnessing the mechanistic details required to produce polyaminoboranes to order.

3.8 References

1. Pons, V.; Baker, R. T.; Szymczak, N. K.; Heldebrant, D. J.; Linehan, J. C.; Matus, M. H.; Grant, D. J.; Dixon, D. A., Coordination of aminoborane, NH_2BH_2, dictates selectivity and extent of H_2 release in metal-catalysed ammonia borane dehydrogenation. *Chem. Commun.* **2008,** (48), 6597-6599.
2. Marziale, A. N.; Friedrich, A.; Klopsch, I.; Drees, M.; Celinski, V. R.; Guenne, J.; Schneider, S., The Mechanism of Borane-Amine Dehydrocoupling with Bifunctional Ruthenium Catalysts. *J. Am. Chem. Soc.* **2013,** *135* (36), 13342-13355.
3. Johnson, H. C.; Leitao, E. M.; Whittell, G. R.; Manners, I.; Lloyd-Jones, G. C.; Weller, A. S., Mechanistic Studies of the Dehydrocoupling and Dehydropolymerization of Amine-Boranes Using a $[Rh(Xantphos)]^+$ Catalyst. *J. Am. Chem. Soc.* **2014,** *136* (25), 9078-9093.
4. Staubitz, A.; Sloan, M. E.; Robertson, A. P. M.; Friedrich, A.; Schneider, S.; Gates, P. J.; Schmedt auf der Günne, J.; Manners, I., Catalytic Dehydrocoupling/Dehydrogenation of N-Methylamine-Borane and Ammonia-Borane: Synthesis and Characterization of High Molecular Weight Polyaminoboranes. *J. Am. Chem. Soc.* **2010,** *132* (38), 13332-13345.
5. Dallanegra, R.; Robertson, A. P. M.; Chaplin, A. B.; Manners, I.; Weller, A. S., Tuning the $[L_2Rh\cdots H_3B{\cdot}NR_3]^+$ interaction using phosphine bite angle. Demonstration by the catalytic formation of polyaminoboranes. *Chem. Commun.* **2011,** *47* (13), 3763-3765.
6. Esteruelas, M. A.; Nolis, P.; Oliván, M.; Oñate, E.; Vallribera, A.; Vélez, A., Ammonia Borane Dehydrogenation Promoted by a Pincer-Square-Planar Rhodium(I) Monohydride: A Stepwise Hydrogen Transfer from the Substrate to the Catalyst. *Inorg. Chem.* **2016,** *55* (14), 7176-7181.
7. Vogt, M.; de Bruin, B.; Berke, H.; Trincado, M.; Grützmacher, H., Amino olefin nickel(I) and nickel(0) complexes as dehydrogenation catalysts for amine boranes. *Chemical Science* **2011,** *2* (4), 723-727.
8. Colebatch, A. L.; McKay, A. I.; Beattie, N. A.; Macgregor, S. A.; Weller, A. S., Fluoroarene Complexes with Small Bite Angle Bisphosphines: Routes to Amine-Borane and Aminoborylene Complexes. *Eur. J. Inorg. Chem.* **2017,** (38-39), 4533-4540.
9. Pike, S. D.; Crimmin, M. R.; Chaplin, A. B., Organometallic chemistry using partially fluorinated benzenes. *Chem. Commun.* **2017,** *53* (26), 3615-3633.
10. Widegren, J. A.; Finke, R. G., A review of the problem of distinguishing true homogeneous catalysis from soluble or other metal-particle heterogeneous catalysis under reducing conditions. *J. Mol. Catal. A: Chem.* **2003,** *198* (1-2), 317-341.
11. Jaska, C. A.; Manners, I., Heterogeneous or Homogeneous Catalysis? Mechanistic Studies of the Rhodium-Catalyzed Dehydrocoupling of Amine-Borane and Phosphine-Borane Adducts. *J. Am. Chem. Soc.* **2004,** *126* (31), 9776-9785.
12. Mikhailine, A. A.; Maishan, M. I.; Lough, A. J.; Morris, R. H., The Mechanism of Efficient Asymmetric Transfer Hydrogenation of Acetophenone Using an Iron(II) Complex Containing an (*S*,*S*)-$Ph_2PCH_2CH{=}NCHPhCHPhN{=}CHCH_2PPh_2$ Ligand: Partial Ligand Reduction Is the Key. *J. Am. Chem. Soc.* **2012,** *134* (29), 12266-12280.
13. Kumar, A.; Ishibashi, J. S. A.; Hooper, T. N.; Mikulas, T. C.; Dixon, D. A.; Liu, S.-Y.; Weller, A. S., The Synthesis, Characterization and Dehydrogenation of Sigma-Complexes of BN-Cyclohexanes. *Chem. Eur. J.* **2016,** *22* (1), 310-322.
14. Kumar, A.; Beattie, N. A.; Pike, S. D.; Macgregor, S. A.; Weller, A. S., The Simplest Amino-Borane $H_2B{=}NH_2$ Trapped on a Rhodium Dimer: Pre-Catalysts for Amine-Borane Dehydropolymerization. *Angew. Chem. Int. Ed.* **2016,** *55* (23), 6651-6656.
15. Sloan, M. E.; Staubitz, A.; Clark, T. J.; Russell, C. A.; Lloyd-Jones, G. C.; Manners, I., Homogeneous Catalytic Dehydrocoupling/Dehydrogenation of Amine-Borane Adducts by Early Transition Metal, Group 4 Metallocene Complexes. *J. Am. Chem. Soc.* **2010,** *132* (11), 3831-3841.
16. Sewell, L. J.; Huertos, M. A.; Dickinson, M. E.; Weller, A. S.; Lloyd-Jones, G. C., Dehydrocoupling of Dimethylamine Borane Catalyzed by $Rh(PCy_3)_2H_2Cl$. *Inorg. Chem.* **2013,** *52* (8), 4509-4516.
17. Jones, W. D., Isotope Effects in C–H Bond Activation Reactions by Transition Metals. *Acc. Chem. Res.* **2003,** *36* (2), 140-146.
18. Simmons, E. M.; Hartwig, J. F., On the Interpretation of Deuterium Kinetic Isotope Effects in C–H Bond Functionalizations by Transition-Metal Complexes. *Angew. Chem. Int. Ed.* **2012,** *51* (13), 3066-3072.
19. Keaton, R. J.; Blacquiere, J. M.; Baker, R. T., Base Metal Catalyzed Dehydrogenation of Ammonia-Borane for Chemical Hydrogen Storage. *J. Am. Chem. Soc.* **2007,** *129* (7), 1844-1845.
20. Bhattacharya, P.; Krause, J. A.; Guan, H., Mechanistic Studies of Ammonia Borane Dehydrogenation Catalyzed by Iron Pincer Complexes. *J. Am. Chem. Soc.* **2014,** *136* (31), 11153-11161.
21. Todisco, S.; Luconi, L.; Giambastiani, G.; Rossin, A.; Peruzzini, M.; Golub, I. E.; Filippov, O. A.; Belkova, N. V.; Shubina, E. S., Ammonia Borane Dehydrogenation Catalyzed by (κ^4-EP_3)Co(H) [EP_3 =

$E(CH_2CH_2PPh_2)_3$; E = N, P] and H_2 Evolution from Their Interaction with NH Acids. *Inorg. Chem.* **2017,** *56* (8), 4296-4307.
22. Pons, V.; Baker, R. T.; Szymczak, N. K.; Heldebrant, D. J.; Linehan, J. C.; Matus, M. H.; Grant, D. J.; Dixon, D. A., Coordination of aminoborane, NH_2BH_2, dictates selectivity and extent of H_2 release in metal-catalysed ammonia borane dehydrogenation. *Chem. Commun.* **2008,** *48*, 6597-6599.
23. Robertson, A. P. M.; Leitao, E. M.; Manners, I., Catalytic Redistribution and Polymerization of Diborazanes: Unexpected Observation of Metal-Free Hydrogen Transfer between Aminoboranes and Amine-Boranes. *J. Am. Chem. Soc.* **2011,** *133* (48), 19322-19325.
24. Metters, O. J.; Chapman, A. M.; Robertson, A. P. M.; Woodall, C. H.; Gates, P. J.; Wass, D. F.; Manners, I., Generation of aminoborane monomers RR'NH=BH_2 from amine-boronium cations $[RR'NH–BH_2L]^+$: metal catalyst-free formation of polyaminoboranes at ambient temperature. *Chem. Commun.* **2014,** *50* (81), 12146-12149.
25. Ewing, W. C.; Marchione, A.; Himmelberger, D. W.; Carroll, P. J.; Sneddon, L. G., Syntheses and Structural Characterizations of Anionic Borane-Capped Ammonia Borane Oligomers: Evidence for Ammonia Borane H_2 Release via a Base-Promoted Anionic Dehydropolymerization Mechanism. *J. Am. Chem. Soc.* **2011,** *133* (42), 17093-17099.
26. Jurca, T.; Dellermann, T.; Stubbs, N. E.; Resendiz-Lara, D. A.; Whittell, G. R.; Manners, I., Step-growth titanium-catalysed dehydropolymerisation of amine-boranes. *Chem. Sci.* **2018,** *9* (13), 3360-3366.
27. Anke, F.; Han, D.; Klahn, M.; Spannenberg, A.; Beweries, T., Formation of high-molecular weight polyaminoborane by Fe hydride catalysed dehydrocoupling of methylamine borane. *Dalton Trans.* **2017,** *46* (21), 6843-6847.
28. Marquardt, C.; Jurca, T.; Schwan, K.-C.; Stauber, A.; Virovets, A. V.; Whittell, G. R.; Manners, I.; Scheer, M., Metal-Free Addition/Head-to-Tail Polymerization of Transient Phosphinoboranes, RPH–BH_2: A Route to Poly(alkylphosphinoboranes). *Angew. Chem. Int. Ed.* **2015,** *54* (46), 13782-13786.
29. Ewing, W. C.; Carroll, P. J.; Sneddon, L. G., Syntheses and Characterizations of Linear Triborazanes. *Inorg. Chem.* **2013,** *52* (18), 10690-10697.
30. Colebatch, A. L.; Hawkey Gilder, B. W.; Whittell, G. R.; Oldroyd, N. L.; Manners, I.; Weller, A. S., A General, Rhodium-Catalyzed, Synthesis of Deuterated Boranes and N-Methyl Polyaminoboranes. *Chem. Eur. J.* **2018,** *24* (21), 5450-5455.
31. Adams, G. M.; Colebatch, A. L.; Skornia, J. T.; McKay, A. I.; Johnson, H. C.; Lloyd-Jones, G. C.; Macgregor, S. A.; Beattie, N. A.; Weller, A. S., Dehydropolymerization of $H_3B{\cdot}NMeH_2$ To Form Polyaminoboranes Using [Rh(Xantphos-alkyl)] Catalysts. *J. Am. Chem. Soc.* **2018,** *140* (4), 1481-1495.
32. Semsarilar, M.; Jones, E. R.; Armes, S. P., Comparison of pseudo-living character of RAFT polymerizations conducted under homogeneous and heterogeneous conditions. *Polym. Chem.* **2014,** *5* (1), 195-203.
33. M., E. J., Gel permeation chromatography: A guide to data interpretation. *Polymer Engineering & Science* **1973,** *13* (6), 401-408.
34. Moré, J. J.; Sorensen, D. C.; Hillstrom, K. E.; Garbow, B. S., The MINPACK Project. In *Sources and Development of Mathematical Software*, Cowell, W. R., Ed. Prentice-Hall, Inc: Upper Saddle River, NJ, USA, 1984.
35. Yang, C.-J.; Jenekhe, S. A., Effects of Structure on Refractive Index of Conjugated Polyimines. *Chem. Mater.* **1994,** *6* (2), 196-203.
36. Turner, J. R.; Resendiz-Lara, D. A.; Jurca, T.; Schäfer, A.; Vance, J. R.; Beckett, L.; Whittell, G. R.; Musgrave, R. A.; Sparkes, H. A.; Manners, I., Synthesis, Characterization, and Properties of Poly(aryl)phosphinoboranes Formed via Iron-Catalyzed Dehydropolymerization. *Macromol. Chem. Phys.* **2017,** *218* (19), 1700120.
37. European Parliament and Council Directive 94/62/EC of 20 December 1994 on packaging and packaging waste. *OJ* **1994,** *L365*, 10-23.
38. Diemer, J.; Heumann, K. G., Development of an ICP-IDMS method for accurate routine analyses of toxic heavy metals in polyolefins and comparison with results by TI-IDMS. *Fresenius J. Anal. Chem.* **2000,** *368* (1), 103-108.
39. Johnson, H. C.; Robertson, A. P. M.; Chaplin, A. B.; Sewell, L. J.; Thompson, A. L.; Haddow, M. F.; Manners, I.; Weller, A. S., Catching the First Oligomerization Event in the Catalytic Formation of Polyaminoboranes: $H_3B{\cdot}NMeHBH_2{\cdot}NMeH_2$ Bound to Iridium. *J. Am. Chem. Soc.* **2011,** *133* (29), 11076-11079.
40. Raave, A., *Principles of Polymer Chemistry*. 3rd ed.; Springer: New York, USA, 2012.
41. Chen, E. Y. X., Coordination Polymerization of Polar Vinyl Monomers by Single-Site Metal Catalysts. *Chem. Rev.* **2009,** *109* (11), 5157-5214.

42. Schäfer, A.; Jurca, T.; Turner, J.; Vance, J. R.; Lee, K.; Du, V. A.; Haddow, M. F.; Whittell, G. R.; Manners, I., Iron-Catalyzed Dehydropolymerization: A Convenient Route to Poly(phosphinoboranes) with Molecular-Weight Control. *Angew. Chem. Int. Ed.* **2015,** *54* (16), 4836-4841.
43. Hartwig, J. F., *Organotransition Metal Chemistry*. University Science Books: 2010.
44. Kim, J. D.; Soares, J. B. P.; Rempel, G. L., Use of hydrogen for the tailoring of the molecular weight distribution of polyethylene in a bimetallic supported metallocene catalyst system. *Macromol. Rapid Commun.* **1998,** *19* (4), 197-199.
45. Shuttleworth, T. A.; Huertos, M. A.; Pernik, I.; Young, R. D.; Weller, A. S., Bis(phosphine)boronium salts. Synthesis, structures and coordination chemistry. *Dalton Trans.* **2013,** *42* (36), 12917-12925.
46. Stephens, F. H.; Baker, R. T.; Matus, M. H.; Grant, D. J.; Dixon, D. A., Acid Initiation of Ammonia-Borane Dehydrogenation for Hydrogen Storage. *Angew. Chem. Int. Ed.* **2007,** *46* (5), 746-749.
47. Roselló-Merino, M.; López-Serrano, J.; Conejero, S., Dehydrocoupling Reactions of Dimethylamine-Borane by Pt(II) Complexes: A New Mechanism Involving Deprotonation of Boronium Cations. *J. Am. Chem. Soc.* **2013,** *135* (30), 10910-10913.
48. Rosello-Merino, M.; Rama, R. J.; Diez, J.; Conejero, S., Catalytic dehydrocoupling of amine-boranes and amines into diaminoboranes: isolation of a Pt(II), Shimoi-type, η^1-BH complex. *Chem. Commun.* **2016,** *52* (54), 8389-8392.
49. Addy, D. A.; Bates, J. I.; Kelly, M. J.; Riddlestone, I. M.; Aldridge, S., Aminoborane σ Complexes: Significance of Hydride Co-ligands in Dynamic Processes and Dehydrogenative Borylene Formation. *Organometallics* **2013,** *32* (6), 1583-1586.
50. Drover, M. W.; Bowes, E. G.; Schafer, L. L.; Love, J. A.; Weller, A. S., Phosphoramidate-Supported Cp^*Ir^{III} Aminoborane $H_2B{=}NR_2$ Complexes: Synthesis, Structure, and Solution Dynamics. *Chem. Eur. J.* **2016,** *22* (20), 6793-6797.
51. Bhunya, S.; Malakar, T.; Paul, A., Unfolding the crucial role of a nucleophile in Ziegler-Natta type Ir catalyzed polyaminoborane formation. *Chem. Commun.* **2014,** *50* (44), 5919-5922.
52. Baker, R. T.; Gordon, J. C.; Hamilton, C. W.; Henson, N. J.; Lin, P.-H.; Maguire, S.; Murugesu, M.; Scott, B. L.; Smythe, N. C., Iron Complex-Catalyzed Ammonia–Borane Dehydrogenation. A Potential Route toward B–N-Containing Polymer Motifs Using Earth-Abundant Metal Catalysts. *J. Am. Chem. Soc.* **2012,** *134* (12), 5598-5609.
53. Mo, Z.; Rit, A.; Campos, J.; Kolychev, E. L.; Aldridge, S., Catalytic B–N Dehydrogenation Using Frustrated Lewis Pairs: Evidence for a Chain-Growth Coupling Mechanism. *J. Am. Chem. Soc.* **2016,** *138* (10), 3306-3309.

4 {Rh(DPEphos)}$^+$ complexes as precatalysts for the dehydropolymerisation of $H_3B{\cdot}NMeH_2$

4.1 Introduction

As discussed in Chapter 1, the Xantphos-Ph system **i-13** (Figure 4.1) was valuable in gaining mechanistic insight into rhodium catalysed dehydropolymerisation of $H_3B{\cdot}NMeH_2$ – a coordination/dehydrogenation/insertion mechanism was proposed, where hydrogenolysis was responsible for termination of the growing polyaminoborane chain (Scheme 1.17).[1] Thus far, this thesis has probed a structure/activity relationship by modifying the PPh_2 groups of the Xantphos-Ph ligand to P^iPr_2. However, this led to a mechanistic switch induced by the bulky alkyl groups (Chapters 2 and 3) which in turn led to rigid mer κ^3-P,O,P Xantphos-^{i}Pr complexes present in catalysis. In fact mer κ^3-P,O,P is the most common geometry for the Xantphos-^{i}Pr ligand (Figure 1.8).

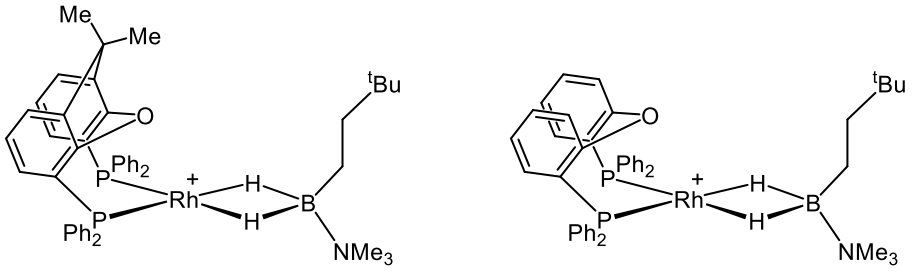


Figure 4.1 Structure of [Rh(κ^2-P,P-Xantphos-Ph)(η^2-$H_2B(CH_2CH_2{}^tBu){\cdot}NMe_3$)][$BAr^F{}_4$] (**i-13**) and target DPEphos analogue [Rh(κ^2-P,P-DPEphos)(η^2-$H_2B(CH_2CH_2{}^tBu){\cdot}NMe_3$)][$BAr^F{}_4$]. [$BAr^F{}_4$]$^-$ anions not shown for clarity.

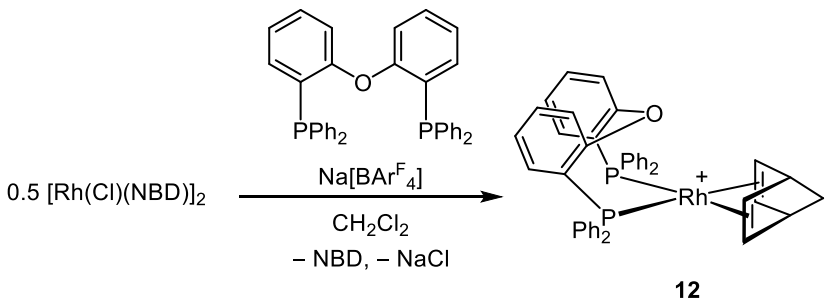
With this knowledge in hand, a ligand which retained the electronics of Xantphos-Ph (i.e. the PPh_2 groups), but with additional flexibility (to contrast rigid Xantphos-^{i}Pr), was sought to enable a similar mechanism to the Xantphos-Ph system **i-13**, whilst providing extra mechanistic insight or potentially stabilise different, but related, complexes. Therefore, the DPEphos analogue of **i-13**, [Rh(κ^2-P,P-DPEphos)(η^2-$H_2B(CH_2CH_2{}^tBu){\cdot}NMe_3$)][$BAr^F{}_4$] (Figure 4.1), was targeted for direct comparison to the successful Xantphos-Ph system.[1] The DPEphos ligand was first synthesised in

1995 by van Leeuwen and co-workers, in the same report as Xantphos-Ph.[2] Its bite angle of 102.2° is narrower than that of Xantphos-Ph (111.7°), and this may lead to greater inclination towards cis κ^2-P,P coordination to transition metals. In fact, Figure 1.8 shows that DPEphos has the greatest relative propensity for cis κ^2-P,P coordination compared to both Xantphos-^{i}Pr and Xantphos-Ph. In addition, Weller and co-workers have previously reported contrasting reactivity of $[Rh(POP)(H)_2(PCyp_3)][BAr^F_4]$ (POP = DPEphos, Xantphos-Ph) complexes,[3] whereby DPEphos preferred cis P,P coordination whilst Xantphos-Ph preferred trans P,P (Scheme 1.27).

This Chapter involves the synthesis of the $[Rh(\kappa^2\text{-P,P-DPEphos})(\eta^2\text{-}H_2B(CH_2CH_2{}^tBu)\cdot NMe_3)][BAr^F_4]$ precatalyst, and investigates $\{Rh(DPEphos)\}^+$ complexes derived from $H_3B\cdot NMeH_2$ which may be implicated or observed during $H_3B\cdot NMeH_2$ dehydropolymerisation catalysis, detailed in Chapter 5.

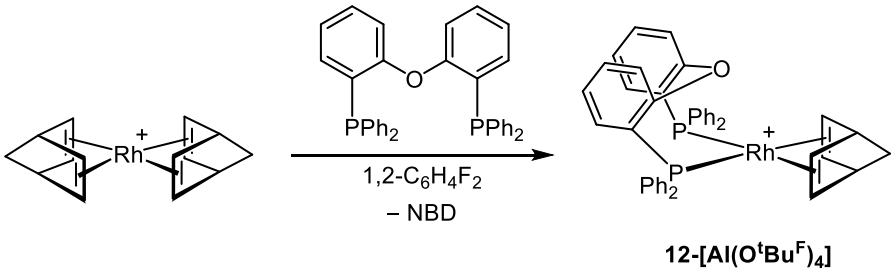
4.2 Formation of $[Rh(DPEphos)(NBD)][BAr^F_4]$ (**12**) and $[Rh(DPEphos)(NBD)][Al(O^tBu^F)_4]$ (**12-[Al(O^{t}Bu^F)$_4$]**)

Using the strategy discussed in Chapter 2, a useful starting point for accessing a suitable $\{Rh(DPEphos)\}^+$ precursor is the formation of the norbornadiene (NBD) adduct $[Rh(\kappa^2\text{-P,P-DPEphos})(NBD)]^+$. This cationic species has previously been reported as the $[BAr^F_4]^-$ salt, as well as carborane-type anions such as $[CB_{11}H_6Cl_6]^-$.[4] $[Rh(\kappa^2\text{-P,P-DPEphos})(NBD)][BAr^F_4]$ (**12**) was therefore synthesised by dropwise addition of DPEphos to a suspension of $[Rh(Cl)(NBD)]_2$ and $Na[BAr^F_4]$ in CH_2Cl_2 solvent (Scheme 4.1).[4]



Scheme 4.1 Synthesis of $[Rh(\kappa^2\text{-P,P-DPEphos})(NBD)][BAr^F_4]$ (**12**). $[BAr^F_4]^-$ anion not shown for clarity.

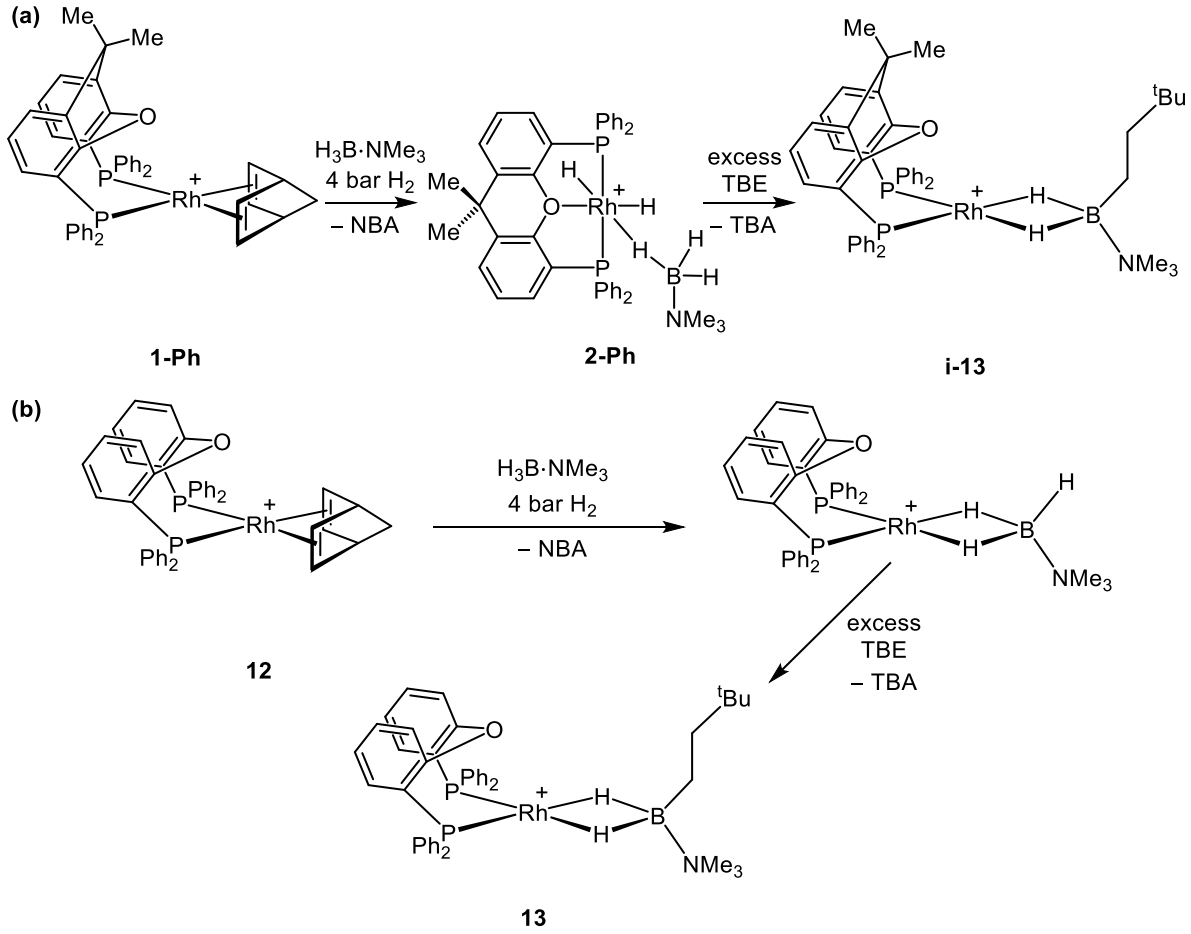
Anions other than $[BAr^{F}_{4}]^{-}$ are often required in order to form crystals of complexes that are suitable for single crystal X-ray diffraction.[5] For example, $[\{Rh(\kappa^3\text{-P,O,P-Xantphos-}^{i}Pr)\}_2B]^{+}$ (**8**) could only be crystallised using the $[BAr^{Cl}_{4}]^{-}$ counterion, as discussed in Chapter 2. $[Al(O^{t}Bu^{F})_4]^{-}$ ($^{t}Bu^{F}$ = $C(CF_3)_3$) can also be considered a suitable weakly coordinating anion (Section 1.4),[6-7] therefore $[Rh(\kappa^2\text{-P,P-DPEphos})(NBD)][Al(O^{t}Bu^{F})_4]$ (**12-[Al(O^{t}Bu^{F})$_4$]**) was synthesised by the dropwise addition of DPEphos to a solution of $[Rh(NBD)_2][Al(O^{t}Bu^{F})_4]$ in 1,2-$C_6H_4F_2$ solvent (Scheme 4.2). **12-[Al(O^{t}Bu^{F})$_4$]** was characterised by NMR spectroscopy, ESI-MS and elemental microanalysis, which revealed closely analogous data to previously reported examples of $[Rh(\kappa^2\text{-P,P-DPEphos})(NBD)][X]$ ([X] = weakly coordinating anion).[4]



Scheme 4.2 Synthesis of $[Rh(\kappa^2\text{-P,P-DPEphos})(NBD)][Al(O^{t}Bu^{F})_4]$ (**12-[Al(O^{t}Bu^{F})$_4$]**). $[Al(O^{t}Bu^{F})_4]^{-}$ anions not shown for clarity.

4.3 Formation of a suitable $\{Rh(DPEphos)\}^{+}$ amine borane dehydropolymerisation precatalyst

With complex **12** in hand as its $[BAr^{F}_{4}]^{-}$ salt, the synthesis of the DPEphos analogue of **i-13**, $[Rh(\kappa^2\text{-P,P-DPEphos})(\eta^2\text{-}H_2B(CH_2CH_2{}^{t}Bu)\cdot NMe_3)][BAr^{F}_{4}]$ was carried out (Scheme 4.3). Previous reports using the Xantphos-Ph ligand showed that the synthesis of $[Rh(\kappa^2\text{-P,P-Xantphos-Ph})(\eta^2\text{-}H_2B(CH_2CH_2{}^{t}Bu)\cdot NMe_3)][BAr^{F}_{4}]$ (**i-13**) could be achieved via the hydrogenation of $[Rh(\kappa^2\text{-P,P-Xantphos-Ph})(NBD)][BAr^{F}_{4}]$ (**1-Ph**) in the presence of $H_3B\cdot NMe_3$ to initially form $[Rh(\kappa^2\text{-P,P-Xantphos-Ph})(H)_2(\eta^1\text{-}H_3B\cdot NMe_3)][BAr^{F}_{4}]$ (**2-Ph**) in situ (Scheme 4.3(a)).[8] Degassing this mixture and adding an excess of 3,3-dimethyl-bute-1-ene (TBE) under argon led to the formation of **i-13** through hydroboration of the alkene by $H_3B\cdot NMe_3$ (Scheme 4.3(a)).[8] This same methodology was employed for the DPEphos system to form $[Rh(\kappa^2\text{-P,P-DPEphos})(\eta^2\text{-}H_2B(CH_2CH_2{}^{t}Bu)\cdot NMe_3)][BAr^{F}_{4}]$ (**13**) (Scheme 4.3(b)).



Scheme 4.3 (a) Previous synthesis of [Rh(κ^2-P,P-Xantphos-Ph)(η^2-$H_2B(CH_2CH_2{}^tBu)\cdot NMe_3$)][$BAr^F{}_4$] (**i-13**) via Rh(III) [Rh(κ^3-P,O,P-Xantphos-Ph)$(H)_2$(η^1-$H_3B\cdot NMe_3$)][$BAr^F{}_4$] (**2-Ph**). (b) Synthesis of [Rh(κ^2-P,P-DPEphos)(η^2-$H_2B(CH_2CH_2{}^tBu)\cdot NMe_3$)][$BAr^F{}_4$] (**13**) via Rh(I) [Rh(κ^2-P,P-DPEphos)(η^2-$H_3B\cdot NMe_3$)][$BAr^F{}_4$]. All steps use 1,2-$C_6H_4F_2$ solvent. NBA = norbornane, TBE = 3,3-dimethylbutene, TBA = 3,3-dimethylbutane. $[BAr^F{}_4]^-$ anions not shown for clarity.

The overall $H_2/H_3B\cdot NMe_3$/TBE reaction for both ligands gave analogous final products, namely hydroborated Rh(I) complexes **i-13** and **13**. However, initial hydrogenation of **12** (4 bar H_2) in the presence of $H_3B\cdot NMe_3$ afforded an intermediate Rh(I) complex: [Rh(κ^2-P,P-DPEphos)(η^2-$H_3B\cdot NMe_3$)][$BAr^F{}_4$] (Scheme 4.3),[9] rather than the Rh(III) Xantphos-Ph analogy (**2-Ph**). [Rh(κ^2-P,P-DPEphos)(η^2-$H_3B\cdot NMe_3$)][$BAr^F{}_4$] has been previously reported.[9] This was shown by observation of a doublet in the $^{31}P\{^1H\}$ NMR spectrum of the in situ reaction mixture at δ 41.3 ($^1J_{RhP}$ 182 Hz) with a coupling constant indicative of a Rh(I) DPEphos ligated complex.[4] A broad signal observed at δ −0.99 in the ^1H NMR spectrum with relative integral 3 H was attributed to a fluxional Rh···H–B environment, with no signals indicative of classical Rh–H resonances at lower

chemical shifts. Using ^{11}B NMR spectroscopy, a broad resonance at δ 16.2 was observed in the ^{11}B NMR spectrum, shifted downfield to that of free $H_3B{\cdot}NMe_3$, (δ −8.4, q, $^1J_{BH}$ 97 Hz),[10] indicative of an η^2 bound amine borane.[9, 11] Degassing the reaction mixture to remove the H_2 pressure and placing it under an argon atmosphere showed no change in the ^{31}P{^{1}H} NMR data (δ 41.3, $^1J_{RhP}$ 182 Hz), ^{1}H NMR data (δ −0.99), or ^{11}B chemical shift (δ 16.2) suggesting that even under high H_2 pressure [Rh(κ^2-P,P-DPEphos)(η^2-$H_3B{\cdot}NMe_3$)][BAr^F_4] is the sole product formed, and that the Rh(III) dihydride is therefore inaccessible under these conditions. Sufficiently pure, bulk solid of [Rh(κ^2-P,P-DPEphos)(η^2-$H_3B{\cdot}NMe_3$)][BAr^F_4] could not be isolated, however a few single crystals of [Rh(κ^2-P,P-DPEphos)(η^2-$H_3B{\cdot}NMe_3$)][BAr^F_4] could be grown in previous work from 2011, where X-ray analysis confirmed the proposed structure.[9] However the organometallic complex derived from the hydroboration of 3-dimethyl-bute-1-ene by $H_3B{\cdot}NMe_3$, complex **13**, could be isolated as a purple powder in good yields of up to 80%.

Complex **13** could be characterised by NMR spectroscopy, ESI-MS and elemental microanalysis. The ^{31}P{^{1}H} NMR spectrum of **13** in CD_2Cl_2 solution showed a doublet at δ 40.0 with a $^1J_{RhP}$ coupling constant of 180 Hz, consistent with DPEphos coordinated to a Rh(I) centre in a κ^2-P,P manner.[12] A broad signal at δ 33.3 was observed in the ^{11}B NMR spectrum, downfield shifted by 32.5 ppm relative to free $H_2B(CH_2CH_2{}^tBu){\cdot}NMe_3$, which resonates at δ −0.8 (t, $^1J_{BH}$ 96 Hz, 1,2-$C_6H_4F_2$ solvent).[13] This is consistent with an η^2 interaction between $H_2B(CH_2CH_2{}^tBu){\cdot}NMe_3$ and the metal, where a higher Rh···B contribution to the bonding occurs due to the bidentate mode of the amine borane ligand. In the ^{1}H NMR spectrum, a broad resonance at δ −5.55 of relative integral 2 H is attributed to the η^2 BH_2 protons of the amine borane, which sharpens on ^{11}B decoupling. Two signals at δ 0.49 and δ 1.49 are assigned to the CH_2 group adjacent to the ^{t}Bu group, and the CH_2 group bound to boron respectively. Their relative 2 H integration confirms that the hydroboration reaction forms the anti-Markovnikov product of $H_2B(CH_2CH_2{}^tBu){\cdot}NMe_3$, as seen in complex **i-13**,[8] as well as [Rh($P^iBu_2{}^tBu$)$_2$(η^2-$H_2B(CH_2CH_2{}^tBu){\cdot}NMe_3$)][$BAr^F_4$], reported in 2011 by Weller co-workers.[13] In contrast, the Markovnikov product would show integrals of 1 H and 3 H for the alkyl chain protons due to the formation of η^2 $H_2B(CH(CH_3){}^tBu){\cdot}NMe_3$.

Layering a CH_2Cl_2 solution of **13** with pentane and storing at −20°C yielded a small number of crystals suitable for single crystal X-ray diffraction. These crystals were of poor quality and high angle data was lacking, which led to a final crystallographic refinement of poor quality (R = 15.2%). Nevertheless, the data was adequate for confirming the atom connectivity in the structure, shown in Figure 4.2.Whilst bond metrics should therefore be treated with caution, the cis κ^2-P,P coordination of the DPEphos ligand was evident, and confirmed by the long Rh···O distance of 3.477(7) Å. This value is similar to the Rh···O distances in the Xantphos-Ph analogue **i-13** (3.431(3) Å),[8] and also [Rh(κ^2-P,P-DPEphos)(η^2-$H_3B{\cdot}NMe_3$)][BAr^F_4] (3.547(2) Å).[9] The close Rh···B distance in **13** of 2.208(13) Å is shorter than the sum of the covalent radii of rhodium and boron (2.26 Å),[14] indicative of the η^2 interaction of the BH_2 fragment with rhodium, compared to longer Rh···B distances found in the η^1 amine borane complexes [Rh(κ^3-P,O,P-Xantphos-R)$(H)_2$(η^2-$H_3B{\cdot}NMe_3$)][BAr^F_4] (R = ^{i}Pr (**2**), Ph (**2-Ph**)) of 2.783(6) (**2**) and 2.759(6) Å (**2-Ph**).[8] This suggests that a shorter Rh···B distance leads to a more downfield chemical shift of the bound amine borane relative to the free amine borane, reflecting the differences in orbital contribution of η^2 versus η^1 binding of amine boranes to transition metal centres.

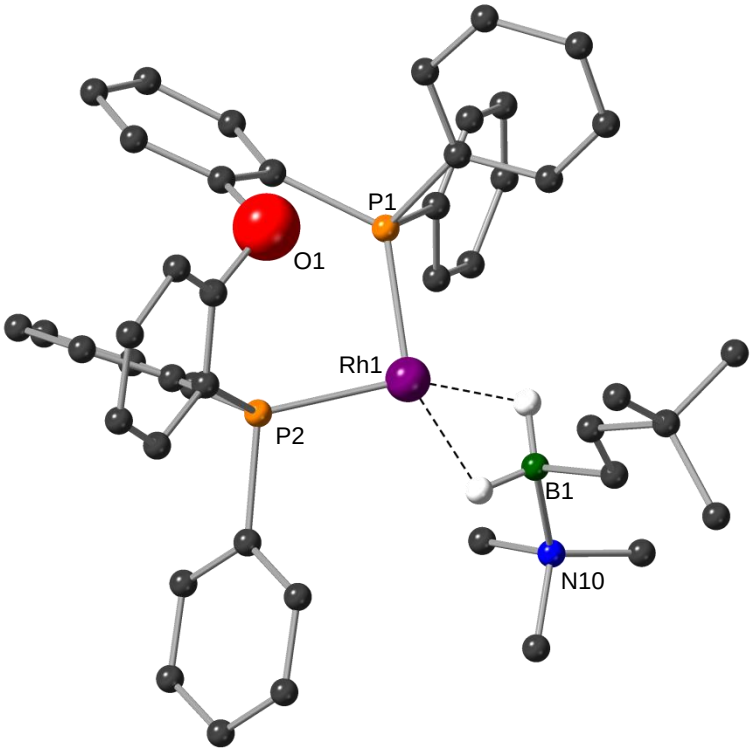


Figure 4.2 Crystal structure of the cationic portion of [Rh(κ²-P,P-DPEphos)(η²-$H_2B(CH_2CH_2{}^tBu)\cdot NMe_3$)][$BAr^F{}_4$] (**13**). The ball-and-stick model confirms the expected connectivity. C-bound H atoms are not shown for clarity. Selected bond lengths (Å) and angles (°): Rh1–P1, 2.240(3); Rh1–P2, 2.232(3); Rh1–O1, 3.477(7); Rh1–B1, 2.208(13); B1–N10, 1.617(14); P1–Rh1–P2, 96.42(11).

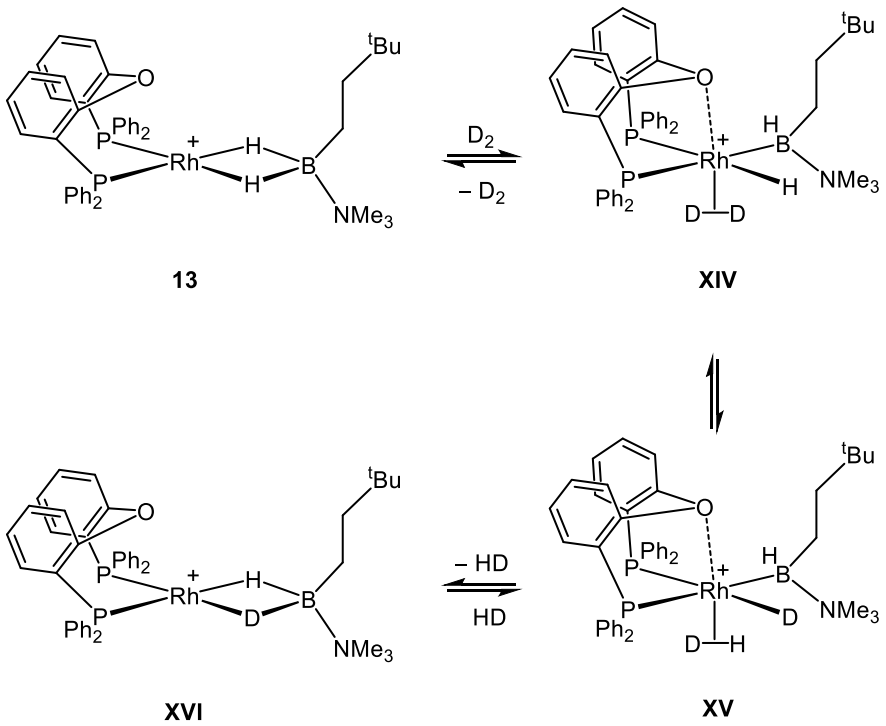
4.4 Reactivity of [Rh(DPEphos)($H_2B(CH_2CH_2{}^tBu)\cdot NMe_3$)][$BAr^F{}_4$] (**13**)

*4.4.1 Reaction of **13** with D_2: H/D exchange*

As B–H activation at a metal centre is a key step during inner sphere dehydrogenation of amine boranes (Section 1.6.6),[15] isolated complex **13** was dissolved in CD_2Cl_2 under an atmosphere of D_2 (298 K, ~1 bar) to study deuterium incorporation into Rh(I) η² amine borane complexes of {Rh(DPEphos)}$^+$ via metal mediated H/D exchange. After 5 minutes, H/D exchange had occurred at the Rh···H–B groups,[16] demonstrated by a reduction for the integral associated with the Rh···H–B environment from 2 H to 1.3 H, relative to 8 H for the [$BAr^F{}_4$]$^-$ anion in the ^{1}H NMR spectrum. This was additionally confirmed by the presence of the corresponding signal in the ^{2}H NMR spectrum for the Rh···D–B environment at δ −5.51. The $^{31}P\{^1H\}$ NMR spectrum showed that **13** remained Rh(I) under a pressure of D_2, though the chemical shift was slightly shifted, likely due to

an isotopic perturbation of chemical shift inflicted by the binding of B–D to the metal rather than B–H (δ 40.3, d, $^{1}J_{RhP}$ 180 Hz).

With this in mind, H/D exchange likely operates through a slightly different mechanism to that seen in [Rh(κ^{3}-P,O,P-Xantphos-^{i}Pr)(H)$_2$(η^{1}-H$_3$B·NMe$_3$)][BAr$^{F}_4$] (**2**, Scheme 2.7), as this occurred through a σ CAM process in which the Rh(III) oxidation state was present throughout. In comparison, the Rh(I) oxidation state in complex **13** appears dominant, even under 1 bar pressure of D_2 (or 4 bar H_2), though the Rh(III) oxidation state may be accessible for H/D exchange to occur. A mechanistic proposal for this process is detailed in Scheme 4.4. B–H activation at the Rh(I) centre and coordination of D_2 gives a rhodium base stabilised boryl complex, **XIV**, where coordination of the DPEphos linker may provide additional stabilisation. **XIV** can rearrange to form **XV** via a σ CAM process, followed by loss of HD and reductive coupling of the boryl and deuteride fragments which forms **XVI** where deuterium incorporation has occurred at the Rh···H–B positions.



Scheme 4.4 Proposed mechanism for the H/D exchange between **13** and D_2. [BAr$^{F}_4$]$^{-}$ anions not shown for clarity. Not all pathways or H/D combinations are shown.

This indicates that relatively fast Rh···H(D)–B exchange occurs in complex **13**, therefore there is a low energetic barrier to the formation of boryl complexes such as **XIV**, and access to the Rh(III) oxidation state. This may have further implications in terms of possible mechanisms for amine borane dehydrocoupling using the {Rh(DPEphos)}$^+$ system, which will be discussed further in Chapter 5.

*4.4.2 Speciation studies of **13** with 10 equivalents of $H_3B{\cdot}NMeH_2$*

To provide insight into the organometallic species that may be formed during the dehydropolymerisation of $H_3B{\cdot}NMeH_2$ using **13** – further detailed in Chapter 5 – 10 equivalents of $H_3B{\cdot}NMeH_2$ was added to complex **13** (i.e. 10 mol% catalyst loading) in 1,2-$C_6H_4F_2$ solvent in a sealed NMR tube.

The initial ^{11}B NMR spectrum (t = 5 min, Figure 4.3) of this reaction showed that a significant proportion of the boron-containing species present was unreacted $H_3B{\cdot}NMeH_2$, alongside evidence of $(H_2BNMeH)_n$ by a broad signal at δ −6.0 and $(BH_2)_2(\mu\text{-}H)(NMeH)$ at δ −22.3 (td, $^1J_{BH}$ 130 Hz, 32 Hz).[5] The latter species indicative of possible B–N bond cleavage processes in the reaction mixture, as $(BH_2)_2(\mu\text{-}H)(NMeH)$ is a product of formal addition of free BH_3 to $H_2B{=}NMeH$. A triplet identified as free $H_2B(CH_2CH_2{}^tBu){\cdot}NMe_3$ was observed at δ −1.2 ($^1J_{BH}$ 92 Hz),[13] in comparison to the broad, η^2 bound $H_2B(CH_2CH_2{}^tBu){\cdot}NMe_3$ resonance at δ 33.3 in precatalyst **13**, suggesting that this masking ligand could be displaced under these conditions. Full consumption of $H_3B{\cdot}NMeH_2$ occurred over approximately 5 hours, forming $(HBNMe)_3$ (δ 33.2, d, $^1J_{BH}$ 133 Hz), likely polymeric species between δ 5.0 and δ −10.0, and $(BH_2)_2(\mu\text{-}H)(NMeH)$ (Figure 4.3). The timescale for this reaction using {Rh(DPEphos)}$^+$ precatalyst **13** of 5 hours contrasts with {Rh(Xantphos-^{i}Pr)}$^+$ system **2** in which $H_3B{\cdot}NMeH_2$ dehydrocoupling was complete after approximately 30 seconds (Section 2.4.2), under the same reaction conditions.

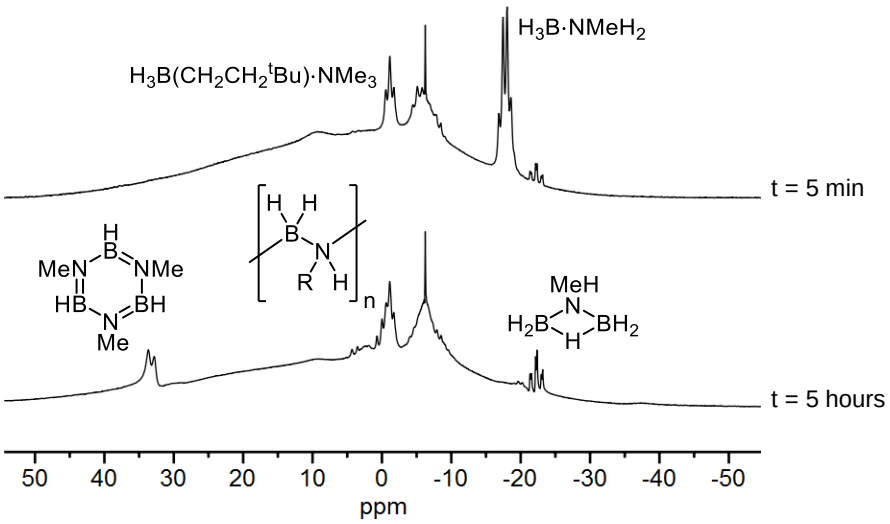


Figure 4.3 Stacked ^{11}B NMR spectra of the reaction of $H_3B{\cdot}NMeH_2$ with 10 mol% **13** in 1,2-$C_6H_4F_2$ solvent over time. The broad baseline signals observed in the ^{11}B NMR spectra at δ ~20.0 are due to background from the tube and probe (borosilicate glass).

Monitoring the reaction mixture by $^{31}P\{^1H\}$ NMR spectroscopy at approximately 5 minutes, 2 hours and 5 hours showed an apparently complex mixture of many phosphorous containing species that evolves with time (Figure 4.4). The earliest spectrum shows that only 5% of precatalyst **13** remains (δ 40.0), however after 2 hours this peak had completely disappeared. Noticeably present over the entire timescale of the reaction are signals at δ 31.7 (dd), δ 28.9 (dd), δ 28.3 (d), δ 15.7 (m) and δ 12.8 (m). The four signals δ 31.7 (dd), δ 28.9 (dd), δ 15.7 (m) and δ 12.8 (m) (*, Figure 4.4) appear to increase or decrease in relative intensity on the same timescale, therefore may be related. In particular, the latter two resonances appear roofed with one another, indicating that these two phosphorous environments may exist in the same species. Broader, but minor, resonances at δ 45.6, δ 33.0 and δ 18.0 are present earlier in the reaction, however these are minimal after a reaction time of 5 hours at the end of catalysis.

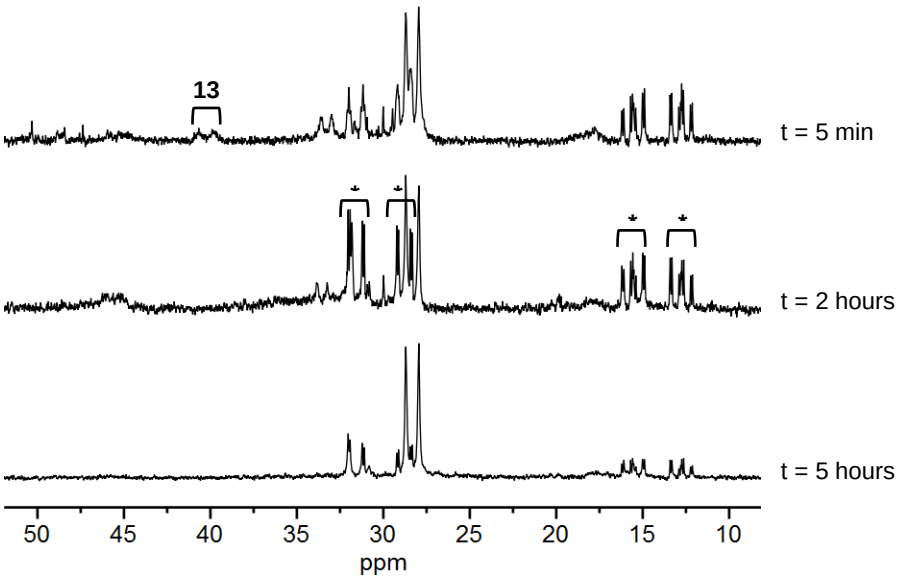


Figure 4.4 Stacked $^{31}P\{^{1}H\}$ NMR spectra of the reaction of $H_3B{\cdot}NMeH_2$ with 10 mol% **13** in 1,2-$C_6H_4F_2$ solvent over time. * = phosphorus environments which appear to be related.

In order to gain further information about the identity of the species present during productive $H_3B{\cdot}NMeH_2$ dehydrocoupling, analysis by ESI-MS of the 10 mol% reaction mixture after 2 hours was attempted. The resulting mass spectrum is shown in Figure 4.5, and shows three major peaks with *m/z* values of 1309.20, 1326.21 and 1338.23. These peaks and their corresponding isotope patterns demonstrate that each have gross formulations of a monocationic $\{Rh(DPEphos)\}_2^+$ fragment, containing B_2H_5 (calculated *m/z* 1309.19), $BNCH_7$ (calculated *m/z* 1326.20) and B_2NCH_8 (calculated *m/z* 1338.22) moieties respectively.

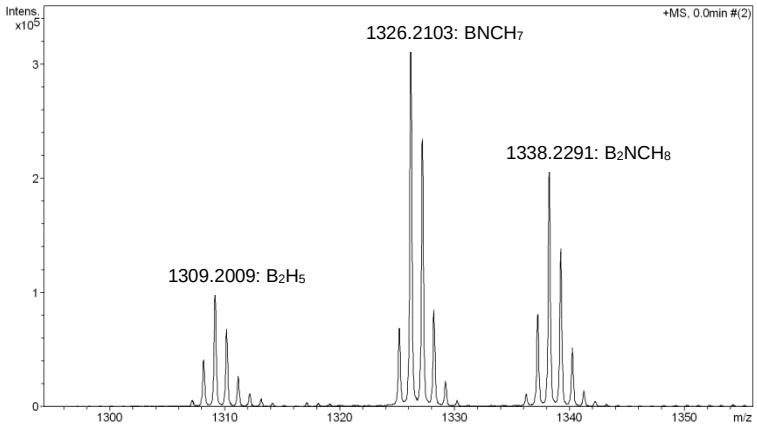


Figure 4.5 ESI-MS spectrum of the reaction of $H_3B{\cdot}NMeH_2$ with 10 mol% **13** in 1,2-$C_6H_4F_2$ solvent after 2 hours. Each peak is assigned to $[\{Rh(DPEphos)\}_2(X)]^+$ where X = B_2H_5, $BNCH_7$ or B_2NCH_8.

These results suggest that complexes of the type $[\{Rh(DPEphos)\}_2(B_2H_5)]^+$, $[\{Rh(DPEphos)\}_2(BNCH_7)]^+$ and $[\{Rh(DPEphos)\}_2(B_2NCH_8)]^+$ may be implicated in catalysis. Investigation of the possible identities of these complexes, as well as others which may form in catalysis, will be focused upon throughout the rest of this Chapter.

4.5 Formation of $\{Rh(DPEphos)\}^+$ complexes from $H_3B{\cdot}NMeH_2$

Given the complexity of the NMR data provided for the reaction of $H_3B{\cdot}NMeH_2$ with 10 mol% **13**, the ESI-MS study provided a simpler view of possible species present during catalysis. Two of these complexes likely contain amine borane frameworks, as the isotope patterns suggested by ESI-MS indicate monocationic species incorporating both boron and nitrogen. Hence the true identities of the species with gross formulations of $[\{Rh(DPEphos)\}_2(BNCH_7)]^+$ and $[\{Rh(DPEphos)\}_2(B_2NCH_8)]^+$ were studied in more detail.

*4.5.1 Formation of [{Rh(DPEphos)}$_2$(H)(H$_2$BNMeH)][BAr$^F{}_4$] (**14**)*

The formulation of $[\{Rh(DPEphos)\}_2(BNCH_7)]^+$ may indicate the more specific molecular formula of $[\{Rh(DPEphos)\}_2(H)(H_2BNMeH)]^+$. Complexes of this type have previously been reported, for example $[\{Rh(R_2P(CH_2)_3PR_2)\}_2(\mu\text{-}H)(\mu\text{-}H_2BNR'H)][BAr^F{}_4]$ (R = Ph, R′ = H (**i-22**), Me; R = ^{i}Pr, R′ = H (**i-23**)) (Figure 4.6),[11] and $[\{Rh(\kappa^2\text{-}P,P\text{-}Xantphos\text{-}Et)\}_2(\mu\text{-}H)(\mu\text{-}H_2BNMeH)][BAr^F{}_4]$ (Figure 4.6).[17]

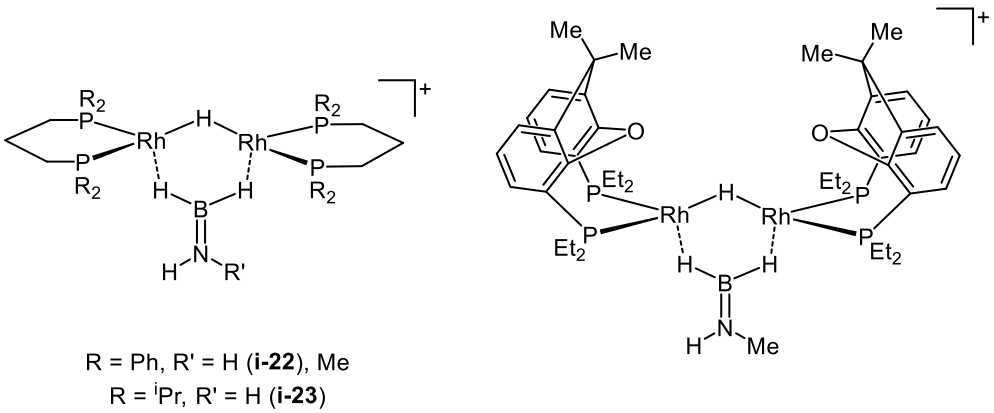
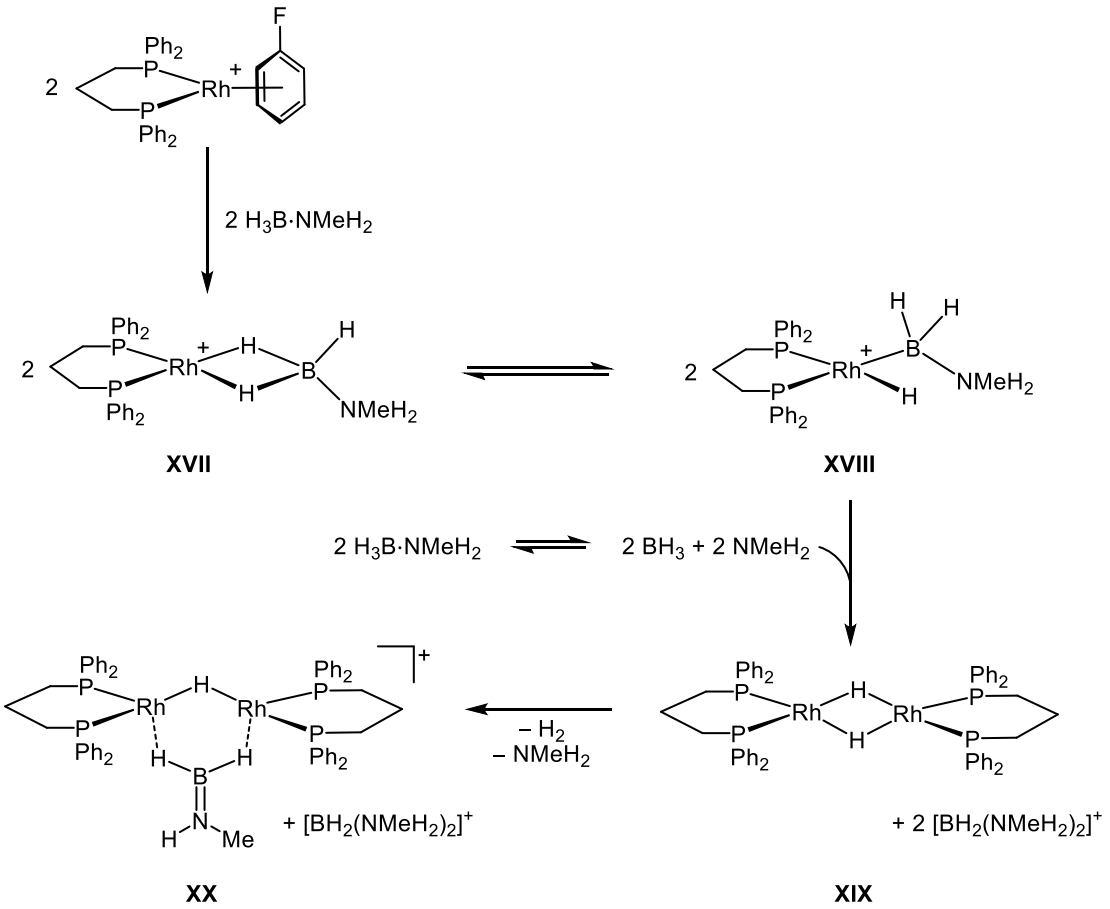


Figure 4.6 Structures of bimetallic bridging aminoborane complexes $[\{Rh(R_2P(CH_2)_3PR_2)\}_2(\mu\text{-}H)(\mu\text{-}H_2BNR'H)][BAr^F{}_4]$ (R = Ph, R′ = H (**i-22**), Me; R = ^{i}Pr, R′ = H (**i-23**) and $[\{Rh(\kappa^2\text{-}P,P\text{-}Xantphos\text{-}Et)\}_2(\mu\text{-}H)(\mu\text{-}H_2BNMeH)][BAr^F{}_4]$. $[BAr^F{}_4]^-$ anions not shown for clarity.

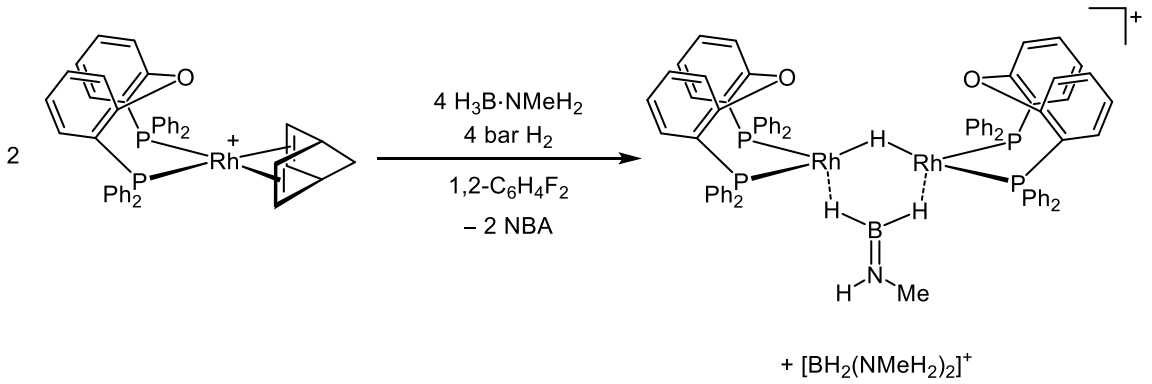
The proposed mechanism for the formation of $[\{Rh(Ph_2P(CH_2)_3PPh_2)\}_2(\mu\text{-}H)(\mu\text{-}H_2BNMeH)][BAr^F{}_4]$ from the precursor complex $[Rh(Ph_2P(CH_2)_3PPh_2)(\eta^6\text{-}C_6H_5F)][BAr^F{}_4]$ in 1,2-$C_6H_4F_2$ solvent has previously been reported (Scheme 4.5),[18] and has parallels with Conejero and López-Serrano's $H_3B{\cdot}NMeH_2$ dehydrocoupling mechanism detailed in Scheme 1.21.[19] $[Rh(Ph_2P(CH_2)_3PPh_2)(\eta^6\text{-}C_6H_5F)][BAr^F{}_4]$ reacts with $H_3B{\cdot}NMeH_2$ to form the σ amine borane complex **XVII**. Oxidative cleavage of $H_3B{\cdot}NMeH_2$ forms the Rh(III) intermediate **XVIII**. **XVIII** reacts with $NMeH_2$ (from B–N cleavage of $H_3B{\cdot}NMeH_2$) and dimerises, forming the neutral Fryzuk-type dimer $[Rh(Ph_2P(CH_2)_3PPh_2)(\mu\text{-}H)]_2$ **XIX**,[20] and two equivalents of the boronium cation $[BH_2(NMeH_2)_2][BAr^F{}_4]$. Protonation of **XIX** by one equivalent of $[BH_2(NMeH_2)_2][BAr^F{}_4]$ furnishes $[\{Rh(Ph_2P(CH_2)_3PPh_2)\}_2(\mu\text{-}H)(\mu\text{-}H_2BNMeH)][BAr^F{}_4]$ (**XX**) with loss of H_2, the overall reaction forming one equivalent of $[BH_2(NMeH_2)_2][BAr^F{}_4]$ alongside **XX**. A similar methodology for the formation of a $[\{Rh(DPEphos)\}_2(H)(H_2BNMeH)]^+$ complex was therefore employed in the DPEphos system.



Scheme 4.5 Weller's previously reported mechanism for the formation of [{Rh($Ph_2P(CH_2)_3PPh_2$)}$_2$(μ-H)(μ-H_2BNMeH)][BAr^F_4] (**XX**) in 1,2-$C_6H_4F_2$ solvent. [BAr^F_4]$^-$ anions not shown for clarity.

In order to investigate this further, the synthesis of the DPEphos analogue of **XVII** was attempted, and its onward reactivity probed. Hydrogenation of [Rh(κ^2-P,P-DPEphos)(NBD)][BAr^F_4] (**12**) in 1,2-$C_6H_4F_2$ solvent in the presence of 2 equivalents of $H_3B{\cdot}NMeH_2$ was performed (Scheme 4.6). The $^{31}P\{^1H\}$ NMR spectrum of the reaction mixture on time of mixing showed one signal at δ 28.3 (d, $^1J_{RhP}$ 150 Hz), corresponding to the formation of proposed new complex [{Rh(κ^2-P,P-DPEphos)}$_2$(μ-H)(μ-H_2BNMeH)][BAr^F_4] (**14**), where the DPEphos analogue of **XVII** had undergone further reaction to form **14**. Notable is that this signal is omnipresent in the $^{31}P\{^1H\}$ NMR spectrum of the reaction mixture of $H_3B{\cdot}NMeH_2$ with 10 mol% **13** (Figure 4.4). These data, in particular the value of the rhodium-phosphorus coupling constant (150 Hz), is consistent with well-studied bridging aminoborane complex [{Rh($Ph_2P(CH_2)_3PPh_2$)}$_2$(μ-H)(μ-H_2BNH_2)][BAr^F_4] (**i-22**, δ 18.2, $^1J_{RhP}$ 142 Hz, d^8-THF solvent).[11] In the ^{11}B NMR spectrum of **14**, a broad signal at

δ 55.8 was present, alongside a triplet at δ −7.1 ($^1J_{BH}$ 120 Hz), indicating the formation of $[BH_2(NMeH_2)_2][BAr^F{}_4]$ (**11**) (δ −7.4, $^1J_{BH}$ 117 Hz, CD_2Cl_2 solvent). The broad signal at δ 55.8 is indicative of a bridging μ-H_2BNMeH unit across two rhodium centres, and in agreement with reported values for similar boron environments – a chemical shift of δ 51.5 was noted in complex **i-22**.[11] The ^{1}H NMR spectrum of **14** shows one peak in the hydride region (δ −9.12) with relative integral 1.5 H with respect to the $[BAr^F{}_4]^-$ anion. This can be explained as the bridging Rh–H–Rh and Rh···H–B are therefore fluxional. The equivalent data for **i-22** also showed the same fluxionality, with the room temperature ^{1}H NMR data indicating a single resonance at δ −7.45.[11] The NMR data for **14** hence fit well with those previously reported for **i-22**, and combined with ESI-MS of this in situ reaction mixture which showed a major species at *m/z* 1326.20 (calculated *m/z* 1326.20), the identity of **14** was proposed to be [{Rh(κ^2-P,P-DPEphos)}$_2$(μ-H)(μ-H_2BNMeH)][$BAr^F{}_4$] (Scheme 4.6).



Scheme 4.6 Synthesis of [{Rh(κ^2-P,P-DPEphos)}$_2$(μ-H)(μ-H_2BNMeH)][$BAr^F{}_4$] (**14**). $[BAr^F{}_4]^-$ anions not shown for clarity. NBA = norbornane.

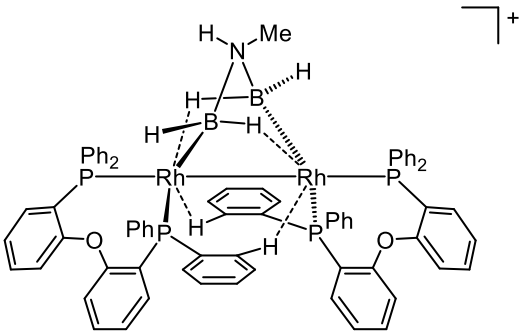
Isolation of complex **14** was unsuccessful, though its crystallisation was attempted multiple times. Layering a 1,2-$C_6H_4F_2$ solution of **14** with pentane at −40°C led to the isolation of a few orange single crystals, for which a solid state structure determination was undertaken. Unfortunately, these crystals were of too poor quality to obtain a definitive structure, however a bridging Rh···B(NC)B···Rh motif gave the best fit, contrasting the expected Rh···B(N)···Rh structure proposed for **14**. In fact, further work showed that on the timescale of crystallisation, **14** forms a

new complex (**15**, vide infra). Nevertheless, **14** is identified as the first formed species under these conditions.

*4.5.2 Formation of [{Rh(DPEphos)}$_2${(H$_2$B)$_2$NMeH}][BAr$^F{}_4$] (**15**) and [{Rh(DPEphos)}$_2${(H$_2$B)$_2$NMeH}][Al(O^{t}Bu^F)$_4$] (**15-[Al(O^{t}Bu^F)$_4$]**)*

The other amine borane-type species suggested to be present by ESI-MS during 10 mol% $H_3B{\cdot}NMeH_2$ catalysis had the formulation $[\{Rh(DPEphos)\}_2(B_2NCH_8)]^+$. Hydrogenation of **12** in the presence of 4 equivalents of $H_3B{\cdot}NMeH_2$ in 1,2-$C_6H_4F_2$ solvent initially led to the in situ formation of **14**, however after 10 minutes, new resonances were present in the $^{31}P\{^1H\}$ NMR spectrum. On degassing this solution and backfilling with argon, after a further 30 minutes $^{31}P\{^1H\}$ NMR spectroscopy showed that 25% of the reaction mixture was complex **14**, the rest being peaks matching four of the resonances detailed in Figure 4.4: δ 31.7 (dd), δ 28.9 (dd), δ 15.7 (ddd) and δ 12.8 (ddd). Attempts to isolate any new complexes from this reaction mixture (i.e. complex **15**) by layering the solution with pentane yielded intractable orange oils. However, by using the $[Al(O^tBu^F)_4]^-$ anion, single crystalline material could be obtained.[6-7]

Hydrogenating [Rh(κ^2-P,P-DPEphos)(NBD)][Al(O^{t}Bu^F)$_4$] (**12-[Al(O^{t}Bu^F)$_4$]**) in 1,2-$C_6H_4F_2$ solvent alongside 4 equivalents of $H_3B{\cdot}NMeH_2$ formed **14-[Al(O^{t}Bu^F)$_4$]** in situ, analogous to Scheme 4.6. Layering this reaction mixture with pentane under an argon atmosphere at room temperature led to the formation of orange needles, and these were suitable for single crystal X-ray diffraction studies. The identity of the complex that had formed on the timescale of crystallisation was found to be [{Rh(κ^2-P,P-DPEphos)}$_2${μ-(H$_2$B)$_2$NMeH}][Al(O^{t}Bu^F)$_4$] (**15-[Al(O^{t}Bu^F)$_4$]**, Figure 4.7), where the solid state structure of **15-[Al(O^{t}Bu^F)$_4$]** is shown in Figure 4.8.



15-[Al(O^{t}Bu^F)$_4$]

Figure 4.7 Structure of [{Rh(κ^2-P,P-DPEphos)}$_2${μ-(H$_2$B)$_2$NMeH}][Al(O^{t}Bu^F)$_4$] (**15-[Al(O^{t}Bu^F)$_4$]**). [Al(O^{t}Bu^F)$_4$]$^-$ anion not shown for clarity.

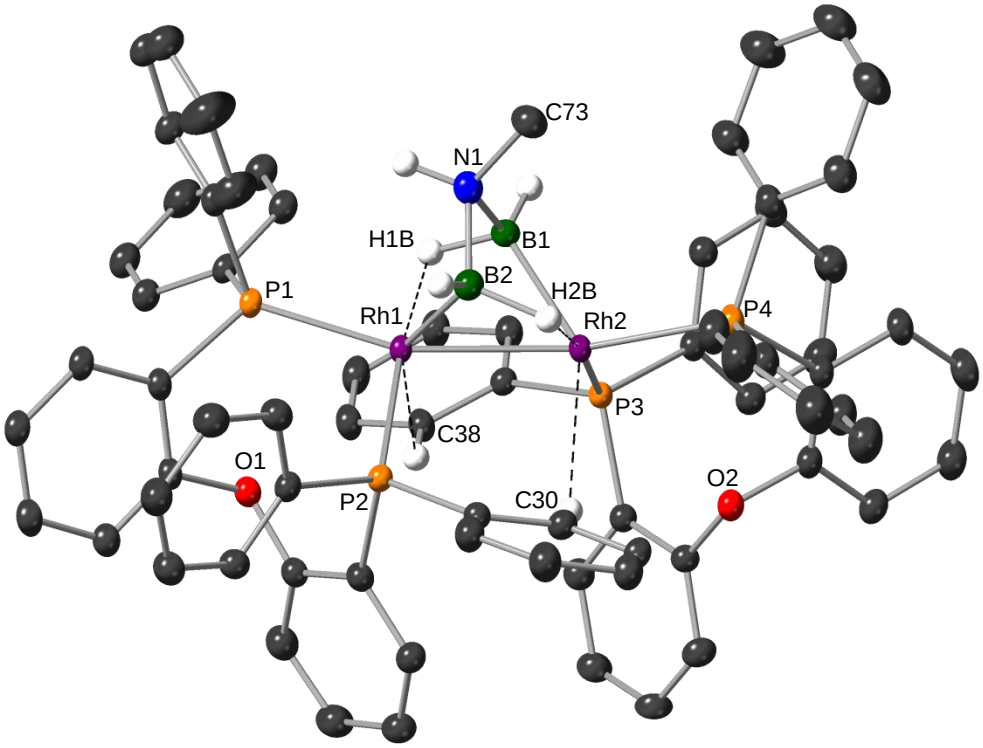


Figure 4.8 Crystal structure of the cationic portion of [{Rh(κ^2-P,P-DPEphos)}$_2${μ-(H$_2$B)$_2$NMeH}][Al(O^{t}Bu^F)$_4$] (**15-[Al(O^{t}Bu^F)$_4$]**). Displacement ellipsoids are drawn at the 30% probability level. C-bound H atoms, except those bound to C30 and C38, are not shown for clarity. Selected bond lengths (Å) and angles (°): Rh1−Rh2 2.6422(5); Rh1–P1 2.329(1); Rh1–P2 2.2788(9); Rh2–P3 2.286(1); Rh2–P4 2.341(1); Rh1–O1 3.273(3); Rh2–O2 3.233(4); Rh1–B2 2.096(6); Rh1–B1 2.326(5); Rh2–B1 2.107(6); Rh2–B2 2.328(5); Rh1–C38 2.997(5); Rh2–C30 2.968(3); B1–N1 1.59(1); B2–N1 1.56(1); N1–C73 1.49(1); P1–Rh1–P2 100.69(4); P3–Rh2–P4 98.64(4); B1–N1–B2 87.5(6); Rh1–Rh2–P3 93.03(3); Rh2–Rh1–P2 95.30(3); Rh1–Rh2–P4 166.53(3); Rh2–Rh1–P1 162.59(3); P2–Rh1–H1B 174(2); P3–Rh2–H2B 172.2(19).

The DPEphos ligands adopt a κ^2-P,P geometry, shown by the relatively long Rh···O distances of 3.273(3) Å and 3.233(4) Å, however these distances are within error shorter than those measured in

DPEphos complex **13** and Xantphos-Ph complex **i-13** (Scheme 4.3, 3.477(7) Å and 3.431(3) Å respectively).[8] The terminal and bridging B–H hydrogen atoms were located, with each BH_2 fragment coordinated to both rhodium centres through a direct Rh–B bond to one rhodium centre, and a bridging Rh···H–B bond to the other. The respective Rh1–B2 and Rh2–B1 bond lengths of 2.096(6) Å and 2.107(6) Å are similar to the Rh–B distances present in Weller's base-stabilised aminoboryl complex [Rh(κ^3-P,O,P-Xantphos-Ph)(H)(BH=N^{i}Pr$_2$)(NCMe)][BAr$^F{}_4$] (2.034(3) Å, Figure 4.9),[1] and Aldridge's aminoboryl complex [Rh(IMes)$_2$(H)(BH=NMe$_2$)][BAr$^F{}_4$] (1.960(9) Å, Figure 4.9),[21] which both contain formal 2-centre 2-electron Rh–B bonds. They are also comparable to the Rh–B bond lengths in the bimetallic bridging aminoborylene structure [{Rh(μ-Cy$_2$PCH$_2$PCy$_2$)(H)}$_2$(μ-H)(μ-BNMe$_2$)][Al(O^{t}Bu^F)$_4$] of 2.015(6) Å and 1.983(7) Å (Figure 4.10).[22]

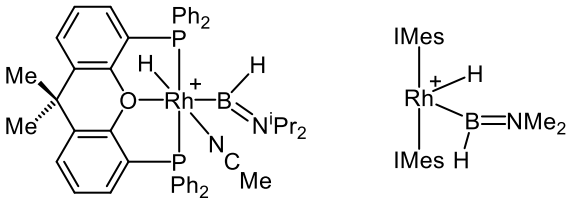
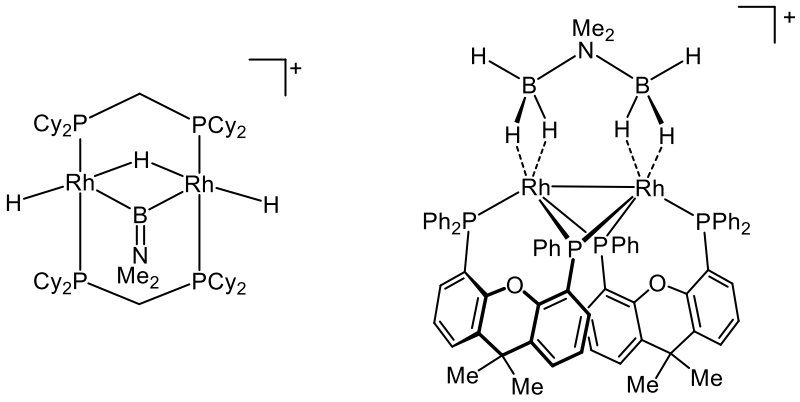


Figure 4.9 Left: Structure of Weller's [Rh(κ^3-P,O,P-Xantphos-Ph)(H)(BH=N^{i}Pr$_2$)(NCMe)][BAr$^F{}_4$]. Right: Structure of Aldridge's [Rh(IMes)$_2$(H)(BH=NMe$_2$)][BAr$^F{}_4$] (IMes = N,N′-bis(2,4,6-trimethylphenyl)imidazol-2-ylidene). [BAr$^F{}_4$]$^-$ anions not shown for clarity.

The Rh1–Rh2 distance of 2.6422(5) in **15-[Al(O^{t}Bu^F)$_4$]** suggests that there may a metal-metal bond present in the bimetallic structure. This length is shorter than the Rh···Rh distance in [{Rh(μ-Cy$_2$PCH$_2$PCy$_2$)(H)}$_2$(μ-H)(μ-BNMe$_2$)][Al(O^{t}Bu^F)$_4$] (2.8266(5) Å, Figure 4.10) – for which a Quantum Theory Atoms in Molecules analysis did not suggest a bond path between the two rhodium centres.[22] Instead, it is more similar to the Rh–Rh distance of 2.5928(4) Å present in the monocationic Xantphos-Ph bimetallic complex [{Rh(κ^2-P,P-Xantphos-Ph′)}$_2$(η^{2}η^2-H$_3$BNMe$_2$BH$_3$)][BAr$^F{}_4$] (**i-18**, Figure 4.10, Xantphos-Ph′ = 4-phenylphosphido-5-diphenylphosphino-9,9-dimethylxanthene), for which a Rh–Rh bond was proposed on the basis of the diamagnetism observed and the formal electron count of the complex.[23]



i-18

Figure 4.10 Left: Structure of Weller's [{Rh(μ-$Cy_2PCH_2PCy_2$)(H)}$_2$(μ-H)(μ-$BNMe_2$)][Al(O^{t}Bu^F)$_4$]. Right: Structure of Weller's [{Rh(κ^2-P,P-Xantphos-Ph′)}$_2$(η^{2}η^2-$H_3BNMe_2BH_3$)][BAr$^F{}_4$] (**i-18**). [Al(O^{t}Bu^F)$_4$]$^-$ and [BAr$^F{}_4$]$^-$ anions not shown for clarity.

In order to gather further information about the formal structure of complex **15-[Al(O^{t}Bu^F)$_4$]**, DFT calculations were undertaken by Dr Nicholas A. Beattie and Prof. Stuart A. Macgregor (Heriot-Watt University, Edinburgh). A QTAIM (Quantum Theory of Atoms in Molecules) analysis was carried out (Figure 4.11), similar to complex **8-[BAr$^{Cl}{}_4$]** in Chapter 2. The electron density (ρ(r)) and bond ellipticity values (ε) for selected bond critical points are shown in Table 4.1.

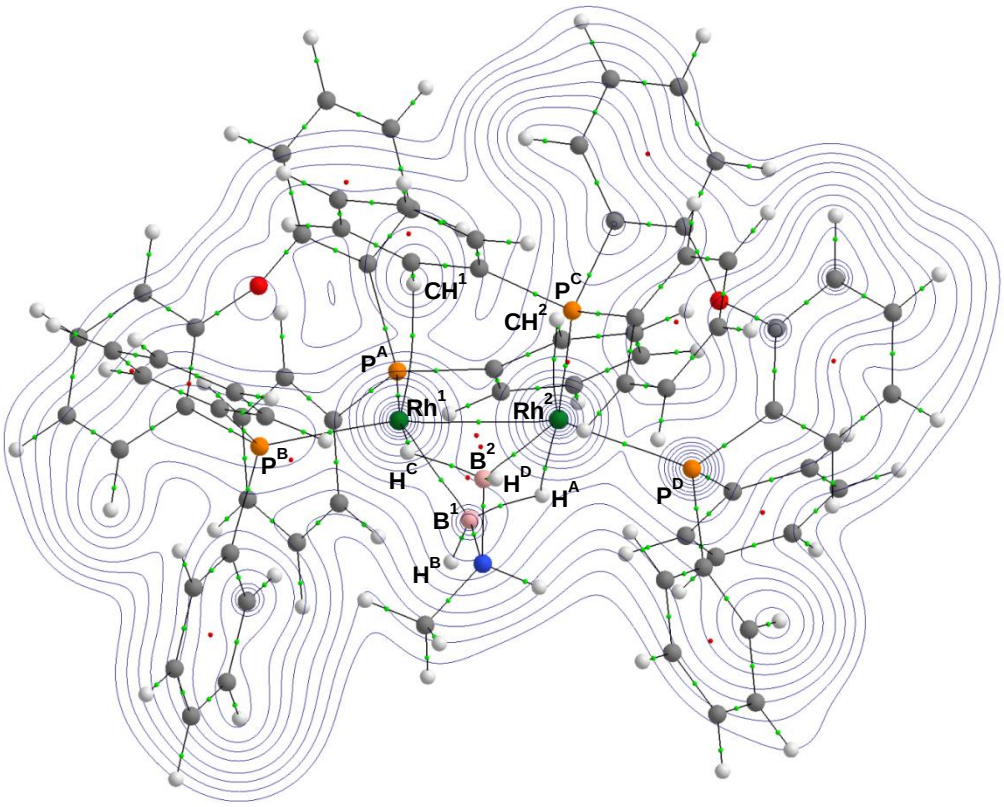


Figure 4.11 Molecular graph of the cationic portion of **15-[Al(O^{t}Bu^F)$_4$]** with 2D contour plot of the electron density present. Bond critical points are shown in green and ring critical points in red. Diagram courtesy of Dr Nicholas A. Beattie and Prof. Stuart A. Macgregor.

Bond	ρ(r)	ε	Bond	ρ(r)	ε
Rh^1–Rh^2	0.05	0.32	Rh^2–B^2	0.10	0.10
Rh^1–H^CB^2	0.10	0.39	B^1–H^B	0.17	0.03
Rh^2–H^AB^1	0.09	0.39	B^2–H^D	0.17	0.03
B^2–H^C	0.12	0.40	Rh^1–HC	0.02	0.28
B^1–H^A	0.12	0.32	Rh^2–HC	0.02	0.37
Rh^1–B^1	0.10	0.10			

Table 4.1 Quantum Theory of Atoms and Molecules calculated parameters for **15-[Al(O^{t}Bu^F)$_4$]** courtesy of Dr Nicholas A. Beattie and Prof. Stuart A. Macgregor.

The Rh–Rh bond suggested by the crystal structure, though relatively long, was confirmed by the calculations, as a bond critical point was located between the two rhodium atoms ($\rho(r) = 0.05$, $\varepsilon = 0.32$). The reasonably high ellipticity value implies that the bonding has a level of asymmetry, and therefore likely contains elements of π and δ bonding, rather than purely σ which would show an ellipticity value closer to 0. The values of $\rho(r)$ for the $Rh^1\cdots H^CB^2$ (0.10) and $Rh^2\cdots H^AB^1$ (0.09) interactions are significant, with high ellipticity values (0.39), indicative of 3-centre 2-electron bonds. These values for the bridging Rh···H–B environments are in agreement with those reported for the similar Rh···H–B bonding motifs in $[\{Rh(^iPr_2P(CH_2)_3P^iPr_2)\}_2(\mu\text{-}H)(\mu\text{-}H_2BNH_2)][BAr^F{}_4]$ (**i-23**, $\rho(r) = 0.09$, $\varepsilon = 0.37$).[11] The 3-centre 2-electron bonding nature of the Rh···H–B interactions in **15-[Al(O^{t}Bu^F)$_4$]** are also reflected in the $\rho(r)$ values of B^2–H^C (0.12) and B^1–H^A (0.12) bonds with respective ellipticities of 0.40 and 0.32. These ellipticity values are higher than those reported for the B^1–H^B and B^2–H^D bonds (0.03), consistent with the 2-centre 2-electron nature expected for terminal B–H groups, in addition to higher $\rho(r)$ values for these terminal bonds (0.17) due to a stronger covalent interaction. Bond critical points observed between Rh^1–B^1 and Rh^2–B^2 with a $\rho(r)$ value of 0.10 and low value of ε (0.10) provide strong evidence for the presence of 2-electron 2-centre bonding. The aminoborylene complex $[\{Rh(\mu\text{-}Cy_2PCH_2PCy_2)(H)\}_2(\mu\text{-}H)(\mu\text{-}BNMe_2)][Al(O^tBu^F)_4]$ (Figure 4.10) had similar calculated parameters for the Rh–B interactions ($\rho(r) = 0.12$, $\varepsilon = 0.05$), and these were shown to be definitively 2-centre 2-electron Rh–B bonds.[22]

Interestingly, bond critical points were also located between Rh1 and C(38)–H ($\rho(r) = 0.02$, $\varepsilon = 0.28$) as well as between Rh2 and C(30)–H ($\rho(r) = 0.02$, $\varepsilon = 0.27$), due to the presence of a stabilising C–H agostic interaction between one of the phenyl rings to the adjacent rhodium (i.e. those shown in Figure 4.7, Figure 4.8 and Figure 4.11). These occupy a vacant site approximately trans to the Rh–B bonds. Although the DPEphos ligand does not use the ether group to coordinate, it was proposed that the shorter than expected Rh···O distances are likely due to the DPEphos ligand orientating itself to accommodate these stabilising Rh···H–C agostic interactions. The Rh1–C38 and Rh2–C30 distances of 2.997(5) Å and 2.968(3) Å shown in Figure 4.8 are smaller than the sum of the van der Waals radii of rhodium and carbon (4.21 Å),[24] and can be considered to be

within the range known for phenyl C–H agostics to transition metals. For example, Kubas and co-workers reported distances of 2.89(6) Å and 2.98(6) Å for the phenyl agostic interactions in $[Mn(Ph_2P(CH_2)_2PPh_2)_2(CO)][BAr^F_4]$ (Figure 4.12),[25] where the sum of the van der Waals radii for manganese and hydrogen is 3.65 Å.[24] This type of interaction has also been observed in Sabo-Etienne's ruthenium complex $[Ru(P^iPr_3)_2(H)(H_2)(ortho\text{-}C_6H_5\text{-}C_5H_4N)[BAr^F_4]$ (Figure 4.12) whereby a Ru···H–C distance of 1.924(33) Å was reported.[26]

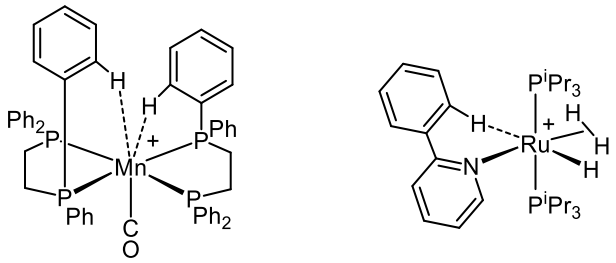


Figure 4.12 Left: Structure of Kubas's $[Mn(Ph_2P(CH_2)_2PPh_2)_2(CO)][BAr^F_4]$. Right: Structure of Sabo-Etienne's $[Ru(P^iPr_3)_2(H)(H_2)(ortho\text{-}C_6H_5\text{-}C_5H_4N)[BAr^F_4]$. $[BAr^F_4]^-$ anions not shown for clarity.

Alongside the crystal structure determination and computational information, the formation of single crystals of **15-[Al(O^{t}Bu^F)$_4$]** allowed for ESI-MS and NMR spectroscopic data of this complex to be acquired, though this material consistently contained some 5% of $[\{Rh(\kappa^2\text{-P,P-DPEphos})\}_2(\mu\text{-H})(\mu\text{-}H_2BNMeH)][Al(O^tBu^F)_4]$ (**14-[Al(O^{t}Bu^F)$_4$]**), pentane solvent and $(H_2BNMeH)_n$ in the bulk. ESI-MS showed that the major peak corresponded to *m/z* 1338.33 (calculated *m/z* 1338.22 for the $[\{Rh(\kappa^2\text{-P,P-DPEphos})\}_2\{\mu\text{-}(H_2B)_2NMeH\}]^+$ fragment. The $^{31}P\{^1H\}$ NMR spectrum showed four phosphorus environments each of relative integral 1 P – all of which were present during 10 mol% catalysis using **13** (Figure 4.4), at δ 31.7 (dd, $^1J_{RhP}$ 163 Hz, $^2J_{PP}$ 23 Hz), δ 28.8 (dd, $^1J_{RhP}$ 158 Hz, $^2J_{PP}$ 21 Hz), δ 15.7 (ddd, $^1J_{RhP}$ 138 Hz, $^2J_{RhP}$ 102 Hz, $^2J_{PP}$ 23 Hz) and δ 13.0 (ddd, $^1J_{RhP}$ 135 Hz, $^2J_{RhP}$ 102 Hz, $^2J_{PP}$ 21 Hz) (Figure 4.13). These were therefore in agreement with the four phosphorus environments shown in the solid state structure (Figure 4.8). The two signals at δ 15.7 and δ 13.0 indicate the phosphorus environments located along the P–Rh–Rh–P axis, as these both show large $^1J_{RhP}$ and $^2J_{RhP}$ couplings due to their trans orientation to both rhodium centres – the Rh1–Rh2–P4 and Rh2–Rh1–P1 bond angles are 166.53(3)° and 162.59(3) respectively (Figure 4.8). These data additionally confirms the presence

of the Rh–Rh bond.[27] The smaller coupling of ~20 Hz is due to the $^{2}J_{PP}$ interaction with the phosphorus environment that lies cis. The equivalent $^{2}J_{PP}$ coupling is reiterated in the two phosphorus signals downfield at δ 31.7 and δ 28.8, alongside one $^{1}J_{RhP}$ coupling for each phosphorus atom. A second $^{2}J_{RhP}$ is not present, likely due to the Rh1–Rh2–P3 and Rh2–Rh1–P2 bond angles of 93.03(3)° and 95.30(3)° respectively (Figure 4.8), as cis coupling is often small.

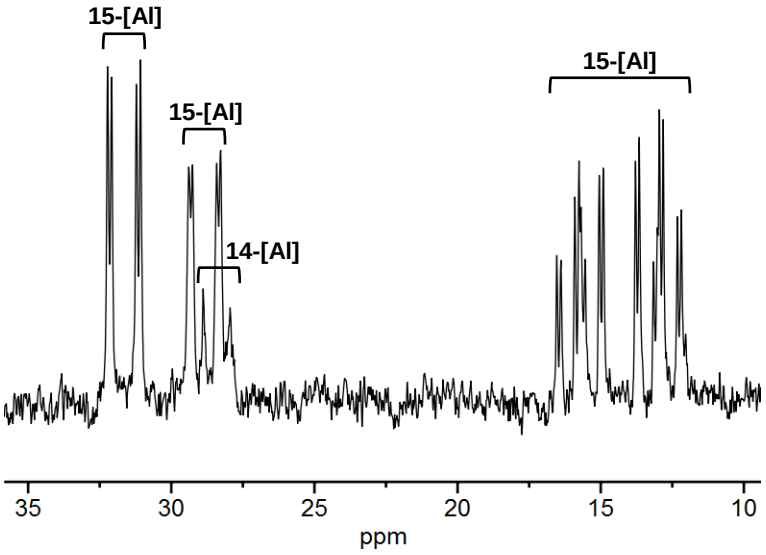


Figure 4.13 $^{31}P\{^{1}H\}$ NMR spectrum of isolated crystals of complex **15-[Al(O^{t}Bu^{F})$_4$]** in CD_2Cl_2 solvent. For simplicity, **15-[Al(O^{t}Bu^{F})$_4$]** is labelled **15-[Al]** and **14-[Al(O^{t}Bu^{F})$_4$]** is labelled **14-[Al]**.

In the ^{11}B NMR spectrum, a broad signal observed at δ 9.4 is attributed to the overlap of two similar boron environments in **15-[Al(O^{t}Bu^{F})$_4$]**, as the $^{31}P\{^{1}H\}$ NMR spectral data at room temperature and solid state structure suggest inequivalent boron environments should be observed. Gaussian NMR calculations performed by Dr Nicholas A. Beattie suggest that the boron environments would resonate at similar values of δ 14.4 and δ 13.3, a Δδ of 4 – 5 ppm between calculated and experimental values, as expected for saturated boron centres. The broad nature could be a result of the η^1 coordination of the bridging Rh···H–B bonds, also observed in η^1 amine borane complexes such as [Rh(κ^2-P,P-Xantphos-Ph)(H)$_2$(η^1-H$_3$B·NMe$_3$)][BAr$^F_4$] (**2-Ph**, Scheme 4.3), as well as the bimetallic complex [{Rh(PCy$_3$)(H)}$_2$(μ-H$_2$BNMe$_3$)$_2$(μ-

$H_3B{\cdot}NMe_3)][BAr^F{}_4]_2$ (Figure 4.14),[27] which contains a similar Rh–B(H)–H···Rh motif to that in **15-[Al(O^{t}Bu^F)$_4$]**.

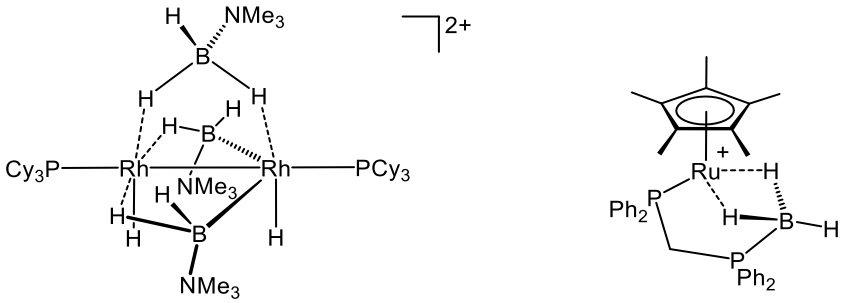


Figure 4.14 Left: Structure of Weller's $[\{Rh(PCy_3)(H)\}_2(\mu\text{-}H_2BNMe_3)_2(\mu\text{-}H_3B{\cdot}NMe_3][BAr^F{}_4]_2$. Right: Structure of Weller's $[Cp^*Ru(\mu^2\text{-}H_3B{\cdot}PPh_2CH_2PPh_2)][PF_6]$. $[BAr^F{}_4]^-$ and $[PF_6]^-$ anions not shown for clarity.

The two bridging Rh···H–B environments in **15-[Al(O^{t}Bu^F)$_4$]** are observed as broad multiplets at δ −8.65 and δ −9.44 in the hydride region of the ^{1}H NMR spectrum, integrating 1 H with respect to each other. These peaks both sharpen to broad doublets (δ −8.65, $^2J_{PH}$ 73.9 Hz and δ −9.44, $^2J_{PH}$ 68.8 Hz) on ^{11}B decoupling (Figure 4.15), indicative of a B–H bond, and the large coupling constants suggest that these agostic Rh···H–B groups lie trans to phosphine ligands.[3, 28] A broad peak at δ 4.64 of relative integral 2 H, which also sharpens on $\{^{11}B\}$ decoupling, suggests coincident terminal B–H environments. These chemical shifts are similar to those reported in $[\{Rh(PCy_3)(H)\}_2(\mu\text{-}H_2BNMe_3)_2(\mu\text{-}H_3B{\cdot}NMe_3][BAr^F{}_4]$ (Figure 4.14), where the terminal B–H signals resonated at δ 5.38 and the bridging Rh···H–B at δ −9.44.[27] Similar data was also found in Weller's $[Cp^*Ru(\mu^2\text{-}H_3B{\cdot}PPh_2CH_2PPh_2)][PF_6]$ complex (Figure 4.14),[10] in which chemical shift values for the terminal and bridging B−H signals were reported at δ 5.12 and δ −9.08 respectively by ^{1}H NMR spectroscopy.

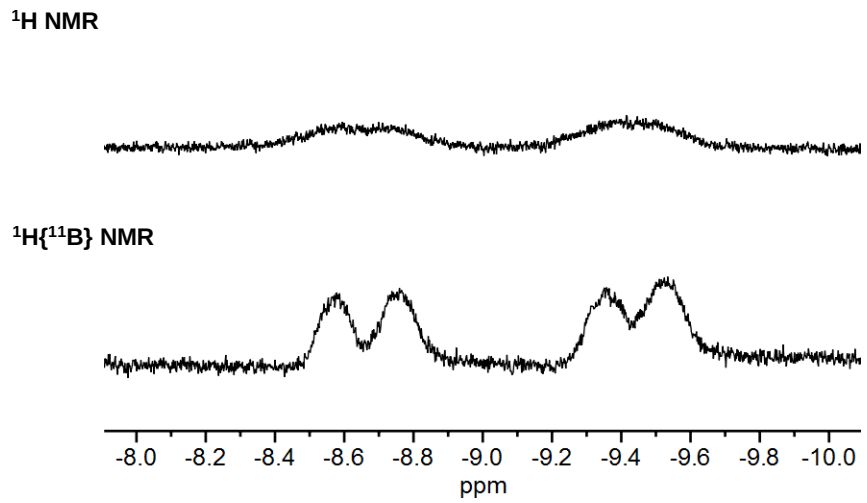


Figure 4.15 Hydride region of the ^{1}H NMR spectrum (top) and ^{1}H{^{11}B} NMR (bottom) of complex **15-[Al(O^{t}Bu^{F})$_4$]** in CD_2Cl_2 solvent.

Other diagnostic features of **15-[Al(O^{t}Bu^{F})$_4$]** are the Rh···H–C phenyl agostic interactions which stabilise each rhodium centre. Sabo-Etienne's [Ru(P^{i}Pr$_3$)$_2$(H)(H$_2$)(ortho-C$_6$H$_5$-C$_5$H$_4$N)[BAr$^{F}_4$] complex (Figure 4.12),[26, 29] with a crystallographically confirmed phenyl agostic interaction, provided a limiting low temperature ^{1}H NMR spectrum in which this proton environment could be observed at a chemical shift of δ 4.14 with relative integral 1 H. In comparison, Kubas's manganese complex (Figure 4.12) remained fluxional even at 198 K, however a resonance significantly upfield shifted relative to the other phenyl protons was observed at δ 6.16 (relative integral 8 H) – this resonance attributed to the phenyl agostic interaction measured in the solid state.[25] For comparison, the ^{1}H NMR spectrum of **15-[Al(O^{t}Bu^{F})$_4$]** at 298 K shows a broad resonance at δ 3.94 of relative integral 2 H which may indicate the phenyl agostic interactions, the chemical shift in particular agreement with Sabo-Etienne's findings in the {Ru(P^{i}Pr$_3$)}$^{+}$ system detailed in Figure 4.12.[26, 29]

With these data, all of which support the proposed structure from X-ray crystallography, two valence extremes can be proposed for **15-[Al(O^{t}Bu^{F})$_4$]**, shown in Figure 4.16. Proposal (a) is a bimetallic base stabilised amidodiboryl complex in which a formally negatively charged nitrogen provides base stabilisation to two boron centres engaging with a Rh(II) centre – a formal positive charge is therefore associated with each rhodium, along with a Rh–Rh bond, to account for the

diamagnetism. The second valence structure, (b), can be described as a bimetallic amidodiboryl with a mixed valent Rh(I)–Rh(III) core, again with a negative charge formally at nitrogen, however the Rh(III) centre is formally 2+, with a dative bond operating from the Rh(I) centre to the Rh(III).

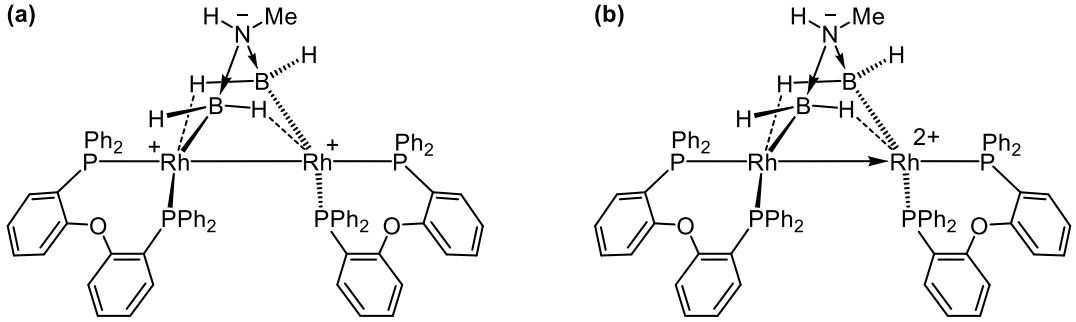


Figure 4.16 Possible bonding schemes for **15-[Al(O^{t}Bu^F)$_4$]**. (a) A base stabilised amidodiboryl with a Rh(II)–Rh(II) core. (b) A base stabilised amidodiboryl with a Rh(I)–Rh(III) core. The phenyl agostic Rh···H–C interactions and [Al(O^{t}Bu^F)$_4$]$^-$ anions are not shown for clarity.

Both of these two valence structures contain a Rh–Rh bond, as suggested by the solid state structure of **15-[Al(O^{t}Bu^F)$_4$]**, and confirmed by the DFT calculations as well as the trans $^2J_{RhP}$ coupling constants measured by $^{31}P\{^1H\}$ NMR spectroscopy which can only operate if a covalent Rh–Rh interaction is present. Mixed valent Rh(I)–Rh(III) complexes have been shown to contain dative Rh–Rh bonds,[30-31] and Rh(II)–Rh(II) motifs contain electronic structures which allow a Rh–Rh bond.[30] Due to the approximate symmetric structure of **15-[Al(O^{t}Bu^F)$_4$]**, with a formal electron count of 18 per rhodium centre (including the phenyl C–H···Rh agostic contributions and Rh–Rh bond) a formal Rh(II)–Rh(II) core seems most sensible, hence **15-[Al(O^{t}Bu^F)$_4$]** is best described by a bridging μ-[(H$_2$B)$_2$NMeH]$^-$ fragment across two Rh(II) metal centres, i.e. formulation (a).

4.5.3 Conclusions: formation of {Rh(DPEphos)}$^+$ complexes from H$_3$B·NMeH$_2$

The formation of complexes **14** and **15** and their associated NMR data shows that these complexes can be observed during the reaction of H$_3$B·NMeH$_2$ using precatalyst **13** at 10 mol% catalyst loading. Bridging aminoborane complex **14**, [{Rh(κ^2-P,P-DPEphos)}$_2$(μ-H)(μ-H$_2$BNMeH)][BAr$^F_4$], likely forms due to initial formation of amine borane complex [Rh(κ^2-P,P-DPEphos)(η^2-H$_3$B·NMeH$_2$)][BAr$^F_4$]. This can then react with free NMeH$_2$, for which there is literature precedent (Scheme 4.5).[11] Furthermore, complex **15**, [{Rh(κ^2-P,P-DPEphos)}$_2${μ-

$(H_2B)_2NMeH\}]^+$, contains an unusual bridging μ-$(H_2B)_2NMeH$ motif which may form via BH_3 addition to **14**, with loss of H_2, or alternatively **15** may be product of chain termination to form $(H_2BNMeH)_n$ through a B–N bond cleavage event. From these results it appears that in catalysis, **14** initially forms, over time converting to **15**. Noteworthy however is that in 10 mol% catalysis using **13**, **14** is also the dominant species at the end of dehydrocoupling (Figure 4.4) The nature of these complexes in dehydropolymerisation is further explored in Chapter 5.

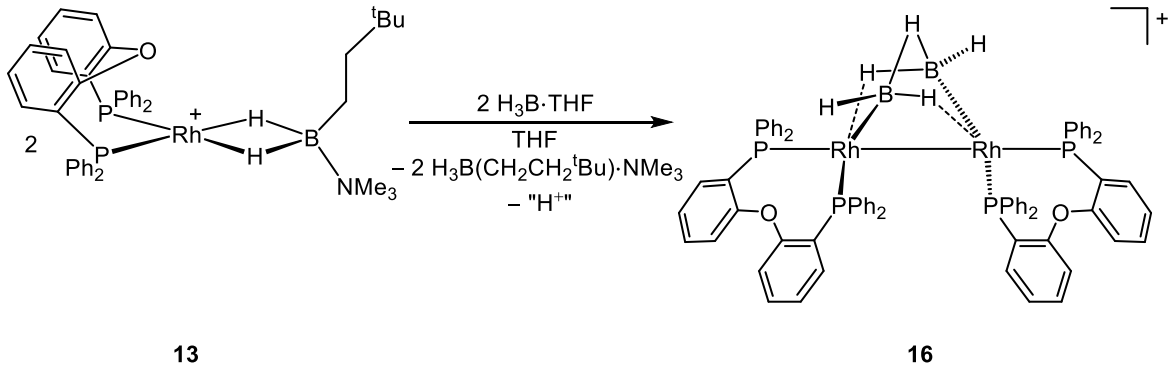
4.6 Reactivity of the $\{Rh(DPEphos)\}^+$ fragment with BH_3 or $NMeH_2$

The ESI-MS data obtained from the reaction mixture of $H_3B{\cdot}NMeH_2$ with 10 mol% **13** (Figure 4.5) suggested that a monocationic bimetallic species, $[\{Rh(DPEphos)\}_2(B_2H_5)]^+$, was formed also during catalysis over 2 hours. The lack of nitrogen present in this boron-containing species suggested that B–N bond cleavage processes may be in operation. This information, in addition to the detailed studies undertaken on the Xantphos-^{i}Pr system using borane or amine in Section 2.6, led to the investigation of the $\{Rh(DPEphos)\}^+$ fragment with both BH_3 and $NMeH_2$ reagents.

*4.6.1 Formation of [{Rh(DPEphos)}$_2$(B$_2$H$_5$)][BAr$^F{}_4$] (**16**)*

The $[\{Rh(DPEphos)\}_2(B_2H_5)]^+$ species suggested by ESI-MS analysis of the reaction mixture of $H_3B{\cdot}NMeH_2$ with 10 mol% **13** (Figure 4.5) was probed by the addition of 1 equivalent of $H_3B{\cdot}THF$ to solution of complex **13** in THF solvent (Scheme 4.7). On time of mixing, the purple solution turned orange and the reaction mixture was analysed by ESI-MS and NMR spectroscopy. ESI-MS of the resultant solution showed a major peak at *m/z* 1309.16 for the $[\{Rh(DPEphos)\}_2(B_2H_5)]^+$ fragment (calculated *m/z* 1309.19), with the correct isotope pattern. The corresponding $^{31}P\{^1H\}$ NMR spectrum showed that the major phosphorus environments present resonated at δ 32.0 and δ 17.5, integrating 1:1 with respect to one another – contributing to 90% of phosphorus in the sample. The former resonance is a doublet with a $^1J_{RhP}$ value of 151 Hz, whilst for the latter, broader, resonance a $^1J_{RhP}$ of ca. 120 Hz could be measured. The hydride region in the ^1H NMR spectrum showed one multiplet at δ −8.14, which sharpened on ^{11}B decoupling, indicating the

presence of a Rh···H–B interaction. In comparison, the ^{11}B NMR spectrum showed many boron environments, and was therefore difficult to interpret with certainty. Free $H_2B(CH_2CH_2{}^tBu)\cdot NMe_3$ was present at δ −0.9 (t, $^1J_{BH}$ 96 Hz), alongside peaks due to unassigned boron species at δ 8.9 (t, $^1J_{BH}$ 133 Hz) and δ −7.6 (q, $^1J_{BH}$ 100 Hz). A small, broad resonance at δ 12.9 may indicate a Rh···B environment. Attempts to crystallise the organometallic species formed by this reaction using $[BAr^F{}_4]^-$ or $[Al(O^tBu^F)_4]^-$ counterions was unsuccessful. However these data, in particular that obtained from the ^{31}P{^{1}H} and ^{1}H NMR spectra, shows similarities to that of $[\{Rh(\kappa^2\text{-P,P-DPEphos})\}_2\{\mu\text{-}(H_2B)_2NMeH\}][Al(O^tBu^F)_4]$ (**15-[Al(O^{t}Bu^F)$_4$]**), therefore the tentative structure of $[\{Rh(\kappa^2\text{-P,P-DPEphos})\}_2(\mu\text{-}B_2H_5)]^+$ may be analogous (complex **16**, Scheme 4.7).

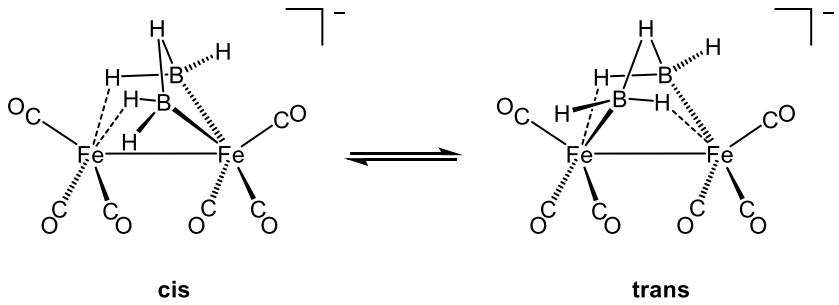


13 **16**

Scheme 4.7 Synthesis and proposed structure of $[\{Rh(\kappa^2\text{-P,P-DPEphos})\}_2(\mu\text{-}B_2H_5)][BAr^F{}_4]$ (**16**). $[BAr^F{}_4]^-$ anions not shown for clarity.

The similar NMR data for **15** and **16** suggests that the B_2H_5 moiety sits symmetrically across the $\{Rh(DPEphos)\}_2^+$ fragment, likewise to the orientation of the $(H_2B)_2NMeH$ fragment in **15-[Al(O^{t}Bu^F)$_4$]**. In this instance, the $[NMeH]^-$ group in **15-[Al(O^{t}Bu^F)$_4$]** has been replaced by H^- in **16**, hence leading to C_2 symmetry in **16** and therefore half the number of phosphorus and hydride environments relative to **15-[Al(O^{t}Bu^F)$_4$]**. Bimetallic B_2H_5 complexes have previously been reported,[32-38] and a similar structure to that proposed for **16** was suggested by Fehlner and co-workers: $[B_2H_5Fe_2(CO)_6][AsPh_4]$ (Scheme 4.8).[32] At 20°C, the diiron complex showed 3 resonances in the ^{1}H NMR spectrum (CD_2Cl_2 solvent) for the B_2H_5 fragment at δ 2.2 (2 H, terminal B–H), δ −2.6 (1 H, bridging B–H–B) and δ −14.2 (2 H, bridging Fe···H–B). The ^{11}B NMR data at 20°C showed a triplet of doublets at δ −17.4, with $^1J_{BH}$ coupling constants of 105 Hz and 25 Hz.

The smaller coupling was attributed to the bridging B–H–B proton, and the larger coupling proposed to be the average of the terminal B–H and the bridging Fe···H–B protons due to fluxionality between "cis" and "trans" forms of $[B_2H_5Fe_2(CO)_6]^-$ (Scheme 4.8). Comparing Fehlner's findings to the in situ ^{11}B NMR data of **16** may suggest that the triplet seen at δ 8.9 ($^1J_{BH}$ 133 Hz) is due to coupling of boron to an average of both terminal and bridging protons in the Rh–BH_2 fragment, whilst coupling to the bridging B–H–B proton is suggested to be small and lost in the line width. Due to the protio THF solvent used for the in situ ^{1}H NMR data for **16**, evidence for the terminal B–H and bridging B–H–B groups could not be obtained, therefore it is unknown whether **16** displays similar fluxionality to $[B_2H_5Fe_2(CO)_6]^-$ as shown in Scheme 4.8. However, given that **15-[Al(O^{t}Bu^F)$_4$]** does not appear fluxional in solution, and its structure is related to **16**, it may be that **16** is non-fluxional as well. Fehlner later reported the synthesis of {Cp*IrH}$_2$(μ-H)(B_2H_5) in 2000.[37] ^{11}B NMR spectroscopy of the bimetallic iridium complex showed two boron environments at δ 14.2 (d, $^1J_{BH}$ 130 Hz) and δ −14.6 (apparent t), within the range of the chemical shifts reported for the possible ^{11}B environments in complex **16**, further agreeing with the formulation of **16** as [{Rh(κ^2-P,P-DPEphos)}$_2$(μ-B_2H_5)][BAr^F_4] in Scheme 4.7.



Scheme 4.8 Fluxional process between "cis" and "trans" isomers of Fehlner's $[B_2H_5Fe_2(CO)_6]^-$ complex. $[AsPh_4]^+$ cation not shown for clarity.

*4.6.2 Formation of [Rh(DPEphos)(H)$_2$(NMeH$_2$)$_x$][BAr$^F_4$] (x = 1 or 2, **17**)*

Given the proposed formation of borane complex **16** in the dehydrocoupling of $H_3B{\cdot}NMeH_2$, amine complexes of the {Rh(DPEphos)}$^+$ fragment were also investigated – since free BH_3 is formed during the reaction, $NMeH_2$ must also be present. Hydrogenation of a 1,2-$C_6H_4F_2$ solution of [Rh(κ^2-P,P-DPEphos)(NBD)][BAr^F_4] (**12**) in the presence of 10 equivalents of $NMeH_2$ (as a

1.0 M solution in THF) led to the formation a new organometallic complex as determined by NMR spectroscopy. This in situ spectroscopic data showed sharp proton environments in the hydride region of the ^{1}H NMR spectrum, at δ −9.61 and δ −16.61, each integrating 1 H with respect to one another (Figure 4.17). Both resonances showed complicated splitting patterns: the downfield Rh–H resonance showed coupling indicative of a doublet of doublets of doublets of doublets (dddd, *J* 182 Hz, 24 Hz, 18 Hz, 5 Hz), whilst the upfield resonance appeared to be a multiplet, of which the individual couplings could not be delineated. On ^{31}P decoupling (Figure 4.17), the dddd collapsed to a doublet of doublets (*J* 18 Hz, 5 Hz), whilst the peak at δ −16.61 collapsed to a broad doublet (*J* 18 Hz).

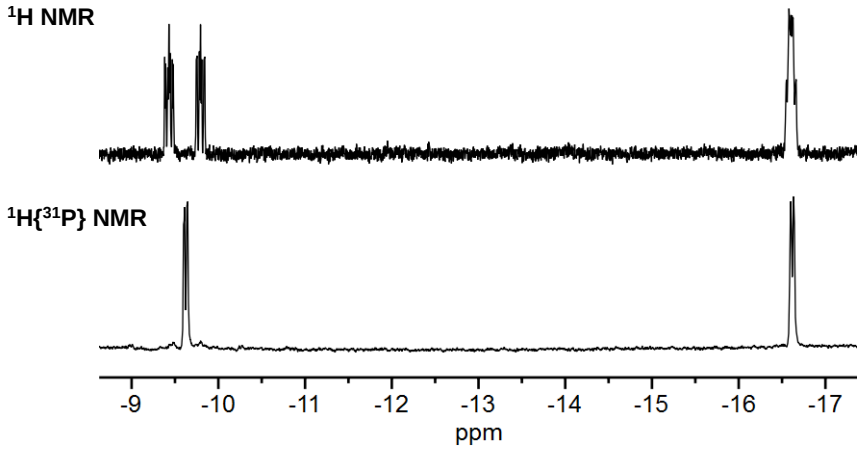


Figure 4.17 Hydride region of the ^{1}H NMR spectrum (top) and ^{1}H{^{31}P} NMR (bottom) of complex **17** in 1,2-$C_6H_4F_2$ solvent.

This suggests that the Rh–H group responsible for the dddd splitting pattern couples to two phosphorus environments. A large coupling constant of 182 Hz is indicative of a hydride trans to phosphorus, whilst the smaller $^{2}J_{PH}$ value of 24 Hz is within that expected of coupling to a phosphorus atom that lies cis.[3, 28] On the other hand, the Rh–H resonance at δ −16.61 does not show an analogous large coupling constant, therefore likely lies cis to both phosphorus environments. In the ^{31}P{^{1}H} NMR spectrum two doublets were observed at δ 52.2 ($^{1}J_{RhP}$ 137 Hz) and δ 23.8 ($^{1}J_{RhP}$ 86 Hz) – the smaller coupling indicative of a ^{31}P environment trans to a strong trans influence ligand, such as a hydride.[3, 28] Unfortunately, complex **17** could not be isolated despite

repeated attempts, and ESI-MS of the reaction mixture was intractable to analysis. Due to the use of excess amine, the number of amine molecules bound to the metal centre could not be confirmed, however two proposed structures for complex **17**, with differing numbers of amine ligands were proposed (Figure 4.18). Importantly, both show the required inequivalent, phosphine environments, with one hydride trans to a phosphorus. Complex **fac-17** (Figure 4.18) has the DPEphos ligand coordinated in a fac κ^3-P,O,P manner, with the second hydride trans to the DPEphos ether group, and the final coordination site filled by $NMeH_2$. The alternative structure **cis-17** suggests a κ^2-P,P-DPEphos motif, in which two $NMeH_2$ molecules bind to the metal centre. Unfortunately, the current data cannot distinguish between these two structures.

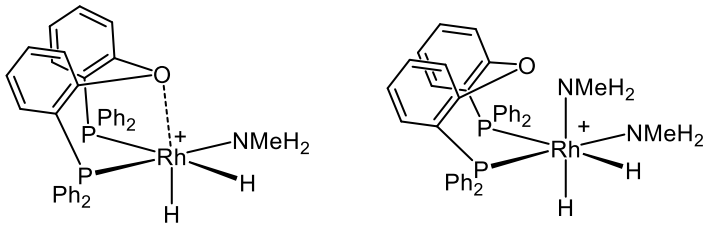
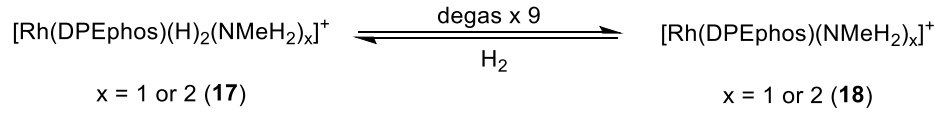


Figure 4.18 Possible structures for $[Rh(DPEphos)(H)_2(NMeH_2)_x][BAr^F{}_4]$ (x = 1 or 2, **17**). Left: fac-$[Rh(\kappa^3\text{-P,O,P-DPEphos})(H)_2(NMeH_2)][BAr^F{}_4]$ (**fac-17**). Right: cis-$[Rh(\kappa^2\text{-P,P-DPEphos})(H)_2(NMeH_2)_2][BAr^F{}_4]$ (**cis-17**). $[BAr^F{}_4]^-$ anions not shown for clarity.

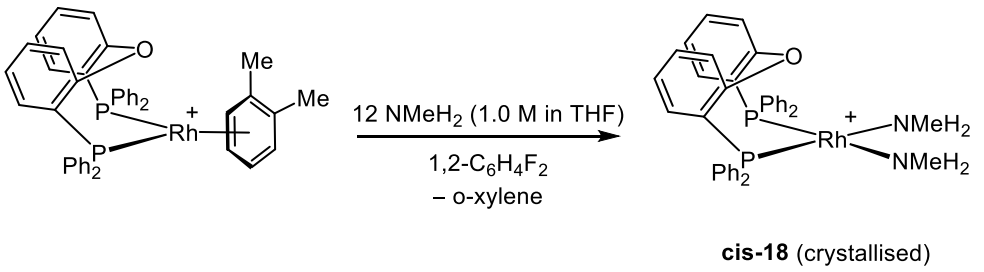
On degassing this reaction mixture containing **17** and backfilling the NMR tube with argon, a new species (**18**) appeared in the $^{31}P\{^1H\}$ NMR spectrum at δ 39.7 (d, $^1J_{RhP}$ 180 Hz). In addition, a decrease in intensity of the hydride signals relative to the $[BAr^F{}_4]^-$ anion was observed in the ^1H NMR spectrum, alongside no new hydride resonances. The coupling constant of 180 Hz is indicative of equivalent DPEphos phosphorus environments bound to a Rh(I) centre,[12] and therefore this new species was proposed to be the product of H_2 loss from **17**. However, even on degassing the solution nine times, half of the sample remained to be dihydride complex **17** by $^{31}P\{^1H\}$ NMR spectroscopy. Addition of 4 bar H_2 reformed **17**, suggesting an equilibrium dependent on H_2 pressure (Scheme 4.9). The identity of the new complex, **18**, is examined in Section 4.6.3.



Scheme 4.9 Degassing of $[Rh(DPEphos)(H)_2(NMeH_2)_x][BAr^F{}_4]$ (x = 1 or 2, **17**) to form $[Rh(DPEphos)(NMeH_2)_x][BAr^F{}_4]$ (x = 1 or 2, **18**), and addition of H_2 to reform **17** in 1,2-$C_6H_4F_2$ solvent. $[BAr^F{}_4]^-$ anions not shown for clarity.

*4.6.3 Formation of [Rh(DPEphos)(NMeH2)x][BArF4] (x = 1 or 2, **18**)*

Despite thorough degassing of a 1,2-$C_6H_4F_2$ solution of $[Rh(DPEphos)(H)_2(NMeH_2)_x][BAr^F{}_4]$ (x = 1 or 2, **17**), it was apparent that even small amounts of H_2 present in the reaction mixture led to complications in cleanly forming Rh(I) complex **18** in situ, therefore a different route without the use of H_2 was developed. 12 equivalents of $NMeH_2$ in THF (0.15 mL of a 1.0 M solution) was added to the known complex $[Rh(\kappa^2\text{-P,P-DPEphos})(\eta^6\text{-ortho-xylene})][BAr^F{}_4]$,[39] in 1,2-$C_6H_4F_2$ solvent (Scheme 4.10). NMR spectroscopic analysis of the reaction mixture indicated the formation of a clean doublet in the $^{31}P\{^1H\}$ NMR spectrum at δ 39.7 (d, $^1J_{RhP}$ 180 Hz), as previously seen when a solution of the proposed dihydride complex **17** was degassed and placed under an argon atmosphere. The intense, broad signals due to the THF-based $NMeH_2$ reagent do not allow for interrogation of the NH or NMe groups of the bound amine signals in the in situ ^1H NMR spectrum. Therefore isolation of this complex as a solid was attempted.



Scheme 4.10 Addition of $NMeH_2$ to $[Rh(\kappa^2\text{-P,P-DPEphos})(\eta^6\text{-ortho-xylene})][BAr^F{}_4]$ to form amine complex $[Rh(\kappa^2\text{-P,P-DPEphos})(NMeH_2)_2][BAr^F{}_4]$ (**cis-18**) which was the crystallographically characterised component of $[Rh(\kappa^2\text{-P,P-DPEphos})(NMeH_2)_x][BAr^F{}_4]$ (x = 1 or 2, **18**) by single crystal X-ray diffraction studies. $[BAr^F{}_4]^-$ anions not shown for clarity.

A very small amount of complex **18** in the form of an oily orange solid (15% yield) could be obtained by layering a 1,2-$C_6H_4F_2$ solution of **18** with pentane at room temperature. A single

crystal could be picked from the resultant oily mixture, and studied by single crystal X-ray diffraction. The solid state structure shown in Figure 4.19 suggests that the formulation of **18** is [Rh(κ^2-P,P-DPEphos)($NMeH_2$)$_2$][BAr^F_4] (**cis-18**), containing two $NMeH_2$ molecules bound to the approximately square planar rhodium centre with Rh–N distances of 2.162(3) Å and 2.176(2) Å. These values are similar to the Rh–N distance in complex **6**, [Rh(κ^3-P,O,P-Xantphos-^{i}Pr)(H)$_2$($NMeH_2$)][BAr^F_4], of 2.242(3) Å (Figure 2.10). The long Rh···O distance of 3.667(3) Å is consistent with κ^2-P,P coordination of the DPEphos ligand, as also seen in complex **13** (Figure 4.2), and similar to the M···O (M = Rh or Pd) distances in related complexes [Rh(κ^2-P,P-DPEphos)($OCMe_2$)][$CB_{11}H_6Cl_6$],[4] and [Pd(κ^2-P,P-DPEphos)($NCMe)_2$][BF_4]$_2$,[40] of 3.562(1) Å and 3.527 Å respectively. In comparison, the van der Waals radii for oxygen, rhodium and palladium are 1.50 Å, 2.44 Å and 2.15 Å respectively, which may indicate a slight Rh···O interaction in all cases, though this may simply be a result of the restricted geometry imposed by κ^2-P,P coordination of the DPEphos ligand.

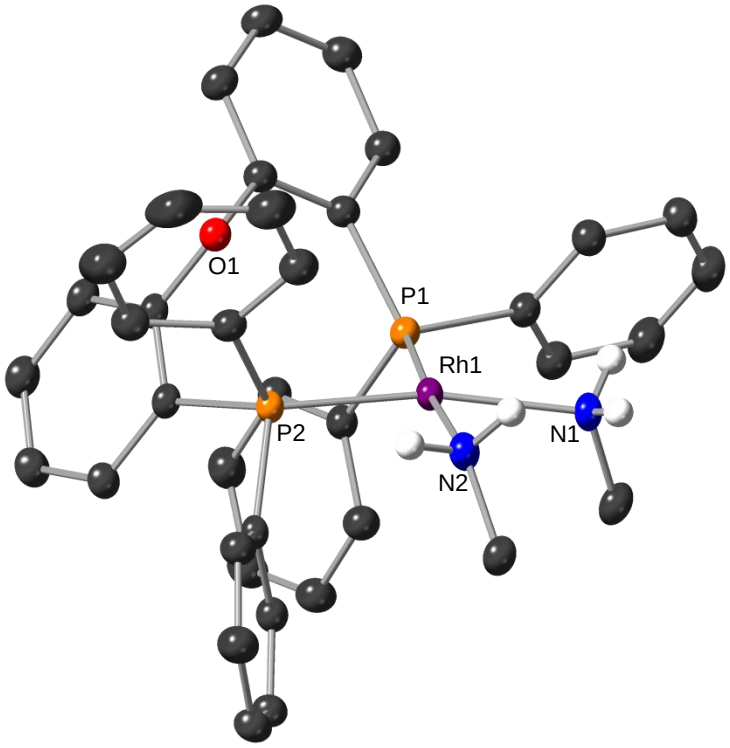
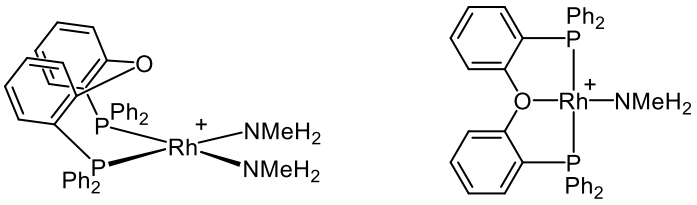


Figure 4.19 Crystal structure of the cationic portion of [Rh(κ^2-P,P-DPEphos)($NMeH_2$)$_2$][BAr^F_4] (**cis-18**). Displacement ellipsoids are drawn at the 30% probability level. C-bound H atoms are not shown for clarity. Selected bond lengths (Å) and angles (°): Rh1–P1, 2.2392(7); Rh1–P2, 2.2218(7); Rh1–O1, 3.667(3); Rh1–N1, 2.162(3); Rh1–N2, 2.176(2); P1–Rh1–P2, 97.22(3).

Surprisingly, NMR spectroscopy of the bulk isolated oily material suggested an alternative structure for complex **18** in solution. In CD_2Cl_2 solvent, the $^{31}P\{^1H\}$ NMR spectrum showed a clean doublet at δ 39.5 (d, $^1J_{RhP}$ 182 Hz), similar to the in situ reaction mixture in 1,2-$C_6H_4F_2$/THF solvent. However, this ^1H NMR spectrum of the isolated oily material showed that peaks responsible for the NMe groups and NH groups could be observed at δ 2.04 and δ 1.75 respectively, with integrals 3.6 H and 2.2 H relative to the $[BAr^F_4]^-$ anion. These relative integrals instead suggest that the bulk solid more likely contains a single $NMeH_2$ molecule per rhodium centre, rather than two amines as seen in the crystal structure (Figure 4.19). Therefore a [Rh(κ^3-P,O,P-DPEphos)($NMeH_2$)][BAr^F_4] structure for complex **18** (**trans-18**) cannot be discounted (Figure 4.20). Precedence for this type of rhodium monoamine complex with a κ^3-bound POP-type ligand has been reported in work by Hartwig and co-workers, in the formation of [Rh(κ^3-P,O,P-Xantphos-NEt_2)($NH_2CH_2CH(Ph)CH_2CHCH_2$)][BF_4].[41] Unfortunately ESI-MS studies were unable to further provide insight on the [Rh(DPEphos)($NMeH_2$)$_x$][BAr^F_4] (x = 1 or 2) system, as the major peak was assigned to [Rh(DPEphos)(N_2)]$^+$ (*m/z* 669.06, calculated *m/z* 669.07), formed due to the presence of N_2 gas in the flow gas.[42]



cis-18 **trans-18**

Figure 4.20 Possible structures for [Rh(κ^2-P,P-DPEphos)($NMeH_2$)$_x$][BAr^F_4] (x = 1 or 2, **18**). Left: [Rh(κ^2-P,P-DPEphos)($NMeH_2$)$_2$][BAr^F_4] (**cis-18**). Right: [Rh(κ^3-P,O,P-DPEphos)($NMeH_2$)][BAr^F_4] (**trans-18**). [BAr^F_4]$^-$ anions not shown for clarity.

4.6.4 Conclusions: formation of {Rh(DPEphos)}$^+$ complexes from BH_3 or $NMeH_2$

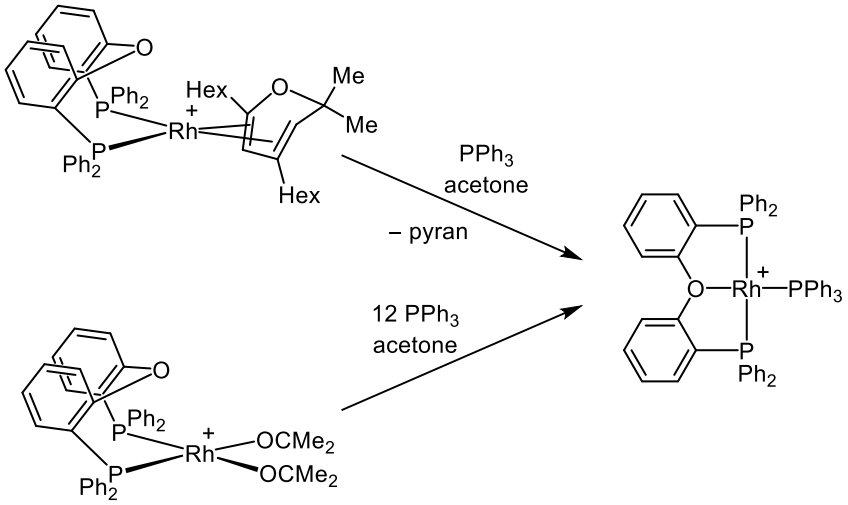
The postulated formation of [{Rh(κ^2-P,P-DPEphos)}$_2$(μ-B_2H_5)][BAr^F_4] (**16**) using a BH_3 source and [Rh(DPEphos)$(H)_2$($NMeH_2$)$_x$][BAr^F_4] (x = 1 or 2, **17**) or [Rh(DPEphos)($NMeH_2$)$_x$][BAr^F_4] (x = 1 or 2, **18**) using $NMeH_2$ has allowed for analysis of the complexes that may result if B–N cleavage of $H_3B{\cdot}NMeH_2$ takes place during catalysis. Complex **16** was showed to form in the

reaction of $H_3B{\cdot}NMeH_2$ with 10 mol% **13** by ESI-MS studies, and may be present in the $^{31}P\{^1H\}$ NMR spectrum of the reaction mixture, however its resonances would overlap with those of higher intensity **15**. On the other hand, **17** and **18** could not be identified by NMR spectroscopy or ESI-MS. Therefore, if formed during catalysis, **17** and **18** are likely transient species dominated by the presence of **14**, **15** and **16**. The implication of each of these complexes in $H_3B{\cdot}NMeH_2$ dehydropolymerisation will be discussed in Chapter 5.

4.7 Catalyst poisoning: [Rh(DPEphos)(PPh_3)][BAr^F_4]

In Chapter 2 (Section 2.11), the triphenylphosphine complex [Rh(κ^3-P,O,P-Xantphos-^{i}Pr)(PPh_3)][BAr^F_4] (**10**) was synthesised. There it was shown that excess PPh_3 can be used to suppress homogeneous catalysis in molecular weight versus conversion experiments, or utilised sub-stoichiometrically in testing for heterogeneous behaviour in the Xantphos-^{i}Pr system (Chapter 3).[43]

The DPEphos analogue to complex **10**, [Rh(κ^3-P,O,P-DPEphos)(PPh_3)][BAr^F_4], was in fact reported by Weller and co-workers in 2018.[12] Addition of 1.6 equivalents of PPh_3 to the pyran complex [Rh(κ^2-P,P-DPEphos)($\eta^2\eta^2$-2,2-methyl-4,6-n-hexyl-α-pyran)][BAr^F_4] in acetone solvent displaced the organic pyran molecule, forming [Rh(κ^3-P,O,P-DPEphos)(PPh_3)][BAr^F_4] as the sole organometallic product (Scheme 4.11). [Rh(κ^3-P,O,P-DPEphos)(PPh_3)][BAr^F_4] could also be independently synthesised from the addition of excess PPh_3 to in situ formed [Rh(κ^2-P,P-DPEphos)($OCMe_2$)$_2$][BAr^F_4] (Scheme 4.11).



Scheme 4.11 Previously reported synthesis of [Rh(κ^3-P,O,P-DPEphos)(PPh_3)][BAr^F_4] from PPh_3 addition to [Rh(κ^2-P,P-DPEphos)(η^{2}η^2-2,2-methyl-4,6-n-hexyl-α-pyran)][BAr^F_4] or [Rh(κ^2-P,P-DPEphos)($OCMe_2$)$_2$][BAr^F_4]. Pyran = 2,2-methyl-4,6-n-hexyl-α-pyran. [BAr^F_4]$^-$ anions not shown for clarity.

The ability for PPh_3 to displace both pyran and acetone in Scheme 4.11 hence suggested that PPh_3 was a suitable reagent to carry out $(H_2BNMeH)_n$ versus conversion experiments and heterogeneous catalysis testing for the DPEphos system in Chapter 5.

4.8 Summary

In this Chapter, a Rh(I) DPEphos complex containing η^2 bound $H_2B(CH_2CH_2{}^tBu)\cdot NMe_3$, [Rh(κ^2-P,P-DPEphos)(η^2-$H_2B(CH_2CH_2{}^tBu)\cdot NMe_3$][$BAr^F_4$] (**13**), was synthesised and found to be a suitable precatalyst for the dehydrocoupling of $H_3B\cdot NMeH_2$ at 10 mol% catalyst loading. Speciation experiments suggest that organometallic complexes [{Rh(κ^2-P,P-DPEphos)}$_2$(μ-H)(μ-H_2BNMeH][BAr^F_4] (**14**) and [{Rh(κ^2-P,P-DPEphos)}$_2${μ-$(H_2B)_2NMeH$}][BAr^F_4] (**15**) may be involved in the dehydrocoupling mechanism, whilst borane-based complex [{Rh(κ^2-P,P-DPEphos)}$_2$(μ-B_2H_5)][BAr^F_4] (**16**) and amine-based complexes [Rh(DPEphos)$(H)_2(NMeH_2)_x$][BAr^F_4] (x = 1 or 2, **17**) and [Rh(DPEphos)$(NMeH_2)_x$][BAr^F_4] (x = 1 or 2, **18**) could also play a role, though could not be fully observed in 10 mol% catalysis by the detection limit of NMR spectroscopy. For example the chemical shifts of the phosphorus environments in **16** appear to overlap with those of **15**. Complex **14** is only the second example of a

bimetallic bridging aminoborane complex supported by a POP-type ligand.[17] **15-[Al(O^{t}Bu^F)$_4$]**, a proposed bimetallic base stabilised amidodiboryl complex for which there is little precedence in the literature, has been characterised by single crystal X-ray diffraction combined with computational analysis. Further exploration of the dehydropolymerisation ability of precatalyst **13** will be discussed in Chapter 5, as well as how complexes **14**, **15**, **16**, **17** and **18** may be relevant to the catalytic process.

4.9 References

1. Johnson, H. C.; Leitao, E. M.; Whittell, G. R.; Manners, I.; Lloyd-Jones, G. C.; Weller, A. S., Mechanistic Studies of the Dehydrocoupling and Dehydropolymerization of Amine-Boranes Using a [Rh(Xantphos)]$^+$ Catalyst. *J. Am. Chem. Soc.* **2014,** *136* (25), 9078-9093.
2. Kranenburg, M.; van der Burgt, Y. E. M.; Kamer, P. C. J.; van Leeuwen, P. W. N. M.; Goubitz, K.; Fraanje, J., New Diphosphine Ligands Based on Heterocyclic Aromatics Inducing Very High Regioselectivity in Rhodium-Catalyzed Hydroformylation: Effect of the Bite Angle. *Organometallics* **1995,** *14* (6), 3081-3089.
3. Dallanegra, R.; Chaplin, A. B.; Weller, A. S., Rhodium Cyclopentyl Phosphine Complexes of Wide-Bite-Angle Ligands DPEphos and Xantphos. *Organometallics* **2012,** *31* (7), 2720-2728.
4. Moxham, G. L.; Randell-Sly, H. E.; Brayshaw, S. K.; Woodward, R. L.; Weller, A. S.; Willis, M. C., A Second-Generation Catalyst for Intermolecular Hydroacylation of Alkenes and Alkynes Using β-S-Substituted Aldehydes: The Role of a Hemilabile P-O-P Ligand. *Angew. Chem. Int. Ed.* **2006,** *45* (45), 7618-7622.
5. Johnson, H. C.; Robertson, A. P. M.; Chaplin, A. B.; Sewell, L. J.; Thompson, A. L.; Haddow, M. F.; Manners, I.; Weller, A. S., Catching the First Oligomerization Event in the Catalytic Formation of Polyaminoboranes: $H_3B{\cdot}NMeHBH_2{\cdot}NMeH_2$ Bound to Iridium. *J. Am. Chem. Soc.* **2011,** *133* (29), 11076-11079.
6. Krossing, I., The Facile Preparation of Weakly Coordinating Anions: Structure and Characterisation of Silverpolyfluoroalkoxyaluminates $AgAl(OR_F)_4$, Calculation of the Alkoxide Ion Affinity. *Chem. Eur. J.* **2001,** *7* (2), 490-502.
7. Krossing, I.; Raabe, I., Noncoordinating anions - Fact or fiction? A survey of likely candidates. *Angew. Chem. Int. Ed.* **2004,** *43* (16), 2066-2090.
8. Johnson, H. C.; McMullin, C. L.; Pike, S. D.; Macgregor, S. A.; Weller, A. S., Dehydrogenative Boron Homocoupling of an Amine-Borane. *Angew. Chem. Int. Ed.* **2013,** *52* (37), 9776-9780.
9. Dallanegra, R. Cationic Rhodium Complexes with Chelating Phosphine and Phosphine Alkene Ligands. Application in Dehydrogenation and Dehydrocoupling Reactions. University of Oxford, Oxford, 2011.
10. Merle, N.; Koicok-Köhn, G.; Mahon, M. F.; Frost, C. G.; Ruggerio, G. D.; Weller, A. S.; Willis, M. C., Transition metal complexes of the chelating phosphine borane ligand $Ph_2PCH_2Ph_2P{\cdot}BH_3$. *Dalton Trans.* **2004,** (22), 3883-3892.
11. Kumar, A.; Beattie, N. A.; Pike, S. D.; Macgregor, S. A.; Weller, A. S., The Simplest Amino-Borane $H_2B{=}NH_2$ Trapped on a Rhodium Dimer: Pre-Catalysts for Amine-Borane Dehydropolymerization. *Angew. Chem. Int. Ed.* **2016,** *55* (23), 6651-6656.
12. Barwick-Silk, J.; Hardy, S.; Willis, M. C.; Weller, A. S., Rh(DPEPhos)-Catalyzed Alkyne Hydroacylation Using β-Carbonyl-Substituted Aldehydes: Mechanistic Insight Leads to Low Catalyst Loadings that Enables Selective Catalysis on Gram-Scale. *J. Am. Chem. Soc.* **2018,** *140* (23), 7347-7357.
13. Sewell, L. J.; Chaplin, A. B.; Weller, A. S., Hydroboration of an alkene by amine-boranes catalysed by a $[Rh(PR_3)_2]^+$ fragment. Mechanistic insight and tandem hydroboration/dehydrogenation. *Dalton Trans.* **2011,** *40* (29), 7499-7501.
14. Cordero, B.; Gómez, V.; Platero-Prats, A. E.; Réves, M.; Echeverría, J.; Cremades, E.; Barragán, F.; Alvarez, S., Covalent radii revisited. *Dalton Trans.* **2008,** (21), 2832-2838.

15. Johnson, H. C.; Hooper, T. N.; Weller, A. S., The Catalytic Dehydrocoupling of Amine-Boranes and Phosphine-Boranes. In *Synthesis and Application of Organoboron Compounds*, Springer-Verlag Berlin: 2015; Vol. 49, pp 153-220.
16. Algarra, A. G.; Sewell, L. J.; Johnson, H. C.; Macgregor, S. A.; Weller, A. S., A combined experimental and computational study of fluxional processes in sigma amine-borane complexes of rhodium and iridium. *Dalton Trans.* **2014,** *43* (29), 11118-11128.
17. Adams, G. M.; Colebatch, A. L.; Skornia, J. T.; McKay, A. I.; Johnson, H. C.; Lloyd-Jones, G. C.; Macgregor, S. A.; Beattie, N. A.; Weller, A. S., Dehydropolymerization of $H_3B{\cdot}NMeH_2$ To Form Polyaminoboranes Using [Rh(Xantphos-alkyl)] Catalysts. *J. Am. Chem. Soc.* **2018,** *140* (4), 1481-1495.
18. Kumar, A. Exploring the Reactivity of Iridium and Rhodium Bis-Phosphine Complexes with Amine-Boranes. University of Oxford, Oxford, 2016.
19. Roselló-Merino, M.; López-Serrano, J.; Conejero, S., Dehydrocoupling Reactions of Dimethylamine-Borane by Pt(II) Complexes: A New Mechanism Involving Deprotonation of Boronium Cations. *J. Am. Chem. Soc.* **2013,** *135* (30), 10910-10913.
20. Fryzuk, M. D.; Piers, W. E.; Einstein, F. W. B.; Jones, T., Coordinatively unsaturated binuclear clusters of rhodium. The reactivity of $[\{i\mathrm{Pr_2P(CH_2)_nPi Pr_2}\}\mathrm{Rh}]_2(\mu\text{-H})_2$ (n = 2, 3, and 4) with dihydrogen, and their use in the catalytic hydrogenation of olefins. *Can. J. Chem.* **1989,** *67* (5), 883-896.
21. Tang, C. Y.; Phillips, N.; Bates, J. I.; Thompson, A. L.; Gutmann, M. J.; Aldridge, S., Dimethylamine borane dehydrogenation chemistry: syntheses, X-ray and neutron diffraction studies of 18-electron aminoborane and 14-electron aminoboryl complexes. *Chem. Commun.* **2012,** *48* (65), 8096-8098.
22. Colebatch, A. L.; McKay, A. I.; Beattie, N. A.; Macgregor, S. A.; Weller, A. S., Fluoroarene Complexes with Small Bite Angle Bisphosphines: Routes to Amine-Borane and Aminoborylene Complexes. *Eur. J. Inorg. Chem.* **2017,** (38-39), 4533-4540.
23. Johnson, H. C.; Weller, A. S., P–C-Activated Bimetallic Rhodium Xantphos Complexes: Formation and Catalytic Dehydrocoupling of Amine-Boranes. *Angew. Chem. Int. Ed.* **2015,** *54* (35), 10173-10177.
24. Alvarez, S., A cartography of the van der Waals territories. *Dalton Trans.* **2013,** *42* (24), 8617-8636.
25. King, W. A.; Luo, X.-L.; Scott, B. L.; Kubas, G. J.; Zilm, K. W., Cationic Manganese(I) Dihydrogen and Dinitrogen Complexes Derived from a Formally 16-Electron Complex with a Bis-Agostic Interaction, $[\mathrm{Mn(CO)(Ph_2PC_2H_4PPh_2)_2}]^+$. *J. Am. Chem. Soc.* **1996,** *118* (28), 6782-6783.
26. Toner, A. J.; Gründemann, S.; Clot, E.; Limbach, H.-H.; Donnadieu, B.; Sabo-Etienne, S.; Chaudret, B., Ruthenium Assisted Reversible Proton Transfer from an Aromatic Carbon to a Hydride. *J. Am. Chem. Soc.* **2000,** *122* (28), 6777-6778.
27. Chaplin, A. B.; Weller, A. S., B–H Activation at a Rhodium(I) Center: Isolation of a Bimetallic Complex Relevant to the Transition-Metal-Catalyzed Dehydrocoupling of Amine-Boranes. *Angew. Chem. Int. Ed.* **2010,** *49* (3), 581-584.
28. Douglas, T. M.; Brayshaw, S. K.; Dallanegra, R.; Kociok-Köhn, G.; Macgregor, S. A.; Moxham, G. L.; Weller, A. S.; Wondimagegn, T.; Vadivelu, P., Intramolecular Alkyl Phosphine Dehydrogenation in Cationic Rhodium Complexes of Tris(cyclopentylphosphine). *Chem. Eur. J.* **2008,** *14* (3), 1004-1022.
29. Toner, A.; Matthes, J.; Gründemann, S.; Limbach, H.-H.; Chaudret, B.; Clot, E.; Sabo-Etienne, S., Agostic interaction and intramolecular proton transfer from the protonation of dihydrogen ortho metalated ruthenium complexes. *PNAS* **2007,** *104* (17), 6945-6950.
30. Gray, T. G.; Nocera, D. G., A model for two-electron mixed valence in metal–metal bonded dirhodium compounds. *Chem. Commun.* **2005,** (12), 1540-1542.
31. Molinos, E.; Brayshaw, S. K.; Kociok-Köhn, G.; Weller, A. S., Cationic rhodium mono-phosphine fragments partnered with carborane monoanions $[\mathrm{closo\text{-}CB_{11}H_6X_6}]^-$ (X = H, Br). Synthesis, structures and reactivity with alkenes. *Dalton Trans.* **2007,** (42), 4829-4844.
32. Jacobsen, G. B.; Andersen, E.; Housecroft, C. E.; Hong, F. E.; Buhl, M. L.; Long, G. J.; Fehlner, T. P., Main-group chemistry in a metal framework: preparation and characterization of (diborane)hexacarbonyldiiron and its conjugate base $[\mathrm{B_2H_5Fe_2(CO)_6}]$. *Inorg. Chem.* **1987,** *26* (24), 4040-4046.
33. Feilong, J.; Fehlner, T. P.; Rheingold, A. L., Preparation and characterization of $(\eta^5\text{-}\mathrm{C_5H_5Co})_2(\mu\text{-}\mathrm{PPh_2})\mathrm{B_2H_5}$: evidence for multicenter cluster bonding in σ-π vinyl transition metal complexes. *J. Organomet. Chem.* **1988,** *348* (2), C22-C26.
34. Jun, C. S.; Fehlner, T. P., Which Metallaborane, $\mathrm{B_2H_5FeCo(CO)_6}$ or $\mathrm{B_2H_6Fe_2(CO)_6}$, Has the Higher Brønsted Acidity? *Organometallics* **1994,** *13* (6), 2145-2146.
35. Bould, J.; Rath, N. P.; Barton, L., Synthesis and Characterization of nido-$[1,1,2,2\text{-}(\mathrm{CO})_4\text{-}1,2\text{-}(\mathrm{PPh_3})_2\text{-}1,2\text{-}\mathrm{FeIrB_2H_5}]$: A Heterobimetallaborane Analogue of nido-$[\mathrm{B_4H_7}]$. *Inorg. Chem.* **1996,** *35* (1), 35-39.

36. Kawano, Y.; Matsumoto, H.; Shimoi, M., Syntheses of Diruthenaborane Clusters, [{Cp*Ru(μ-H)}$_2$B$_3$H$_7$], [{(Cp*Ru)$_2$(μ-H)}B$_4$H$_9$], and [(Cp*Ru)$_2$(μ-H)(PMe$_3$)(μ-η^4-B$_2$H$_5$)]. *Chem. Lett.* **1999,** *28* (6), 489-490.
37. Lei, X.; Shang, M.; Fehlner, T. P., Fine-Tuning of Metallaborane Geometries: Chemistry of Iridaboranes Derived from the Reaction of [(Cp*Ir)$_2$H$_x$Cl$_{4-x}$] (x=0-2; Cp*=η^5-C$_5$Me$_5$) with LiBH$_4$. *Chem. Eur. J.* **2000,** *6* (14), 2653-2664.
38. Geetharani, K.; Kumar Bose, S.; Varghese, B.; Ghosh, S., From Metallaborane to Borylene Complexes: Syntheses and Structures of Triply Bridged Ruthenium and Tantalum Borylene Complexes. *Chem. Eur. J.* **2010,** *16* (37), 11357-11366.
39. Hooper, J. F.; Chaplin, A. B.; González-Rodríguez, C.; Thompson, A. L.; Weller, A. S.; Willis, M. C., Aryl Methyl Sulfides as Substrates for Rhodium-Catalyzed Alkyne Carbothiolation: Arene Functionalization with Activating Group Recycling. *J. Am. Chem. Soc.* **2012,** *134* (6), 2906-2909.
40. Rheingold, A. L.; Nguyen, S., CCDC 1441303: Experimental Crystal Structure Determination. *CSD Communication* **2015**.
41. Julian, L. D.; Hartwig, J. F., Intramolecular Hydroamination of Unbiased and Functionalized Primary Aminoalkenes Catalyzed by a Rhodium Aminophosphine Complex. *J. Am. Chem. Soc.* **2010,** *132* (39), 13813-13822.
42. Adams, G. M.; Chadwick, F. M.; Pike, S. D.; Weller, A. S., A CH_2Cl_2 complex of a [Rh(pincer)]$^+$ cation. *Dalton Trans.* **2015,** *44* (14), 6340-6342.
43. Widegren, J. A.; Finke, R. G., A review of the problem of distinguishing true homogeneous catalysis from soluble or other metal-particle heterogeneous catalysis under reducing conditions. *J. Mol. Catal. A: Chem.* **2003,** *198* (1-2), 317-341.

5 Dehydropolymerisation of $H_3B{\cdot}NMeH_2$ using the $\{Rh(DPEphos)\}^+$ system

5.1 Introduction

In Chapter 4, the activity of the DPEphos complex [Rh(κ^2-P,P-DPEphos)(η^2-$H_2B(CH_2CH_2{}^tBu){\cdot}NMe_3$)][$BAr^F{}_4$] (**13**, Figure 5.1) was tested in $H_3B{\cdot}NMeH_2$ dehydrocoupling at 10 mol% catalyst loading, and took approximately 5 hours to reach completion. Despite being much slower than the analogous reaction using the Xantphos-^{i}Pr precatalyst [Rh(κ^3-P,O,P-Xantphos-^{i}Pr)$(H)_2$(η^1-$H_3B{\cdot}NMe_3$)][$BAr^F{}_4$] (**2**, Figure 5.1), which itself took only 30 seconds to complete under the same conditions, **13** was still of interest to test in the dehydropolymerisation of $H_3B{\cdot}NMeH_2$ using lower catalyst loadings. Of particular interest is that **13** is a direct analogue of successful Xantphos-Ph $H_3B{\cdot}NMeH_2$ dehydrocoupling precatalyst [Rh(κ^2-P,P-Xantphos)(η^2-$H_2B(CH_2CH_2{}^tBu){\cdot}NMe_3$)][$BAr^F{}_4$] (**i-13**, Figure 5.1),[1] while $H_3B{\cdot}NMeH_2$-derived complexes of the $\{Rh(DPEphos)\}^+$ fragment showed similarities with previous examples of $\{Rh(L_2)\}^+$ (L_2 = bidentate bisphosphine) systems, i.e. the bridging aminoborane motif in [$\{Rh(\kappa^2$-P,P-DPEphos$)\}_2$(μ-H)(μ-H_2BNMeH)][$BAr^F{}_4$] (**14**, Figure 5.2) has been previously reported in [$\{Rh(Ph_2P(CH_2)_3PPh_2\}_2$($\mu$-H)($\mu$-$H_2BNMeH$)][$BAr^F{}_4$] (**i-22**, Figure 5.2).[2] This suggested potentially rich catalytic chemistry.

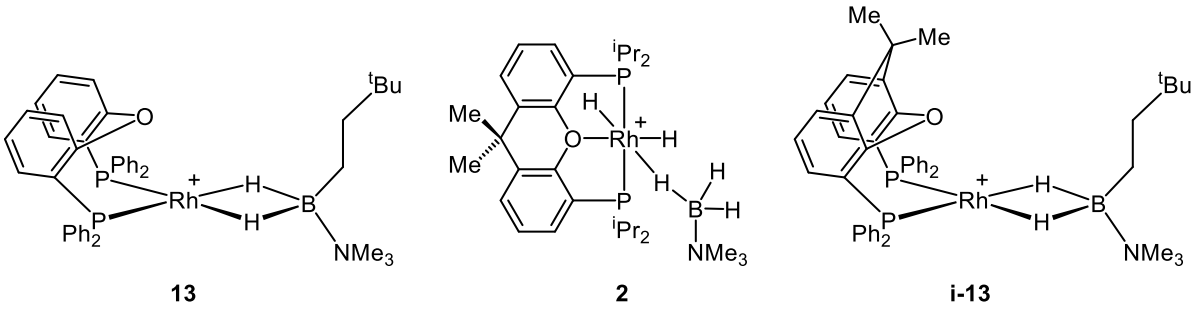
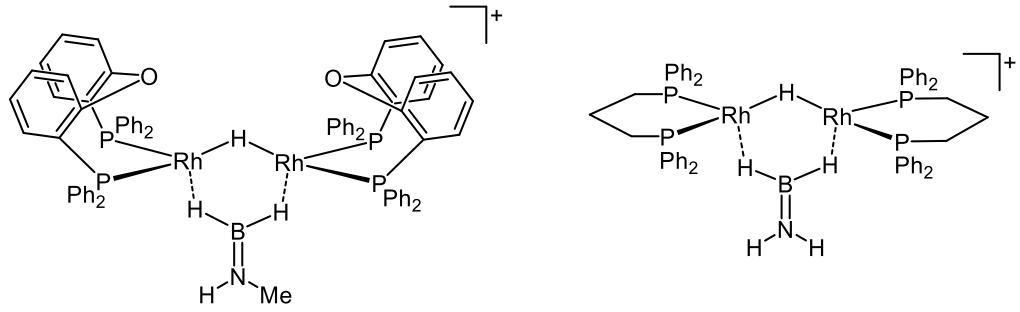


Figure 5.1 Structures of complexes **13**, **2**, and **i-13**. [$BAr^F{}_4$]$^-$ anions not shown for clarity.



14 **i-22**

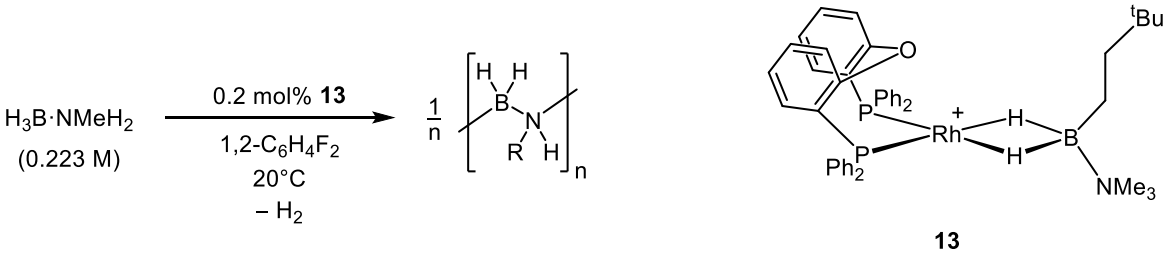
Figure 5.2 Structures of complexes **14** and **i-22**. $[BAr^F_4]^-$ anions not shown for clarity.

The differing speciation between complexes **2** and **13** described in Chapters 2 and 4 respectively also poses questions over whether these contrasting ligand backbones dictate different dehydropolymerisation mechanisms. This may be governed by clear differences between the preferred coordination geometries of Xantphos-^{i}Pr and DPEphos – Xantphos-^{i}Pr generally binds in a mer-κ^3-P,O,P manner, whereas DPEphos more likely exists in a cis κ^2-P,P orientation as determined by ground state X-ray structures (Figure 1.8). DPEphos also exhibits a greater cis κ^2-P,P preference compared to Xantphos-Ph (Figure 1.8), therefore comparisons in dehydropolymerisation mechanisms between $\{Rh(DPEphos)\}^+$ (**13**) and the parent $\{Rh(Xantphos\text{-}Ph)\}^+$ (**i-13**) systems may also show important similarities or differences. During this Chapter, analysis of polyaminoborane growth kinetics and $H_3B{\cdot}NMeH_2$ dehydrogenation kinetics using precatalyst **13** and its $H_3B{\cdot}NMeH_2$ derivatives will be explored.

5.2 Dehydropolymerisation of $H_3B{\cdot}NMeH_2$ using precatalyst $[Rh(DPEphos)(H_2B(CH_2CH_2{}^tBu){\cdot}NMe_3)][BAr^F_4]$ (**13**): initial screening

Precatalyst **13**, $[Rh(\kappa^2\text{-P,P-DPEphos})(\eta^2\text{-}H_2B(CH_2CH_2{}^tBu){\cdot}NMe_3)][BAr^F_4]$, was tested in $H_3B{\cdot}NMeH_2$ dehydropolymerisation at 0.2 mol% catalyst loading using a $H_3B{\cdot}NMeH_2$ concentration of 0.223 M in 1,2-$C_6H_4F_2$ solvent under open conditions (H_2 released via a mineral oil bubbler under controlled argon flow, Scheme 5.1). After 4 hours, the major product formed was $(H_2BNMeH)_n$, as confirmed by ^{11}B NMR spectroscopy of the in situ reaction mixture, in which the

characteristic broad signal is observed at δ −5.1 (Figure 5.3). This timeframe is notably slower than that of Xantphos-^{i}Pr precatalyst **2**, [Rh(κ^3-P,O,P-Xantphos-^{i}Pr)(H)$_2$(η^1-H$_3$B·NMe$_3$)][BAr$^F_4$], which under the same concentration regime afforded complete conversion of H$_3$B·NMeH$_2$ in 25 minutes (Figure 3.6). In fact, the activity of DPEphos precatalyst **13** appears more similar to that of Xantphos-Ph system **i-13**, [Rh(κ^2-P,P-Xantphos-Ph)(η^2-H$_2$B(CH$_2$CH$_2$^{t}Bu)·NMe$_3$)][BAr$^F_4$], which took 2 hours to reach completion at 0.2 mol% catalyst loading, albeit at a higher concentration regime of 0.446 M H$_3$B·NMeH$_2$.[1]



Scheme 5.1 Dehydropolymerisation of H$_3$B·NMeH$_2$ using precatalyst **13**. [BAr$^F_4$]$^-$ anion not shown for clarity.

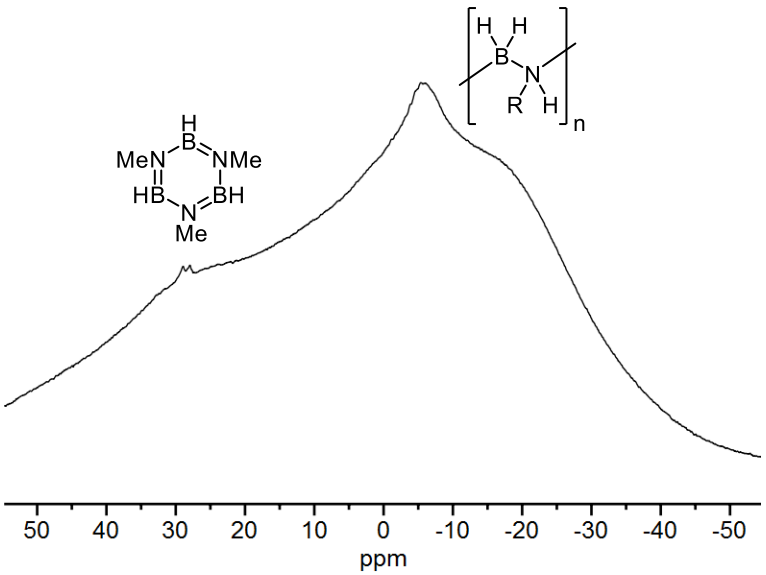


Figure 5.3 Representative ^{11}B NMR spectrum of the dehydropolymerisation reaction mixture using precatalyst **13** (0.2 mol% **13**, 0.223 M H$_3$B·NMeH$_2$, 1,2-C$_6$H$_4$F$_2$ solvent, open conditions). The broad baseline signal observed in the ^{11}B NMR spectrum at δ ~20.0 is due to background from the tube and probe (borosilicate glass).

With this initial data obtained, (H$_2$BNMeH)$_n$ growth kinetics and H$_3$B·NMeH$_2$ dehydrogenation kinetics for the [Rh(κ^2-P,P-DPEphos)(η^2-H$_2$B(CH$_2$CH$_2$^{t}Bu)·NMe$_3$)][BAr$^F_4$] system (precatalyst **13**) were investigated.

5.3 Polyaminoborane growth kinetics

The molecular weight of $(H_2BNMeH)_n$ samples formed by precatalyst **13** were analysed by gel permeation chromatography (GPC) using a refractive index (RI) detector, as calibrated using polystyrene standards. As for the Xantphos-^{i}Pr precatalyst [Rh(κ^3-P,O,P-Xantphos-^{i}Pr)(H)$_2$(η^1-$H_3B{\cdot}NMe_3$)][$BAr^F{}_4$] (**2**) discussed in Chapter 3, all of the polyaminoborane samples produced by precatalyst **13** gave GPC traces which contained a broad peak characteristic of $(H_2BNMeH)_n$, overlapping with a sharp peak at lower M_n indicative of the $[BAr^F{}_4]^-$ anion (i.e. those in Figure 3.13). Given that the modelled fits described in Chapter 3 gave similar M_n and Đ values to the raw data, only raw data was used to compare the GPC data for DPEphos precatalyst **13**. This was further confirmed to be a valid method to report GPC molecular weight data in the DPEphos system as, for example, polyaminoborane that provided a raw M_n value of 11,600 g mol^{-1} (Đ = 1.8) gave a very similar corresponding fitted M_n value of 11,000 g mol^{-1} (Đ = 2.1).

5.3.1 Polyaminoborane molecular weight versus conversion

The relationship between degree of polymerisation and reaction progress using dehydropolymerisation precatalyst **13** at 0.2 mol% loading was explored by analysing the molecular weight of $(H_2BNMeH)_n$ formed under open conditions (H_2 released via a mineral oil bubbler under controlled argon flow) against the corresponding percentage conversion of $H_3B{\cdot}NMeH_2$ (measured by ^{11}B NMR spectroscopy). The plot is detailed in Figure 5.4, which shows that even at 10% $H_3B{\cdot}NMeH_2$ conversion, polyaminoborane of medium molecular weight (M_n = 24,800 g mol^{-1}, Đ = 1.2) was formed. M_n increased to 33,800 g mol^{-1} (Đ = 1.5) at 40% conversion, with this molecular weight very similar to that of $(H_2BNMeH)_n$ produced at full $H_3B{\cdot}NMeH_2$ conversion (M_n = 34,900 g mol^{-1}, Đ = 1.5). Likewise to Xantphos-^{i}Pr precatalyst **2**, these data are consistent with a chain growth polymerisation process in which a chain termination event is in operation,[3-4] though the levelling of molecular weight between 40% and full conversion may be due to a switch in mechanism due to H_2 build up. The lower molecular weight material formed up to 30% conversion may be related to the presence of the long induction period that

proceeds productive dehydrogenation, which will be further discussed in Section 5.4. The presence of an induction period suggests an evolution of the organometallic complexes present before formation of the true active catalytic species, which are likely to be dependent upon the complexes identified in 10 mol% catalysis using **13** (Section 4.4.2), such as [{Rh(κ^2-P,P-DPEphos)}$_2$(μ-H)(μ-H$_2$BNMeH)][BAr$^F{}_4$] (**14**), [{Rh(κ^2-P,P-DPEphos)}$_2${μ-(H$_2$B)$_2$NMeH}][BAr$^F{}_4$] (**15**) and [{Rh(κ^2-P,P-DPEphos)}$_2$(μ-B$_2$H$_5$)][BAr$^F{}_4$] **16**, and others.

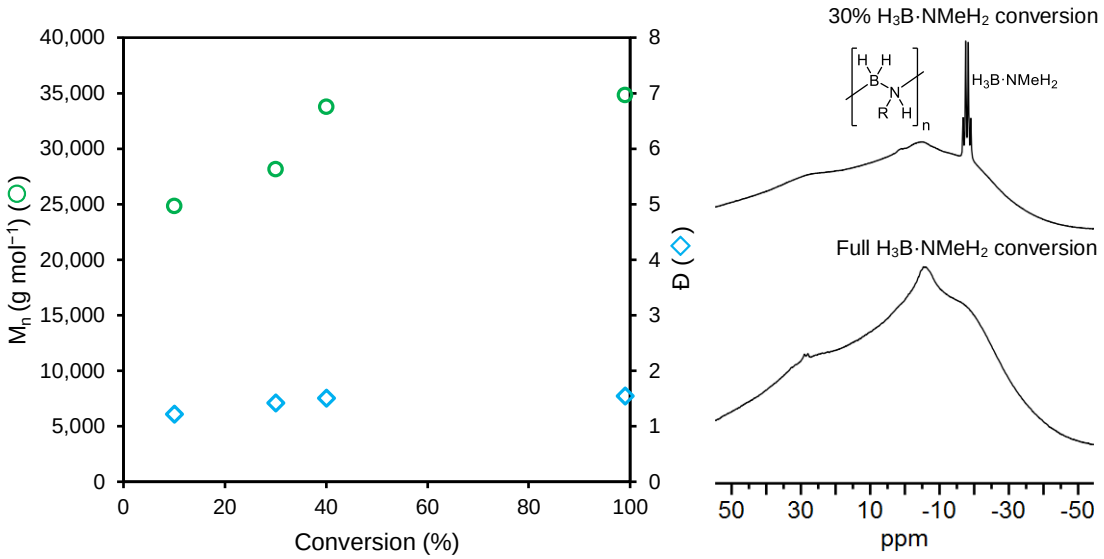


Figure 5.4 Left: M_n (○**;** g mol^{-1}) and Đ (◇) versus $H_3B{\cdot}NMeH_2$ conversion (%) plot. [**13**] = 4.45 × 10^{-4} M (0.2 mol%), [$H_3B{\cdot}NMeH_2$] = 0.223 M, 1,2-$C_6H_4F_2$ solvent. Open conditions via controlled argon flow. Right: Stacked ^{11}B NMR spectra of the polyaminoborane samples in THF solvent from molecular weight versus conversion reaction mixtures using precatalyst **13** ([**13**] = 4.45 × 10^{-4} M (0.2 mol%), [$H_3B{\cdot}NMeH_2$] = 0.223 M, 1,2-$C_6H_4F_2$, open conditions) at 30% $H_3B{\cdot}NMeH_2$ conversion (top) and full $H_3B{\cdot}NMeH_2$ conversion (bottom). The broad baseline signals observed at δ ~20.0 are due to background from the tube and probe (borosilicate glass).

5.3.2 Polyaminoborane molecular weight versus catalyst loading

Figure 5.5 shows the effect of increasing catalyst loading from 0.1 mol% to 1.0 mol% of precatalyst **13** on the dehydropolymerisation of $H_3B{\cdot}NMeH_2$ under open conditions controlled via argon flow. Increasing the catalyst loading 5-fold from 0.2 mol% to 1.0 mol% leads to an approximate 5-fold decrease in $(H_2BNMeH)_n$ molecular weight (0.2 mol%: M_n = 34,900 g mol^{-1}, Đ = 1.5; 1.0 mol%: M_n = 6,400 g mol^{-1}, Đ = 1.8), as shown in Figure 5.5. This is a much more significant trend compared to that seen for Xantphos-^{i}Pr precatalyst **2** (Figure 3.16) in which a 2-

fold decrease in M_n was observed over the same catalyst loading increase (0.2 mol%: M_n = 9,600 g mol^{-1}, Đ = 2.8; 1.0 mol%: M_n = 5,000 g mol^{-1}, Đ = 2.4). This shows that the DPEphos system has a strong, inverse, catalyst loading versus molecular weight trend (Figure 5.5, inset), more indicative of a single site chain growth mechanism compared to the Xantphos-^{i}Pr system, as an increase in initiating polymerisation sites should result in shorter polyaminoborane chains. In fact, this effect is even more pronounced compared to the parent Xantphos-Ph system for which a 0.2 mol% catalyst loading gave polyaminoborane with M_n = 22,700 g mol^{-1} (Đ = 2.1), whereas at 1.0 mol% the polyaminoborane was shorter, but only by approximately 3-fold (M_n = 7,500 g mol^{-1}, Đ = 1.5).[1] However, the plot in Figure 5.5 also shows that the polyaminoborane formed at 0.1 mol% catalyst loading (M_n = 34,600 g mol^{-1}, Đ = 1.7) was of similar molecular weight to that at 0.2 mol% and therefore that the catalyst loading dependence on molecular weight reaches a limit of approximately 35,000 g mol^{-1} under these reaction conditions.

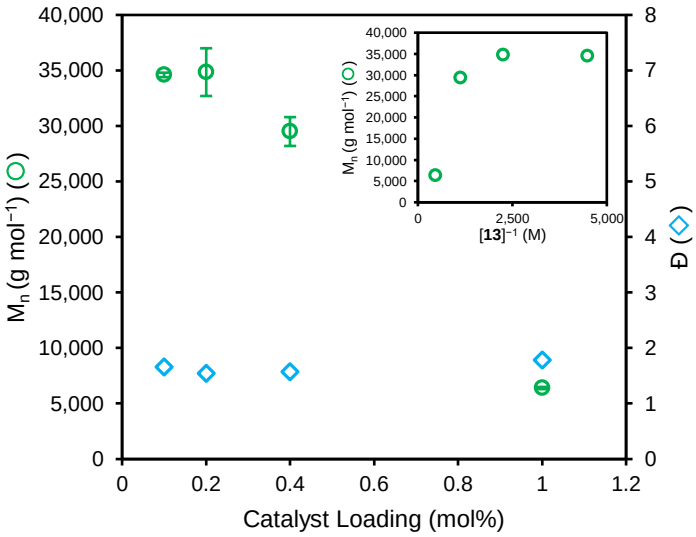


Figure 5.5 M_n (○; g mol^{-1}) and Đ (◇) versus catalyst loading of **13** (mol%). [$H_3B{\cdot}NMeH_2$] = 0.223 M, 1,2-$C_6H_4F_2$ solvent. Open conditions with the reaction flask under controlled argon flow via a mineral oil bubbler. Inset: M_n (g mol^{-1}) versus [**13**]$^{-1}$ (M) under the same conditions showing the approximate inverse dependence on polyaminoborane M_n versus catalyst concentration.

Hydrogen measurement conditions were deployed to study the amine borane dehydrogenation kinetics (discussed in detail in Section 5.4) at catalyst loadings between 0.1 mol% and 1.0 mol%. Under these conditions, the molecular weight distributions of polyaminoborane formed at each

catalyst loading are shown in Figure 5.6. The inverse dependence of catalyst loading versus M_n previously demonstrated in Figure 5.5 was again observed under these hydrogen measurement conditions, though in this case polyaminoborane M_n does not level off between 0.1 mol% and 0.2 mol% catalyst loading, and the M_n versus $[\mathbf{13}]^{-1}$ correlation was strong across all data points (Figure 5.6, inset). However, the M_n values appear shorter across the board. This is most notable for polyaminoborane produced at 0.2 mol% and 0.4 mol% catalyst loadings where decreases of 20,400 g mol^{-1} and 19,500 g mol^{-1} respectively were observed on changing from controlled argon flow conditions to those of hydrogen measurement. It was speculated that this was due to the increase in the hydrogen pressure as a consequence of the hydrogen measurement conditions used – although H_2 loss from the system is measured, it is technically a closed system as the gas is trapped in a water-filled burette. On the other hand, in open conditions, evolved H_2 gas is flushed out of the system by the constant argon flow through the reaction vessel into the outside atmosphere.

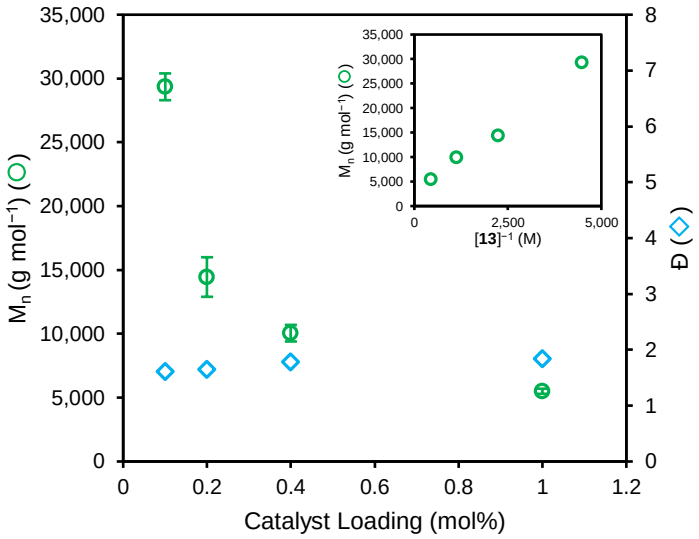


Figure 5.6 M_n (○**;** g mol^{-1}) and Đ (◇) versus catalyst loading of **13** (mol%). $[H_3B{\cdot}NMeH_2]$ = 0.223 M, 1,2-$C_6H_4F_2$ solvent. Hydrogen measurement conditions with the reaction flask isolated from the argon supply and connected to a 100.0 mL water-filled burette. Inset: M_n (g mol^{-1}) versus $[\mathbf{13}]^{-1}$ (M) under the same conditions showing the approximate inverse dependence on polyaminoborane M_n versus catalyst concentration.

5.3.3 H_2 dependence on polyaminoborane molecular weight

To investigate this effect of hydrogen on the chain termination event, dehydropolymerisation was carried out at 0.4 mol% catalyst loading in a sealed J. Young flask of 30.0 mL volume. Using

50.0 mg of $H_3B{\cdot}NMeH_2$ (0.223 M), this leads to the generation of approximately 1 bar of H_2 pressure over the lifetime of catalysis. The ^{11}B NMR spectrum of the isolated material from the reaction is shown in Figure 5.7, and contains the characteristic peak centred at δ –5.1. However, this appears much more resolved compared to polyaminoborane formed using Xantphos-^{i}Pr precatalyst **2** shown in Figure 3.12, as well as that produced by DPEphos precatalyst **13** under argon flow conditions (Figure 5.10, vide infra). Instead, this suggests that fewer BH_2 environments are present in the sample. In particular, the sharpest peak centred at δ –5.1 is similar to that of the linear dimer $H_3B{\cdot}NMeHBH_2{\cdot}NMeH_2$ which has a triplet coupling pattern for the internal BH_2 group (δ −4.8, t, $^{1}J_{BH}$ 112 Hz, 1,2-$C_6H_4F_2$ solvent),[5] as well as short chain oligomers with chemical shifts in a similar region. Furthermore, a resonance at δ –18.0 was also observed (Figure 5.7), coincident with $H_3B{\cdot}NMeH_2$,[6] which may indicate end groups of the short chain oligomers. Though it cannot be discounted that this peak is in fact entrained, unreacted $H_3B{\cdot}NMeH_2$, leaving the reaction for up to 24 hours longer does not lead to a reduction in intensity of this resonance in the isolated material.

Consistent with the proposed oligomeric nature of the sample, analysis of the material by GPC showed that low molecular weight $(H_2BNMeH)_n$ (M_n = 5,600 g mol^{-1}, Đ = 2.0) had been produced under closed conditions with a degree of polymerisation of approximately 130. This is a considerable decrease in M_n relative to both open conditions and hydrogen measurement conditions which led to degrees of polymerisation of 690 and 230 respectively (Figure 5.8) at 0.4 mol% **13**. Therefore, H_2 appears to act as a chain transfer agent in the DPEphos system, analogous to single-site Ziegler-Natta olefin polymerisation,[7-8] and the parent Xantphos-Ph system.[1] This contrasts with the Xantphos-^{i}Pr system described in Chapter 3 where H_2 has no effect on the system, and suggests that, alongside the correlation of inverse catalyst loading versus M_n in system **13**, a different mechanism is operating.

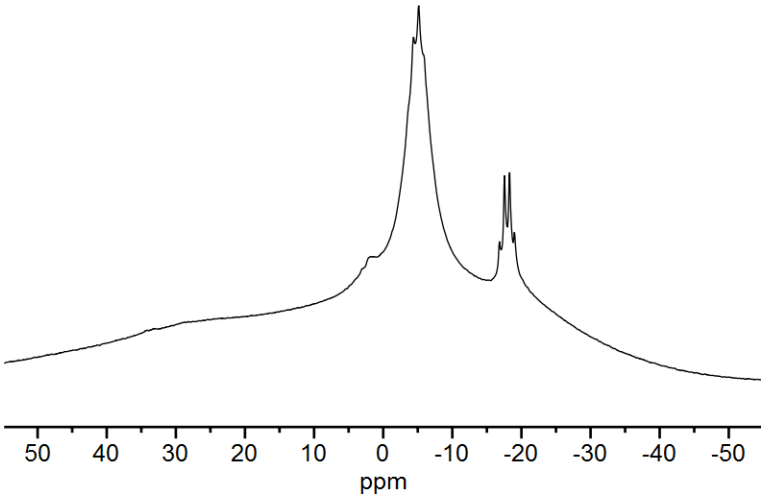


Figure 5.7 ^{11}B NMR spectrum (THF, 298 K) for isolated $(H_2BNMeH)_n$ produced by precatalyst **13** (0.4 mol%, 0.223 M $H_3B{\cdot}NMeH_2$, 1,2-$C_6H_4F_2$ solvent, closed conditions). The broad baseline signal observed in the ^{11}B NMR spectrum at δ ~20.0 is due to background from the tube and probe (borosilicate glass).

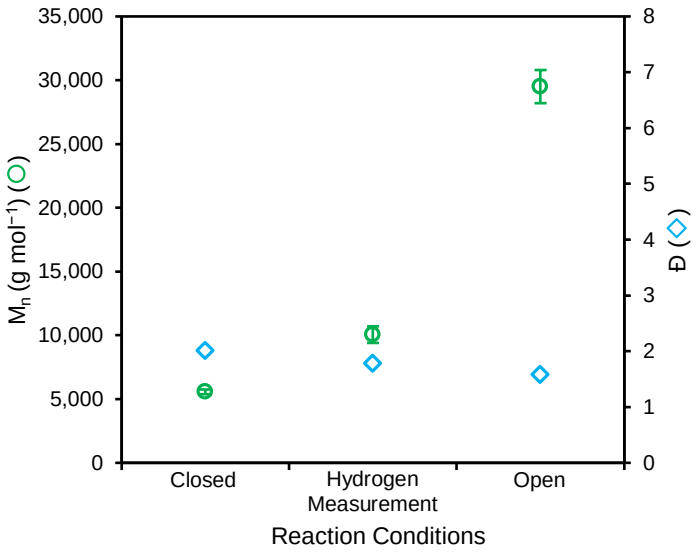


Figure 5.8 M_n (○; g mol^{-1}) and Đ (◇) versus reaction conditions (closed, hydrogen measurement or open). [**13**] = 8.92 × 10^{-4} M (0.4 mol%), [$H_3B{\cdot}NMeH_2$] = 0.223 M, 1,2-$C_6H_4F_2$ solvent. Closed conditions with the reaction carried out in a sealed J. Young flask. Hydrogen measurement conditions with the reaction flask isolated from the argon supply and connected to a 100.0 mL water-filled burette. Open conditions with the reaction flask under controlled argon flow via a mineral oil bubbler.

5.3.4 Further polyaminoborane analysis

It was noted that the dehydropolymerisation reaction mixtures (all carried out in 1,2-$C_6H_4F_2$ solvent) using precatalyst **13**, which formed higher molecular weight polyaminoborane

(>10,000 g mol^{-1}, i.e. 0.1 mol% – 0.4 mol% **13** under open conditions and 0.1 mol% – 0.2 mol% **13** under hydrogen measurement conditions) led to the observation of some (~ 10 mg) off-white precipitate over the course of the reaction. The light colour of this material, and the negative results for heterogeneous catalysis detailed in Figure 5.12 (vide infra), suggested that this did not point to the formation of rhodium nanoparticles. The material insoluble in the 1,2-$C_6H_4F_2$ reaction solvent was separated from the soluble portion, and instead found to be THF-soluble. The solubility of $(H_2BNMeH)_n$ has not been fully detailed in the literature, and whilst previous reports have utilised its solubility in solvents such as THF,[1] chloroform,[9] and CD_2Cl_2,[10] Grützmacher and co-workers have reported $(H_2BNMeH)_n$ that was poorly soluble in THF, toluene, chloroform and DMF.[11] Grützmacher's insoluble polyaminoborane was only characterised by mass spectrometry, and this showed a degree of polymerisation of up to 22 monomer units,[11] rather than the longer material that is produced by precatalyst **13**, however it should be noted that mass spectrometry is not a reliable technique for determining chain length as the maximum observed *m/z* is only around 3,000.[12] As shown next, the identity of the 1,2-$C_6H_4F_2$-insoluble material was determined by GPC and NMR studies to in fact be $(H_2BNMeH)_n$ polyaminoborane.

GPC analysis (in THF containing 0.1% w/w $[N^nBu_4]Br$) of the isolated material obtained from the dehydropolymerisation of $H_3B{\cdot}NMeH_2$ carried out under open conditions using 0.2 mol% **13** provided molecular weight data for the 1,2-$C_6H_4F_2$-soluble (M_n = 41,700 g mol^{-1}, Đ = 1.6) and 1,2-$C_6H_4F_2$-insoluble (M_n = 34,200 g mol^{-1}, Đ = 1.6) portions. The average of these values (M_n = 38,000 g mol^{-1}) is close to the upper limit found for the unseparated mixture (M_n = 34,900 ± 2,200 g mol^{-1}, Figure 5.5), in agreement with the similar amounts of 1,2-$C_6H_4F_2$-soluble and 1,2-$C_6H_4F_2$-insoluble polyaminoborane formed (~ 10 mg each) during the reaction. This trend, where the 1,2-$C_6H_4F_2$-insoluble polyaminoborane was observed to be shorter than the 1,2-$C_6H_4F_2$-soluble was repeated, though to a lesser extent, using a 0.4 mol% catalyst loading of **13**, where the insoluble portion gave an M_n value of 29,000 g mol^{-1} (Đ = 1.5) – slightly shorter than the soluble component (M_n = 30,800 g mol^{-1}, Đ = 1.6). Also of interest was that the GPC chromatogram for the 1,2-$C_6H_4F_2$-insoluble polyaminoborane sample showed a much lower

intensity $[BAr^{F}{}_4]^-$ signal (Figure 5.9), unlike the 1,2-$C_6H_4F_2$-soluble portion, therefore may indicate that $[BAr^{F}{}_4]^-$ is present in a lower quantity and possibly less rhodium may be present also, although this was not tested for. Another big difference between the two components was observed by NMR spectroscopy (Figure 5.10).

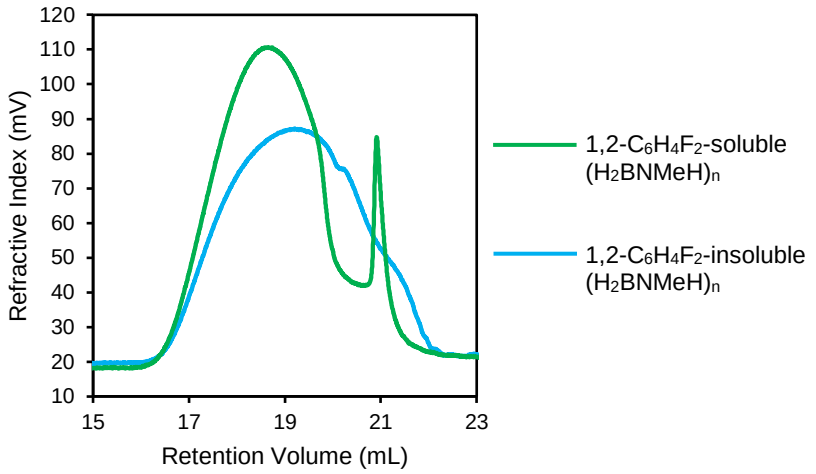


Figure 5.9 Refractive Index (mV) versus Retention Volume (mL) GPC data for 1,2-$C_6H_4F_2$-soluble polyaminoborane (green line) versus 1,2-$C_6H_4F_2$-insoluble polyaminoborane (blue line) showing the different intensities of the $[BAr^{F}{}_4]^-$ anion peak.

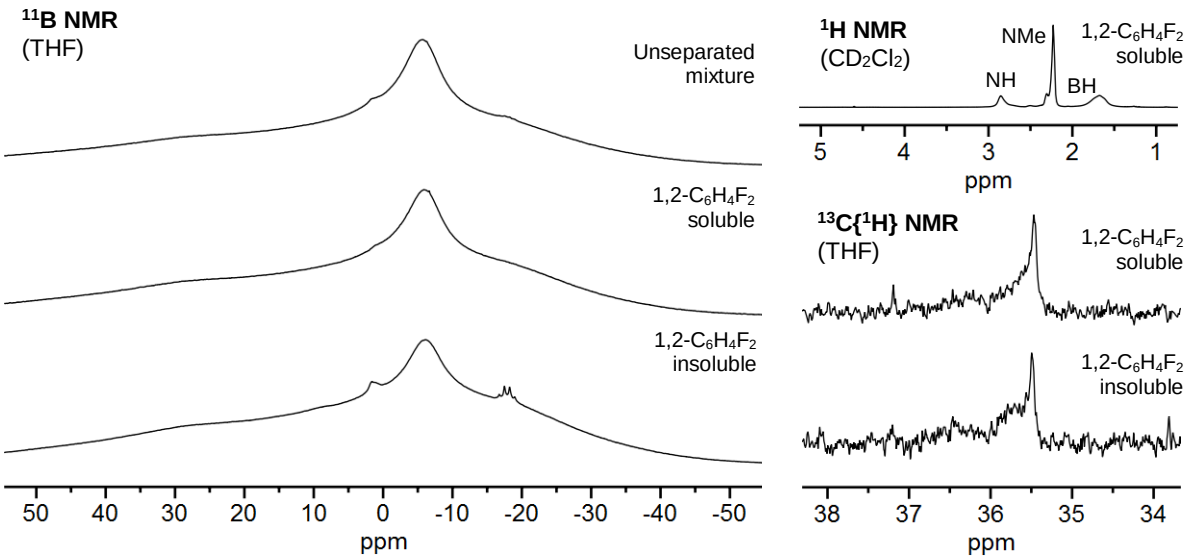


Figure 5.10 NMR spectra (THF solvent unless otherwise stated, 298 K) for isolated $(H_2BNMeH)_n$ produced by precatalyst **13** (0.2 mol%, 0.223 M $H_3B{\cdot}NMeH_2$, 1,2-$C_6H_4F_2$ solvent, open conditions). The ^{1}H NMR spectrum of $(H_2BNMeH)_n$ recorded in CD_2Cl_2 is the 1,2-$C_6H_4F_2$ soluble fraction. The broad baseline signals observed in the ^{11}B NMR spectra at δ ~20.0 are due to background from the tube and probe (borosilicate glass).

In order to compare 1,2-$C_6H_4F_2$-soluble polyaminoborane, 1,2-$C_6H_4F_2$-insoluble polyaminoborane, and the analogous unseparated mixtures by NMR spectroscopy, THF solvent was used to ensure all samples were fully dissolved, as the 1,2-$C_6H_4F_2$-insoluble portion was also insoluble in CD_2Cl_2 solvent. The ^{11}B NMR spectra of these isolated polyaminoborane samples are shown in Figure 5.10, and in all cases the major resonance is a broad peak centred at δ −6.0. A very low intensity shoulder at δ 1.0 can also be seen in the unseparated mixture and 1,2-$C_6H_4F_2$-soluble components, however in the 1,2-$C_6H_4F_2$-insoluble case this shoulder is of much greater intensity, and therefore may signify heightened chain branching, i.e. the presence of tertiary or quaternary boron centres.[13] Also evident in the ^{11}B NMR spectrum for the 1,2-$C_6H_4F_2$-insoluble component is the quartet at δ −17.9. In this case, due to the high molecular weight of the 1,2-$C_6H_4F_2$-insoluble polyaminoborane produced under open conditions using 0.2 mol% **13** (M_n = 34,200 g mol^{-1}, Đ = 1.6), this is suggested to be entrained $H_3B{\cdot}NMeH_2$ that cannot react once the polyaminoborane precipitates from the reaction mixture.

This effect of chain branching may also be signalled in the $^{13}C\{^1H\}$ NMR spectra of both the 1,2-$C_6H_4F_2$-soluble and 1,2-$C_6H_4F_2$-insoluble $(H_2BNMeH)_n$ samples (Figure 5.10). Whilst the sharpest peak for both samples lies at δ 35.5, there is an underlying broader resonance in both cases centred at δ ~35.7. This broader resonance appears to be of much higher relative intensity for 1,2-$C_6H_4F_2$-insoluble polyaminoborane. This, combined with the ^{11}B NMR spectrum, may further signify chain branching due to a greater abundance of differing ^{13}C environments imposed by the increased number of tertiary or quaternary boron centres. Despite the discussion in Chapter 3 regarding the complications in ^{13}C NMR analysis due to coupling to both quadrupolar ^{10}B and ^{11}B environments, the clear differences between the two samples in this case may help to support the proposed chain branching hypothesis, or at the very least a different polyaminoborane structure. The ^{1}H NMR spectrum of 1,2-$C_6H_4F_2$-soluble polyaminoborane could be recorded in CD_2Cl_2 solvent and captures the characteristic signals for $(H_2BNMeH)_n$ presented previously in Figure 3.12. Since 1,2-$C_6H_4F_2$-insoluble polyaminoborane is also insoluble in CD_2Cl_2, and in THF solvent the solvent

signals overlap with the characteristic polyaminoborane resonances, the equivalent ^{1}H NMR spectrum for 1,2-$C_6H_4F_2$-insoluble polyaminoborane could not be obtained.

The increased chain branching proposed for 1,2-$C_6H_4F_2$-insoluble polyaminoborane versus 1,2-$C_6H_4F_2$-soluble polyaminoboranes may explain the lower molecular weight reported for the 1,2-$C_6H_4F_2$-insoluble portion. Given that GPC separation coupled with RI detection are relative size measurements, rather than an indication of absolute chain length, polyaminoborane with greater chain branching in its structure could lead to a more compact, smaller size when dissolved in THF solution compared to a sample with less chain branching (i.e. 1,2-$C_6H_4F_2$-soluble $(H_2BNMeH)_n$) despite possibly being composed of a similar or even greater number of monomer units, or absolute molecular weight.[14]

5.3.5 Probing for living polymerisation

Catalyst recharging experiments at 0.4 mol% **13** (0.223 M $H_3B{\cdot}NMeH_2$, 8.92× 10^{-4} M **13**) under H_2 measurement conditions showed that the $(H_2BNMeH)_n$ formed (M_n = 10,100 g mol^{-1}, Đ = 1.8) did not change significantly in molecular weight on two further additions of $H_3B{\cdot}NMeH_2$ to the reaction vessel (M_n = 9,500 g mol^{-1}, Đ = 1.8), and therefore that living polymerisation was not in operation. However, it was clear that the organometallic species present at the end of catalysis remained active – the temporal reaction profile for this reaction is detailed in Section 5.4.3.

5.3.6 Aminoborane trapping experiments

The presence of free aminoborane, $H_2B{=}NMeH$, formed during the dehydropolymerisation of $H_3B{\cdot}NMeH_2$ by {Rh(DPEphos)}$^{+}$ precatalyst **13**, was investigated by probing the hydroboration of cyclohexene by $H_2B{=}NMeH$ to form the hydroborated cyclohexene product $Cy_2B{=}NMeH$.[15] Addition of 2.7 equivalents of cyclohexene (i.e. 270 mol%) to the dehydropolymerisation of $H_3B{\cdot}NMeH_2$ using **13** at 0.2 mol% catalyst loading under open conditions did not result in the observation of $Cy_2B{=}NMeH$ in the ^{11}B NMR spectrum of the reaction mixture (i.e. a resonance at

δ 45.9, br, shown in Figure 3.11). This suggests that at this low catalyst loading, any free H_2B=NMeH that may form is consumed faster by polymerisation rather than being involved in hydroboration processes, or that H_2B=NMeH remains metal bound during both the dehydrogenation of $H_3B{\cdot}NMeH_2$ and the subsequent chain propagation of $(H_2BNMeH)_n$. This was further confirmed as polyaminoborane formed under these conditions was of very similar molecular weight (M_n = 33,000 g mol^{-1}, Đ = 1.6) to that obtained without additional cyclohexene (M_n = 34,900 g mol^{-1}, Đ = 1.5). Either way, this result, combined with the clear inverse dependence of polyaminoborane molecular weight versus catalyst loading (Figure 5.5 and Figure 5.6), strongly suggests that polymerisation of H_2B=NMeH by the {Rh(DPEphos)}$^+$ fragment is metal mediated rather than off-metal.

5.4 Amine borane dehydrogenation kinetics

The dehydrogenation of $H_3B{\cdot}NMeH_2$ to aminoborane monomer H_2B=NMeH can be indirectly quantified by measuring the volume of H_2 gas given off over time. This was achieved by carrying out the reaction in a jacketed two-neck Schlenk flask attached to a recirculating cooler to ensure a reproducible constant temperature of 20°C. The flask can then be connected to a water-filled gas burette via Teflon tubing. Sealing the system from the argon flow allows the volume of H_2 to be measured in single millilitre intervals.

Using 0.4 mol% **13** and 0.223 M $H_3B{\cdot}NMeH_2$ in 1,2-$C_6H_4F_2$ solvent, 1.1 equivalents of H_2 were released over approximately 3.5 hours (Figure 5.11), consistent with the major product of $(H_2BNMeH)_n$ alongside a small amount of borazine $(HBNMe)_3$ (Figure 5.3 shows the ^{11}B NMR spectrum of a reaction mixture at 0.2 mol% **13**). For this system, likewise to Xantphos-^{i}Pr precatalyst **2**, the volume of H_2 released from the reaction can be used to represent generation of the H_2B=NMeH monomer (Equations 3.1 and 3.2), which can then polymerise to form $(H_2BNMeH)_n$. The temporal plot in Figure 5.11 shows a long induction period of approximately 60 minutes, which varies depending on the batch of 1,2-$C_6H_4F_2$ solvent used – for example the

plots detailed in Figure 5.12 show induction periods of closer to 35 minutes. This difference is likely due to the presence of impurities in different batches of 1,2-$C_6H_4F_2$ solvent, confirmed by GC-MS (Figure 3.3). However likewise to the Xantphos-^{i}Pr system described in Section 3.3.1, the induction periods are consistent within each batch of solvent for repeat runs, therefore direct comparisons between kinetic data are only made between experiments using the same batch of solvent. Despite the 25 minute difference, the 35 minute and 60 minute induction periods reported for different solvent batches in the DPEphos system are both remarkably long compared to those of the order of 20 – 150 s reported in the Xantphos-^{i}Pr system, therefore the induction period in the DPEphos system was of importance to investigate and understand.

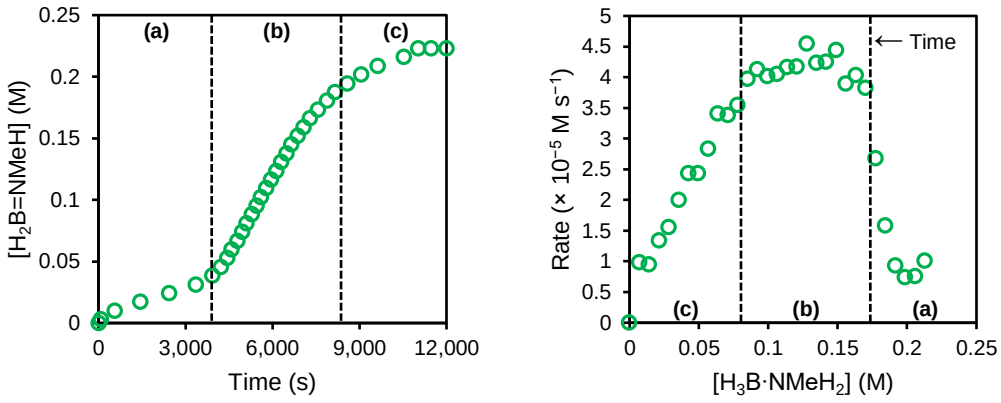


Figure 5.11 Left: Temporal data plot for H_2B=NMeH formation (as measured by H_2 evolution). [**13**] = 8.92 × 10^{-4} M, [$H_3B{\cdot}NMeH_2$] = 0.223 M, 1,2-$C_6H_4F_2$ solvent. Right: Rate versus [$H_3B{\cdot}NMeH_2$] over time. [**13**] = 8.92 × 10^{-4} M, [$H_3B{\cdot}NMeH_2$] = 0.223 M, 1,2-$C_6H_4F_2$ solvent. (a) Induction period. (b) Apparent zero order region. (c) Proposed first order region.

Figure 5.11 also details a rate versus [$H_3B{\cdot}NMeH_2$] plot for the dehydropolymerisation reaction. Post induction period (Figure 5.11(a)), between 0.17 M and 0.08 M, there is an apparent zero order dependence on $H_3B{\cdot}NMeH_2$ (Figure 5.11(b)). At concentrations below 0.08 M $H_3B{\cdot}NMeH_2$, a dependence of [$H_3B{\cdot}NMeH_2$] on the rate of reaction is apparent (Figure 5.11(c)), from which a proposed first order fit gives a reasonable R^2 value of 0.940. This profile indicates complicated kinetics which will be investigated further during this Chapter.

5.4.1 Tests for catalyst homogeneity

To discount the formation of catalytically active rhodium nanoparticles in the dehydropolymerisation of $H_3B{\cdot}NMeH_2$ using precatalyst **13**, exogeneous PPh_3 and Hg were added to the reaction mixture once turnover was established (Figure 5.12),[16] in an analogous manner to that of Xantphos-^{i}Pr precatalyst **2** discussed in detail in Section 3.3.2. In both cases, the reactions reached completion, suggesting that catalysis is likely to be homogeneous, and there is an alternative explanation for the observed long induction period. This will be investigated later in this Chapter.

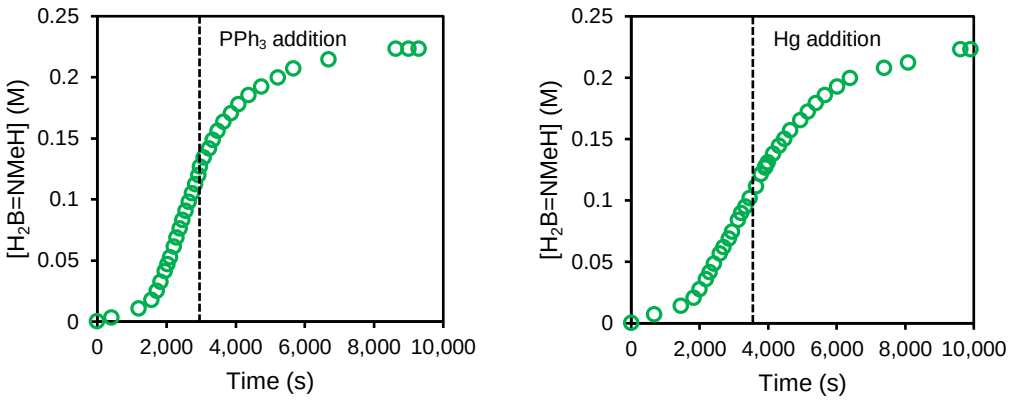


Figure 5.12 Temporal data plots for $H_2B{=}NMeH$ formation (as measured by H_2 evolution). [**13**] = 8.92×10^{-4} M, [$H_3B{\cdot}NMeH_2$] = 0.223 M, 1,2-$C_6H_4F_2$ solvent. Left: Effect of 0.2 equivalents of PPh_3 added at 2,800 s. Right: Effect of 1500 equivalents of Hg added at 3,600 s.

*5.4.2 Determining order in precatalyst **13** and $H_3B{\cdot}NMeH_2$*

To analyse the effect of the concentration of precatalyst **13** on catalysis, dehydropolymerisation was carried out at 0.223 M $H_3B{\cdot}NMeH_2$ and catalyst loadings of 0.1 mol% – 1.0 mol% **13** and the hydrogen evolution kinetics measured (the GPC data for the polyaminoborane produced under these conditions is graphically represented in Figure 5.6). Due to the nature of the induction period and the apparent zero order relationship of rate on $H_3B{\cdot}NMeH_2$ shown in Figure 5.11, the average rate between 25% and 75% conversion, i.e. the apparent zero order rate, at each catalyst loading was compared (Figure 5.13).

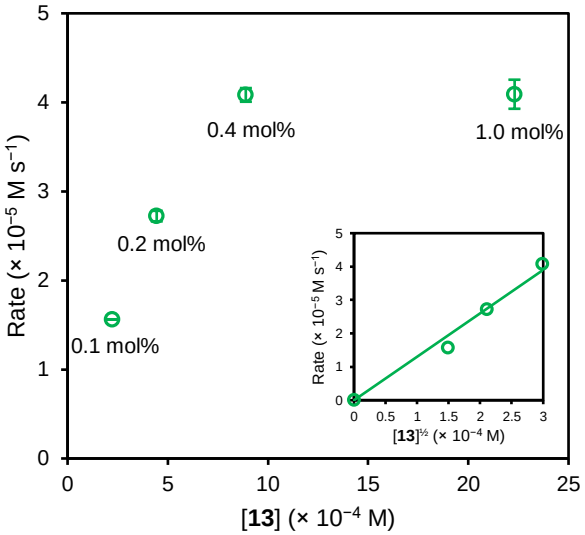


Figure 5.13 Rate (measured in the apparent zero order region between 25% – 75% $H_3B{\cdot}NMeH_2$ conversion) versus [**13**] plot for the dehydropolymerisation of $H_3B{\cdot}NMeH_2$ using precatalyst **13**. [$H_3B{\cdot}NMeH_2$] = 0.223 M, 1,2-$C_6H_4F_2$ solvent. Inset: Apparent zero order rate versus [**13**]^{½} plot for the dehydropolymerisation of $H_3B{\cdot}NMeH_2$ using **13** between 2.23 × 10^{-4} M (0.1 mol%) and 8.92 × 10^{-4} M (0.4 mol%) **13**. [$H_3B{\cdot}NMeH_2$] = 0.223 M, 1,2-$C_6H_4F_2$ solvent. A line of best fit is shown for a hypothetical half order dependence on [**13**] (R^2 = 0.979).

Between 0.1 mol% **13** (2.23 × 10^{-4} M) and 0.4 mol% **13** (8.92 × 10^{-4} M), rate increases from 1.6 × 10^{-5} M s^{-1} to 4.1 × 10^{-5} M s^{-1}, however increasing the catalyst loading further to 1.0 mol% (2.23 × 10^{-3} M) did not lead to an increase in rate, staying almost constant at a value of 4.1 × 10^{-5} M s^{-1}. In addition, the relationship between rate and [**13**] between 0.1 mol% and 0.4 mol% catalyst loading does not appear linear (R^2 = 0.817), instead a better, though still imperfect, fit of R^2 = 0.983 can be achieved when rate is plotted against [**13**]^{½} which indicates a kinetic regime of more half order precatalyst dependence rather than first order (Figure 5.13, inset). This half order catalyst dependence, in addition the observed maximum rate limit of approximately 4.1 × 10^{-5} M s^{-1}, suggests a complicated kinetic landscape of dehydropolymerisation using precatalyst **13**. This is further reiterated by the catalyst loading dependence on the induction period (Figure 5.14).

5.4.3 Induction period prior to the onset of H_2 evolution

In Chapter 3 the short length of the induction period (< 150 s) and fast $H_3B{\cdot}NMeH_2$ dehydrogenation using Xantphos-^{i}Pr system **2** made induction period comparisons between catalyst loadings difficult to interpret. However, the very slow, 60 minute induction period in the DPEphos system at 0.4 mol% **13** (Figure 5.11) was of interest to investigate. Figure 5.14 shows that surprisingly, the induction period increases in length as catalyst concentration increases when using the same batch of 1,2-$C_6H_4F_2$ solvent. The shortest induction period of 33 minutes was reported at 0.1 mol% **13**, and the highest at 1.0 mol% **13** (110 minutes). This seemingly counterintuitive dependence has been documented previously in amine borane dehydrocoupling by Weller and Manners,[17] where the induction period prior to dehydrocoupling of $H_3B{\cdot}NMe_2H$ using $[Rh(Ph_2P(CH_2)_xPPh_2)(\eta^6\text{-}C_6H_5F)][BAr^F{}_4]$ (x = 3 – 5) in 1,2-$C_6H_4F_2$ solvent increased in length on increasing the catalyst loading. This was speculated to be due to the formation of the bimetallic complexes $[\{Rh(Ph_2P(CH_2)_xPPh_2)\}_2(\mu\text{-}H)(\mu\text{-}H_2BNMe_2)][BAr^F{}_4]$ (x = 3 – 5), although these structures were only resolved later.[2] Interestingly these complexes are analogous to $[\{Rh(\kappa^2\text{-}P,P\text{-}DPEphos)\}_2(\mu\text{-}H)(\mu\text{-}H_2BNMeH)][BAr^F{}_4]$ (**14**), which was observed in the reaction of **13** with 10 equivalents of $H_3B{\cdot}NMeH_2$ detailed in Figure 4.4.

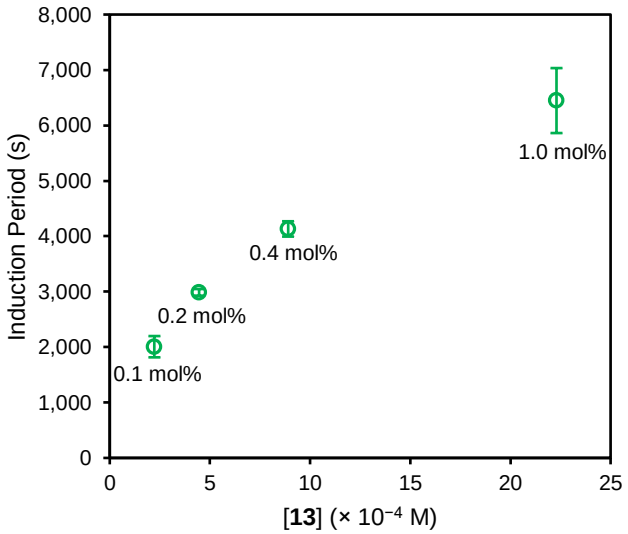


Figure 5.14 Induction period prior to the onset on H_2 evolution versus [**13**] plot for the dehydropolymerisation of $H_3B{\cdot}NMeH_2$ using precatalyst **13**. $[H_3B{\cdot}NMeH_2]$ = 0.223 M, 1,2-$C_6H_4F_2$ solvent.

These results further indicate complicated reaction kinetics, which may be due to the presence of bimetallic complexes formed throughout the reaction, implied by Weller and Manners' previous work,[17] as well as the apparent half order dependence of **13** on dehydrogenation rate (Figure 5.13, inset) between 2.23×10^{-4} M and 8.92×10^{-4} M **13**.

5.4.4 Catalyst recharging experiments

Addition of two successive batches of $H_3B{\cdot}NMeH_2$ to the catalysis solution post dehydropolymerisation (0.4 mol% **13**, 0.223 M [$H_3B{\cdot}NMeH_2$]) resulted in full consumption of $H_3B{\cdot}NMeH_2$. The equivalents of H_2 versus time plot for all three consecutive experiments are shown in Figure 5.15. Whilst significantly shorter in length, there still appeared to be an induction period for the second and third additions of $H_3B{\cdot}NMeH_2$ of approximately 5 minutes, indicating that although the organometallic species at the end of catalysis remain active, conversion to the active catalytic species is required on the addition of further $H_3B{\cdot}NMeH_2$. Likewise to the Xantphos-^{i}Pr system described in Chapter 3, the third catalytic run shows a reduction in rate, most likely due to catalyst deactivation on manipulation of the reaction mixture over the 9 hour time frame of the total reaction.

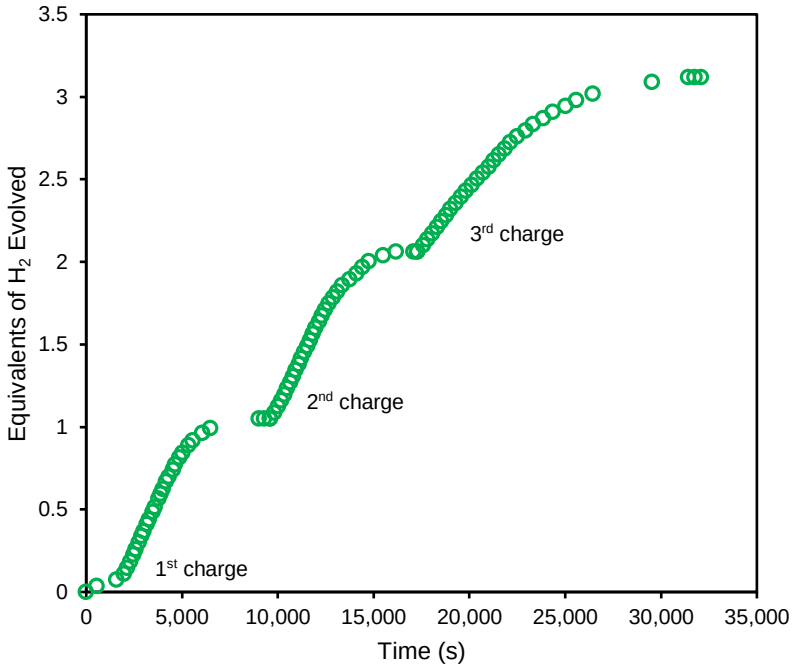


Figure 5.15 Temporal data plots for the equivalents of H_2 formed over 3 successive catalytic runs (as measured by H_2 evolution) in 1,2-$C_6H_4F_2$ solvent. [**13**] = 8.92×10^{-4} M, [$H_3B{\cdot}NMeH_2$] = 0.223 M × 3.

5.4.5 Kinetic isotope effect on dehydrogenation catalysis

Kinetic isotope effects of the dehydrogenation process (KIE = k_H/k_D) were explored using the deuterated amine borane substrates $D_3B{\cdot}NMeH_2$ and $H_3B{\cdot}NMeD_2$. By using $D_3B{\cdot}NMeH_2$ at 0.223 M ([**13**] = 8.92×10^{-4} M, 0.4 mol%), a KIE of 1.1 ± 0.1 for B–H/B–D substitution was measured, while $H_3B{\cdot}NMeD_2$ resulted in a KIE of 2.2 ± 0.1 for N–H/N–D substitution as shown in Figure 5.16, by comparing the apparent zero order rates for each amine borane substrate.

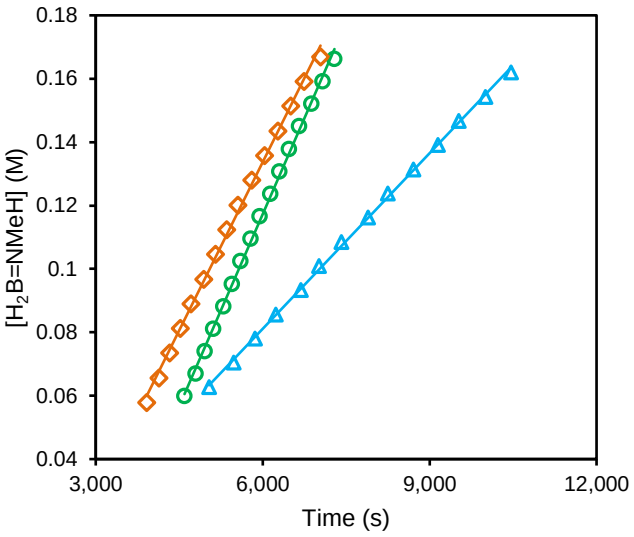
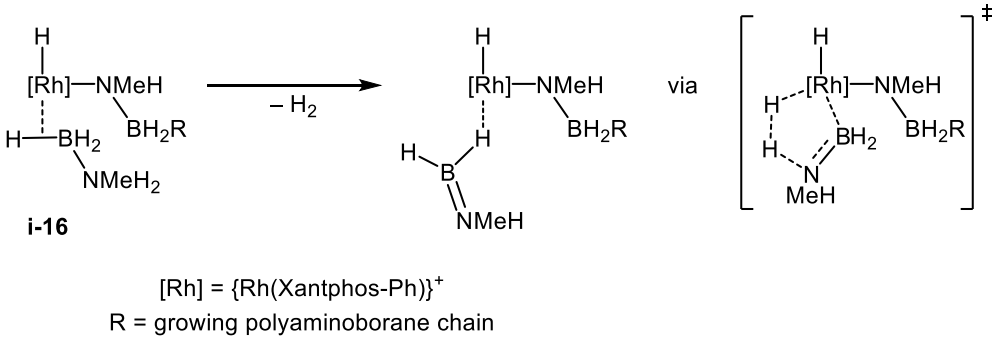


Figure 5.16 Temporal data plot for $H_2B{=}NMeH$ formation (in the apparent zero order region between 25% – 75% $H_3B{\cdot}NMeH_2$ conversion, as measured by H_2 evolution). [**13**] = 8.92×10^{-4} M, 1,2-$C_6H_4F_2$ solvent. ○ = 0.223 M $H_3B{\cdot}NMeH_2$ (rate = $4.0 \pm 0.1 \times 10^{-5}$ M s^{-1}); ◇ = 0.223 M $D_3B{\cdot}NMeH_2$ (rate = $3.5 \pm 0.1 \times 10^{-5}$ s^{-1}); △ = 0.223 M $H_3B{\cdot}NMeD_2$ (rate = $1.9 \pm 0.1 \times 10^{-5}$ s^{-1}).

The KIE associated with B–H activation using precatalyst **13** is close to unity and likely indicates that B–H activation is not involved in the rate limiting process. This is further corroborated by the fast incorporation of deuterium into the Rh···H–B groups in [Rh(κ^2-P,P-DPEphos)(η^2-$H_2B(CH_2CH_2{}^tBu){\cdot}NMe_3$)][$BAr^F{}_4$] by a possible mechanism detailed in Scheme 4.4. The KIE of 2.2 ± 0.1 associated with catalysis performed using $H_3B{\cdot}NMeD_2$ suggests that N–H cleavage is involved in the turnover limiting step of dehydrogenation, or in an equilibrium process prior to it. This value is much smaller than reported for Xantphos-^{i}Pr system **2** (k_{NH}/k_{ND} = 4.4 ± 0.1, Figure 3.9), suggesting that a different dehydrogenation mechanism operates in the DPEphos system. Instead, the DPEphos system appears more consistent with that of {Rh(Xantphos-Ph)}$^+$ precatalyst **i-13**, in which a KIE of 2.1 ± 0.2 was reported on deuteration at the nitrogen in the dehydrocoupling of secondary amine borane $H_3B{\cdot}NMe_2H$.[1] This was associated with rate limiting N–H activation in the formation of $H_2B{=}NMe_2$, which then dimerised to form $(H_2BNMe_2)_2$. With this result, the analogous dehydrocoupling of primary amine borane $H_3B{\cdot}NMeH_2$ using **i-13** was proposed to occur through an on metal dehydrogenation mechanism whereby the resultant

aminoborane $H_2B{=}NMeH$ remained metal-bound (Scheme 5.2).[1] Therefore, a similar dehydrogenation mechanism may occur in DPEphos system **13**.



Scheme 5.2 $H_3B{\cdot}NMeH_2$ dehydrogenation mechanism proposed in Xantphos-Ph system **i-13**. $[BAr^F{}_4]^-$ anions not shown for clarity. The full dehydropolymerisation mechanism for this system in shown in Scheme 1.17.

In addition to differences in rates of dehydrogenation for the deuterated amine borane substrates, differences in the induction periods were also apparent. The relationship of induction period length versus deuteration of amine borane substrate in Figure 5.17 shows that deuteration at the boron leads to the shortest induction period – 20 minutes shorter than non-deuterated $H_3B{\cdot}NMeH_2$. On deuteration at nitrogen, a shorter induction period is also seen, however to a lesser extent of approximately 10 minutes. Given that these values lie outside of the error obtained for non-deuterated $H_3B{\cdot}NMeH_2$ over three catalytic runs, this decrease is proposed to be significant. In this instance, the deuterated species react faster than the fully protio analogue, therefore a qualitative inverse kinetic isotope effect is in operation. Whilst the origin of this trend is currently unclear, if amine borane dissociation is necessary for the true active catalytic species to form, deuterating the amine borane may stabilise the free amine and borane components and therefore lower the dissociation energy. Alternatively, an intermediate sigma complex may form during the induction period which forms a strong B–D or H(D)–D bond which is more favourable on deuterium substitution over protium.

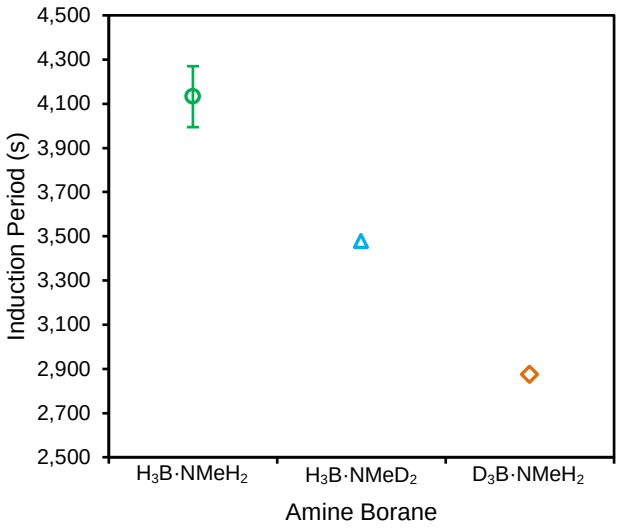


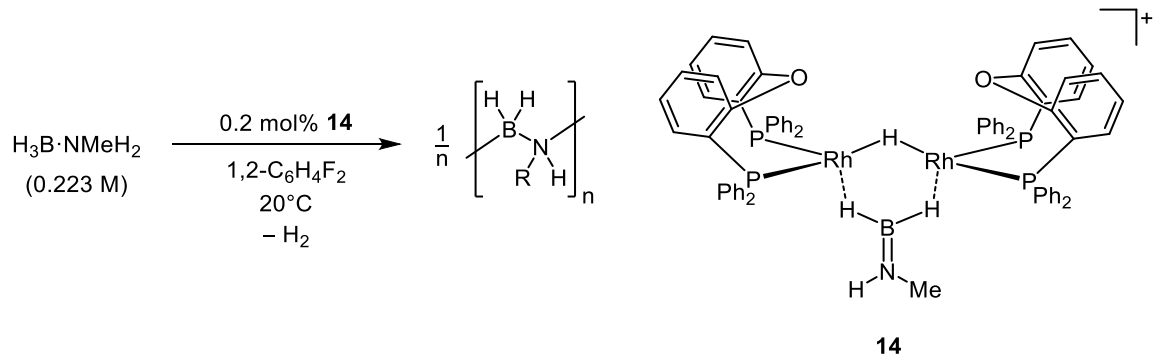
Figure 5.17 Induction period prior to the onset on H_2 evolution for the dehydropolymerisation of $H_3B{\cdot}NMeH_2$, $H_3B{\cdot}NMeD_2$ and $D_3B{\cdot}NMeH_2$ using precatalyst **13**. [**13**] = 8.92×10^{-4} M, [amine borane] = 0.223 M, 1,2-$C_6H_4F_2$ solvent.

5.5 Involvement of [{Rh(DPEphos)}$_2$(H)(H$_2$BNMeH)]$^+$ (**14**) and [{Rh(DPEphos)}$_2${(H$_2$B)$_2$NMeH}]$^+$ (**15**) in the dehydropolymerisation of H$_3$B·NMeH$_2$ using [Rh(DPEphos)(H$_2$B(CH$_2$CH$_2$^{t}Bu)·NMe$_3$)]$^+$ (**13**)

The NMR data obtained for the speciation experiments of precatalyst **13** with 10 equivalents of $H_3B{\cdot}NMeH_2$ is detailed in Figure 4.4, allowing for the identification of complexes **14**, [{Rh(κ^2-P,P-DPEphos)}$_2$(μ-H)(μ-H$_2$BNMeH)][BAr$^F{}_4$], and **15**, [{Rh(κ^2-P,P-DPEphos)}$_2${μ-(H$_2$B)$_2$NMeH}][BAr$^F{}_4$], to be present in the reaction mixture. This suggests that these complexes may also be present at the lower catalyst loadings used in dehydropolymerisation outlined during this Chapter. This work also suggested that although both **14** and **15** appear present throughout the reaction using 10 mol% **13**, complex **14** is in its highest concentration at the beginning and end of dehydrocoupling, and **15** reaches its highest concentration after the start of dehydrocoupling, diminishing towards the end of catalysis. This observation was confirmed further, as at the end of dehydropolymerisation conducted at 1.0 mol% catalyst loading of **13**, complex **14** was the only species present by $^{31}P\{^1H\}$ NMR spectroscopy of the concentrated reaction mixture.

*5.5.1 Role of [{Rh(DPEphos)}$_2$(H)(H$_2$BNMeH)]$^+$ (**14**)*

Due to the observation of [{Rh(κ^2-P,P-DPEphos)}$_2$(μ-H)(μ-H$_2$BNMeH)][BAr$^F{}_4$] (**14**) in the dehydrocoupling of H$_3$B·NMeH$_2$ both at high catalyst loadings such as 10 mol% (Figure 4.3), as well as at the end of dehydropolymerisation at lower catalyst loadings of 1.0 mol%, its role as an in situ synthesised precatalyst (according to Scheme 4.6) was determined. Catalysis was carried out using the same conditions employed previously for precatalyst **13** (0.2 mol% **14** i.e. 0.4 mol% Rh$_1$, 0.223 M H$_3$B·NMeH$_2$, Scheme 5.3), and the resulting temporal profile as measured by hydrogen evolution is plotted in Figure 5.18. Comparison with the analogous temporal profile of **13** shows that **14** also shows an induction period, albeit shorter, and undergoes dehydrogenation of H$_3$B·NMeH$_2$ between 25% and 75% conversion at an apparent zero order rate of $4.4 \pm 0.1 \times 10^{-5}$ M s^{-1} – very similar to that of precatalyst **13** ($4.1 \pm 0.2 \times 10^{-5}$ M s^{-1}). These observations suggest that **14** is in fact also a dehydropolymerisation precatalyst and requires conversion to the true active catalytic species. Further confirmation that **14** is involved in the overall mechanism of the dehydropolymerisation of H$_3$B·NMeH$_2$ by **13** was shown by GPC analysis of the polyaminoborane produced using in situ formed **14** at 0.2 mol% loading (M_n = 14,800 g mol^{-1}, Đ = 1.6) which was slightly longer than that produced by 0.4 mol% **13** under the same reaction conditions (M_n = 10,100 g mol^{-1}, Đ = 1.8). This may be due to a difference in the number of chain propagation sites present when using **14** instead of **13**, and a higher molecular weight implies a lower number of propagating sites.



14

Scheme 5.3 Dehydropolymerisation of H$_3$B·NMeH$_2$ using in situ formed **14** under hydrogen measurement conditions. [BAr$^F{}_4$]$^-$ anion not shown for clarity.

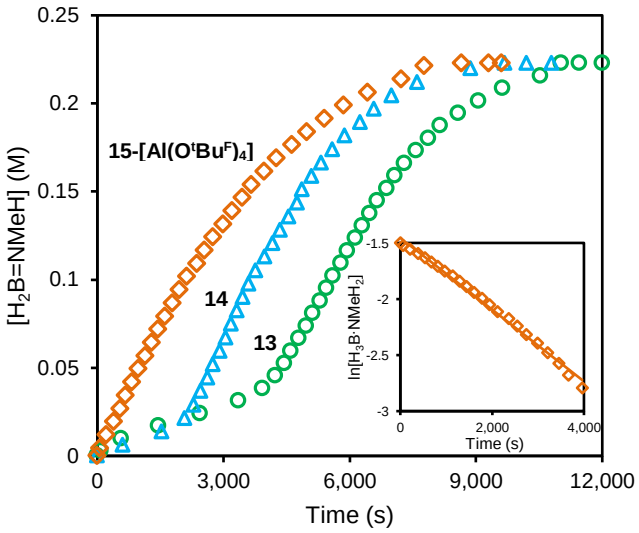
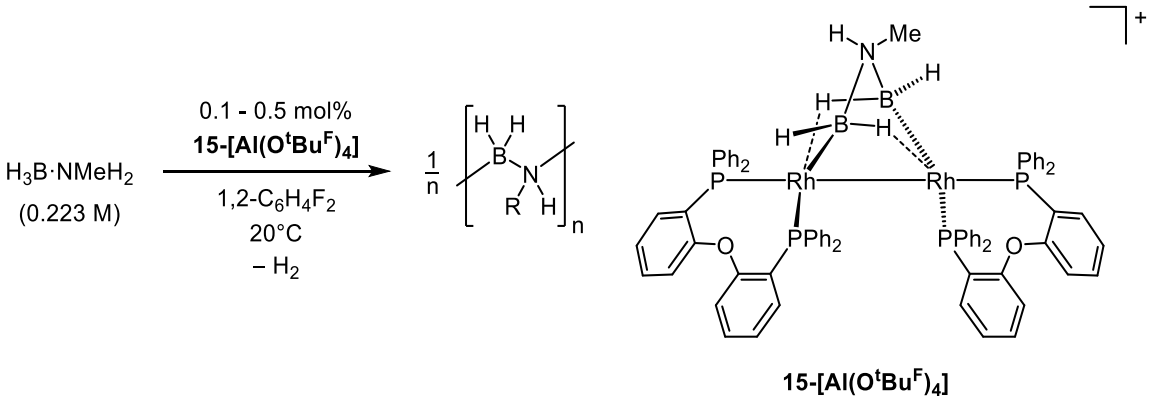


Figure 5.18 Temporal data plots for $H_2B{=}NMeH$ formation (as measured by H_2 evolution). $[H_3B{\cdot}NMeH_2]$ = 0.223 M, 1,2-$C_6H_4F_2$ solvent. ○ = 8.92×10^{-4} M **13**; ◇ = 4.45×10^{-4} M **15-[Al(O^{t}Bu^F)$_4$]**; △ = 4.45×10^{-4} M in situ formed **14**. Inset: First order rate plot under these conditions for **15-[Al(O^{t}Bu^F)$_4$]** (k_{obs} = 3.2 ± 0.1 × 10^{-4} s^{-1}).

5.5.2 Role of [{Rh(DPEphos)}$_2${(H$_2$B)$_2$NMeH}]$^+$ (15)

Complex **15** was also implicated in $H_3B{\cdot}NMeH_2$ dehydrocoupling using a 10 mol% loading of **13** (Figure 4.3). As its $[Al(O^tBu^F)_4]^-$ salt, for which the crystalline material contained some 5% [{Rh(κ^2-P,P-DPEphos)}$_2$(μ-H)(μ-H_2BNMeH)][Al(O^{t}Bu^F)$_4$] (**14-[Al(O^{t}Bu^F)$_4$]**) (Figure 4.13) and $(H_2BNMeH)_n$, **15-[Al(O^{t}Bu^F)$_4$]** was tested in catalysis (0.2 mol% **15-[Al(O^{t}Bu^F)$_4$]** i.e. 0.4 mol% Rh_1, 0.223 M $H_3B{\cdot}NMeH_2$, Scheme 5.4). In fact, on using this complex as a precatalyst, the induction period essentially vanished, leading to a first order profile for the temporal hydrogen evolution plot (Figure 5.18) with a corresponding k_{obs} value of 3.2 ± 0.1 × 10^{-4} s^{-1}, calculated for the first 75% of $H_3B{\cdot}NMeH_2$ conversion.



Scheme 5.4 Dehydropolymerisation of $H_3B{\cdot}NMeH_2$ using **15-[Al(O^{t}Bu^F)$_4$]** under hydrogen measurement conditions. $[Al(O^tBu^F)_4]^-$ anion not shown for clarity.

With this simplified kinetic profile obtained using complex **15-[Al(O^{t}Bu^F)$_4$]**, further mechanistic insight was obtained by measuring the pseudo first order k_{obs} of the reaction over a range of catalyst concentrations (Figure 5.19, inset). Interestingly, this data led to the observation of a half order dependence of **15-[Al(O^{t}Bu^F)$_4$]** on k_{obs} (R^2 = 0.989, Figure 5.19), chiming with the observation of precatalyst order using **13** (Figure 5.13).

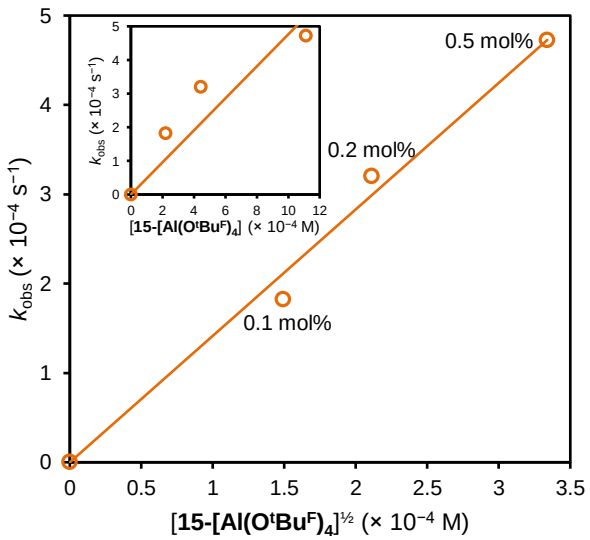
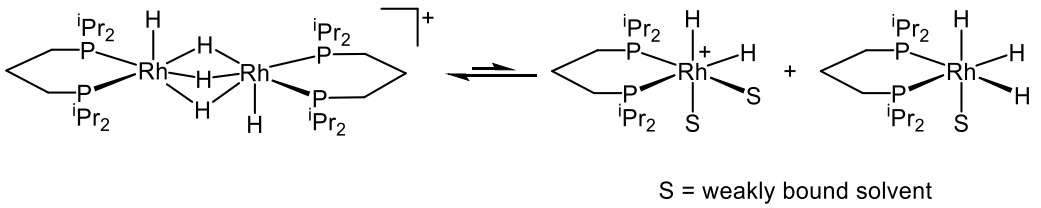


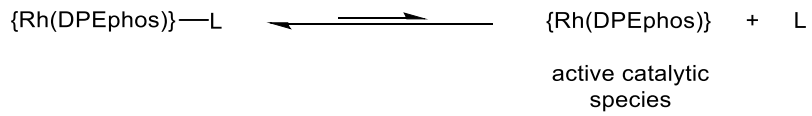
Figure 5.19 First order k_{obs} versus $[$**15-[Al(O^{t}Bu^F)$_4$]**$]^{½}$ plot for the dehydropolymerisation of $H_3B{\cdot}NMeH_2$ using **15-[Al(O^{t}Bu^F)$_4$]**. $[H_3B{\cdot}NMeH_2]$ = 0.223 M, 1,2-$C_6H_4F_2$ solvent. A line of best fit is shown for the proposed half order dependence on $[$**15-[Al(O^{t}Bu^F)$_4$]**$]$ (R^2 = 0.989). Inset: First order k_{obs} versus $[$**15-[Al(O^{t}Bu^F)$_4$]**$]$ plot for the dehydropolymerisation of $H_3B{\cdot}NMeH_2$ using **15-[Al(O^{t}Bu^F)$_4$]**. $[H_3B{\cdot}NMeH_2]$ = 0.223 M, 1,2-$C_6H_4F_2$ solvent. A line of best fit is shown for a hypothetical first order dependence on $[$**15-[Al(O^{t}Bu^F)$_4$]**$]$ (R^2 = 0.827).

Half order kinetics in catalytic reactions using bimetallic complexes may be a result of a rapid dimer/monomer equilibrium where the dimer is the dominant species but sits off-cycle, and several literature examples related to amine borane dehydrogenation have shown half order kinetic profiles.[18-23] If a bimetallic complex is in equilibrium with monometallic complexes which are catalytically active, this will lead to a half order dependence of k_{obs} on the concentration of the bimetallic precatalyst. In 2016, Liu, Weller and co-workers found that in the dehydrogenation of the BN-cyclohexane 2,2-H,Me-1,2-B,N-C_4H_{10}, the bimetallic precatalyst [{Rh(^{i}Pr$_2$P(CH$_2$)$_3$P^{i}Pr$_2$)(H)}$_2$(μ-H)$_3$][BAr$^F_4$] (Scheme 5.5) showed half order kinetics.[18] This was proposed to be due to [{Rh(^{i}Pr$_2$P(CH$_2$)$_3$P^{i}Pr$_2$)(H)}$_2$(μ-H)$_3$][BAr$^F_4$] being in equilibrium with one cationic and one neutral monomeric species, with only one of the monomers active in catalysis (Scheme 5.5). Hence, similar reactivity may occur in dehydropolymerisation catalysis using **15-[Al(O^{t}Bu^F)$_4$]**.



Scheme 5.5 The equilibrium between bimetallic amine borane dehydrogenation precatalyst [{Rh(^{i}Pr$_2$P(CH$_2$)$_3$P^{i}Pr$_2$)(H)}$_2$(μ-H)$_3$][BAr$^F_4$] and cationic species [Rh(^{i}Pr$_2$P(CH$_2$)$_3$P^{i}Pr$_2$)(H)$_2$(S)$_2$][BAr$^F_4$] and neutral species Rh(^{i}Pr$_2$P(CH$_2$)$_3$P^{i}Pr$_2$)(H)$_3$(S), where one of the monomeric complexes in catalytically active, hence leading to half order kinetics. S = weakly bound solvent. [BAr$^F_4$]$^-$ anions not shown for clarity.

Alternatively, half order kinetics may occur when ligand dissociation is vital for the formation of the active catalytic species, but where this ligand dissociation is also an equilibrium process (Scheme 5.6).[24-25] Therefore the reversible loss of H_2 or the $H_2BNMeHBH_2$ bridge from **15-[Al(O^{t}Bu^F)$_4$]** may be possibilities for ligand dissociation that would lead to half order kinetics.



Scheme 5.6 Equilibrium process which forms the active catalytic species {Rh(DPEphos)} via ligand dissociation, leading to half order kinetics. {Rh(DPEphos)} = unknown DPEphos-ligated rhodium complex – this may be bimetallic or monometallic.

The kinetics of polyaminoborane growth using **15-[Al(O^{t}Bu^F)$_4$]** under hydrogen measurement conditions were investigated, and showed a strong inverse effect of catalyst loading on $(H_2BNMeH)_n$ molecular weight – a 5-fold increase on catalyst loading led to a 4-fold decrease in M_n (Figure 5.20). This agrees with the overall trend observed using parent precatalyst **13** under the same reaction conditions, however the individual M_n values for the equivalent rhodium concentrations for **15-[Al(O^{t}Bu^F)$_4$]** are higher than those found for **13**. In the case of 0.2 mol% Rh_1, $(H_2BNMeH)_n$ formed by precatalyst **13** (0.2 mol%) compared to that of **15-[Al(O^{t}Bu^F)$_4$]** (0.1 mol%) gave significantly different M_n values of 14,500 g mol^{-1} (Đ = 1.7) and 33,400 g mol^{-1} (Đ = 1.7) respectively. However the values were more similar for 0.4 mol% Rh_1 (**13**: M_n = 10,500 g mol^{-1}, Đ = 1.8; **15-[Al(O^{t}Bu^F)$_4$]**: M_n = 15,900 g mol^{-1}, Đ = 1.8) and 1.0 mol% Rh_1 (**13**: M_n = 5,500 g mol^{-1}, Đ = 1.8; **15-[Al(O^{t}Bu^F)$_4$]**: M_n = 8,300 g mol^{-1}, Đ = 1.9), by comparing the data graphically presented in Figure 5.6 and Figure 5.20. This may be linked to the lower purity of **15-[Al(O^{t}Bu^F)$_4$]** (as **14-[Al(O^{t}Bu^F)$_4$]** and dehydrocoupling products were also present in the bulk solid of the isolated material), leading to a lower than calculated Rh content, and a lower number of initiating sites – therefore longer chains.

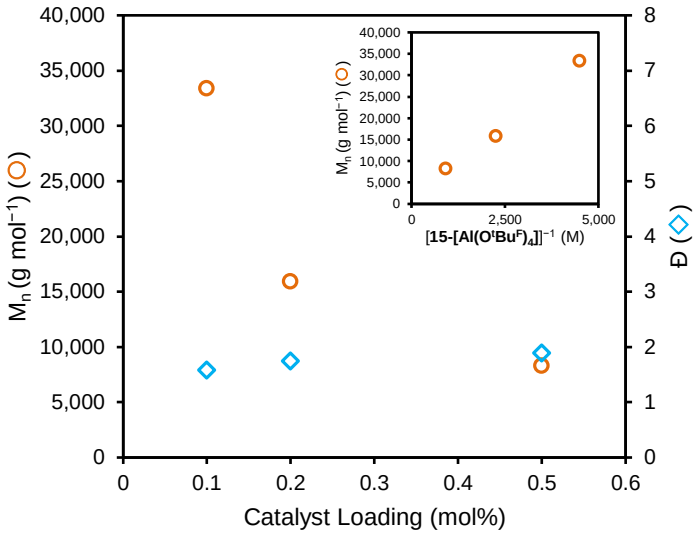


Figure 5.20 M_n (○**;** g mol^{-1}) and Đ (◇) versus catalyst loading of **15-[Al(O^{t}Bu^F)$_4$]** (mol%). [$H_3B{\cdot}NMeH_2$] = 0.223 M, 1,2-$C_6H_4F_2$ solvent. Hydrogen measurement conditions with the reaction flask isolated from the argon supply and connected to a 100.0 mL water-filled burette. Inset: M_n (g mol^{-1}) versus [**15-[Al(O^{t}Bu^F)$_4$]**]$^{-1}$ (M) under the same conditions showing the approximate inverse dependence on polyaminoborane M_n versus catalyst concentration.

These results suggest that complex **15** may be involved in the dehydropolymerisation of $H_3B{\cdot}NMeH_2$ by parent precatalyst **13**. However, in particular, the lack of induction period on performing catalysis with **15-[Al(O^{t}Bu^F)$_4$]** suggests that this complex is very closely connected to the true active catalytic species, whilst the half order dependence of **15-[Al(O^{t}Bu^F)$_4$]** on the rate of dehydrogenation shows that **15** itself is not the true active catalyst.

5.6 Involvement of $[BH_2(NMeH_2)_2][BAr^F{}_4]$ (**11**), BH_3 and $NMeH_2$ in the dehydropolymerisation of $H_3B{\cdot}NMeH_2$ using $[Rh(DPEphos)(H_2B(CH_2CH_2{}^tBu){\cdot}NMe_3)]^+$ (**13**)

The results described in Chapter 4 and thus far in Chapter 5 have presented the following points with regard to the possible mechanism of dehydrogenation and the identity of the true active catalytic species in this $\{Rh(DPEphos)\}^+$ system:

(1) The presence of [{Rh(κ^2-P,P-DPEphos)}$_2$(μ-H)(μ-H_2BNMeH)]$^+$ (**14**) in the dehydrocoupling of $H_3B{\cdot}NMeH_2$ by **13** suggests that concomitant formation of boronium [$BH_2(NMeH_2)_2$][$BAr^F{}_4$] (**11**) also occurs, as **11** was identified in the reaction mixture of the independent synthesis of **14** by ^{11}B NMR spectroscopy, as discussed in Section 4.5.1.

(2) The boron-rich amine borane-derived complex [{Rh(κ^2-P,P-DPEphos)}$_2${μ-(H_2B)$_2$NMeH}]$^+$ (**15**) is implicated in catalysis by NMR spectroscopy and ESI-MS, and borane-containing [{Rh(κ^2-P,P-DPEphos)}$_2$(μ-B_2H_5)]$^+$ (**16**) is also observed by ESI-MS, which suggests that free BH_3 is likely present in the reaction mixture, pointing towards B–N cleavage events in this system.[26-28]

(3) B–N cleavage would also result in the formation of free $NMeH_2$;[26-28] therefore the presence of $NMeH_2$ is likely. This is further confirmed as $NMeH_2$ may be involved in the formation of **14** from **13** in a mechanism analogous to that shown in Scheme 4.5 involving hydride transfer processes.

(4) Neither **14** nor **15** are the true active catalytic species. Catalysis using in situ formed **14** is accompanied by an induction period prior to the onset of H_2 evolution, and a kinetic study on the dehydropolymerisation of $H_3B{\cdot}NMeH_2$ by **15-[Al(O^{t}Bu^F)$_4$]** showed half order dependence on **15-[Al(O^{t}Bu^F)$_4$]**, suggesting that it sits off the catalytic cycle.

With these findings in mind, the action of [$BH_2(NMeH_2)_2$][$BAr^F{}_4$] (**11**), BH_3 or $NMeH_2$ on catalysis using **13** was investigated.

*5.6.1 Doping the reaction with [$BH_2(NMeH_2)_2$][$BAr^F{}_4$] (**11**)*

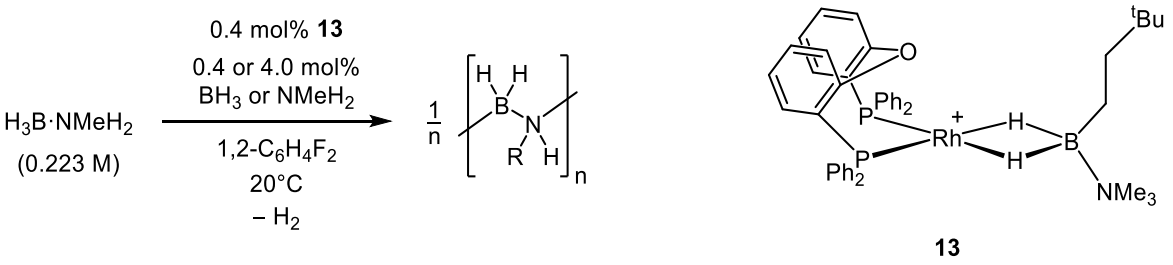
Given that [$BH_2(NMeH_2)_2$][$BAr^F{}_4$] (**11**) is formed in the dehydrocoupling of $H_3B{\cdot}NMeH_2$ by precatalyst **13**, the effect of exogeneous **11** on catalysis was probed. Interestingly, the presence of 10 equivalents of **11** with respect to the precatalyst was shown to increase the rate of $H_3B{\cdot}NMeH_2$ dehydrogenation approximately 3-fold in Xantphos-^{i}Pr system **2** (Figure 3.20), leading to a

proposed catalytic cycle which intimately involved **11** in the rate determining step (Scheme 3.6), as well as the KIE of 4.4 ± 0.1 obtained for N–H activation indicative of protonation involved in the rate determining step, therefore analogous reactivity was investigated in the DPEphos system.

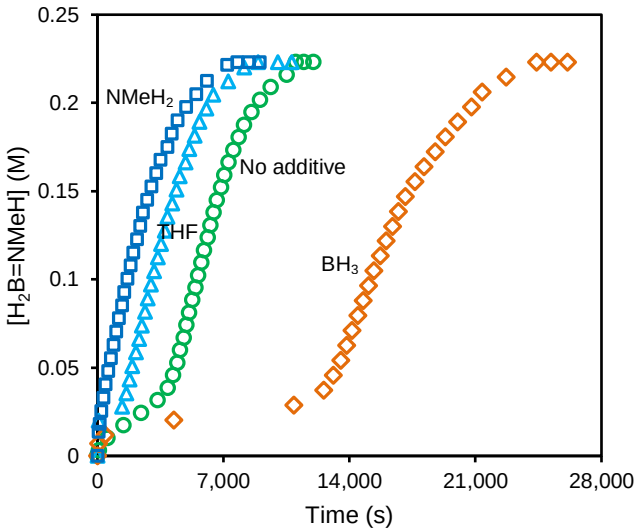
Dehydropolymerisation was carried out at 0.223 M $H_3B{\cdot}NMeH_2$, 0.4 mol% **13** under hydrogen measurement conditions with the addition of 10 equivalents of independently synthesised **11** (4 mol%). The reaction took approximately 24 hours to reach completion, providing polyaminoborane of very low molecular weight (M_n = 2,800 g mol^{-1}, Đ = 2.3). This directly contrasts the non-doped dehydropolymerisation experiment, which took approximately 3.5 hours to complete (Figure 5.11) and produced higher molecular weight polyaminoborane (M_n = 10,100 g mol^{-1}, Đ = 1.8), suggesting that in the DPEphos system, $[BH_2(NMeH_2)_2][BAr^F{}_4]$ is not involved in productive catalysis, and may in fact hamper it. As discussed previously in Section 3.5.2 with respect to the {Rh(Xantphos-^{i}Pr)}$^+$ system, the suppressive effect of boronium may increase stabilising dihydrogen bonding between $[BH_2(NMeH_2)_2]^+$ and amine borane,[29] or $NMeH_2$, leading to decreased activity.

5.6.2 Doping the reaction with THF solutions of BH_3 or $NMeH_2$

The effect of free BH_3 or free $NMeH_2$ on the dehydropolymerisation of $H_3B{\cdot}NMeH_2$ by 0.4 mol% precatalyst **13** was investigated by the addition of 1 or 10 equivalents of exogenous BH_3 or $NMeH_2$ (relative to rhodium concentration) as 0.05 mL THF solutions (Scheme 5.7). The effect of adding 0.05 mL plain THF was also probed as a direct control. The temporal hydrogen evolution profiles for the THF-doped, BH_3-doped (0.4 mol%) and $NMeH_2$-doped (0.4 mol%) reactions are shown in Figure 5.21, alongside the equivalent non-doped experiment under the same reaction conditions. The respective apparent zero order rates and induction periods are also outlined in the corresponding table in Figure 5.21.



Scheme 5.7 Dehydropolymerisation of $H_3B{\cdot}NMeH_2$ using precatalyst **13** doped with 1 or 10 equivalents of BH_3 or $NMeH_2$ via 0.05 mL THF at 5 seconds. $[BAr^F{}_4]^-$ anion not shown for clarity.



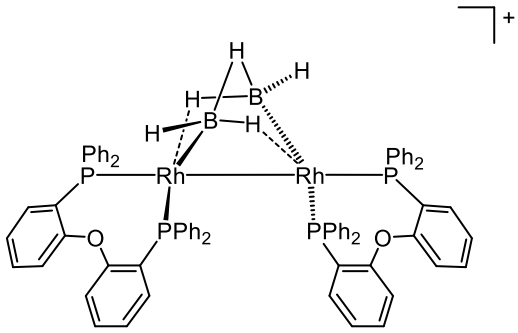
Additive	Apparent zero order rate ($\times 10^{-5}$ M s^{-1})	Induction period (minutes)
None	4.1 ± 0.2	60
0.05 mL THF	4.0 ± 0.1	30
1 equivalent BH_3 (via 0.05 mL THF)	2.4 ± 0.1	220
1 equivalent $NMeH_2$ (via 0.05 mL THF)	4.3 ± 0.1	0

Figure 5.21 Top: Temporal data plots for $H_2B{=}NMeH$ formation (as measured by H_2 evolution). [**13**] = 8.92×10^{-4} M, $[H_3B{\cdot}NMeH_2]$ = 0.223 M, 1,2-$C_6H_4F_2$ solvent. Additives injected into reaction vessel after 5 seconds. ○ = no additive; ◇ = 8.92×10^{-4} M BH_3 (via 0.05 mL THF); △ = 0.05 mL THF; □ = 8.92×10^{-4} M $NMeH_2$ (via 0.05 mL THF). Bottom: Table showing the apparent zero order rate and induction period for each of the doped experiments shown in the temporal data plot above.

As discussed previously, the non-doped experiment showed an induction period of approximately 60 minutes, with an overall reaction time of 3.5 hours and an apparent zero order rate between 25% – 75% $H_3B{\cdot}NMeH_2$ conversion of 4.1 ± 0.2 × 10^{-5} M s^{-1}. The control for the doping experiments

where 0.05 mL plain THF was added to the reaction after 5 seconds showed a decrease in the induction period to a value of 30 minutes, taking 3 hours to reach completion with an apparent zero order rate of $4.0 \pm 0.1 \times 10^{-5}$ M s^{-1}, indicating that THF shortens the induction period by half, whilst the dehydrogenation rate remained very similar. This may suggest that THF acts to encourage the formation of the true active catalytic species. GPC results of the corresponding $(H_2BNMeH)_n$ formed were also similar between the non-doped and THF-doped experiments, of M_n = 10,100 g mol^{-1} (Đ = 1.8) and M_n = 11,000 g mol^{-1} (Đ = 1.6) respectively.

In comparison, addition of 1 equivalent of BH_3 in 0.05 mL THF to the reaction mixture after 5 seconds led to a large increase in the induction period to approximately 220 minutes, and a halving of the apparent zero order rate to $2.4 \pm 0.1 \times 10^{-5}$ M s^{-1}: leading to an overall reaction time of 7 hours. The polyaminoborane produced was also shorter (M_n = 6,600 g mol^{-1}, Đ = 1.9), but not dramatically so. Interestingly, addition of 10 equivalents of BH_3 via a 0.05 mL THF solution halted catalysis entirely. These results suggest that BH_3 suppresses catalysis, and that any organometallic species formed by addition of BH_3 to the reaction mixture are inactive in catalysis. It is proposed that its identity could be the boron-rich bimetallic complex **16**, $[\{Rh(\kappa^2\text{-P,P-DPEphos})\}_2(\mu\text{-}B_2H_5)]^+$ (Figure 5.22), though this was not experimentally confirmed by NMR spectroscopy nor ESI-MS under these catalytic conditions. It is pertinent however that **16** was indicated in 10 mol% catalysis using ESI-MS (Figure 4.5), and by the addition of BH_3·THF to precatalyst **13** (Section 4.6.1).



16

Figure 5.22 Suggested structure of complex **16**, the proposed identity of the inactive organometallic complex formed on the addition of BH_3 (in THF) to $H_3B{\cdot}NMeH_2$ dehydropolymerisation catalysis using precatalyst **13**. $[BAr^F{}_4]^-$ anion not shown for clarity.

The suppression of amine borane dehydrogenation by free BH_3 has been previously reported by Chirik and co-workers,[30] where $(C_5Me_4H)_2Zr(\eta^2\text{-}BH_4)H$ was formed by capture of free BH_3 by $(C_5Me_4H)_2Zr(H)_2$, subsequently lowering the activity of the dihydride precatalyst (Figure 5.23). Similar findings were also observed by Heinekey and Goldberg in their Ir(POCOP-^{t}Bu)$(H)_2$ system, in which over time the dormant BH_3-trapped complex Ir(POCOP-^{t}Bu)$(H)_2(\eta^1\text{-}BH_3)$ formed during the dehydrogenation of $H_3B{\cdot}NH_3$ (Figure 5.23).[31-32] Schneider and co-workers also reported improved $H_3B{\cdot}NH_3$ dehydropolymerisation activity in their Fe(H)(CO)(PNP) (PNP = N(CH$_2$CH$_2$P^{i}Pr$_2$)$_2$) system on addition of a catalytic amount of NMe_2Et, which prevented catalyst deactivation through formation of an inactive BH_3 complex.[33] With these reports in mind with regard to DPEphos system **13**, it appears that if free BH_3 is formed during catalysis, it also suppresses it, and therefore the decrease in induction period found on THF doping or $NMeH_2$ doping (Figure 5.21) may operate by acting as Lewis bases to sequester the action of free BH_3.

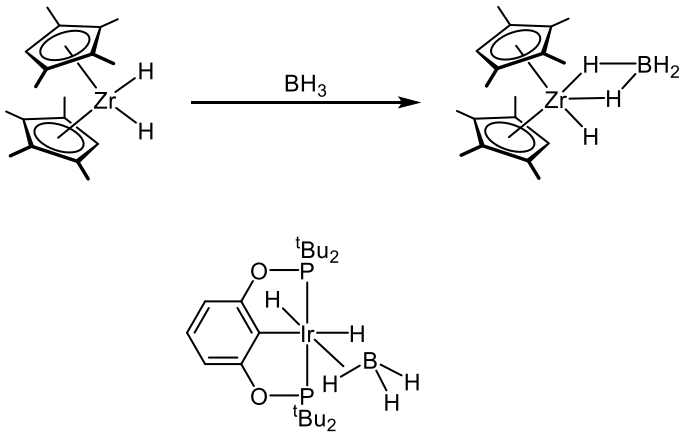


Figure 5.23 Top: Chirik's $(C_5Me_4H)_2Zr(H)_2$ system for the dehydrocoupling of $H_3B{\cdot}NMe_2H$ which can trap BH_3 to form $(C_5Me_4H)_2Zr(\eta^2\text{-}BH_4)H$ which shows decreased catalytic activity. Bottom: Heinekey and Goldberg's Ir(POCOP-^{t}Bu)$(H)_2(\eta^1\text{-}BH_3)$ complex which was proposed to be dormant in $H_3B{\cdot}NH_3$ dehydrogenation.

Figure 5.21 also shows the result of adding 1 equivalent of $NMeH_2$ via 0.05 mL THF to the dehydropolymerisation reaction. Not only did the induction period completely diminish, but the so-called apparent zero order rate region shown in Figure 5.11 simplified to straightforward first order curve in which the first order k_{obs} was calculated to be $3.7 \pm 0.1 \times 10^{-4}$ s^{-1}. Interestingly, the polyaminoborane produced was much longer in length (M_n = 27,400 g mol^{-1}, Đ = 1.6), which may suggest different relative rates of initiation, propagation and termination in the $NMeH_2$-doped

system relative to the THF-doped or non-doped experiments. As more initiating sites would lead to lower M_n values in the single site chain growth mechanism proposed for **13** by the observations in Section 5.3, this suggests that propagation (i.e. dehydrogenation and B–N coupling) or termination are appropriately affected on addition of $NMeH_2$. The effect of $NMeH_2$ was probed further by addition of 10 equivalents of $NMeH_2$ which led to very little change in the value of k_{obs} (4.2 ± 0.1 × 10^{-4} s^{-1}), suggesting that the reaction is zero order in $NMeH_2$ concentration.

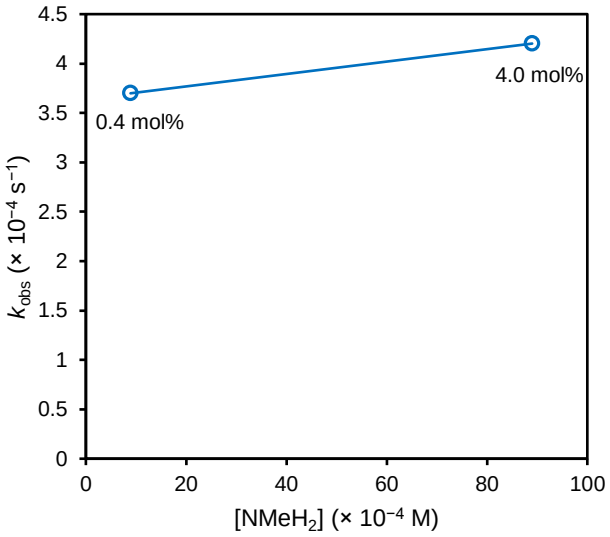
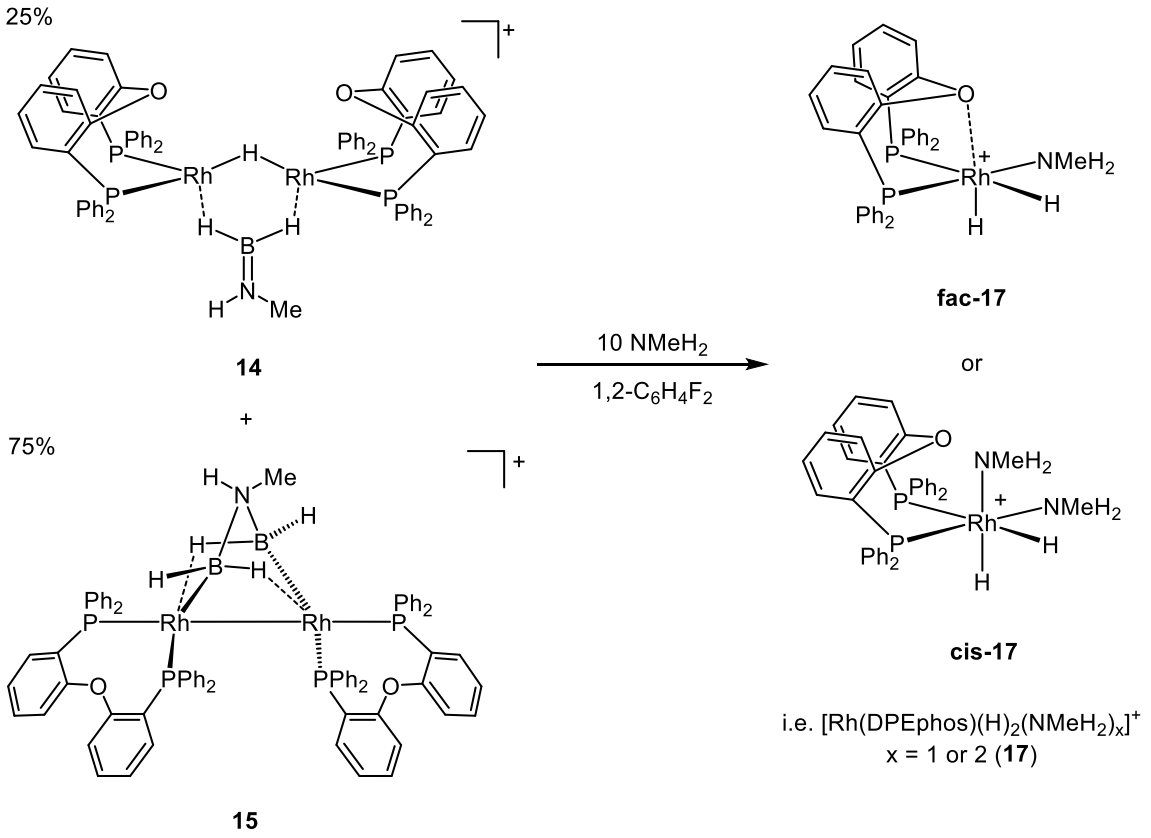


Figure 5.24 First order k_{obs} versus [$NMeH_2$] plot for the dehydropolymerisation of $H_3B{\cdot}NMeH_2$ using precatalyst **13** doped with $NMeH_2$ (in 0.05 mL THF) after 5 seconds. [**13**] = 8.92 × 10^{-4} M, [$H_3B{\cdot}NMeH_2$] = 0.223 M, 1,2-$C_6H_4F_2$ solvent. The line between the two points has the equation k_{obs} = 0.0063[$NMeH_2$] + 0.00036 which is consistent with the proposed zero order dependence on [$NMeH_2$] (gradient = 0.0063 ≈ 0).

The identity of the organometallic species formed on addition of $NMeH_2$ to the dehydropolymerisation reaction mixture was probed. Hydrogenating an NMR sample containing [Rh(κ^2-P,P-DPEphos)(NBD)][$BAr^F{}_4$] (**12**) with 4 equivalents of $H_3B{\cdot}NMeH_2$ in 1,2-$C_6H_4F_2$ solvent and subsequent freeze-pump-thawing of the solution and backfilling with argon led to a 1:3 mixture of complexes **14** and **15** after 30 minutes by $^{31}P\{^1H\}$ NMR spectroscopy. Addition of 10 equivalents of $NMeH_2$ (via THF solution) to this NMR sample under an argon atmosphere gave [Rh(κ^2-P,P-DPEphos)$(H)_2(NMeH_2)_x$][$BAr^F{}_4$] (x = 1 or 2, **17**) as the sole product by $^{31}P\{^1H\}$ NMR spectroscopy (Scheme 5.8). $BH(NMeH_2)_2$ was the major boron-containing product of the reaction, demonstrated by a characteristic doublet in the ^{11}B NMR spectrum of the reaction mixture (δ 28.6,

d, $^{1}J_{BH}$ 127 Hz),[34] which may result from the formal addition of the excess $NMeH_2$ present with $H_2B{=}NMeH$ equivalents in the form of $(H_2BNMeH)_n$, for example. As described in Section 4.6.2, **17** is only stable under an H_2 atmosphere (when synthesised in the absence of any $H_3B{\cdot}NMeH_2$ dehydrocoupling products), therefore given that this reaction was carried out under argon, 5% $[Rh(\kappa^2\text{-P,P-DPEphos})(NMeH_2)_x][BAr^F{}_4]$ (x = 1 or 2, **18**) could be observed in the $^{31}P\{^{1}H\}$ NMR spectrum of the mixture after 1 hour due to reductive elimination of H_2 from **17**.



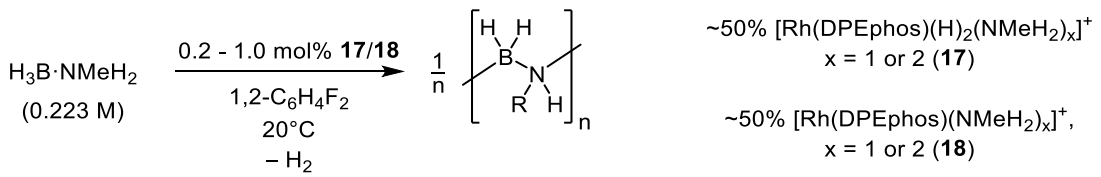
Scheme 5.8 Formation of $[Rh(\kappa^2\text{-P,P-DPEphos})(H)_2(NMeH_2)_x][BAr^F{}_4]$ (x = 1 or 2, **17**) from complexes **14** and **15**. $[BAr^F{}_4]^-$ anions not shown for clarity.

Therefore the dehydropolymerisation of $H_3B{\cdot}NMeH_2$ using $NMeH_2$ complexes **17** and **18** was probed.

5.7 Involvement of $NMeH_2$ complexes $[Rh(DPEphos)(H)_2(NMeH_2)_x][BAr^F{}_4]$ (x = 1 or 2, **17**) and $[Rh(DPEphos)(NMeH_2)_x][BAr^F{}_4]$ (x = 1 or 2, **18**) in the dehydropolymerisation of $H_3B{\cdot}NMeH_2$

In Chapter 4, it was reported that complex **17** could only be characterised in situ, and **18** could not be formed consistently and only in very poor yield (15%). Instead, a 1:1 mixture of complexes **17** and **18** could be formed in situ by initially hydrogenating $[Rh(\kappa^2\text{-P,P-DPEphos})(NBD)][BAr^F{}_4]$ (**12**) in 1,2-$C_6H_4F_2$ solvent in the presence of two equivalents of $NMeH_2$ (in THF). On degassing the reaction mixture and placing it under an argon atmosphere, in situ $^{31}P\{^1H\}$ NMR spectroscopy showed that the mixture contained ~50% each of complexes **17** and **18**.

Catalysis was subsequently performed using these in situ formed $NMeH_2$ complexes **17** and **18** at catalyst loadings between 0.2 mol% and 1.0 mol% (Scheme 5.9), ensuring that each reaction mixture contained 0.05 mL THF to directly compare to the other doped experiments (Section 5.6.2). The resultant temporal plots for hydrogen evolution from the systems showed pseudo first order kinetics in all cases, with the pseudo first order rate constants (k_{obs}) at each concentration recorded in Figure 5.25. The k_{obs} on using 8.92×10^{-4} M **17**/**18** ($k_{obs} = 4.1 \pm 0.1 \times 10^{-4}$ s^{-1}) was very similar to the value using 8.92×10^{-4} M **13** doped with one equivalent $NMeH_2$ ($k_{obs} = 3.7 \pm 0.1 \times 10^{-4}$ s^{-1}), suggesting that complexes **17** and **18** may be implicated in the $NMeH_2$-doped reaction, and further confirms the zero order dependence on $[NMeH_2]$ as two equivalents of $NMeH_2$ (1.78×10^{-4} M) relative to Rh were used to form **17**/**18** in situ.



Scheme 5.9 Dehydropolymerisation of $H_3B{\cdot}NMeH_2$ using in situ formed **17**/**18** under hydrogen measurement conditions. $[BAr^F{}_4]^-$ anions not shown for clarity.

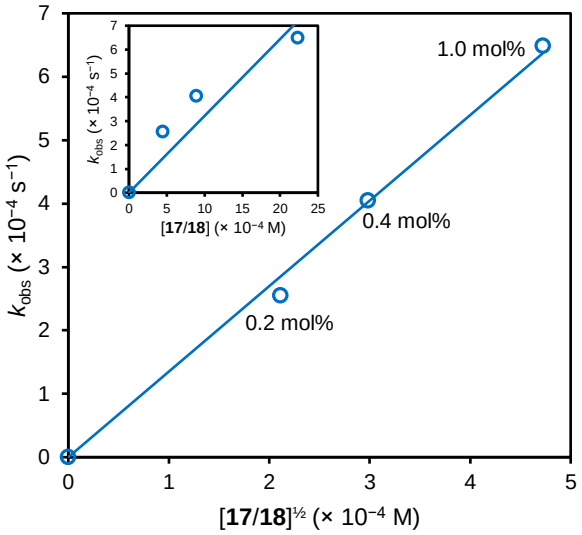


Figure 5.25 First order k_{obs} versus [**17**/**18**]^{½} plot for the dehydropolymerisation of $H_3B{\cdot}NMeH_2$ using in situ formed **17**/**18**. [$H_3B{\cdot}NMeH_2$] = 0.223 M, 1,2-$C_6H_4F_2$ solvent. A line of best fit is shown for the proposed half order dependence on [**17**/**18**] (R^2 = 0.995). Inset: First order k_{obs} versus [**17**/**18**] plot for the dehydropolymerisation of $H_3B{\cdot}NMeH_2$ using in situ formed **17**/**18**. [$H_3B{\cdot}NMeH_2$] = 0.223 M, 1,2-$C_6H_4F_2$ solvent. A line of best fit is shown for a hypothetical first order dependence on [**17**/**18**] (R^2 = 0.859).

Figure 5.25 shows that the order in **17**/**18** concentration with respect to the pseudo first order k_{obs} values best fit half order kinetics, similar to that found for complex **15-[Al(O^{t}Bu^F)$_4$]** (Figure 5.19). As previously discussed for **15-[Al(O^{t}Bu^F)$_4$]**, half order kinetics can occur when fast and reversible ligand dissociation is required for the formation of the active catalytic species, in an equilibrium process (Scheme 5.6).[24-25] Possibilities for ligand dissociation in this system include the reversible loss of H_2 from complex **17** to form **18**, or reversible loss of one equivalent of $NMeH_2$ from either **17** or **18**. Recalling that Figure 5.24 showed that the reaction is most likely zero order in $NMeH_2$ concentration, it is proposed that H_2 loss is reversible. Hence, tentatively, the loss of H_2 from **17** to form **18**, with **18** the true active catalytic species was proposed. Future work will be guided to synthesise and fully characterise complex **18** to ascertain its true identity as either **cis-18** ([Rh(κ^2-P,P-DPEphos)($NMeH_2$)$_2$][BAr^F_4]) or **mer-18** ([Rh(κ^3-P,O,P-DPEphos)($NMeH_2$)][BAr^F_4]). However, given that the crystal structure of **cis-18** was obtained (Figure 4.19) and the propensity for DPEphos complexes to prefer cis κ^2-P,P coordination over mer κ^3-P,O,P – or even fac κ^3-P,O,P – as shown in Figure 1.8, **cis-18** is thus far considered the best fit to the structure of **18**. If **18** is the

true active catalytic species, then the dependence of [**18**] on k_{obs} should be first order, however given that H_2 is formed during the dehydropolymerisation process, this may difficult to probe unless H_2 can be fully driven from the system via a chemical or mechanical process.

GPC analysis of the polyaminoborane samples formed using in situ synthesised **17**/**18** showed an inverse dependence of catalyst loading on $(H_2BNMeH)_n$ molecular weight (Figure 5.26). This trend is consistent with those shown by other $\{Rh(DPEphos)\}^+$ precatalysts such as **13** (Figure 5.6) and **15-[Al(O^{t}Bu^F)$_4$]** (Figure 5.20), further suggesting that complexes **17** and **18** may be involved in dehydropolymerisation using precatalyst **13**.

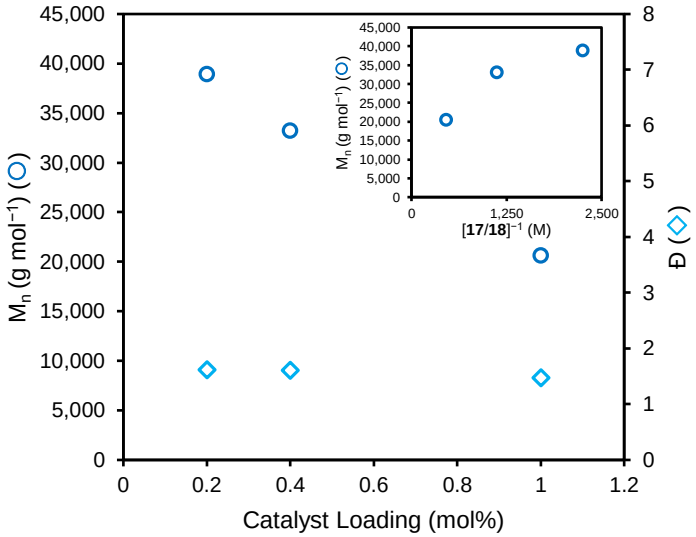


Figure 5.26 M_n (○**;** g mol^{-1}) and Đ (◇) versus catalyst loading of in situ formed **17**/**18** (mol%). [$H_3B{\cdot}NMeH_2$] = 0.223 M, 1,2-$C_6H_4F_2$ solvent. Hydrogen measurement conditions with the reaction flask isolated from the argon supply and connected to a 100.0 mL water-filled burette. Inset: M_n (g mol^{-1}) versus [**17**/**18**]$^{-1}$ (M) under the same conditions showing the approximate inverse dependence on polyaminoborane M_n versus catalyst concentration.

Despite neither complex **17** nor **18** being directly observed in catalysis using parent DPEphos precatalyst **13**, the data obtained thus far suggests that these complexes may in fact be the true active catalysts. Final confirmation that these amine complexes can be implicated in catalysis is that the organometallic complex formed at the end of the reaction of $H_3B{\cdot}NMeH_2$ with 10 mol% **17**/**18** was in fact the bridging aminoborane complex **14**, as confirmed by in situ $^{31}P\{^1H\}$ NMR

spectroscopy of the reaction mixture by the characteristic doublet at δ 28.3 ($^1J_{RhP}$ 150 Hz), detailed in Figure 5.27. Note that complex **14** was the sole phosphorus containing species present at the end of the dehydropolymerisation of $H_3B{\cdot}NMeH_2$ by 1.0 mol% parent DPEphos precatalyst **13**.

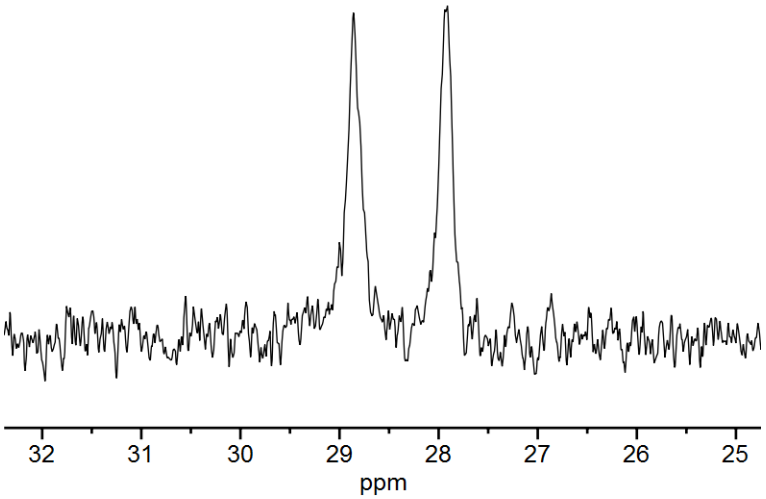


Figure 5.27 $^{31}P\{^1H\}$ NMR spectrum of the reaction mixture at the end of dehydrocoupling of $H_3B{\cdot}NMeH_2$ using in situ formed **17**/**18** at 10 mol% loading in 1,2-$C_6H_4F_2$ solvent performed in a sealed NMR tube.

5.8 Proposed mechanism for the dehydropolymerisation of $H_3B{\cdot}NMeH_2$ using the $\{Rh(DPEphos)\}^+$ system

The catalytic studies presented throughout this Chapter, and speciation experiments performed during Chapter 4, combine together to provide the following observations for the dehydropolymerisation of $H_3B{\cdot}NMeH_2$ using $\{Rh(DPEphos)\}^+$ precatalyst **13**, [Rh(κ^2-P,P-DPEphos)(η^2-$H_2B(CH_2CH_2{}^tBu){\cdot}NMe_3$)][$BAr^F{}_4$]:

(1) The temporal kinetic profiles of the dehydrogenation of $H_3B{\cdot}NMeH_2$ to form $H_2B{=}NMeH$ using precatalyst **13** appear complicated and hence are intractable to obtaining the reaction order in [**13**] or [$H_3B{\cdot}NMeH_2$].

(2) A KIE for B–H activation of 1.1 ± 0.1 and for N–H activation of 2.2 ± 0.1 as measured by the apparent zero order rate for the productive stage of $H_3B{\cdot}NMeH_2$ dehydrogenation by **13** suggests that N–H activation is involved in the rate limiting step during the dehydrogenation of

$H_3B{\cdot}NMeH_2$, by a mechanism analogous to that in the Xantphos-Ph system as shown in Scheme 5.2.

(3) Recharging experiments show that the catalyst remains active and is not irreversibly consumed in the dehydropolymerisation process, though there is an induction period prior to the onset of H_2 evolution on further additions of $H_3B{\cdot}NMeH_2$. The end organometallic species of catalysis is complex **14**, $[\{Rh(\kappa^2\text{-P,P-DPEphos})\}_2(\mu\text{-H})(\mu\text{-}H_2BNMeH)]^+$.

(4) The boronium cation $[BH_2(NMeH_2)_2]^+$ is observed in the ^{11}B NMR spectrum during the reaction of $H_3B{\cdot}NMeH_2$ with 10 mol% **13**, most likely due to the concomitant formation of $[\{Rh(\kappa^2\text{-P,P-DPEphos})\}_2(\mu\text{-H})(\mu\text{-}H_2BNMeH)]^+$ (**14**). However, the addition of 10 equivalents (relative to rhodium) of **11** in catalysis using precatalyst **13** led to a much longer total reaction time. In addition, very low molecular weight $(H_2BNMeH)_n$ uncharacteristic of the system was formed, suggesting that unlike in the Xantphos-^{i}Pr system, $[BH_2(NMeH_2)_2]^+$ is not involved in the dehydrogenation catalytic cycle.

(5) An observed speciation manifold that operates **13** → **14** → **15** → **14** in the non-doped reaction mixture, where neither **14** (induction period), nor **15** (half order kinetics) are the true active catalytic species, however the lack of induction period using **15-[Al(O^{t}Bu^F)$_4$]** as a precatalyst indicates that it may be close in identity to the true active catalytic species.

(6) A speciation manifold that operates **13** → **14**/**15** → **16** in the BH_3-doped reaction mixture leading to very slow catalysis as **16** is inactive.

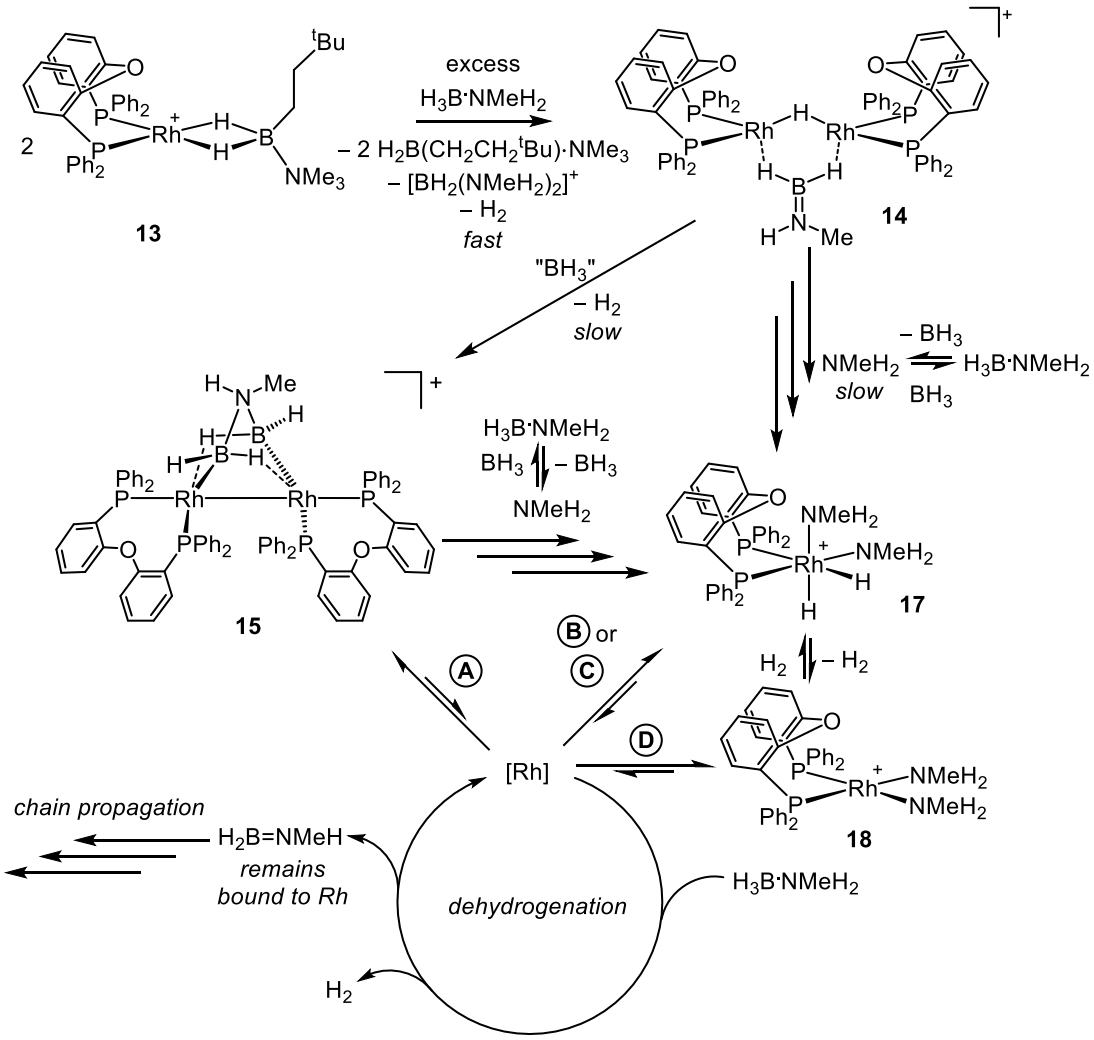
(7) A speciation manifold that operates **13** → **14**/**15** → **17**/**18** → **14** in the $NMeH_2$-doped reaction mixture, where **17** may lose H_2 to form **18** which may be the true active catalytic species, or alternatively loss of $NMeH_2$ from **17** or **18** may be the cause of half order kinetics observed using a mixture of **17**/**18** as a precatalyst.

(8) It is likely that small amounts of **16**, **17** and **18** (alongside the major organometallic components of **14** and **15**) are all present in low amounts in the non-doped dehydropolymerisation reaction using **13**, and since BH_3-derived **16** and $NMeH_2$-derived **17**/**18** show conflicting dehydrocoupling activities, this leads to the complicated kinetic profile (including the apparent zero order region) using precatalyst **13**.

(9) The chain growth characteristics of $H_2B{=}NMeH$ polymerisation suggest a mechanism that involves rapid addition of the reactive monomer $H_2B{=}NMeH$ to a growing polyaminoborane chain with a well-defined termination event.

(10) A strong effect of catalyst loading on the degree of polymerisation and control of polymerisation using H_2 suggests a single site coordination/dehydrogenation/insertion mechanism where H_2 is involved in the chain termination event.

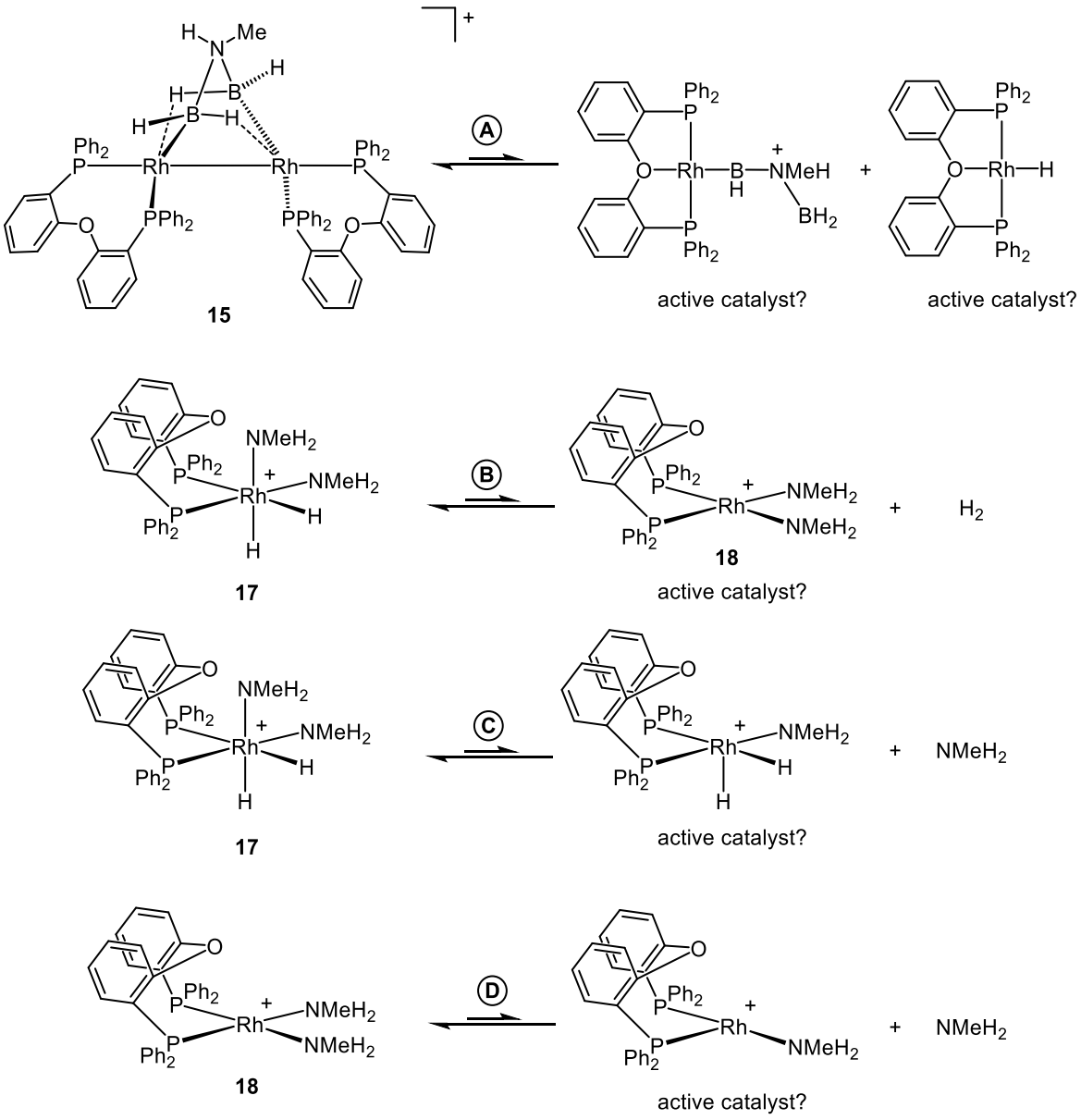
This information led to the proposal in Scheme 5.10 for the possible routes to the true active catalytic species, [Rh], for the dehydrogenation of $H_3B{\cdot}NMeH_2$.



Scheme 5.10 Proposed mechanism for the formation of the true active catalyst [Rh] in the dehydrogenation of $H_3B{\cdot}NMeH_2$ to $H_2B{=}NMeH$ using precatalyst **13**. The identity of **17** may be fac-[Rh(κ^3-P,O,P-DPEphos)$(H)_2(NMeH_2)$][$BAr^F{}_4$] and the identity of **18** may be mer-[Rh(κ^3-P,O,P-DPEphos)$(NMeH_2)$][$BAr^F{}_4$]. [$BAr^F{}_4$]$^-$ anions not shown for clarity.

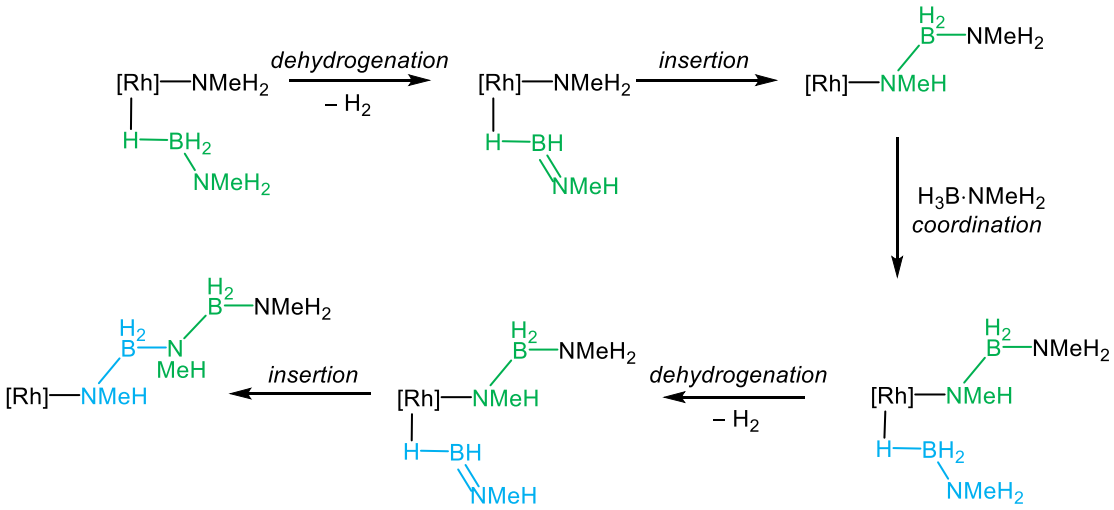
Overall loss of $H_2B(CH_2CH_2{}^tBu){\cdot}NMe_3$ from precatalyst **13** and reaction with $H_3B{\cdot}NMeH_2$ as per an analogous pathway to that in Scheme 4.5 leads to **14**. **17** then forms slowly via an undetermined mechanism which involves $NMeH_2$, formed by $H_3B{\cdot}NMeH_2$ dissociation. **15** may also form slowly from formal BH_3 addition to **14**. Adding further complexity, **17** can reversibly lose H_2 to form **18**. The lack of induction period on using **15-[Al(O^{t}Bu^F)$_4$]** or **17**/**18** as dehydropolymerisation precatalysts, and the half order kinetics observed, show that these species could all be connected to the true active species, [Rh], by a dimer/monomer equilibrium in **15-[Al(O^{t}Bu^F)$_4$]** or reversible loss

of a ligand in **17** or **18**. Options for this process from each of **15**, **17** and **18** (pathways A, B, C and D) are shown in Scheme 5.11. Equilibria B, C and D result from the reversible loss of H_2 from **17** (B), $NMeH_2$ from **17** (C) or $NMeH_2$ from **18** (D), respectively. However, equilibrium A tentatively postulates that **15** may dissociate to form a cationic primary boryl complex,[35-36] and a neutral hydride complex, both of which are known for rhodium complexes of POP-type ligands.[1, 37-38]



Scheme 5.11 Possible equilibria between complexes **15**, **17** and **18** and the true active species. All structures for the proposed active catalysts are tentative. $[BAr^F{}_4]^-$ anions not shown for clarity.

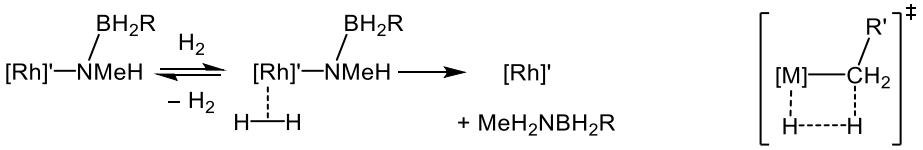
In terms of connecting dehydrogenation and chain propagation, the following mechanism is proposed in Scheme 5.12 due to the strong dependence on polyaminoborane on H_2 pressure and catalyst loading, evident of an on-metal coordination/insertion mechanism. Whilst the true active species is unknown, insertion of the H_2B=NMeH monomer into a Rh–$NMeH_2$ moiety may be a reasonable starting point if the active catalytic species is formed via equilibria B, C or D (Scheme 5.11). Alternatively, insertion of H_2B=NMeH into a Rh–B or Rh–H fragment may occur if the active catalytic species is formed via equilibrium A (Scheme 5.11). On-metal dehydrogenation of $H_3B{\cdot}NMeH_2$ forms a bound H_2B=NMeH complex.[39-40] B–N coupling then occurs through insertion of the bound aminoborane monomer in to the Rh–N bond. Such a mechanism has been proposed previously, for example in Xantphos-Ph system **i-13**,[1] and during amine borane dehydrogenation mediated by Hill's alkali earth metal system,[41] and also draws similarities to the mechanism of Ziegler-Natta polymerisation of olefins.[7]



Scheme 5.12 A proposed pathway for B–N coupling in the dehydropolymerisation of $H_3B{\cdot}NMeH_2$ using the $\{Rh(DPEphos)\}^+$ fragment. [Rh] = unknown {Rh(DPEphos)} complex.

In terms of the chain termination event, it is likely that H_2 is involved due to the lower molecular weight polyaminoborane formed under closed conditions when H_2 pressure was allowed to build up. Whilst this may occur via a sigma bond metathesis process similar to that in Ziegler-Natta polymerisation, the exact nature of this mechanism for the DPEphos system is opaque to

experiment. Hydrogenolysis may occur through heterolytic cleavage of H_2[42] via [Rh]′ (Scheme 5.13), however its subsequent conversion back to active species [Rh] is currently unknown.



Scheme 5.13 Left: Possible intermediates involved in the hydrogenolysis of the growing polyaminoborane chain in the DPEphos system. [Rh]′ may be different to [Rh] in Schemes 5.10 and 5.12, R = growing polyaminoborane chain. Right: Possible transition state for the chain termination of polyolefins by sigma bond metathesis of H_2 with [M]–CH_2–R′. [M] = early transition metal catalyst, R′ = growing polyolefin chain.

5.9 Summary and future of the {Rh(DPEphos)}$^+$ system

This Chapter has described a mechanistic investigation into the dehydropolymerisation of $H_3B{\cdot}NMeH_2$ using [Rh(κ^2-P,P-DPEphos)(η^2-$H_2B(CH_2CH_2{}^tBu){\cdot}NMe_3$)][$BAr^F{}_4$] (**13**). Its selectivity for $(H_2BNMeH)_n$ and ability to control the molecular weight of the resultant polyaminoborane through catalyst loading or H_2 pressure shows that this system may have the ability to produce polyaminoboranes of specific molecular weight to order. However, the complicated kinetic profile makes the fundamental dehydropolymerisation mechanism using **13** difficult to probe. Nonetheless, catalytic systems based upon {Rh(DPEphos)}$^+$ with apparently simpler kinetic profiles were discovered through the isolation of the precatalyst [{Rh(κ^2-P,P-DPEphos)}$_2${μ-$(H_2B)_2$NMeH}][Al(O^tBu^F)$_4$] (**15-[Al(O^tBu^F)$_4$]**) or addition of $NMeH_2$ to catalysis performed using **13**. The clean synthesis of bimetallic complexes based upon **15**, or amine complexes such as **17** and **18**, are still required in order to study these systems in-depth, in particular to examine the speciation of these complexes with $H_3B{\cdot}NMeH_2$. Ongoing work in the Weller group is focused upon exploring these complexes for $H_3B{\cdot}NMeH_2$ dehydropolymerisation.

5.10 References

1. Johnson, H. C.; Leitao, E. M.; Whittell, G. R.; Manners, I.; Lloyd-Jones, G. C.; Weller, A. S., Mechanistic Studies of the Dehydrocoupling and Dehydropolymerization of Amine-Boranes Using a [Rh(Xantphos)]$^+$ Catalyst. *J. Am. Chem. Soc.* **2014,** *136* (25), 9078-9093.
2. Kumar, A.; Beattie, N. A.; Pike, S. D.; Macgregor, S. A.; Weller, A. S., The Simplest Amino-Borane $H_2B{=}NH_2$ Trapped on a Rhodium Dimer: Pre-Catalysts for Amine-Borane Dehydropolymerization. *Angew. Chem. Int. Ed.* **2016,** *55* (23), 6651-6656.

3. Raave, A., *Principles of Polymer Chemistry*. 3rd ed.; Springer: New York, USA, 2012.
4. Chen, E. Y. X., Coordination Polymerization of Polar Vinyl Monomers by Single-Site Metal Catalysts. *Chem. Rev.* **2009,** *109* (11), 5157-5214.
5. Johnson, H. C.; Robertson, A. P. M.; Chaplin, A. B.; Sewell, L. J.; Thompson, A. L.; Haddow, M. F.; Manners, I.; Weller, A. S., Catching the First Oligomerization Event in the Catalytic Formation of Polyaminoboranes: $H_3B{\cdot}NMeHBH_2{\cdot}NMeH_2$ Bound to Iridium. *J. Am. Chem. Soc.* **2011,** *133* (29), 11076-11079.
6. Jaska, C. A.; Temple, K.; Lough, A. J.; Manners, I., Transition Metal-Catalyzed Formation of Boron–Nitrogen Bonds: Catalytic Dehydrocoupling of Amine-Borane Adducts to Form Aminoboranes and Borazines. *J. Am. Chem. Soc.* **2003,** *125* (31), 9424-9434.
7. Hartwig, J. F., *Organotransition Metal Chemistry*. University Science Books: 2010.
8. Kim, J. D.; Soares, J. B. P.; Rempel, G. L., Use of hydrogen for the tailoring of the molecular weight distribution of polyethylene in a bimetallic supported metallocene catalyst system. *Macromol. Rapid Commun.* **1998,** *19* (4), 197-199.
9. Staubitz, A.; Sloan, M. E.; Robertson, A. P. M.; Friedrich, A.; Schneider, S.; Gates, P. J.; Schmedt auf der Günne, J.; Manners, I., Catalytic Dehydrocoupling/Dehydrogenation of N-Methylamine-Borane and Ammonia-Borane: Synthesis and Characterization of High Molecular Weight Polyaminoboranes. *J. Am. Chem. Soc.* **2010,** *132* (38), 13332-13345.
10. Adams, G. M.; Colebatch, A. L.; Skornia, J. T.; McKay, A. I.; Johnson, H. C.; Lloyd-Jones, G. C.; Macgregor, S. A.; Beattie, N. A.; Weller, A. S., Dehydropolymerization of $H_3B{\cdot}NMeH_2$ To Form Polyaminoboranes Using [Rh(Xantphos-alkyl)] Catalysts. *J. Am. Chem. Soc.* **2018,** *140* (4), 1481-1495.
11. Lichtenberg, C.; Adelhardt, M.; Gianetti, T. L.; Meyer, K.; de Bruin, B.; Grützmacher, H., Low-Valent Iron Mono-Diazadiene Compounds: Electronic Structure and Catalytic Application. *ACS Catal.* **2015,** *5* (10), 6230-6240.
12. Colebatch, A. L.; Hawkey Gilder, B. W.; Whittell, G. R.; Oldroyd, N. L.; Manners, I.; Weller, A. S., A General, Rhodium-Catalyzed, Synthesis of Deuterated Boranes and N-Methyl Polyaminoboranes. *Chem. Eur. J.* **2018,** *24* (21), 5450-5455.
13. Ewing, W. C.; Marchione, A.; Himmelberger, D. W.; Carroll, P. J.; Sneddon, L. G., Syntheses and Structural Characterizations of Anionic Borane-Capped Ammonia Borane Oligomers: Evidence for Ammonia Borane H_2 Release via a Base-Promoted Anionic Dehydropolymerization Mechanism. *J. Am. Chem. Soc.* **2011,** *133* (42), 17093-17099.
14. Scholte, T. G.; Meijerink, N. L. J., Gel Permeation Chromatography on Branched Polymers. *Br. Polym. J.* **1977,** *9* (2), 133-139.
15. Pons, V.; Baker, R. T.; Szymczak, N. K.; Heldebrant, D. J.; Linehan, J. C.; Matus, M. H.; Grant, D. J.; Dixon, D. A., Coordination of aminoborane, NH_2BH_2, dictates selectivity and extent of H_2 release in metal-catalysed ammonia borane dehydrogenation. *Chem. Commun.* **2008,** (48), 6597-6599.
16. Widegren, J. A.; Finke, R. G., A review of the problem of distinguishing true homogeneous catalysis from soluble or other metal-particle heterogeneous catalysis under reducing conditions. *J. Mol. Catal. A: Chem.* **2003,** *198* (1-2), 317-341.
17. Dallanegra, R.; Robertson, A. P. M.; Chaplin, A. B.; Manners, I.; Weller, A. S., Tuning the $[L_2Rh{\cdots}H_3B{\cdot}NR_3]^+$ interaction using phosphine bite angle. Demonstration by the catalytic formation of polyaminoboranes. *Chem. Commun.* **2011,** *47* (13), 3763-3765.
18. Kumar, A.; Ishibashi, J. S. A.; Hooper, T. N.; Mikulas, T. C.; Dixon, D. A.; Liu, S.-Y.; Weller, A. S., The Synthesis, Characterization and Dehydrogenation of Sigma-Complexes of BN-Cyclohexanes. *Chem. Eur. J.* **2016,** *22* (1), 310-322.
19. Sewell, L. J.; Lloyd-Jones, G. C.; Weller, A. S., Development of a Generic Mechanism for the Dehydrocoupling of Amine-Boranes: A Stoichiometric, Catalytic, and Kinetic Study of $H_3B{\cdot}NMe_2H$ Using the $[Rh(PCy_3)_2]^+$ Fragment. *J. Am. Chem. Soc.* **2012,** *134* (7), 3598-3610.
20. Sewell, L. J.; Huertos, M. A.; Dickinson, M. E.; Weller, A. S.; Lloyd-Jones, G. C., Dehydrocoupling of Dimethylamine Borane Catalyzed by $Rh(PCy_3)_2H_2Cl$. *Inorg. Chem.* **2013,** *52* (8), 4509-4516.
21. Conley, B. L.; Guess, D.; Williams, T. J., A Robust, Air-Stable, Reusable Ruthenium Catalyst for Dehydrogenation of Ammonia Borane. *J. Am. Chem. Soc.* **2011,** *133* (36), 14212-14215.
22. Lu, Z.; Conley, B. L.; Williams, T. J., A Three-Stage Mechanistic Model for Ammonia–Borane Dehydrogenation by Shvo's Catalyst. *Organometallics* **2012,** *31* (19), 6705-6714.
23. Beweries, T.; Thomas, J.; Klahn, M.; Schulz, A.; Heller, D.; Rosenthal, U., Catalytic and Kinetic Studies of the Dehydrogenation of Dimethylamine Borane with an *i*Pr Substituted Titanocene Catalyst. *ChemCatChem* **2011,** *3* (12), 1865-1868.
24. Boller, T. M.; Murphy, J. M.; Hapke, M.; Ishiyama, T.; Miyaura, N.; Hartwig, J. F., Mechanism of the Mild Functionalization of Arenes by Diboron Reagents Catalyzed by Iridium Complexes. Intermediacy

and Chemistry of Bipyridine-Ligated Iridium Trisboryl Complexes. *J. Am. Chem. Soc.* **2005,** *127* (41), 14263-14278.
25. Marshall, J. E.; Keister, J. B.; Diver, S. T., Mechanism of Intermolecular Ene-yne Metathesis Promoted by the Grubbs First-Generation Catalyst: An Alternative Entry Point to Catalysis. *Organometallics* **2011,** *30* (6), 1319-1321.
26. Anane, H.; Jarid, A.; Boutalib, A.; Nebot-Gil, I.; Tomás, F., Substituent effect on ammonia-borane donor-acceptor complexes: a G2(MP2) molecular orbital study. *J. Mol. Struct. (Theochem)* **1998,** *455* (1), 51-57.
27. Stubbs, N. E.; Schäfer, A.; Robertson, A. P. M.; Leitao, E. M.; Jurca, T.; Sparkes, H. A.; Woodall, C. H.; Haddow, M. F.; Manners, I., B-Methylated Amine-Boranes: Substituent Redistribution, Catalytic Dehydrogenation, and Facile Metal-Free Hydrogen Transfer Reactions. *Inorg. Chem.* **2015,** *54* (22), 10878-10889.
28. Metters, O. J.; Flynn, S. R.; Dowds, C. K.; Sparkes, H. A.; Manners, I.; Wass, D. F., Catalytic Dehydrocoupling of Amine-Boranes using Cationic Zirconium(IV)-Phosphine Frustrated Lewis Pairs. *ACS Catal.* **2016,** *6* (10), 6601-6611.
29. Shuttleworth, T. A.; Huertos, M. A.; Pernik, I.; Young, R. D.; Weller, A. S., Bis(phosphine)boronium salts. Synthesis, structures and coordination chemistry. *Dalton Trans.* **2013,** *42* (36), 12917-12925.
30. Pun, D.; Lobkovsky, E.; Chirik, P. J., Amineborane dehydrogenation promoted by isolable zirconium sandwich, titanium sandwich and N_2 complexes. *Chem. Commun.* **2007,** (31), 3297-3299.
31. Denney, M. C.; Pons, V.; Hebden, T. J.; Heinekey, D. M.; Goldberg, K. I., Efficient Catalysis of Ammonia Borane Dehydrogenation. *J. Am. Chem. Soc.* **2006,** *128* (37), 12048-12049.
32. Hebden, T. J.; Denney, M. C.; Pons, V.; Piccoli, P. M. B.; Koetzle, T. F.; Schultz, A. J.; Kaminsky, W.; Goldberg, K. I.; Heinekey, D. M., σ-Borane Complexes of Iridium: Synthesis and Structural Characterization. *J. Am. Chem. Soc.* **2008,** *130* (32), 10812-10820.
33. Glüer, A.; Förster, M.; Celinski, V. R.; Schmedt auf der Günne, J.; Holthausen, M. C.; Schneider, S., Highly Active Iron Catalyst for Ammonia Borane Dehydrocoupling at Room Temperature. *ACS Catal.* **2015,** *5* (12), 7214-7217.
34. Robertson, A. P. M.; Haddow, M. F.; Manners, I., Synthesis and the Thermal and Catalytic Dehydrogenation Reactions of Amine-Thioboranes. *Inorg. Chem.* **2012,** *51* (15), 8254-8264.
35. O'Neill, M.; A. Addy, D.; Riddlestone, I.; Kelly, M.; Phillips, N.; Aldridge, S., Borane to Boryl Hydride to Borylene Dihydride: Explicit Demonstration of Boron-to-Metal α-Hydride Migration in Aminoborane Activation. *J. Am. Chem. Soc.* **2011,** *133* (30), 11500-11503.
36. Bénac-Lestrille, G.; Helmstedt, U.; Vendier, L.; Alcaraz, G.; Clot, E.; Sabo-Etienne, S., Dimethylaminoborane (H_2BNMe_2) Coordination to Late Transition Metal Centers: Snapshots of the B–H Oxidative Addition Process. *Inorg. Chem.* **2011,** *50* (21), 11039-11045.
37. Haibach, M. C.; Wang, D. Y.; Emge, T. J.; Krogh-Jespersen, K.; Goldman, A. S., (POP)Rh pincer hydride complexes: unusual reactivity and selectivity in oxidative addition and olefin insertion reactions. *Chem. Sci.* **2013,** *4* (9), 3683-3692.
38. Esteruelas, M. A.; Oliván, M.; Vélez, A., Xantphos-Type Complexes of Group 9: Rhodium versus Iridium. *Inorg. Chem.* **2013,** *52* (9), 5339-5349.
39. Addy, D. A.; Bates, J. I.; Kelly, M. J.; Riddlestone, I. M.; Aldridge, S., Aminoborane σ Complexes: Significance of Hydride Co-ligands in Dynamic Processes and Dehydrogenative Borylene Formation. *Organometallics* **2013,** *32* (6), 1583-1586.
40. Vidovic, D.; Addy, D. A.; Krämer, T.; McGrady, J.; Aldridge, S., Probing the Intrinisic Structure and Dynamics of Aminoborane Coordination at Late Transition Metal Centers: Mono(σ-BH) Binding in $[CpRu(PR_3)_2(H_2BNCy_2)]^+$. *J. Am. Chem. Soc.* **2011,** *133* (22), 8494-8497.
41. Bellham, P.; Hill, M. S.; Kociok-Köhn, G.; Liptrot, D. J., Bespoke synthesis of unsymmetrical diaminoboranes by alkaline earth catalysis. *Chem. Commun.* **2013,** *49* (19), 1960-1962.
42. Kubas, G. J., Activation of dihydrogen and coordination of molecular H_2 on transition metals. *J. Organomet. Chem.* **2014,** *751*, 33-49.

6 Summary and future outlook

The $H_3B{\cdot}NMeH_2$ dehydropolymerisation efficiency of POP-type rhodium precatalysts based upon $\{Rh(Xantphos\text{-}^iPr)\}^+$ and $\{Rh(DPEphos)\}^+$ to form $(H_2BNMeH)_n$ has been explored. Work towards a universal dehydropolymerisation mechanism through developing structure/activity relationships showed significant differences between the two systems, likely due to the contrasting geometries of Xantphos-^{i}Pr versus DPEphos complexes – though a common mechanistic thread was apparent.

Importantly, both systems appear dependent upon B–N bond cleavage of $H_3B{\cdot}NMeH_2$ to form free $NMeH_2$ and BH_3. The $\{Rh(Xantphos\text{-}^iPr)\}^+$ system was proposed to operate by the formation of a boronium cation, $[BH_2(NMeH_2)_2]^+$, via $NMeH_2$ attack of a boryl hydride intermediate, and its subsequent deprotonation to form $H_2B{=}NMeH$. Due to lack of dependence on H_2 pressure and catalyst loading, an on-metal end-chain propagation mechanism was proposed for $(H_2BNMeH)_n$ formation. Boron-rich complexes were observed in catalysis, and a dimetalloborylene could be crystallographically characterised. In contrast, the DPEphos system was proposed to operate by an on-metal coordination/dehydrogenation/insertion mechanism, as suggested by its strong catalyst loading and H_2 dependence. Here, $NMeH_2$ may play a role in the formation of the active catalyst; however an unprecedented, crystallographically characterised, boron-rich rhodium amidodiboryl complex may also be close in identity to the active species. The identity of the active catalyst was not defined, and future work must consider the benefits of added $NMeH_2$ to metal catalysed $H_3B{\cdot}NMeH_2$ dehydropolymerisation, and probe the wider applicability of this approach.

Proposed chain branched $(H_2BNMeH)_n$ formed by $\{Rh(DPEphos)\}^+$ points to the need for in-depth, critical analysis of the polyaminoborane formed, in addition to the dehydrogenation kinetics. Therefore, in order for polyaminoboranes to become as widely utilised as polyolefins, systematic methods for probing dehydropolymerisation are still required. Future work which continues to report upon mechanistic intricacies will help towards a universal mechanism, which in turn can lead to the production of polyaminoboranes to order.

7 Experimental methods

7.1 General techniques

All manipulations, unless otherwise stated, were performed under an argon atmosphere using standard Schlenk line and glovebox techniques. Glassware was oven dried at 130°C overnight and flame dried under vacuum prior to use. Pentane, hexane, toluene, Et_2O and CH_2Cl_2 were dried using a Grubbs-type solvent purification system (MBraun SPS-800) and degassed by three successive freeze-pump-thaw cycles.[1] THF was dried over Na/benzophenone, vacuum distilled, degassed by three successive freeze-pump-thaw cycles and stored over 3.0 Å molecular sieves. 1,2-$C_6H_4F_2$ (pre-treated with alumina), C_6H_5F (pre-treated with alumina) and CD_2Cl_2 were dried over CaH_2, vacuum distilled, degassed by three successive freeze-pump-thaw cycles and stored over 3.0 Å molecular sieves.

7.1.1 Procedure for hydrogenation

The sample was freeze-pump-thaw degassed once and backfilled with H_2 at 77 K (flask immersed in liquid N_2). The internal H_2 pressure on warming was ca. 4 bar.

7.1.2 Nuclear magnetic resonance (NMR) spectroscopy

NMR spectra were recorded on a Bruker AVIIIHD 500 or Bruker AVIIIHD 400 nanobay spectrometer at room temperature, unless otherwise stated. Residual protio solvent was used as a reference for ^{1}H NMR spectra in deuterated solvent samples. For NMR samples in 1,2-$C_6H_4F_2$ or THF, ^{1}H NMR spectra were pre-locked to a sample of C_6D_6 (25%) and 1,2-$C_6H_4F_2$ (75%) and referenced to the centre of the downfield solvent multiplet, δ = 7.07 and 3.57 respectively. ^{31}P and ^{11}B NMR spectra were referenced against 85% H_3PO_4 (external) and $BF_3{\cdot}OEt_2$ (external) respectively. Chemical shifts (δ) are quoted in ppm and coupling constants (*J*) in Hz.

7.1.3 Mass spectrometry

ESI-MS (electrospray ionisation mass spectrometry) of organometallic complexes were recorded using a Bruker MicrOTOF instrument directly connected to a modified Innovative Technology glovebox. The mass spectrometer was calibrated in positive ion mode using a 10.0 ng mL^{-1} mixture of tetraalkylammonium bromide salts $[N(C_nH_{2n+1})_4]Br$ (n = 2 – 8, 12, 16, 18) in CH_2Cl_2. Typical experimental acquisition parameters were: sample flow rate, 4.0 μL min^{-1}; nebuliser gas pressure, 0.4 bar; drying gas (argon) at 60°C flowing at 4.0 L min^{-1}; capillary voltage, 4.5 kV. The solvents used were 1,2-$C_6H_4F_2$ or CH_2Cl_2. Samples were diluted to a concentration of approximately 1.0×10^{-6} M and filtered (0.2 μm pore size) before running.

ICP-MS (inductively coupled plasma mass spectrometry) experiments were performed by Philip Holdship at the Department of Earth Sciences, University of Oxford.

GC-MS (gas chromatography mass spectrometry) experiments were performed by Dr Colin Sparrow at the Department of Chemistry, University of Oxford.

7.1.4 Gel permeation chromatography (GPC)

Gel permeation chromatography (GPC) was performed on a Malvern Viscotek GPCmax chromatograph fitted with a refractive index (RI) detector. The columns were contained within an oven (35°C) and consisted of a porous styrene divinylbenzene copolymer with a maximum pore size of 1,500 Å. THF containing 0.1% w/w $[N^nBu_4]Br$ was used as the eluent at a flow rate of 1.0 mL min^{-1}. Samples were dissolved in the eluent (2.0 mg mL^{-1}), filtered (0.2 μm pore size) and run immediately. The calibration was conducted using a series of monodisperse polystyrene standards obtained from Sigma-Aldrich.

7.1.5 Elemental microanalysis

Elemental microanalyses were performed by Stephen Boyer at London Metropolitan University.

7.1.6 Infrared spectroscopy

Infrared spectra were recorded as thin films on a Bruker Tensor 27 FT-IR spectrometer.

7.2 Synthesis and characterisation

7.2.1 Starting materials

$H_3B{\cdot}NMe_3$ was purchased from Sigma-Aldrich and sublimed prior to use (5.0×10^{-2} mbar, 298 K). $H_3B{\cdot}NMeH_2$ was purchased from Boron Specialities and recrystallised twice from Et_2O at −18°C. Cyclohexene was purchased from Sigma-Aldrich, dried over Na, vacuum distilled and stored over 3.0 Å molecular sieves. Hg (99.9995%) was purchased from Sigma-Aldrich, washed with 1,2-$C_6H_4F_2$ and dried in vacuo prior to use. 3,3-dimethyl-1-butene was purchased from Sigma-Aldrich, dried over Na, vacuum distilled and stored over 3.0 Å molecular sieves. $[N^nBu_4][BH_4]$ and PPh_3 were purchased from Sigma-Aldrich and used as received. DPEphos was purchased from Strem Chemicals and used as received. $H_3B{\cdot}THF$ (1.0 M in THF) and $NMeH_2$ (2.0 M in THF) were purchased from Fisher Scientific and used as received. Xantphos-^{i}Pr,[2] Rh(Xantphos-^{i}Pr)$(H)_2Cl$,[3] $Na[BAr^F{}_4]$,[4] $Na[BAr^{Cl}{}_4]$,[5] $H_3B{\cdot}NMeHBH_2{\cdot}NMeH_2$,[6] $BH_2(NMeH_2)_2Cl$,[7] $D_3B{\cdot}NMeH_2$,[8] $H_3B{\cdot}NMeD_2$,[8] [Rh(DPEphos)(NBD)][$BAr^F{}_4$] (**12**),[9] and [Rh(DPEphos)(η^6-ortho-xylene)][$BAr^F{}_4$][10] were prepared by literature methods. [$Rh(NBD)_2$][$BAr^F{}_4$] and [$Rh(NBD)_2$][$Al(O^tBu^F)_4$] were prepared according to the literature procedures for [$Rh(COD)_2$][$BAr^F{}_4$] and [$Rh(COD)_2$][$Al(O^tBu^F)_4$] respectively.[11-12]

*7.2.2 Synthesis of [Rh(Xantphos-^{i}Pr)(NBD)][$BAr^F{}_4$] (**1**)*

A solution of Xantphos-^{i}Pr (0.09 mL, 215.4 μmol) in CH_2Cl_2 (3.6 mL) was added dropwise to a solution of [$Rh(NBD)_2$][$BAr^F{}_4$] (225.0 mg, 195.8 μmol) in CH_2Cl_2 (2.0 mL) in a Schlenk flask over 10 minutes. The resulting light orange solution was concentrated to ca. 1.0 mL under vacuum, and pentane (30.0 mL) was added with stirring to afford an orange powder. Following removal of the supernatant by filtration, the orange solid was washed with pentane (5.0 mL × 3) and dried in

vacuo. Yield: 200.0 mg (133.3 μmol, 68%). Dissolving the isolated solid in CH_2Cl_2 (1.0 mL) and layering with pentane (20 mL) yielded orange crystals suitable for single crystal X-ray diffraction. **^{1}H NMR** (500 MHz, CD_2Cl_2, 298 K): δ 7.72 (s, br, 8 H, $[BAr^F_4]^-$-ortho-CH), 7.64 (d, 2 H, $^2J_{HH}$ 8, aryl CH para to P), 7.56 (s, br, 4 H, $[BAr^F_4]^-$-para-CH), 7.37 (app t, 2 H, $^2J_{HH}$ 8, aryl CH meta to P), 7.30 (dd, 2 H, $^2J_{HH}$ 8, $^2J_{PH}$ 6, aryl CH ortho to P), 4.00 (s, br, 4 H, NBD-HC=CH), 3.32 (s, br, 2 H, NBD-CH), 2.51 (s, 4 H, ^{i}Pr-CH), 1.69 (s, 6 H, Xantphos 'backbone' $C(CH_3)_2$), 1.59 (m, 12 H, ^{i}Pr-CH_3), 1.36 (m, 12 H, ^{i}Pr-CH_3), 1.32 (s, 2 H, NBD-CH_2). Upon decoupling to ^{31}P, the resonances at δ 7.30, 1.59 and 1.36 each sharpened into doublets, revealing $^2J_{HH}$ coupling constants of 8, 7 and 7, respectively. **^{31}P{^{1}H} NMR** (202 MHz, CD_2Cl_2, 298 K): δ 26.3 (d, $^1J_{RhP}$ 145). **ESI-MS** (1,2-$C_6H_4F_2$, 60˚C, 4.5 kV): *m/z* 637.23 (calculated 637.22 for the $[Rh(Xantphos\text{-}^iPr)(NBD)]^+$ fragment, showing the correct isotope pattern). **Microanalysis**: Calc. ($C_{66}H_{60}B_1F_{24}O_1P_2Rh_1$): C, 52.82; H, 4.03. Found: C, 52.85; H, 3.94.

*7.2.3 Synthesis of [Rh(Xantphos-^{i}Pr)(H)$_2$(H$_3$B·NMe$_3$)][BAr$^F_4$] (**2**)*

Route A: $[Rh(Xantphos\text{-}^iPr)(NBD)][BAr^F_4]$ (**1**) (100.0 mg, 66.7 μmol) and $H_3B{\cdot}NMe_3$ (4.9 mg, 66.7 μmol) were dissolved in 1,2-$C_6H_4F_2$ (1.0 mL) in a J. Young flask. The resulting orange solution was immediately frozen and hydrogenated. Upon thawing and shaking the orange solution turned pale yellow. The solution was shaken for 5 minutes, then layered with H_2-saturated pentane (30.0 mL) and stored at 5˚C, which yielded pale yellow crystals suitable for single crystal X-ray diffraction. The crystals were isolated by filtration, washed with pentane (5.0 mL × 3) and dried under vacuum. Yield 75.0 mg (50.6 μmol, 76%).

Route B: $Rh(Xantphos\text{-}^iPr)(H)_2Cl$ (79.9 mg, 137.1 μmol), $Na[BAr^F_4]$ (121.5 mg, 137.1 μmol) and $H_3B{\cdot}NMe_3$ (10.0 mg, 137.1 μmol) were dissolved in 1,2-$C_6H_4F_2$ (1.0 mL) in a J. Young flask. The pale yellow solution was stirred for 30 minutes, filtered, then layered with pentane and stored at 5˚C. The pale yellow crystals were isolated by filtration, washed with pentane (5.0 mL × 3) and dried under vacuum. Yield 160.6 mg (108.0 μmol, 79%).

^{1}H NMR (500 MHz, CD_2Cl_2, 298 K): δ 7.72 (s, br, 8 H, $[BAr^{F}_4]^-$-ortho-CH), 7.64 (d, 2 H, $^{2}J_{HH}$ 8, aryl CH para to P), 7.56 (s, br, 4 H, $[BAr^{F}_4]^-$-para-CH), 7.54 (m, obscured by $[BAr^{F}_4]^-$ peak, 2 H, aryl CH meta to P), 7.39 (dd, 2 H, $^{2}J_{HH}$ 8, $^{2}J_{PH}$ 8, aryl CH ortho to P), 2.64 (m, 4 H, ^{i}Pr-CH), 2.61 (s, 9 H, NMe_3), 1.62 (s, br, 6 H, Xantphos 'backbone' $C(CH_3)_2$), 1.36 (m, 12 H, ^{i}Pr-CH_3), 1.08 (m, 12 H, ^{i}Pr-CH_3), 0.08 (s, br, 3 H, RhH_3B), −19.09 (s, br, 2 H, RhH). Upon decoupling to ^{11}B, the resonance at δ 0.08 sharpened. **^{1}H NMR** (500 MHz, CD_2Cl_2, 200 K): δ 7.71 (s, br, 8 H, $[BAr^{F}_4]^-$-ortho-CH), 7.59 (d, 2 H, $^{2}J_{HH}$ 8, aryl CH para to P), 7.53 (s, br, 4 H, $[BAr^{F}_4]^-$-para-CH), 7.52 (m, obscured by $[BAr^{F}_4]^-$ peak, 2 H, aryl CH meta to P), 7.33 (dd, 2 H, $^{2}J_{HH}$ 8, $^{2}J_{PH}$ 8, aryl CH ortho to P), 2.66 (br, 2 H, ^{i}Pr-CH), 2.56 (s, 9 H, NMe_3), 2.52 (br, 2 H, ^{i}Pr-CH), 1.83 (s, 3 H, Xantphos 'backbone' $C(CH_3)$), 1.42 (m, 12 H, ^{i}Pr-CH_3), 1.22 (s, 3 H, Xantphos 'backbone' $C(CH_3)$), 1.19 (m, 6 H, ^{i}Pr-CH_3), 0.62 (m, 6 H, ^{i}Pr-CH_3), −0.58 (s, br, 3 H, RhH_3B), −17.62 (br, 1 H, RhH), −19.97 (br, 1 H, RhH). **^{11}B{^{1}H} NMR** (160 MHz, CD_2Cl_2, 298 K): δ −6.6 (s, $[BAr^{F}_4]^-$), −9.9 (s, br, RhH_3B). **^{31}P{^{1}H} NMR** (202 MHz, CD_2Cl_2, 298 K): δ 66.5 (d, $^{1}J_{RhP}$ 111). **^{31}P{^{1}H} NMR** (202 MHz, CD_2Cl_2, 200 K): δ 68.4 (d, $^{1}J_{RhP}$ 111). **ESI-MS** (1,2-$C_6H_4F_2$, 60˚C, 4.5 kV): *m/z* 547.19 (calculated 547.18 for the $[Rh(Xantphos\text{-}^{i}Pr)(H)_2]^+$ fragment, showing the correct isotope pattern). **Microanalysis**: Calc. ($C_{62}H_{66}B_2F_{24}N_1O_1P_2Rh$): C, 50.19; H, 4.48; N, 0.94. Found: C, 49.99; H, 4.39; N, 1.00.

*7.2.4 Synthesis of [Rh(Xantphos-^{i}Pr)(H)$_2$($H_3B{\cdot}NMe_3$)][BAr^{Cl}_4] (**2-[BAr^{Cl}_4]**)*

$Rh(Xantphos\text{-}^{i}Pr)(H)_2Cl$ (79.9 mg, 137.1 μmol), $Na[BAr^{Cl}_4]$ (88.9 mg, 143.9 μmol) and $H_3B{\cdot}NMe_3$ (10.0 mg, 137.1 μmol) were dissolved in CH_2Cl_2 (3.0 mL) in a J. Young flask. The pale yellow solution was stirred for 20 hours, filtered and the solvent removed in vacuo. The light yellow powder was then dissolved in CH_2Cl_2 (1.0 mL), layered with pentane and stored at room temperature. The pale yellow crystals were isolated by filtration, washed with pentane (5.0 mL × 3) and dried under vacuum. Yield 105.0 mg (86.4 μmol, 63%).

^{1}H NMR (400 MHz, CD_2Cl_2, 298 K): 7.64 (d, 2 H, $^{2}J_{HH}$ 8, aryl CH para to P), 7.52 (m, 2 H, aryl CH meta to P), 7.37 (dd, 2 H, $^{2}J_{HH}$ 8, $^{2}J_{PH}$ 8, aryl CH ortho to P), δ 7.04 – 7.02 (m, 8 H, $[BAr^{Cl}_4]^-$-

ortho-CH), 6.99 – 6.98 (m, 4 H, $[BAr^{Cl}{}_4]^-$-para-CH), 2.62 (m, 4 H, ^{i}Pr-CH), 2.60 (s, 9 H, NMe_3), 1.62 (s, br, 6 H, Xantphos 'backbone' $C(CH_3)_2$), 1.32 (m, 12 H, ^{i}Pr-CH_3), 1.04 (m, 12 H, ^{i}Pr-CH_3), −0.04 (s, br, 3 H, RhH_3B), −19.33 (s, br, 2 H, RhH). Upon decoupling to ^{11}B, the resonance at δ −0.04 sharpened. **^{11}B{^{1}H} NMR** (128 MHz, CD_2Cl_2, 298 K): δ −7.0 (s, $[BAr^{Cl}{}_4]^-$), −10.2 (s, br, RhH_3B). **^{31}P{^{1}H} NMR** (162 MHz, CD_2Cl_2, 298 K): δ 65.8 (d, $^1J_{RhP}$ 111). **ESI-MS** (1,2-$C_6H_4F_2$, 60˚C, 4.5 kV): *m/z* 547.20 (calculated 547.18 for the $[Rh(Xantphos\text{-}^iPr)(H)_2]^+$ fragment, showing the correct isotope pattern). **Microanalysis**: Calc. ($C_{54}H_{66}B_2N_1Cl_8O_1P_2Rh_1$): C, 53.37; H, 5.47; N, 1.15. Found: C, 53.29; H, 5.62; N, 1.09.

*7.2.5 Synthesis of [Rh(Xantphos-^{i}Pr)(H)$_2$(H$_3$B·NMeH$_2$)][BAr$^F{}_4$] (**3**)*

Rh(Xantphos-^{i}Pr)$(H)_2Cl$ (26.0 mg, 44.6 μmol), Na[$BAr^F{}_4$] (39.4 mg, 44.6 μmol) and $H_3B{\cdot}NMeH_2$ (2.2 mg, 49.1 μmol) were dissolved in 1,2-$C_6H_4F_2$ (0.6 mL) in a J. Young NMR tube. The mixture was shaken and immediately formed a yellow solution with a colourless precipitate.

Selected spectroscopic data: **^{1}H NMR** (400 MHz, 1,2-$C_6H_4F_2$, 298 K): δ −0.33 (s, br, 3 H, RhH_3B), −16.75 (br, 1 H, RhH), −20.18 (br, 1 H, RhH). Upon decoupling to ^{11}B, the resonance at δ −0.33 sharpened. **^{11}B{^{1}H} NMR** (128 MHz, 1,2-$C_6H_4F_2$, 298 K): δ −6.2 (s, $[BAr^F{}_4]^-$), −19.0 (s, br, RhH_3B). **^{31}P{^{1}H} NMR** (162 MHz, 1,2-$C_6H_4F_2$, 298 K): δ 67.6 (d, $^1J_{RhP}$ 110).

*7.2.6 Synthesis of [Rh(Xantphos-^{i}Pr)(H)$_2$(H$_3$B·NMeHBH$_2$·NMeH$_2$)][BAr$^F{}_4$] (**4**)*

Rh(Xantphos-^{i}Pr)$(H)_2Cl$ (20.0 mg, 34.3 μmol), Na[$BAr^F{}_4$] (30.4 mg, 34.3 μmol) and $H_3B{\cdot}NMeHBH_2{\cdot}NMeH_2$ (3.3 mg, 37.7 μmol) were dissolved in 1,2-$C_6H_4F_2$ (0.6 mL) in a J. Young NMR tube. The mixture was shaken and immediately formed a yellow solution with a colourless precipitate.

Selected spectroscopic data: **^{1}H NMR** (400 MHz, 1,2-$C_6H_4F_2$, 298 K): δ −0.53 (s, br, 3 H, RhH_3B), −16.62 (br, 1 H, RhH), −20.19 (br, 1 H, RhH). Upon decoupling to ^{11}B, the resonance at δ −0.53 sharpened. **^{11}B{^{1}H} NMR** (128 MHz, 1,2-$C_6H_4F_2$, 298 K): δ −4.8 (s, br, RhH_2B), −6.2 (s, [$BAr^F{}_4$]),

−18.0 (s, br, RhH_3B). **$^{31}P\{^1H\}$ NMR** (162 MHz, 1,2-$C_6H_4F_2$, 298 K): δ 68.1 (app t, $^1J_{RhP}$ 112, $^2J_{PP}$ ~340).

*7.2.7 Synthesis of [Rh(Xantphos-^{i}Pr)(H)$_2$(H$_3$B·NMe$_2$H)][BAr$^F_4$] (**5**)*

Rh(Xantphos-^{i}Pr)(H)$_2$Cl (20.8 mg, 35.7 μmol), Na[BAr^F_4] (31.6 mg, 35.7 μmol) and $H_3B{\cdot}NMe_2H$ (2.0 mg, 35.8 μmol) were dissolved in 1,2-$C_6H_4F_2$ (0.3 mL) in a high pressure J. Young NMR tube. The reaction mixture was shaken and immediately formed a yellow solution with a colourless precipitate. The reaction mixture was filtered into a J. Young crystallisation flask and layered with pentane, which yielded a small number of pale yellow crystals suitable for single crystal X-ray diffraction.

Selected spectroscopic data: **^{1}H NMR** (400 MHz, 1,2-$C_6H_4F_2$, 298 K): δ −0.38 (s, br, 3 H, RhH_3B), −17.30 (br, 1 H, RhH), −19.86 (br, 1 H, RhH). Upon decoupling to ^{11}B, the resonance at δ −0.38 sharpened. **$^{11}B\{^1H\}$ NMR** (128 MHz, 1,2-$C_6H_4F_2$, 298 K): δ −6.1 (s, $[BAr^F_4]^-$), −14.9 (s, br, RhH_3B). **$^{31}P\{^1H\}$ NMR** (162 MHz, 1,2-$C_6H_4F_2$, 298 K): δ 67.8 (d, $^1J_{RhP}$ 111).

*7.2.8 Synthesis of [Rh(Xantphos-^{i}Pr)(H)$_2$(NMeH$_2$)][BAr$^F_4$] (**6**)*

Rh(Xantphos-^{i}Pr)(H)$_2$Cl (35.1 mg, 60.0 μmol) and Na[BAr^F_4] (53.2 mg, 60.0 μmol) were dissolved in 1.0 mL THF in a J. Young crystallisation tube. Immediately, 0.15 mL of a 2.0 M solution of $NMeH_2$ in THF (300.0 μmol) was added. The solution was stirred for 1 hour to give a pale yellow solution and white precipitate. The reaction mixture was filtered and layered with pentane (30.0 mL) and stored at 5˚C, which yielded pale yellow crystals suitable for single crystal X-ray diffraction. The crystals were isolated by filtration, washed with pentane (5.0 mL × 3) and dried under vacuum. Yield 53.2 mg (36.9 μmol, 62%).

^{1}H NMR (500 MHz, CD_2Cl_2, 298 K): δ 7.72 (s, br, 8 H, $[BAr^F_4]^-$-ortho-CH), 7.67 (d, 2 H, $^2J_{HH}$ 8, aryl CH para to P), 7.56 (s, br, 4 H, $[BAr^F_4]^-$-para-CH), 7.52 (m, 2 H, aryl CH meta to P), 7.42 (dd, 2 H, $^2J_{HH}$ 8, $^2J_{PH}$ 8, aryl CH ortho to P), 2.62 (br, 2 H, NH), 2.51 (s, br, 4 H, ^{i}Pr-CH), 2.32 (t, 3 H, $^3J_{HH}$ 6, NMe), 1.89 (s, 3 H, Xantphos 'backbone' C(CH_3)), 1.44 (m, 6 H, ^{i}Pr-CH_3), 1.34 (s, 3 H,

Xantphos 'backbone' C(CH_3)), 1.26 (m, 6 H, ^{i}Pr-CH_3), 1.19 (m, 6 H, ^{i}Pr-CH_3), 0.75 (m, 6 H, ^{i}Pr-CH_3), −17.73 (br, 1 H, RhH), −20.40 (br, 1 H, RhH). **^{31}P{^{1}H} NMR** (202 MHz, CD_2Cl_2, 298 K): δ 64.0 (d, $^{1}J_{RhP}$ 111). **ESI-MS** (1,2-$C_6H_4F_2$, 60˚C, 4.5 kV): *m/z* 547.20 (calculated 547.18 for the [Rh(Xantphos-^{i}Pr)]$^{+}$ fragment, showing the correct isotope pattern). **Microanalysis**: Calc. ($C_{60}H_{59}B_1F_{24}N_1O_1P_2Rh_1$): C, 49.98; H, 4.12; N, 0.97. Found: C, 49.83; H, 3.97; N, 0.92.

7.2.9 Synthesis of [{Rh(Xantphos-^{i}Pr)(H)$_2$}$_2$BH$_4$][BAr$^{F}_4$] (7)

Route A: [Rh(Xantphos-^{i}Pr)(H)$_2$($H_3B{\cdot}NMe_3$)][BAr$^{F}_4$] (**2**) (14.8 mg, 10.0 μmol) and 0.5 mL of a 0.02 M solution of $H_3B{\cdot}THF$ (10.0 μmol) were placed in a J. Young NMR tube, giving a pale yellow solution. The sample was immediately placed into the NMR spectrometer. ^{31}P{^{1}H} NMR spectroscopy indicated that the mixture contained 35% [{Rh(Xantphos-^{i}Pr)(H)$_2$}$_2$BH$_4$][BAr$^{F}_4$] (**7**) and 5% [{Rh(Xantphos-^{i}Pr)}$_2$B][BAr$^{F}_4$] (**8**), the rest being unidentified species with the major species proposed to be [Rh(Xantphos-^{i}Pr)(H)$_2$(THF)][BAr$^{F}_4$].

Route B: [Rh(Xantphos-^{i}Pr)(H)$_2$($H_3B{\cdot}NMe_3$)][BAr$^{F}_4$] (**2**) (11.5 mg, 7.7 μmol) and [N^{n}Bu$_4$][BH_4] (1.0 mg, 3.9 μmol) were dissolved in 0.4 mL 1,2-$C_6H_4F_2$ in a J. Young NMR tube, giving a pale yellow solution. The sample was immediately placed into the NMR spectrometer. ^{31}P{^{1}H} NMR spectroscopy indicated that the mixture contained 79% [{Rh(Xantphos-^{i}Pr)(H)$_2$}$_2$BH$_4$][BAr$^{F}_4$] (**7**) and 21% [{Rh(Xantphos-^{i}Pr)}$_2$B][BAr$^{F}_4$] (**8**).

Selected spectroscopic data: **^{1}H NMR** (400 MHz, 1,2-$C_6H_4F_2$, 298 K): δ −2.77 (s, br, 2 H, RhHB), −16.07 (br, 1 H, RhH), −20.41 (br, 1 H, RhH). Upon decoupling to ^{11}B, the resonance at δ −2.77 sharpened. **^{11}B{^{1}H} NMR** (128 MHz, 1,2-$C_6H_4F_2$, 298 K): δ −6.2 (s, [BAr$^{F}_4$]), −37.5 (s, br, Rh(H_2BH_2)Rh). **^{31}P{^{1}H} NMR** (162 MHz, 1,2-$C_6H_4F_2$, 298 K): δ 67.2 (d, $^{1}J_{RhP}$ 111).

7.2.10 Synthesis of [{Rh(Xantphos-^{i}Pr)}$_2$B][BAr$^{F}_4$] (8)

Route A: [Rh(Xantphos-^{i}Pr)(H)$_2$($H_3B{\cdot}NMe_3$)][BAr$^{F}_4$] (**2**) (15.0 mg, 10.1 μmol) and $H_3B{\cdot}NMeH_2$ (4.6 mg, 101.0 μmol) were dissolved in 0.4 mL 1,2-$C_6H_4F_2$ in a J. Young NMR tube. After being

shaken for 5 minutes and agitated for a further 20 minutes, $^{31}P\{^{1}H\}$ NMR spectroscopy indicated that the mixture contained 82% [{Rh(Xantphos-^{i}Pr)}$_2$B][BAr$^{F}_4$] (**8**).

Route B: [Rh(Xantphos-^{i}Pr)(H)$_2$(H$_3$B·NMe$_3$)][BAr$^{F}_4$] (**2**) (14.8 mg, 10.0 μmol) and 0.5 mL of a 0.02 M solution of H$_3$B·THF (10.0 μmol) were placed in a J. Young NMR tube, initially giving a pale yellow solution. Over 40 minutes, effervescence was observed and a darkening of the solution to orange. $^{31}P\{^{1}H\}$ NMR spectroscopy indicated that the mixture contained 50% [{Rh(Xantphos-^{i}Pr)}$_2$B][BAr$^{F}_4$] (**8**). After 12 hours, [{Rh(Xantphos-^{i}Pr)}$_2$B][BAr$^{F}_4$] (**8**) was the sole phosphorus-containing species in solution by $^{31}P\{^{1}H\}$ NMR spectroscopy.

Route C: [Rh(Xantphos-^{i}Pr)(H)$_2$(H$_3$B·NMe$_3$)][BAr$^{F}_4$] (**2**) (11.5 mg, 7.7 μmol) and [N^{n}Bu$_4$][BH$_4$] (1.0 mg, 3.9 μmol) were dissolved in 0.4 mL 1,2-C$_6$H$_4$F$_2$ in a J. Young NMR tube, giving a pale yellow solution. Over 30 mins, effervescence was observed and a darkening of the solution to orange. $^{31}P\{^{1}H\}$ NMR spectroscopy indicated that the mixture contained 80% [{Rh(Xantphos-^{i}Pr)}$_2$B][BAr$^{F}_4$] (**8**).

For all routes, attempts to isolate **14** were unsuccessful. In our hands, transferral of the above reaction mixtures to stirring pentane at −30°C gave brown/orange powders which could not be interrogated by NMR spectroscopy. Attempts to crystallise **14** gave brown oils across a range of temperatures.

Selected spectroscopic data: **^{11}B{^{1}H} NMR** (128 MHz, THF, 298 K): δ 132, (v br, Rh$_2$B), −6.1 (s, [BAr$^{F}_4$]$^-$). **^{31}P{^{1}H} NMR** (162 MHz, THF, 298 K): δ 48.1 (dd, $^{1}J_{RhP}$ 174, $^{3}J_{RhP}$ 6).**^{11}B{^{1}H} NMR** (160 MHz, 1,2-C$_6$H$_4$F$_2$, 298 K): δ 135, (v br, Rh$_2$B), −6.2 (s, [BAr$^{F}_4$]$^-$). **^{31}P{^{1}H} NMR** (202 MHz, 1,2-C$_6$H$_4$F$_2$, 298 K): δ 47.5 (dd, $^{1}J_{RhP}$ 174, $^{3}J_{RhP}$ 6). **ESI-MS** (1,2-C$_6$H$_4$F$_2$, 60˚C, 4.5 kV): *m/z* 1101.34 (calculated 1101.33 for the [{Rh(Xantphos-^{i}Pr)}$_2$B]$^+$ fragment, showing the correct isotope pattern).

*7.2.11 Synthesis of [{Rh(Xantphos-^{i}Pr)}$_2$B][BAr$^{Cl}_4$] (**8-[BAr$^{Cl}_4$]**)*

[Rh(Xantphos-^{i}Pr)(H)$_2$(H$_3$B·NMe$_3$)][BAr$^{Cl}_4$] (**2-[BAr$^{Cl}_4$]**) (18.9 mg, 15.5 μmol) and [N^{n}Bu$_4$][BH$_4$] (2.0 mg, 7.8 μmol) were dissolved in 0.5 mL CH$_2$Cl$_2$ in a J. Young flask. After 3 hours, the

solution was filtered and layered with pentane to yield orange needles suitable for single crystal X-ray diffraction, though a significant quantity of $[N^nBu_4][BAr^{Cl}{}_4]$ was identified in the bulk by ^{1}H NMR spectroscopy.

Selected spectroscopic data: **^{1}H NMR** (400 MHz, CD_2Cl_2, 298 K): δ 7.60 (d, $^2J_{HH}$ 8, aryl CH para to P), 7.44 (m, aryl CH meta to P), 7.28 (dd, $^2J_{HH}$ 8, $^2J_{PH}$ 8, aryl CH ortho to P). The aliphatic region was obscured by the presence of $[N^nBu_4][BAr^{Cl}{}_4]$ and pentane. There are no signals < 0 ppm. **^{11}B{^{1}H} NMR** (128 MHz, CD_2Cl_2, 298 K): δ 131.0, (v br, Rh_2B), −7.0 (s, $[BAr^{Cl}{}_4]^-$). **^{31}P{^{1}H} NMR** (162 MHz, CD_2Cl_2, 298 K): δ 47.5 (dd, $^1J_{RhP}$ 175, $^3J_{RhP}$ 7). **ESI-MS** (1,2-$C_6H_4F_2$, 60˚C, 4.5 kV): *m/z* 1101.32 (calculated 1101.33 for the $[\{Rh(Xantphos\text{-}^iPr)\}_2B]^+$ fragment, showing the correct isotope pattern).

*7.2.12 Synthesis of [Rh(Xantphos-^{i}Pr)(CO)][BAr$^{Cl}{}_4$] (**9**)*

$[\{Rh(Xantphos\text{-}^iPr)\}_2B][BAr^{Cl}{}_4]$ (**8-[BAr$^{Cl}{}_4$]**) (5.0 mg of bulk material, ~2.9 μmol) was dissolved in CD_2Cl_2 (0.5 mL) in a J. Young NMR tube. The sample was freeze-pump-thaw degassed three times and backfilled with CO_2 at room temperature. The internal CO_2 pressure was ca. 1 bar. The sample was agitated for 48 hours, then degassed with three successive freeze-pump-thaw cycles and placed under an atmosphere of argon. The light yellow solution was filtered to a J. Young crystallisation flask and layered with pentane (20.0 mL), which yielded pale yellow crystals suitable for single crystal X-ray diffraction, though significant a quantity of $[N^nBu_4][BAr^{Cl}{}_4]$ was identified in the bulk by NMR spectroscopy.

Selected spectroscopic data: **^{31}P{^{1}H} NMR** (162 MHz, CD_2Cl_2, 298 K): δ 62.8 (d, $^1J_{RhP}$ 116). **ESI-MS** (CH_2Cl_2, 60˚C, 4.5 kV): *m/z* 573.15 (calculated 573.16 for the $[Rh(Xantphos\text{-}^iPr)(CO)]^+$ fragment, showing the correct isotope pattern). **IR** (film): 1999.7 cm^{-1} (CO).

*7.2.13 Synthesis of [Rh(Xantphos-^{i}Pr)(PPh$_3$)][BAr$^F{}_4$] (**10**)*

$[Rh(Xantphos\text{-}^iPr)(H)_2(H_3B{\cdot}NMe_3)][BAr^F{}_4]$ (**2**) (20.0 mg, 13.5 μmol) and PPh_3 (8.8 mg, 33.8 μmol) were dissolved in 1,2-$C_6H_4F_2$ (0.4 mL) in a J. Young NMR tube. The resulting orange

solution was left to stand for 3 hours, before being filtered into a J. Young crystallisation flask. The solution was layered with pentane and stored at room temperature, which yielded orange crystals suitable for single crystal X-ray diffraction. The crystals were isolated by filtration, washed with pentane (5.0 mL × 3) and dried under vacuum. Yield 10.0 mg (6.0 μmol, 44%).

^{1}H NMR (400 MHz, CD_2Cl_2, 298 K): δ 7.98 (m, 6 H, PPh_3-CH), δ 7.72 (s, br, 8 H, $[BAr^{F}_4]^-$-ortho-CH), 7.68 (d, 2 H, $^{2}J_{HH}$ 8, aryl CH para to P), 7.56 (s, br, 4 H, $[BAr^{F}_4]^-$-para-CH), 7.49 (m, 9 H, PPh_3-CH), 7.39 (m, 2 H, aryl CH meta to P), 7.33 (dd, 2 H, $^{2}J_{HH}$ 8, $^{2}J_{PH}$ 8, aryl CH ortho to P), 1.66 (s, 6 H, Xantphos 'backbone' $C(CH_3)$), 1.48 (m, br, 4 H, ^{i}Pr-CH), 0.97 (m, 12 H, ^{i}Pr-CH_3), 0.86 (m, 12 H, ^{i}Pr-CH_3). **^{31}P{^{1}H} NMR** (162 MHz, CD_2Cl_2, 298 K): δ 47.4 (dt, 1 P, $^{1}J_{RhP}$ 217, $^{2}J_{PP}$ 39, PPh_3), 44.7 (dd, 2 P, $^{1}J_{RhP}$ 131, $^{2}J_{PP}$ 39, P^{i}Pr$_2$). **ESI-MS** (1,2-$C_6H_4F_2$, 60˚C, 4.5 kV): *m/z* 807.25 (calculated 807.25 for the $[Rh(PPh_3)(Xantphos\text{-}^{i}Pr)]^+$ fragment, showing the correct isotope pattern). **Microanalysis**: Calc. ($C_{77}H_{67}B_1F_{24}O_1P_3Rh_1$): C, 55.35; H, 4.04. Found: C, 55.44; H, 4.00.

*7.2.14 Synthesis of $[BH_2(NMeH_2)_2][BAr^{F}_4]$ (**11**)*

$[BH_2(NMeH_2)_2][BAr^{F}_4]$ was prepared by an analogous method to that of $[BH_2(NMe_2H)_2][BAr^{F}_4]$ as described by López-Serrano, Conejero and co-workers.[12] $BH_2(NMeH_2)_2Cl$ (30.0 mg, 27.2 μmol) and $Na[BAr^{F}_4]$ (240.8 mg, 27.2 μmol) were dissolved in 3.0 mL THF and stirred for 15 minutes to form a white precipitate (NaCl) and a colourless solution. The solution was filtered and the solvent removed in vacuo. The remaining white solid was dissolved in CH_2Cl_2 (3.0 mL) and the resultant solution was filtered into a J. Young crystallisation tube. The colourless solution was layered with hexane and stored at room temperature to give colourless, crystalline material. The crystals were isolated by filtration, washed with hexane (5.0 mL × 3) and dried under vacuum. Yield 207.8 mg (22.1 μmol, 81%).

^{1}H NMR (500 MHz, CD_2Cl_2, 298 K): δ 7.72 (s, br, 8 H, $[BAr^{F}_4]^-$-ortho-CH), 7.57 (s, br, 4 H, $[BAr^{F}_4]^-$-para-CH), 4.03 (br, 4 H, NH), 2.71 (t, 6 H, $^{3}J_{HH}$ 6, NMe), 2.22 (q, br, 2 H, $^{1}J_{BH}$ ~120, BH_2). **^{11}B NMR** (160 MHz, CD_2Cl_2, 298 K): δ −6.6 (s, $[BAr^{F}_4]^-$), −7.4 (t, $^{1}J_{BH}$ 117, $[BH_2(NMeH_2)_2]^+$). **^{11}B{^{1}H} NMR** (160 MHz, CD_2Cl_2, 298 K): δ −6.6 (s, $[BAr^{F}_4]^-$), −7.4 (s,

$[BH_2(NMeH_2)_2]^+$). **$^{13}C\{^1H\}$ NMR** (126 MHz, CD_2Cl_2, 298 K): δ 162.1 (q, $^1J_{CB}$ 50, $[BAr^F{}_4]^-$-ipso-C), 135.2 (s, br, $[BAr^F{}_4]^-$-ortho-C), 129.3 (q, $^2J_{CF}$ 32, $[BAr^F{}_4]^-$-meta-C), 125.0 (q, $^1J_{CF}$ 272, $[BAr^F{}_4]^-$-CF_3), 117.9 (m, $[BAr^F{}_4]^-$-para-C), 32.3 (s, $NMeH_2$-C). **Microanalysis**: Calc. ($C_{34}H_{24}B_2F_{24}N_2$): C, 43.53; H, 2.58; N, 2.99. Found: C, 43.40; H, 2.43; N, 3.34.

*7.2.15 Synthesis of [Rh(DPEphos)(NBD)][Al(O^{t}Bu^F)$_4$] (**12-[Al(O^{t}Bu^F)$_4$]**)*

A solution of DPEphos (129.0 mg, 239.5 μmol) in 1,2-$C_6H_4F_2$ (10.0 mL) was added dropwise to a Schlenk flask containing a solution of $[Rh(NBD)_2][Al(O^tBu^F)_4]$ (300.0 mg, 239.2 μmol) in 1,2-$C_6H_4F_2$ (8.0 mL). The resulting orange solution was left to stir for 12 hours. The solution was filtered, concentrated to ca. 3.0 mL under vacuum, layered with pentane (40.0 mL) and left to crystallise for ca. 48 hours at room temperature. Following removal of the supernatant by filtration, the dark orange crystalline material was washed with pentane (10.0 mL × 3) and dried under vacuum. Yield: 350.0 mg (206.0 μmol, 86%).

^{1}H NMR (400 MHz, CD_2Cl_2, 298 K): δ 7.55 – 7.31 (m, 22 H, aryl CH), 7.07 – 6.10 (m, 6 H, aryl CH), 4.30 (s, br, 4 H, NBD-HC=CH), 3.85 (s, br, 2 H, NBD-CH), 1.53 (s, 2 H, NBD-CH_2). **$^{31}P\{^1H\}$ NMR** (162 MHz, CD_2Cl_2, 298 K): δ 17.0 (d, $^1J_{RhP}$ 159). **ESI-MS** (1,2-$C_6H_4F_2$, 60˚C, 4.5 kV): *m/z* 733.13 (calculated 733.13 for the $[Rh(DPEphos)(NBD)]^+$ fragment, showing the correct isotope pattern). **Microanalysis**: Calc. ($C_{59}H_{36}Al_1F_{36}O_5P_2Rh_1$): C, 41.67; H, 2.13. Found: C, 41.76; H, 2.23.

*7.2.16 Synthesis of [Rh(DPEphos)(H$_2$B(CH$_2$CH$_2$^{t}Bu)·NMe$_3$)][BAr$^F{}_4$] (**13**)*

$[Rh(DPEphos)(NBD)][BAr^F{}_4]$ (**12**) (547.2 mg, 342.7 μmol) and $H_3B{\cdot}NMe_3$ (32.0 mg, 438.7 μmol) were dissolved in C_6H_5F (5.0 mL) in a J. Young flask. The mixture was immediately frozen in liquid N_2 and hydrogenated. On warming to room temperature, the mixture was shaken, yielding a dark blue solution, forming $[Rh(DPEphos)(H_3B{\cdot}NMe_3)][BAr^F{}_4]$ in situ.[13] The solution was rapidly degassed with three successive freeze-pump-thaw cycles and placed under an atmosphere of argon. 3,3-dimethylbut-1-ene (0.3 mL, 2327.7 μmol) was added to the J. Young flask, and a further

3.0 mL of C_6H_5F was added to ensure all of the 3,3-dimethylbut-1-ene had entered the reaction mixture. The reaction mixture was stirred for 90 minutes, turning from dark blue to purple in colour. The solution was filtered; the solvent removed in vacuo and the resultant purple powder was washed with hexane (10.0 mL × 3), and dried under vacuum. Yield 452.5 mg (272.3 μmol, 79%). Purple crystals suitable for single crystal X-ray diffraction were obtained by recrystallisation from CH_2Cl_2/pentane at −20°C.

^{1}H NMR (500 MHz, CD_2Cl_2, 298 K): δ 7.72 (s, br, 8 H, $[BAr^F_4]^-$-ortho-CH), 7.56 (s, br, 4 H, $[BAr^F_4]^-$-para-CH), 7.45 – 7.28 (m, 22 H, aryl CH), 7.13 (d, 2 H, $^2J_{HH}$ 8, aryl CH), 6.87 (t, 2 H, $^2J_{HH}$ 8, aryl CH), 6.63 (m, 2 H, aryl CH), 2.59 (s, 9 H, NMe_3), 1.49 (m, 2 H, $CH_2C\underline{H_2}^tBu$), 0.78 (s, 9 H, ^{t}Bu), 0.49 (m, 2 H, $C\underline{H_2}CH_2{}^tBu$), −5.55 (br, 2 H, RhH_2B). Upon decoupling to ^{11}B, the resonance at δ −5.55 sharpened slightly. **^{11}B{^{1}H} NMR** (160 MHz, CD_2Cl_2, 298 K): δ 33.3 (s, br, RhH_2B), −6.6 (s, $[BAr^F_4]^-$). **^{31}P{^{1}H} NMR** (202 MHz, CD_2Cl_2, 298 K): δ 40.0 (d, $^1J_{RhP}$ 180). **ESI-MS** (CH_2Cl_2, 60˚C, 4.5 kV): *m/z* 798.22 (calculated 798.27 for the $[Rh(DPEphos)(H_2B(CH_2CH_2{}^tBu)\cdot NMe_3)]^+$ fragment, showing the correct isotope pattern). **Microanalysis**: Calc. ($C_{77}H_{64}B_2F_{24}N_1O_1P_2Rh_1$): C, 55.65; H, 3.88; N, 0.84. Found: C, 55.78; H, 3.95; N, 0.82.

*7.2.17 Synthesis of [{Rh(DPEphos)}$_2$(H)(H$_2$BNMeH)][BAr$^F_4$] (**14**)*

[Rh(DPEphos)(NBD)][BAr^F_4] (**12**) (35.0 mg, 21.9 μmol) and $H_3B\cdot NMeH_2$ (2.0 mg, 44.6 μmol) were dissolved in 1,2-$C_6H_4F_2$ (0.35 mL) in a high pressure J. Young NMR tube. The sample was immediately frozen in liquid N_2 and hydrogenated. On warming to room temperature, the mixture was shaken, and the light orange solution turned darker in colour. The sample was immediately placed into the NMR spectrometer.

Selected spectroscopic data: **^{1}H NMR** (500 MHz, 1,2-$C_6H_4F_2$, 298 K): δ 8.33 (s, br, 8 H, $[BAr^F_4]^-$-ortho-CH), −9.12 (br, ~1 H, $Rh_2(\mu\text{-}BH_2)$ and $Rh_2(\mu\text{-}H)$). Upon decoupling to ^{31}P, the resonance at δ −9.13 sharpened. **^{11}B NMR** (160 MHz, 1,2-$C_6H_4F_2$, 298 K): δ 55.8 (br, RhH_2B), −6.3 (s, $[BAr^F_4]^-$), –7.1 (t, $^1J_{BH}$ ~120, $[BH_2(NMeH_2)_2]^+$). **^{11}B{^{1}H} NMR** (160 MHz, CD_2Cl_2, 298 K): δ 55.8 (br, RhH_2B), −6.3 (s, $[BAr^F_4]^-$), −7.1 (s, $[BH_2(NMeH_2)_2]^+$). **^{31}P{^{1}H} NMR** (202 MHz, 1,2-$C_6H_4F_2$,

298 K): δ 28.3 (d, $^{1}J_{RhP}$ 150). **ESI-MS** (1,2-$C_6H_4F_2$, 60˚C, 4.5 kV): *m/z* 1326.20 (calculated 1326.20 for the [{Rh(DPEphos)}$_2$(H)(H_2BNMeH)]$^+$ fragment, showing the correct isotope pattern). These data are analogous to the well-studied $PR_2(CH_2)_3PR_2$ (R = Ph, ^{i}Pr) analogues of complex **14**.[14]

*7.2.18 Synthesis of [{Rh(DPEphos)}$_2${($H_2B)_2$NMeH}][BAr$^F_4$] (**15**)*

[Rh(DPEphos)(NBD)][BAr$^F_4$] (**12**) (35.0 mg, 21.9 μmol) and $H_3B{\cdot}NMeH_2$ (4.0 mg, 89.1 μmol) were dissolved in 1,2-$C_6H_4F_2$ (0.4 mL) in a high pressure J. Young NMR tube. The sample was immediately frozen in liquid N_2 and hydrogenated. On warming to room temperature, the mixture was shaken and agitated for 10 minutes, and the light orange solution turned darker in colour. The sample was freeze-pump-thaw degassed three times, backfilled with argon, and agitated for 30 minutes before being placed into the NMR spectrometer. $^{31}P\{^{1}H\}$ NMR spectroscopy of the fully degassed NMR sample indicated that the mixture subsequently contained 25% [{Rh(DPEphos)}$_2$(H)(H_2BNMeH)][BAr$^F_4$] (**14**) and 75% [{Rh(DPEphos)}$_2${($H_2B)_2$NMeH}][BAr$^F_4$] (**15**).

Selected spectroscopic data: **^{1}H NMR** (400 MHz, 1,2-$C_6H_4F_2$, 298 K): δ −8.41 (d, br, $^{2}J_{PH}$ 76, Rh_2(μ-BH)), −9.25 (m, obscured by **14** Rh_2(μ-BH_2) and Rh_2(μ-H), Rh_2(μ-BH)). Upon decoupling to ^{11}B, the resonance at δ −8.41 sharpened. Upon decoupling to ^{31}P, the resonance at δ −8.41 collapsed to a broad singlet. **^{11}B{^{1}H} NMR** (128 MHz, 1,2-$C_6H_4F_2$, 298 K): δ 9.7 (br, Rh(μ-($H_2B)_2$), −6.2 (s, [BAr$^F_4$]$^-$). **^{31}P{^{1}H} NMR** (162 MHz, 1,2-$C_6H_4F_2$, 298 K): δ 31.7 (dd, 1 P, $^{1}J_{RhP}$ 163, $^{2}J_{PP}$ 23), 28.9 (dd, 1 P, $^{1}J_{RhP}$ 159, $^{2}J_{PP}$ 21), 15.7 (ddd, 1 P, $^{1}J_{RhP}$ 138, $^{2}J_{RhP}$ 103, $^{2}J_{PP}$ 23), 12.8 (ddd, 1 P, $^{1}J_{RhP}$ 136, $^{2}J_{RhP}$ 103, $^{2}J_{PP}$ 21).

*7.2.19 Synthesis of [{Rh(DPEphos)}$_2${($H_2B)_2$NMeH}][Al(O^{t}Bu^F)$_4$] (**15-[Al(O^{t}Bu^F)$_4$]**)*

[Rh(DPEphos)(NBD)][Al(O^{t}Bu^F)$_4$] (**12-[Al(O^{t}Bu^F)$_4$]**) (40.4 mg, 23.8 μmol) and $H_3B{\cdot}NMeH_2$ (4.2 mg, 93.6 μmol) were dissolved in 1,2-$C_6H_4F_2$ (0.4 mL) in a high pressure J. Young NMR tube. The sample was immediately frozen in liquid N_2 and hydrogenated. On warming to room

temperature, the mixture was shaken and agitated for 10 minutes, and the light orange solution turned darker in colour. The sample was freeze-pump-thaw degassed three times, backfilled with argon, and agitated for 30 minutes before being filtered into a J. Young crystallisation flask. The solution was layered with pentane (20.0 mL) at room temperature to yield orange crystals suitable for single crystal X-ray diffraction. The bulk solid of **15-[Al(O^{t}Bu^F)$_4$]** was analysed by NMR spectroscopy which showed that 5% [{Rh(DPEphos)}$_2$(H)(H$_2$BNMeH)][Al(O^{t}Bu^F)$_4$] (**14-[Al(O^{t}Bu^F)$_4$]**) was present by ^{31}P{^{1}H} spectroscopy, and dehydrocoupling products of H$_3$B·NMeH$_2$ were also identified by ^{11}B NMR spectroscopy. Yield: 18.0 mg.

Selected spectroscopic data: **^{1}H NMR** (400 MHz, CD_2Cl_2, 298 K): δ 8.06 – 5.78 (m, 54 H, aryl CH), 4.64 (br, 2 H, BH), 3.94 (br, 2 H, aryl CH···Rh), 1.07 (d, 3 H, $^3J_{HH}$ 6, NMe), −8.65 (br, 1 H, Rh$_2$(μ-HB)), −9.44 (br, 1 H, Rh$_2$(μ-HB). Upon decoupling to ^{11}B, the resonance at δ 4.64 sharpened, and the resonances at δ −8.65 and −9.44 each sharpened into doublets, revealing $^2J_{PH}$ coupling constants of 73.9 and 68.8, respectively. Upon decoupling to ^{31}P, the resonances at δ −8.65 and −9.44 each collapsed to broad singlets. **^{11}B{^{1}H} NMR** (128 MHz, CD_2Cl_2, 298 K): δ 9.4 (br, Rh(μ-(H$_2$B)$_2$)). **^{31}P{^{1}H} NMR** (162 MHz, CD_2Cl_2, 298 K): δ 31.7 (dd, 1 P, $^1J_{RhP}$ 163, $^2J_{PP}$ 23), 28.8 (dd, 1 P, $^1J_{RhP}$ 158, $^2J_{PP}$ 21), 15.7 (ddd, 1 P, $^1J_{RhP}$ 138, $^2J_{RhP}$ 102, $^2J_{PP}$ 23), 13.0 (ddd, 1 P, $^1J_{RhP}$ 135, $^3J_{RhP}$ 102, $^2J_{PP}$ 21). **ESI-MS** (1,2-C$_6$H$_4$F$_2$, 60˚C, 4.5 kV): *m/z* 1338.33 (calculated 1338.22 for the [{Rh(DPEphos)}$_2${(H$_2$B)$_2$NMeH}]$^+$ fragment, showing the correct isotope pattern).

*7.2.20 Synthesis of [{Rh(DPEphos)}$_2$(B$_2$H$_5$)][BAr$^F_4$] (**16**)*

[Rh(DPEphos)(H$_2$B(CH$_2$CH$_2$^{t}Bu)·NMe$_3$)][BAr$^F_4$] (**13**) (14.0 mg, 8.4 μmol) was dissolved in THF (0.35 mL) in a J. Young NMR tube. 0.11 mL of a 0.08 M solution of H$_3$B·THF (8.8 μmol) was added. The purple solution turned orange on addition of H$_3$B·THF. The sample was immediately placed into the NMR spectrometer.

Selected spectroscopic data: **^{1}H NMR** (400 MHz, THF, 298 K): δ −8.14 (m, Rh$_2$(μ-BH)). **^{31}P{^{1}H} NMR** (162 MHz, THF, 298 K): δ 32.0 (d, 2 P, $^1J_{RhP}$ 151), 17.5 (d, br, 2 P, $^1J_{RhP}$ ~120).

ESI-MS (1,2-$C_6H_4F_2$, 60˚C, 4.5 kV): *m/z* 1309.16 (calculated 1309.19 for the $[\{Rh(DPEphos)\}_2(B_2H_5)]^+$ fragment, showing the correct isotope pattern).

*7.2.21 Synthesis of [Rh(DPEphos)(H)$_2$(NMeH$_2$)$_x$][BAr$^F{}_4$] (x = 1 or 2, **17**)*

Route A: [Rh(DPEphos)(NBD)][BAr$^F{}_4$] (**12**) (15.0 mg, 9.4 μmol) was dissolved in 1,2-$C_6H_4F_2$ (0.3 mL) in a high pressure J. Young NMR tube. 0.1 mL of a 1.0 M solution of $NMeH_2$ in THF (100.0 μmol) was added. The reaction mixture was immediately frozen in liquid N_2 and hydrogenated. On warming to room temperature, the mixture was shaken, and the light orange solution turned darker in colour. The sample was immediately placed into the NMR spectrometer. $^{31}P\{^1H\}$ NMR spectroscopy indicated that the mixture contained 97% [Rh(DPEphos)(H)$_2$(NMeH$_2$)$_x$][BAr$^F{}_4$] (**17**) and 3% [Rh(DPEphos)(NMeH$_2$)$_x$][BAr$^F{}_4$] (**18**).

Route B: [Rh(DPEphos)(NBD)][BAr$^F{}_4$] (**12**) (35.0 mg, 21.9 μmol) and $H_3B{\cdot}NMeH_2$ (4.0 mg, 89.1 μmol) were dissolved in 1,2-$C_6H_4F_2$ (0.4 mL) in a high pressure J. Young NMR tube. The sample was immediately frozen in liquid N_2 and hydrogenated. On warming to room temperature, the mixture was shaken and agitated for 10 minutes, and the light orange solution turned darker in colour. The sample was freeze-pump-thaw degassed three times and agitated for 30 minutes before being placed into the NMR spectrometer. $^{31}P\{^1H\}$ NMR spectroscopy of the NMR sample indicated that the mixture subsequently contained 25% [{Rh(DPEphos)}$_2$(H)(H$_2$BNMeH)][BAr$^F{}_4$] (**14**) and 75% [{Rh(DPEphos)}$_2${(H$_2$B)$_2$NMeH}][BAr$^F{}_4$] (**15**). 0.2 mL of a 1.0 M solution of $NMeH_2$ in THF (200.0 μmol) was added to the sample. $^{31}P\{^1H\}$ NMR spectroscopy of the NMR sample indicated that the mixture contained [Rh(DPEphos)(H)$_2$(NMeH$_2$)$_x$][BAr$^F{}_4$] (**17**) only. Attempts to crystallise this complex by filtration of the reaction mixture and layering with pentane (20.0 mL) were unsuccessful, however a small number of orange crystals ([Rh(κ^2-P,P-DPEphos)(NMeH$_2$)$_2$][BAr$^F{}_4$], **cis-18**) suitable for single crystal X-ray diffraction were obtained.

Selected spectroscopic data: **^{1}H NMR** (400 MHz, 1,2-$C_6H_4F_2$, 298 K): δ −9.61 (dddd, 1 H, $^2J_{PtransH}$ 182, $^2J_{PcisH}$ 24, $^1J_{RhH}$ 18, $^2J_{HH}$ 5, RhH trans to P), −16.61 (m, 1 H, RhH cis to P). **^{1}H{^{31}P} NMR** (400 MHz, 1,2-$C_6H_4F_2$, 298 K): δ −9.61 (dd, 1 H, $^1J_{RhH}$ 18, $^2J_{HH}$ 5, RhH trans to

DPEphos-PPh_2), −16.61 (d, br, 1 H, $^1J_{RhH}$ 15, RhH trans to $NMeH_2$ or DPEphos-O). **$^{31}P\{^1H\}$ NMR** (162 MHz, 1,2-$C_6H_4F_2$, 298 K): δ 52.2 (d, 1 P, $^1J_{RhP}$ 137), 23.8 (d, br, 1 P, $^1J_{RhP}$ 86).

*7.2.22 Synthesis of [Rh(DPEphos)(NMeH$_2$)$_x$][BAr$^F_4$] (x = 1 or 2, **18**)*

Route A: [Rh(DPEphos)(η^6-ortho-xylene)][BAr^F_4] (20.0 mg, 12.4 μmol) was dissolved in 1,2-$C_6H_4F_2$ (0.35 mL) in a J. Young NMR tube. 0.15 mL of a 1.0 M solution of $NMeH_2$ in THF (150.0 μmol) was added. The resulting orange solution was agitated and turned dark yellow. The sample was filtered into a J. Young crystallisation flask and layered with pentane (20.0 mL) to give an oily orange solid which was washed with pentane (20.0 mL) and dried under vacuum. Yield 3.0 mg (1.9 μmol, 15%).

Route B: [Rh(DPEphos)(NBD)][BAr^F_4] (**12**) (17.8 mg, 11.2 μmol) was dissolved in 1,2-$C_6H_4F_2$ (2.25 mL) in a J. Young flask. 0.25 mL of a 0.0892 M solution of $NMeH_2$ in THF (22.3 μmol) was added. The reaction mixture was immediately frozen in liquid N_2 and hydrogenated. On warming to room temperature, the mixture was shaken, and the light orange solution turned darker in colour. The hydrogen pressure was released under an argon atmosphere and 0.3 mL of the reaction mixture was removed from the flask and placed into a J. Young NMR tube. The sample was immediately placed into the NMR spectrometer. $^{31}P\{^1H\}$ NMR spectroscopy indicated that the mixture contained 74% [Rh(DPEphos)$(H)_2(NMeH_2)_2$][BAr^F_4] (**17**) and 26% [Rh(DPEphos)$(NMeH_2)_x$][BAr^F_4] (**18**). The NMR sample was freeze-pump-thaw degassed nine times and backfilled with argon at room temperature. $^{31}P\{^1H\}$ NMR spectroscopy of the fully degassed NMR sample indicated that the mixture contained 50% [Rh(DPEphos)$(H)_2(NMeH_2)_x$][BAr^F_4] (**17**) and 50% [Rh(DPEphos)$(NMeH_2)_x$][BAr^F_4] (**18**).

Route C: [Rh(DPEphos)(NBD)][BAr^F_4] (**12**) (35.0 mg, 21.9 μmol) and $H_3B{\cdot}NMeH_2$ (4.0 mg, 89.1 μmol) were dissolved in 1,2-$C_6H_4F_2$ (0.4 mL) in a high pressure J. Young NMR tube. The sample was immediately frozen in liquid N_2 and hydrogenated. On warming to room temperature, the mixture was shaken and agitated for 10 minutes, and the light orange solution turned darker in colour. The sample was freeze-pump-thaw degassed three times and agitated for 30 minutes before

being placed into the NMR spectrometer. $^{31}P\{^{1}H\}$ NMR spectroscopy of the NMR sample indicated that the mixture subsequently contained 25% [{Rh(DPEphos)}$_2$(H)(H_2BNMeH)][BAr^F_4] (**14**) and 75% [{Rh(DPEphos)}$_2${(H_2B)$_2$NMeH}][BAr^F_4] (**15**). 0.2 mL of a 1.0 M solution of $NMeH_2$ in THF (200.0 μmol) was added to the sample. $^{31}P\{^{1}H\}$ NMR spectroscopy of the NMR sample indicated that the mixture contained [Rh(DPEphos)$(H)_2(NMeH_2)_x$][BAr^F_4] (**17**) only. The sample was filtered into a J. Young crystallisation tube and layered with pentane (20.0 mL) to yield a small number of orange crystals ([Rh(κ^2-P,P-DPEphos)$(NMeH_2)_2$][BAr^F_4], **cis-18**) suitable for single crystal X-ray diffraction.

Selected spectroscopic data: **^{1}H NMR** (400 MHz, CD_2Cl_2, 298 K): δ 7.96 – 6.62 (m, 40 H, [BAr^F_4]$^-$-CH, aryl CH), 2.04 (br, 3.6 H, NCH_3), 1.75 (br, 2.2 H, NH). **^{31}P{^{1}H} NMR** (162 MHz, CD_2Cl_2, 298 K): δ 39.5 (d, $^1J_{RhP}$ 182). **^{31}P{^{1}H} NMR** (162 MHz, 1,2-$C_6H_4F_2$, 298 K): δ 39.7 (d, $^1J_{RhP}$ 180). **ESI-MS** (CH_2Cl_2, 60˚C, 4.5 kV): *m/z* 669.06 (calculated 669.07 for the [Rh(DPEphos)(N_2)]$^+$ fragment, showing the correct isotope pattern). Only the corresponding N_2 complex was found due to the presence of N_2 in the flow gas, as noted previously.[15]

7.3 Catalytic procedures

7.3.1 Dehydropolymerisation under open conditions

In a typical experiment (e.g. 0.223 M [$H_3B{\cdot}NMeH_2$], 0.2 mol% catalyst loading), $H_3B{\cdot}NMeH_2$ (50.0 mg, 1110.0 μmol) was suspended in 4.5 mL 1,2-$C_6H_4F_2$ in a two-neck Schlenk flask. Double the desired amount of the precatalyst was weighed into a separate flask and dissolved in 1.0 mL 1,2-$C_6H_4F_2$. The $H_3B{\cdot}NMeH_2$-containing flask was connected to an external mineral oil bubbler and the argon flow was controlled to achieve a rate of bubbling of approximately 2 bubbles s^{-1}. 0.5 mL of the precatalyst solution was added to the reaction mixture and the resultant solution was stirred for the desired reaction time at 400 rpm. 0.3 mL of the reaction mixture was removed for analysis by NMR spectroscopy. The remaining solution was decanted into 40.0 mL of rapidly stirring hexane to give an off-white suspension which was stirred for 5 minutes to allow polymer

precipitation, then isolated by filtration. The off-white solid $(H_2B{\cdot}NMeH)_n$ was dried under vacuum overnight. Isolated yields of $(H_2BNMeH)_n$ varied from 30% to 65%.

7.3.2 Dehydropolymerisation under hydrogen evolution measurement conditions

In a typical experiment (e.g. 0.223 M $[H_3B{\cdot}NMeH_2]$, 0.2 mol% catalyst loading), $H_3B{\cdot}NMeH_2$ (50.0 mg, 1110.0 μmol) was suspended in 4.5 mL 1,2-$C_6H_4F_2$ in a jacketed two-neck Schlenk flask connected to a recirculating cooler and the temperature set at 20°C. Double the desired amount of the precatalyst was weighed into a separate flask and dissolved in 1.0 mL 1,2-$C_6H_4F_2$. The $H_3B{\cdot}NMeH_2$-containing flask was sealed off from the argon supply and connected to a water-filled 100.0 mL gas burette. 0.5 mL of the precatalyst solution was added to the reaction mixture and the resultant solution was stirred at 400 rpm. The time taken per 1.0 mL of gas to evolve was recorded. Upon completion of gas evolution, 0.3 mL of the reaction mixture was removed for analysis by NMR spectroscopy. The remaining solution was decanted into 40.0 mL of rapidly stirring hexane to give an off-white suspension which was stirred for 5 minutes to allow polymer precipitation, then isolated by filtration. The off-white solid $(H_2B{\cdot}NMeH)_n$ was dried under vacuum overnight. Isolated yields of $(H_2BNMeH)_n$ varied from 30% to 60%.

7.3.3 Dehydropolymerisation under closed conditions

In a typical experiment (e.g. 0.223 M $[H_3B{\cdot}NMeH_2]$, 0.2 mol% catalyst loading), $H_3B{\cdot}NMeH_2$ (50.0 mg, 1110.0 μmol) was suspended in 4.5 mL 1,2-$C_6H_4F_2$ in a J. Young flask. Double the desired amount of the precatalyst was weighed into a separate flask and dissolved in 1.0 mL 1,2-$C_6H_4F_2$. 0.5 mL of the precatalyst solution was added to the reaction mixture and the flask was sealed and stirred for the desired reaction time at 400 rpm. 0.3 mL of the reaction mixture was removed for analysis by NMR spectroscopy. The remaining solution was decanted into 40.0 mL of rapidly stirring hexane to give an off-white suspension which was stirred for 5 minutes to allow polymer precipitation, then isolated by filtration. The off-white solid $(H_2B{\cdot}NMeH)_n$ was dried under vacuum overnight. Isolated yields of $(H_2BNMeH)_n$ varied from 20% to 45%.

7.3.4 Dehydropolymerisation in the presence of cyclohexene

$H_3B{\cdot}NMeH_2$ (50.0 mg, 1110 μmol) was suspended in 4.2 mL 1,2-$C_6H_4F_2$ in a two-neck Schlenk flask and cyclohexene (0.3 mL, 3000 mmol) was added. Double the desired amount of the precatalyst was weighed into a separate flask and dissolved in 1.0 mL 1,2-$C_6H_4F_2$. The $H_3B{\cdot}NMeH_2$-containing flask was connected to an external mineral oil bubbler and the argon flow was controlled to achieve a rate of bubbling of approximately 2 bubbles s^{-1}. 0.5 mL of the precatalyst solution was added to the reaction mixture and the resultant solution was stirred for the desired reaction time at 400 rpm. 0.3 mL of the reaction mixture was removed for analysis by NMR spectroscopy. The remaining solution was decanted into 40.0 mL of rapidly stirring hexane to give an off-white suspension which was stirred for 5 minutes to allow polymer precipitation, then isolated by filtration. The off-white solid $(H_2B{\cdot}NMeH)_n$ was dried under vacuum overnight. Isolated yield of $(H_2BNMeH)_n$ 18.0 mg (36%).

7.3.5 Dehydropolymerisation recycling experiments

Dehydropolymerisation was conducted as per standard gas evolution measurement conditions. After cessation of gas evolution, the reaction mixture was transferred by syringe into a second jacketed, two-neck Schlenk flask connected to a recirculating cooler at 20°C containing $H_3B{\cdot}NMeH_2$ (50.0 mg, 1110 μmol). Gas evolution was recorded by gas burette. After cessation of gas evolution, the reaction mixture was transferred by syringe into a third jacketed, two-neck Schlenk flask connected to a recirculating cooler at 20°C containing $H_3B{\cdot}NMeH_2$ (50.0 mg, 1110 μmol). Gas evolution was recorded by gas burette. After cessation of gas evolution, 0.3 mL of the reaction mixture was removed for analysis by NMR spectroscopy. The remaining solution was decanted into 40.0 mL of rapidly stirring hexane, stirred for 5 minutes to allow polymer precipitation, then isolated by filtration. The off-white solid $(H_2B{\cdot}NMeH)_n$ was dried under vacuum overnight. Isolated yield of $(H_2BNMeH)_n$ 80.0 mg (53%).

7.3.6 Molecular weight versus conversion procedure

For molecular weight versus conversion experiments, the general dehydropolymerisation procedure under open conditions was followed. At various time points, 5.0 equivalents (relative to precatalyst) of PPh_3 in 0.2 mL 1,2-$C_6H_4F_2$ was added to stop catalysis. Hexane (30.0 mL) was added to the reaction flask and the precipitate was isolated by filtration and dried under vacuum for 30 minutes. A sample was dissolved in THF and analysed by ^{11}B NMR spectroscopy to determine the percentage conversion calculated by integration of the relevant signals. Polyaminoborane samples were dried overnight prior to GPC analysis.

7.3.7 Tests for catalyst homogeneity: mercury poisoning

Dehydropolymerisation was conducted as per standard gas evolution measurement conditions. After a short time, an excess of elemental mercury (ca. 0.05 mL) was added. No inhibition of gas evolution was observed, consistent with homogeneous catalysis.

7.3.8 Tests for catalyst homogeneity: PPh_3 fractional poisoning

Dehydropolymerisation was conducted as per standard gas evolution measurement conditions. After a short time, 0.2 equivalents (relative to precatalyst) of PPh_3 in 0.2 mL 1,2-$C_6H_4F_2$ was added. A minor decrease in the rate of gas evolution was observed, consistent with homogeneous catalysis.

7.3.9 Dehydropolymerisation under THF, BH_3 or $NMeH_2$-doped conditions

$H_3B{\cdot}NMeH_2$ (50.0 mg, 1110.0 µmol) was suspended in 4.45 mL 1,2-$C_6H_4F_2$ in a jacketed two-neck Schlenk flask connected to a recirculating cooler and the temperature set at 20°C. Double the desired amount of the precatalyst was weighed into a separate flask and dissolved in 1.0 mL 1,2-$C_6H_4F_2$. The $H_3B{\cdot}NMeH_2$-containing flask was sealed off from the argon supply and connected to a water-filled 100.0 mL gas burette. 0.5 mL of the precatalyst solution was added to the reaction mixture and the resultant solution was stirred at 400 rpm. After 5 seconds, 1.0 equivalent (relative

to precatalyst) of the desired doping agent in 0.05 mL THF was added. The time taken per 1.0 mL of gas to evolve was recorded. Upon completion of gas evolution, 0.3 mL of the reaction mixture was removed for analysis by NMR spectroscopy. The remaining solution was decanted into 40.0 mL of rapidly stirring hexane to give an off-white suspension which was stirred for 5 minutes to allow polymer precipitation, then isolated by filtration. The off-white solid $(H_2B{\cdot}NMeH)_n$ was dried under vacuum overnight. Isolated yields of $(H_2BNMeH)_n$ varied from 25% to 50%.

7.4 Computational details

The computational work in Chapters 2 and 4 was carried out by Professor Stuart A. Macgregor and Dr Nicholas A. Beattie at Heriot-Watt University. The geometry optimisations of **8-[BAr$^{Cl}_4$]** and **15-[Al(O^{t}Bu^F)$_4$]** were run with Gaussian 03 Revision D.01[16] and performed using the BP86[17-18] functional. Rh and P centres were described with Stuttgart RECPs and associated basis sets,[19] with added d-orbital polarisation on P (ζ = 0.387)[20] and 6-31G** basis sets for C, H, O, B and N.[21-22] Stationary points were fully characterised via analytical frequency calculations as minima with all positive eigenvalues. Frequency calculations and NMR spectroscopy calculations were run using Gaussian 09 Revision D.01.[23] Atoms in Molecules[24] analyses were performed with the AIMALL program[25] using the same functional and basis sets described above. NBO calculations were run with NBO 6.0[26] using the same functional and basis sets described above.

7.5 X-ray crystallography

Structure determinations were carried out by Dr Heather C. Johnson (**1** and **2**), Dr Alasdair I. McKay (**5**, **6**, **8-[BAr$^{Cl}_4$]**, **9**, **10**, **15-[Al(O^{t}Bu^F)$_4$]** and **cis-18**) or Dr F. Mark Chadwick (**13**). The crystallographic data obtained are contained in the electronic appendix affixed to the inside back cover of this thesis. Crystallographic data were collected on a Nonius Kappa-CCD (**13**) or Agilent SuperNova diffractometer fitted with an Oxford CryoSystems CryoStream unit (**1**, **2**, **5**, **6**, **8-[BAr$^{Cl}_4$]**, **9**, **10**, **15-[Al(O^{t}Bu^F)$_4$]** and **cis-18**).[27] Raw frame data were reduced using CrysAlisPro, including unit cell determination and refinement, integration of intensities and associated

correction, or the DENZO-SMN package.[28] The structures were solved using direct methods with SIR92,[29] SuperFlip[30] or SHELXT[31] and refined using full-matrix least squares refinement on all F^2 data using the CRYSTALS program suite[32-33] (**1**, **2** and **13**) or using SHELXL[34] (**5**, **6**, **8-[BAr$^{Cl}_4$]**, **9**, **10**, **15-[Al(O^{t}Bu^F)$_4$]** and **cis-18**) using the interface OLEX2.[35] In certain cases some of the CF_3 groups in the $[BAr^F_4]^-$ anion refined to give highly prolate[36] displacement ellipsoids. For each structure a split site model was used and same distance restraints were applied to maintain a sensible geometry. Similarity and vibrational restraints were also used to ensure the displacement ellipsoids behaved as expected. In general, the hydrogen atoms were located in the difference Fourier maps and refined independently using soft restraints.[33] Hydrogen atoms were refined in this way at intervals following inclusion in the refinement using a riding model.

Hydrides on the rhodium and the boron atoms in **2** were placed in calculated positions and refined using a riding model. The $H_3B{\cdot}NMe_2H$ molecule in **5** displayed highly prolate ellipsoids. This was modelled as disorder over two sites. Hydrides on the rhodium and boron ligand atoms were located in the difference map and freely refined. Restraints to distances and displacement parameters were applied to maintain the expected geometry. In complex **6**, two ^{i}Pr substituents on a single phosphorus atom were found to be disordered. The disorder was modelled over two sites. A molecule of THF was located in the lattice which is disordered over a special position. Distance and displacement parameter restraints were applied to give the expected geometry. Single crystals of **8-[BAr$^{Cl}_4$]** repeatedly grow with two very small dimensions for an X-ray structure determination. A significant fall-off in diffraction intensity at relatively low Bragg angles was observed, nevertheless the refinement converged well and atom connectivity was unambiguous. The final Fourier difference map revealed notable peaks of electron density proximal to each rhodium atom and diametrically opposed across the atom at ca. 1.00 Å, these are of each of magnitude ca. 2.00 e Å^{-3}. In addition, positive residual densities (ca. 2.00 e Å^{-3}) on each of the heavy atom sites were observed. Twinning was investigated, but twin scale factors refine to zero for all sensible twin laws. The locations of the electron densities are such that a chemically sensible disorder model could not be generated. These are therefore attributed to Fourier truncation errors.

The atoms of one aryl group of the anion displayed prolate ellipsoids. This was treated by modelling the atoms over two sites and restraining their geometries and displacement parameters. The lattice of **8-[BAr$^{Cl}_4$]** contained a number of disordered solvent molecules; these were modelled with the aid of the DSR tool.[37] All hydrogen atoms were placed in calculated positions using a riding model. A molecule of pentane was located in the lattice for **9**, which was disordered over a special position. Distance and displacement parameter restraints were applied to give the expected geometry. For **13**, the dataset showed poor completeness (95%) out to $\theta = 23°$. Significant thermal motion of both the cation and $[BAr^F_4]^-$ anion was observed, which was modelled as disorder over two sites, and displacement parameter restraints were applied to give the expected geometry. The final model is poor (R_1 [$I > 2\sigma(I)$] = 0.1518) and the quality is such that it is suitable for demonstrating atom connectivity only.

In **15-[Al(O^{t}Bu^F)$_4$]**, highly disordered solvent molecules were found in the lattice that could not be identified or refined. Reflection contributions from these molecules were removed using the solvent mask function in OLEX2, which determined there to be 176 electrons in 738 Å^3 removed per unit cell. This was suspected to be three molecules of 1,2-$C_6H_4F_2$ based on the electron count, however, these were not included in the molecular formula. Thus all fields that derive from the molecular formula (e.g. F(000), calculated density) are known to be incorrect. The atoms of all the ^{t}Bu^F groups on the anion as well as the bridging NMeH group displayed highly prolate displacement ellipsoids. This was treated by modelling the atoms as disordered over two sites and restraining their geometries and displacement parameters. Hydrides on the rhodium and boron ligand atoms were located in the difference map and freely refined. A disordered molecule of toluene was located in the lattice of **cis-18** which was modelled over two sites. Distance and displacement parameter restraints were applied to give the expected geometry.

7.5.1 Crystallographic data

Complex	**1**	**2**	**5**
Chemical formula	$C_{66}H_{60}B_1F_{24}O_1P_2Rh_1$	$C_{62}H_{66}B_2F_{24}N_1O_1P_2Rh_1$	$C_{61}H_{64}B_2F_{24}N_1O_1P_2Rh_1$
Formula weight	1500.82	1483.64	1469.60
Temperature (K)	150	150	150
Crystal system	Monoclinic	Orthorhombic	Orthorhombic
Space group	$P2_1/c$	$Pca2_1$	$Pca2_1$
a (Å)	22.8626(2)	19.32780(10)	19.2876(2)
b (Å)	25.0729(2)	13.11580(10)	13.17180(10)
c (Å)	24.0283(2)	26.1296(2)	25.7831(2)
α (deg)	90	90	90
β (deg)	106.5796(9)	90	90
γ (deg)	90	90	90
V (Å^3)	13201.1(2)	6623.84(8)	6550.26(10)
Z	8	4	4
ρ (calcd) (g cm^{-1})	1.510	1.488	1.490
μ (mm^{-1})	3.535	3.514	3.548
Reflections collected	79001	80376	186830
Unique reflections	22184	6888	13644
Restraints/parameters	912/1823	285/894	890/1059
R_{int}	0.036	0.056	0.0836
R_1 [$I > 2\sigma(I)$]	0.0456	0.040	0.0591
wR_2 [$I > 2\sigma(I)$]	0.1117	0.1039	0.1590
GoF	0.9798	0.9794	1.027
Residual electron density (e Å^{-3})	1.49, −1.08	1.33, −0.70	2.02, −1.41
CCDC no.	1580255	1580253	N/A

Table 7.5.1 Crystallographic data for complexes **1**, **2** and **5**.

Complex	**6**	**8-[BAr$^{Cl}_4$]**	**9**
Chemical formula	$C_{62}H_{63}B_1F_{24}N_1O_{1.5}P_2Rh_1$	$C_{89}H_{92}B_2Cl_{10}O_2P_4Rh_2$	$C_{54.5}H_{58}B_1Cl_8O_2P_2Rh_1$
Formula weight	1477.79	1899.44	1204.27
Temperature (K)	150	150	150
Crystal system	Monoclinic	Triclinic	Triclinic
Space group	$P2_1/c$	$P\bar{1}$	$P\bar{1}$
a (Å)	14.4409(3)	14.1034(4)	12.4114(3)
b (Å)	18.6068(4)	14.4749(9)	13.7487(4)
c (Å)	24.1763(4)	23.9437(10)	17.1563(5)
α (deg)	90	82.527(4)	105.055(2)
β (deg)	90.062(2)	85.664(3)	100.615(2)
γ (deg)	90	83.694(3)	90.458(2)
V (Å^3)	6496.1(2)	4807.8(4)	2773.89(14)
Z	4	2	2
ρ (calcd) (g cm^{-1})	1.511	1.312	1.442
μ (mm^{-1})	3.590	6.293	6.890
Reflections collected	38858	46942	29390
Unique reflections	13113	18124	11457
Restraints/parameters	674/1075	575/1192	54/652
R_{int}	0.0370	0.0913	0.0608
R_1 [$I > 2\sigma(I)$]	0.0440	0.0787	0.0613
wR_2 [$I > 2\sigma(I)$]	0.1031	0.1904	0.1630
GoF	1.057	1.022	1.024
Residual electron density (e Å^{-3})	0.45, −1.17	2.34, −1.21	1.89, −1.03
CCDC no.	N/A	1580256	N/A

Table 7.5.2 Crystallographic data for complexes **6**, **8-[BAr$^{Cl}_4$]** and **9**.

Compound	**10**	**13**
Chemical formula	$C_{77}H_{67}B_1F_{24}O_1P_3Rh_1$	$C_{77}H_{64}B_2F_{24}N_1O_1P_2Rh_1$
Formula weight	1670.93	1661.79
Temperature (K)	150	150
Crystal system	Triclinic	Orthorhombic
Space group	*P*−1	*Pcab*
a (Å)	14.3481(3)	19.0784(3)
b (Å)	15.4366(4)	25.3142(3)
c (Å)	19.5398(5)	30.8853(6)
α (deg)	108.570(2)	90
β (deg)	111.362(2)	90
γ (deg)	96.035(2)	90
V (Å^3)	3698.80(17)	14916.2(4)
Z	2	8
ρ (calcd) (g cm^{-1})	1.500	1.480
μ (mm^{-1})	3.418	0.377
Reflections collected	40127	19168
Unique reflections	15310	10553
Restraints/parameters	306/1058	5084/1523
R_{int}	0.0238	0.043
R_1 [$I > 2\sigma(I)$]	0.0282	0.1518
wR_2 [$I > 2\sigma(I)$]	0.0729	0.2928
GoF	1.028	1.0368
Residual electron density (e Å^{-3})	0.56, −0.92	1.09, −1.19
CCDC no.	N/A	N/A

Table 7.5.3 Crystallographic data for complexes **10** and **13**.

Compound	**15-[Al(O^{t}Bu^F)$_4$]**	**cis-18**
Chemical formula	$C_{89}H_{64}Al_1B_2F_{36}N_1O_6P_4Rh_2$	$C_{86}H_{78}B_1F_{24}N_2O_2P_2Rh_1$
Formula weight	2305.71	1803.16
Temperature (K)	150	150
Crystal system	Triclinic	Triclinic
Space group	*P*−1	*P*−1
a (Å)	14.5138(2)	13.1588(5)
b (Å)	18.5644(3)	16.5371(6)
c (Å)	21.4620(3)	20.3822(7)
α (deg)	104.3850(10)	71.918(3)
β (deg)	102.6830(10)	76.956(3)
γ (deg)	107.5450(10)	88.653(3)
V (Å^3)	5062.15(13)	4102.3(3)
Z	2	2
ρ (calcd) (g cm^{-1})	1.513	1.460
μ (mm^{-1})	4.361	2.964
Reflections collected	59592	47803
Unique reflections	20898	16981
Restraints/parameters	2883/1761	613/1161
R_{int}	0.0478	0.0451
R_1 [$I > 2\sigma(I)$]	0.0549	0.0478
wR_2 [$I > 2\sigma(I)$]	0.1465	0.1204
GoF	1.026	1.027
Residual electron density (e Å^{-3})	1.66, −0.85	1.55, −0.59
CCDC no.	N/A	N/A

Table 7.5.4 Crystallographic data for complexes **15-[Al(O^{t}Bu^F)$_4$]** and **cis-18**.

7.6 References

1. Pangborn, A. B.; Giardello, M. A.; Grubbs, R. H.; Rosen, R. K.; Timmers, F. J., Safe and Convenient Procedure for Solvent Purification. *Organometallics* **1996,** *15* (5), 1518-1520.
2. Asensio, G.; Cuenca, A. B.; Esteruelas, M. A.; Medio-Simón, M.; Oliván, M.; Valencia, M., Osmium(III) Complexes with POP Pincer Ligands: Preparation from Commercially Available $OsCl_3 \cdot 3H_2O$ and Their X-ray Structures. *Inorg. Chem.* **2010,** *49* (19), 8665-8667.
3. Esteruelas, M. A.; Oliván, M.; Vélez, A., Xantphos-Type Complexes of Group 9: Rhodium versus Iridium. *Inorg. Chem.* **2013,** *52* (9), 5339-5349.
4. Buschmann, W. E.; Miller, J. S., Synthesis of $[M^{II}(NCMe)_6]^{2+}$ (M = V, Cr, Mn, Fe, Co, Ni) Salts of Tetra[3,5-bis(trifluoromethyl)phenyl]borate. *Inorg. Synth.* **2002,** *33*, 83-91.
5. Chaplin, A. B.; Weller, A. S., $[B(3,5\text{-}C_6H_3Cl_2)_4]^-$ as a Useful Anion for Organometallic Chemistry. *Eur. J. Inorg. Chem.* **2010,** *2010* (32), 5124-5128.
6. Johnson, H. C.; Robertson, A. P. M.; Chaplin, A. B.; Sewell, L. J.; Thompson, A. L.; Haddow, M. F.; Manners, I.; Weller, A. S., Catching the First Oligomerization Event in the Catalytic Formation of Polyaminoboranes: $H_3B \cdot NMeHBH_2 \cdot NMeH_2$ Bound to Iridium. *J. Am. Chem. Soc.* **2011,** *133* (29), 11076-11079.
7. Inoue, M.; Kodama, G., The Preparation and Some Properties of Dihydridobis(monomethylamine)- and Dihydridobis(dimethylamine)boron(III) Tetrahydridoborate(III). *Inorg. Chem.* **1968,** *7* (3), 430-433.

8. Colebatch, A. L.; Hawkey Gilder, B. W.; Whittell, G. R.; Oldroyd, N. L.; Manners, I.; Weller, A. S., A General, Rhodium-Catalyzed, Synthesis of Deuterated Boranes and N-Methyl Polyaminoboranes. *Chem. Eur. J.* **2018,** *24* (21), 5450-5455.
9. Moxham, G. L.; Randell-Sly, H. E.; Brayshaw, S. K.; Woodward, R. L.; Weller, A. S.; Willis, M. C., A Second-Generation Catalyst for Intermolecular Hydroacylation of Alkenes and Alkynes Using β-S-Substituted Aldehydes: The Role of a Hemilabile P-O-P Ligand. *Angew. Chem. Int. Ed.* **2006,** *45* (45), 7618-7622.
10. Hooper, J. F.; Chaplin, A. B.; González-Rodríguez, C.; Thompson, A. L.; Weller, A. S.; Willis, M. C., Aryl Methyl Sulfides as Substrates for Rhodium-Catalyzed Alkyne Carbothiolation: Arene Functionalization with Activating Group Recycling. *J. Am. Chem. Soc.* **2012,** *134* (6), 2906-2909.
11. Guzel, B.; Omary, M. A.; Fackler Jr., J. P.; Akgerman, A., Synthesis and characterization of {[(COD)Rh(bis-(2R,3R)-2,5-diethylphospholanobenzene)]$^+$BARF$^-$} for use in homogeneous catalysis in supercritical carbon dioxide. *Inorg. Chim. Acta* **2001,** *325* (1), 45-50.
12. Colebatch, A. L.; McKay, A. I.; Beattie, N. A.; Macgregor, S. A.; Weller, A. S., Fluoroarene Complexes with Small Bite Angle Bisphosphines: Routes to Amine-Borane and Aminoborylene Complexes. *Eur. J. Inorg. Chem.* **2017,** *2017* (38-39), 4533-4540.
13. Dallanegra, R. Cationic Rhodium Complexes with Chelating Phosphine and Phosphine Alkene Ligands. Application in Dehydrogenation and Dehydrocoupling Reactions. University of Oxford, Oxford, 2011.
14. Kumar, A.; Beattie, N. A.; Pike, S. D.; Macgregor, S. A.; Weller, A. S., The Simplest Amino-Borane $H_2B{=}NH_2$ Trapped on a Rhodium Dimer: Pre-Catalysts for Amine-Borane Dehydropolymerization. *Angew. Chem. Int. Ed.* **2016,** *55* (23), 6651-6656.
15. Adams, G. M.; Chadwick, F. M.; Pike, S. D.; Weller, A. S., A CH_2Cl_2 complex of a [Rh(pincer)]$^+$ cation. *Dalton Trans.* **2015,** *44* (14), 6340-6342.
16. Frisch, M. J.; Trucks, G. W.; Schlegel, H. B.; Scuseria, G. E.; Robb, M. A.; Cheeseman, J. R.; Montgomery, J., J. A.; Vreven, T.; Kudin, K. N.; Burant, J. C.; Millam, J. M.; Iyengar, S. S.; Tomasi, J.; Barone, V.; Mennucci, B.; Cossi, M.; Scalmani, G.; Rega, N.; Petersson, G. A.; Nakatsuji, H.; Hada, M.; Ehara, M.; Toyota, K.; Fukuda, R.; Hasegawa, J.; Ishida, M.; Nakajima, T.; Honda, Y.; Kitao, O.; Nakai, H.; Klene, M.; Li, X.; Knox, J. E.; Hratchian, H. P.; Cross, J. B.; Bakken, V.; Adamo, C.; Jaramillo, J.; Gomperts, R.; Stratmann, R. E.; Yazyev, O.; Austin, A. J.; Cammi, R.; Pomelli, C.; Ochterski, J. W.; Ayala, P. Y.; Morokuma, K.; Voth, G. A.; Salvador, P.; Dannenberg, J. J.; Zakrzewski, V. G.; Dapprich, S.; Daniels, A. D.; Strain, M. C.; Farkas, O.; Malick, D. K.; Rabuck, A. D.; Raghavachari, K.; Foresman, J. B.; Ortiz, J. V.; Cui, Q.; Baboul, A. G.; Clifford, S.; Cioslowski, J.; Stefanov, B. B.; Liu, G.; Liashenko, A.; Piskorz, P.; Komaromi, I.; Martin, R. L.; Fox, D. J.; Keith, T.; Al-Laham, M. A.; Peng, C. Y.; Nanayakkara, A.; Challacombe, M.; Gill, P. M. W.; Johnson, B.; Chen, W.; Wong, M. W.; Gonzalez, C.; Pople, J. A. *Gaussian 03, Revision D.01*, Gaussian, Inc.: Wallingford CT, 2004.
17. Becke, A. D., Density-functional exchange-energy approximation with correct asymptotic behavior. *Phys. Rev. A* **1988,** *38* (6), 3098-3100.
18. Perdew, J. P., Density-functional approximation for the correlation energy of the inhomogeneous electron gas. *Phys. Rev. B* **1986,** *33* (12), 8822-8824.
19. Andrae, D.; Häußermann, U.; Dolg, M.; Stoll, H.; Preuß, H., Energy-adjusted *ab initio* pseudopotentials for the second and third row transition elements. *Theor. Chim. Acta* **1990,** *77* (2), 123-141.
20. Höllwarth, A.; Böhme, M.; Dapprich, S.; Ehlers, A. W.; Gobbi, A.; Jonas, V.; Köhler, K. F.; Stegmann, R.; Veldkamp, A.; Frenking, G., A set of d-polarization functions for pseudo-potential basis sets of the main group elements Al–Bi and f-type polarization functions for Zn, Cd, Hg. *Chem. Phys. Lett.* **1993,** *208* (3), 237-240.
21. Hehre, W. J.; Ditchfield, R.; Pople, J. A., Self-Consistent Molecular Orbital Methods. XII. Further Extensions of Gaussian-Type Basis Sets for Use in Molecular Orbital Studies of Organic Molecules. *J. Chem. Phys.* **1972,** *56* (5), 2257-2261.
22. Hariharan, P. C.; Pople, J. A., The Influence of Polarization Functions on Molecular Orbital Hydrogenation Energies. *Theor. Chim. Acta* **1973,** *28* (3), 213-222.
23. Frisch, M. J.; Trucks, G. W.; Schlegel, H. B.; Scuseria, G. E.; Robb, M. A.; Cheeseman, J. R.; Scalmani, G.; Barone, V.; Petersson, G. A.; Nakatsuji, H.; Li, X.; Caricato, M.; Marenich, A.; Bloino, J.; Janesko, B. G.; Gomperts, R.; Mennucci, B.; Hratchian, H. P.; Ortiz, J. V.; Izmaylov, A. F.; Sonnenberg, J. L.; Williams-Young, D.; Ding, F.; Lipparini, F.; Egidi, F.; Goings, J.; Peng, B.; Petrone, A.; Henderson, T.; Ranasinghe, D.; Zakrzewski, V. G.; Gao, J.; Rega, N.; Zheng, G.; Liang, W.; Hada, M.; Ehara, M.; Toyota, K.; Fukuda, R.; Hasegawa, J.; Ishida, M.; Nakajima, T.; Honda, Y.; Kitao, O.; Nakai, H.; Vreven, T.; Throssell, K.; Montgomery, J., J. A. ; Peralta, J. E.; Ogliaro, F.; Bearpark, M.; Heyd, J. J.; Brothers, E.; Kudin, K. N.; Staroverov, V. N.; Keith, T.; Kobayashi, R.; Normand, J.; Raghavachari, K.; Rendell, A.; Burant, J. C.; Iyengar, S. S.; Tomasi, J.; Cossi, M.; Millam, J. M.; Klene, M.; Adamo, C.; Cammi, R.;

Ochterski, J. W.; Martin, R. L.; Morokuma, K.; Farkas, O.; Foresman, J. B.; Fox, D. J. *Gaussian 09, Revision D.01*, Gaussian, Inc.: Wallingford CT, 2009.
24. Bader, R. F. W., *Atoms in Molecules - A Quantum Theory*. Oxford University Press: Oxford, 1990.
25. Keith, T. A. *AIMAII (Version 13.02.26, Professional)*, TK Gristmill Software (aim.tkgristmill.com): Overland Park KS, USA, 2015.
26. Glendening, E. D.; Badenhoop, J. K.; Reed, A. E.; Carpenter, J. E.; Bohmann, J. A.; Morales, C. M.; Landis, C. R.; Weinhold, F. *NBO 6.0*, Theoretical Chemistry Institute, University of Wisconsin, Madison (nbo6.chem.wisc.edu): Madison, WI, 2013.
27. Cosier, J.; Glazer, A. M., A nitrogen-gas-stream cryostat for general X-ray diffraction studies. *J. Appl. Crystallogr.* **1986,** *19* (2), 105-107.
28. Otwinowski, Z.; Minor, W., [20] Processing of X-ray diffraction data collected in oscillation mode. In *Methods in Enzymology*, Academic Press: 1997; Vol. 276, pp 307-326.
29. Altomare, A.; Cascarano, G.; Giacovazzo, C.; Guagliardi, A.; Burla, M. C.; Polidori, G.; Camalli, M., SIR92 - a program for automatic solution of crystal structures by direct methods. *J. Appl. Crystallogr.* **1994,** *27* (3), 435.
30. Palatinus, L.; Chapuis, G., SUPERFLIP - a computer program for the solution of crystal structures by charge flipping in arbitrary dimensions. *J. Appl. Crystallogr.* **2007,** *40* (4), 786-790.
31. Sheldrick, G., SHELXT - Integrated space-group and crystal-structure determination. *Acta Cryst. A* **2015,** *71* (1), 3-8.
32. Betteridge, P. W.; Carruthers, J. R.; Cooper, R. I.; Prout, K.; Watkin, D. J., CRYSTALS version 12: software for guided crystal structure analysis. *J. Appl. Crystallogr.* **2003,** *36* (6), 1487.
33. Cooper, R. I.; Thompson, A. L.; Watkin, D. J., CRYSTALS enhancements: dealing with hydrogen atoms in refinement. *J. Appl. Crystallogr.* **2010,** *43* (5), 1100-1107.
34. Sheldrick, G., Crystal structure refinement with SHELXL. *Acta Cryst. C* **2015,** *71* (1), 3-8.
35. Dolomanov, O. V.; Bourhis, L. J.; Gildea, R. J.; Howard, J. A. K.; Puschmann, H., OLEX2: a complete structure solution, refinement and analysis program. *J. Appl. Crystallogr.* **2009,** *42* (2), 339-341.
36. Guzei, I. A.; Wendt, M., An improved method for the computation of ligand steric effects based on solid angles. *Dalton Trans.* **2006,** (33), 3991-3999.
37. Kratzert, D.; Holstein, J. J.; Krossing, I., DSR: enhanced modelling and refinement of disordered structures with SHELXL. *J. Appl. Crystallogr.* **2015,** *48* (3), 933-938.